Analytical Application of
Charged Particle Induced Prompt
Photon Emission

A thesis submitted for the
Degree of Doctor of Philosophy

Brendan O'Connell, B.Sc. M.Sc.
Department of Physics
University of Aston in Birmingham
Gosta Green
Birmingham

June, 1976

ABSTRACT

The development of suitable instrumentation and data acquisition systems for prompt nuclear microanalysis are presented. The reaction $F^{19}(p,\alpha\gamma)O^{16}$ has been used to determine the fluorine concentration in samples of microcracked chromium plate, using the charged particle beams of the 0.5 MV Aston Van de Graaff and the 3 MV Birmingham Radiation Centre Dynamitron.

Disadvantages associated with the use of molecular hydrogen ion beams and the intrinsic variables of prompt nuclear analysis are considered in detail.

The complementary techniques of convolution and deconvolution for the determination of concentration profiles from experimental data are compared and contrasted.

The inherent difficulty of obtaining precise analytical information from charged particle induced resonance reaction data is established.

ACKNOWLEDGMENT

I would like to thank Dr.D.Crumpton for supervising this project and the University of Aston in Birmingham for providing a research studentship.

I wish to acknowledge the assistance of H.Arrowsmith, F.Lane and the Technical Staff of the main workshop, J.Phull, H.Biggs of the Aston Nuclear Physics Laboratory, the Staff of the Aston University Computer Centre, J.Litherland, M.Stillman and the Staff of the Birmingham Radiation Centre.

I am particularly grateful to R.Bassett for many helpful discussions on all aspects of the work, Dr.L.Hazlewood for guidance on numerical analysis and Mrs.D.Hill for typing the manuscript.

I would also like to acknowledge the contribution of my Collaborator ICL 1904S.

TABLE OF CONTENTS

Chapter I

Prompt Nuclear Analysis

Prompt Nuclear Analysis

The study of physical and chemical phenomena taking place near the surface of solids requires the quantitative determination and localization in depth of very small isotopic or elemental concentrations. Such studies are fundamental to all fields where surface phenomena are of interest. Conventional analytical techniques are not always suitable especially when high sensitivity and good depth resolution are required.

Activation analysis has been established as an analytical technique for over thirty years and has been the subject of intense investigation [LUTZ et al. (1968) contains over 4,000 references to activation measurements by neutrons, gamma-rays and charged particles]. In the past decade considerable interest has been shown in the technique of prompt nuclear analysis.

Prompt nuclear analysis may be defined as a method which uses the prompt radiation accompanying a nuclear reaction for determining isotopic or elemental concentrations. Such radiation is produced in a time which is characteristically 10^{-14} seconds, or less, and this provides a distinction from activation analysis which relies on radioactive decay occurring on a longer time scale and is therefore restricted to reactions which yield radioactive product nuclei of suitable half-life. The number of possible reactions which may be employed in prompt analysis is considerable. The requirements of analytical work, however, such as sensitivity and selectivity, favour the use of the simpler and more prolific reactions.

The techniques of analysis may be classified according to the type of incident and emergent radiation used. Most applications involve the use of charged particles as the incident beam, but neutrons and gamma-rays have important advantages for some applications. For each type of incident beam it is possible to measure scattered particles or reaction products which again may be charged particles, neutrons or gamma-rays.

The principle of elastic charged particle scattering as applied to analysis has been described by RUBIN(1963) in some detail and more recently in reviews by MACKINTOSH and DAVIES (1969), KRIVAN (1972), NICOLET et al.(1972) and PIERCE (1971). In elastic scattering it is difficult to differentiate between particles scattered from a light nuclide near the surface of the sample and those scattered from a heavier nuclide deeper within the sample. Application of this technique to the analysis of complex samples therefore requires careful consideration of the number of different cases for which useful information can be obtained. The method is most usefully applied to the determination of a thin film of a heavy element present on a lighter substrate. COHEN and MOYER (1971) have obtained sensitivities of 1 ppm (under favourable conditions 1 ppb) in the analysis of thin-film impurities. Depth distributions may be obtained by comparison of observed and calculated spectra or by deconvolution of the observed spectrum, GYULAI et al. (1971), POATE et al.(1973), NICOLET et al.(1972), SIPPEL (1959) ZEIGLER and BAGLIN (1971), ECONOMOU et al. (1973), HABANEC et al.(1973), WILLIAMS (1975). Typical examples of the measurement of depth distributions are the diffusion of gold in copper, SIPPEL (1959), in which a depth resolution of 6.5 nm was achieved and the study of arsenic impurities in silicon, ZEIGLER and BAGLIN (1971), with a depth resolution of ∿ 200 Å. A compact analytical instrument based on the elastic scattering of alpha-particles from a curium-242 source was used for instrumental lunar missions, PATTERSON et al. (1965) and subsequently operated successfully on the moon's surface, TURKEVITCH et al. (1968).

Nuclear reactions involving charged particles as both incident and emergent radiation offer a wide range of possibilities. Because of the variety of reactions available analytical work usually concentrates on establishing conditions in which a reaction provides a specific measurement for one nuclide. The most frequently used reactions are (p,α), (d,p) and (d,α). Heavy-ion reactions are the subject of much current research but because of the higher energies that are usually required and the greater complexity of these reactions, they have been used less frequently for analytical purposes. The cross-section for the reaction $O^{17}(He^{3},\alpha)O^{18}$ is approximately constant for incident energies close to 5 MeV and the reaction has been used to determine oxygen-17 to depths of 6 μm with a resolution of 0.1 μm, OLLERHEAD et al.(1966),COX and ROY (1966). Carbon and oxygen-16 have been determined in various metals and oxides by SANDERS et al. (1972) with a sensitivity of 1 ppm using the (He^{3},p) reaction. The development of heavy ion techniques has made possible sensitive methods for detecting hydrogen by means of the reaction $H^{1}(Li^{7}, p\gamma)Be^{8}$, PADAWER and SCHNEID (1969), LEICH and TOMBRELLO (1973) and LEA et al. (1974) have made use of the reaction $H^{1}(F^{19},\alpha\gamma)O^{16}$ to study the distribution of hydrogen implanted by solar winds in lunar soil and rock, at depths from 20 to 40 μm with a resolution of 0.02 μm.

Extensive use has been made of the (p,α) reaction for the study of oxygen -18, AMSEL and SAMUEL (1967), AMSEL et al. (1969) GASS et al. (1973), NEILD et al. (1972), AMSEL et al. (1971) CALVERT et al. (1972), CHERKI and SIEJKA (1973), LINDSTROM and HEUER (1974). Although the Q-valves for (p,α) reactions on lithium-6, lithim-7. boron-11 nitrogen-15 and fluorine-19 are higher than for oxygen-18 there has been less interest in the analysis of these isotopes, PRETORIUS (1972), PRETORIUS and COETZEE (1972), MONNIER et al. (1972), AMSEL et al. (1971). Typical sensitivities for (p,α) reactions are 1 ppm, or less, with a depth resolution of the order of 20 nm. For the oxygen-18 reaction a spatial resolution of 50 μm has been achieved, PRICE and BIRD (1969), MAK et al. (1966). The use of special focussing techniques can provide a beam as small as 3 μm for use in surface scans [COOKSEN et al. (1972)].

Deuterons with energies below 1 MeV are particularly suitable for studying carbon, nitrogen and oxygen. Experimental conditions can be optimized so that these nuclides may be studied with either (d,p) or (d,α) reactions. Other product particles may also be present and this has been used to advantage in a coincidence technique for the study of lithium [PRETOREUS (1972)]. For deuteron energies from 1 MeV to 2 MeV the Coulomb barrier limits reactions with appreciable yields to light nuclei, but as the incident deuteron energy is increased more reactions are observed. Estimation of oxygen-16 in thickness layers of 2 nm has been been made using this reaction AMSEL et al. (1969). Oxygen has been the favourite nuclide studied by means of deuteron induced reactions but the detection of sulphur [WOLICKI and KNUDSON (1967)], silicon, [AMSEL et al. (1969) , CACHARD et al. (1971) , QUAGLIA et al. (1971)], carbon, [PIERCE et al. (1974)] and metals from calcium to strontium [OLIVER and PEISACH (1972)] indicate the general sensitivity of the reaction for many light and medium weight nuclei. PRONKO and PRONKO (1974) have recently used the reaction $He^{3}(d,p)^{4}He$ to study the depth profile of hydrogen and helium isotopes implanted in niobium.

The major advantage of analytical techniques based on the detection of prompt particulate reaction products is that by suitable choice of experimental conditions particle groups can occur in a region of the spectrum where there is a very low background, and hence the sensitivity of the measurement is high.

Prompt gamma emission accompanies most nuclear reactions and gamma-ray energies are often quite high. Because of the occurrence of resonances in many reaction cross-sections, it is possible to select a type and energy of incident particle which will favour one reaction and minimize others so as to reduce difficulties in interpreting the observed gamma-ray spectra. Gamma-ray detection has been one of the most common methods of nuclear analysis and almost all isotopes upto calcium and a number of medium and heavy isotopes have been studied by this method [SHABASON and COHEN (1973)].

Most analytical applications have made use of sodium-iodide detectors, particularly for the study of light nuclei. The limited energy resolution is more than offset by the high detection efficiency and large solid angles attainable using large crystals which provide a very sensitive method of detecting nuclear reactions. Several workers have determined fluorine by the reaction $F^{19}(p,\alpha\gamma)O^{16}$ counting the 6-7 MeV gamma-rays, B EWERS and FLACK (1969), PADAWER (1970), MÖLLER and STARFELT (1967), PORTE et al. (1973), THOMAS and GREA (1975). A sensitivity of $0.01\ \mu g.cm^{-2}$ has been demonstrated for the detection of fluorine by this method . GOLICHEFF et al. (1972) have investigated the use of prompt gamma-ray detection for the study of the elements, lithium, boron, carbon, nitrogen, oxygen and fluorine.

The improved resolution of Ge(Li) detectors, provides a more reliable allocation of each gamma-ray to a particular reaction. This increases the versatility of the method as it is possible to analyse for several nuclides at once, COOTE et al. (1972), SHABASON and COHEN (1973), DECONNINECK (1972), MACEY and GILBOYS (1971). Using the reaction C^{12} $(p,\gamma)N^{13}$, LORENZEN (1974) has reported carbon concentration profiles in steel to depths of 20 μm with a depth resolution between 0.26 μm and 1.7 μm and a sensitivity of 0.1 per cent. A sensitivity of 0.3 pg has been reported by ANTILLA and KEINONEN (1973), and 1 ppb by FIARMAN and SCHNEIDER (1972) for the detection of a number of light elements in evaporated solutions. The major disadvantage in the use of Ge(Li) detectors in analytical work is their low detection efficiency and small size which limits the sensitivity that can be achieved.

For reactions which exhibit narrow resonances in the reaction cross-section it is necessary to perform a series of measurements for different incident particle energies to obtain a depth profile. When analysis is based on the detection of prompt gamma-rays a knowledge of the stopping-power of the target medium for the incident beam is required to establish an absolute depth scale. Beam induced deposition of contaminants on the target surface is a serious problem as it is not possible to use the energy of emergent radiation as an additional parameter to determine the depth at which a reaction occurs. It is also possible for gamma-rays to reach the detector from surfaces within the vacuum system such as slits or apertures which are struck by the incident beam. The sensitivity of analysis based on the detection of prompt gamma radiation is ultimately limited by background radiation.

Neutron producing reactions have also been used in analytical work. Neutron counting has been applied to (α,n) reactions for the detection of elements upto sodium using radioactive nuclides as the source of alpha-particles, [ADLOF et al. (1966)]. The (d,n) reaction has been used to study deuterium in surface layers of corroded zirconium at depths to 20 μm with a sensitivity of 5 ppm [BUTLER (1965)] The presence of competing nuclei introduces a major limitation to reactions of this type although reliability is greatly improved if neutron energies are also measured. The (d,n) reaction has been used by MÖLLER et al. (1967), together with time of flight techniques, to determine carbon, oxygen and nitrogen in steel samples with a sensitivity of 0.1 $\mu g.cm^{-2}$ and a depth resolution of 0.45 μm.

Neutron or photon induced reactions are most suitable for the analysis of bulk material. Because of their high penetrating power these radiations can initiate reactions over a relatively large sample volume and provide information on the average or bulk concentration of a particular nuclide. Charged particle techniques in contrast exploit low penetration to provide specific analytical information from a very limited thickness of sample.

Neutron induced charged particle production can be employed for depth analysis of surface layers. The large thermal cross-section for (n,α) reactions in lithium-6 and boron-10 have been exploited to measure concentration profiles of these nuclides. ZIEGLER et al. (1972) determined boron in aluminium using this reaction with a depth resolution of 20 nm and a sensitivity of 3 ppm.

Prompt analysis employing charged particles as incident or emergent radiation has, in general, the following characteristics. Analysis is restricted to the first few microns of the sample unless high energy incident beams are available. Natural background is low or non-existent. High positive Q-values are frequently encountered and low energy particles lead to high yields for low Z nuclei. At low incident particle energies medium and high Z nuclei have small cross-sections for charged particle induced reactions permitting traces of low Z nuclei to be detected in heavier substrates. Nuclear reactions are specific and isotopes of the same element behave quite differently. The results are generally independent of the matrix in which the observed nucleus is embedded as the reaction depends only on the nuclear cross-section. The physical or chemical state of the target is unimportant provided the sample remains stable under bombardment. The method is quantitative, a precision of one per cent is easily achieved, and in general, is non-destructive. The sensitivity of the method can be high; 10^{-12}g of matter may be determined in favourable cases, and concentration profiles can be obtained. The most serious limitation of the method is that only reasonably uniform samples may be examined as the lateral resolution is poor.

The technique of prompt nuclear analysis has been applied by the author to the determination of fluorine on and below the surface of microcracked chromium plate. Bright chromium electro deposits may be obtained by the electrolysis of solutions containing chromic and sulphuric acids, using an insoluble lead anode. The addition of fluorosilicates to the plating solution results in a microcracked deposit. The mechanism of the electrodeposition of microcracked chromium is not fully established, although it is known that the deposit is highly stressed, relief occurring through microcracking [DENNIS (1965)]. The role of fluorine in the production of microcracked chromium is at present being investigated in the Department of Metallurgy of the University of Aston in Birmingham. It is thus of interest to determine the amount of fluorine on the surface and its possible depth penetration. Analysis by means of the nuclear reaction $F^{19}(p,\alpha\gamma)O^{16}$ is a sensitive method by which such information can be obtained. A number of samples of microcracked chromium have been investigated to establish if a correlation exists between fluorine concentration and plating conditions. Sample homogeneity has been studied by repeated surface scans with a lateral resolution of 2 mm. Fluorine depth concentration profiles have been determined from measured counting rates by application of the technique of deconvolution. Formulae have been derived for the observed yield curve from samples of uniform concentration and for the intrinsic sensitivity of detection of a given element in a given matrix. The extrinsic sensitivity has been estimated for the detection of fluorine, lithium and aluminium.

The use of charged particles as incident or emergent radiation requires an accurate knowledge of stopping-power and range data. The status of modern stopping-power theory has been considered and selected data compared for a series of nine target media covering a wide spectrum of the periodic table.

Molecular hydrogen-ion beams have found use in the calibration of accelerators [PARKINSON and BARDWICK (1970)] and in extending the range of effective proton energies available. It is shown that possible advantages resulting from the use of molecular hydrogen-ion beams are gained at the expense of energy homogeneity. Difficulties associated with the use of molecular hydrogen-ion beams in nuclear microanalysis and the effect of beam energy dispersion have been considered.

Chapter II

Instrumentation

Instrumentation on the Aston Van de Graaff

The air insulated electrostatic generator was originally constructed in 1933 to Van de Graaffs' specifications. In the early 1950's it was used to supply the high voltage for an accelerator designed and built at the Associated Electrical Industries Research Laboratory at Aldermaston, Berkshire. The accelerator and generator were installed in the Physics Department of the University of Aston in 1963. The machine has a nominal maximum terminal voltage of 0.5 MV and can deliver a proton current of 40 μA. A full description of the accelerator, its installation and calibration has been given by CRUMPTON (1967).

The mixed-mass positive ion beam from the accelerator, obtained by applying an extractor potential to a THONEMANN (1948) radio-frequency ion-source, was mass analysed by a 90° magnetic deflector. The terminal potential was measured by a generating voltmeter and stabilized in the conventional manner by monitoring the current on the exit-slits of the mass-analyser. In practice the beam was found to sweep the exit-slits in an irregular manner making it difficult to determine the setting of the generating voltmeter. The main factors contributing to machine instability were beam profile distortion introduced by the mass-analysis and corona discharge from the accelerator resistor chain and generator belt. The transmitted beam was found to emerge from the analyser at a downward angle of approximately 4° to the horizontal. Re-design to correct these aberrations was not considered to be practical. The magnetic-deflector and beam transport system were fitted with gate-valves to allow the system to be maintained under vacuum when not in use and permit rapid changes of target during experiments.

The target assembly is illustrated in Figure 1 and Plate 1. The design allowed the detector to be placed close to the target for maximum efficiency and as far from the magnetic-analyser and diffusion-pump heaters as possible to minimise their effect on the photomultiplier. The target holder formed a Faraday-cup to trap secondary electrons emitted from the target. A liquid nitrogen trap was situated close to the target to reduce the hydrocarbon vapour pressure in the vicinity of the target and minimise carbon build-up.

The gamma-ray spectra were measured using a 10.16 cm x 10.16 cm NaI(Tl) scintillation-crystal, optically coupled to an eleven-stage E.M.I. photomuliplier tube number 9030B, employing a 12.7 cm diameter photocathode and a venetian blind dynode structure. A mu-metal shield was used to minimise the effect of magnetic fields. The counting assembly was initially used by VILLAITHONG (1972) with a standard dynode chain employing all eleven stages and operated at 1100 volts. The system was found to introduce spectral distortion and to exhibit a non-linear response for gamma-rays of energy greater than 2.5 MeV as a result of space charge limitations.

In the modified system only nine stages of the photomultiplier were used in conjunction with a non-linear chain operated at 940 volts, with the cathode earthed, the first stage zener stabilized, and capacitative decoupling of the last four diodes. Stages ten and eleven were connected directly to the anode. COATES (1973) has shown that shorting the later stages of the photomultiplier to the anode produces a negligible change in the electrical characteristics of the tube.

TARGET ASSEMBLY

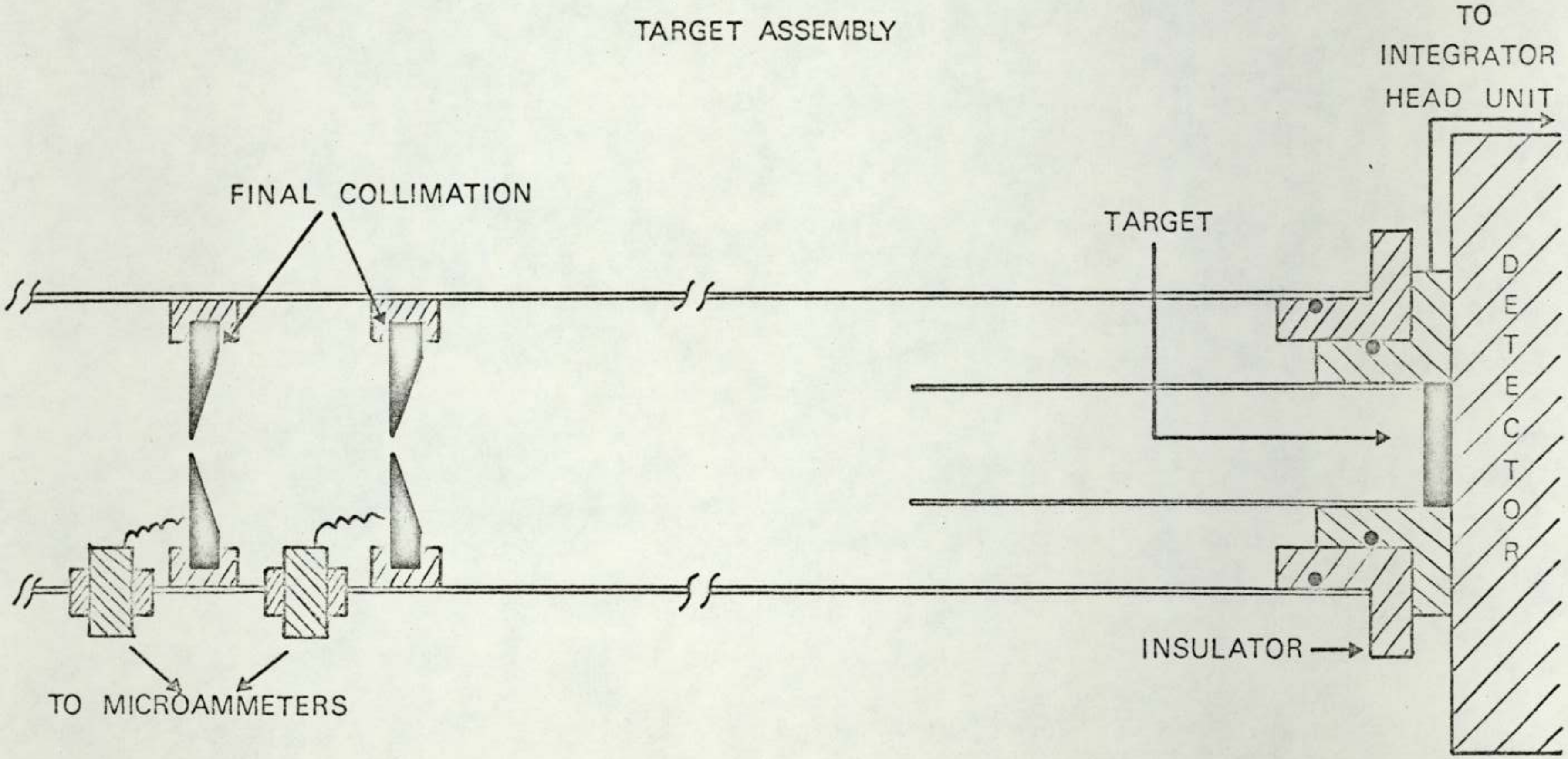

Figure 1

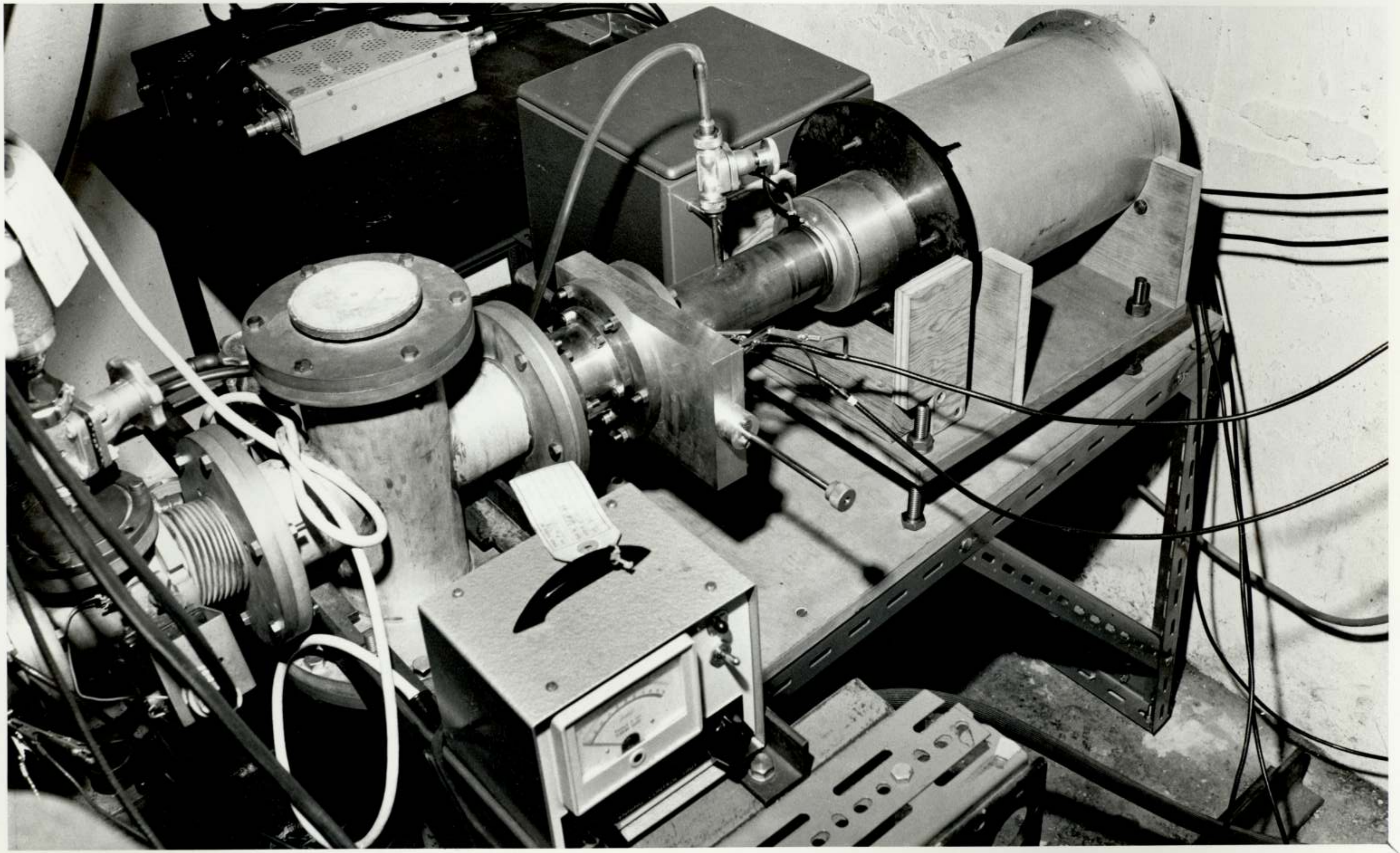

Plate 1

The preamplifier was based on the Nuclear Enterprises Model NE 5285. Plate 2 shows the pulse-height spectrum for gamma-rays from the $F^{19}(p,\alpha\gamma)O^{16}$ reaction at 340 keV before and after dynode and preamplifier modifications.

A block diagram of the data-acquisition system is shown in Figure 2. It is essentially a standard scintillation spectrometer and the operation of all units was controlled by monitoring the target current.

The beam current was measured by means of an AERE Harwell unit type 3008, comprising head-unit type 1679A and control unit type 2040A. This equipment integrates beam currents in the range 10^{-10} to 10^{-4}A. The beam current is integrated over a period to obtain the total quantity of charge delivered to the target with an absolute accuracy of 3 per cent. After each charge integration constituting between 10^{-5} and 10^{-9} coulombs a cycle-pulse is generated and converted in the control unit to an earthing contact which closes for 100 milli-seconds. The integrator was calibrated by connecting a precision low current source, O'CONNELL (1971), to the target assembly and counting the number of integrator cycle-pulses recorded in a known time. Calibration was performed before and after each set of measurements.

The circuit diagram of the main control unit is shown in Figures 3 and 4. When used in conjunction with a Nuclear Enterprises five-decade scaler, type NE 5097, it permitted data acquisition to be controlled by the target current monitor. Normally the total integrated charge was preset on the "count-limit" switches of the scaler and planned interruptions of a run carried out with the start/stop switch .

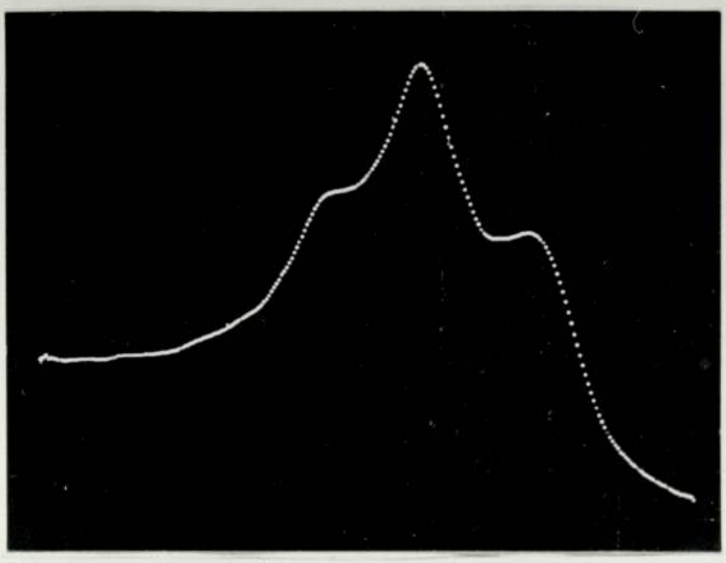

Photon pulse-height spectrum from the reaction $F^{19}(p,\alpha\gamma)\ O^{16}$ at E_o = 340 keV, before dynode and preamplifier modifications NaI(Tl) .

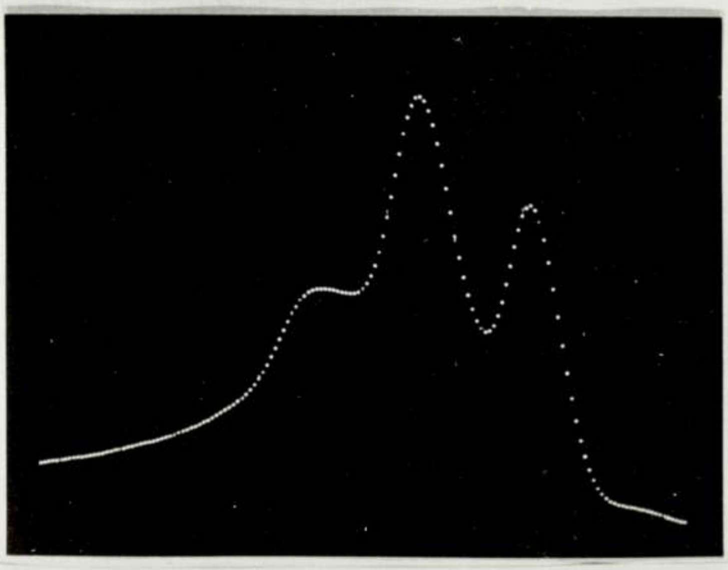

Photon pulse-height spectrum from the reaction $F^{19}(p,\alpha\gamma)\ O^{16}$ at E_o = 340 keV, after dynode and preamplifier modifications NaI(Tl) .

BLOCK DIAGRAM OF THE DATA AQUISITION SYSTEM(ASTON VAN DE GRAAFF)

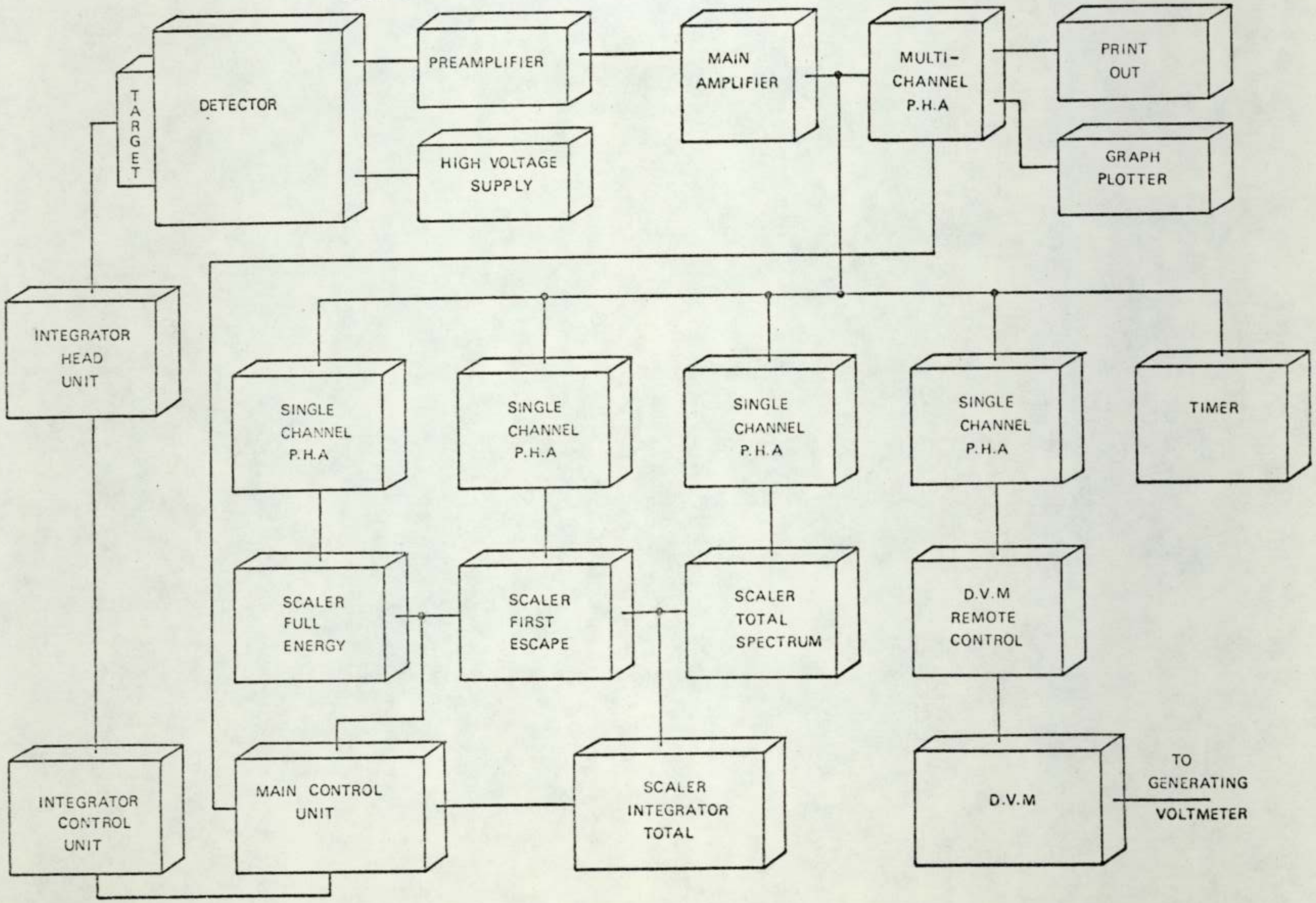

Figure 2

When the switch, S1, was placed in the "start" position, the closing contact to ground caused the generation of pulses suitable for driving the "remote-start" inputs of all units, and their operation was coincident with the first closure of the contact, and protected against relay bounce, within a few milliseconds. When the preset count was reached the "remote-stop" signal from the scaler raised a latched inhibit level on the integrator input and stopped all units. The remote "set acquire" and"set display" outputs to the multichannel pulse-height analyser were also latched; that is they did not disappear on removal of the input. The multi-channel pulse-height analyser logic inputs were isolated, by reed-relays, to prevent damage in the event of malfunction of the main control unit, and protected against high frequency pick-up by low pass filters. It was found necessary to introduce low pass filters in the power-rails of the control unit and use adequate screening in order to operate the unit in the intense radio-frequency environment of the accelerator. At the end of a run the switch was placed in the "stop" position and all units reset. If, during a run, the switch was raised to "stop" the unit waited until the next integrator cycle-pulse before raising the inhibit level. When the switch was returned to "start" it would similarly remove the inhibit level on the next integrator cycle-pulse. As it was necessary to operate the accelerator controls during an experiment the main control unit was fitted with an audio-visual alarm to indicate the termination of a run. The alarm was set when the inhibit level was raised.

The terminal potential was measured by a generating voltmeter, mounted close to the top terminal, the limit of approach being set

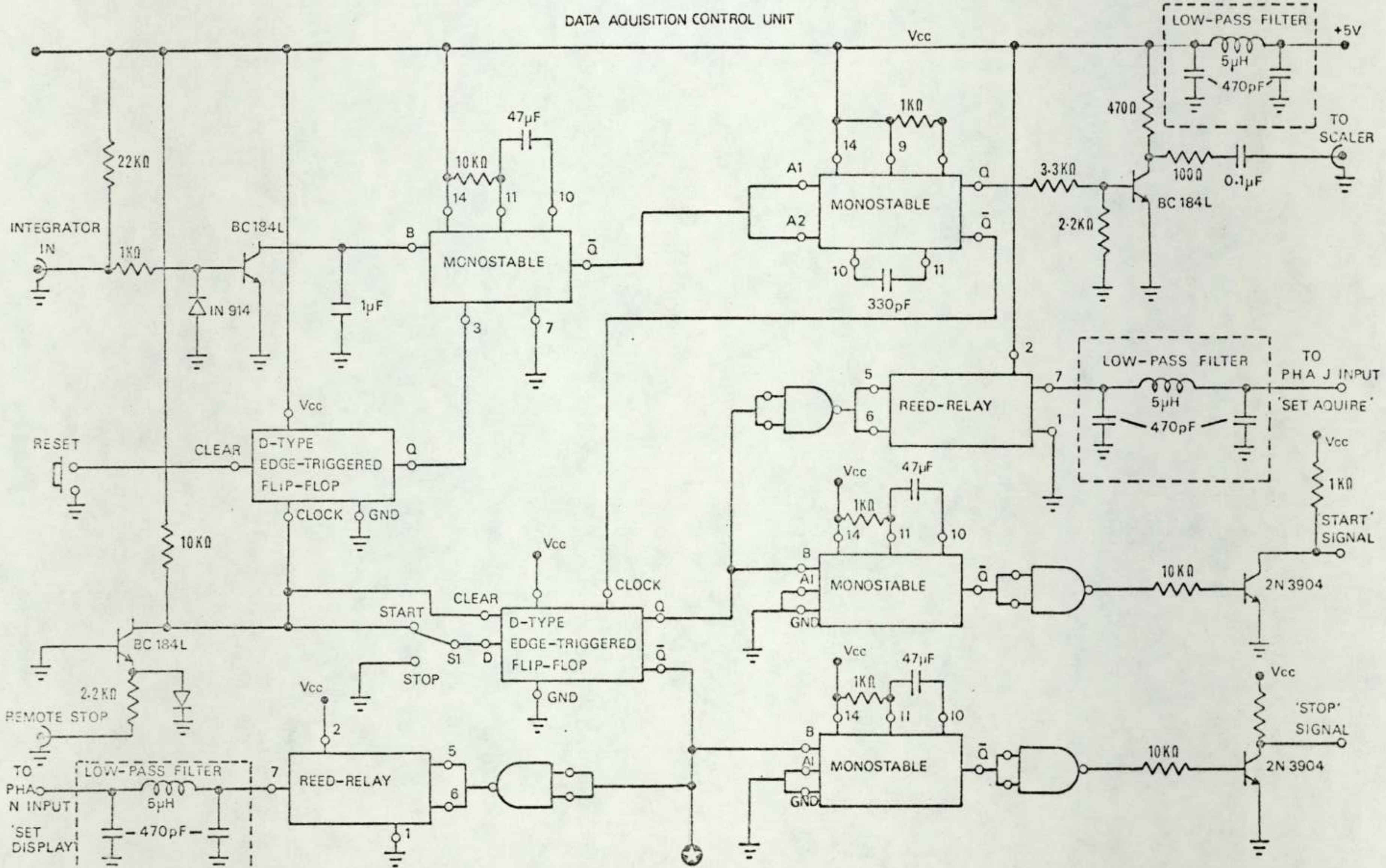
DATA AQUISITION CONTROL UNIT
Vcc
+5V
LOW-PASS FILTER
5μH
470pF
470Ω
TO SCALER
100Ω
0.1μF
BC 184L
3·3KΩ
2·2KΩ
1KΩ
14
9
A1
A2
MONOSTABLE
Q
Q̄
10
11
330pF
INTEGRATOR IN
22KΩ
1KΩ
IN 914
BC184L
1μF
47μF
10KΩ
14
11
10
B
MONOSTABLE
Q̄
3
7
RESET
CLEAR
D-TYPE EDGE-TRIGGERED FLIP-FLOP
Vcc
Q
CLOCK
GND
10KΩ
2
5
6
REED-RELAY
7
1
LOW-PASS FILTER
5μH
470pF
TO PHA J INPUT 'SET AQUIRE'
Vcc
1KΩ
'START' SIGNAL
Vcc
47μF
1KΩ
14
11
10
B
A1
GND
MONOSTABLE
Q̄
10KΩ
2N 3904
CLEAR
START
S1
D
STOP
Vcc
CLOCK
D-TYPE EDGE-TRIGGERED FLIP-FLOP
Q
Q̄
GND
BC 184L
2·2KΩ
REMOTE STOP
TO PHA N INPUT 'SET DISPLAY'
LOW-PASS FILTER
5μH
470pF
Vcc
2
7
REED-RELAY
5
6
1
Vcc
47μF
1KΩ
14
11
10
B
A1
GND
MONOSTABLE
Q̄
10KΩ
Vcc
'STOP' SIGNAL
2N 3904

Figure 3

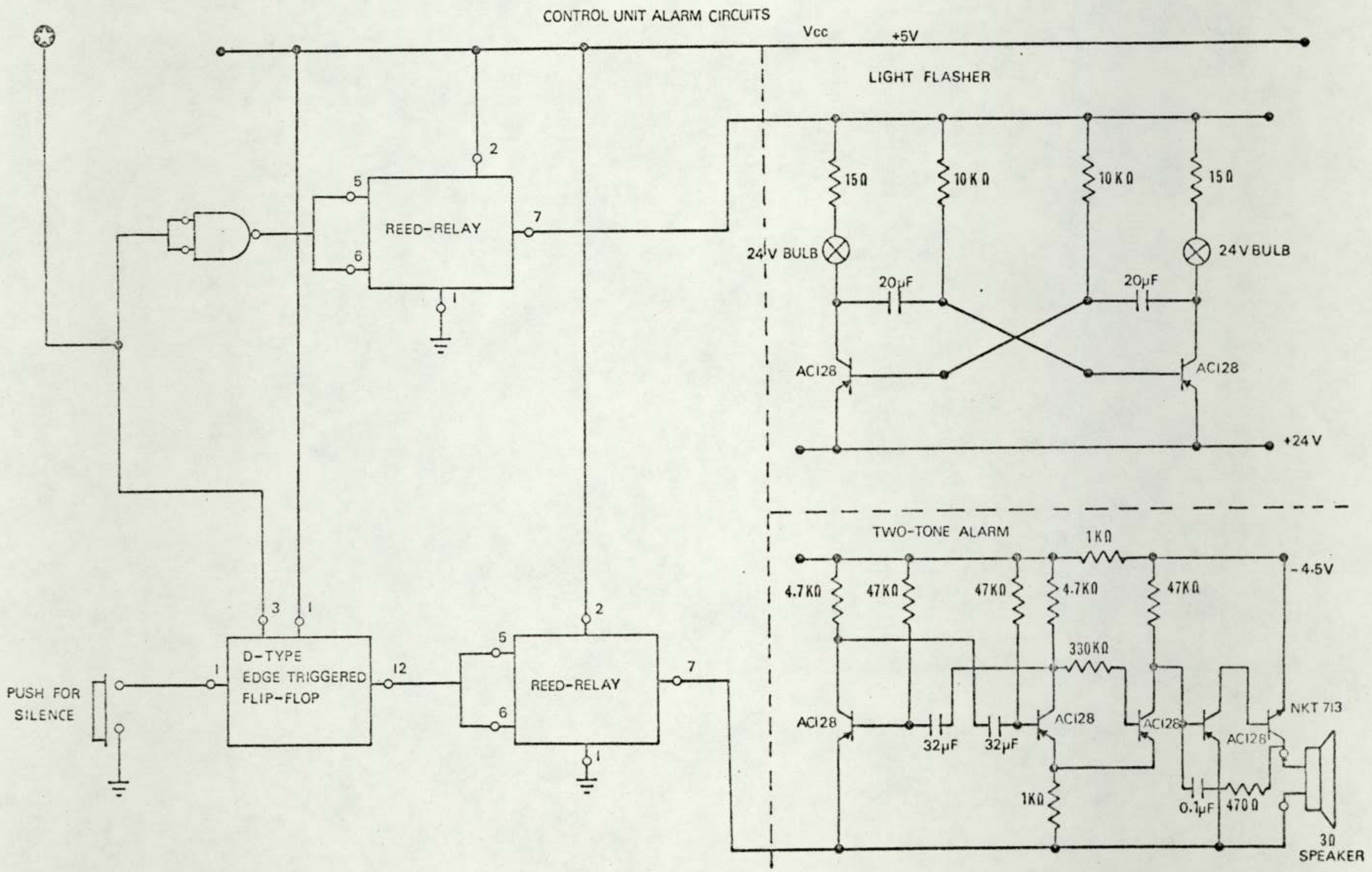
CONTROL UNIT ALARM CIRCUITS
Vcc
+5V
LIGHT FLASHER
15Ω
10KΩ
10KΩ
15Ω
24V BULB
24V BULB
20µF
20µF
AC128
AC128
+24V
REED-RELAY
2
5
6
7
1
D-TYPE EDGE TRIGGERED FLIP-FLOP
3
1
1
12
REED-RELAY
2
5
6
7
1
PUSH FOR SILENCE
TWO-TONE ALARM
1KΩ
-4.5V
4.7KΩ
47KΩ
47KΩ
4.7KΩ
47KΩ
330KΩ
AC128
32µF
32µF
AC128
AC128
AC128
NKT 713
1KΩ
0.1µF
470Ω
3Ω SPEAKER

Figure 4

by the electrical breakdown of air at 500 kV. Two sets of eight stator plates were exposed alternately by an eight vane rotor to the electrostatic field produced by the terminal potential. The resulting alternating voltage on the stator segments was proportional to the terminal voltage. CHURCHILL (1951) has shown that if a capacitative load is employed the induced voltage is independent of the speed of the rotor. This was achieved by using a MILLAR (1957) feed-back circuit which produced an output voltage of approximately 1 volt per 10 kV on the generator. Because of accelerator instabilities the meter reading fluctuated by one scale division or more (approximately 6 per cent at 340 kV) as the proton beam scanned the exit slits of the analyser. A method was therefore devised to "sample" the terminal voltage only when beam was transmitted through the analyser system to the target.

The output voltage from the generating voltmeter circuit was observed on a SOLARTRON, four decade digital-voltmeter, type LM1604DC, with a remote sampling facility. Sampling of the terminal voltage was triggered by pulses arising from the detection of gamma-rays from proton induced reactions in the target. The output of a single channel pulse height analyser, "gated" across the full-energy peak of the pulse height spectrum, was used to trigger a monolithic timing circuit type MC1455, operated in the monostable mode. In this mode, once triggered by an input signal, the circuit cannot be re-triggered until a set timing period has been completed. The timing period is determined by an external R-C network which was adjusted to give a maximum operating rate of 25 Hz, the maximum sampling speed of the digital-voltmeter. The digital-voltmeter logic circuitry was isolated by a reed-relay to prevent possible damage.

The circuit diagram of the unit is shown in Figure 5.

The system was recalibrated, as described by CRUMPTON (1967) using the F^{19} $(p,\alpha\gamma)O^{16}$, Al^{27} (p,γ) Si^{28} and $Li^{7}(p,\gamma)$ Be^{8} reactions.

Instrumentation on the Birmingham Radiation Centre Dynamitron

The experimental programme was transferred to the Birmingham Radiation Centre when this facility became available. The move was stimulated, both by access to a greatly improved data acquisition system and the by the expansion of the work made possible by the increased energy range of the accelerator. The "Dynamitron" accelerator, manufactured by Radiation Dynamics Incorporated, is situated in the Birmingham Radiation Centre sited on the Edgbaston Campus of the University of Birmingham and serves both Universities in common.

The accelerator is a variable energy, potential drop device which can operate at terminal potentials from 1 to 3 MV. It is powered by a 130 kHz R.F. oscillator. The power is fed to two large semi-circulard "dees" inside the pressure vessel which are capacitively coupled to semi-circular corona rings about the accelerator column. There are 64 corona rings separated by rectifier tubes; rectification of the R.F. produces a D.C. potential on the terminal. The rectifier heaters are powered by transforming a portion of the R.F. between adjacent corona rings and this effectively sets the low energy limit of the machine at 1 MV. Below this value there is a

DIGITAL-VOLTMETER CONTROL CIRCUIT

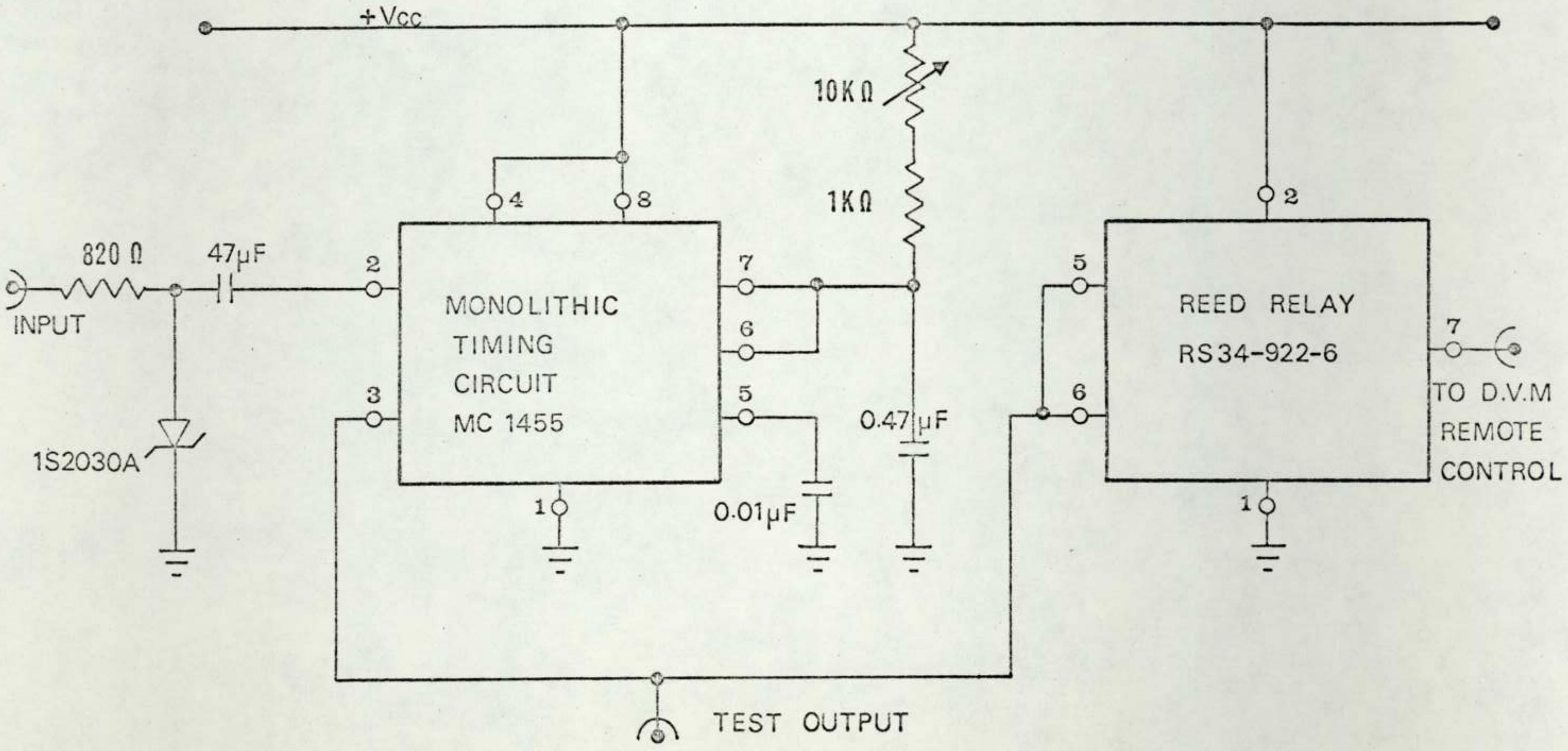

Figure 5

possibility of tube failure causing voltage-breakdown in the machine.

Both electron and positive ion beams can be accelerated. In the electron mode up to 10 mA(30 kW at 3 MV) can be obtained. In the positive mode ions are produced in a duoplasmatron ion source. The source is placed at an angle of 20 degrees to the accelerator column and the ions are bent into the line of the accelerator by a permanent magnet. Mass analysis is achieved by varying the extractor potential. Up to 2 mA of protons can be produced (6 kW at 3 MV). A full description of the duoplasmatron ion-source may be found in HANDLEY and WELLS (1973). Further details of the accelerator may be found in the literature, CLELAND and FARRELL (1965),CLELAND (1968) and CLELAND et al.(1969). The Dynamitron is stabilized through the current drawn down a resistor chain from the top terminal in the machine. The total resistance of this chain is approximately 10^{10} ohm. The standing current serves as input to a control circuit which provides a feed-back signal to the oscillator. Terminal potential is indicated by a digital voltmeter reading across a 500 ohm resistor at the base of the chain.

To make full use of the limited machine time available it was considered necessary to construct a multiple target assembly with a remote sample change facility. The target chamber is shown dismantled in Plate 3. The target holder, a 6.25 cm hollow cylinder could accommodate six samples, held in place by grub-screws. It was mounted on an A.E.I. 5 cm linear drive type LM 50, with a clearance of 0.25 mm. The precision drive permitted lateral translation, over the full diameter of the sample, along the axis of the target holder.

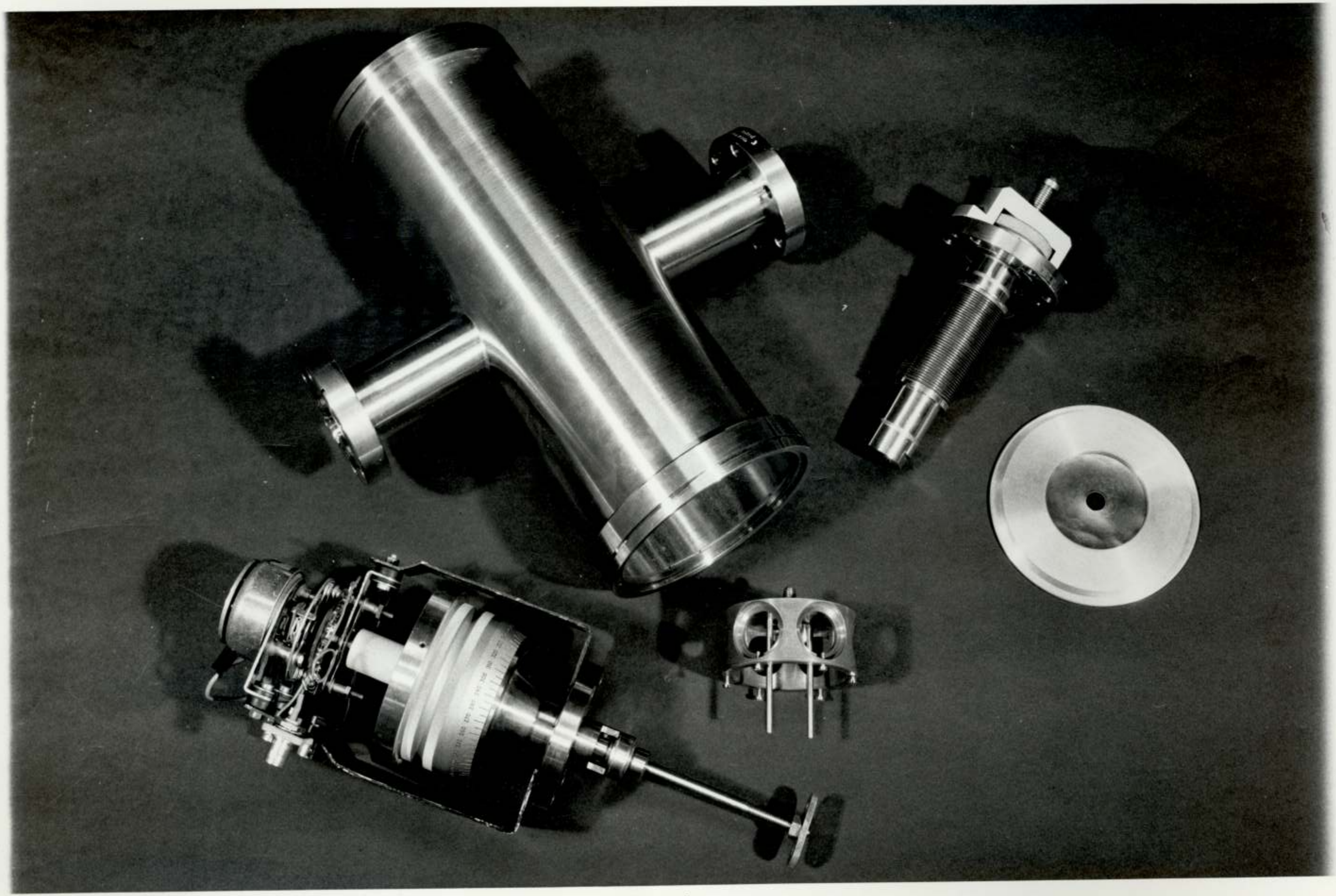

Plate 3

The target holder was rotated, to bring different samples into the beam, by means of an A.E.I. 360 degree rotary-drive type RM 2, carrying a sliding collet which located in the target holder. Efficient secondary electron suppression was achieved by using the whole target chamber as a Faraday cage. The beam entered the chamber through an end-plate with a 1 cm diameter aperture to reduce the possibility of secondary electrons leaving the chamber and giving a false indication of target current. No target cooling was provided as low beam currents were used, typically 1.0μA.

A remote change facility was obtained by attaching a twelve position uniselector to the rotary drive through a P.T.F.E. insulating bush. Application of a slow (1 second) 25-30 volt pulse to the uniselector winding produced a 30 degree rotation of the sample holder. Target position was indicated by a 12-way single-pole wafer-switch, wired as a potential divider network, mounted on the uniselector drive-shaft. Between measurements the beam was "dumped" on the target holder in intermediate positions to reduce unnecessary target irradiation.

A large surface area, baffled, liquid nitrogen cold trap was situated close to the target to minimise carbon build-up and reduce possible fluorine contamination of the beam transport system. Because of the poor thermal conductivity of stainless steel, copper was used for the trap and for the base of the liquid nitrogen reservoir. The trap also served to locate two tantalum foils for final beam collimation. Aperture sizes used ranged from 0.5 mm to 2.0 mm. The components of the trap are shown in Plate 4. A gate-valve and roughing port were introduced between the cold-trap and target chamber so that

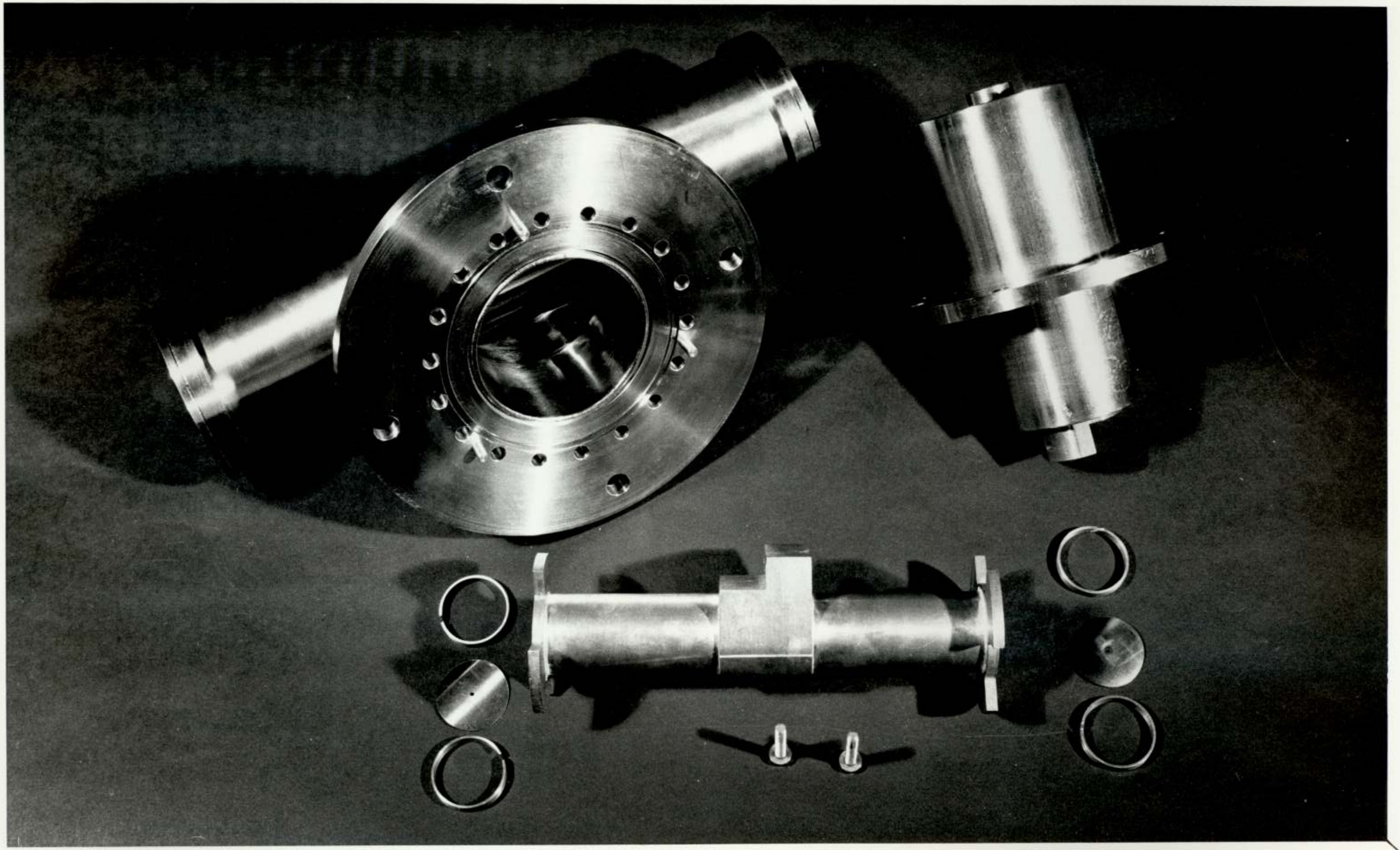

Plate 4

the latter could be isolated from the vacuum system to change samples. The target chamber and cold-trap assembly were electrically isolated by insulating vacuum seals. A perspex holder mounted on the target chamber served to locate the sodium-iodide crystal accurately and close to the target.

For the detection of charged-particles a lithium drifted solid-state detector, type Ne 100-3, could be mounted in the target chamber at an angle of 155 degrees (beam direction zero degrees). It was electrically isolated from the target chamber and fitted with variable collimation and aluminium foils to exclude scattered protons. The complete assembly is shown in Plate 5 mounted on one of the Dynamitron beam-lines. A liquid nitrogen pump and level sensing device were used to maintain the level in the cold trap.

A block diagram of the data acquisition system is shown in Figure 6, together with the twin processor Hewlett-Packard computer system installed in the Radiation Centre. One processor, a type 2116 can operate three terminals. Each station has a teletype and display and one has a plotter. The analogue-to-digital converters are 8192 channel devices with a 200MHz clock and can run in the multiparameter or multiplex modes. Approximately 6000 channels are available in the 2116 computer for data storage, and this part of the system is known as the 5406B Nuclear Package. A link exists between the two processors so that the 5406B can pass information to the type 2100 computer to which are attached the input output peripherals, paper-tape reader, punch, line-printer and 7-track magnetic tape. This computer operates the real-time executive in which several levels of programme can exist at one time. The real time executive has a 3/4M word drum backing store.

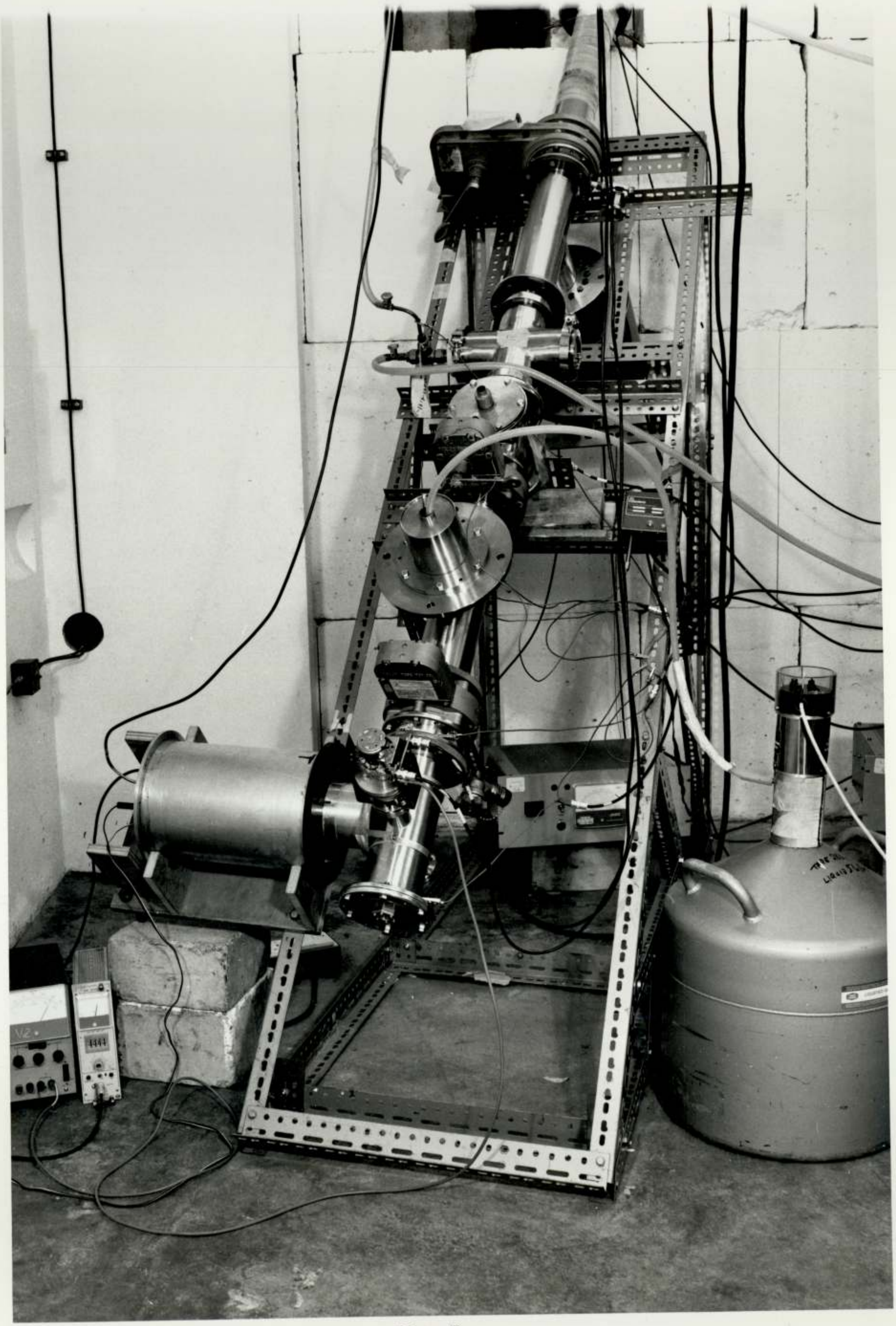

Plate 5

Gamma-rays and charged particle pulse-height spectra could be accumulated simultaneously in two 1024 channel regions, using one analogue-to-digital converter in the multiplex mode. The spectra were stored on magnetic tape and analysed later.

The target current-monitor was based on a Kiethley electrometer, a high-input impedance current meter which produces a one volt output for full scale deflection on each range, with an accuracy of one per cent of full scale. The output of the Kiethley electrometer was fed to a voltage to frequency converter which produced a negative-going pulse chain of 10^5 Hz for a one volt input. The pulse chain was converted into positive-going, "NIM" compatible, pulses by a scaling unit which provided outputs from one to five decades slower in frequency, suitable for counting on a scaler. To accumulate spectra for a preset charge the inhibit level from the integrator total count scaler was used to gate the anticoincidence input of the analogue-to-digital converter. The high input impedence of the Kiethley electrometer was a contributary factor in the decision not to provide target cooling. Range selection is achieved by switching the impedance (1 MΩ for 1 μA F.S.D. 10 MΩ for 0.1 μA F.S.D.). A water cooling circuit would introduce an impedance, of typically 10 MΩ, in parallel with the integrator input and lead to significant charge loss on the lower ranges.

Targets were prepared on a backing of highly polished copper, in the form of 2.5 cm diameter discs of 3 mm thickness. Copper was chosen as the backing material as it has a very small cross-section for gamma-ray production when irradiated with protons of energy less than 1 MeV,

BLOCK DIAGRAM OF THE DATA AQUISITION SYSTEM (RADIATION CENTRE DYNAMITRON)

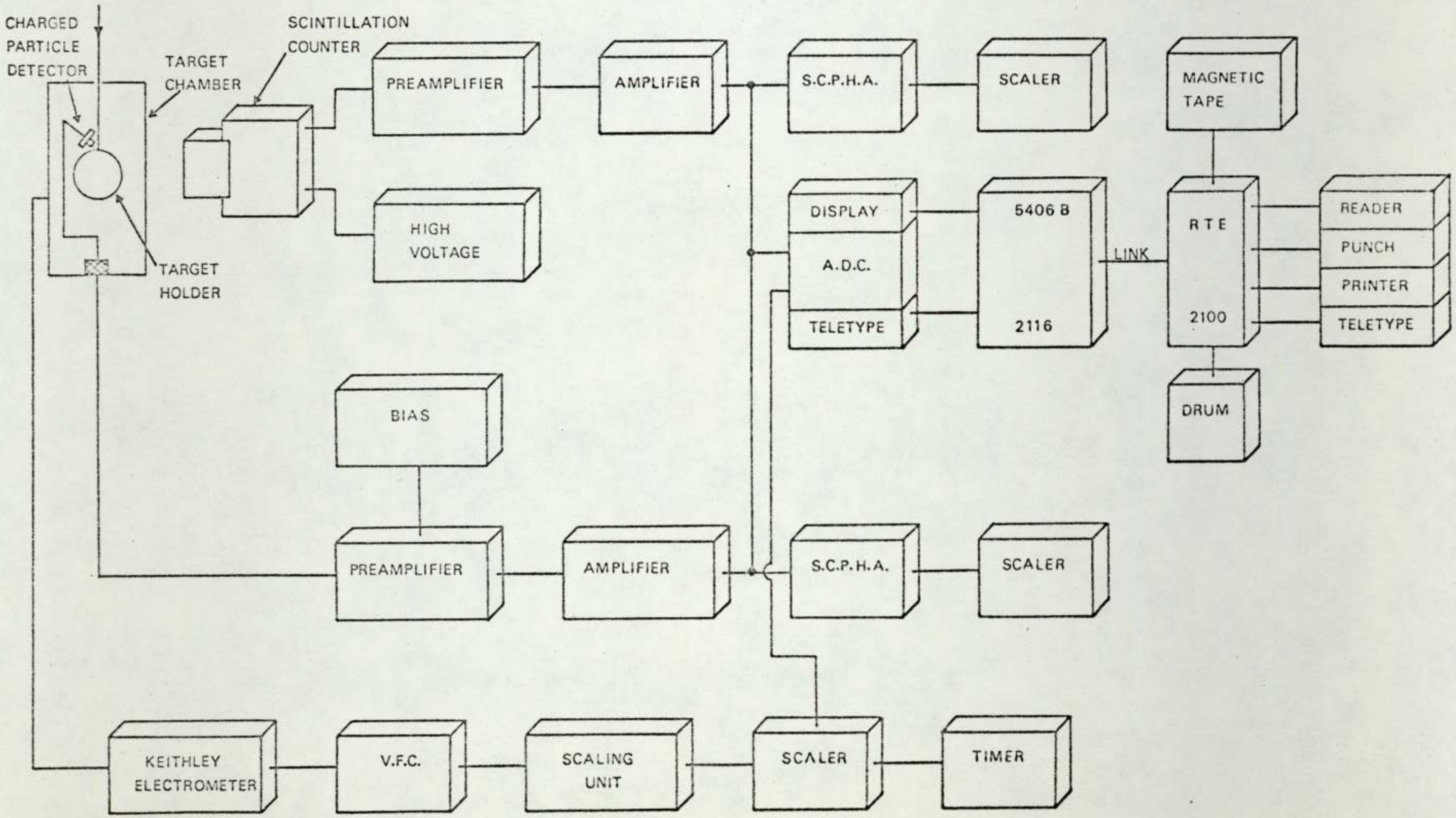

Figure 6

HUNT et al.(1958). The discs were machined without the use of cutting oil to minimise possible contamination and mounted in thermosetting plastic to facilitate polishing.

Microcracked chromium samples were prepared by electro plating the discs on a 5 cm x 5 cm copper cathode, using two anodes to reduce thickness inhomogenity. The constituents of the plating solution are shown in Table 1. Other samples and comparison standards were prepared by vacuum evaporation.

Interferometric and polorimetry techniques were used to measure target thickness. A full description of the methods employed may be found in AGUADO-BOMBIN (1975).

TABLE 1

Constituents of the Plating Solution for the Production of Microcracked Chromium Plate.

Chromic Acid	0.150 kg. litre^{-1}
Sulphuric Acid	0.00035 kg. litre^{-1}
Sodium Fluoride	0.003 kg. litre^{-1}

Chapter III

The Form Factors of Charged Particle Induced Reactions

The Form Factors of Charged Particle Induced Reactions

The yield from a charged particle induced reaction is a function of the reaction cross-section, the thickness, composition and stopping power of the target medium, incident beam energy dispersion, Doppler broadening and straggling. Each of these factors will be considered in turn to determine their relative contribution to the shape of observed yield curves from resonance reactions.

DOPPLER BROADENING

Doppler broadening arises because the target nuclei have random thermal velocities and the effective reaction cross-section must be obtained by averaging over an appropriate distribution of relative velocities. If the target is a gas (a rather unusual situation) the distribution of particle energies about the mean incident proton energy, Ep, due to Doppler broadening may be represented by the Maxwellian distribution function

$$N(E) = \frac{1}{(2\pi)^{\frac{1}{2}} \sigma_D} \exp \left[- (Ep - E)^2/2\sigma_D^2\right]$$

The standard deviation, σ_D, is given by

$$\sigma_D = \left[2m\ EpKT/M\right]^{\frac{1}{2}}$$

with

m = mass of incident particle

M = mass of target nucleus

T = absolute temperature

K = Boltzmanns constant

For a solid target N(E) is given, from Debye theory, by approximately the same function, with

$$\sigma_D = \left[(2m/M)EpKT(1 + \lambda^2/20T^2)\right]^{\frac{1}{2}} \qquad \text{.........} \qquad (1)$$

where, λ, is the Debye temperature. The full-width at half-maximum, R, of the function N(E) is given by

$$R = 2.35\sigma_D$$

We shall assume that the true reaction cross-section, σ(E), is of the Breit-Wigner form, that is

$$\sigma(E) = \sigma_r \frac{\Gamma^2/4}{(E-E_o)^2 + \Gamma^2/4}$$

where

E_o = resonance energy

Γ = resonance width

σ_r = cross-section at $E = E_o$

In the absence of all other factors contributing to observed width, the experimentally observed function, I(E) is the correlation of the two functions N(E) and σ(E),

$$I(E) = \int_{\infty}^{\infty} \sigma(E')N(E+E')dE' \qquad \text{........ ...} \qquad (2)$$

The function I(E) cannot be expressed in terms of elementary functions. WILKINSON (1971) has investigated the analogous case of the function formed by the convolution of a Gaussian and a Breit-Wigner. The operations of convolution and correlation must normally be considered as distinct. However, the functions formed by the convolution or correlation of two centre symmetric functions are identical in shape, though not necessarily in position. It has been shown by WILKINSON (1971) that the FWHM, $W(0.5)$ of the function formed by the convolution of a Gaussian and a Breit-Wigner, is given by the quadratic addition of Γ and R, if the ratio $\Gamma/R \geqslant 4$. That is,

$$W(0.5)^2 = \Gamma^2 + R^2 \qquad \ldots\ldots\ldots\ldots \qquad (3)$$

If the ratio $\Gamma/R \leqslant 0.1$, a Breit-Wigner and a Gaussian add linearly rather than quadratically, and $W(0.5)$ is given by

$$W(0.5) = R + 0.5323\Gamma \qquad \ldots\ldots\ldots\ldots\ldots \qquad (4)$$

The Doppler broadened widths of several prominent resonances in the $F^{19}(p,\alpha\gamma)O^{16}$ reaction cross-section have been calculated using equations (1) and (3). It was assumed that the Debye temperature is the same as the target temperature ($T = 723^{o}K$). The results are shown in Table 2 together with the resonance energies and natural widths taken from GOLICHEFF et al. (1972). Apart from the resonance at 483 keV the error entailed by neglecting Doppler broadening is less than 0.2 per cent. Table 3 shows a similar calculation for a number of resonances in the $Al^{27}(p,\gamma)Si^{28}$ reaction cross-section. The Doppler broadened width were calculated using equations (1) and (4). The resonance energies and natural widths were taken from LYONS et al. (1969) and ENDT and VAN DER LEUN (1973). For very narrow resonances the observed width is almost exclusively due to Doppler broadening and such

TABLE 2

Doppler Widths for a Number of Prominent Resonances in the $F^{19}(p,\alpha\gamma)O^{16}$ Reaction Cross-Section

$T = 723^{\circ}$ K

E_o keV	Γ keV	R keV	Γ/R	W(0.5) keV	$\lvert(W(0.5)-\Gamma)/\Gamma\rvert.100$
340.0	2.4	0.11	21.1	2.403	0.11
483.0	0.9	0.14	6.6	0.910	1.14
672.0	6.0	0.16	37.5	6.002	0.04
872.0	4.5	0.182	24.7	4.504	0.08
902.0	5.1	0.185	27.6	5.103	0.06
935.0	8.6	0.188	45.7	8.602	0.02
1140.0	5.0	0.208	24.0	5.004	0.08
1189.0	11.0	0.213	516.4	110.0002	1.9×10^{-4}
1283.0	19.0	0.221	86.0	19.001	6.8×10^{-4}
1348.0	5.6	0.23	24.8	5.605	0.81
1735.0	11.0	0.26	42.8	11.003	

TABLE 3

Doppler Widths for a Number of Prominent Resonances in the $Al^{27}(p,\gamma)Si^{28}$ Reaction Cross-section.

$T = 723^{\circ}K$

E_o keV	Γ keV	R keV	Γ/R	W(0.5) keV	$\lvert(W(0.5)-\Gamma)/\Gamma\rvert.100$
405.5	1.5×10^{-4}	0.1040	1.4×10^{-3}	0.1041	96000.0
612.1	1.1×10^{-4}	0.1280	8.5×10^{-4}	0.1281	116300.0
733.7	1.0×10^{-4}	0.141	0.07	0.146	1360.0
1118.4	1.45×10^{-2}	0.173	0.08	0.181	1146.0
1213.0	1.0×10^{-2}	0.180	0.06	0.185	1753.0
1262.2	8.2×10^{-3}	0.171	0.05	0.175	2039.0
1316.9	1.0×10^{-2}	0.188	0.05	0.193	1833.0

resonances are said to exhibit a pure Doppler shape.

INCIDENT BEAM ENERGY DISPERSION

The factors which contribute to a spread in the incident beam energy arise from the resolution of the analyser system and modulation of the incident beam due to power supply ripple and regulation.

The terminal potential of the Dynamitron accelerator is developed by rectification of a 130 kHz R.F. signal. The power supply for the top terminal operates at a frequency of 629 Hz, and all other supplies at the mains frequency of 50 Hz. During acceleration the beam is modulated at these frequencies, and their harmonics, producing an energy ripple. A further ripple component is introduced by R.F. frequencies in the duoplasmatron ion-source. The terminal mass analyser and accelerator lens system also induce spatial modulation of the beam at frequencies of 130 kHz and 629 Hz.

The trajectory of the emergent beam from the accelerator is defined by a 3 cm aperture, 2 m from the base of the accelerator and 1m from the main analyser or "H" magnet, which deflects the beam through an angle of 45 degrees. The "H" magnet has a 1 cm entrance aperture, the exit aperture is unstopped. In the configuration used, the flight-path from the analyser to the final collimation and target assembly was 7 m. No beam steering or focussing were used between the analyser and target assembly. All active components built onto the beam-line were degaussed before a run to minimise beam steering caused by residual magnetic fields ($\sim 35 \times 10^{-12}$ tesla on the pole-tips of the quadrapole lenses). Under these conditions beam energy dispersion at the target is limited by the stability of the analyser magnet and the size of the final collimator. The analyser magnet has a current stability of 2 parts in 10^5 and a total ripple of $\leqslant 5$ mA at all currents. Ripple introduced by the analyser magnet is therefore small compared to that introduced by the accelerator. BASSETT (1975) has shown that for the configuration described, with a 2 mm aperture 7 m from the analyser, the energy spread at the target is of the order of 2 to 3 keV. The precise shape of the energy distribution of protons at the target is unknown, but is considered to be described by a distribution intermediate in shape between a Gaussian and a slit-function.

If all other factors are neglected and incident beam energy dispersion is represented by a unit-area slit-function, D(E), given by

$$\begin{aligned} D(E) &= H = \frac{1}{n} \qquad a \leqslant E \leqslant b \\ &= 0 \qquad\quad\; a > E > b \end{aligned}$$

of width $n = b - a$, the observed function, $\phi_1(E)$, is the correlation of D(E) with the reaction cross-section, $\sigma(E)$, that is

$$\phi_1\ (E) \quad = \quad \int_{-\infty}^{\infty} \sigma(E')\ D\ (E + E')dE' \quad \ldots\ldots\ldots\ldots \qquad (5)$$

Substituting for $\sigma(E)$ and integrating by parts

$$\phi_1(Eb) \quad = \quad \frac{\Gamma^2\ \sigma_r}{4n} \int_{Eb-n/2}^{Eb+n/2} \frac{dE'}{(E'-E_o)^2 + (\Gamma/2)^2}$$

$$\phi_1\ (Eb) = \frac{\Gamma\sigma_r}{2n}\left\{\tan^{-1}\frac{Eb + n/2 - Eo}{\Gamma/2} - \tan^{-1}\frac{Eb - n/2 - Eo}{\Gamma/2}\right\} \ldots (6)$$

where Eb is the mean incident energy. The maximum value of Equation (6) occurs at Eb = E_o, and is given by

$$\phi_1\ (\max) = \frac{\Gamma\sigma_r}{n}\tan^{-1}\frac{n}{\Gamma} \quad \ldots\ldots\ldots\ldots \quad (7)$$

The FWHM, S(0.5), of the correlate ϕ_1(Eb) is given by the quadratic addition of n and Γ, that is

$$S(0.5)^2 = n^2 + \Gamma^2 \quad \ldots\ldots\ldots\ldots \quad (8)$$

Equation (8) is valid for all values of n and Γ.

If beam energy dispersion is represented by a pure Gaussian, Equation (5) may be redefined as

$$\phi_2\ (E) = \int_{-\infty}^{\infty} \sigma(E')\ G(E + E')\ dE' \quad \ldots\ldots\ldots \quad (9)$$

where G(E) is the Gaussian

$$G\ (E) = (1/\theta\sqrt{\pi})\ .\exp - (E/\theta)^2$$

of FWHM, R, given by

$$R = 2(\ln 2)^{\frac{1}{2}}\ \theta = 1.6551\theta$$

The general solution of Equation (9) is, (See Appendix I)

$$\phi_2\ (E) = (1/\theta\sqrt{\pi})\ \mathrm{Re}\,\omega\left(\frac{E}{\theta} + \frac{i\Gamma}{2\theta}\right) \quad \ldots\ldots\ldots \quad (10)$$

where ω(z) is the complex error function

$$\omega(z) = \exp(-z^2)\text{erfc}\ (-iz)$$

$$\text{erfc}\ z = 1 - \text{erf}\ z$$

$$\text{erf}\ z = 2/\sqrt{\pi}\int_0^z \exp(-t^2)dt$$

The asymptotic approximations ($\Gamma/R \geqslant 4$ and $\Gamma/R \leqslant 0.1$) for the FWHM of the function ϕ_2 (E) have been considered (Equations (3) and (4)). The intermediate region, $0.1 < \Gamma/R < 4$, has been parameterized by WILKINSON (1971) for the case in which W(0.5) (the FWHM of $\phi_2(E)$) and R are known and Γ is unknown. If Γ_1 is the width that would be deduced by a quadratic subtraction of the FWHM, R, of the Gaussian from the FWHM, W (0.5), of the function $\phi_2(E)$:

$$\Gamma_1 = (W(0.5)^2 - R^2)^{\frac{1}{2}} \qquad \text{............} \quad (11)$$

The true width of the Breit-Wigner, Γ, is

$$\Gamma = \Gamma_1/\ \Omega \qquad \text{.................} \quad (12)$$

where Ω is given approximately by

$$\ln\ (\Omega-1) = a_o + a_1\ \ln\ (\Gamma_1/R) + a_2\left[\ \ln(\Gamma_1/R)\right]^2 \qquad \text{....} \quad (13)$$

with

$$a_o = -0.774 \quad a_1 = -1.652 \quad a_2 = -0.153$$

The parameterization reproduces the value of Ω to better than one per cent in the range $0.1 < \Gamma/R < 4$. The maximum value of the correlate ϕ_2 (E) is given by

$$\phi_2\ (\text{max}) = \sigma_\Gamma \sqrt{\pi}\, y\, \omega\ (iy) \qquad \text{..................(14)}$$

with

$$y = (\ln 2)^{\frac{1}{2}}\ \Gamma/R$$

$$\omega\ (iy) = \exp\ (y^2)\ \text{erfc}\ y\ \text{(See note}^*\text{)}$$

Experimental data, presented in a later section, for the $F^{19}(p,\alpha\gamma)O^{16}$ reaction at E_o = 340 keV, for which Γ = 2.4 keV, indicates that 3.3 ± 0.5 is the minimum observable FWHM for the resonance in the experimental configuration described. A value of 3.3 keV for the FWHM of the correlate will therefore be used as a basis for comparison of Equations (6) and (9).

For the Gaussian smearing function the ratio $\Gamma/R \sim 1.0$ ($R \sim 2$ keV) is in the intermediate region parameterized in Equations (11) to (13). Equation (13) was adapted, by substitution from Equations (11) and (12) to yield an equation with R as the only unknown :

---

[*] NOTE. In WILKINSON'S paper ω (iy) is incorrectly given as $\omega\ (iy) = \exp\ (y)\ \text{erfc}\ y$, due to a printing error.

$$\ln\left[\frac{(W(0.5)^2 - R^2)^{\frac{1}{2}}}{\Gamma} - 1\right] = a_o + a_1 \ln\left[\frac{(W(0.5)^2 - R^2)^{\frac{1}{2}}}{R}\right] + a_2\left[\ln\left\{\frac{(W(0.5)^2 - R^2)^{\frac{1}{2}}}{R}\right\}\right]^2 \quad ..(15)$$

Equation (15) was solved numerically for R (using the search and binary search methods) in the bound $W(0.5) \geqslant R \geqslant 0$. For $W(0.5) = 3.3$ keV and $\Gamma = 2.4$ keV the value of R obtained was 1.68 keV. The function $\phi_2(E)$ was then determined by numerically correlating Equation (9) with a unit-area Gaussian of FWHM R = 1.68 keV and a Breit-Wigner with $E_o = 340$ keV, $\sigma_\Gamma = 102$ mb and $\Gamma = 2.4$ keV. The numerical solution yielded a value of 81.93 mb for $\phi_2(\max)$. The same value was obtained from Equation (14).

For the slit-function case, substitution of $\Gamma = 2.4$ keV and $S(0.5) = 3.3$ keV in Equation (8) gives n = 2.265 keV. The function $\phi_1(Eb)$ was then evaluated, for a unit-area slit-function, from the analytical solution (Equation (6))with identical parameter values for the Breit-Wigner. From Equation (7) ϕ_1 (max) was obtained as 81.76 mb.

The function ϕ_1 (Eb) and ϕ_2 (E) are shown in Figure 7. The curves for ϕ_1 (Eb) and $\phi_2(E)$ are virtually indistinguishable and are shown as a single curve with a FWHM of 3.3 keV. For both types of smearing function the maximum values of the correlates, $\phi_1(\max)$ and $\phi_2(\max)$ respectively, agree to within 0.2 per cent.

The correlates ϕ_1 (Eb) and ϕ_2 (E) are not equivalent mathematically but are very similar. Knowledge of the correlate,

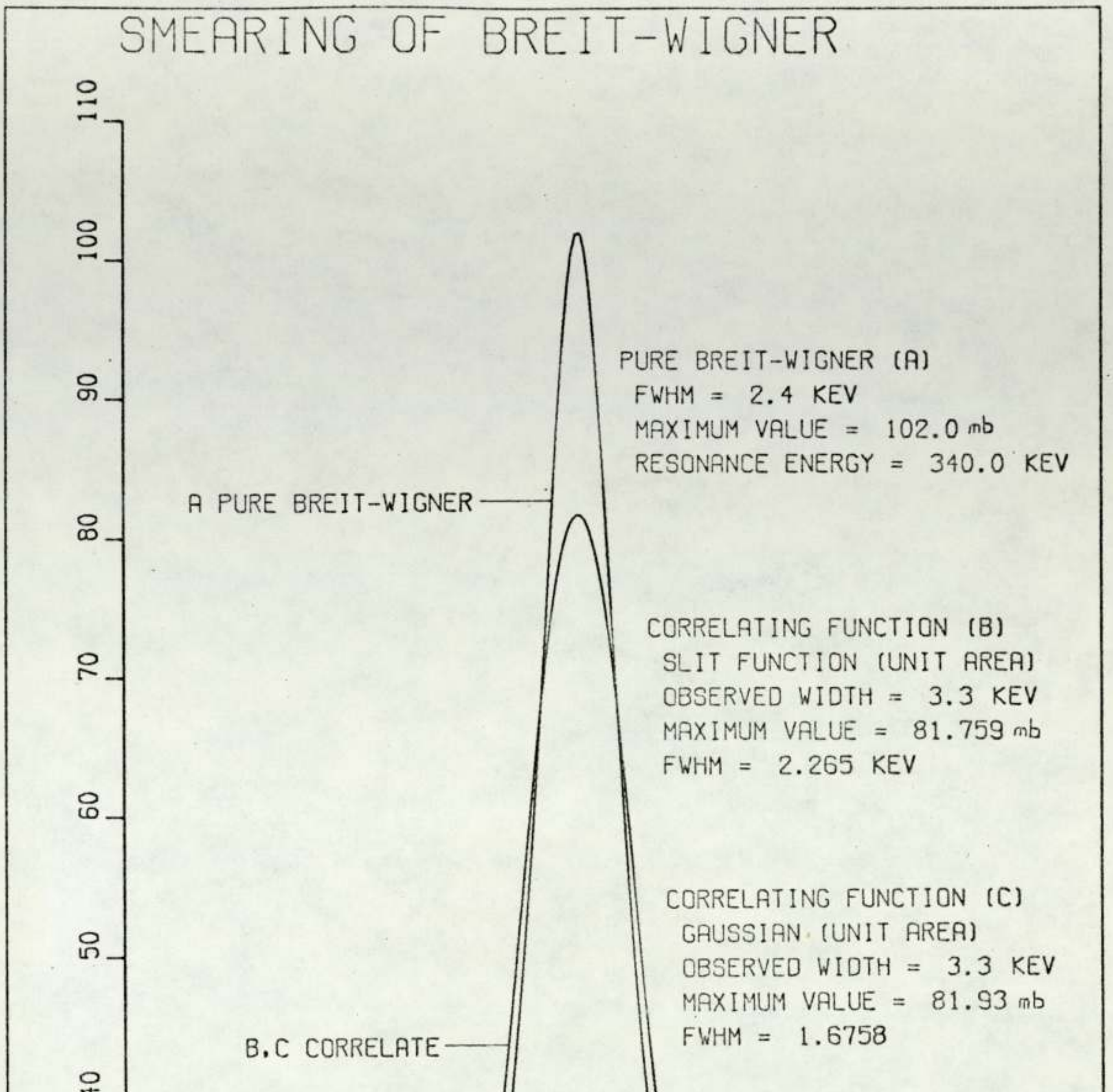
SMEARING OF BREIT-WIGNER
PURE BREIT-WIGNER (A)
FWHM = 2.4 KEV
MAXIMUM VALUE = 102.0 mb
RESONANCE ENERGY = 340.0 KEV
A PURE BREIT-WIGNER
CORRELATING FUNCTION (B)
SLIT FUNCTION (UNIT AREA)
OBSERVED WIDTH = 3.3 KEV
MAXIMUM VALUE = 81.759 mb
FWHM = 2.265 KEV
CORRELATING FUNCTION (C)
GAUSSIAN (UNIT AREA)
OBSERVED WIDTH = 3.3 KEV
MAXIMUM VALUE = 81.93 mb
FWHM = 1.6758
B.C CORRELATE
CROSS-SECTION (MILLIBARNS)
0
10
20
30
40
50
60
70
80
90
100
110
330
332
334
336
338
340
342
344
346
348
350
ENERGY (KEV)

Figure 7

which is the only experimental observable, is not therefore sufficient to uniquely determine the form of the smearing function unless the correlate is known to high accuracy. To differentiate between the functions ϕ_1 (Eb) and ϕ_2(E) from discrete (that is, point recorded) experimental data would require an absolute accuracy of better than 0.1 per cent. Accuracy of this order must normally be considered unattainable.

In practice a pure Gaussian distribution of particle energies cannot be transmitted through a finite beam transport system. The energy distribution at the target will therefore tend more to that of a slit-function.

TARGET THICKNESS EFFECTS

In the general case, if incident beam energy dispersion is neglected, the observed yield per incident proton, ϕ_3(E), is given by the convolution,

$$\phi_3\ (E) \ = \ \int_{-\infty}^{\infty} \sigma(E')\left(\frac{dE'}{dx}\right)^{-1} C\ (E - E')dE' \qquad \ldots\ldots\ldots\ldots \quad (16)$$

where σ(E) is the reaction cross-section, C(E) is the concentration profile and dE/dx is the stopping power of the target medium. Only targets of uniform concentration will be considered. When the proton range is greater than the target thickness the concentration profile is represented by a slit-function; when the proton range is less than the target thickness, at all energies considered, the concentration profile is represented by a step-function.

Consider a target of thickness, t, containing C reaction centres per unit volume, and assume that the reaction cross-section, σ (E), is of the Breit-Wigner form. If we make the further assumption that the stopping cross-section, $\varepsilon = (1/C).(dE/dx)$, of the target medium and the energy loss, $\xi = Ct\varepsilon$ of the particle beam in the target are independent of energy in the vicinity of the resonance, Equation (16) may be integrated by parts to yield

$$\phi_4 (E) = \varepsilon^{-1} \int_{E-\xi}^{E} \sigma (E')dE' \qquad \ldots\ldots\ldots\ldots\ldots \qquad (17)$$

Substituting for σ (E) and integrating gives

$$\phi_4 (E) = \frac{\sigma_r \Gamma}{2\varepsilon} \left\{ \tan^{-1} \frac{E - E_o}{\Gamma/2} - \tan^{-1} \frac{E - E_o - \xi}{\Gamma/2} \right\} \ldots\ldots \qquad (18)$$

For a given ξ Equation (18) has a maximum at $E = E_o + \xi/2$ given by

$$\phi_4 \max (\xi) = \frac{\sigma_r \Gamma}{\varepsilon} \tan^{-1} \frac{\xi}{\Gamma}$$

The FWHM, P(0.5), of the function ϕ_4 (E) is given by,

$$P (0.5) = [\Gamma^2 + \xi^2]^{\frac{1}{2}}$$

We now reintroduce beam energy dispersion, represented by the slit-function D (E_v) defined previously. The observed yield. ϕ_5 (E), is now given by

$$\phi_5 (E) = \int_{E_v = Eb - n/2}^{Eb + n/2} D (E_v) \phi_4(E' + E_v) dE_v$$

Substituting and integrating by parts we obtain

$$\phi_5 \; (Eb) = \frac{\sigma_r \Gamma}{2\varepsilon n} \int_{E_v = Eb - n/2}^{Eb + n/2} \left\{ \tan^{-1}\left(\frac{E_v - E_o}{\Gamma/2} \right) - \tan^{-1}\left(\frac{E_v - E_o - \xi}{\Gamma/2} \right) \right\} dE_v$$

$$= \frac{\sigma_r \Gamma}{2\varepsilon n} \left[(Eb + n/2 - E_o) \tan^{-1}\left(\frac{Eb + n/2 - E_o}{\Gamma/2} \right) \right.$$

$$- \frac{\Gamma}{4} \ln\left\{ \frac{\Gamma^2}{4} + (Eb + n/2 - E_o)^2 \right\} - (Eb + n/2 - E_o - \xi) \tan^{-1}\left(\frac{Eb+n/2-E_o-\xi}{\Gamma/2} \right)$$

$$+ \frac{\Gamma}{4} \ln\left\{ \frac{\Gamma^2}{4} + (Eb+n/2-E_o-\xi)^2 \right\} - (Eb-n/2-E_o) \tan^{-1}\left(\frac{Eb-n/2-E_o}{\Gamma/2} \right)$$

$$+ \frac{\Gamma}{4} \ln\left\{ \frac{\Gamma^2}{4} + (Eb-n/2-E_o)^2 \right\} + (Eb-n/2-E_o-\xi) \tan^{-1}\left(\frac{Eb-n/2-E_o-\xi}{\Gamma/2} \right)$$

$$\left. - \frac{\Gamma}{4} \ln\left\{ \frac{\Gamma^2}{4} + (Eb - n/2 - E_o - \xi)^2 \right\} \right] \quad \ldots\ldots\ldots\ldots\ldots \quad (19)$$

For a given ξ the maximum of Equation (19) occurs at $Eb = E_o + \xi/2$ and is given by

$$\phi_5 \max \; (\xi) = \frac{\sigma_r \Gamma}{2\varepsilon n} \left[(\xi + n) \tan^{-1}\left(\frac{\xi + n}{\Gamma} \right) - (\xi - n) \tan^{-2} \left(\frac{\xi - n}{\Gamma} \right) \right.$$

$$\left. - \frac{\Gamma}{2} \ln\left\{ \frac{\Gamma^2}{4} + \left(\frac{n + \xi}{\Gamma} \right)^2 \right\} + \frac{\Gamma}{2} \ln\left\{ \frac{\Gamma^2}{4} + \left(\frac{n - \xi}{\Gamma} \right)^2 \right\} \right] \quad .. \quad (20)$$

Equation (19) has been used to generate a number of simulated thin target yield curves examples of which are shown in Figures 8 and 9 for values of $n = 2.265$ keV and $\xi = 0.1$ keV.

The FWHM, T(0.5), of the function $\phi_5(Eb)$ is not, however, given by the quadratic addition of Γ, ξ and n, that is

$$T(0.5) \neq \left[\Gamma^2 + \xi^2 + n^2\right]^{\frac{1}{2}}$$

We have been unable to find a general parameterization for T(0.5) but can illustrate the deviation from quadratic addition by a number of examples.

For a fixed value of $n = 2.265$ keV, T(0.5) was obtained, as a function of target thickness, for several values of Γ by numerical solution of Equations (19) and (20). The values obtained were compared with the FWHM given by quadratic addition for identical parameter values. Results for three fluorine resonances are shown in Figures 10 to 12. Quadratic addition overestimates the observed FWHM and maximum error occurs when $\xi = (n^2 + \Gamma^2)^{\frac{1}{2}}$. As the ratio $\Gamma/n \rightarrow \infty$ (or approximately $\Gamma/n > 17$) the observed yield curve tends to the integral of a slit-function over a Breit-Wigner. This case has already been considered. As the ratio $\Gamma/n \rightarrow 0$ (or approximately $\Gamma/n < 0.01$) the observed yield curve tends to the integral of a slit-function over another slit function, which for $n = \xi$ is a triangular function of FWHM n. Under the same conditions the FWHM predicted by quadratic addition is $n\sqrt{2}$. The maximum percentage deviation from quadratic addition is therefore asymptotic to the value -41.42 per cent as the ratio $\Gamma/n \rightarrow 0$. The situation is summarized in Figures 13

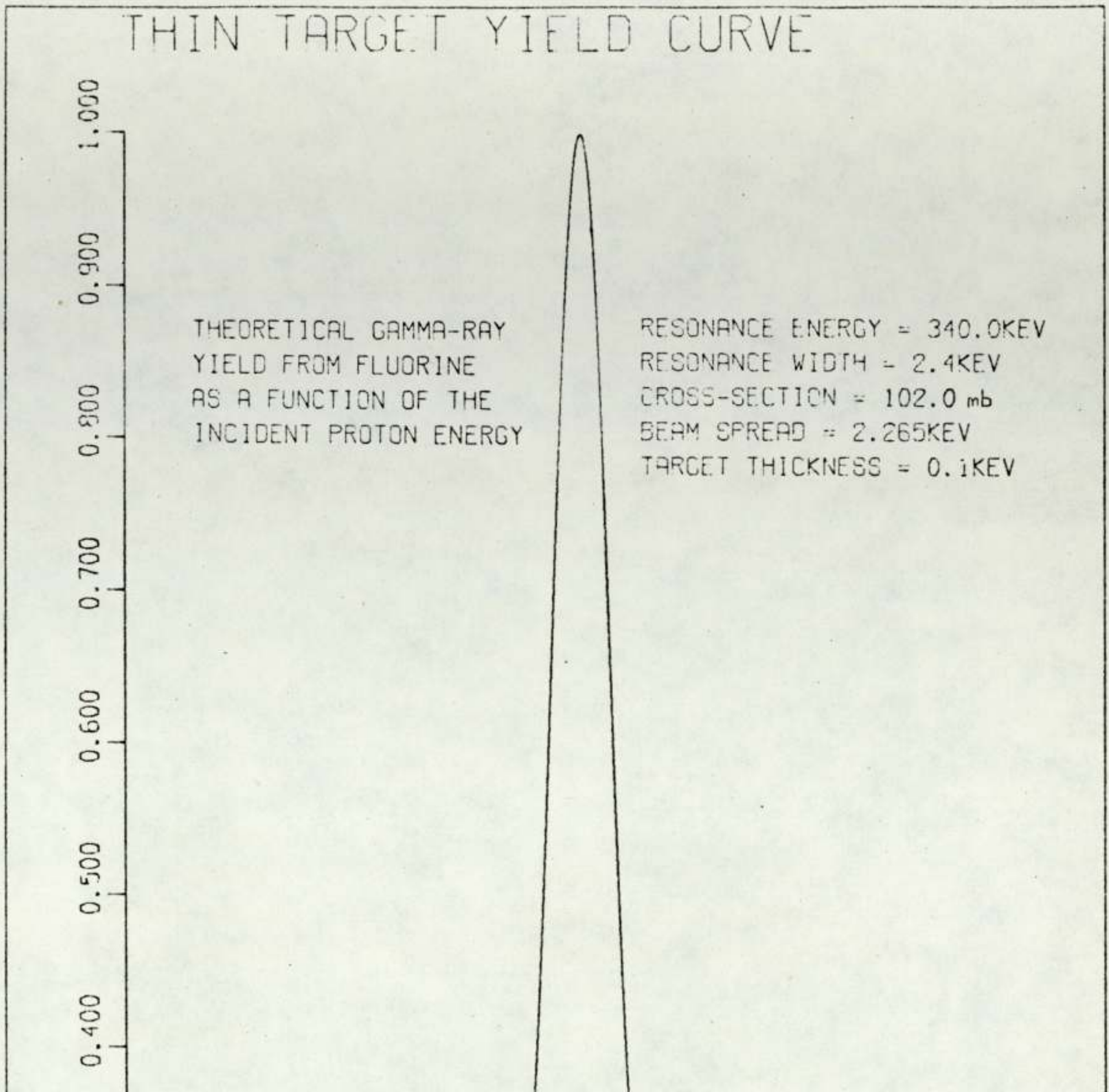
THIN TARGET YIELD CURVE
THEORETICAL GAMMA-RAY
YIELD FROM FLUORINE
AS A FUNCTION OF THE
INCIDENT PROTON ENERGY
RESONANCE ENERGY = 340.0KEV
RESONANCE WIDTH = 2.4KEV
CROSS-SECTION = 102.0 mb
BEAM SPREAD = 2.265KEV
TARGET THICKNESS = 0.1KEV
RELATIVE YIELD/MICROCOULOMB
0.000
0.100
0.200
0.300
0.400
0.500
0.600
0.700
0.800
0.900
1.000
320
330
340
350
360
PROTON ENERGY (KEV)

Figure 8

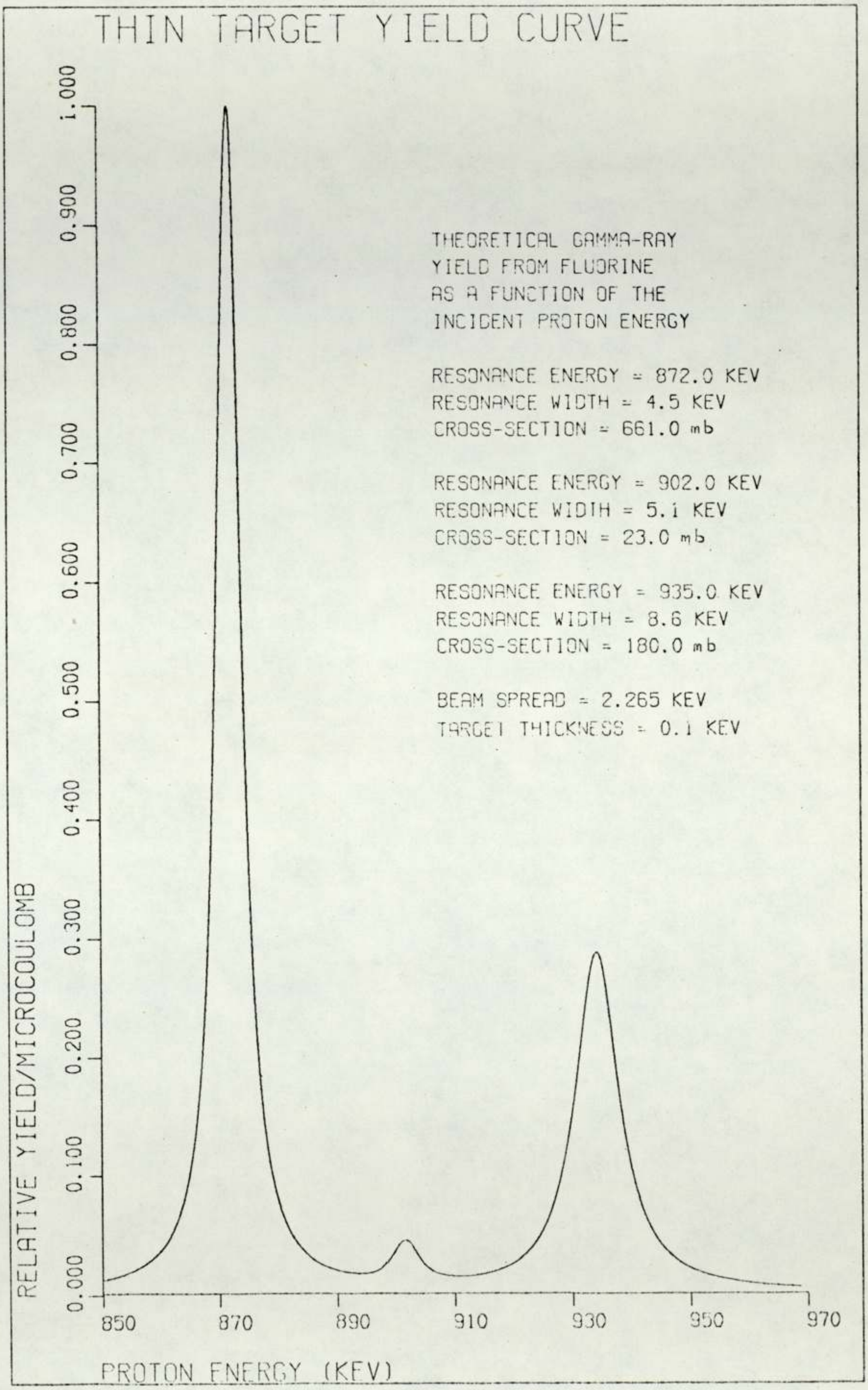
THIN TARGET YIELD CURVE
THEORETICAL GAMMA-RAY
YIELD FROM FLUORINE
AS A FUNCTION OF THE
INCIDENT PROTON ENERGY
RESONANCE ENERGY = 872.0 KEV
RESONANCE WIDTH = 4.5 KEV
CROSS-SECTION = 661.0 mb
RESONANCE ENERGY = 902.0 KEV
RESONANCE WIDTH = 5.1 KEV
CROSS-SECTION = 23.0 mb
RESONANCE ENERGY = 935.0 KEV
RESONANCE WIDTH = 8.6 KEV
CROSS-SECTION = 180.0 mb
BEAM SPREAD = 2.265 KEV
TARGET THICKNESS = 0.1 KEV
RELATIVE YIELD/MICROCOULOMB
0.000
0.100
0.200
0.300
0.400
0.500
0.600
0.700
0.800
0.900
1.000
850
870
890
910
930
950
970
PROTON ENERGY (KEV)

Figure 9

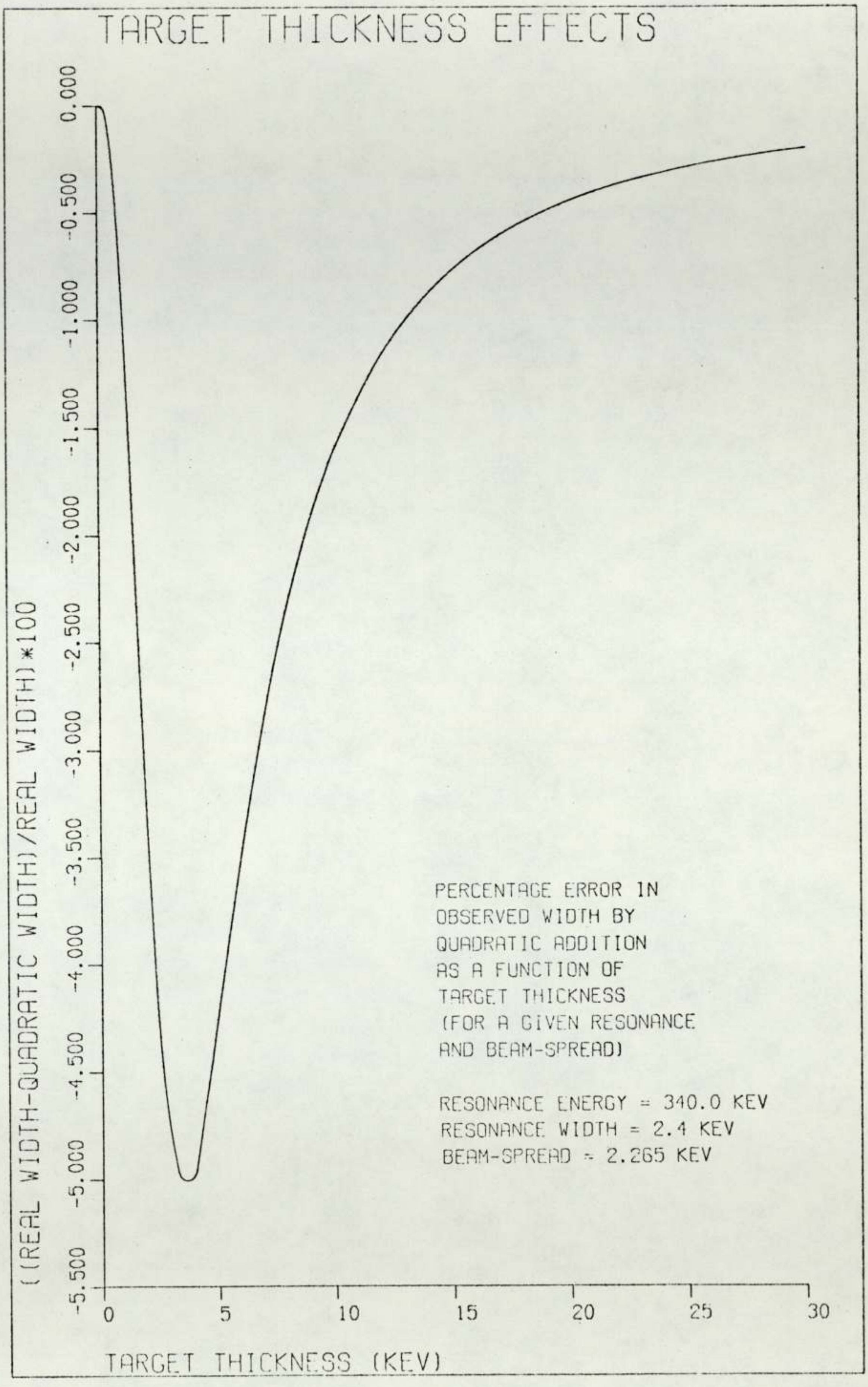
TARGET THICKNESS EFFECTS
((REAL WIDTH-QUADRATIC WIDTH)/REAL WIDTH)*100
0.000
-0.500
-1.000
-1.500
-2.000
-2.500
-3.000
-3.500
-4.000
-4.500
-5.000
-5.500
0
5
10
15
20
25
30
TARGET THICKNESS (KEV)
PERCENTAGE ERROR IN
OBSERVED WIDTH BY
QUADRATIC ADDITION
AS A FUNCTION OF
TARGET THICKNESS
(FOR A GIVEN RESONANCE
AND BEAM-SPREAD)
RESONANCE ENERGY = 340.0 KEV
RESONANCE WIDTH = 2.4 KEV
BEAM-SPREAD = 2.265 KEV

Figure 10

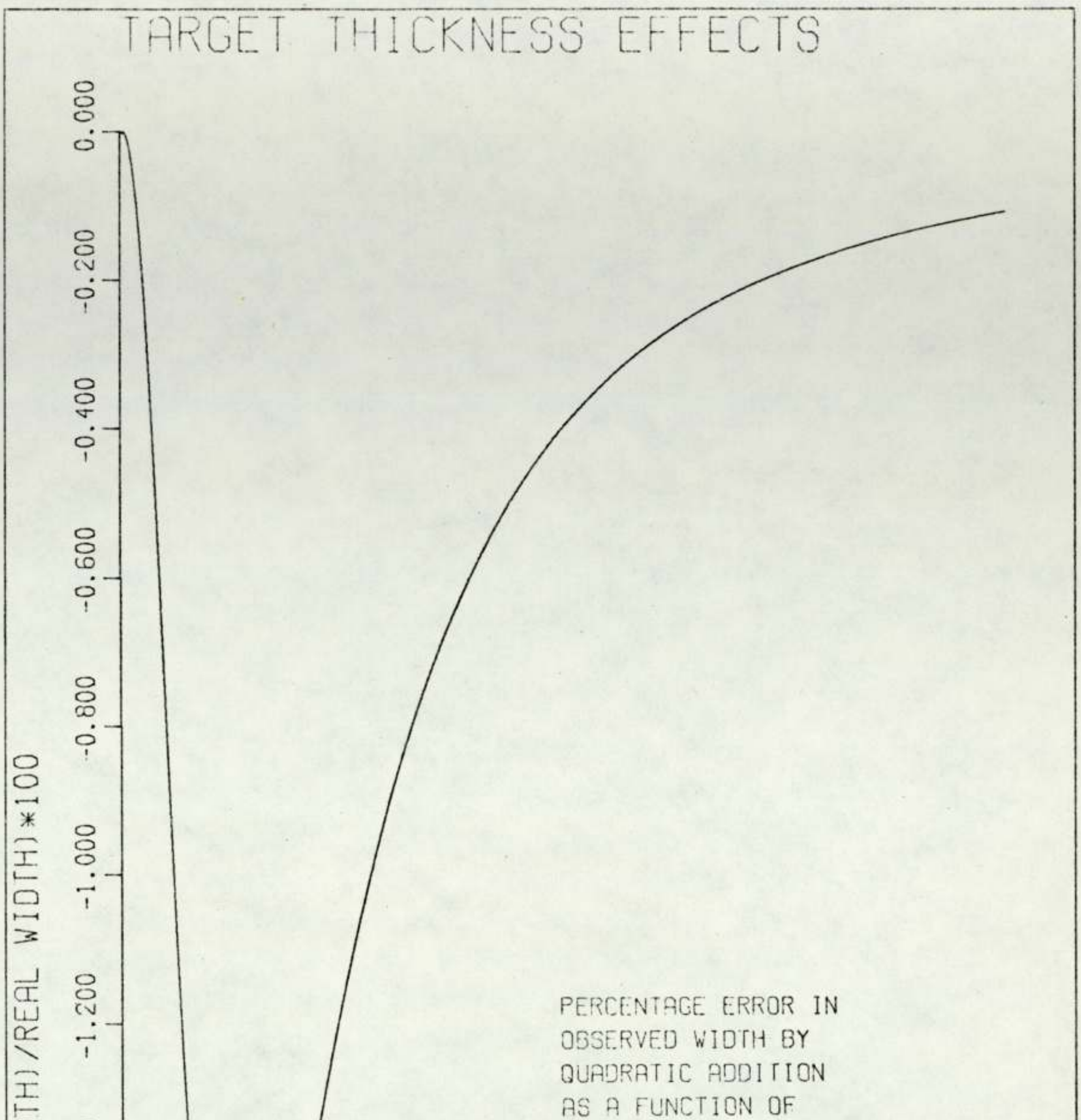
TARGET THICKNESS EFFECTS
((REAL WIDTH-QUADRATIC WIDTH)/REAL WIDTH)*100
0.000
-0.200
-0.400
-0.600
-0.800
-1.000
-1.200
-1.400
-1.600
-1.800
-2.000
0
5
10
15
20
25
30
35
40
TARGET THICKNESS (KEV)
PERCENTAGE ERROR IN
OBSERVED WIDTH BY
QUADRATIC ADDITION
AS A FUNCTION OF
TARGET THICKNESS
(FOR A GIVEN RESONANCE
AND BEAM-SPREAD)
RESONANCE ENERGY = 872.0 KEV
RESONANCE WIDTH = 4.5 KEV
BEAM-SPREAD = 2.265 KEV

Figure 11

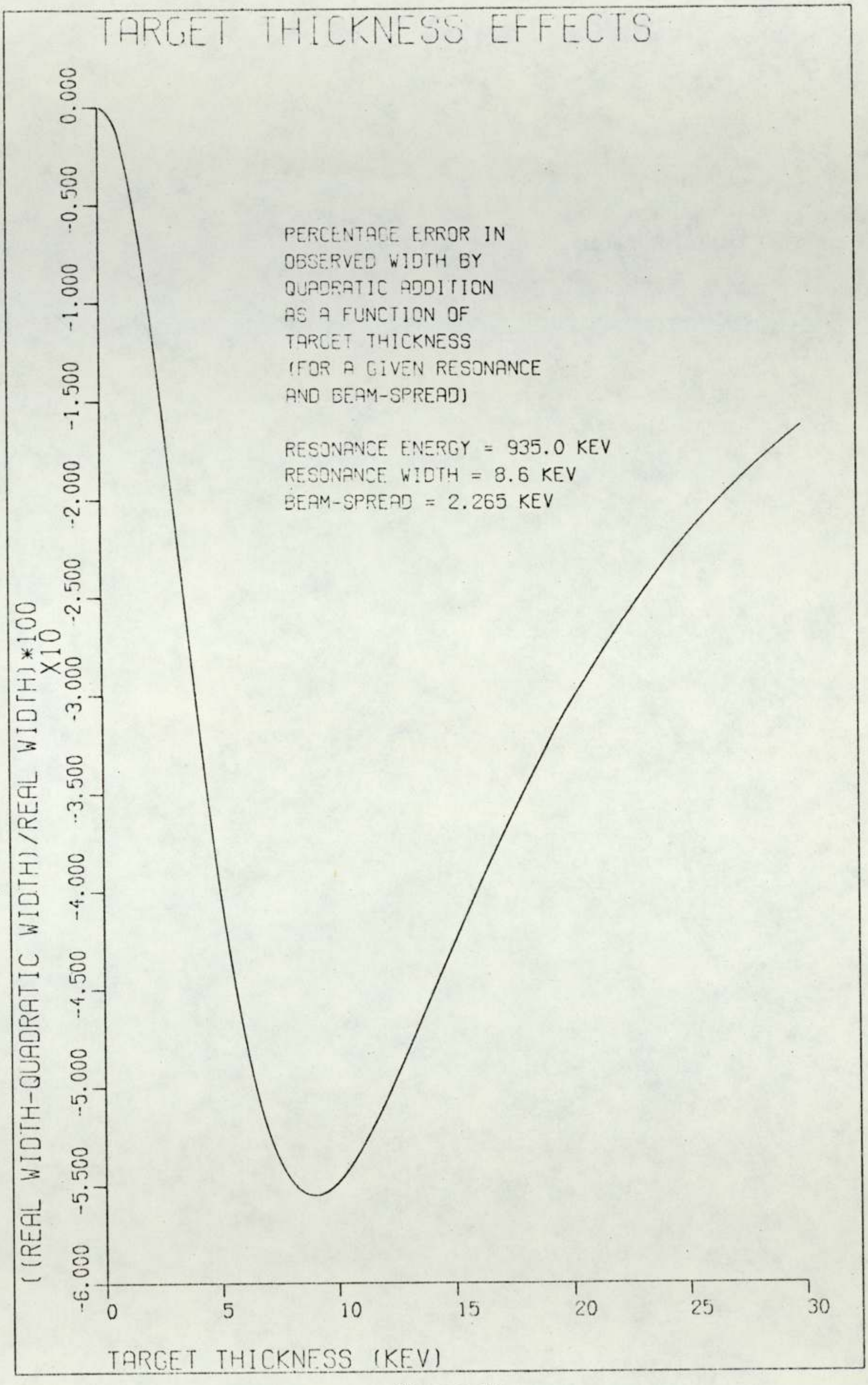
TARGET THICKNESS EFFECTS
PERCENTAGE ERROR IN
OBSERVED WIDTH BY
QUADRATIC ADDITION
AS A FUNCTION OF
TARGET THICKNESS
(FOR A GIVEN RESONANCE
AND BEAM-SPREAD)
RESONANCE ENERGY = 935.0 KEV
RESONANCE WIDTH = 8.6 KEV
BEAM-SPREAD = 2.265 KEV
((REAL WIDTH-QUADRATIC WIDTH)/REAL WIDTH)*100
X10
0.000
-0.500
-1.000
-1.500
-2.000
-2.500
-3.000
-3.500
-4.000
-4.500
-5.000
-5.500
-6.000
0
5
10
15
20
25
30
TARGET THICKNESS (KEV)

Figure 12

and 14 which show the maximum percentage deviation from quadratic addition as a function of the natural resonance width and incident beam energy dispersion respectively.

Quadratic subtraction of n and Γ from the FWHM of an experimental yield curve, therefore, leads to an underestimation of target thickness. For parameter values representative of the author's experimental data the maximum deviation from quadratic addition is less than five per cent. Under high resolution conditions, however, with beam energy dispersion and target thickness of the order of 0.5 keV and natural resonance widths of 100 eV, or less, the maximum deviation from quadratic addition is of the order of 20 per cent.

Figures 15 to 17 show the variation of T(0.5) and ϕ_5 max (ξ) as functions of target thickness. The curves were obtained by numerical solution of Equations (19) and (20) for the parameter values indicated. For a target thickness equivalent to approximately half the natural resonance, or less, T(0.5) is a slowly varying function, and ϕ_5 max (ξ) a rapidly varying function of target thickness.

If we consider the thick target case, as $\xi \to \infty$ Equation (18) reduces to

$$\phi_5 (E) = \frac{\sigma_r \Gamma}{2\varepsilon} \left[\tan^{-1} \frac{E - E_o}{\Gamma/2} + \frac{\pi}{2} \right]$$

And with beam energy dispersion

$$\phi_7 (Eb) = \frac{\sigma_r \Gamma}{2\varepsilon} \int_{Eb-n/2}^{Eb+n/2} \left[\tan^{-1} \frac{E_v - E_o}{\Gamma/2} + \frac{\pi}{2} \right] D (E' + E_v) \, dE_v$$

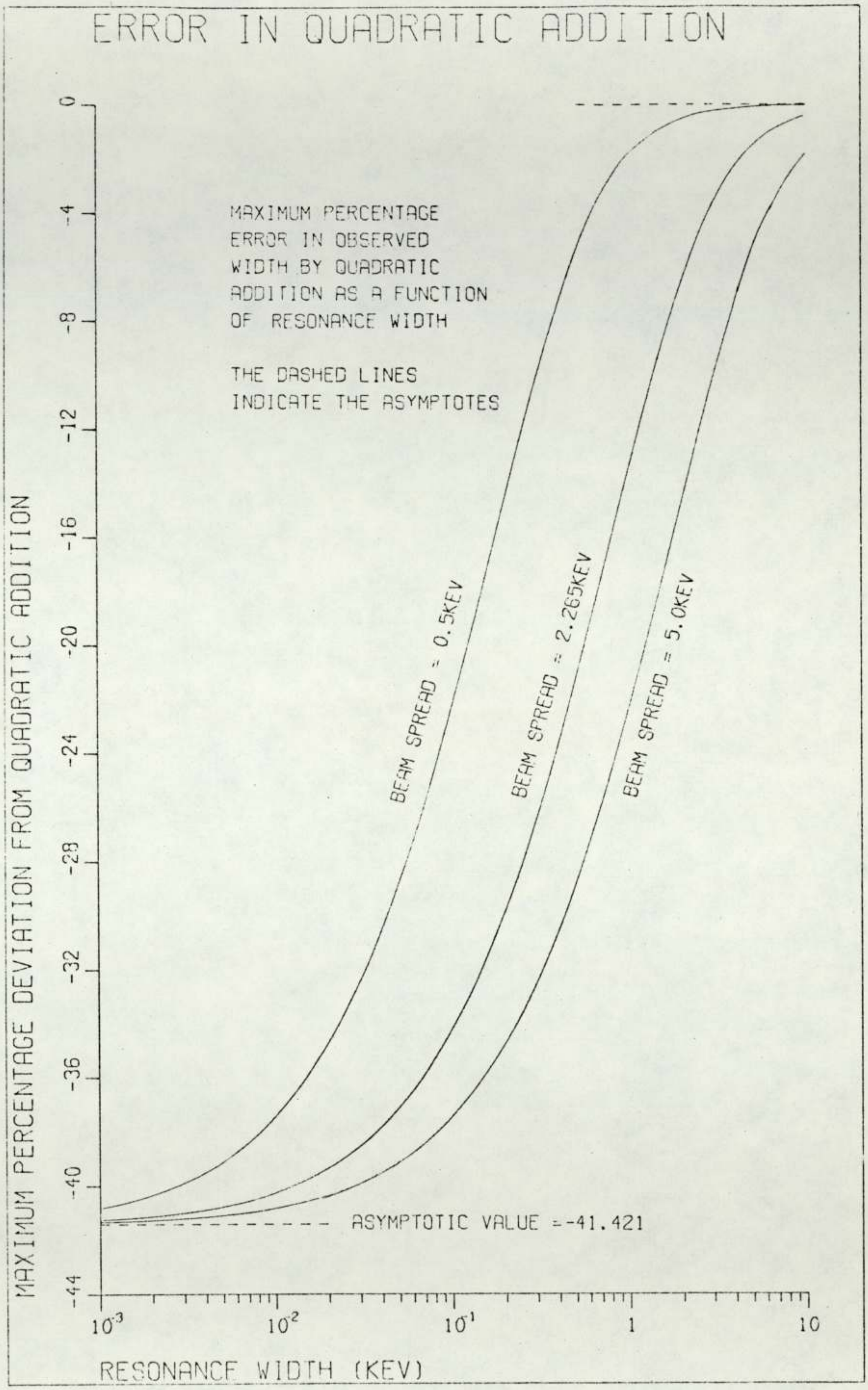

ERROR IN QUADRATIC ADDITION
MAXIMUM PERCENTAGE ERROR IN OBSERVED WIDTH BY QUADRATIC ADDITION AS A FUNCTION OF RESONANCE WIDTH
THE DASHED LINES INDICATE THE ASYMPTOTES
BEAM SPREAD = 0.5KEV
BEAM SPREAD = 2.265KEV
BEAM SPREAD = 5.0KEV
ASYMPTOTIC VALUE =-41.421
MAXIMUM PERCENTAGE DEVIATION FROM QUADRATIC ADDITION
0
-4
-8
-12
-16
-20
-24
-28
-32
-36
-40
-44
10^{-3}
10^{-2}
10^{-1}
1
10
RESONANCE WIDTH (KEV)

Figure 13

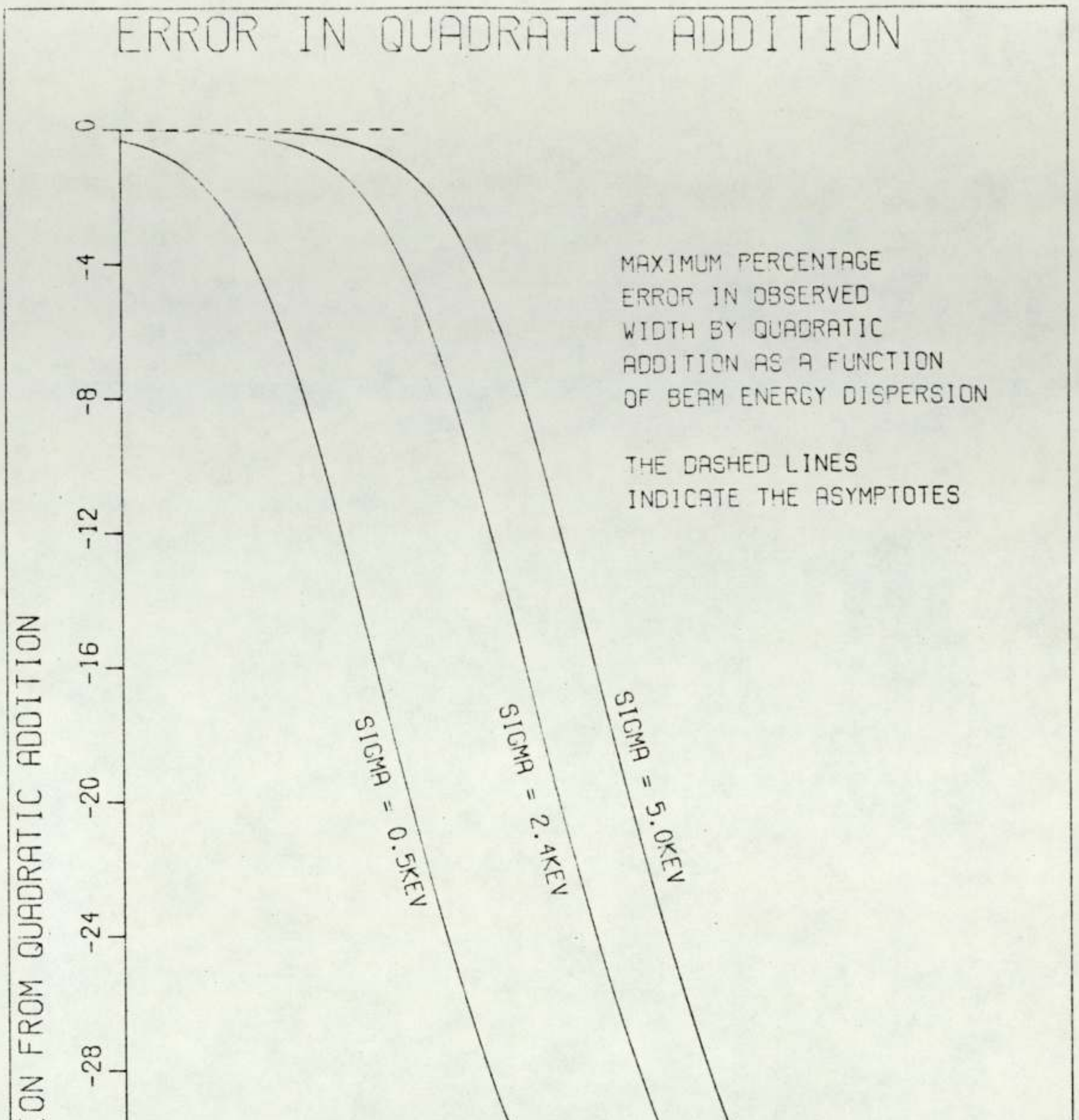
ERROR IN QUADRATIC ADDITION
MAXIMUM PERCENTAGE ERROR IN OBSERVED WIDTH BY QUADRATIC ADDITION AS A FUNCTION OF BEAM ENERGY DISPERSION
THE DASHED LINES INDICATE THE ASYMPTOTES
SIGMA = 0.5KEV
SIGMA = 2.4KEV
SIGMA = 5.0KEV
ASYMPTOTIC VALUE =-41.421
MAXIMUM PERCENTAGE DEVIATION FROM QUADRATIC ADDITION
0
-4
-8
-12
-16
-20
-24
-28
-32
-36
-40
-44
10^{-1}
1
10
10^2
10^3
BEAM ENERGY DISPERSION (KEV)

Figure 14

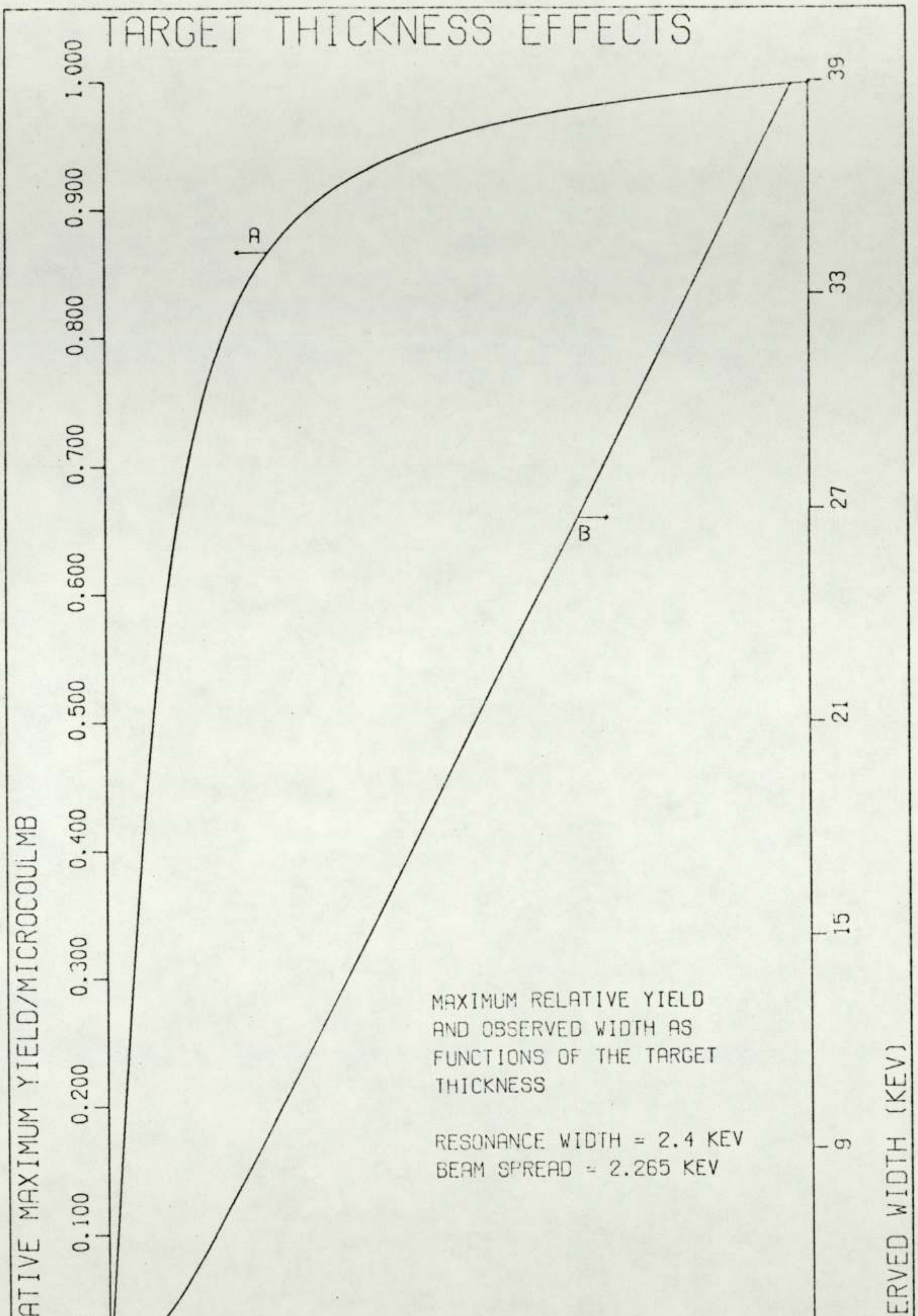
TARGET THICKNESS EFFECTS
RELATIVE MAXIMUM YIELD/MICROCOULMB
0.000
0.100
0.200
0.300
0.400
0.500
0.600
0.700
0.800
0.900
1.000
OBSERVED WIDTH (KEV)
3
9
15
21
27
33
39
TARGET THICKNESS (KEV)
0
4
8
12
16
20
24
28
32
36
40
A
B
MAXIMUM RELATIVE YIELD
AND OBSERVED WIDTH AS
FUNCTIONS OF THE TARGET
THICKNESS
RESONANCE WIDTH = 2.4 KEV
BEAM SPREAD = 2.265 KEV

Figure 15

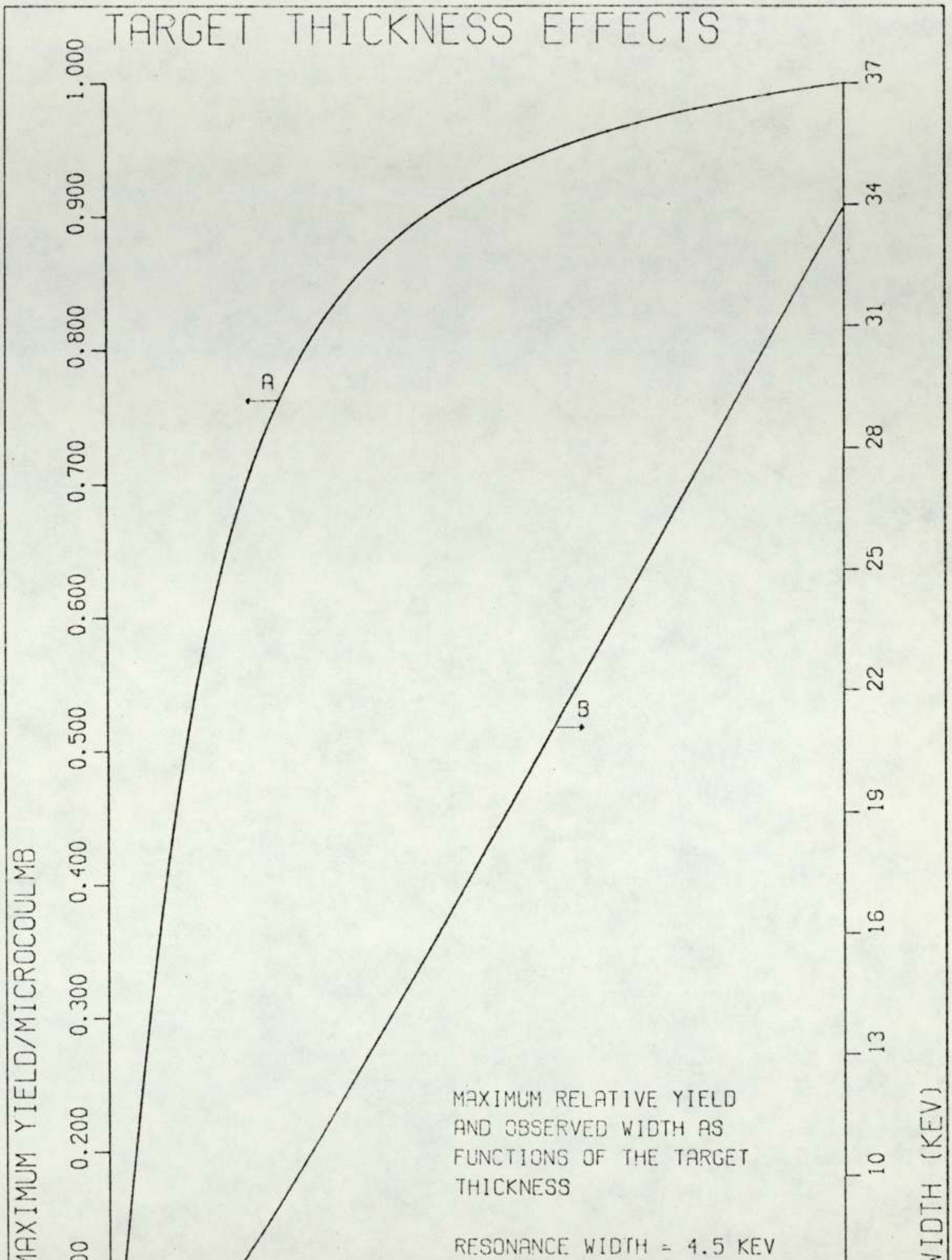
TARGET THICKNESS EFFECTS
RELATIVE MAXIMUM YIELD/MICROCOULMB
0.000
0.100
0.200
0.300
0.400
0.500
0.600
0.700
0.800
0.900
1.000
OBSERVED WIDTH (KEV)
4
7
10
13
16
19
22
25
28
31
34
37
TARGET THICKNESS (KEV)
0
4
8
12
16
20
24
28
32
36
40
A
B
MAXIMUM RELATIVE YIELD
AND OBSERVED WIDTH AS
FUNCTIONS OF THE TARGET
THICKNESS
RESONANCE WIDTH = 4.5 KEV
BEAM SPREAD = 2.265 KEV

Figure 16

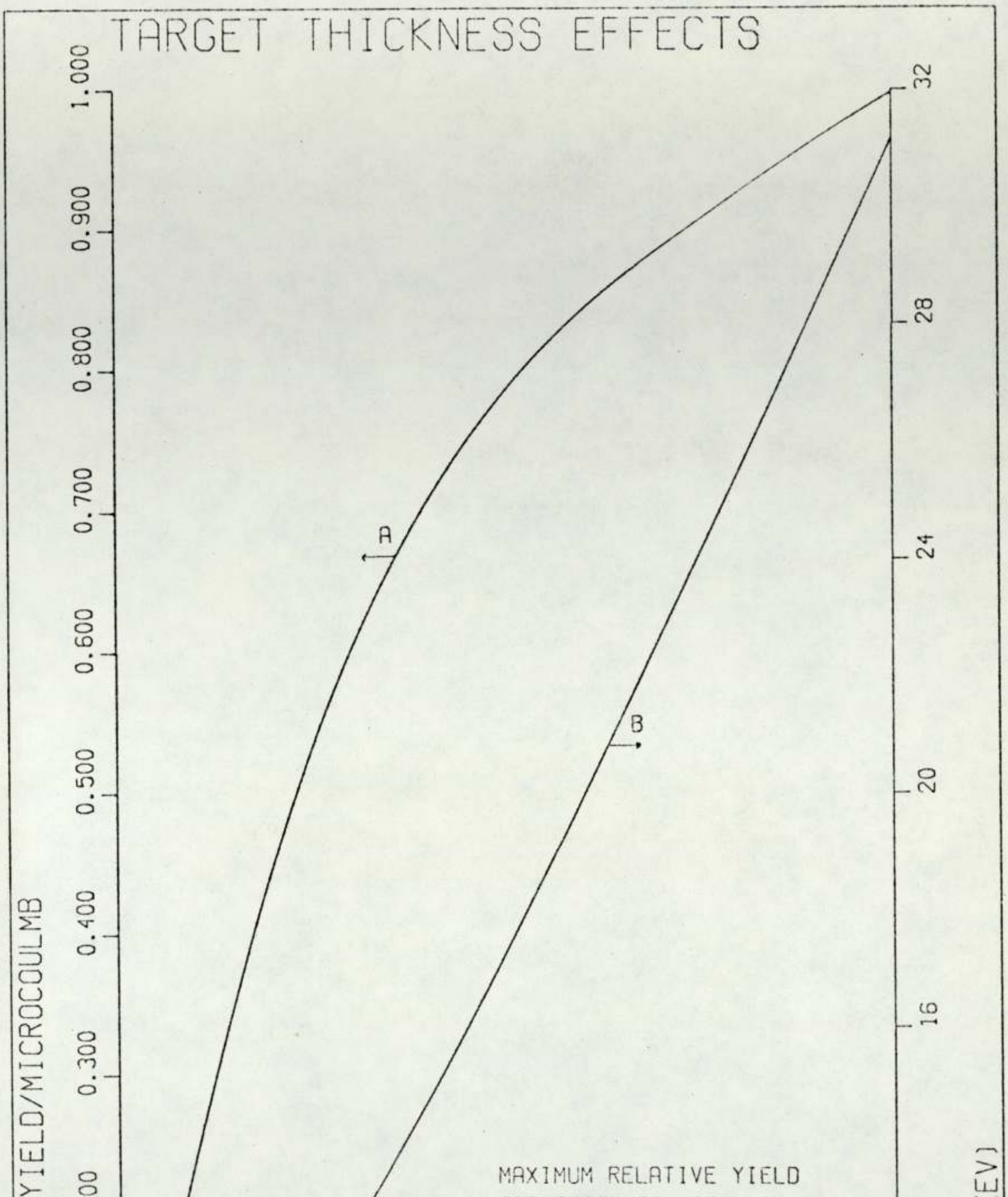
TARGET THICKNESS EFFECTS
RELATIVE MAXIMUM YIELD/MICROCOULMB
0.000
0.100
0.200
0.300
0.400
0.500
0.600
0.700
0.800
0.900
1.000
OBSERVED WIDTH (KEV)
8
12
16
20
24
28
32
0
5
10
15
20
25
30
TARGET THICKNESS (KEV)
A
B
MAXIMUM RELATIVE YIELD
AND OBSERVED WIDTH AS
FUNCTIONS OF THE TARGET
THICKNESS
RESONANCE WIDTH = 8.6 KEV
BEAM SPREAD = 2.265 KEV

Figure 17

Integrating by parts we obtain

$$\phi_7\ (Eb) = \frac{\sigma_r \Gamma}{2\varepsilon n} \left[(Eb + n/2 - E_o) \tan^{-1}\left(\frac{Eb + n/2 - E_o}{\Gamma/2} \right) \right.$$

$$- (Eb - n/2 - E_o) \tan^{-1}\left(\frac{Eb - n/2 - E_o}{\Gamma/2} \right)$$

$$\frac{\Gamma}{4} \ln\left\{ \frac{\Gamma^2}{4} + (Eb + n/2 - E_o)^2 \right\} + \frac{\Gamma}{4} \ln\left\{ \frac{\Gamma^2}{4} + (Eb - n/2 - E_o)^2 \right\}$$

$$\left. + \frac{n\pi}{2} \right] \quad \ldots\ldots\ldots\ldots\ldots\ldots(21)$$

where all terms have been defined previously. Examples of the type of curve generated by Equation (21) are shown in Figures 18 and 19. The energy $E_{\frac{1}{2}}$, at half the plateau yield, corresponds to the resonance energy E_o. The interquartile width, $F_{\frac{3}{4}} - E_{\frac{1}{4}} = (n^2 + \Gamma^2)^{\frac{1}{2}}$.

STRAGGLING EFFECTS

The shape of experimental yield curves is also affected by straggling, that is, the discrete nature of the energy loss of the bombarding particles in the target medium.

Several authors have pointed out that neglecting straggling leads to an underestimation of resonance energy and width as derived from experimental data. Observation of effects associated with straggling are normally considered to be restricted to high resolution beams ($n < 200$ eV) and sharp resonances ($\Gamma < 1$ keV). CUNHA and CORRÊA (1975)

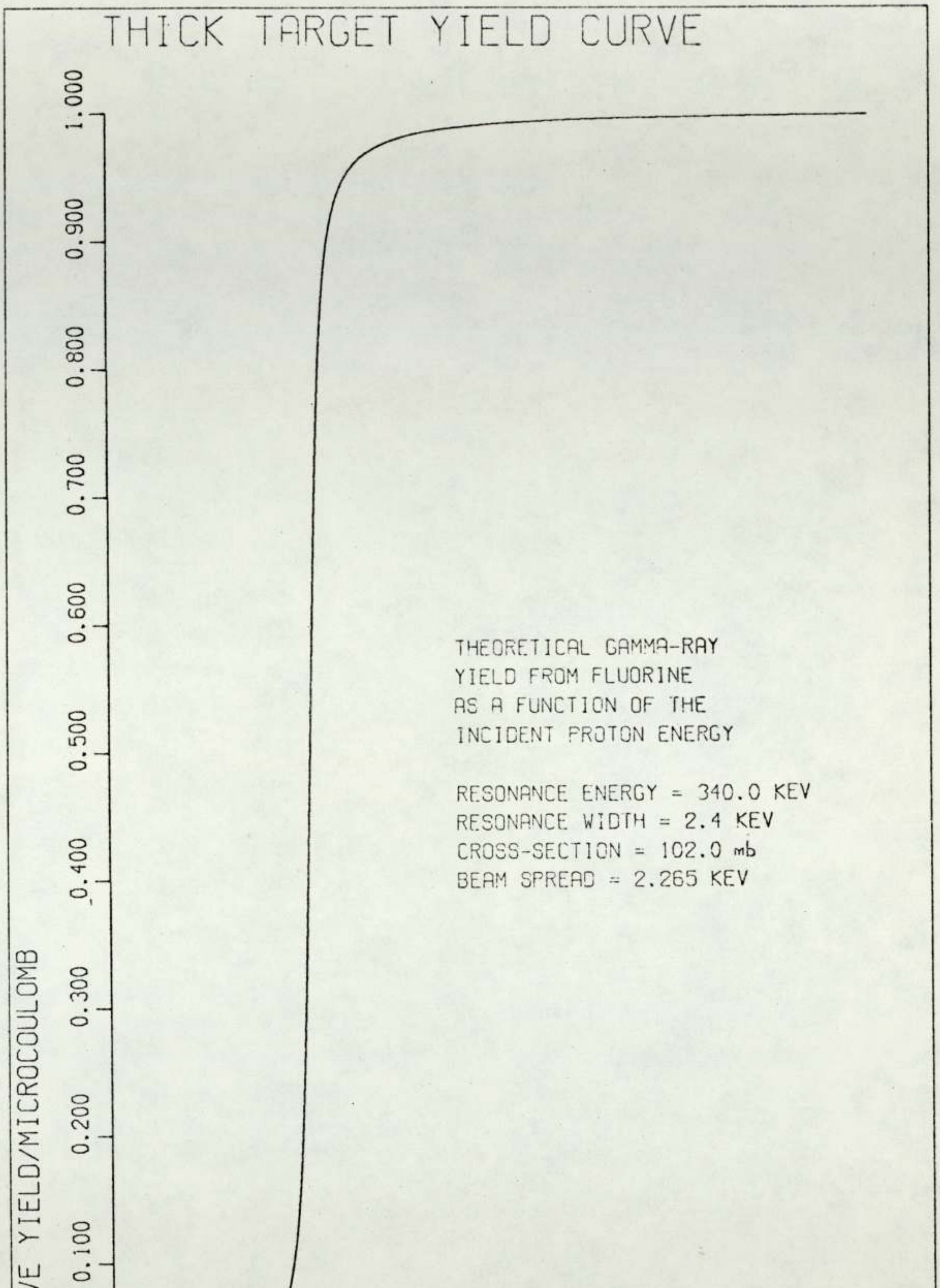
THICK TARGET YIELD CURVE
RELATIVE YIELD/MICROCOULOMB
0.000
0.100
0.200
0.300
0.400
0.500
0.600
0.700
0.800
0.900
1.000
300
325
350
375
400
425
450
PROTON ENERGY (KEV)
THEORETICAL GAMMA-RAY
YIELD FROM FLUORINE
AS A FUNCTION OF THE
INCIDENT PROTON ENERGY
RESONANCE ENERGY = 340.0 KEV
RESONANCE WIDTH = 2.4 KEV
CROSS-SECTION = 102.0 mb
BEAM SPREAD = 2.265 KEV

Figure 18

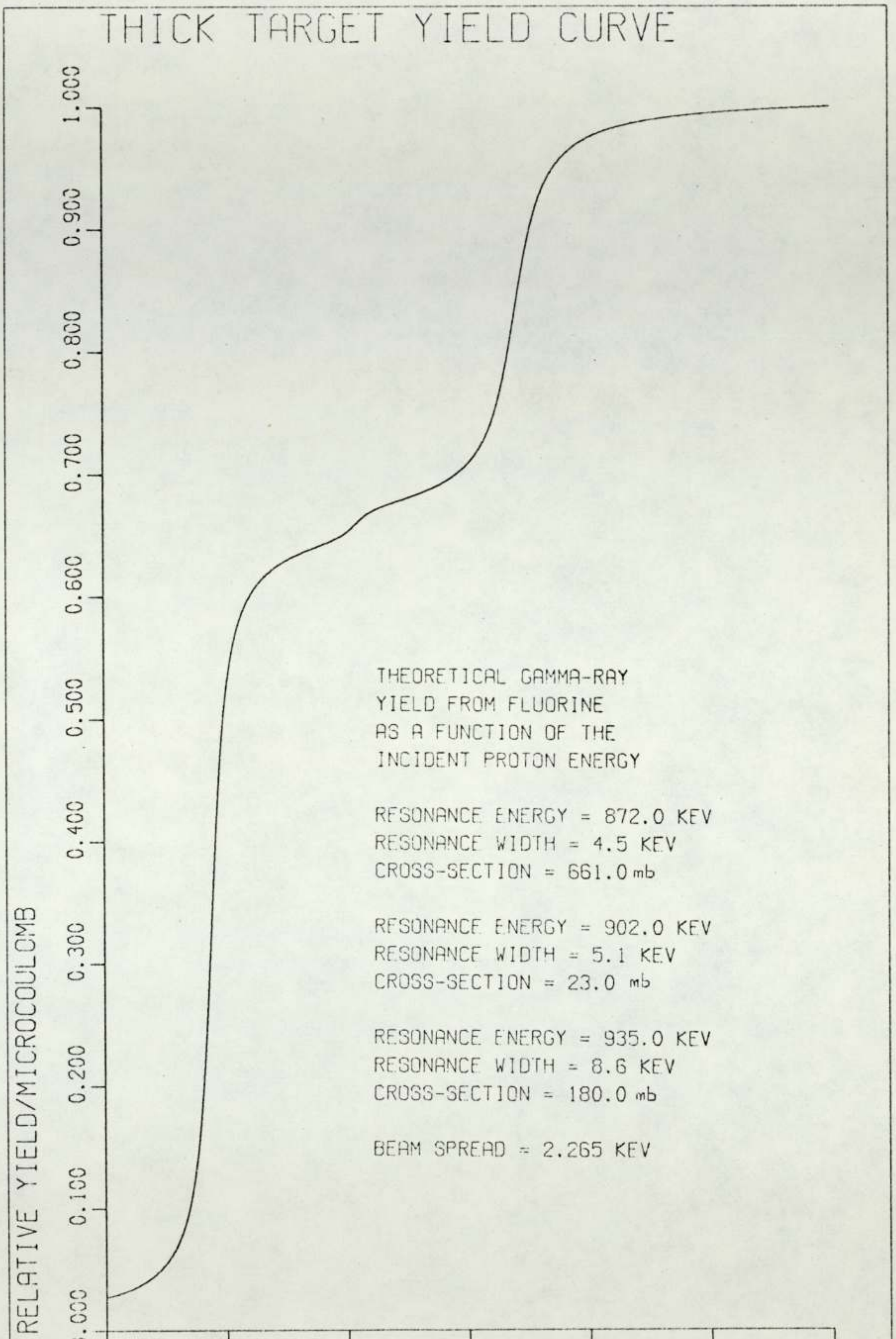

THICK TARGET YIELD CURVE

THEORETICAL GAMMA-RAY
YIELD FROM FLUORINE
AS A FUNCTION OF THE
INCIDENT PROTON ENERGY

RESONANCE ENERGY = 872.0 KEV
RESONANCE WIDTH = 4.5 KEV
CROSS-SECTION = 661.0 mb

RESONANCE ENERGY = 902.0 KEV
RESONANCE WIDTH = 5.1 KEV
CROSS-SECTION = 23.0 mb

RESONANCE ENERGY = 935.0 KEV
RESONANCE WIDTH = 8.6 KEV
CROSS-SECTION = 180.0 mb

BEAM SPREAD = 2.265 KEV

Figure 19

have recently shown that the discrete nature of the energy loss of charged particles must be taken into account for a wide variety of beam energy dispersions and resonance widths. By considering a hypothetical resonance at $E_o = 1$ MeV for the reaction $Al^{27}(p,\gamma)\ Si^{28}$ they have shown that the thin target maximum yield value, ϕ_5 max (ξ), approaches asymptotically the value $E_o + \xi/2$ as n and Γ increase. For thick targets, however, the value $E_o - E_{\frac{1}{2}}$ increases asymptotically to a maximum with increasing n and Γ. By extrapolation of their data for appropriate values of n and Γ we consider that the displacement of the thin target maxima is unlikely to exceed 0.1 keV for our experimental data. Similarly for thick targets $E_{\frac{1}{2}}$ would be lower than E_o by less than 0.2 keV. Displacements of this order are considered negligible in comparison with the absolute accuracy of the calibration of the terminal potential of the accelerator. The phenomenon of charged particle straggling is considered in more detail in Appendix IV.

COMPARISON WITH EXPERIMENTAL DATA

We now examine if the yield curves predicted by Equation (19) and (21) represent a reasonable approximation to experimental yield curves obtained using an incident proton beam.

The operational characteristics of the Dynamitron, discussed in an earlier section, did not normally permit the accelerator to run at terminal potentials below 1 MeV. A number of measurements were, however, obtained in the viscinity of the 872 keV and 935 keV resonances in the $F^{19}(p,\alpha\gamma)O^{16}$ reaction cross-section. At such low terminal potentials the stability of the accelerator is considerably poorer than under normal operating conditions, particularly when supplying the small beam currents required ($\sim 0.1\mu A$).

Table 4 shows a summary of the data obtained.

The maximum yield from the thickest target ($\xi = 1.4$ keV) in set A of Table 4 was normalized to curve B of Figure 16. The observed widths and normalized maximum yields are in good agreement with the predictions of Equations (19) and (20). A more serious discrepancy exists in the location of the maxima which occur some 5 keV higher than expected. The origin of the discrepancy is considered to be error in the calibration of the terminal potential. Comparison of Sets A and B of Table 4 indicates that the calibration error is time dependent.

As it was not possible to use the location of the maxima as a test of the validity of the theoretical predictions, Equation(19) has been fitted to one of the experimental data sets. This was achieved by means of a general purpose fitting procedure developed by SALMON and BOOKER (1972). During preliminary fitting attempts using Equation (19) as the "model" it was found that experimental values were consistently higher than fitted values on the high energy side of the curve. Careful inspection of the data revealed that the yield curve is not quite symmetrical about the maximum value. The observed yield was therefore considered to consist of a thin target yield curve superimposed on a thick target yield curve of much lower intensity. A low intensity "thick target background" would arise from slight fluorine contamination of the beam transport system. A "better" fit to the experimental data was obtained by using a combination of Equations (19) and (21).

TABLE 4

Thin Target Data $F^{19}(p,\alpha\gamma)O^{16}$ Resonances H_1^+ Incident Beam

E_{max} keV	FWHM keV	ξ keV	$E_o + \xi/2$ keV	$E_{max}-(E_o+\xi/2)$ keV	Yield(E_{max}) Counts/μC	*Normalized Yield
^{A}878.0±0.6	5.2 ± 0.1	∿ 1.4	∿ 872.7	∿ 5.3	5057 ± 70	880 ± 12
878.0±0.6	5.2 ± 0.1	< 1.4	∿ 872.7	∿ 5.3	2917 ± 50	508 ± 8
877.6±0.6	5.1 ± 0.1	∿ 0.9	∿ 872.4	∿ 5.1	792 ± 15	138 ± 3
B						
1344.0±0.9	7.2 ± 0.2	< 3.9	∿1346.0	∿ (-2.0)	-	-
876.0±0.6	5.2 ± 0.1	∿ 1.4	∿ 872.7	∿ 3.3	-	-

*Normalized to Curve B of Figure 16 at $\xi = 1.4$ keV

TABLE 5

Thick Target Data $F^{19}(p,\alpha\gamma)O^{16}$ Resonances H_1^+ Incident Beam

$E_{\frac{1}{2}}$ keV	E_o keV	$E_{\frac{1}{2}}-E_o$ keV	$E_{\frac{3}{4}}-E_{\frac{1}{4}}$ keV
878.2 ± 0.05	872.0	6.2 ± 0.05	5.6 ± 0.5
940.6 ± 0.5	935.0	5.6 ± 0.5	9.2 ± 0.6

The experimental data and fitted curve are shown in Figure 20* . The value of chi-squared obtained was 28.89, which, for 28 degrees of freedom gives a relatively high value of 0.43 for P. A plot of residuals for this fit exhibited a U-shaped scatter, however, and there is a large uncertainty in the final estimate for n of 2.4 ± 0.3 keV.

Only one thick target yield curve was obtained, using a proton beam, in the vicinity of the 872 keV, 902 keV and 935 keV resonances in the $F^{19}(p,\alpha\gamma)\ O^{16}$ reaction cross-section. The results are presented in Table 5. The data was fitted using a combination of equations of the same functional form as Equation (21). It was not possible to locate the position of the 902 keV resonance from the experimental data. The position of this resonance was not therefore used as a parameter of the fit but was assumed to occur at an energy 30 keV above the lower resonance. The value of chi-squared obtained was 37.0, which, for 34 degrees of freedom gives a value of 0.33 for P. The final estimate for n was 3.4 ± 0.3 keV. This value is 40 per cent greater than the value obtained from the fit to the thin target data.

The experimental data and fitted curve are shown in Figure 21. A poor fit was obtained in the plateau region above the 935 keV resonance where the experimental data is 2 per cent higher than the

---

* Note : The energy scales in Figures 20 and 21 have been renormalized for presentation purposes.

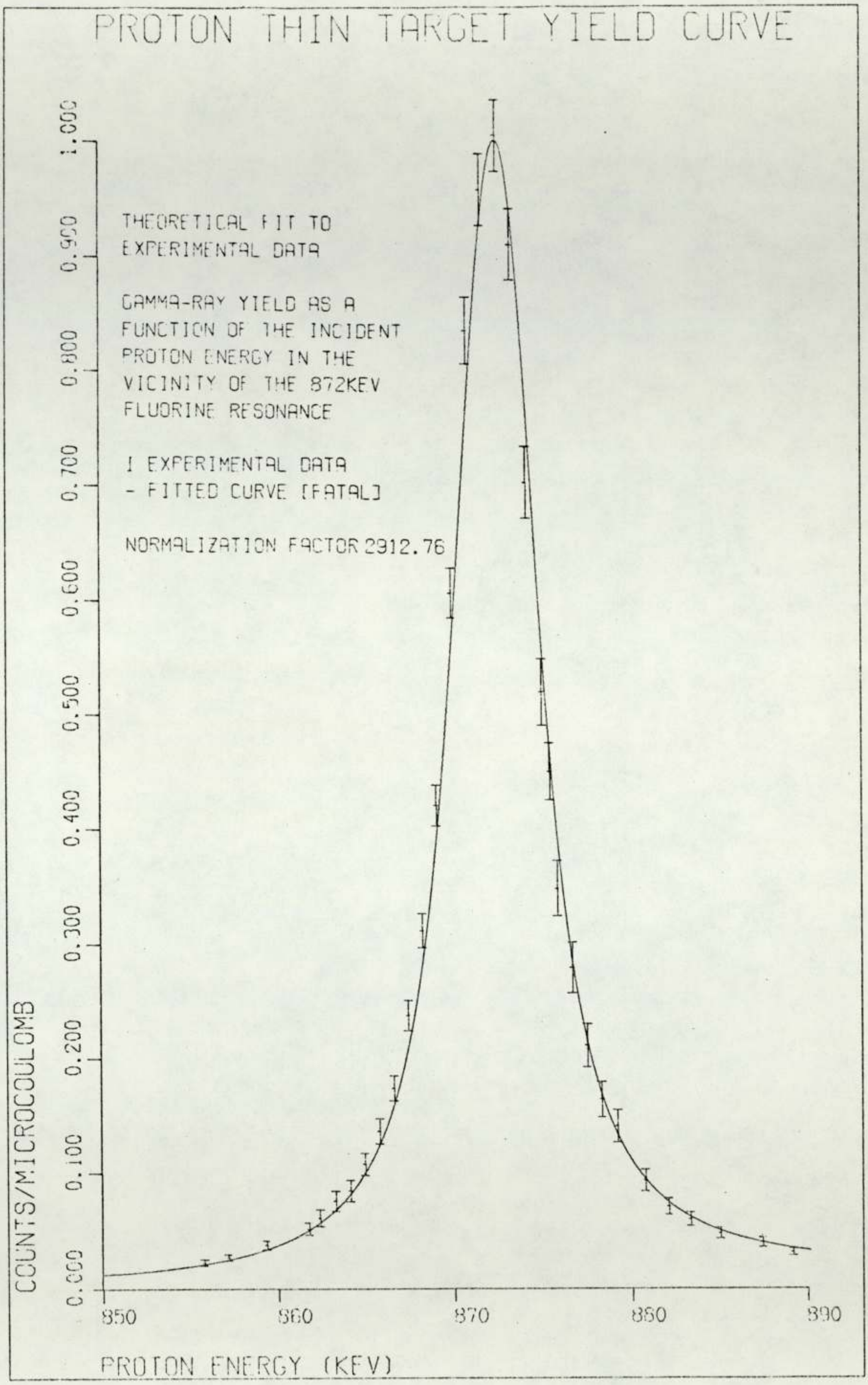
PROTON THIN TARGET YIELD CURVE
THEORETICAL FIT TO
EXPERIMENTAL DATA
GAMMA-RAY YIELD AS A
FUNCTION OF THE INCIDENT
PROTON ENERGY IN THE
VICINITY OF THE 872KEV
FLUORINE RESONANCE
I EXPERIMENTAL DATA
- FITTED CURVE [FATAL]
NORMALIZATION FACTOR 2912.76
COUNTS/MICROCOULOMB
0.000
0.100
0.200
0.300
0.400
0.500
0.600
0.700
0.800
0.900
1.000
850
860
870
880
890
PROTON ENERGY (KEV)

Figure 20

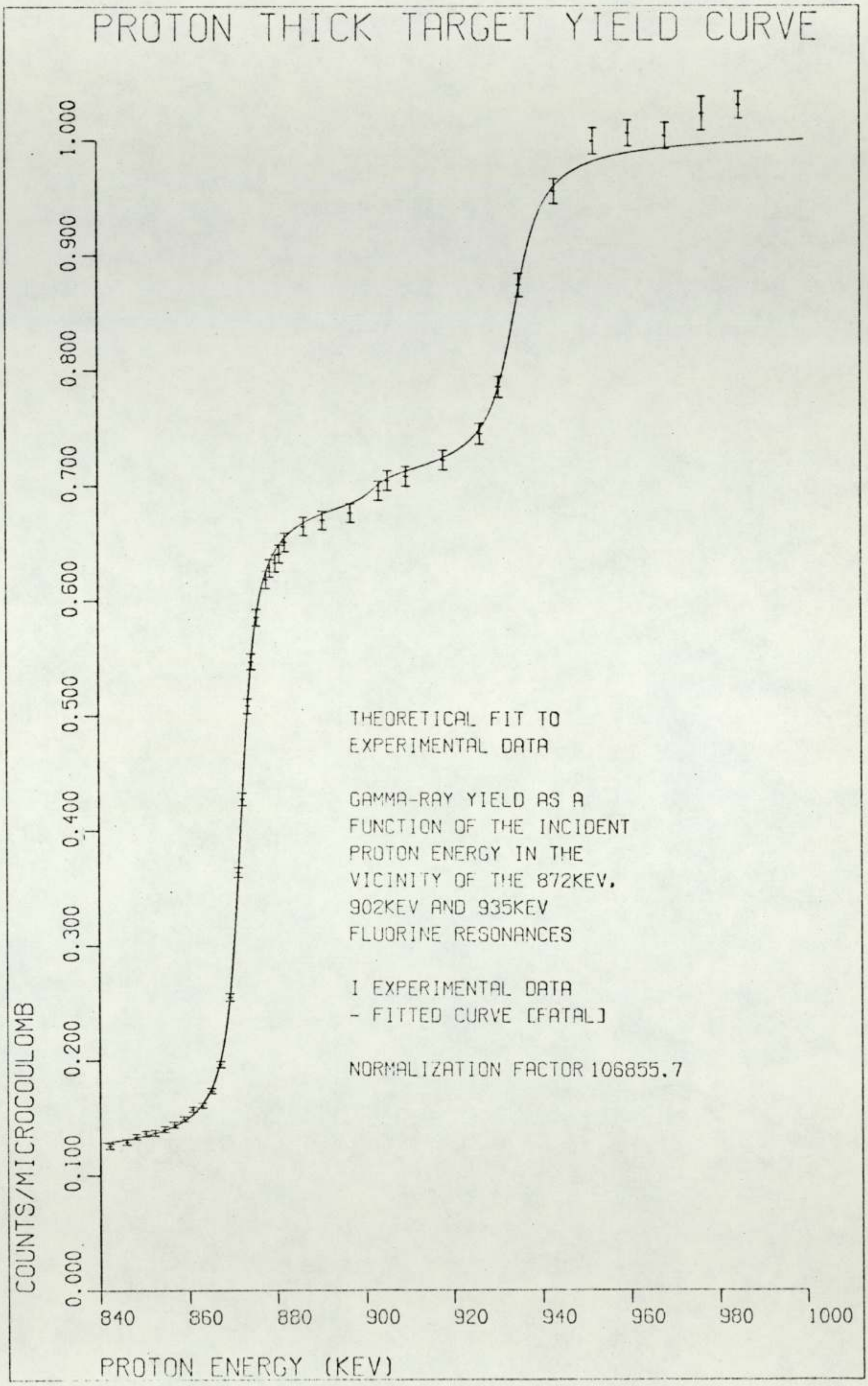
PROTON THICK TARGET YIELD CURVE
COUNTS/MICROCOULOMB
0.000
0.100
0.200
0.300
0.400
0.500
0.600
0.700
0.800
0.900
1.000
840
860
880
900
920
940
960
980
1000
PROTON ENERGY (KEV)
THEORETICAL FIT TO
EXPERIMENTAL DATA
GAMMA-RAY YIELD AS A
FUNCTION OF THE INCIDENT
PROTON ENERGY IN THE
VICINITY OF THE 872KEV,
902KEV AND 935KEV
FLUORINE RESONANCES
I EXPERIMENTAL DATA
- FITTED CURVE [FATAL]
NORMALIZATION FACTOR 106855.7

Figure 21

fitted curve. In fitting Equation (21) the variation of stopping power with energy was neglected. The proton stopping power in calcium fluoride in fact decreases by 5 per cent in the energy region 872 keV to 935 keV and the yield is inversely proportional to the stopping power.

It should be appreciated that even "successful" fitting of data to a model never proves the validity of that model. The computer programme used by the author bears the somewhat facetious acronym "FATAL" (fit anything to anything you like) to indicate that it is possible, after a fashion, to fit data to any empirical function. The fitting technique is one of the most widely used methods of analysis of prompt nuclear activation data. The parameters of the fit must, in general, include the concentration profile as an empirical function. Equations of the type derived are relatively insensitive with respect to the processes of correlation or convolution. That is, large changes in the coefficients (eg one of the functions) result in small changes in the solution. Such equations are said to be well conditioned with respect to these operations. It follows, therefore, that a degree of ambiguity is inherent in the determination of the concentration profile. A variety of empirical functions will, in general, result in a "satisfactory" fit within the accuracy of the experimental data. This point will be more rigorously established in a later section.

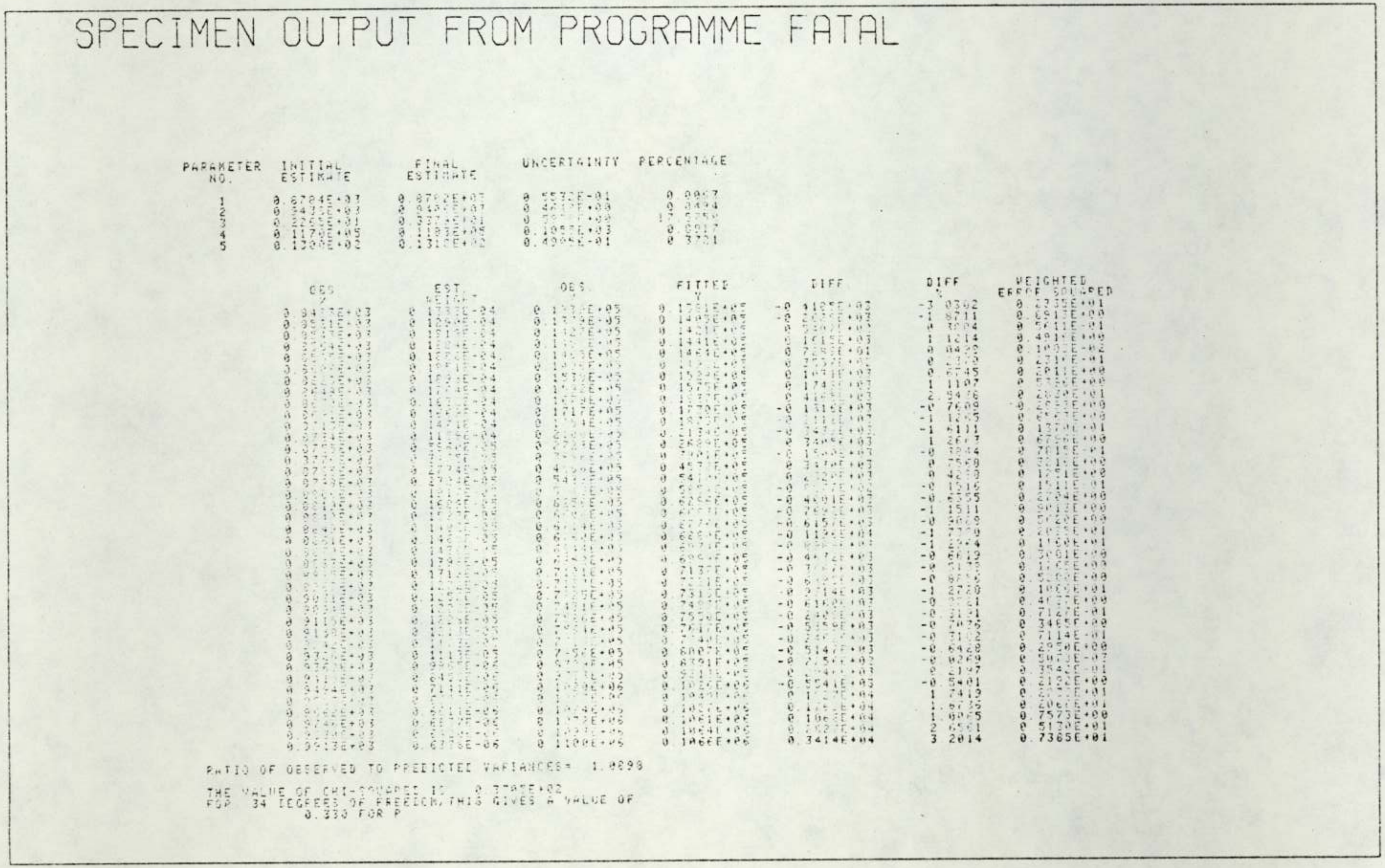

SPECIMEN OUTPUT FROM PROGRAMME FATAL

```
PARAMETER   INITIAL       FINAL       UNCERTAINTY  PERCENTAGE
   NO.      ESTIMATE      ESTIMATE

      OBS          EST.            OBS          FITTED          DIFF          DIFF      WEIGHTED
       Z          WEIGHT                          Y                          %     ERROR SQUARED

RATIO OF OBSERVED TO PREDICTED VARIANCES=  1.0298

THE VALUE OF CHI-SQUARED IS   0.3[illegible]E+02
FOR  34 DEGREES OF FREEDOM,THIS GIVES A VALUE OF
          0.330 FOR P
```

Figure 22

Chapter IV

Reaction Form Factors Using Molecular Ion Beams

Reaction Form Factors Using Molecular Ion Beams

Analytical determination of fluorine by means of the $F^{19}(p,\alpha\gamma)O^{16}$ reaction using the proton beam of the Aston Van de Graaff was limited to measurements in the vicinity of the 340 keV resonance. When the experimental programme was transferred to the Birmingham Radiation Centre, the extended energy range of the Dynamitron accelerator offered the prospect of greater sensitivity by making use of more intense, higher energy, resonances in the $F^{19}(p,\alpha\gamma)O^{16}$ reaction cross-section. To achieve maximum sensitivity the intense resonance at $E_o = 872$ keV (σ_r=661 mb,Γ= 4.5 keV) was considered most suitable. Measurements were continued in the vicinity of the 340 keV $F^{19}(p,\alpha\gamma)O^{16}$ resonance so that data obtained on the Radiation Centre Dynamitron could be directly compared with similar data from the Aston Van de Graaff.

The operational characteristics of the Dynamitron accelerator set a lower limit for the terminal voltage of 1 MV. It was, therefore, necessary to employ molecular hydrogen ion beams to study reactions induced by protons of energy less than 1 MeV. It was initially assumed that results obtained using molecular hydrogen ion beams could be explained in terms of the parameters of the proton beam. It became apparent, however, that anomalies in yield curves from molecular hydrogen ion beams could not be resolved by reference to the proton data.

ANOMALOUS YIELD CURVES FROM MOLECULAR HYDROGEN ION BEAMS

A discrepancy was first noticed in thick target yield curves for the 340 keV $F^{19}(p,\alpha\gamma)O^{16}$ resonance using a mass-three (H_3^+) molecular hydrogen ion beam. A typical curve is shown in Figure 23 *. The curve exhibits a curious asymmetry on the leading edge. The shape of the curve was found to be very sensitive to target contamination as repeated measurements produced a distinct "rounding" in the region between the three-quarter yield point and the plateau. A more serious discrepancy, however, is the large interquartile width, $E_{\frac{3}{4}}-E_{\frac{1}{4}} = 8.0\pm0.3$ keV Quadratic subtraction of the natural resonance width ($\Gamma = 2.4$ keV) from the interquartile width yields a value of $\eta = 7.6 \pm 0.3$ keV for the "effective" energy dispersion per proton. If an approximately equal division of energy is assumed this would imply an energy dispersion of 23.0 keV in the incident H_3^+ beam. BASSETT (1975), however, has shown that for the experimental configuration described, incident energy dispersion is of the order of 2 to 3 keV for mass-one (H_1^+), mass-two (H_2^+) and mass-three (H_3^+) beams.

Figure 24 shows a thin target yield curve for the $F^{19}(p,\alpha\gamma)O^{16}$ reaction at 340 keV using a H_3^+ incident beam. The observed FWHM of the curve is 3.4 ± 0.05 keV. The target thickness, obtained from polarimetry measurements (AGUADO BOMBIN (1975)) was 40 ± 15 Å, equivalent to approximately 0.5 keV for 340 keV protons in calcium fluoride. The data was fitted using the theory developed previously. The value obtained for beam energy dispersion was 2.3 ± 0.1 keV, in good agreement with thin target data for the proton beam. A modest increase in target thickness was found to produce a very significant increase in observed width. Figures 25 and 26 show similar thin

* Note. All yield values for molecular hydrogen ion beams are shown renormalized to proton equivalent yields.

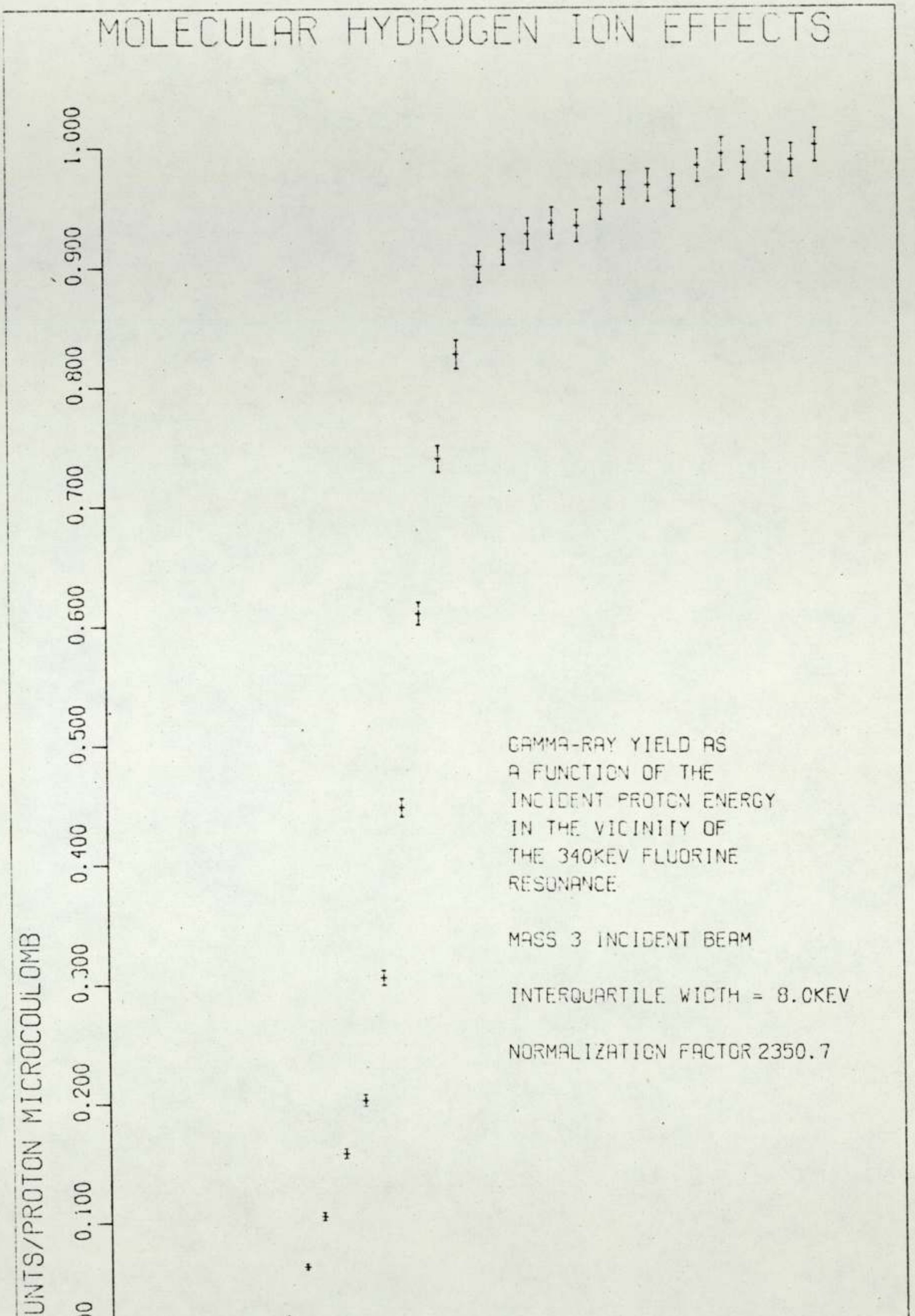
MOLECULAR HYDROGEN ION EFFECTS
COUNTS/PROTON MICROCOULOMB
0.000
0.100
0.200
0.300
0.400
0.500
0.600
0.700
0.800
0.900
1.000
300
310
320
330
340
350
360
370
380
390
400
PROTON ENERGY (KEV)
GAMMA-RAY YIELD AS
A FUNCTION OF THE
INCIDENT PROTON ENERGY
IN THE VICINITY OF
THE 340KEV FLUORINE
RESONANCE
MASS 3 INCIDENT BEAM
INTERQUARTILE WIDTH = 8.0KEV
NORMALIZATION FACTOR 2350.7

Figure 23

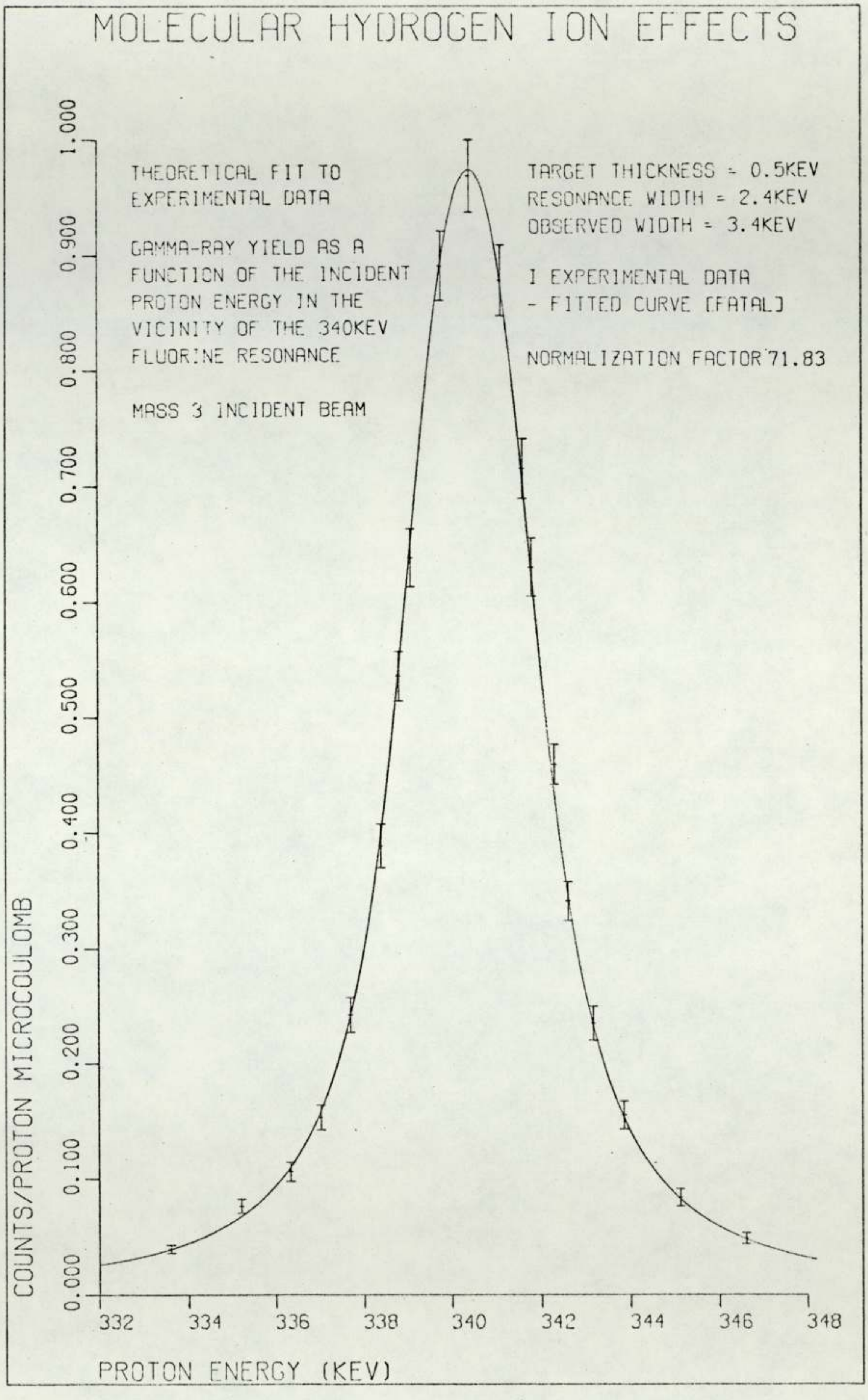
MOLECULAR HYDROGEN ION EFFECTS
THEORETICAL FIT TO
EXPERIMENTAL DATA
GAMMA-RAY YIELD AS A
FUNCTION OF THE INCIDENT
PROTON ENERGY IN THE
VICINITY OF THE 340KEV
FLUORINE RESONANCE
MASS 3 INCIDENT BEAM
TARGET THICKNESS = 0.5KEV
RESONANCE WIDTH = 2.4KEV
OBSERVED WIDTH = 3.4KEV
I EXPERIMENTAL DATA
- FITTED CURVE [FATAL]
NORMALIZATION FACTOR 71.83
COUNTS/PROTON MICROCOULOMB
0.000
0.100
0.200
0.300
0.400
0.500
0.600
0.700
0.800
0.900
1.000
332
334
336
338
340
342
344
346
348
PROTON ENERGY (KEV)

Figure 24

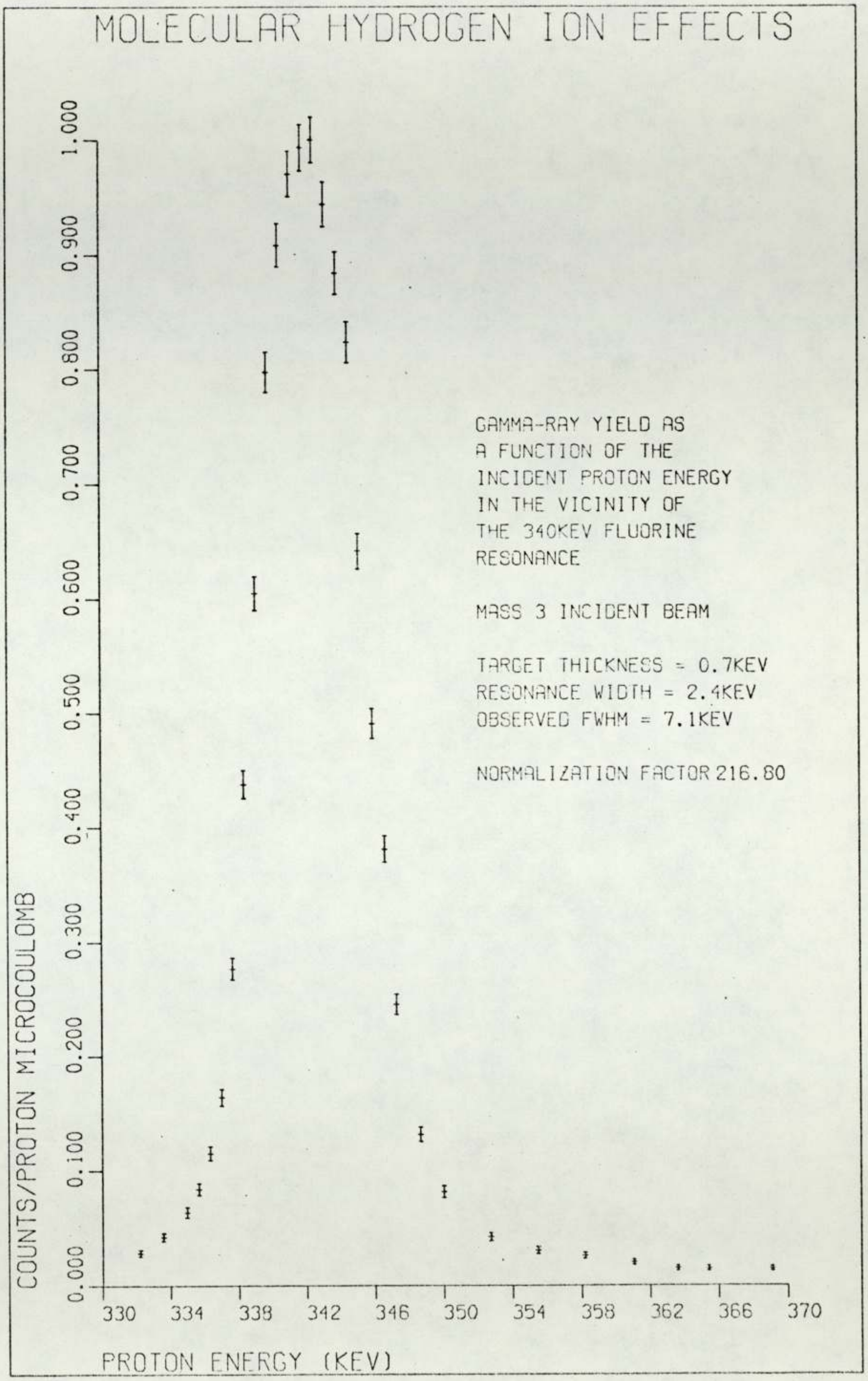
MOLECULAR HYDROGEN ION EFFECTS
COUNTS/PROTON MICROCOULOMB
0.000
0.100
0.200
0.300
0.400
0.500
0.600
0.700
0.800
0.900
1.000
PROTON ENERGY (KEV)
330
334
338
342
346
350
354
358
362
366
370
GAMMA-RAY YIELD AS
A FUNCTION OF THE
INCIDENT PROTON ENERGY
IN THE VICINITY OF
THE 340KEV FLUORINE
RESONANCE
MASS 3 INCIDENT BEAM
TARGET THICKNESS = 0.7KEV
RESONANCE WIDTH = 2.4KEV
OBSERVED FWHM = 7.1KEV
NORMALIZATION FACTOR 216.80

Figure 25

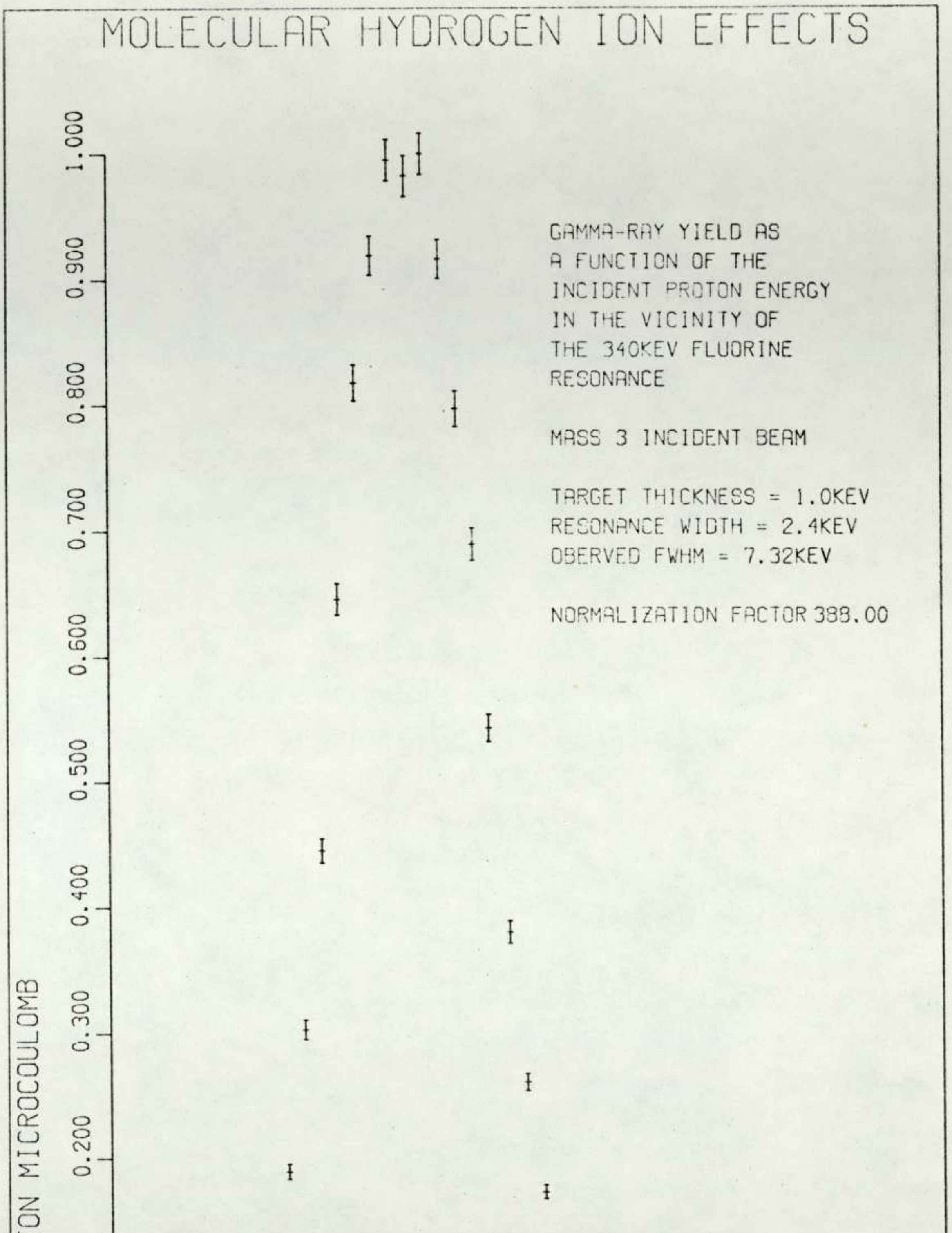
MOLECULAR HYDROGEN ION EFFECTS
GAMMA-RAY YIELD AS
A FUNCTION OF THE
INCIDENT PROTON ENERGY
IN THE VICINITY OF
THE 340KEV FLUORINE
RESONANCE
MASS 3 INCIDENT BEAM
TARGET THICKNESS = 1.0KEV
RESONANCE WIDTH = 2.4KEV
OBERVED FWHM = 7.32KEV
NORMALIZATION FACTOR 388.00
COUNTS/PROTON MICROCOULOMB
0.000
0.100
0.200
0.300
0.400
0.500
0.600
0.700
0.800
0.900
1.000
330
335
340
345
350
355
360
PROTON ENERGY (KEV)

Figure 26

target yield curves for target thicknesses of 70 ± Å (~ 0.75 keV at E_p = 340 keV) and 100 ± 15 Å (~ 1.0 keV at E_p = 340 keV). The FWHM for these curves is 7.1 ± 0.2 keV and 7.3 ± 0.2 keV respectively. A summary of the data is presented in Table 6.

The ratios of observed width to maximum yield are at variance with theoretical predictions for the proton beam. An increase in target thickness from 0.5 keV to 1.0 keV would be expected to produce only a 2 per cent change in observed width for an increase in maximum yield of 146 per cent. In practice the observed width was found to increase by 215 per cent. Figures 25 and 26 exhibit positive skewness which cannot be attributed to a thick target background as the effect is absent in Figure 24 . The anomalously large increase in observed width, as a function of target thickness, for incident molecular hydrogen ion beams must therefore be attributed to effects occurring within the target. Observation of these effects would appear to be strongly target thickness dependent, as they are not observed for very thin targets, and to be very sensitive to target contamination. Target oxidation might, in part, account for these anomalies, although oxidation effects would be considered to be more significant for the thinnest target.

Figure 27 shows a set of three thin target yield curves in the vicinity of the 872 keV $F^{19}(p,\alpha\gamma)O^{16}$ resonance. The data corresponds to measurements on a single target of thickness 100 ± 15 Å (~ 0.7 keV for 872 keV protons in calcium fluoride), using H_1^+, H_2^+ and H_3^+ incident beams. Owing to error in the calibration of the high voltage terminal it is doubtful if any significance can be attributed to the shift (~ 1.5 per cent) in the position of the resonance. The yield

TABLE 6

Thin Target Data 340 keV $F^{19}(p,\alpha\gamma)O^{16}$ Resonance H_3^+ Incident Beam

	FWHM	ξ	*Yield (E_{max})	**Normalized
	keV	keV	Counts/μc	Yield
***340.3 ± 0.	3.4 ± 0.05	∿ 0.5	70.0 ± 0.5	40 ± 0.3
341.1 ± 0.4	7.1 ± 0.2	∿ 0.7	217.0 ± 2.0	123 ± 1.0
341.2 ± 0.5	7.3 ± 0.2	∿ 1.0	388. ± 3.0	221 ± 2.0

* Proton Equivalent Yield

** Normalized to Curve B of Figure 15 at $\xi = 0.5$ keV

*** Fitted

TABLE 7

Thin Target Data 872 keV $F^{19}(p,\alpha\gamma)O^{16}$ Resonance H_1^+, H_2^+ and H_3^+ Incident Beams

Ion	E_{max}	FWHM, T	$(T^2 - \Gamma^2)^{\frac{1}{2}}$	*Yield(E_{max})
	keV	keV	keV	Counts/μc
H_1^+	*877.1 ± 0.6	5.5 ± 0.1	3.1 ± 0.05	2924 ± 90
H_2^+	870.0 ± 0.7	8.5 ± 0.2	7.2 ± 0.2	2210 ± 55
H_3^+	863.3 ± 0.7	11.3 ± 0.2	10.4 ± 0.2	1807 ± 70

* Fitted

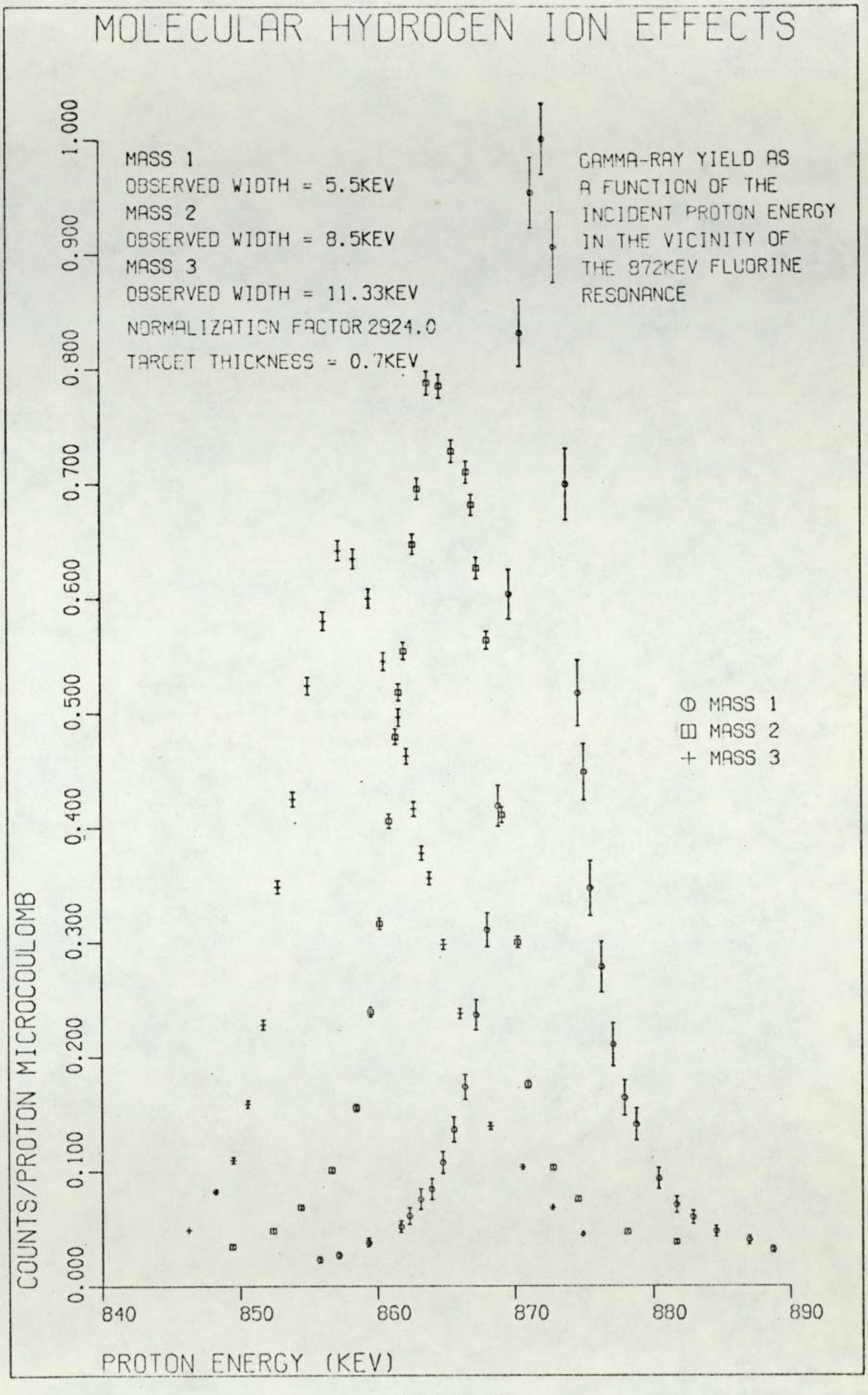
MOLECULAR HYDROGEN ION EFFECTS
MASS 1
OBSERVED WIDTH = 5.5KEV
MASS 2
OBSERVED WIDTH = 8.5KEV
MASS 3
OBSERVED WIDTH = 11.33KEV
NORMALIZATION FACTOR 2924.0
TARGET THICKNESS = 0.7KEV
GAMMA-RAY YIELD AS
A FUNCTION OF THE
INCIDENT PROTON ENERGY
IN THE VICINITY OF
THE 872KEV FLUORINE
RESONANCE
Φ MASS 1
⊞ MASS 2
+ MASS 3
COUNTS/PROTON MICROCOULOMB
0.000
0.100
0.200
0.300
0.400
0.500
0.600
0.700
0.800
0.900
1.000
840
850
860
870
880
890
PROTON ENERGY (KEV)

Figure 27

curves for incident molecular hydrogen ion beams again exhibit positive skewness, which is particularly marked for the H_3^+ beam. The observed FWHM of the curves are 5.5 ± 0.1 keV (H_1^+), 8.5 ± 0.2 keV (H_2^+) and 11.3 ± 0.2 keV (H_3^+) and the relative maximum yields 2924 ± 90 (H_1^+), 2210 ± 55 (H_2^+) and 1807 ± 70 (H_3^+) respectively. For all three curves the total integrated yield (area under the curve) is constant to within 4.0 per cent. A summary of the data is present in Table 7. Figure 28 shows a similar thin target yield curve, for the same target, using an incident H_2^+ beam with an energy dispersion of approximately 0.5 keV. * The FWHM of the curve is 7.0 ± 0.3 keV. As n^2 (0.25) is small compared to Γ^2 (5.76) and ξ^2 (1.0) the contribution of incident beam energy dispersion to observed width may be neglected to a first approximation . Under these conditions the observed FWHM would be expected to be approximately 2.6 keV. The large FWHM observed for incident molecular hydrogen ion beams must therefore result from an "effective" increase in target thickness or energy dispersion within the target.

Effects similar to those observed for thin targets would occur if the stopping power of the target medium was significantly greater for molecular hydrogen ion beams than for a proton beam. A 400 per cent increase in stopping power for molecular hydrogen ion beams, relative to the proton stopping power would, however, produce only a 30 per cent increase in observed width for a 20 per cent reduction in amplitude.

* Note : Attempts to use more finely collimated beams (less than 0.5 mm) were found to result in unuseable peak to background ratios.

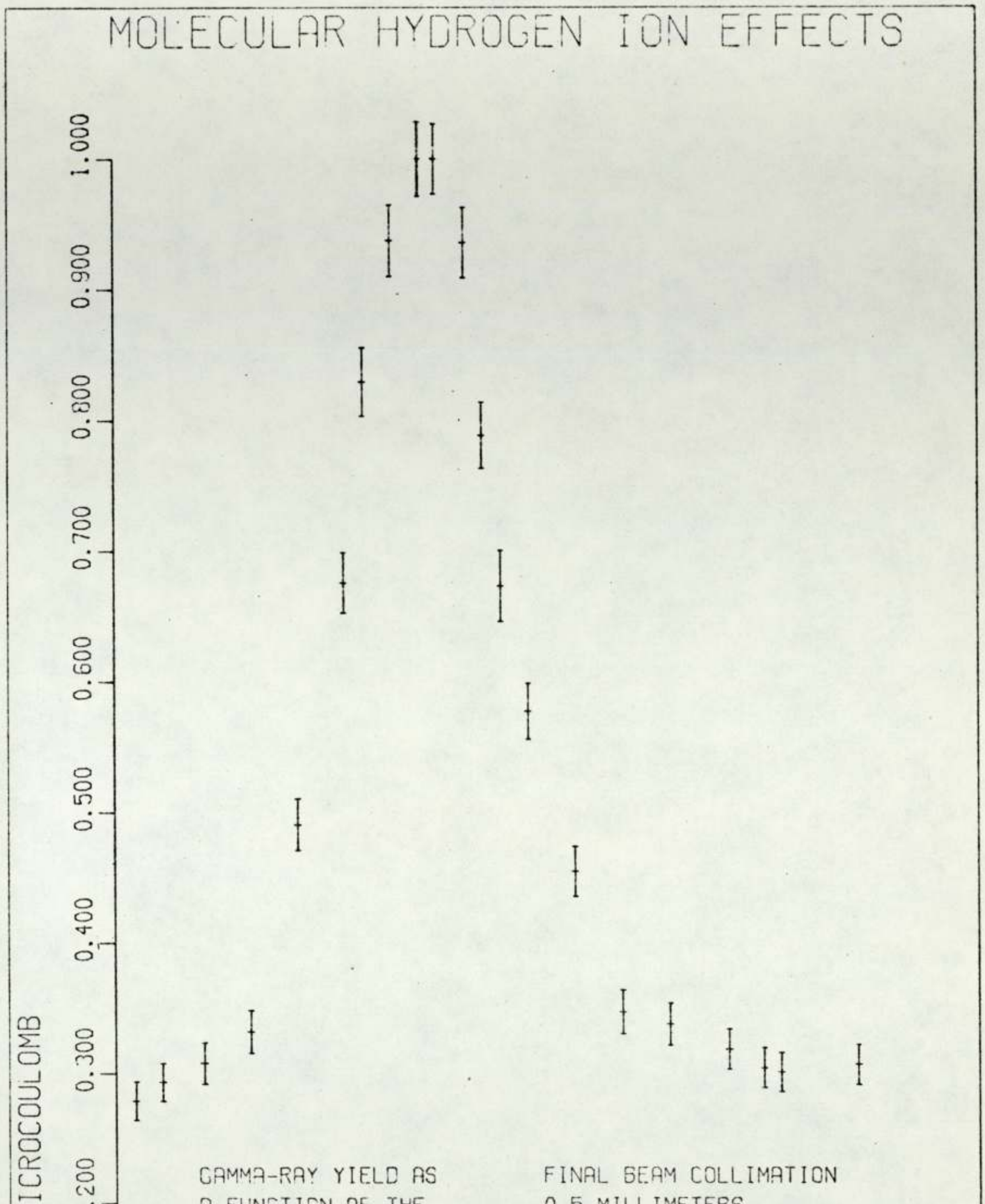
MOLECULAR HYDROGEN ION EFFECTS
COUNTS/PROTON MICROCOULOMB
0.000
0.100
0.200
0.300
0.400
0.500
0.600
0.700
0.800
0.900
1.000
860
865
870
875
880
885
890
PROTON ENERGY (KEV)
GAMMA-RAY YIELD AS
A FUNCTION OF THE
INCIDENT PROTON ENERGY
IN THE VICINITY OF
THE 872KEV FLUORINE
RESONANCE
MASS 2 INCIDENT BEAM
FINAL BEAM COLLIMATION
0.5 MILLIMETERS
TARGET THICKNESS = 0.7KEV
RESONANCE WIDTH = 4.5KEV
OBSERVED FWHM = 7.05KEV
NORMALIZATION FACTOR 206.0

Figure 28

A set of three thick target yield curves in the vicinity of the 872 keV, 902 keV and 935 keV $F^{19}(p,\alpha\gamma)\,O^{16}$ resonances is shown in Figure 29 , for H_1^+ , H_2^+ and H_3^+ incident beams. A summary of the data is presented in Table 8. The energies, $E_{\frac{1}{2}}$, corresponding to the half- plateau yields on the curve for the proton beam (taken as the resonance energies) yield values of 878.2 ± 0.05 keV and 940.6 ± 0.5 keV. These values are respectively 6.2 keV and 5.6 keV higher than accepted values and indicate error in the calibration of the high voltage terminal. The corresponding points on the curves for incident H_2^+ and H_3^+ ions yield slightly lower values; 876.4 ± 1.0 keV 939.7 ± 2.0 keV(H_2^+), 874.6 ± 1.0 keV and 937.4 ± 2.0 keV (H_3^+). The $E_{\frac{1}{2}}$ values for incident H_3^+ ions are approximately 0.3 per cent lower than the $E_{\frac{1}{2}}$ values for an incident proton beam. This value is appreciably smaller than the corresponding shift of 1.5 per cent in the location of the thin target maxima. Although the difference appears to be significant it might be attributable to a change in the calibration of the high voltage terminal (the thick and thin target data sets are separated in time by a period of five months). The interquartile widths, $\Delta E = (E_{\frac{3}{4}} - E_{\frac{1}{4}})$, are respectively;

	E_o = 872 keV	E_o = 935 keV
	ΔE (keV)	ΔE (keV)
H_1^+	5.6 ± 0.5	9.2 ± 0.6
H_2^+	8.2 ± 0.7	12.2 ± 0.9
H_3^+	9.3 ± 0.8	15.4 ± 1.0

The corresponding ratios $\Delta E'(H_3^+)/\Delta E'(H_1^+)$ are 2.5. (E_o = 872 keV) and 4.0 (E_o = 935 keV). Above the resonance energies the curves for incident

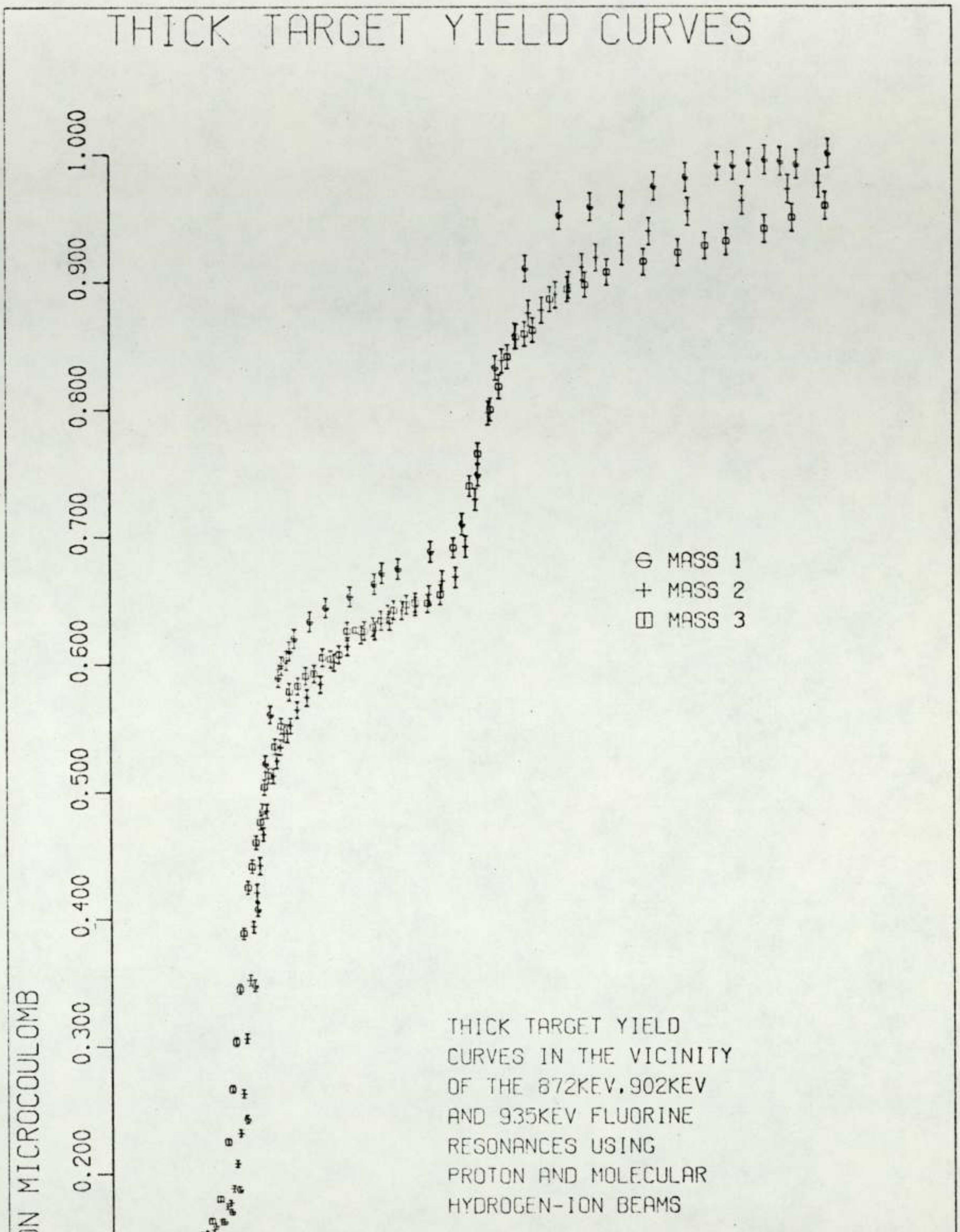
THICK TARGET YIELD CURVES
COUNTS/PROTON MICROCOULOMB
0.000
0.100
0.200
0.300
0.400
0.500
0.600
0.700
0.800
0.900
1.000
840
860
880
900
920
940
960
980
1000
1020
1040
PROTON ENERGY (KEV)
MASS 1
MASS 2
MASS 3
THICK TARGET YIELD CURVES IN THE VICINITY OF THE 872KEV, 902KEV AND 935KEV FLUORINE RESONANCES USING PROTON AND MOLECULAR HYDROGEN-ION BEAMS
NORMALIZATION FACTOR 112140.0

Figure 29

TABLE 8

Thick Target Data 872 keV and 935 keV $F^{19}(p,\alpha\gamma)O^{16}$ Resonances

H_1^{++}, H_2^+ and H_3^+ Incident Beams

ION	$E_{\frac{1}{2}}$ keV	$E_{\frac{3}{4}}-E_{\frac{1}{4}}$ keV	$\Delta E' = (\Delta E^2 - \Gamma^2)^{\frac{1}{2}}$ keV
H_1^+	*878.2 ±0.05	5.6 ± 0.5	3.3 ± 0.3
H_2^+	876.4 ±1.0	8.2 ± 0.7	6.8 ± 0.6
H_3^+	874.6 ±1.0	9.3 ± 0.8	8.1 ± 0.7
H_1^+	*940.6 ±0.5	9.2 ± 0.6	3.2 ± 0.2
H_2^+	939.7 ±2.0	12.2 ± 0.9	8.6 ± 0.6
H_3^+	937.4 ±2.0	15.4 ± 1.0	12.7 ± 0.8

* Fitted

TABLE 9

Simulated Thin Target Data 872 keV $F^{19}(p,\alpha\gamma)O^{16}$ Resonances

H_1^+, H_2^+ and H_3^+ Incident Beams

ION	FWHM keV	$n_{effective}$ keV	ϕ_5 max (ξ) Arbitrary units	*Normalized ϕ_5 max (ξ)	*Normalized Yield (E_{max})
H_1^+	5.5 ± 0.1	3.0	573.3	1.0	1.0 ± 0.04
H_2^+	8.5 ± 0.2	7.14	417.2	0.73	0.75 ± 0.03
H_3^+	11.3 ± 0.2	10.35	332.2	0.56	0.62 ± 0.03

*Normalized to H_1^+ data

H_2^+ and H_3^+ ions are lower, by approximately 5 per cent, than the curve for the incident proton beam and gradually rise to a maximum yield which agrees approximately with the yield for the proton beam.

The results presented above were considered to indicate conclusively that the phenomena observed in yield curves for incident molecular hydrogen ion beams are not instrumental in origin. They must, therefore,be attributed to properties associated with molecular ions. A review of the literature revealed that many of the effects observed are in fact well documented and have been studied by several groups of workers.

Anomalous yield curves from molecular hydrogen ion beams were observed as early as 1940, by HAXBY et al. (1940), during the calibration of an electrostatic generator. The data of other workers exhibit similar phenomena which were largely ignored or attributed to instrumental effects,[HUNT et al.(1952), HERRING et al. (1955), ANDERSEN et al. (1958)] Subsequent work,[BONDELID and KENNEDY (1958) and (1959), DAHL et al. (1960), WALTERS et al.(1961),PURSER et al.(1963)] established that effects observed with molecular hydrogen ion beams were not instrumental in origin.

BONDELID and BUTLER (1963) found that the $E_{\frac{1}{2}}$ point on the thick target yield curve from H_2^+ ions, for the reaction $Al^{27}(p, \gamma)Si^{28}$ at E_o = 992 keV, was 0.05 per cent lower than that from a corresponding observation with a proton beam. The interquartile widths of thick target yield curves taken with H_2^+ ions were considerably broader than those taken with protons and exhibited an asymmetry on the leading edge. The energy shifts, broadening effects and intensity of the "Lewis peak"* were found to be very sensitive to target contamination. For extremely thin targets (< 0.3 keV) the energy co-ordinates of the maxima of the curves from proton and H_2^+ ion beams have agreed to within 0.01 per cent. The observed widths of moderately thin targets were found to increase much more rapidly for H_2^+ ion beams than for proton beams and showed no simple relationship between target thickness and observed width. The effects observed by BONDELID and

* Note :

A peak on high resolution thick target yield curves was predicted by LEWIS (1961), due to the discrete nature of energy loss in the target. Charged particles lose energy in matter in a series of discrete steps. If some of the steps are larger than the natural width of a narrow resonance, some of the particles incident on the target at an energy well above the resonance energy, E_o, will jump over the resonance. Particles incident at an energy E_o, all have, for a finite time, the correct energy to interact. The yield curve will therefore exhibit a peak near E_o. The criterion for the observation of the "Lewis effect" is that the total energy resolution of the experimental system (including the natural and Doppler widths of the resonance) should be much less than the maximum energy loss for the incident particle in a single collision.

BUTLER for H_2^+ ion beams are very similar to those observed by the author for H_2^+ and H_3^+ ion beams. The amount of data available in the scientific literature for incident H_3^+ ion beams is, however, extremely limited.

The phenomena observed with molecular hydrogen ion beams may be understood by reference to the dissociation mechanism of molecular ions. Though molecular binding energies lie in the electron volt range molecular structure effects can produce energy spreads of several keV for beam energies in the MeV range. It is necessary to consider only diatomic molecules as more complex molecules can be dealt with by a two body approximation, particularly in view of the limited precision of available data. The kinetic energy of a proton, E_f, produced during the dissociation of an H_2^+ ion, with initial kinetic energy E_i, is given by the relationship,

$$E_f = \frac{1}{2}\,(E_i - E_d + E) + \cos\phi \left\{ E_i(E - E_d) \right\}^{\frac{1}{2}}$$

where E is the total excess kinetic energy liberated in the centre of mass system and E_d is the excitation energy needed for dissociation. For the particular molecules which have their dissociation axes at 0 degrees and 180 degrees to the beam direction, the energies E_f^+ and E_f^- of the dissociation products is given by,

$$E_f^{\pm} = \frac{1}{2}\,(E_i - E_d + E) \pm \left\{ E_i(E - E_d) \right\}^{\frac{1}{2}} \qquad \ldots\ldots\ldots\ldots \quad (22)$$

It follows from Equation (22) that when E_i is in the keV or MeV range the minute excess energy liberated due to dissociation will be considerably amplified as variations of laboratory energy E_f.

A closely related phenomenon is that of Aston-banding observed in mass spectrometers. If the pressure in a mass spectrometer is so high that many ions in the beam collide with residual gas molecules, broad bands are observed in the mass spectrum. The effect was first observed by ASTON (1920) who, in a subsequent paper [ASTON (1933)] wrote : "Attention is now drawn to the phenomenon again in the hope that research workers interested in the dynamics of molecular combination and dissocation may find in them a possible new line of attack".

BACHER et al. (1972) have established that there are two main molecular phenomena to consider; the zero point vibrational energy of the molecule and the Coulomb interaction of the nucleons in the molecular ion when some of the binding electrons are removed. The first of these effects is independent of the nature of the target and depends only upon the structure of the molecular ion. The latter effect is, however, strongly influenced by the thickness, density and composition of the target material.

In a simple two step model [SWEETMAN (1960), WALTERS et al. (1961), PURSER et al.(1963)MORAN et al. (1969)] collision produces excitation of the ion to an unbound electronic state followed by dissociation. The electronic transition is assumed to obey the Franck-Condon principle, [FRANCK (1925), CONDON(1928)] in that the internuclear separation is constant throughout the collision and approximately that corresponding to the minimum of the $1s\sigma_g$ internuclear potential curve of the H_2^+ ion. The statistical distribution of internuclear spacings in the incident H_2^+ ion, as affected by the initial vibrational state, may be considered by characterising the incoming ion as a simple hormonic oscillator, McCLURE (1963), (1965). It is well established, GIBSON et al. (1968), VOGLER and SEIBT (1968), CAUDANO and DELFOSSE (1968), MORAN et al .(1969), BERKNER et al. (1966), CHENG et al.(1970), that in the case of high energy collisions of H_2^+ ions in gas targets dissociation occurs principally by means of collision excitation to the repulsive $2p\sigma_\mu$ state and to a lower extent by excitation to the $2p\pi_\mu$ and totally ionized states. The vertical transition $1s\sigma g - 2p\sigma_\mu$ is also the main dissociation process for 3 keV to 5 keV H_2^+ ion beams in gaseous targets, DURUP et al. (1969). The energy level diagram is illustrated in Figure 30.

According to DUNN and ZYL (1967) and WALTERS et al.(1961), H_2^+ molecular ions occupy vibrational levels the mean value of which is slightly greater than $\nu = 3$. Observed cross sections are an average over separate cross sections for ions in each state and correspond approximately to those for $\nu = 4$ or $\nu = 5$, which are the two most heavily weighted levels for Franck-Condon transitions (See Figure 31). Both H_3^+ and H_2^+ ions are homonuclear. De-excitation of the vibrational states by electric dipole transition is therefore forbidden. Only relatively improbable quadrapole emission is allowed. If the life-times of some of the excited state levels are large compared to the flight time of ions from source to target it is possible that excited levels are still partially populated.

A number of workers have observed variations in the dissociation cross-section with ion-source conditions, WILLIAMS and DUNBAR (1966), Mc CLURE (1963), CHAMBERS (1965), CAUDINO and DELFOSSE (1968), and

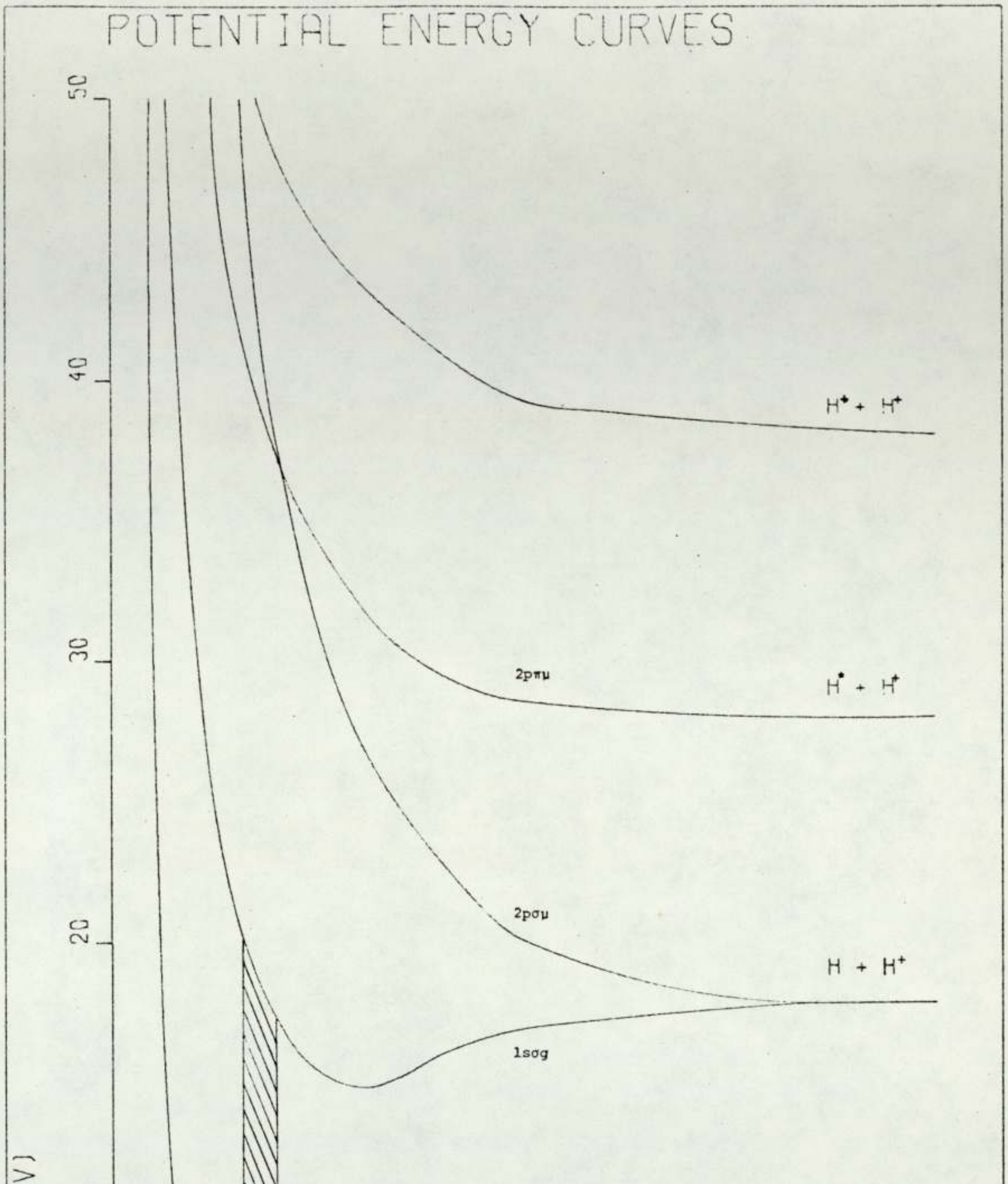
POTENTIAL ENERGY CURVES
POTENTIAL ENERGY(EV)
0
10
20
30
40
50
NUCLEAR SEPARATION (A)
0
1
2
3
4
$H^+ + H^+$
$2p\pi u$
$H^* + H^+$
$2p\sigma u$
$H + H^+$
$1s\sigma g$
CLASSICAL FRANCK-CONDON REGION
$^1\Sigma_g$
H + H

Figure 30

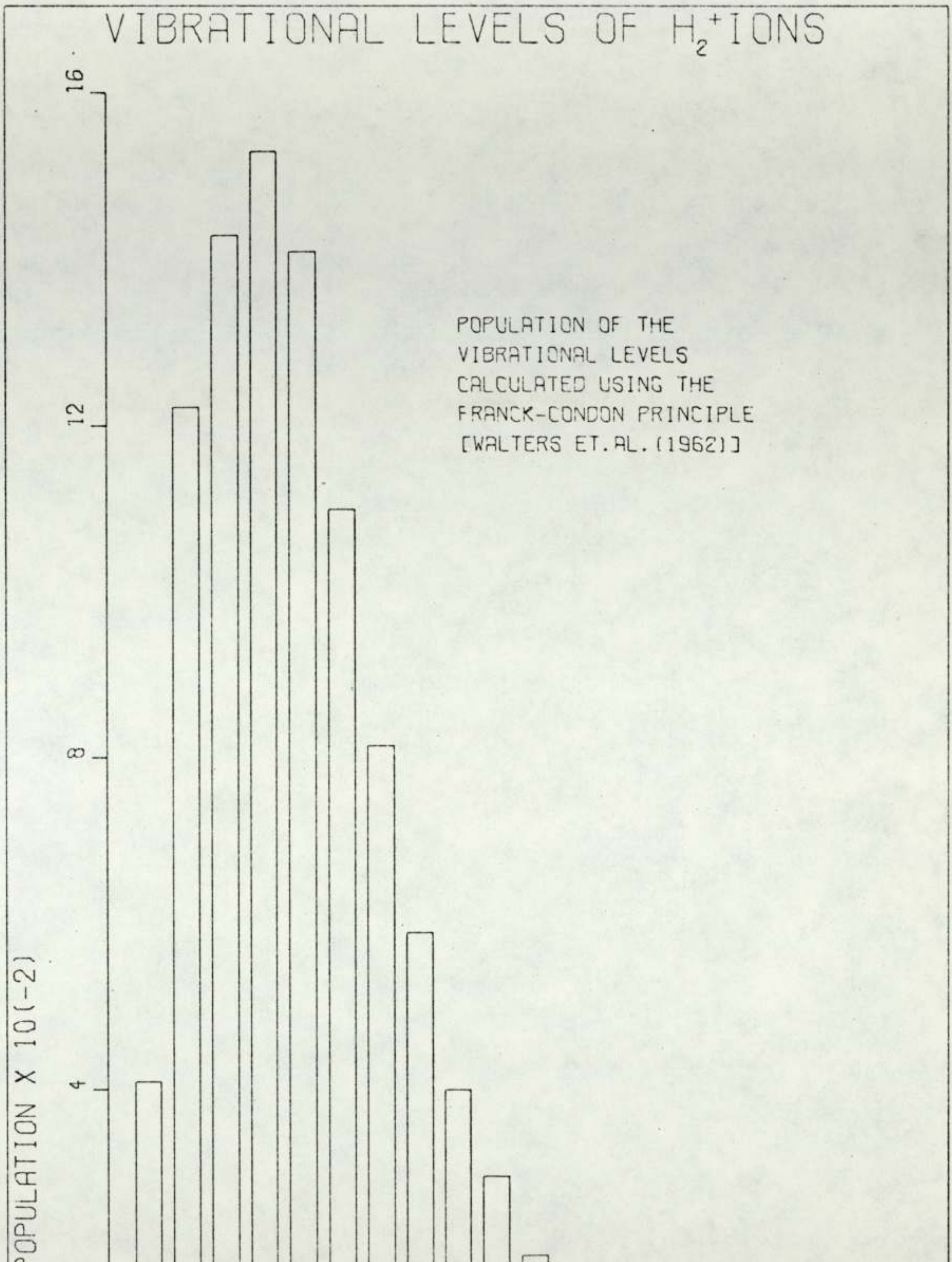
VIBRATIONAL LEVELS OF H_2^+ IONS
RELATIVE POPULATION X 10(-2)
0
4
8
12
16
0 1 2 3 4 5 6 7 8 9 10 11 12 13 14 15 16 17 18
VIBRATIONAL LEVEL
POPULATION OF THE
VIBRATIONAL LEVELS
CALCULATED USING THE
FRANCK-CONDON PRINCIPLE
[WALTERS ET.AL.(1962)]

Figure 31

have attributed these differences to varying vibrational distributions. Other workers have failed to detect this ion source effect, BARNETT and RAY (1963), RIVIERE and SWEETMAN (1961), GIBSON and LOS (1967). The relative population of the nineteen bounded vibrational levels of the $1s\sigma_g$ electronic state of the H_2^+ ion, as a function of energy of the ionizing electrons, is illustrated in Figure 32. McGOWEN and KERWIN (1964) have established that the relative population of the vibrational levels is near saturation if the ionizing electron energy exceeds 24 eV.* It is not established that the experimental H_2^+ ion beam has a vibrational population distribution given by the Franck-Condon principle, even if it were formed with one in the source. MEGGITT et al. (1973) found that incident H_2^+ ion beams in the energy region 60 keV to 300 keV, after mass analysis, consisted of approximately 96 per cent H_2^+ ions and 4 per cent H_1^o and H_1^+, the latter produced by collision with residual gas molecules in the beam transport system.

When molecular ions are incident on a target the binding electrons are stripped-off at, or close to, the surface of the target in a time period of approximately 10^{-17} seconds [BACHER et al. (1972)]. Both H_2^+ and H_3^+ molecular ions have no dipole moment and the internuclear axes are therefore randomly orientated with respect to the beam

* Note ; The electron energy in the ion source of the Radiation Centre Dynamitron is approximately 100 eV. Observed molecular beam phenomena should therefore be independent of ion source conditions.

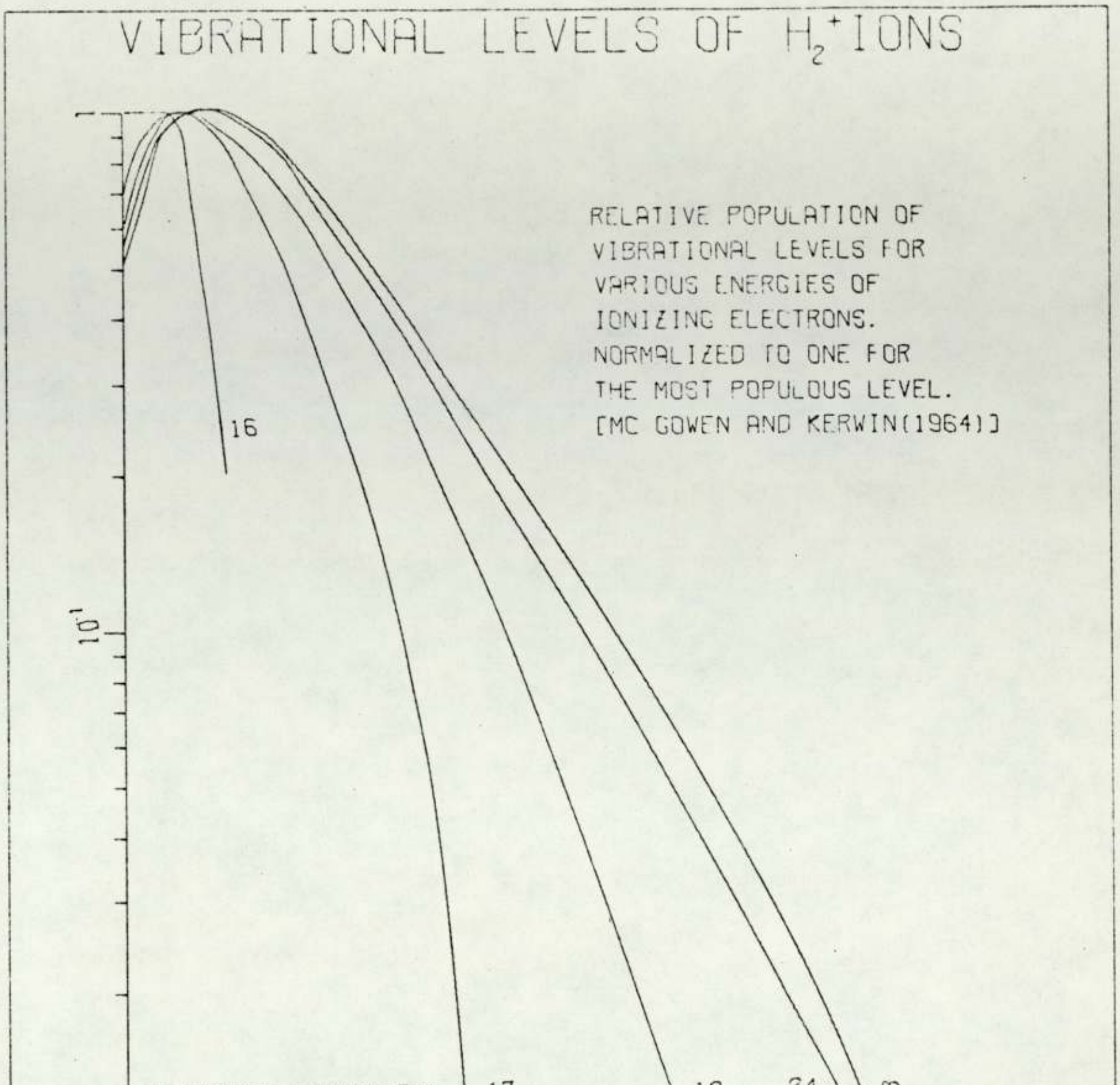
VIBRATIONAL LEVELS OF H_2^+ IONS
RELATIVE POPULATION OF VIBRATIONAL LEVELS FOR VARIOUS ENERGIES OF IONIZING ELECTRONS. NORMALIZED TO ONE FOR THE MOST POPULOUS LEVEL. [MC GOWEN AND KERWIN(1964)]
16
ELECTRON ENERGY(EV)
17
18
24
∞
RELATIVE POPULATION VMAX = 1
1
10^{1}
10^{2}
10^{3}
0
1
2
3
4
5
6
7
8
9
10
11
12
13
14
15
16
17
18
VIBRATIONAL LEVEL

Figure 32

direction. By a comparison of the dissociation time*, ($\sim 10^{-15}$ to 10^{-14} seconds), with the rotational time, ($\sim 10^{-12}$ seconds), the internuclear axis may be assumed to maintain a constant inclination to the direction of motion during the dissociation process. The periods of nuclear vibration of moleculor ions vary from $\sim 10^{-11}$ to 10^{-14} seconds .

The short time of flight in solid targets and the large number of interactions in this time are the main features differentiating dissociation induced in solid target from dissociation induced in a gaseous target. A 2 MeV incident H_2^+ ion has approximately 10^{-7} seconds to dissociate in a 10 cm gas cell. An H_2^+ ion of the same energy incident on a solid target a few hundred Angstroms in thickness has approximately 10^{-15} seconds before it, or the dissociation products, leave the target or lose too much energy to contribute significantly to the yield at bombarding energies close to the resonance energy**. The nuclear reaction samples only the time interval during which the protons are in the target. In this short time the Coulomb force can accelerate the protons to only a fraction of their ultimate terminal velocity and therefore only a small fraction of the maximum energy

Note * The time for ninety per cent of the potential energy to be converted into kinetic energy.

Note** In calcium fluoride a 1 MeV proton loses energy at the rate of approximately 770 eV per 10^{-15} seconds.

dispersion is achieved.

The relative contribution to effective energy dispersion of the vibrational energy of the incident molecular ion and the Coulomb interaction of the nucleons when the binding electrons are removed has been investigated by BACHER et al. (1972), for the $C^{12}(p,p)C^{12}$ resonance at 14.2 MeV using H_1^+, H_2^+ and H_3^+ incident beams. Near the surface of the target, or for very thin targets (0.013μm of carbon, equivalent to approximately 90 eV at 14 MeV) the energy spread is dominated by the zero point motion. At intermediate distances into the target (0.013 μm to 0.066 μm of carbon equivalent approximately to 90 eV to 460 eV at 14 MeV) the contribution from the Coulomb explosion dominates.

The products formed by the dissociation of molecular ions are in close spatial proximity (~ 1 Å). HARRISON (1971) has shown that the dissociation fragments from 60 keV to 300 keV H_2^+ ion beams incident on a 500 Å carbon foil are scattered through only 0.5 degrees after passage through the foil. Their separation does not therefore exceed 10 Å throughout their entire passage through the foil. In a 1 MeV proton beam of microampere intensity the average separation between protons is approximately 10^3 Å . For H_2^+ ion beams in the energy region 60 keV to 300 keV. DETTMANN et al. (1974) observed a specific energy loss per nucleon thirty per cent greater than for protons of the same velocity. They concluded that the discrepancy was due to a spatial correlation effect. Their data for H_3^+ ions was similar to that for H_2^+ ions indicating that the triple correlation does not enhance the effect further [this conclusion has recently been modified, LUCAS (1975)].

The transmission, scattering and channelling of H_2^+ ion beams in aligned crystals have been investigated by several workers, POIZAT and REMILLEUX (1971), (1972), CAYWOOD et al.(1971), TOMBRELLO and CAYWOOD (1973), GEMMELL et al.(1975). Relatively little experimental data has been presented for H_3^+ ion beams. SCHWARTZ and SCHAAD(1967) have performed detailed variational calculations for both H_2^+ and H_3^+ molecular ions. The H_3^+ ion quantum-mechanical problem is sufficiently difficult to have remained unsolved for many years*.

If the zero-point motion of the H_2^+ ion is neglected and it assumed that dissociation takes place by prompt removal of the electron the potential energy function is then given by $E = e^2/4\pi\varepsilon_o r$, where r is the internuclear separation. The classical differential equation which governs the motion of the protons is therefore

$$\frac{d^2r}{dt^2} = e^2/4\pi\varepsilon_o m_p r^2$$

where m_p is the proton mass. The solution of this equation is

$$t(r) = r_o\left(\frac{\pi\varepsilon_o m_p}{e^2}\right)^{\frac{1}{2}} \left[\left(\frac{2r^2}{r_o} - 2r\right)^{\frac{1}{2}} + (2r_o)^{\frac{1}{2}} \ln\left\{\left(\frac{r}{r_o}\right)^{\frac{1}{2}} + \left(\frac{r}{r_o} - 1\right)^{\frac{1}{2}}\right\}\right] \quad \ldots\ldots\ldots\ldots\ldots \quad (23)$$

Note* The H_3^+ ion was quoted by EYRIN (1957) to be "the scandal of modern chemistry".

where r_o is the internuclear spacing of the protons in the molecular ion. If r_o is taken as 1 Å then 90 per cent of the initial potential energy appears as kinetic energy of the protons when their separation is 10 Å. From Equation (23) the dissociation time of the H_2^+ ion is therefore 2.15×10^{-14} seconds. Similarly 60 per cent of the zero-point potential energy would be converted into kinetic energy of the protons in approximately 5.6×10^{-15} seconds ($r = 2.5$ Å).

A 1 MeV proton has a velocity of 1.38×10^{7} m.sec^{-1} and loses only 550 eV in traversing a 100 Å calcium fluoride target. Its time of flight in the target is approximately 7×10^{-16} seconds. In the same target a 340 keV proton has a time of flight of approximately 1.2×10^{-15} seconds ($v_p = 8.06 \times 10^{6}$ m.sec^{-1}) and suffers an energy loss of 1.2 keV. At the energies considered the times of flight in thin targets are appreciably less than the classical dissociation time of the H_2^+ ion. The relevant parameters for the thin target data obtained by the author are summarized below :

Resonance $F^{19}(p,\alpha\gamma)O^{16}$ at E_o=340 keV Γ=2.4 keV

Incident Beam	W (0.5) (keV)	Target Thickness (Å)	Time of Flight (10^{16} seconds)
H_3^+	3.4 ± 0.5	40 ± 15	5.0 ± 1.2
H_3^+	7.1 ± 0.2	70 ± 20	8.7 ± 2.5
H_3^+	7.3 ± 0.2	100 ± 15	12.4 ± 1.2

Resonance $F^{19}(p,\alpha\gamma)O^{16}$ at E_o = 872 keV Γ=4.5 keV

Incident Beam	W (0.5) (keV)	Target Thickness (Å)	Time of Flight (10^{16} seconds)
H_1^+	5.5 ± 0.1	100 ± 15	7.7 ± 1.2
H_2^+	8.5 ± 0.2		
H_3^+	11.3 ± 0.2		

The large increase in effective energy dispersion for the target thickness given would not be expected on the basis of the calculated dissociation time for the H_2^+ ion of 2 x 10^{-14} seconds. For the measurements in the vicinity of the 340 keV $F^{19}(p,\alpha\gamma)O^{16}$ resonance using the H_3^+ incident beam only 2 to 6 per cent of the initial potential energy would be converted into kinetic energy of the protons during their time in the target.

The lack of quantitative agreement between prediction and observation may arise because the simple model chosen overestimates the dissociation time, or the targets carry inert surface coatings arising from target oxidation or beam induced deposition.

From data not presented the maximum rate of beam induced carbon deposition has been estimated as 7×10^{-2} Å per incident microcoulomb At the rate of deposition a 10 Å layer would be formed during the accumulation of the thin target data. The rate of formation of oxide layers is difficult to estimate but their presence would be indicated by the location of the thin target maxima. For data from the $F^{19}(p,\alpha\gamma)O^{16}$ resonance at 340 keV using an H_3^+ incident beam the relative shift observed was less than 1 keV, approximately half of which is attributed to target thickness. If oxide layers were present on the targets studied they could not therefore differ in thickness by more than 50 Å .

The simple model used for the dissociation process applies only to the H_2^+ ion in the ground $1s\sigma_g$ electronic state. No account was taken of the vibrational levels which would still be occupied after the transit time ($\sim 10^{-6}$ to 10^{-5} seconds) from source to target. The mode of operation of the Keithley electrometer used to measure beam current is such that full scale deflection on any range produces a (positive) autobias on the target of 1 volt. A potential difference of only 0.1 volt across the calcium fluoride targets would produce very high field strength ($\sim 10^{7}$ volt. m^{-1}) which may seriously perturb the dissociation process.

The quantitative explanation of effects observed with incident molecular hydrogen ions is relatively simple. The yield curves from very thin targets using incident molecular hydrogen ion beams are essentially similar to equivalent proton induced data as only a small fraction of the dissociation energy of the ions is liberated during the time of flight of the beam in the target. As target thickness is increased the observed width increases rapidly as 40 to 60 per cent of the dissociation energy appears as kinetic energy of the protons in the target. The effective energy dispersion is a function of the time of flight, and therefore of the depth of penetration, of the incident beam in the target. Yield curves from moderately thin targets taken with molecular hydrogen ion beams should therefore exhibit positive skewness. When a thick target is irradiated with a molecular hydrogen ion beam of proton equivalent energy less than the resonance energy a significant portion of the beam is gaining energy from the dissociation process in the front layers of the target faster than it is losing energy through ordinary energy-loss interactions. Though essentially none of the protons in the incident beam have energies great enough to contribute significantly to the yield, some protons will gain enough net energy in the target to reach or exceed the resonance energy and thus contribute significantly to observed yield. It is this feature which gives the long slow rise observed on the leading edge of thick target yield curves taken with molecular hydrogen ion beams. For incident proton equivalent energies above the resonance energy the contribution to observed yield from "leading-protons" occurs after the dissociation process is essentially complete and they pass through the resonance energy zone at a normal rate of energy loss. A net yield loss arises, however, from the "trailing-protons" (those losing energy from the dissociation process) which pass through the resonance energy zone more rapidly than normal. The result is a slowly rising yield, as a function of incident energy, until all the trailing protons pass through the resonance energy zone at a normal rate . For the data obtained by the author a target thickness of 150 keV was insufficient to bring out the full shape of the curves from molecular hydrogen ion beams. A "normal" rate of slowing down is not, therefore, achieved until the beam has penetrated to considerable depth.

The most serious objection to the use of molecular hydrogen ion beams in analytical work is that their influence on observed yield is dependent on the very parameters such experiments seek to determine. A prior knowledge of target thickness and composition, or proton reference data, is required to determine the contribution to observed yield arising from molecular ion effects. In the absence of such knowledge analytical yield curves contain at least two unknown and variable contributions; the concentration profile of the nuclide of interest and the effective energy dispersion resulting from the dissociation of the molecular ions. The latter is a function of the type and energy of the incident molecular ion and and in trace analysis its contribution is essentially determined by the nature of the base matrix.

As a first order approximation it was assumed that all contributions to observed width, other than natural resonance width and target thickness, could be grouped together as effective beam energy dispersion and be represented by a unit-area slit function. Using the theory developed for incident proton beams simulated yield curves from molecular hydrogen ion beams were obtained and compared with experimental data.

A set of synthesized thin target yield curves is shown in Figure 33. It was possible to reproduce the observed width of yield curves taken with incident H_2^+ and H_3^+ ions and the relative maximum yields, normalized to the proton curve, agree with

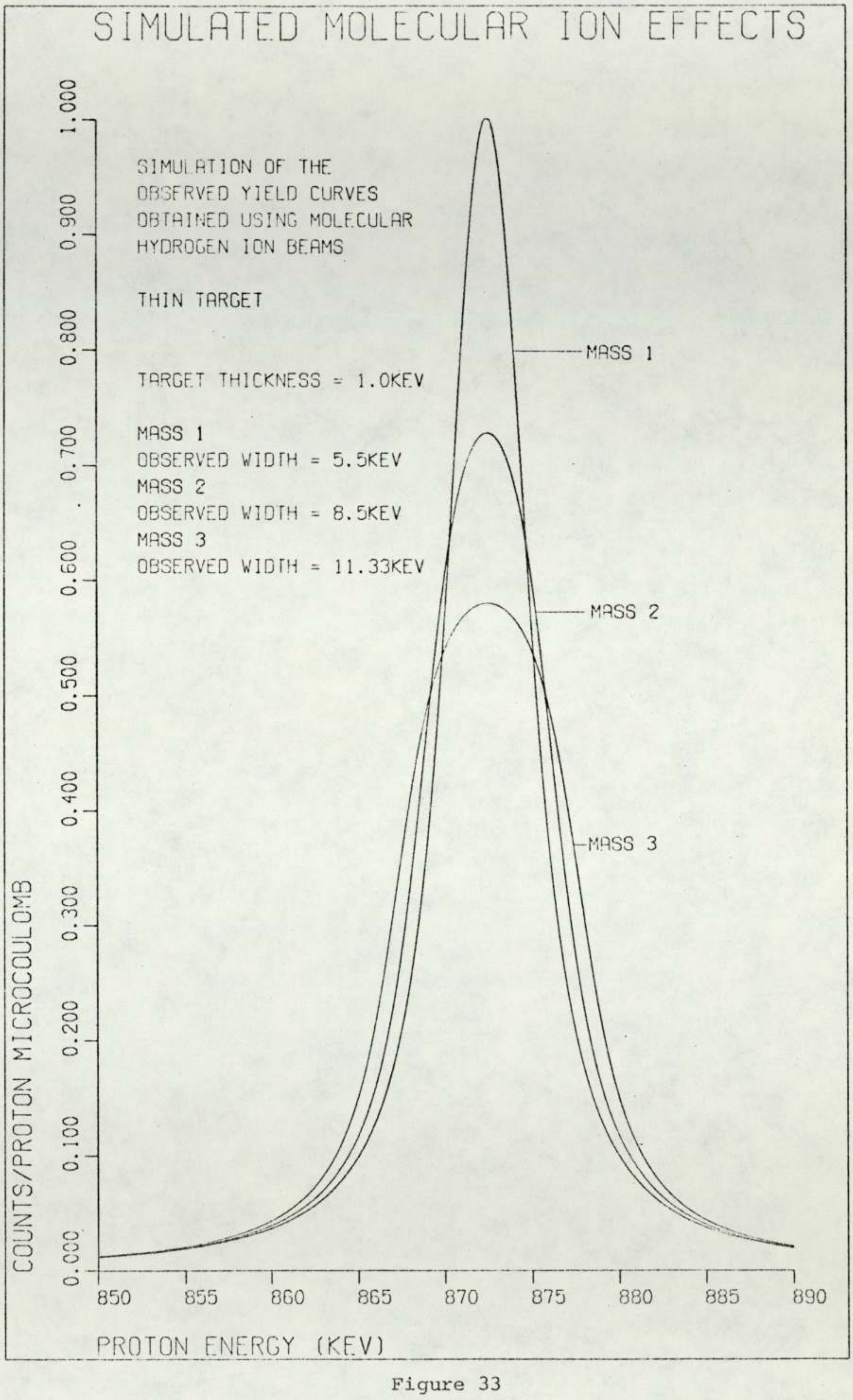
SIMULATED MOLECULAR ION EFFECTS
SIMULATION OF THE
OBSERVED YIELD CURVES
OBTAINED USING MOLECULAR
HYDROGEN ION BEAMS
THIN TARGET
TARGET THICKNESS = 1.0KEV
MASS 1
OBSERVED WIDTH = 5.5KEV
MASS 2
OBSERVED WIDTH = 8.5KEV
MASS 3
OBSERVED WIDTH = 11.33KEV
MASS 1
MASS 2
MASS 3
COUNTS/PROTON MICROCOULOMB
0.000
0.100
0.200
0.300
0.400
0.500
0.600
0.700
0.800
0.900
1.000
850
855
860
865
870
875
880
885
890
PROTON ENERGY (KEV)

Figure 33

experimental data to within 5 per cent. The asymmetry exhibited by experimental yield curves from molecular ion beams was not, however, reproduced as the theoretical formulation used generates symmetrical yield curves. A summary of the data used in the calculations is shown in Table 9.

A set of simulated thick target yield curves is shown in Figure 34. The values for effective beam energy dispersion were taken from the thin target data. The interquartile width of the simulated yield curve for an incident H_2^+ ion beam is in good agreement with experimental data; for the H_3^+ ion beam it is 20 per cent greater than experimental data. In the present context this is not considered to be a serious problem. Thick target yield curves are required mainly as comparison standards for normalization. For curves from molecular ion beams yield points taken well above the resonance energy agree with proton induced yield curves to within 2 per cent. This is of comparable magnitude to experimental uncertainties.

A conclusion of the work described is that it is undesirable to employ molecular hydrogen ion beams in analytical work until the phenomena associated with their use are more fully tabulated, so that quantitative, as distinct from qualitative, corrections can be applied to observed yield curves.

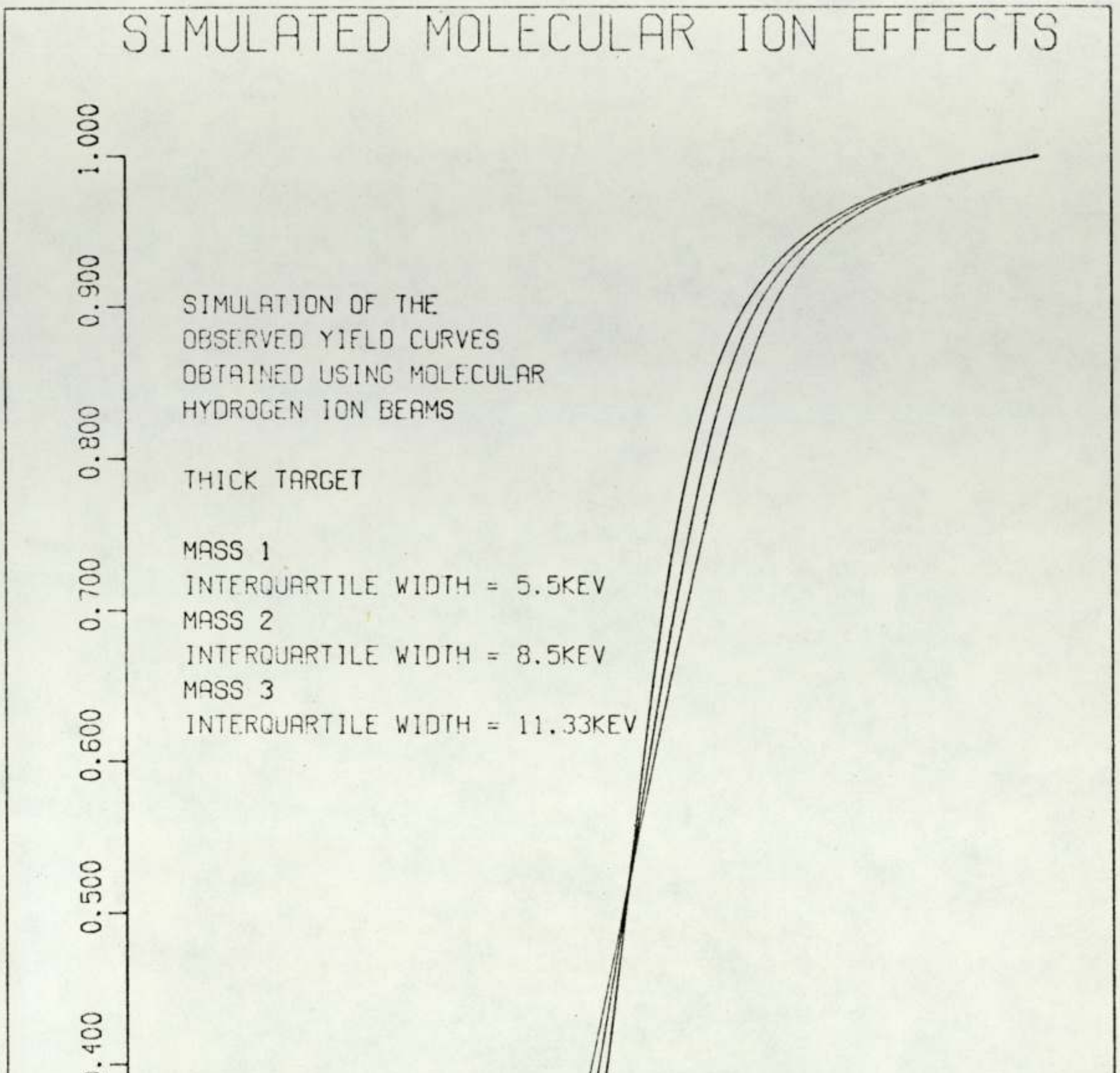
SIMULATED MOLECULAR ION EFFECTS
SIMULATION OF THE
OBSERVED YIELD CURVES
OBTAINED USING MOLECULAR
HYDROGEN ION BEAMS
THICK TARGET
MASS 1
INTERQUARTILE WIDTH = 5.5KEV
MASS 2
INTERQUARTILE WIDTH = 8.5KEV
MASS 3
INTERQUARTILE WIDTH = 11.33KEV
MASS 1
MASS 2
MASS 3
COUNTS/PROTON MICROCOULOMB
0.000
0.100
0.200
0.300
0.400
0.500
0.600
0.700
0.800
0.900
1.000
850
855
860
865
870
875
880
885
890
PROTON ENERGY (KEV)

Figure 34

Chapter V

Charged Particle Stopping Power And Range

Charged Particle Stopping Power and Range

In the analysis of charged particle experiments an essential requirement is comprehensive stopping power and range data. Although a considerable amount of data is generally available a wide disparity exists between published values for projectile particle energies in the region 0 to 10 MeV/amu. It was, therefore, considered appropriate to compare experimental data and theoretical formulations in this energy region to assess the validity of interpolation or computation of such data to less common target media for which information is sparse or non-existent . Discussion is largely restricted to proton data although the energy loss mechanisms of heavier ions are not fundamentally different.

Charged particles traversing matter may lose energy by any one, or all of the following processes; inelastic collision with bound atomic electrons, elastic nuclear scattering, inelastic nuclear scattering and Bremsstrahlung. Atomic excitation and ionization are the dominant modes of energy loss for proton energies in the range 0.01 MeV to 2 GeV. Elastic nuclear scattering is an important mode of energy loss for heavy ions and must be considered for proton energies below 0.01 MeV. Inelastic nuclear collisions and photon emission are significant proton energy loss mechanisms only at very high energies.

The theory of energy loss by fast charged particles due to atomic excitation and ionization was established by BOHR (1913), (1915) through a semiclassical procedure [see also MOTT (1931), LIVINGSTON and BETHE (1937), BOHR(1948)].Purely quantum mechanical formulations were presented by BETHE (1930), (1932) and BLOCH (1933). The most generally useful of the three theories is that due to Bethe which gives the stopping power in the form : -

$$-\frac{dE}{dx} = \frac{e^4}{4\pi\varepsilon_o^2} \frac{Z_1^{*2}}{mV^2} NZ_2 \left[\ln \frac{2mv^2}{I_{adj}} - \ln (1-\beta^2) \right.$$

$$\left. - \beta^2 - \sum_i C_i/Z_2 - \delta/2 \right] \text{joule.m}^{-1} \quad \ldots\ldots \quad (24)$$

where

m = electron rest mass

v = projectile velocity

Z_1^* = effective charge of projectile ion

Z_2 = atomic number of stopping medium

N = atom density of stopping medium

I_{adj} = adjusted ionization potential

$\sum_i C_i/Z_2$ = sum of shell correction terms

The low energy validity of the Bethe equation is given by the numerical value of the first logarithmic term which must generally be greater than zero. The kinetic energy, E, of the incident particle must satisfy the restriction

$$E > \frac{I_{adj}}{4} \cdot \frac{M}{m}$$

The above inequality is always satisfied for 1 MeV protons.

Energy loss is reduced by perturbation of the field of the incident ion caused by electric polarization of the surrounding atoms. The polarization correction term, δ, is generally significant only for condensed matter of low atomic number at high projectile energies. The effect is negligible at the energies considered here and has been discussed in detail by several authors, FERMI (1940), HALPERN and HALL (1948), STERNHEIMER (1952) (1956), NEUFIELD and SYNDER (1957), ARMSTRONG and ALSMILLER (1970).

The shell correction terms, $\sum_i C_i/Z_2$, are required when the velocity of the incident particle is comparable to the velocities of the inner shell electrons in their normal bound states. Electrons in the inner shells cease to contribute to the stopping power in succession as projectile velocity decreases although shell cut-off is gradual. Correction terms which represent the non-participation of excitation-ionization levels in the slowing down process have been presented by several authors; BROWN (1950) and WALSKE (1952), the K-shell, WALSKE (1956), the L-shell, KHANDELWAL and MERZBACHER (1966), the M-shell, BICHSEL (1961), (1963), all shells higher than K and L. A polynomial representation of the shell corrections* has been given by BARKAS and BERGER (1964), and theoretical formulations have been presented by FANO (1963), FANO and TURNER (1964) and CHOI and HERZBACHER (1969).

---

* The low energy validity of the Barkas and Berger polynomial representation for protons is 8 MeV.

The quantity $\bar{I}$, the mean excitation energy is a rigorous and well defined parameter of stopping power theory which represents the average least energy that can be transferred to an atomically bound electron. From its definition [FANO (1963)] $\bar{I}$ depends only upon the ground- excited-state wave functions of the stopping material, and is a property of that material, independent of the energy or type of the projectile particle. Theoretical evaluation of $\bar{I}$ is, however, very difficult and has been performed for only a few simple cases. It is directly related to I_{adj}, the adjusted mean excitation energy, on the assumption of vanishing shell corrections in the extreme relativistic limit,

$$\ln I_{adj} = \ln \bar{I} + \left[\sum_i C_i/Z_2\right]_{\beta = 1}$$

Parametric expressions due to BLOCH (1933) and BRANT (1956) (1958) predict the correct trend of I_{adj} as a function of atomic number but do not give very accurate results. The most extensively used formulation is that presented by STERNHEIMER (1966),

$$I_{adj} = Z_2 \left(9.76 + 58.8 Z_2^{-1.19}\right) \qquad \ldots\ldots\ldots \qquad (25)$$

Equation (25) has been found to give good agreement with experimental data when Z_2 is greater than 10. Values of I_{adj} used by several authors are presented in Figure 35. A departure from the general trend occurs for elements having atomic numbers between 20 and 42. GREEN et al.(1955) and BURKIG and MacKENZIE (1957) have observed deviations of I_{adj} from a smooth dependence on atomic number. The elements calcium, vanadium, thorium and the noble gases appear to be anomalous. ANDERSEN et al.(1969)have suggested that the ratio between I_{adj} and atomic number is not a monotonically increasing function of atomic

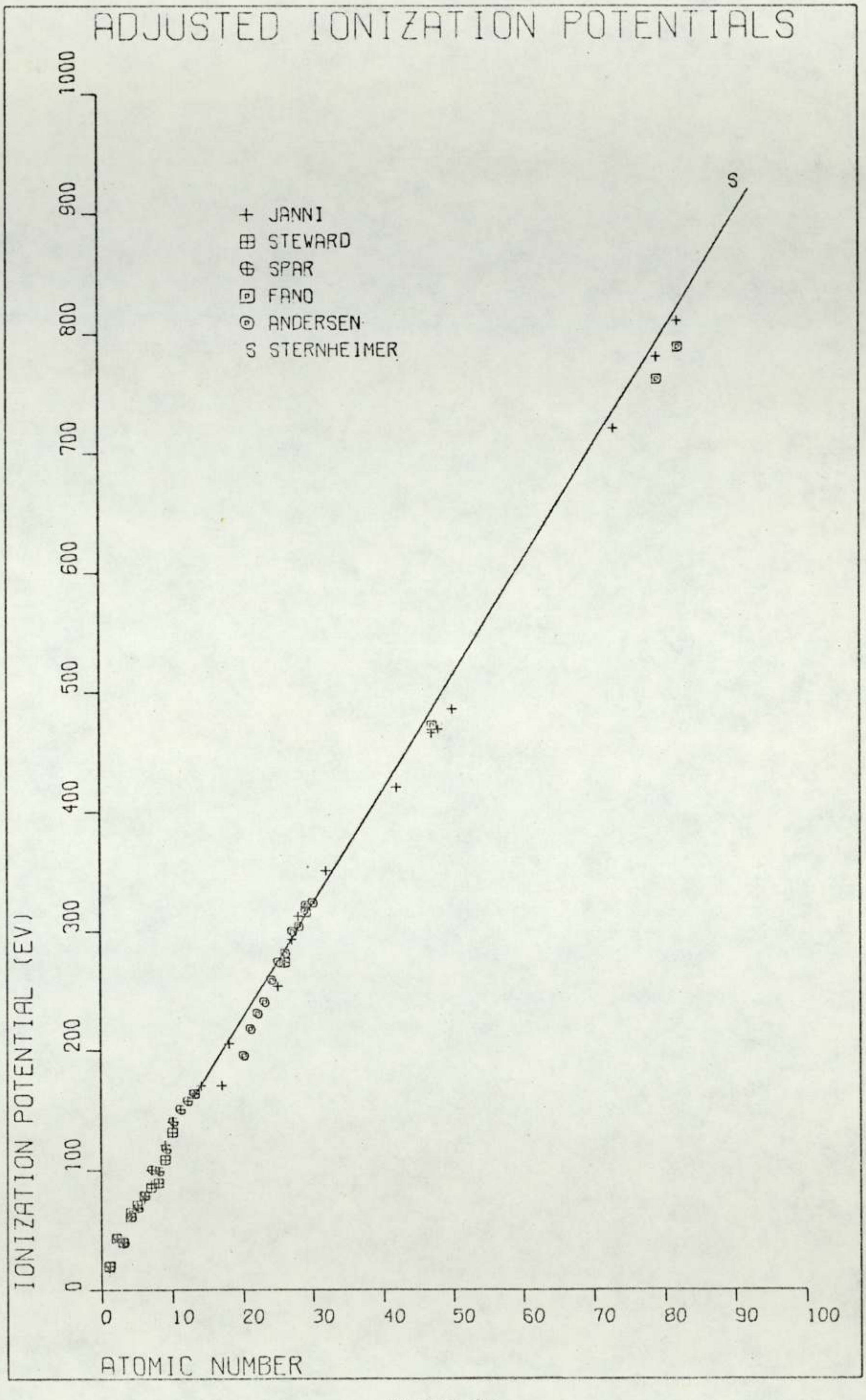
ADJUSTED IONIZATION POTENTIALS
IONIZATION POTENTIAL (EV)
0
100
200
300
400
500
600
700
800
900
1000
ATOMIC NUMBER
0
10
20
30
40
50
60
70
80
90
100
+ JANNI
⊞ STEWARD
⊕ SPAR
⊡ FANO
⊙ ANDERSEN
S STERNHEIMER
S

Figure 35

number but exhibits an oscillatory dependence.

As a projectile ion slows down in matter and approaches velocities comparable to the orbital velocity of an orbital electron the probability of electron capture greatly exceeds the loss probability. For $\beta \geqslant 0.04\ Z_2^{2/3}$ the net charge of the particle is therefore less than the nuclear charge. The cross-sections for electron loss and capture have been determined by KANNER (1951) and HALL (1956). The effective charge of an ion at a given velocity may be obtained from the empirical relationship of BARKAS (1963),

$$Z_1 = Z_1 \left[1 - \exp\ (-125\beta Z_1^{-2/3}) \right]$$

By inclusion of the shell correction terms and the concept of effective charge the Bethe formulation given in Equation (24) may be considered to be valid for projectile velocities such that $\beta \geqslant 0.0046\ Z_1^{1/3}$ and and is therefore applicable for proton energies in excess of 0.01 MeV.

LINDHARD et al. (1961) (1963) have developed the only generally useful theory valid at low projectile velocities ($0 \leqslant \beta \leqslant 0.0046 Z_1^{1/3}$). The theory is expressed in dimensionless units and is based on a proposal first discussed by BOHR (1948) who suggested that the "electronic" and "nuclear" components of the stopping power may be calculated separately and then added together. The unit corresponding to distance is

$$\zeta = 4\pi\ a^2\ N \left(\frac{A_1}{A_1 + A_2} \right)^2 R \quad \ldots\ldots\ldots \quad (26)$$

with

$$a = 0.8853\ a_o\ (Z_1^{\ 2/3} + Z_2^{\ 2/3})^{\ -\ 1/2}$$

where a_o is the first Bohr radius for hydrogen ($5.29\ .\ 10^{-11}$m), A_1, Z_1 and R are the mass, charge and range of the projectile ion, respectively, A_2, Z_2 and N are the mass, charge and atom density of the stopping medium respectively. The unit corresponding to distance is

$$\theta\ = 1.8\dot{4}\ .\ 10^{-26}\ \frac{a}{e^2}\ \left(\frac{A_2\ A_2}{A_1\ +\ A_2} \right) \frac{\varepsilon}{Z_1 Z_2} \qquad \text{..........}\ (27)$$

where ε is the specific energy (joule. kg^{-1}).

The electronic stopping power is given by

$$\left(\frac{d\theta}{d\zeta} \right)_e \ = \ K\zeta^{1/2}$$

where K is a constant defined by

$$K = 8.077\ .\ 10^{-9}\ \ \xi\ \left[\frac{Z_1^{1/2}\ \ Z_2^{1/2}}{Z_1^{2/3}\ +\ Z_2^{2/3}\ \ \ 3/4} \right] \left[\frac{A_1\ \ +\ \ A_2^{3/2}}{A_1^{3/2}\ \ \ A_2^{1/2}} \right]$$

and ξ is approximately $Z_1^{1/6}$. The nuclear component of the stopping power was not expressed in closed form by Lindhard et al., but was presented graphically in the dimensionless units of Equations (26) and (27) as a universal curve valid for all projectile ions and stopping media. An analytical expression for this curve has been obtained by STEWARD (1968), who presented the stopping power in the form*

$$\frac{dE}{dR} = \left(\frac{dE}{dR}\right)_e + \left(\frac{dE}{dR}\right)_n \qquad (\text{joule.m}^{-1})$$

where

$$\left(\frac{dE}{dR}\right)_e = 7.794 \times 10^{-28}\, N\left(Z_1^{1.207}\, Z_2\right)\left(Z_1^{2/3} + Z_2^{2/3}\right)^{-3/2} \varepsilon^{1/2} (\text{joule.m}^{-1})$$

and

$$\left(\frac{dE}{dR}\right) = C_n\, \varepsilon^{1/2} \exp\left[-3947.1\, (C_n' \,\varepsilon)^{0.277}\right] \qquad (\text{joule.m}^{-1})$$

with

$$C_n = 4.365 \times 10^{-26} N \left(\frac{A_1^2}{A_1 + A_2}\right)^{3/2} \left(\frac{Z_1\, Z_2}{A_2}\right)^{1/2} \left(Z_1^{2/3} + Z_2^{2/3}\right)^{-3/4}$$

and

$$C_n' = \left(\frac{A_1\, A_2}{Z_1\, Z_2}\right)\left(A_1 + A_2\right)^{-1}\left(Z_1^{2/3} + Z_2^{2/3}\right)^{-1/2}$$

When there is more than one atomic component to the stopping medium, as in mixtures and compounds, it is usual to assume that the stopping power of each component acts independently and is thus additive to that of the others (Bragg's Rule). At low ion velocities the use of Bragg's rule may not be valid. As projectile velocity decreases the more tightly bound inner electron shells of the atoms of the stopping medium contribute less to the stopping process than the more loosely bound valence shell. In chemical bonding the energy of the valence shell is modified and departure from strict additivity would therefore be expected primarily at low ion velocities, particularly,

---

* Note. Steward presented the equations in C.E.S. units. The conversion to M.K.S. units has been made by the author.

for hydrogen compounds. Experimental studies by THOMPSON (1952) for high energy protons (200 MeV to 340 MeV) have shown that deviations from strict additivity are 2 per cent, or less, for low Z_2 compounds containing hydrogen. As Z_2 is increased the deviation decreases rapidly and is negligible above chlorine. B EWERS and FLACK (1968) found that for 1 MeV protons the stopping powers of sixteen different fluorine compounds (some containing hydrogen) deviated from Bragg's rule by less than 2 per cent. The validity of the additivity rate for gases has been established by REYNOLDS et al. (1953), for proton energies above 0.2 MeV, with the exception of nitrous oxide which had a stopping power approximately 4 per cent higher than expected assuming additivity. For mixtures of elements there are no binding effects and the additivity rule should be strictly correct.

The mean pathlength may be obtained by numerical integration of the stopping power;

$$P\ (E_i) = \int_o^{E_i} (dE/dx)^{-1}\ dE$$

Unfortunately stopping power cross-sections have not been measured at low projectile velocities and there is some doubt as to the reliability with which they can be calculated. Published pathlength data therefore involves a normalization of the type ;

$$P\ (E_i) = P\ (E_N) + \int_{E_N}^{E_i} (dE/dx)^{-1}\ dE$$

where $P\ (E_i)$ is the total mean pathlength of ions of initial energy E_i, and $P\ (E_N)$ is the pathlength at energy E_N. The mean pathlength at E_N is obtained from experimental data and the mean pathlength for all higher energies normalized to this value. The pathlength at high energy has a small dependence on the value selected at the normalization energy; at lower energies a significant error may be introduced.

The range of an ion in an absorbing medium is somewhat shorter than the pathlength as measured from the original angle of incidence into the medium, because the ion undergoes multiple scattering. In general corrections for multiple scattering increase with Z_1 and, for a given ion, decrease with increasing energy. A discussion of the theory of multiple scattering is beyond the scope of the present work. Detailed descriptions of the corrections may be found in the literature, LEWIS (1950), YANG (1951), MATHER and SEGRÈ (1951), BICHSEL and UEHLING (1960), BARKAS and VON FRIESEN (1961), SCOTT (1963), BERGE (1963), BERGER and SELTZER (1964), JANNI (1966), TSCHÄLAR and BICHSEL (1967), (1968), EASTHAM (1975).

Published stopping power and range data is legion. The author has concentrated on the more comprehensive data sets and compared them for a series of eight elements with atomic numbers from $Z_2 = 4$ to $Z_2 = 79$. Chromium and calcium fluoride data was included as these target media are of interest in the present work. Only a brief description of the procedures employed in the generation of the data sets is given as more detailed information can be obtained from the cited references.

Stopping power data was calculated by the author using the Bethe formulation [Equation (24)] but neglecting the shell correction, polarization effect and charge reduction terms. The inclusion of shell corrections was accomplished using the computer programme "KINK" developed by CLARKE (1974) who has derived inner shell correction terms by fitting functional equations to the data of FANO et al.(1964).

The tabulation of WILLIAMSON et al.(1962) includes stopping power and range data for proton, deuteron, helium-3 and alpha particle projectile ions in thirty seven elemental target media with atomic numbers from $Z_2 = 1$ to $Z_2 = 92$. The tables cover the energy range 0.05 MeV to 100 MeV and are based on an empirical modification of the Bethe formulation which asymptotically approaches the Bethe form at high energy.

A comprehensive tabulation for one hundred and three projectile ion types in twenty-four target media has been presented by NORTHCLIFFE and SCHILLING(1970), derived from a series of "master" curves for various ions in aluminium. Theoretical and empirical formulations and experimental data, were used to generate stopping power and range data for other target media and projectile ions relative to the aluminium master curves. The tables are limited to the specific energy region 0.0125 MeV/amu to 12 MeV/amu.

An extensive tabulation of proton stopping power, pathlength, range, multiple scattering and pathlength straggling in seventy-four target media has been produced by JANNI (1966). Values of energy loss between 0.1 MeV and 1.0 MeV were obtained by smoothing and interpolating experimental data. For energies from 1.0 MeV to 1000 MeV the Bethe formulation was usual. Pathlengths were obtained by numerical integration of the stopping power and normalized to experimental data at 0.1 MeV. Multiple Coulomb scattering theory was used to calculate ranges.

STEWARD (1968) has developed a method for calculating stopping power and range data for any heavy ion of specific energy $0.01 \leqslant E/A_1 \leqslant 500$ MeV/amu incident on any nongaseous target medium. The method has been incorporated into a computer programme*. For projectile ions with $Z_1 \leqslant 10$ at low energy ($\varepsilon \leqslant 10$ MeV/amu) the programme uses experimental data. For projectile ions with $Z_1 > 10$ the stopping power theory of Lindhard et al. is adjusted to fission product data at low energy; at intermediate energies charge-state data developed from argon range-energy data in aluminium is extended to other projectile ions and target media. The Bethe formulation is used in all cases for projectile velocities such that $137\beta > 3Z_1$.

The experimental data of ANDERSEN et al. (1967), (1968), (1969) has been included in the comparison because of the high accuracy (0.3 per cent) claimed for the data set. Data obtained by GORODETSKY et al.(1967) was also considered as one of the most recent experimental determinations of proton stopping power in calcium fluoride.

Stopping power data for cited authors is presented in Figures 36 to 44. Between 1 MeV and 10 MeV the curves, in general, converge as all data sets essentially use the Bethe formulation in this energy region. Below 1 MeV, however, the data sets diverge, maximum divergence occurring at approximately 0.1 MeV.

*Note: Data presented here was produced by a version of Steward's programme modified by the author.

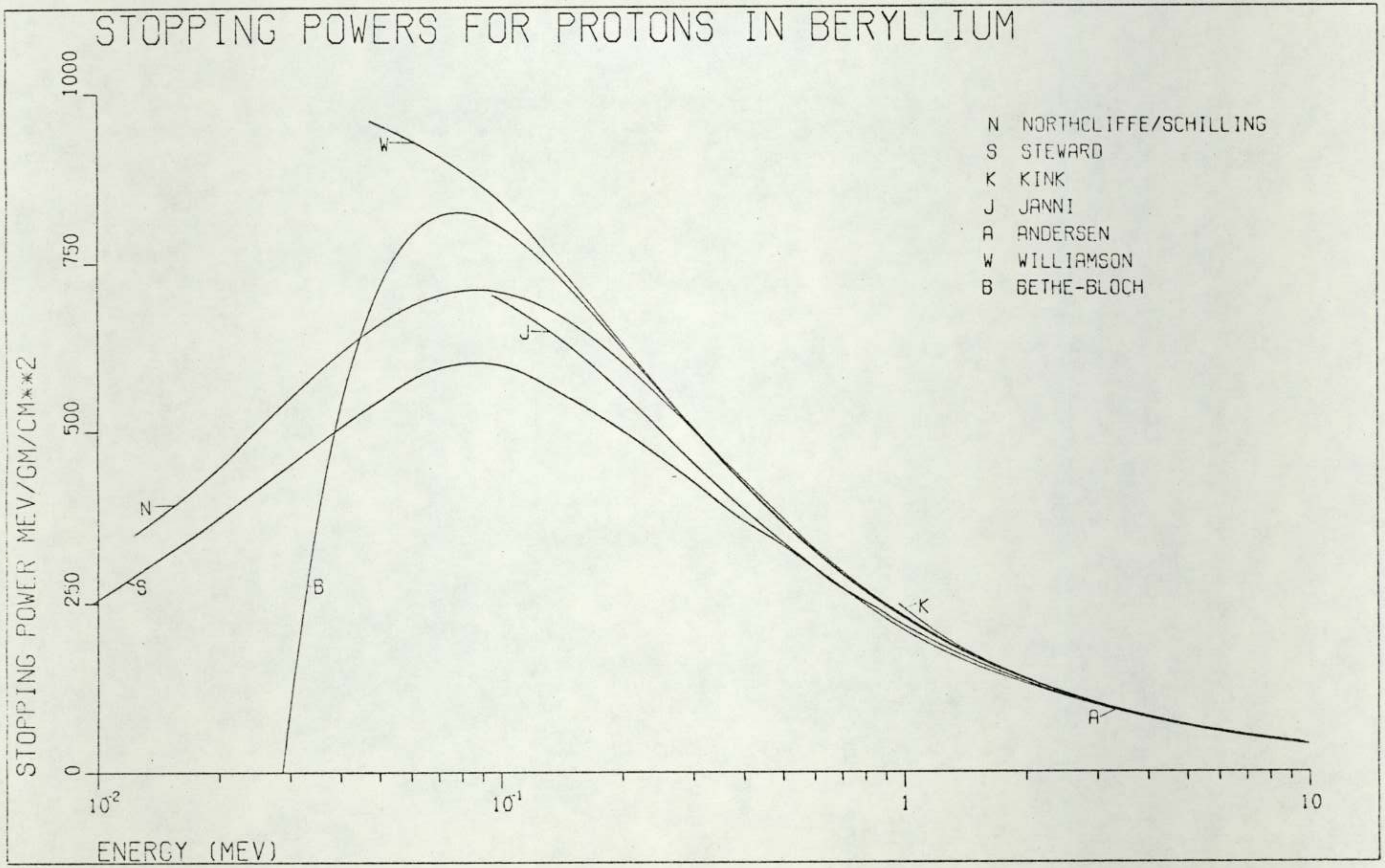
STOPPING POWERS FOR PROTONS IN BERYLLIUM
N NORTHCLIFFE/SCHILLING
S STEWARD
K KINK
J JANNI
A ANDERSEN
W WILLIAMSON
B BETHE-BLOCH
STOPPING POWER MEV/GM/CM**2
1000
750
500
250
0
10^{-2}
10^{-1}
1
10
ENERGY (MEV)
W
J
N
S
B
K
A

Figure 36

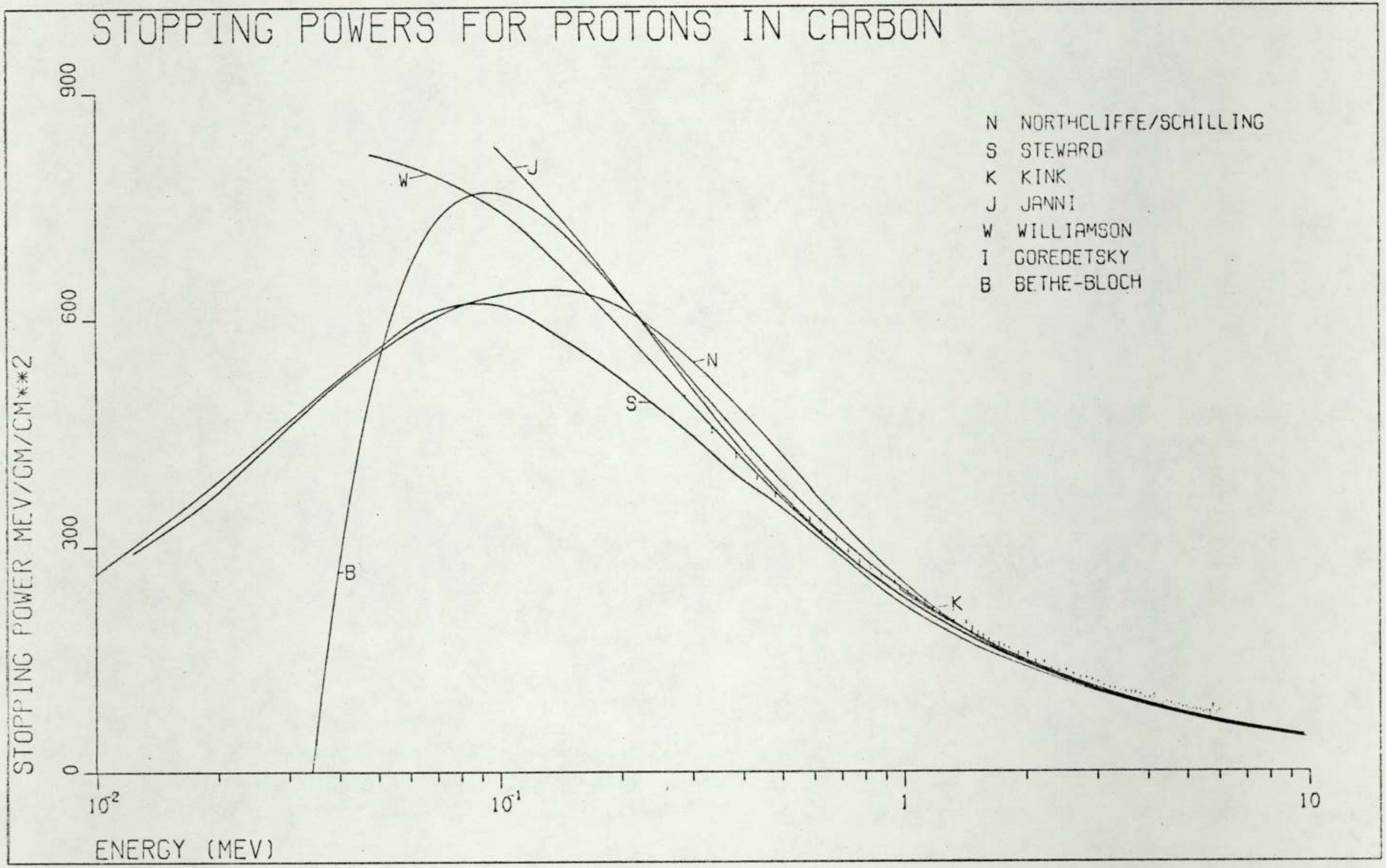
STOPPING POWERS FOR PROTONS IN CARBON
N NORTHCLIFFE/SCHILLING
S STEWARD
K KINK
J JANNI
W WILLIAMSON
I GOREDETSKY
B BETHE-BLOCH
STOPPING POWER MEV/CM/CM**2
900
600
300
0
10^{-2}
10^{-1}
1
10
ENERGY (MEV)
W
J
N
S
B
K

Figure 37

The best overall agreement is found in the data for aluminium (Figure 38) which has long been established as a reference and normalization standard for stopping power data.

The curves generated by the author illustrate the failure of the simplified Bethe formulation at low projectile velocities, particularly for elements with high atomic numbers. Essentially similar qualifications apply to the data produced by the computer programme "KINK". The anomalously high values obtained for chromium in the energy region 1 MeV to 3 MeV (Figure 39) are not clearly understood. The discrepancy may in part be due to the use of Jannis' value for the adjusted ionization energy for chromium (224.4 eV) which is approximately 13 per cent lower than the value used by other authors (256.9 eV).

The data of WILLIAMSON et al. is generally lower than other data sets in the energy region 0.1 MeV to 1 MeV and higher than other data sets below 0.1 MeV. Their low energy data for silver (Figure 41) appears to be particularly in error.

The data of Janni is in general agreement with other data sets for proton energies in excess of 0.5 MeV. For lower energies it gives high values of stopping power, particularly for chromium, silver and calcium fluoride (Figures 39,41 and 44 respectively). A discontinuity in the tantalum data at 1 MeV (Figure 42) indicates incorrect normalization of the high energy Bethe formulation to experimental data used at lower energies.

The most consistent of the data sets investigated are those of Steward and Northcliffe and Schilling, as only for light elements does

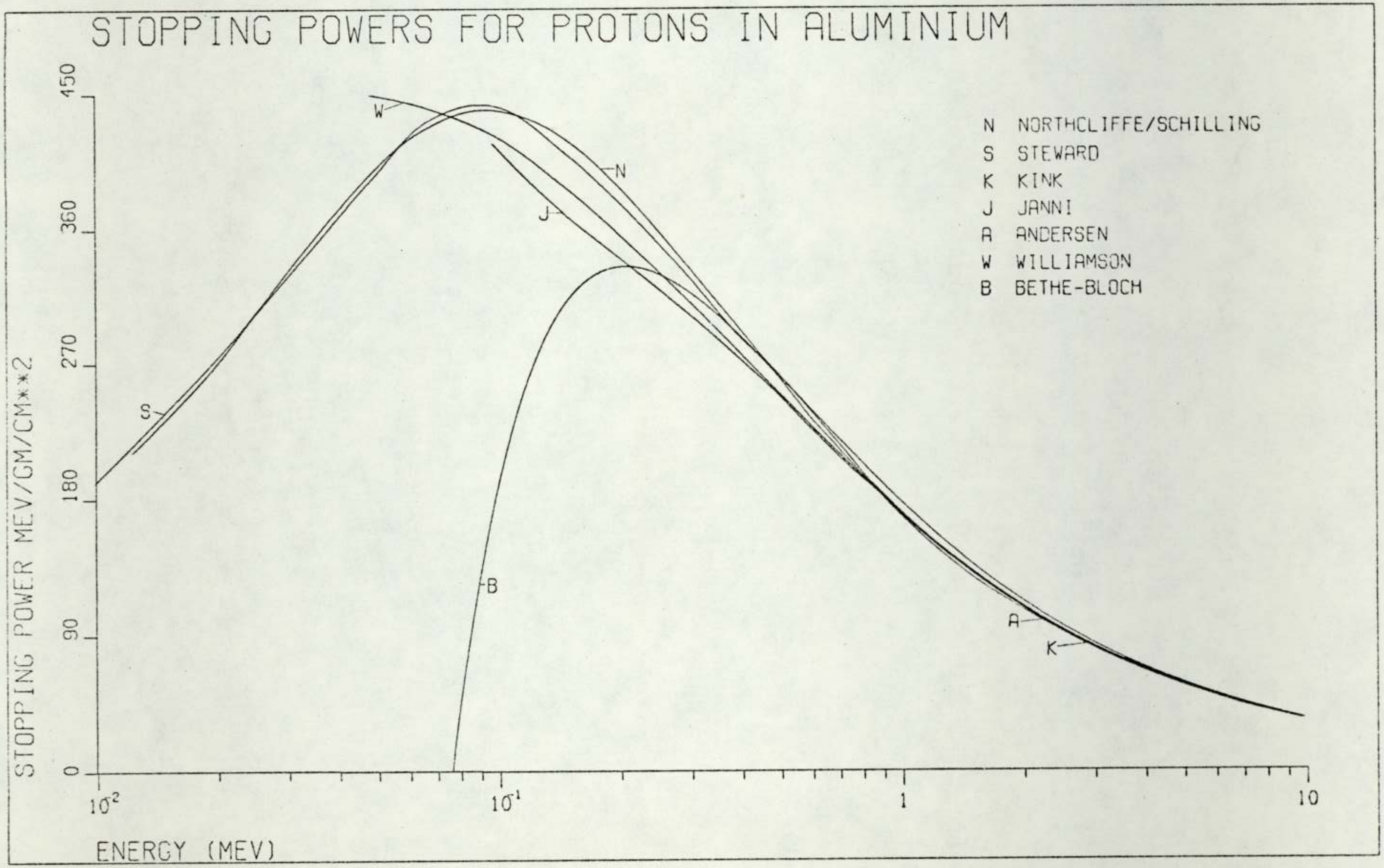
STOPPING POWERS FOR PROTONS IN ALUMINIUM
N NORTHCLIFFE/SCHILLING
S STEWARD
K KINK
J JANNI
A ANDERSEN
W WILLIAMSON
B BETHE-BLOCH
W
N
J
S
B
A
K
450
360
270
180
90
0
STOPPING POWER MEV/GM/CM**2
10^{-2}
10^{-1}
1
10
ENERGY (MEV)

Figure 38

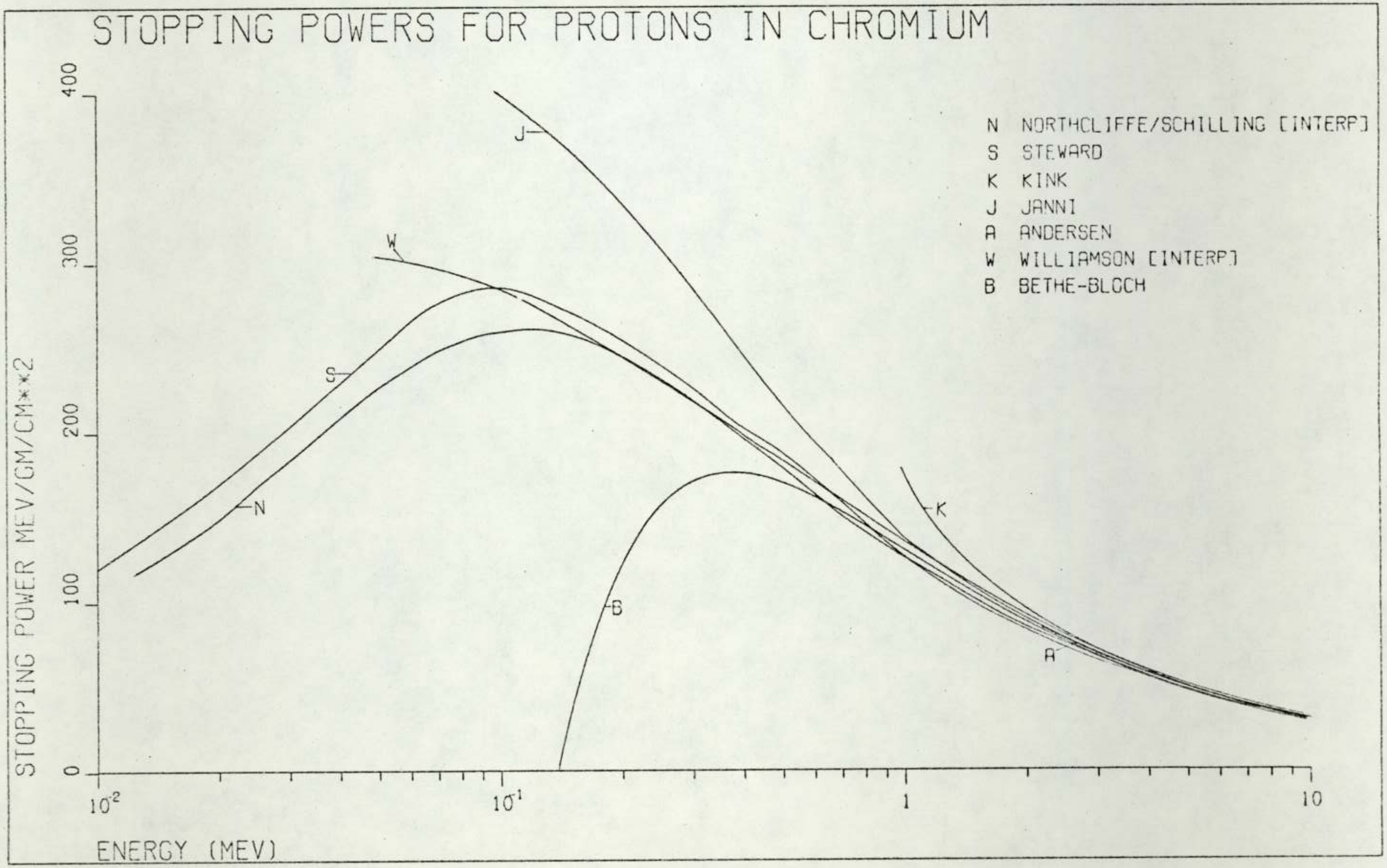
STOPPING POWERS FOR PROTONS IN CHROMIUM
N NORTHCLIFFE/SCHILLING [INTERP]
S STEWARD
K KINK
J JANNI
A ANDERSEN
W WILLIAMSON [INTERP]
B BETHE-BLOCH
STOPPING POWER MEV/GM/CM**2
0
100
200
300
400
ENERGY (MEV)
10^{-2}
10^{-1}
1
10
N
S
W
J
B
K
A

Figure 39

any serious conflict arise. Steward's data includes both electronic and nuclear contributions to the total stopping power and is therefore higher at low energies than the purely electronic stopping power data of Northcliffe and Schilling. A slight inflection, at 0.5 MeV, may be seen in a number of the curves taken from Northcliffe and Schilling*. The tabulation was produced by fitting the energies above 0.5 MeV and those below 0.5 MeV separately, using general second order polynomials, 0.5 MeV being used as an end point of both fits. The smooth curves presented here were obtained by fitting general cubic polynomials to the tabulated points. The inflection therefore indicates that Northcliffe and Schilling did not match the derivatives of the piecewise fit at the 0.5 MeV end point. Inflections were also observed in curves fitted to Steward's data for energies in the region 0.4 MeV and 0.7 MeV. It is considered that this reflects a similar missmatch of derivative values or a normalization error in Steward's data in the transition region between the Lindhard et al. theory and the Bethe formulation.

The experimental data of Gorodetsky et al. tends to follow the Janni tabulation. The accuracy of the data is not, however, sufficient to resolve differences among data sets. Within the resolution of the curves the data of Andersen et al. is in agreement with all data sets.

The data of Northcliffe and Schilling has been selected as an

---

*Note : The more serious cases have been "smoothed".

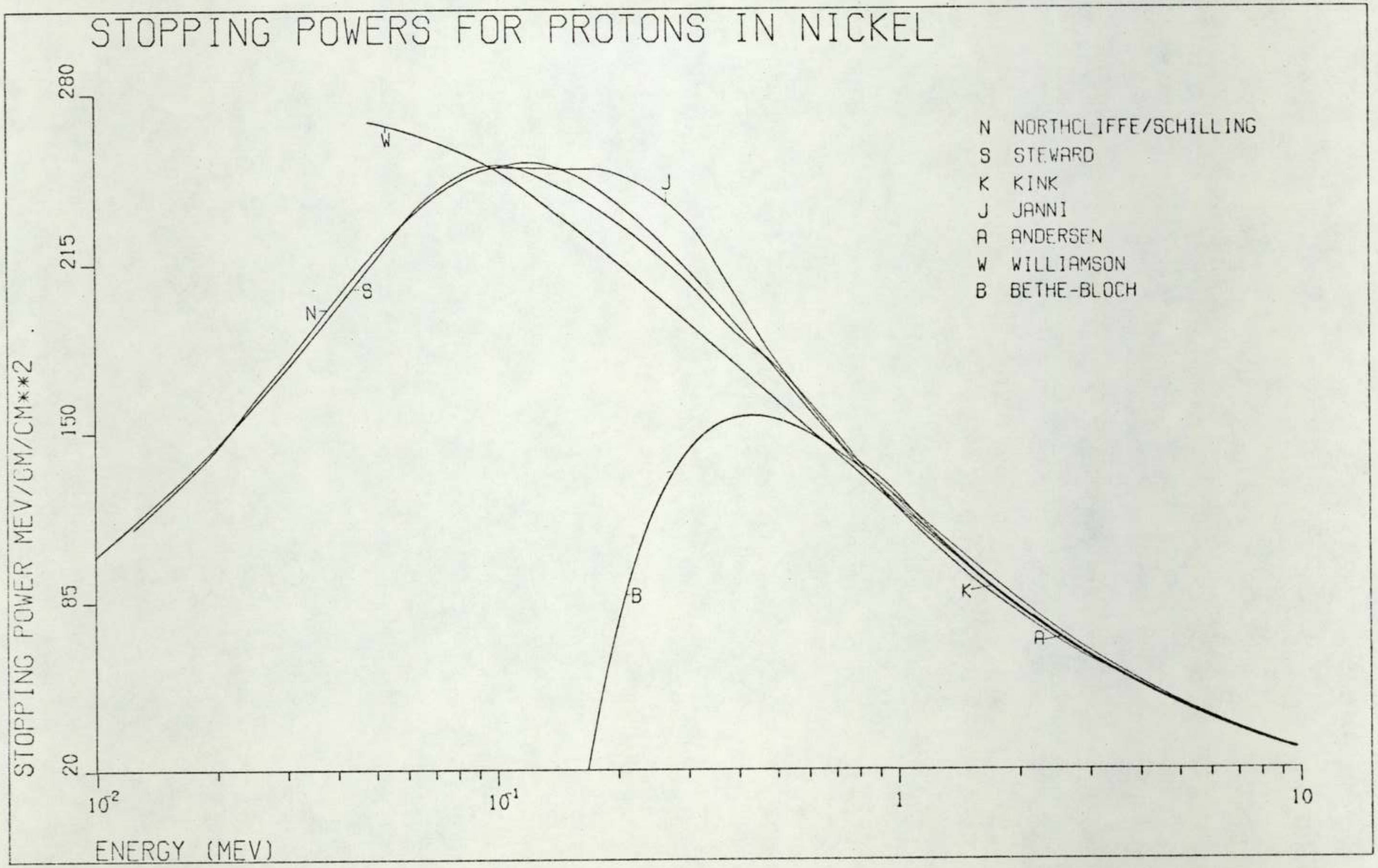
STOPPING POWERS FOR PROTONS IN NICKEL
N NORTHCLIFFE/SCHILLING
S STEWARD
K KINK
J JANNI
A ANDERSEN
W WILLIAMSON
B BETHE-BLOCH
STOPPING POWER MEV/GM/CM**2
280
215
150
85
20
10^{-2}
10^{-1}
1
10
ENERGY (MEV)
W
J
N
S
B
K
A

Figure 40

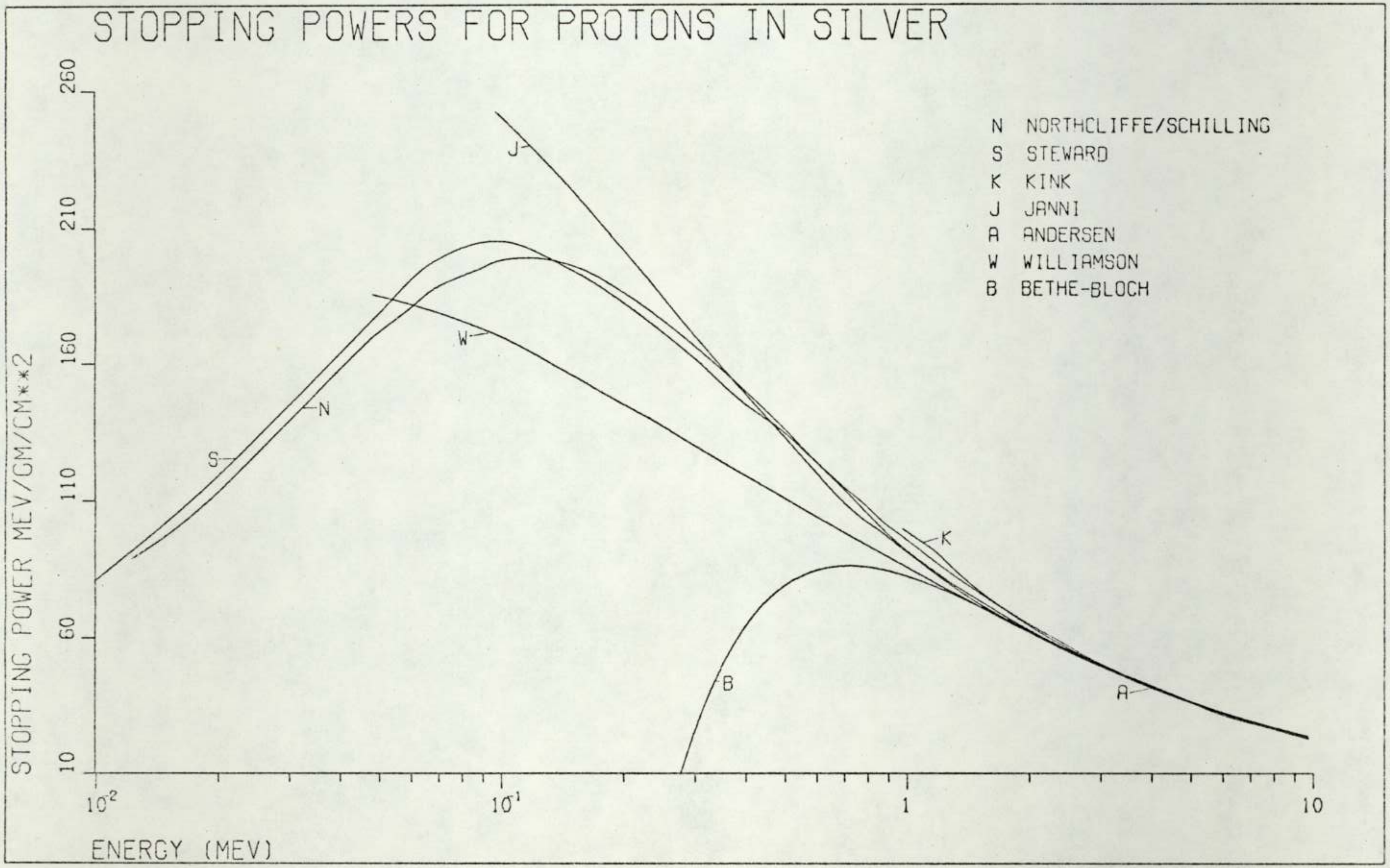
STOPPING POWERS FOR PROTONS IN SILVER
N NORTHCLIFFE/SCHILLING
S STEWARD
K KINK
J JANNI
A ANDERSEN
W WILLIAMSON
B BETHE-BLOCH
STOPPING POWER MEV/GM/CM**2
260
210
160
110
60
10
10^{-2}
10^{-1}
1
10
ENERGY (MEV)
J
W
N
S
K
B
A

Figure 41

arbitrary comparison standard. Deviations from this standard have been expressed as percentage differences at common tabulated data points. The energy regions 0.1 MeV to 1 MeV and 1 MeV to 10 MeV have been considered separately in order to accommodate the wide scatter of results. As this mode of display necessarily produces a large number of similar curves they are presented in Appendix II. The one per cent confidence interval for the Northcliffe and Schilling data is indicated on the figures by broken lines. Northcliffe and Schilling do not claim an overall accuracy of one per cent for their data and make no estimate of the reliability of their proton data *. Error bars associated with points in the percentage difference plots are a combination of the errors attributed by the authors of the individual data sets and a one per cent error assumed for the data of Northcliffe and Schilling.

In the energy region 0.1 MeV to 1.0 MeV no clear or systematic differences are evident. The energy region 1 MeV to 10 MeV, however, reveals a number of significant features. In general, the data of Northcliffe and Schilling represent an average of all other data sets taken as a whole. The apparent exception of chromium (Figure 13, Appendix II) is not necessarily significant as data for chromium is not included in the Northcliffe and Schilling tabulation and has been generated by interpolation from their data for other elements. In the energy region of 5 MeV to 10 MeV data for the simple Bethe

*Note : The one per cent level is possibly a lower limit as Northcliffe and Schilling claim to have fitted the aluminium master curves to within this accuracy.

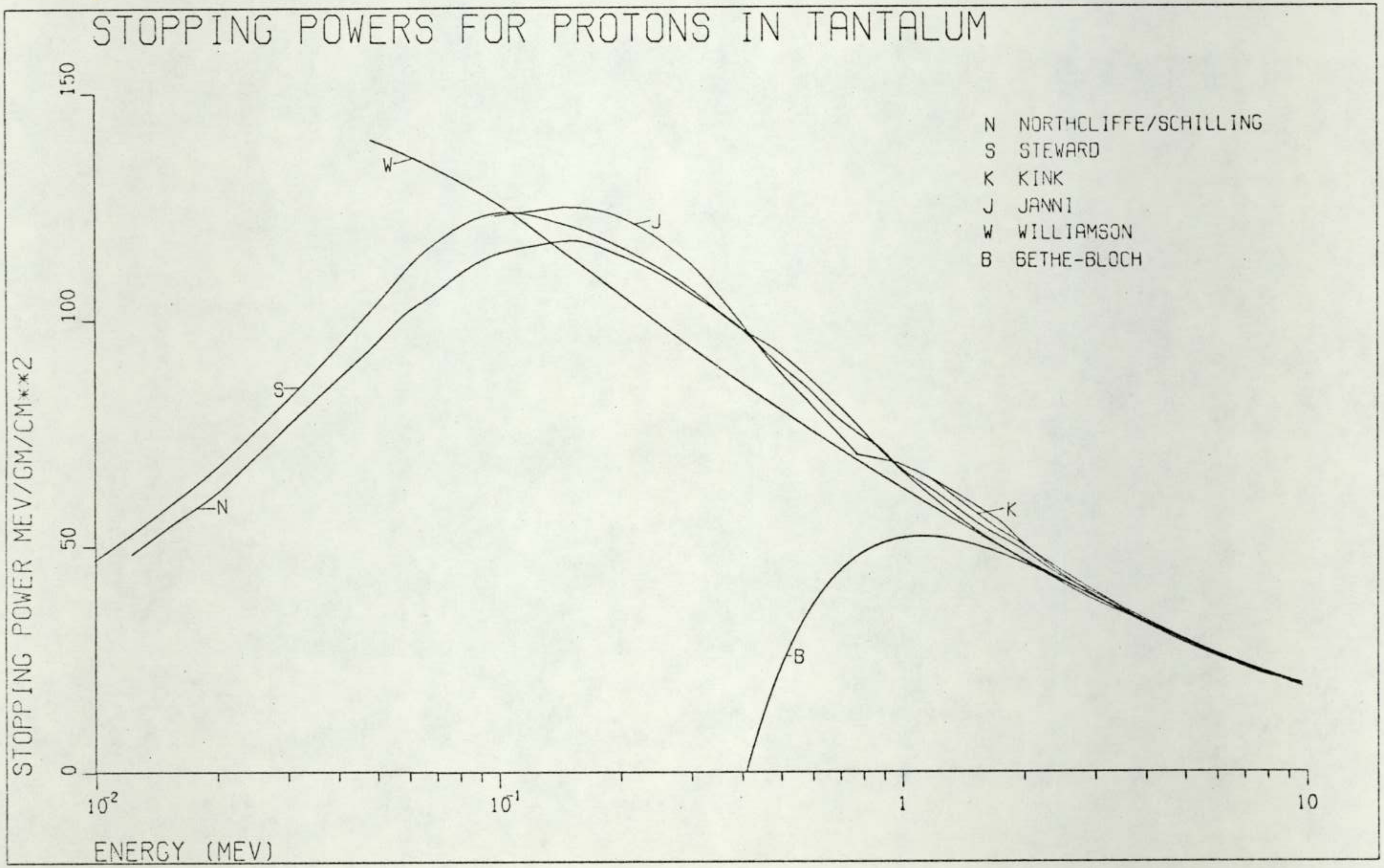
STOPPING POWERS FOR PROTONS IN TANTALUM
N NORTHCLIFFE/SCHILLING
S STEWARD
K KINK
J JANNI
W WILLIAMSON
B BETHE-BLOCH
W
J
S
N
K
B
STOPPING POWER MEV/GM/CM**2
0
50
100
150
10^{-2}
10^{-1}
1
10
ENERGY (MEV)

Figure 42

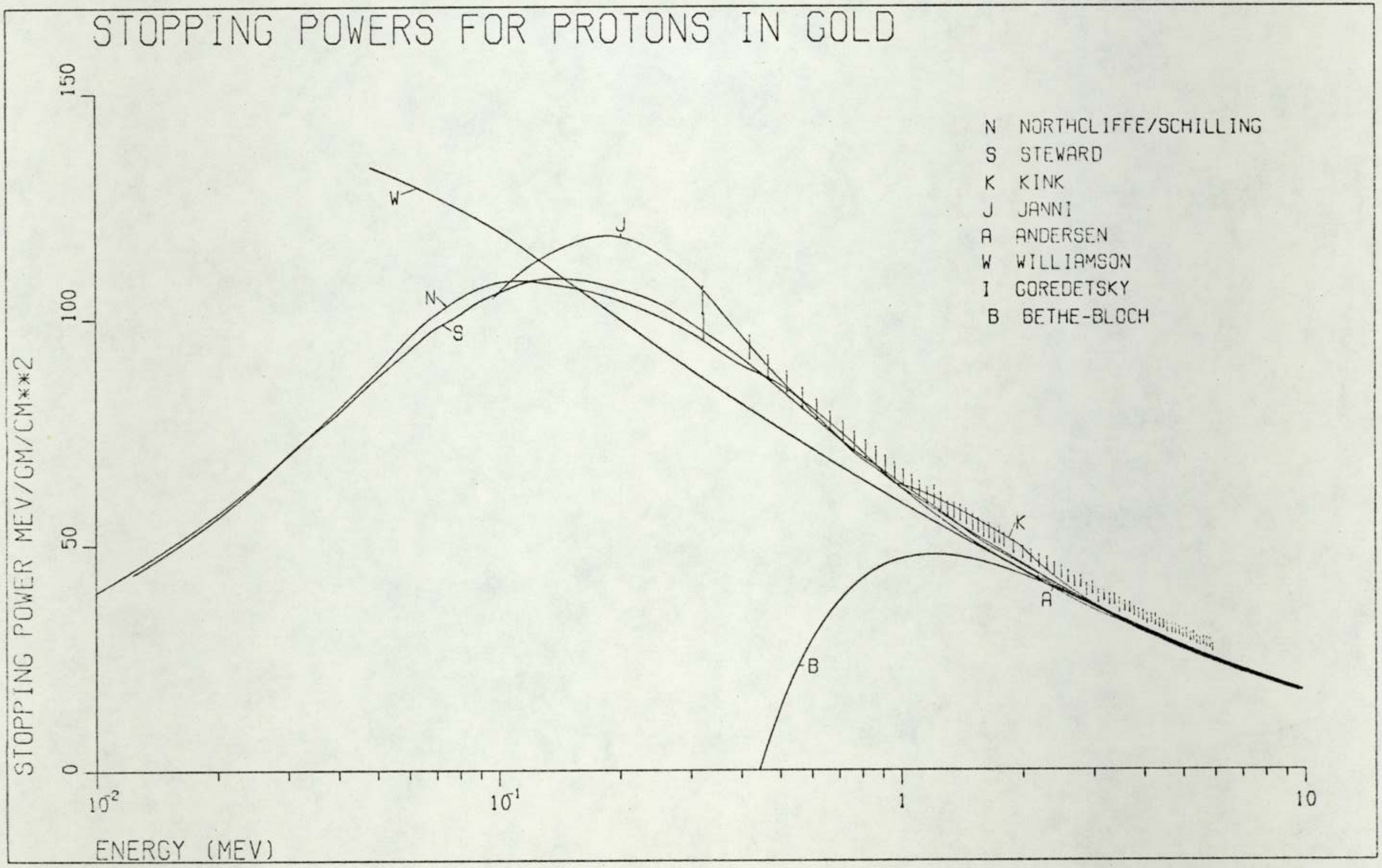
STOPPING POWERS FOR PROTONS IN GOLD
STOPPING POWER MEV/GM/CM**2
150
100
50
0
10^{-2}
10^{-1}
1
10
ENERGY (MEV)
N NORTHCLIFFE/SCHILLING
S STEWARD
K KINK
J JANNI
A ANDERSEN
W WILLIAMSON
I GOREDETSKY
B BETHE-BLOCH
W
J
N
S
K
A
B

Figure 43

formulation oscillates in unison with all other data sets about the Northcliffe and Schilling values. In this energy region the Bethe formulation yields a simple monotonically decreasing function and the observed oscillation must therefore be a feature of the Northcliffe and Schilling data. It is also significant that, in the same energy region, mutual agreement among the data sets of Williamson et al., Janni and Andersen et al.is much better than the agreement between any one of the data sets and the Northcliffe and Schilling tabulation.

The range data has been treated in a similar manner and is presented in Appendix III. In cases where no data exists in the tabulation of Northcliffe and Schilling the data of Steward has been chosen as a comparison standard.

In the energy region 0.1 MeV to 1 MeV the data of Steward and Northcliffe and Schilling generally agree to within 5 per cent. Beryllium and carbon (Figures 10 and 11, Appendix III) are notable exceptions as the disparity in stopping power data for these two elements is reflected in the range data. For beryllium, Steward's data is greater than Northcliffe and Schilling by 31 per cent at 0.1 MeV and 10 per cent at 1 MeV. The corresponding values for carbon are 7 per cent and 18 per cent, respectively. Janni and Williamson et al. ,deviate from Northcliffe and Schilling by approximately 12 per cent in the energy region 0.5 MeV to 1.0 MeV but yield substantially shorter ranges at lower energies (approximately 15 to 35 per cent shorter at 0.1 MeV).

In the energy region 1 MeV to 10 MeV Steward and Northcliffe and Schilling are in general agreement to within 2 per cent. The

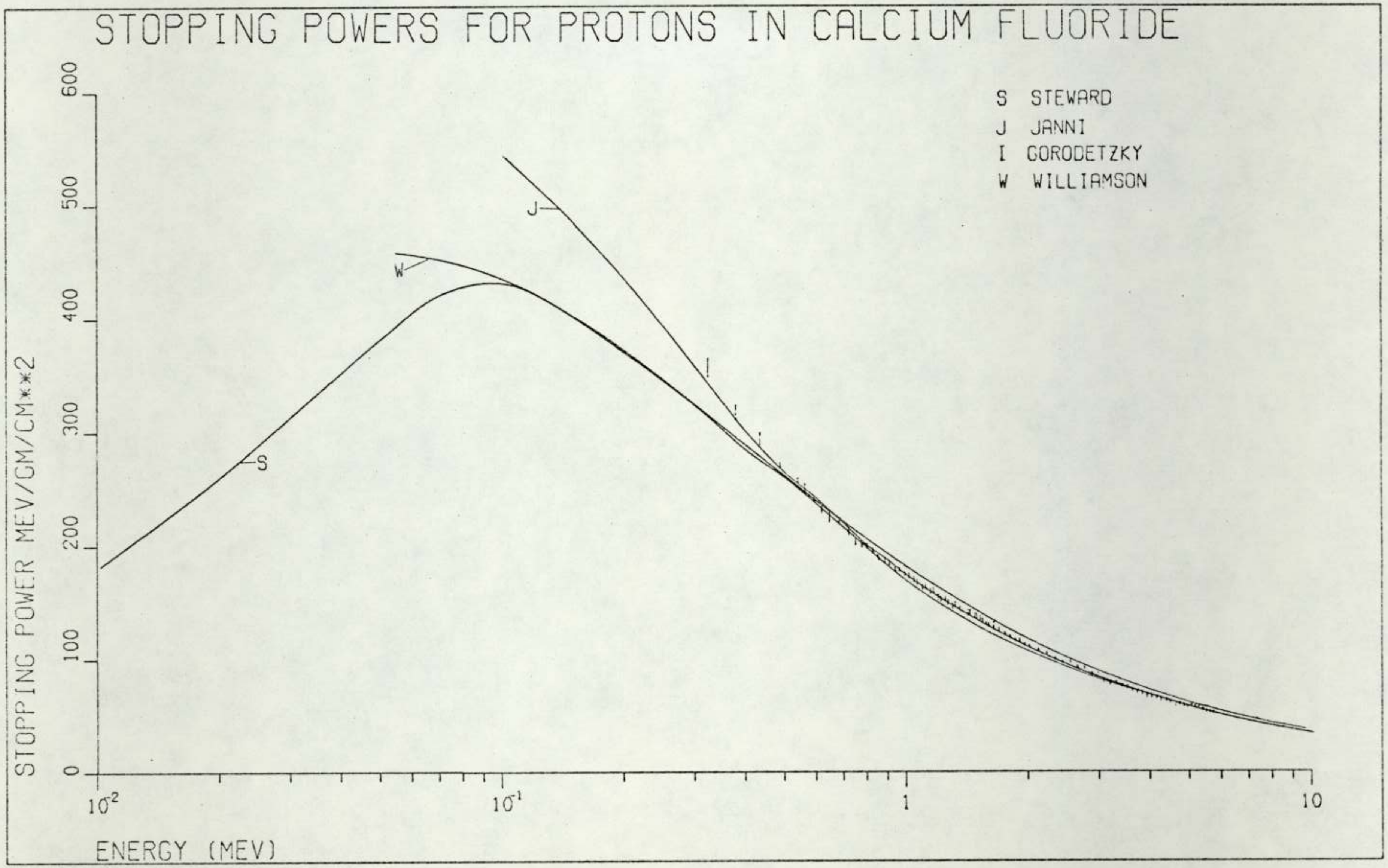
STOPPING POWERS FOR PROTONS IN CALCIUM FLUORIDE
S STEWARD
J JANNI
I GORODETZKY
W WILLIAMSON
J
W
S
STOPPING POWER MEV/GM/CM**2
0
100
200
300
400
500
600
10^{-2}
10^{-1}
1
10
ENERGY (MEV)

Figure 44

poor agreement between the sets for beryllium and carbon is still apparent, however, at the lower end of the interval. Janni and Williamson et al., are generally within 4 per cent of the Northcliffe and Schilling values except at 1 MeV for silver (Figure 24, Appendix III) where the Williamson et al data is high by approximately 15 per cent and gold (Figure 26, Appendix III) where the data of Janni is low by approximately 9 per cent. For aluminium (Figure 21, Appendix III) all data sets are consistent to within 1.5 per cent.

Since the above comparison was undertaken a very comprehensive method of calculating stopping power and range data has been made available. This is the FORTRAN IV computer programme "SPAR" developed by ARMSTRONG and CHADLER (1973), (1974) at the Oak Ridge National Laboratory.

SPAR is designed to calculate stopping powers and ranges for heavy ions in any nongaseous medium at energies from zero to several hundred GeV. Different computational procedures are used for each of the three (β, Z_1) regions. At high energies $(\beta > 0.07 Z_1^{2/3})$, the Bethe theory with shell and density effect corrections is employed. At intermediate energies $(0.0046\ Z_1^{1/3} < \beta \leq 0.07 Z_1^{2/3})$, an empirical expression due to BARKAS (1963) is used, and at low energies $(0 \leq \beta \leq 0.0046\ Z_1^{1/3})$ the theory of Lindhard et al. . In all cases stopping powers are computed using the continuous slowing down approximation and ranges are obtained by numerical integration of the stopping power.*

Stopping power data from the SPAR code is presented in Figures 45 to 53. The data of Northcliffe and Schilling is included for

*Note : The SPAR code has not been extensively tested by Armstrong and Chadler.

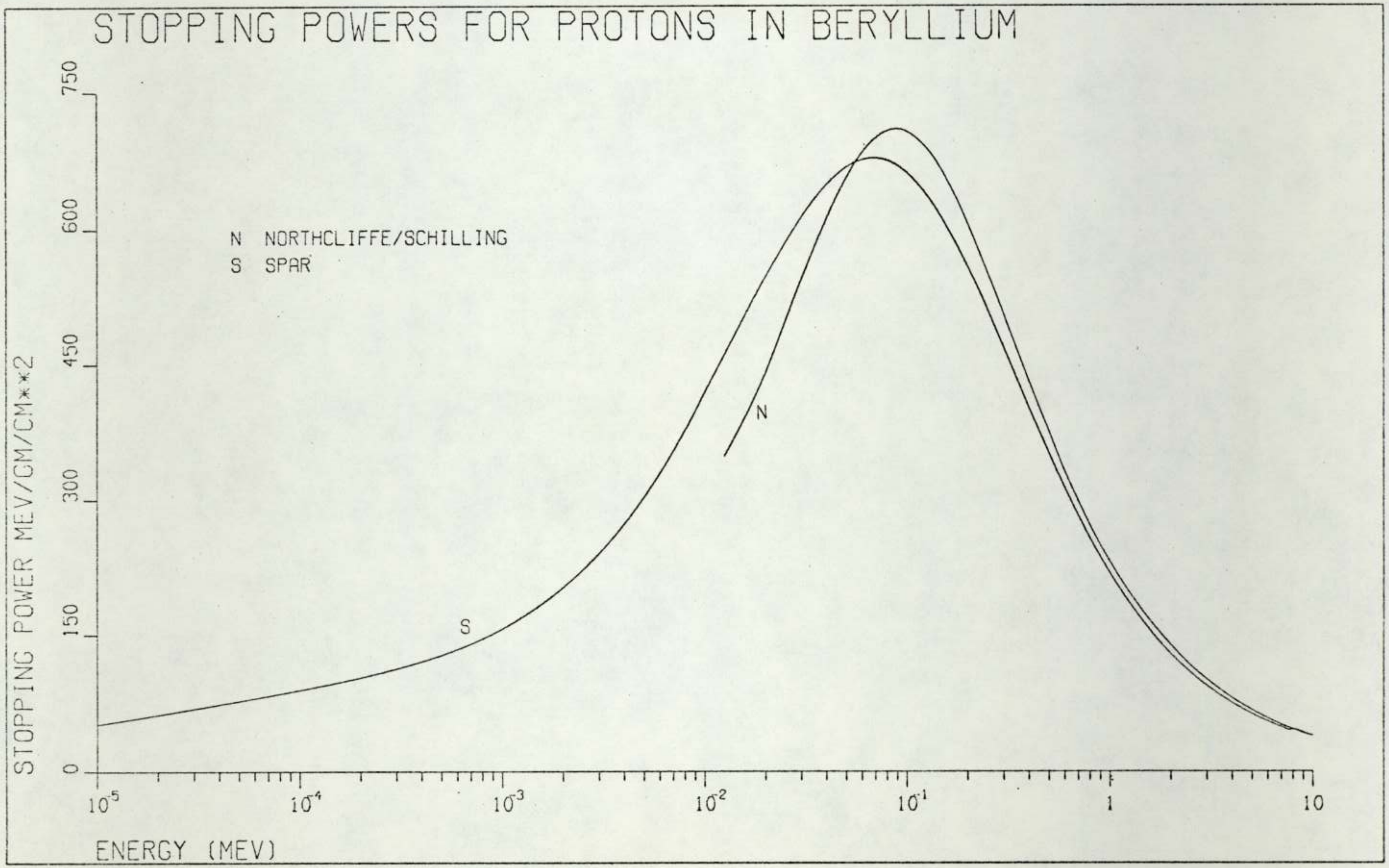
STOPPING POWERS FOR PROTONS IN BERYLLIUM
N NORTHCLIFFE/SCHILLING
S SPAR
N
S
STOPPING POWER MEV/CM/CM**2
0
150
300
450
600
750
10^{-5}
10^{-4}
10^{-3}
10^{-2}
10^{-1}
1
10
ENERGY (MEV)

Figure 45

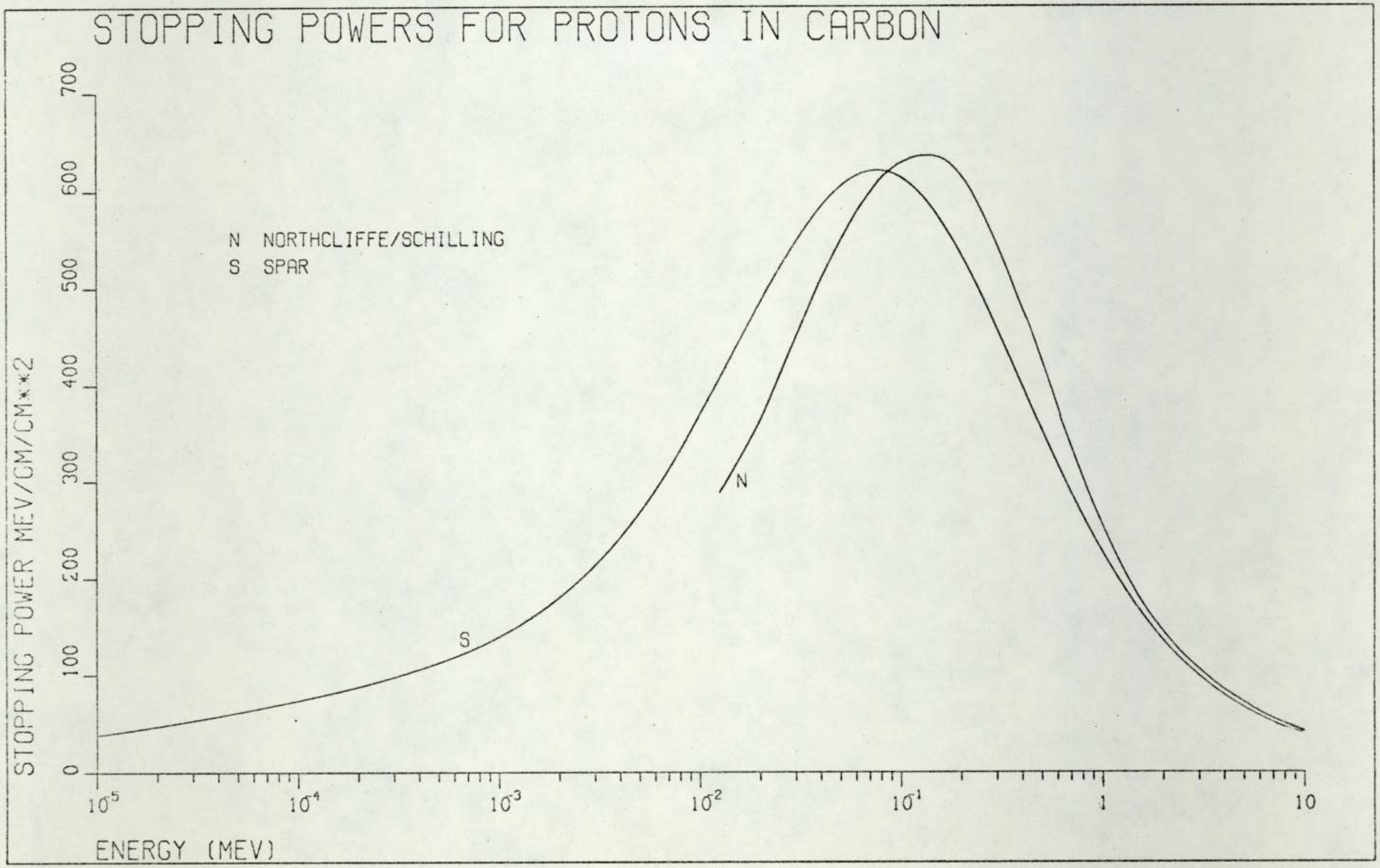
STOPPING POWERS FOR PROTONS IN CARBON
N NORTHCLIFFE/SCHILLING
S SPAR
STOPPING POWER MEV/GM/CM**2
0
100
200
300
400
500
600
700
ENERGY (MEV)
10^{-5}
10^{-4}
10^{-3}
10^{-2}
10^{-1}
1
10
N
S

Figure 46

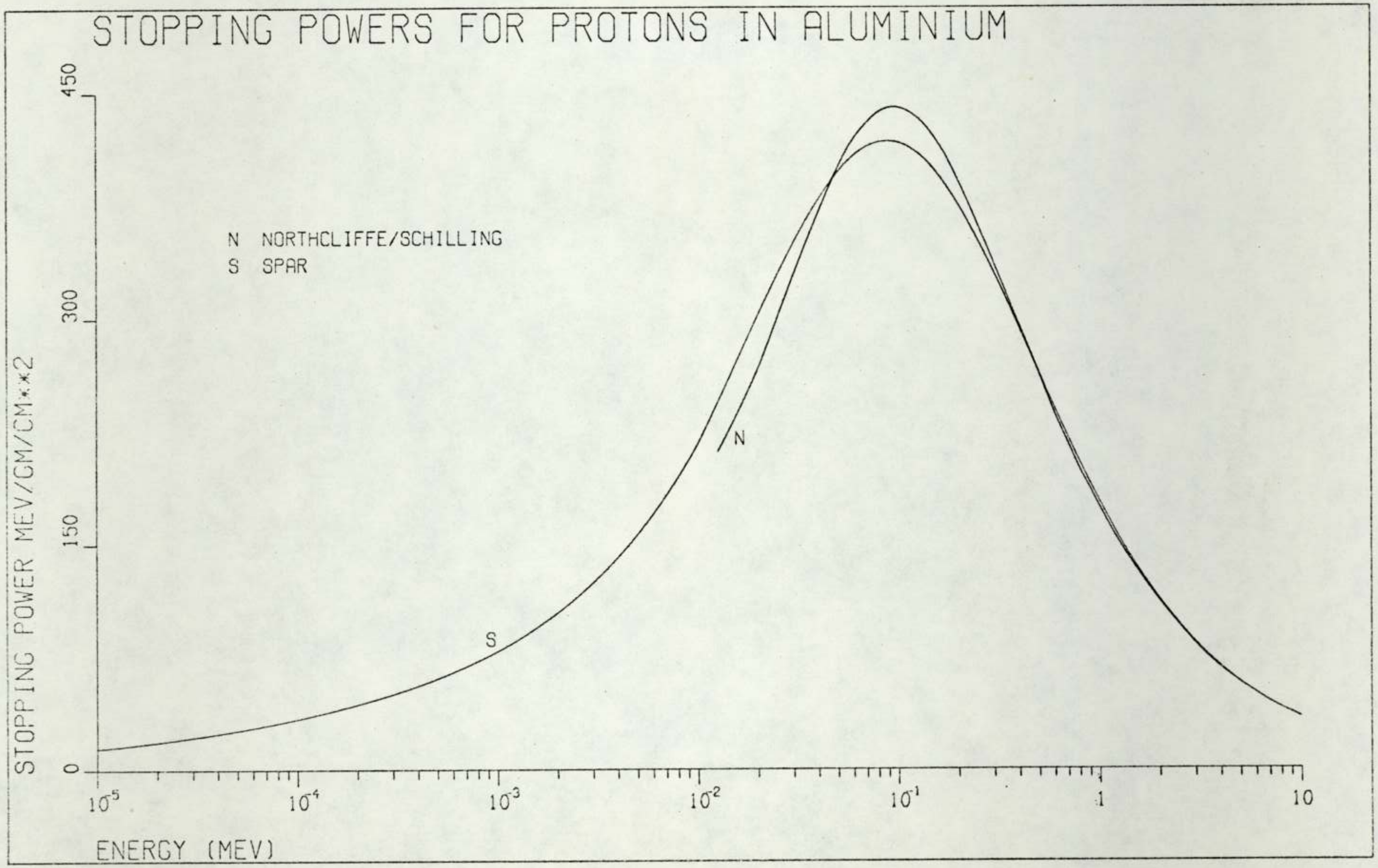
STOPPING POWERS FOR PROTONS IN ALUMINIUM
N NORTHCLIFFE/SCHILLING
S SPAR
N
S
STOPPING POWER MEV/CM/CM**2
450
300
150
0
10^{-5}
10^{-4}
10^{-3}
10^{-2}
10^{-1}
1
10
ENERGY (MEV)

Figure 47

comparison. The main differences between the data sets occur for energies of approximately 0.1 MeV, particularly for beryllium, chromium and silver. Corresponding percentage difference plots are presented in Appendix IV and are limited to the energy interval 0.1 MeV to 10 MeV.

Compared to Northcliffe and Schilling the Spar data is, in general, low (by 1 to 6 per cent) at 0.1 MeV and high (by 2 to 6 per cent) at 1 MeV. The data sets differ by 21 per cent at 0.1 MeV for silver (Figure 6, Appendix IV) and by 19 per cent at 0.5 MeV for carbon (Figure 2 Appendix IV).

In the energy range 1 MeV to 10 MeV agreement taken between the data sets is within 6 per cent. A discontinuity in the Spar stopping power data * at 8 MeV is considered to arise from a change in the shell correction terms at this energy. For proton energies from 1 keV to 8 MeV shell correction terms in the Spar code were chosen to match the ICRU(1970) stopping powers. For proton energies in excess of 8 MeV the shell correction was computed using an expression given by BARKAS and BERGER (1964).

Range data from the Spar code is presented in Appendix V. No systematic deviation from the Northcliffe and Schilling data was observed. Agreement is typically of the order of 10 per cent in the energy region 0.1 MeV to 1 MeV except for carbon (approximately 25 per cent), and approximately 4 per cent in the energy region 1 MeV to 10 MeV

---

*Note: See Appendix IV, Figures 10 to 17.

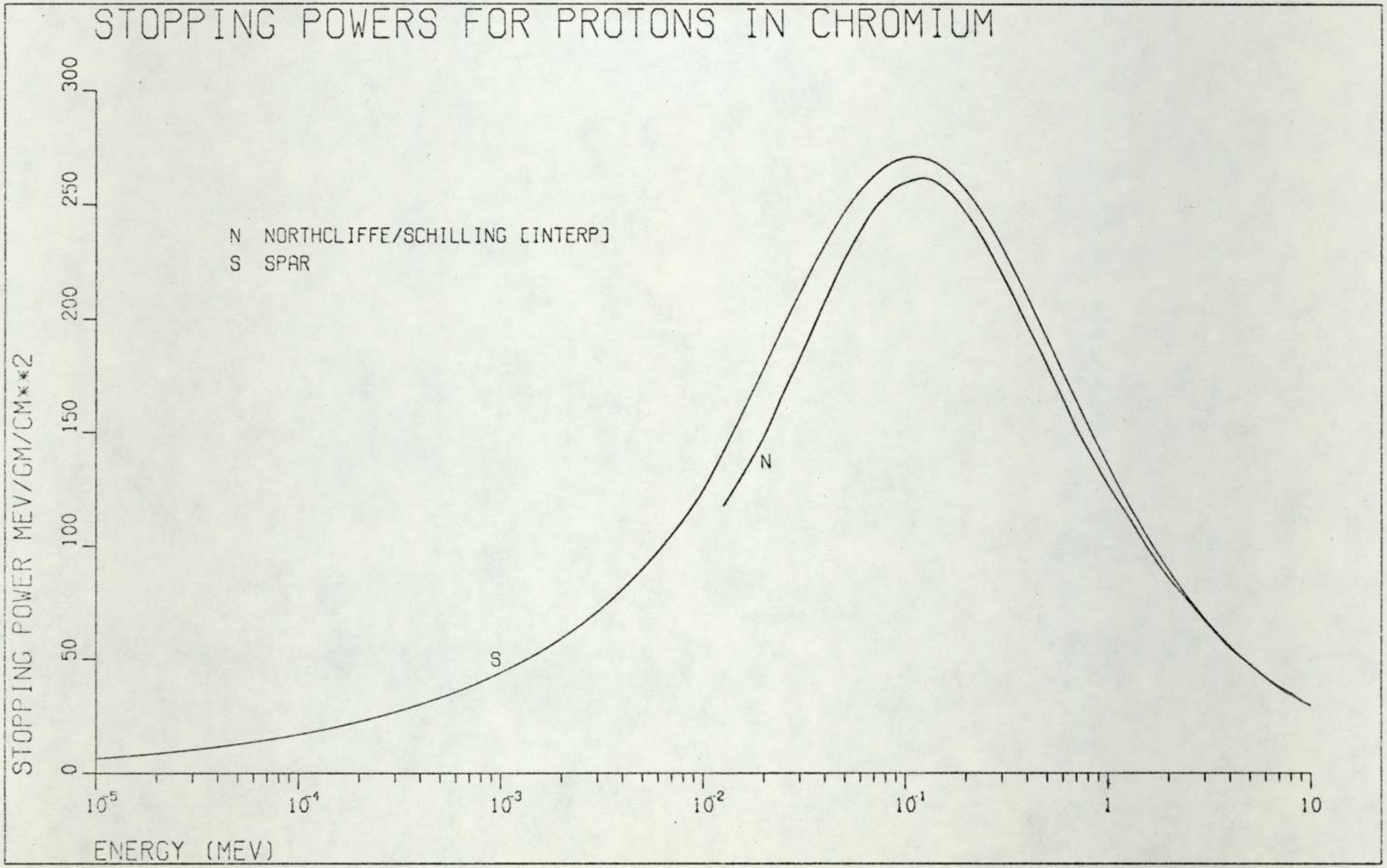
STOPPING POWERS FOR PROTONS IN CHROMIUM
N NORTHCLIFFE/SCHILLING [INTERP]
S SPAR
N
S
STOPPING POWER MEV/CM/CM**2
0
50
100
150
200
250
300
10^{-5}
10^{-4}
10^{-3}
10^{-2}
10^{-1}
1
10
ENERGY (MEV)

Figure 48

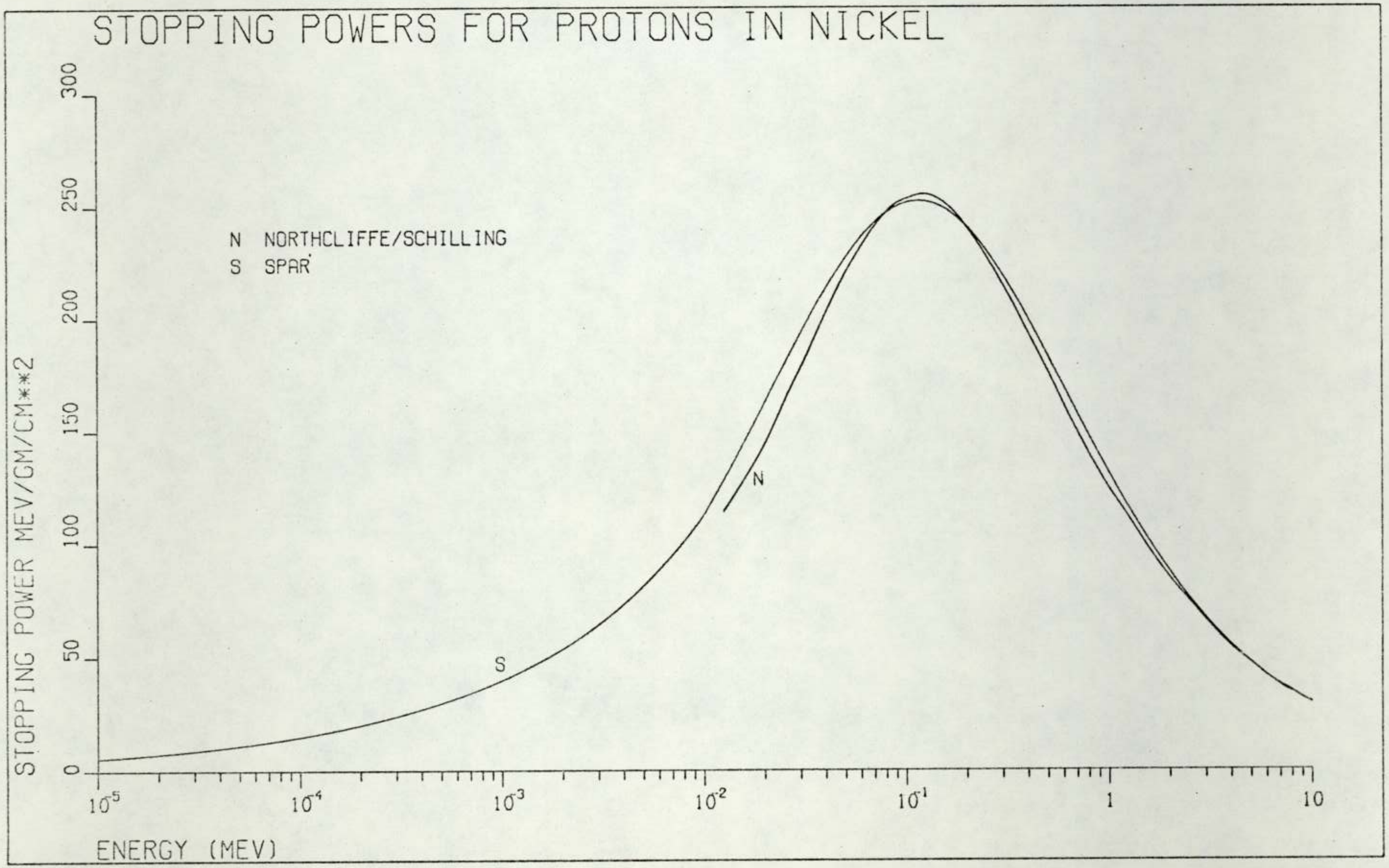
STOPPING POWERS FOR PROTONS IN NICKEL
N NORTHCLIFFE/SCHILLING
S SPAR
STOPPING POWER MEV/GM/CM**2
0
50
100
150
200
250
300
ENERGY (MEV)
10⁻⁵
10⁻⁴
10⁻³
10⁻²
10⁻¹
1
10
N
S

Figure 49

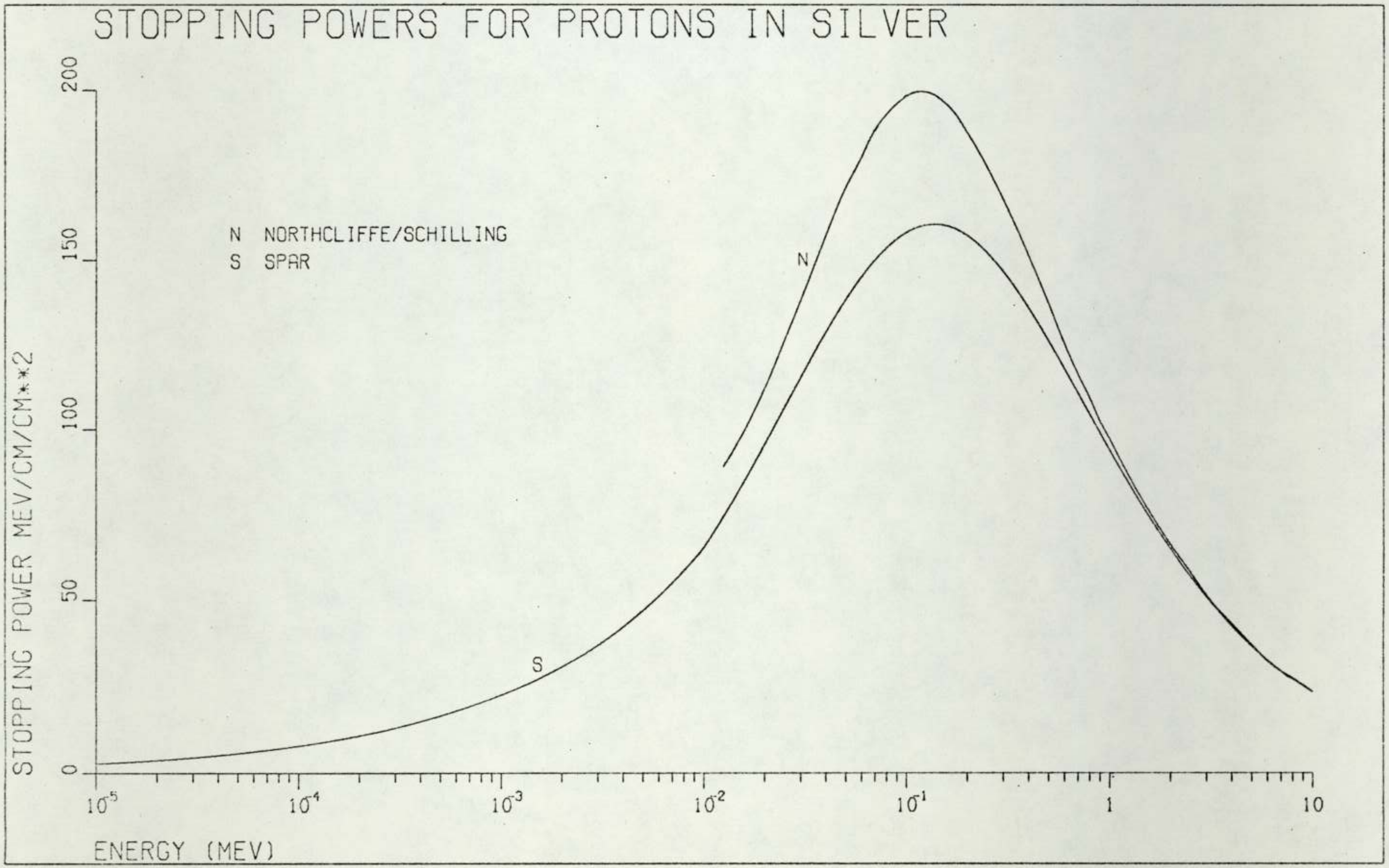
STOPPING POWERS FOR PROTONS IN SILVER
N NORTHCLIFFE/SCHILLING
S SPAR
N
S
STOPPING POWER MEV/CM/CM**2
0
50
100
150
200
ENERGY (MEV)
10^{-5}
10^{-4}
10^{-3}
10^{-2}
10^{-1}
1
10

Figure 50

except for carbon (5 to 12 per cent) and silver (0 to 9 per cent).

Together with data not presented for the elements calcium, iron, copper and lead approximately 30 per cent of the Williamson et al. proton data has been considered * and approximately 16 per cent of the Janni tabulation. For approximately half the target media considered both data sets give stopping power and range values well outside the general consensus of opinion for proton energies below 1 MeV. **

Fifty per cent of the Northcliffe and Schilling data has been considered for protons incident on non gaseous target media. Comparisons of the type are obviously meaningless for the computer codes due to Steward and Armstrong and Chadler ($Z_1 \leqslant 92$ on $Z_1 \leqslant 92$). The most serious discrepancies among these data sets occur for proton energies in the vicinity of 0.1 MeV particularly for the lighter elements. The closest overall agreement was found between data from the Steward and Spar computer codes.

Stopping power and range data is very limited for projectile specific energies less than 0.01 MeV/amu. CASWELL and BERGER (1972) have extended the Northcliffe and Schilling tabulation to specific energies of 1 keV/amu and the ICRU (1970) report provides some

*Note : Approximately 6 per cent of their total data for five incident ion types.

**Note: A universal range energy curve presented by BAROUCH (1968) is claimed to reproduce the range data of Williamson et al. over the whole range $Z_2 = 2$ to 82 inclusive to within an accuracy of 15 per cent.

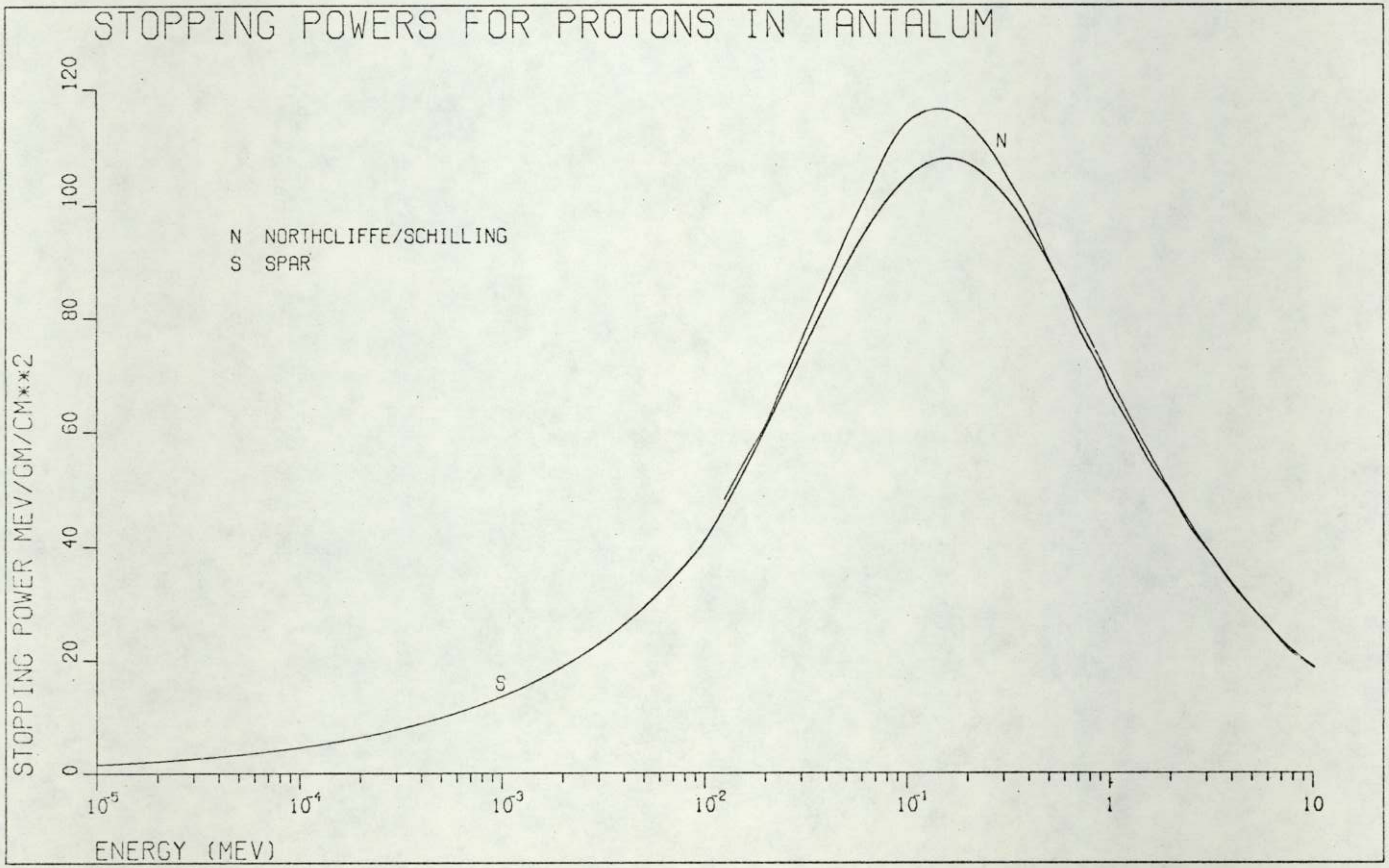
STOPPING POWERS FOR PROTONS IN TANTALUM
N NORTHCLIFFE/SCHILLING
S SPAR
N
S
STOPPING POWER MEV/GM/CM**2
0
20
40
60
80
100
120
10^{-5}
10^{-4}
10^{-3}
10^{-2}
10^{-1}
1
10
ENERGY (MEV)

Figure 51

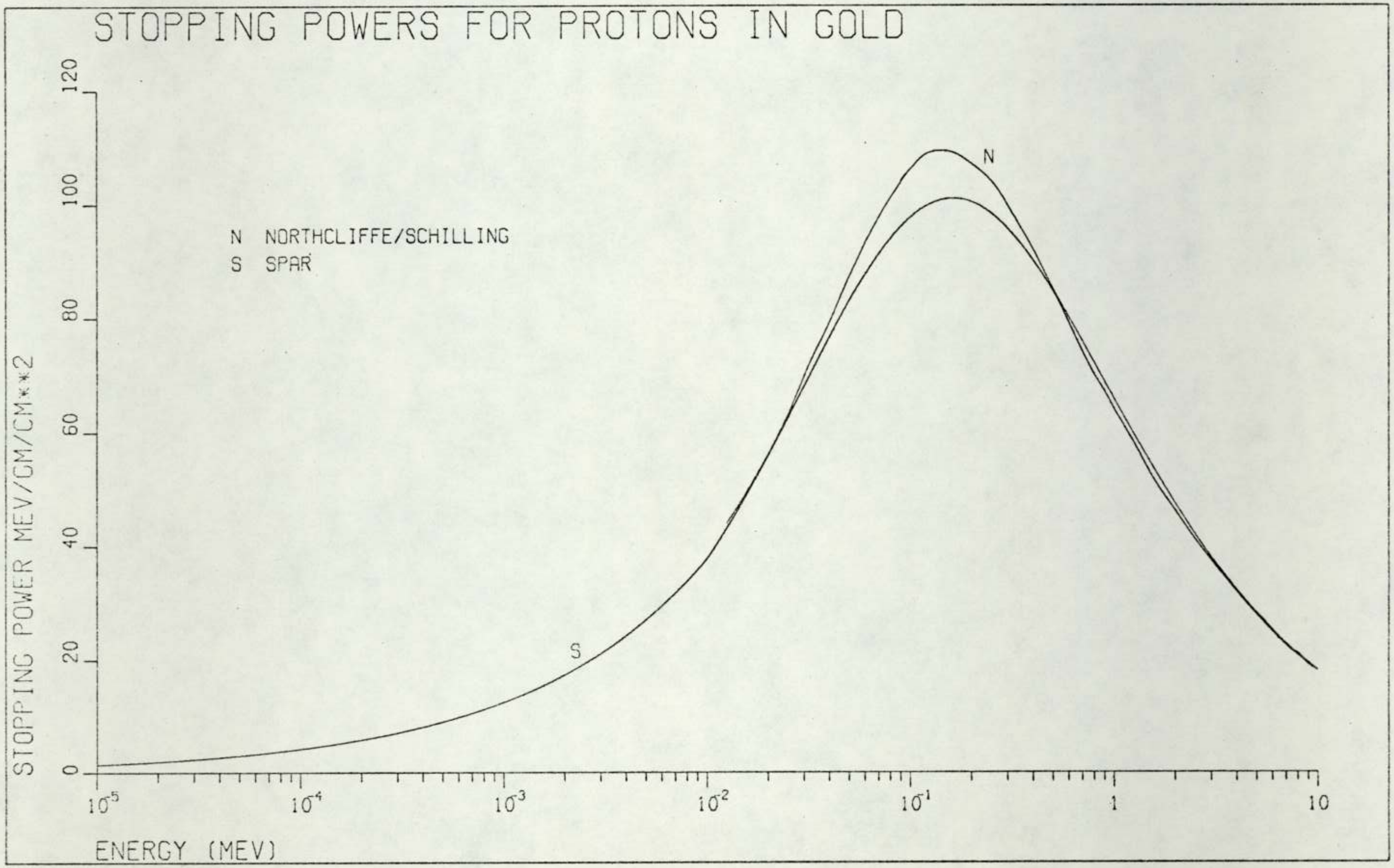
STOPPING POWERS FOR PROTONS IN GOLD
N NORTHCLIFFE/SCHILLING
S SPAR
N
S
STOPPING POWER MEV/GM/CM**2
0
20
40
60
80
100
120
ENERGY (MEV)
10^{-5}
10^{-4}
10^{-3}
10^{-2}
10^{-1}
1
10

Figure 52

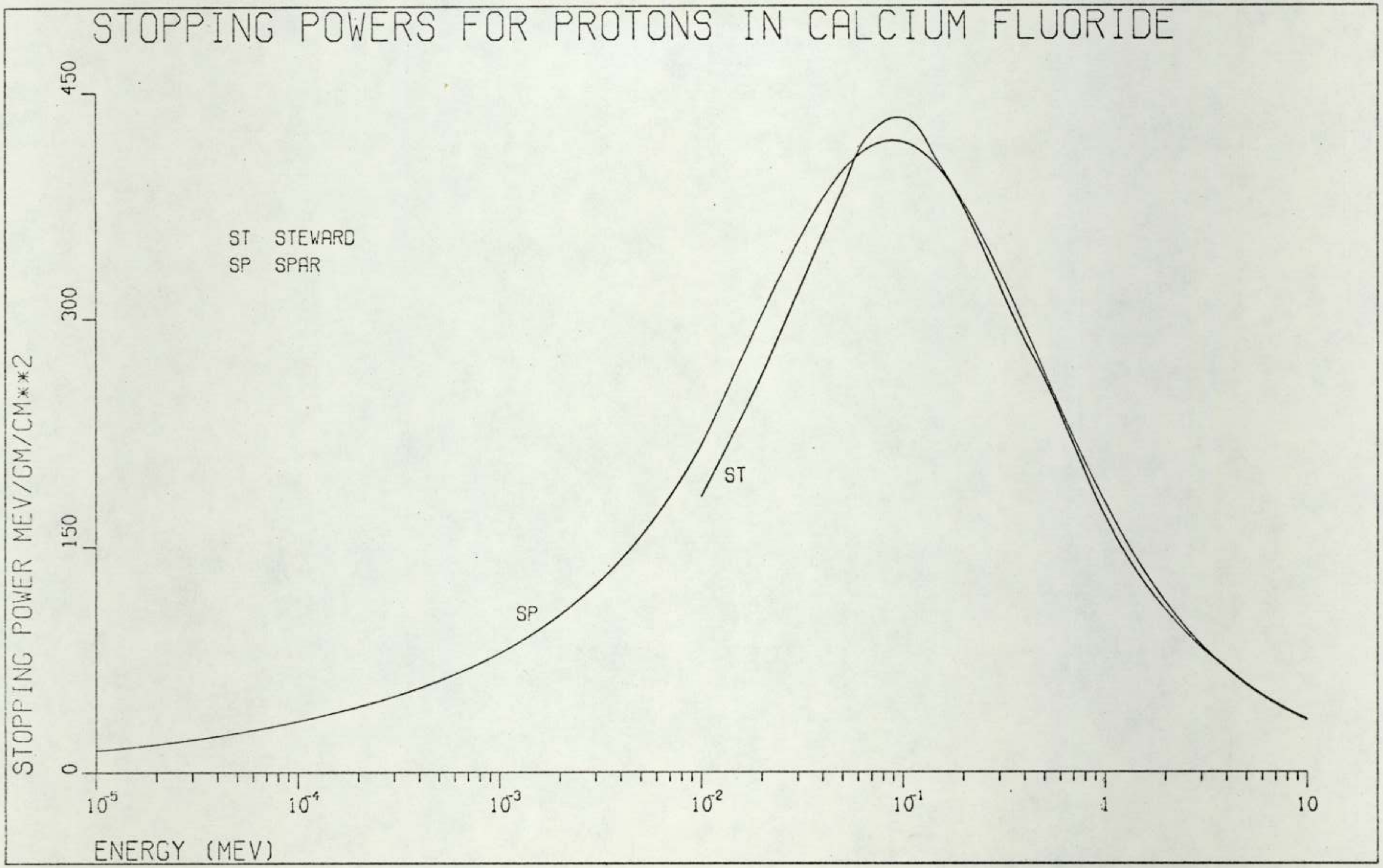
STOPPING POWERS FOR PROTONS IN CALCIUM FLUORIDE
ST STEWARD
SP SPAR
ST
SP
STOPPING POWER MEV/GM/CM**2
0
150
300
450
10^{-5}
10^{-4}
10^{-3}
10^{-2}
10^{-1}
1
10
ENERGY (MEV)

Figure 53

information for specific energies of 10 eV/amu. The Spar code is, however, the only general source of low energy data.

There is no anodyne panacea for problems associated with stopping power and range data. For a particular projectile ion and target medium reference to all available data is the safest course. Generalized tabulations or computational procedures should be employed with some caution especially when used as a basis for parametric fitting or interpolation.

Chapter VI

Analytical Applications

Analytical Applications

In the context of a study of the possibilities of employing proton induced prompt photon emission for depth analysis preliminary investigations have been made to determine the extrinsic sensitivity for the detection of lithium, aluminium and fluorine.

There are two principal features on which identification and measurement of a nuclide in a given sample can be based, the resonance energy and the photon spectrum. The main resonance characteristics for the elements investigated are shown in Table 10. Smoothed [SAVITZKY and GOLAY (1964)] photon pulse-height spectra for these reactions, obtained using NaI(Tl) and Ge(Li) detectors are presented in Plates 6 to 8. Because of the ease with which the spectra may be identified and the absence of competing nuclear reactions producing photons in an equivalent energy band, the high detection efficiency of the NaI(Tl) detector has been utilized in preference to the superior energy resolution but lower detection efficiency of the Ge(Li) detector. The integrated count rate over gated regions of the pulse-height spectrum was used as a measure of the reaction rate. For lithium the region of the pulse-height spectrum corresponding to photon energies between 14 and 18 MeV was used. For aluminium only the peak at approximately 10.8 MeV due to the 992 keV resonance was considered. For fluorine the analyser was set to accept the full energy and first and second escape peaks from the 6 to 7 MeV photons. Thick target yield curves in the vicinity of the 441 keV $Li^7(p,\gamma)Be^8$ resonance and the 992 keV $Al^{27}(p,\gamma)Si^{28}$ resonance are shown in Figures 54 and 55. Examples of similar yield curves for

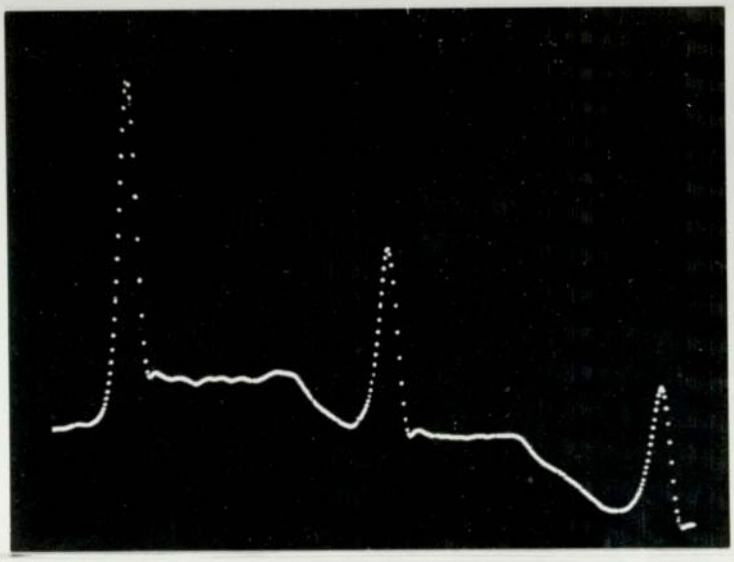

Photon pulse-height spectrum from the reaction $F^{19}(p\alpha,\gamma)\ O^{16}$ at E_o = 340 keV Ge(Li) [Expanded scale].

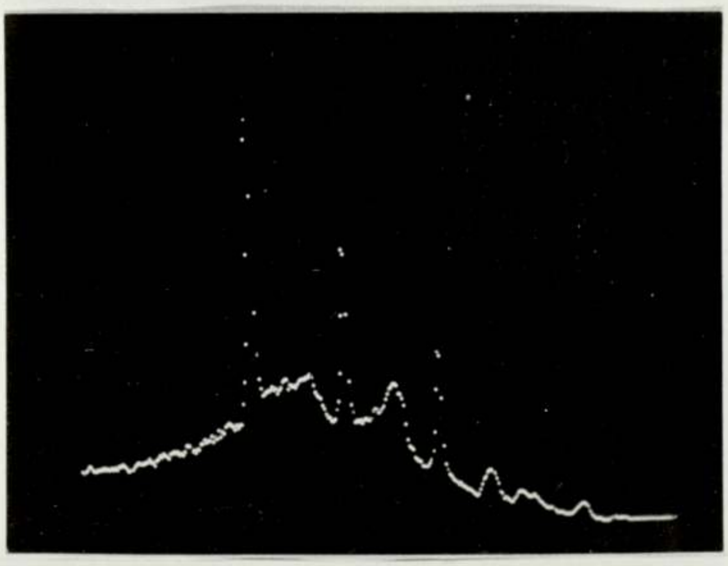

Photon pulse-height spectrum from the reaction $F^{19}(p,\alpha\gamma)\ O^{16}$ at E_o = 872 keV, Ge(Li).

Plate 6

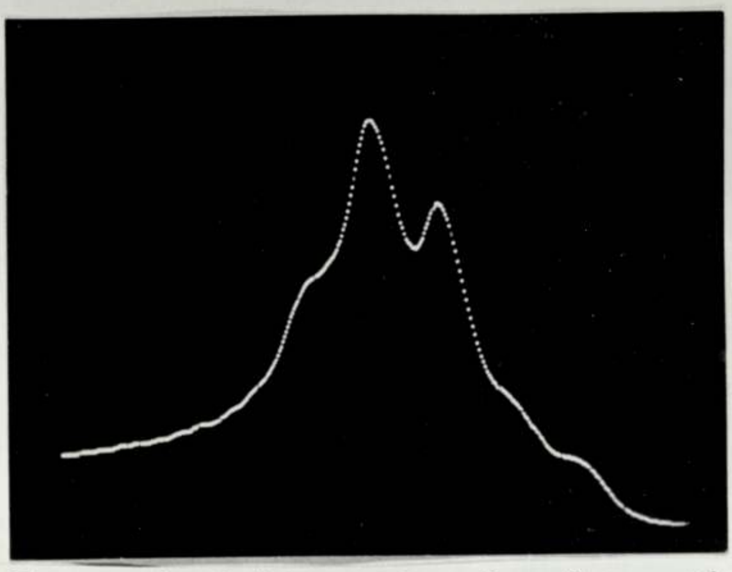

Photon pulse height spectrum from the reaction $F^{19}(p,\alpha\gamma)\ O^{16}$ at E_o = 935 keV, NaI(Tl).

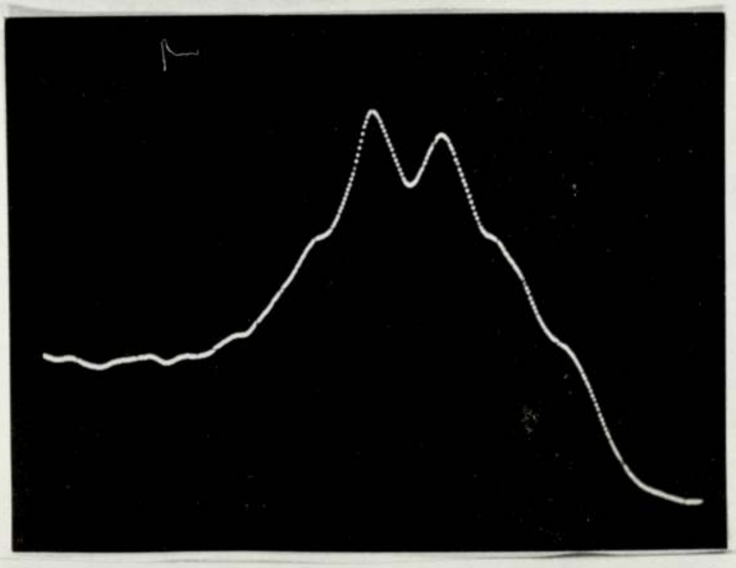

Photon pulse-height spectrum from the reaction $F^{19}(p,\alpha\gamma)\ O^{16}$ at E_o = 1348 keV, NaI(Tl).

Plate 7

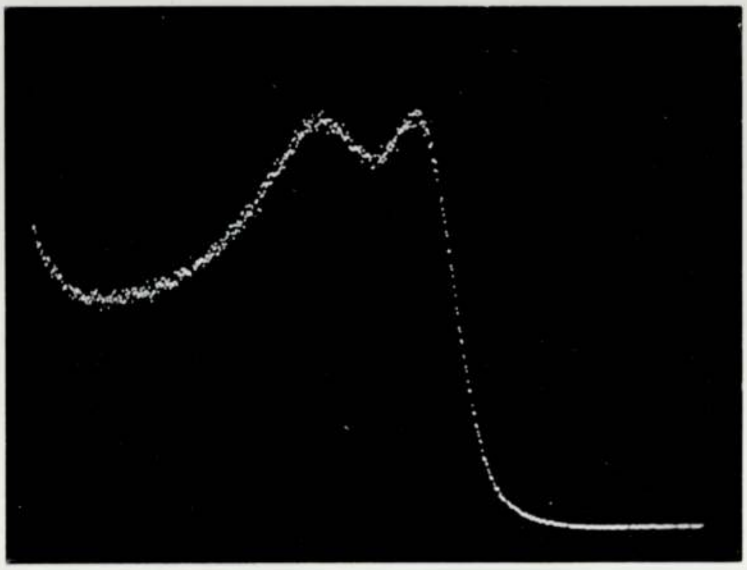

Photon pulse-height spectrum from the reaction $Li^7(p,\gamma)\ Be^8$ at E_o = 441 keV, NaI(Tl).

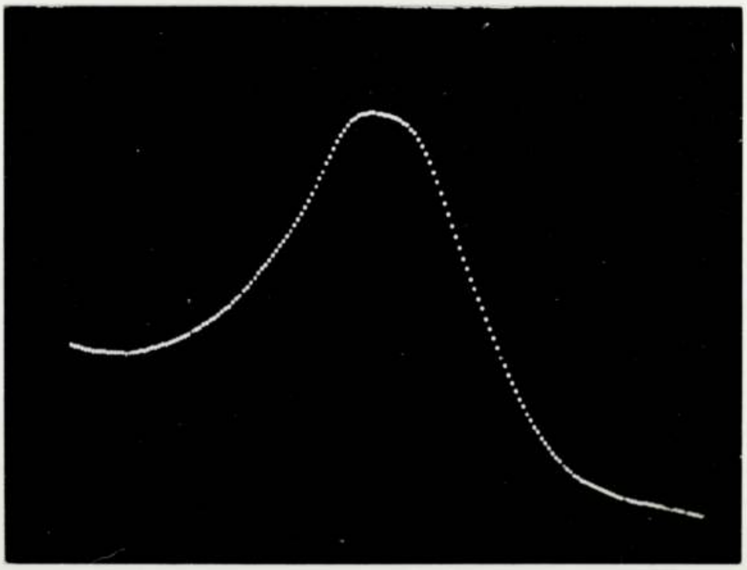

Photon pulse-height spectrum from the reaction $Al^{27}(p,\gamma)\ Si^{28}$ at E_o = 992 keV, NaI(Tl).

Plate 8

TABLE 10

The Main Resonance Characteristics of the Nuclides Studied

Element	Reaction	E_o keV	σ_r mb	Γ keV	E_γ MeV	Percentage Relative Intensity
Lithium	$Li^7(p,\gamma)Be^8$	441	6	12	14.75	37.0
					17.65	63.0
Aluminium	$Al^{27}(p,\gamma Si^{28}$	992		0.1	1.52	1.0
					1.77	44.0
					2.30	1.0
					2.84	2.6
					3.10	1.0
					4.50	2.3
					4.62	2.3
					4.75	4.6
					5.70	0.7
					6.02	3.0
					6.30	0.7
					7.95	2.0
					9.50	<1.0
					10.30	0.7
					10.78	33.0
Fluorine	$F^{19}(p,\alpha\gamma)O^{16}$	340	102	2.4	7.12	3.0
					6.72	0.5
					6.13	96.5
		872	661	4.5	7.12	8.0
					6.72	24.0
					6.13	68.0
		935	180	8.6	7.12	21.0
					6.72	3.0
					6.13	76.0
		1348	89	5.6	7.12	31.0
					6.72	14.0
					6.13	55.0

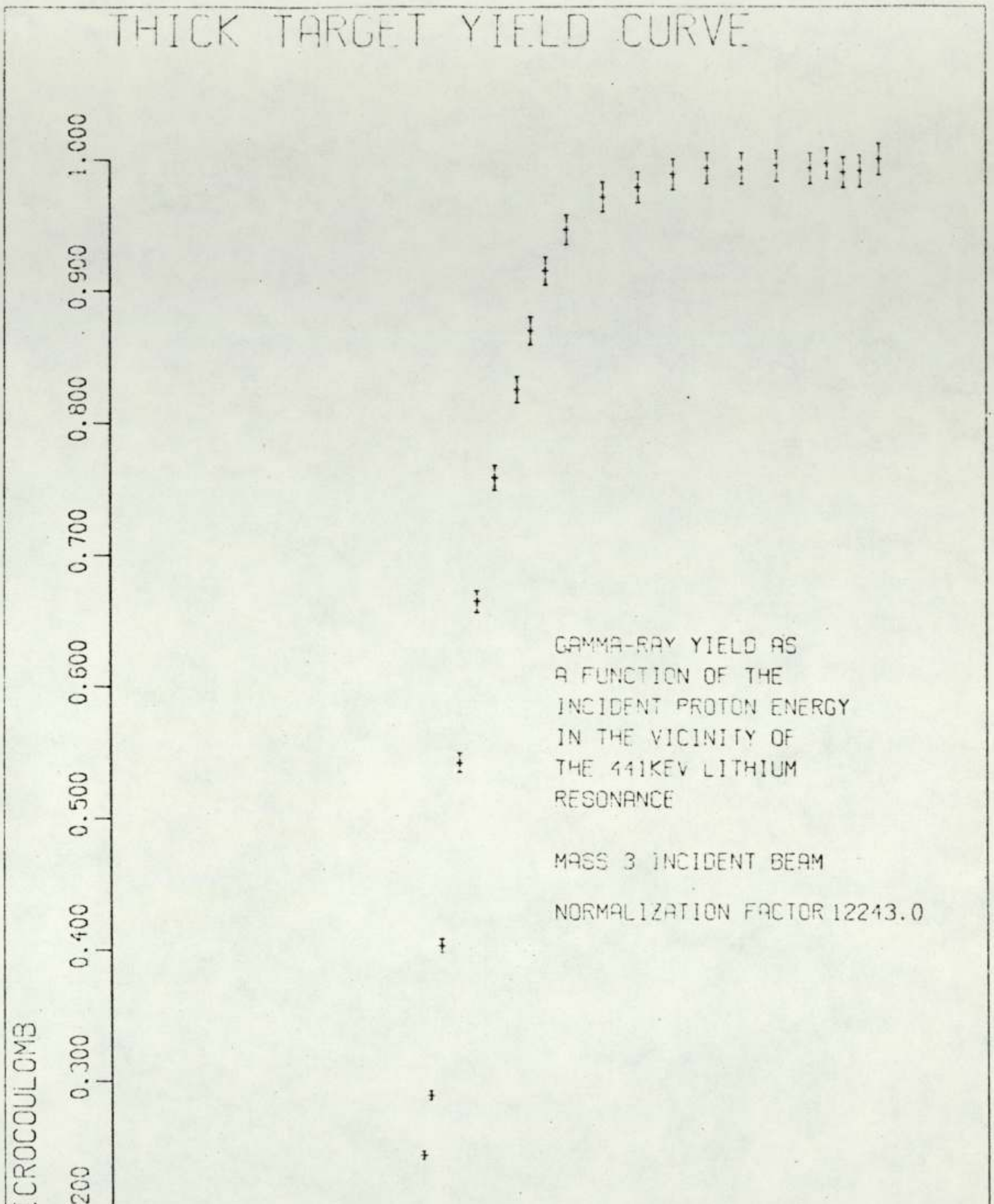
THICK TARGET YIELD CURVE
COUNTS/PROTON MICROCOULOMB
0.000
0.100
0.200
0.300
0.400
0.500
0.600
0.700
0.800
0.900
1.000
320
360
400
440
480
520
560
600
PROTON ENERGY (KEV)
GAMMA-RAY YIELD AS
A FUNCTION OF THE
INCIDENT PROTON ENERGY
IN THE VICINITY OF
THE 441KEV LITHIUM
RESONANCE
MASS 3 INCIDENT BEAM
NORMALIZATION FACTOR 12243.0

Figure 54

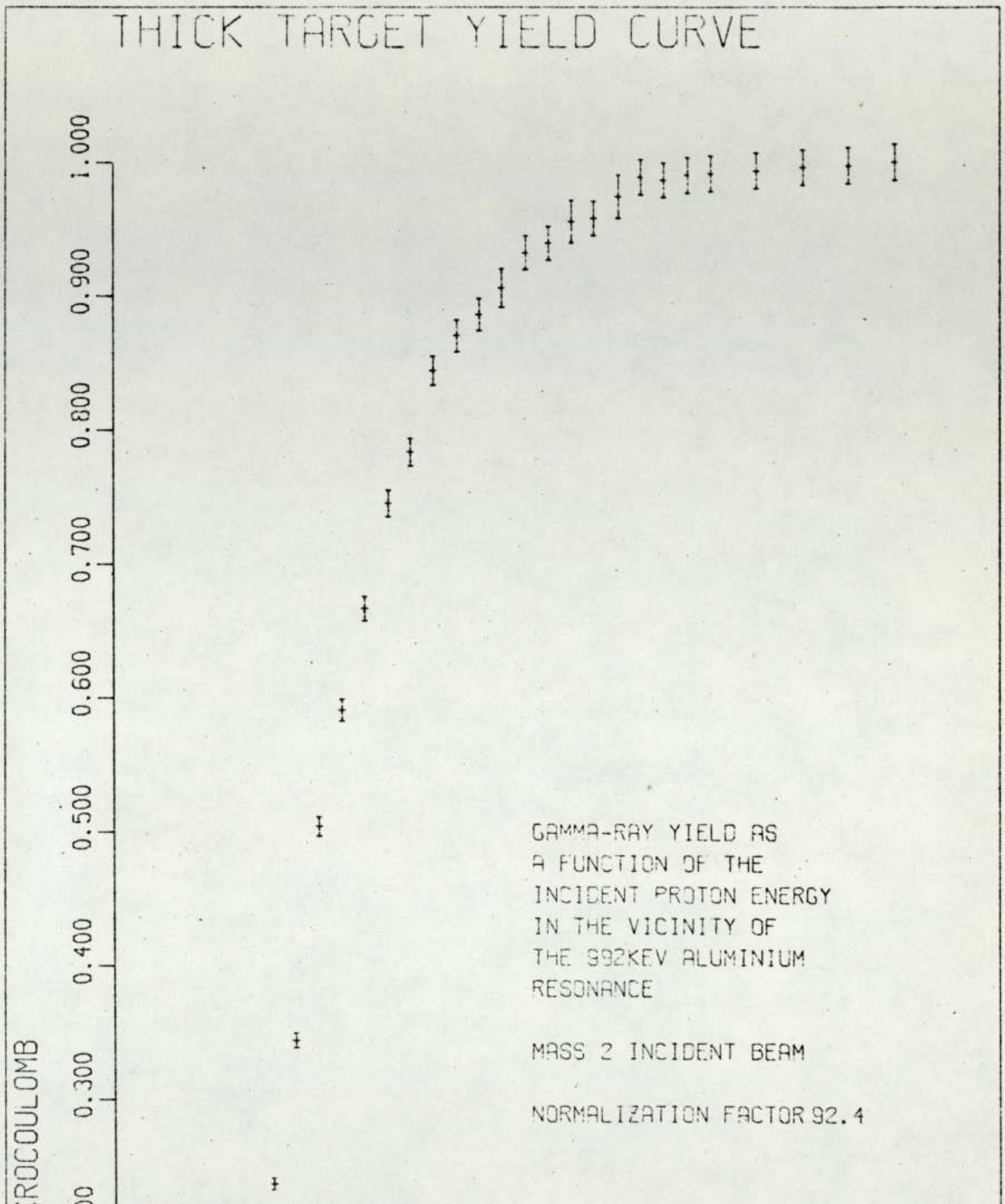
THICK TARGET YIELD CURVE
COUNTS/PROTON MICROCOULOMB
0.000
0.100
0.200
0.300
0.400
0.500
0.600
0.700
0.800
0.900
1.000
980
985
990
995
1000
1005
1010
PROTON ENERGY (KEV)
GAMMA-RAY YIELD AS
A FUNCTION OF THE
INCIDENT PROTON ENERGY
IN THE VICINITY OF
THE 992KEV ALUMINIUM
RESONANCE
MASS 2 INCIDENT BEAM
NORMALIZATION FACTOR 92.4

Figure 55

prominent $F^{19}(p,\alpha\gamma)O^{16}$ resonances have already been presented.

For a reaction from an isolated resonance on a standard thick target containing C_s atoms.m^{-3} of a given nuclide, assume that R_S (Eb) is the integrated count per microcoulomb in an appropriate region of the characteristic photon spectrum for a mean incident proton energy $\bar{E}$b. If R_M(Eb) is the equivalent count rate from a given matrix containing $C_M$atoms.m^{-3} of the same nuclide then, from Equation (21), C_M is given

$$C_M = \frac{R_M\ (Eb)}{R_s\ (Eb)} \cdot \frac{(dE/dx)_M}{(dE/dx)_s} \cdot C_s \quad \ldots\ldots\ldots \qquad (28)$$

where the stopping powers are taken at the resonance energy. The detection limit for a beam intensity IμA may be arbitrarily defined as the amount of the nuclide, assumed to be homogeneously distributed in the sample, which gives a count rate equal to the background recorded by the detector in the corresponding energy band. If the background in this region is B counts per second the limiting integrated count per incident microcoulomb for the sample is equal to B/I. It is usual to quote detection limits with respect to a base matrix with a stopping power equal to that of aluminium. This conversion may be accomplished by multiplying Equation (28) by the ratio $(dE/dx)_{AL}/(dE/dx)_M$. Detection limits for the experimental configuration used in the present work are given below, normalized to an aluminium base matrix.

ELEMENT	RESONANCE ENERGY (keV)	DETECTION LIMIT (ppm)
Lithium	441	25
Aluminium	991	2050
Fluorine	340	80

For the reaction $F^{19}(p,\alpha\gamma)O^{16}$ at E_o = 340 keV the photon emission yield is isotropic [KESZTHELYI et al.(1962)]. By equating the observed thick target yield for this reaction with the theoretical prediction of Equation (21) the absolute counting efficiency of the system for primary photon energies from 6 to 7 MeV has been established as 2 per cent.

The techniques described have been applied to the determination of fluorine in microcracked chromium plate. In order to reduce the number of possible variables all samples were plated for a constant total charge derived from the empirical optimum conditions for the production of microcracked chromium plate, which are a current density of 2045.14 $A.m^{-2}$ and a plating time of thirty minutes. Current density was varied about the optimum value and the plating time adjusted to maintain a constant product. Typical observed yield curves are shown in Figures 56 and 57 taken using incident H_3^+ and H_2^+ ion beams respectively. The data indicates a high fluorine concentration in the surface region of the sample and a lower homogeneous distribution at depth.

For the purpose of analysis the yield curve is assumed to consist of a thick target component, arising from a homogeneous fluorine concentration throughout the sample, on which is superimposed a thin target component arising from an additional fluorine concentration in a surface region of effective thickness ξ . For the model chosen the observed yield curve is a function of the variables E_o, Γ, n and ξ and the bulk to surface component intensity ratio I_R. Analytical determinations are usually performed in the vicinity of a given resonance with a given incident beam energy dispersion. It is

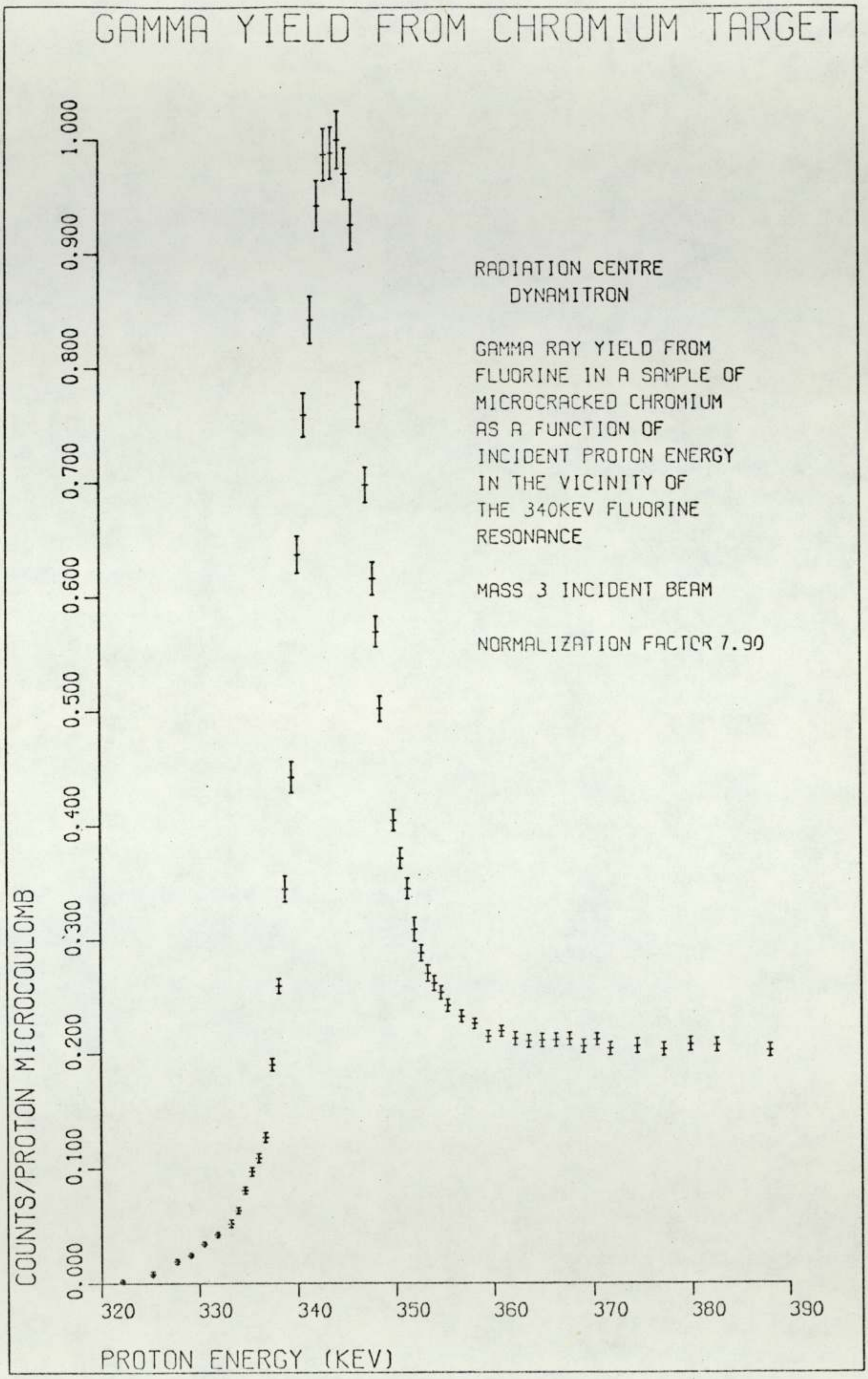
GAMMA YIELD FROM CHROMIUM TARGET
RADIATION CENTRE
DYNAMITRON
GAMMA RAY YIELD FROM
FLUORINE IN A SAMPLE OF
MICROCRACKED CHROMIUM
AS A FUNCTION OF
INCIDENT PROTON ENERGY
IN THE VICINITY OF
THE 340KEV FLUORINE
RESONANCE
MASS 3 INCIDENT BEAM
NORMALIZATION FACTCR 7.90
COUNTS/PROTON MICROCOULOMB
0.000
0.100
0.200
0.300
0.400
0.500
0.600
0.700
0.800
0.900
1.000
320
330
340
350
360
370
380
390
PROTON ENERGY (KEV)

Figure 56

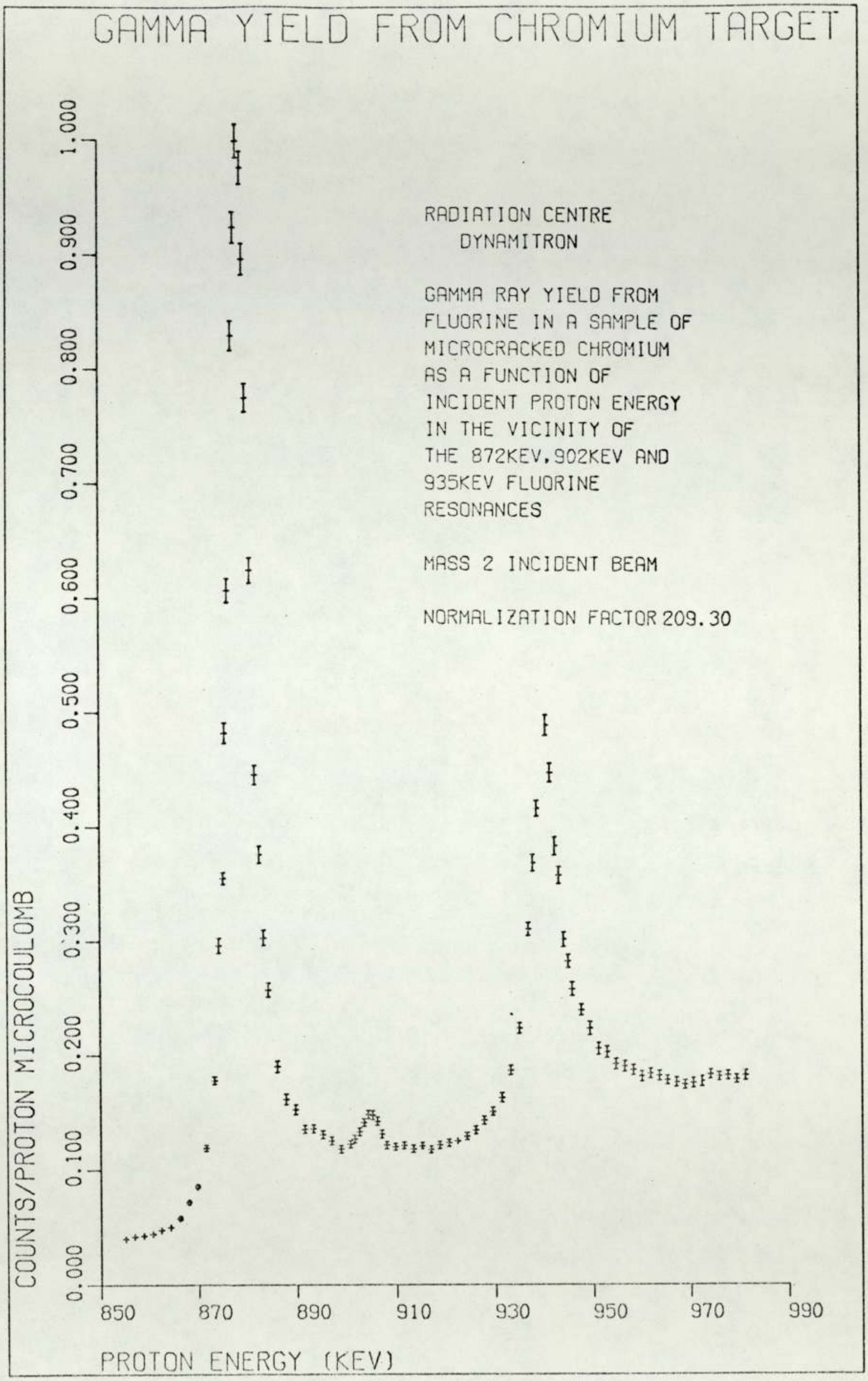
GAMMA YIELD FROM CHROMIUM TARGET

RADIATION CENTRE
DYNAMITRON

GAMMA RAY YIELD FROM
FLUORINE IN A SAMPLE OF
MICROCRACKED CHROMIUM
AS A FUNCTION OF
INCIDENT PROTON ENERGY
IN THE VICINITY OF
THE 872KEV, 902KEV AND
935KEV FLUORINE
RESONANCES

MASS 2 INCIDENT BEAM

NORMALIZATION FACTOR 209.30

Figure 57

normally sufficient therefore to consider the variation of observed yield as a function of the variables ξ and I_R for fixed values of E_o, Γ and n. Simulated yield curves are presented in Figures 58 and 59 for $\xi = 0.5$ keV and $\xi = 5.0$ keV respectively, $E_o = 340$ keV, $\Gamma = 2.4$ keV, n = 2.3 keV and I_R values from 0.25 to 1.0. The most significant feature of the curves is the enhancement of the surface yield due to the thick target substrate. For given values of ξ,Γ, E_o and n the surface yield enhancement may be expressed, in terms of experimental observables, as a function of the ratio of maximum surface yield to the bulk yield at an arbitrarily defined energy. Enhancement factors for several values of ξ are presented in Figure 60 for values of E_o,Γ and n as given above and a bulk normalization energy of 380 keV.

In the evaluation of analytical thin target data the effective target thickness ξ must be known in order to determine the concentration. The only criterion generally available for the estimation of ξ is the FWHM of the observed yield curve. When ξ is large compared to Γ and n, and therefore dominates the observed FWHM, this presents no real difficulty. A non-trivial problem arises, however, when ξ is small compared to Γ and n. Under these conditions, as established in Chapter III, the observed FWHM is insensitive with respect to effective target thickness. This insensitivity is reflected in a large relative uncertainty in the evaluation of ξ obtained by data fitting techniques or from parametric curves of the type shown in Figures 15 and 16. For the assumed model and for I_R ratios of approximately 0.1 the FWHM of the surface peak may be obtained to within an accuracy of two per cent by reflection of the low energy data about the maximum yield the location of which is relatively insensitive to the presence of the substrate. I_R ratios of

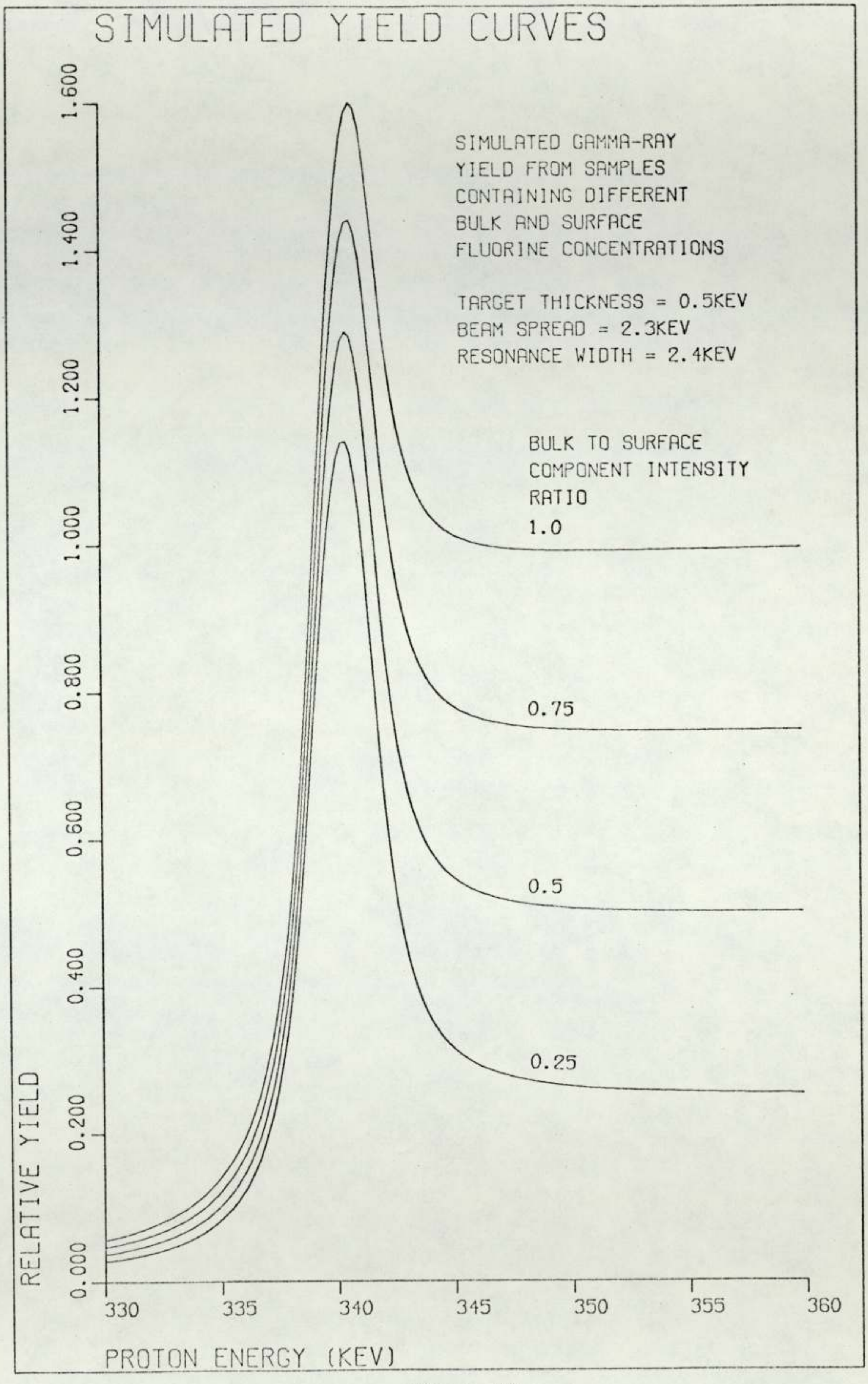
SIMULATED YIELD CURVES
SIMULATED GAMMA-RAY
YIELD FROM SAMPLES
CONTAINING DIFFERENT
BULK AND SURFACE
FLUORINE CONCENTRATIONS
TARGET THICKNESS = 0.5KEV
BEAM SPREAD = 2.3KEV
RESONANCE WIDTH = 2.4KEV
BULK TO SURFACE
COMPONENT INTENSITY
RATIO
1.0
0.75
0.5
0.25
RELATIVE YIELD
0.000
0.200
0.400
0.600
0.800
1.000
1.200
1.400
1.600
330
335
340
345
350
355
360
PROTON ENERGY (KEV)

Figure 58

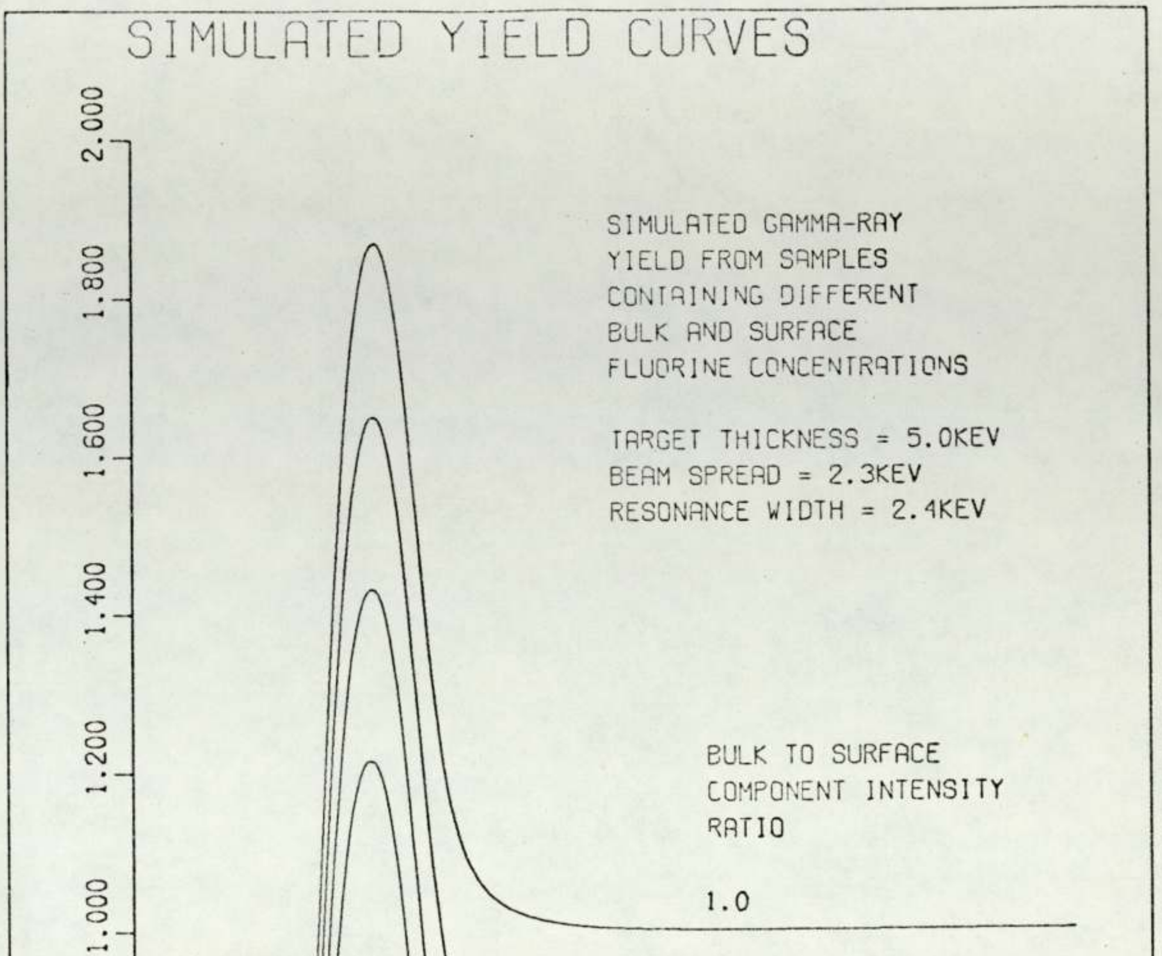
SIMULATED YIELD CURVES
SIMULATED GAMMA-RAY YIELD FROM SAMPLES CONTAINING DIFFERENT BULK AND SURFACE FLUORINE CONCENTRATIONS
TARGET THICKNESS = 5.0KEV
BEAM SPREAD = 2.3KEV
RESONANCE WIDTH = 2.4KEV
BULK TO SURFACE COMPONENT INTENSITY RATIO
1.0
0.75
0.5
0.25
RELATIVE YIELD
0.000
0.200
0.400
0.600
0.800
1.000
1.200
1.400
1.600
1.800
2.000
PROTON ENERGY (KEV)
330
340
350
360
370
380

Figure 59

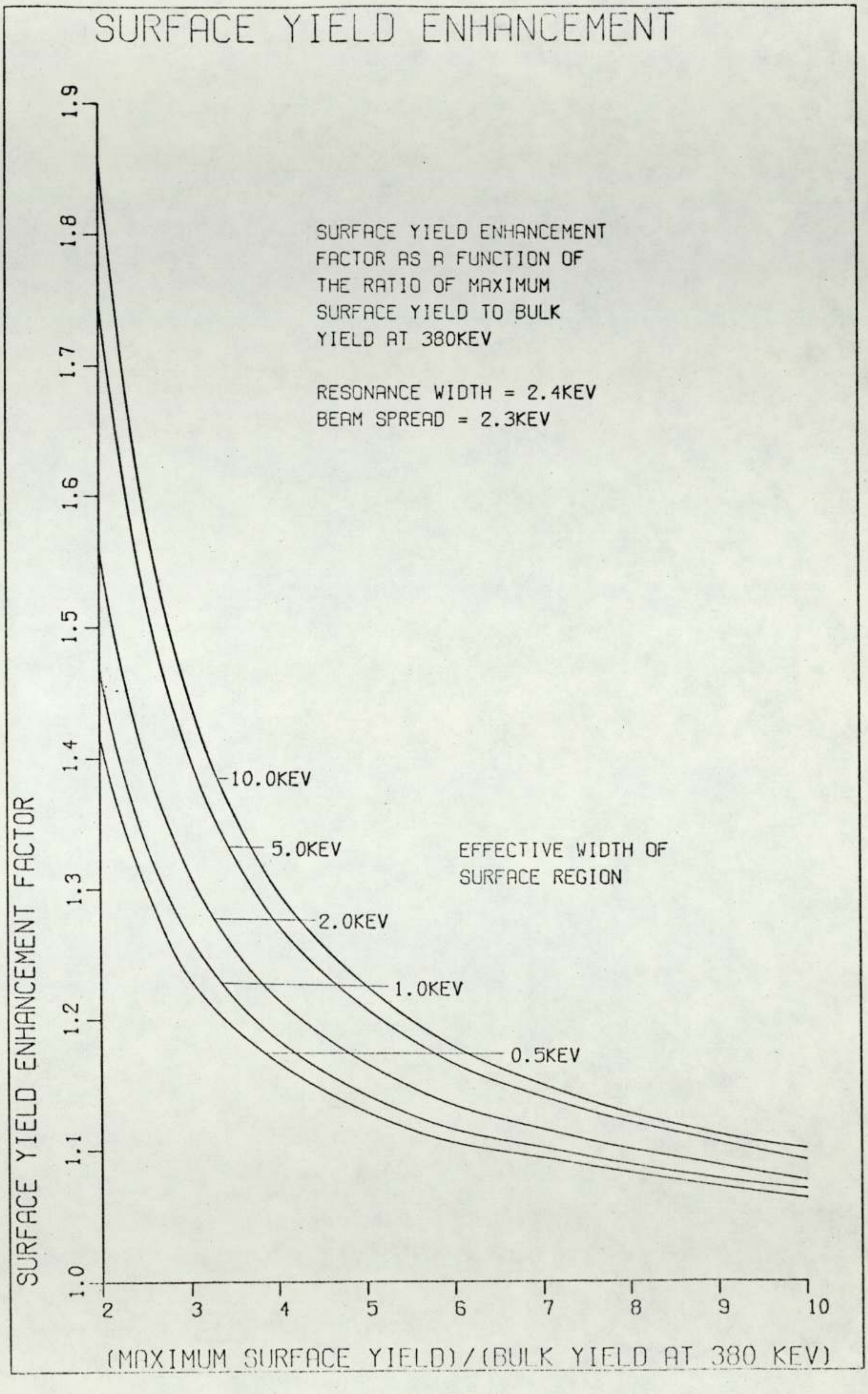
SURFACE YIELD ENHANCEMENT
SURFACE YIELD ENHANCEMENT FACTOR AS A FUNCTION OF THE RATIO OF MAXIMUM SURFACE YIELD TO BULK YIELD AT 380KEV
RESONANCE WIDTH = 2.4KEV
BEAM SPREAD = 2.3KEV
10.0KEV
5.0KEV
2.0KEV
1.0KEV
0.5KEV
EFFECTIVE WIDTH OF SURFACE REGION
SURFACE YIELD ENHANCEMENT FACTOR
1.0
1.1
1.2
1.3
1.4
1.5
1.6
1.7
1.8
1.9
2
3
4
5
6
7
8
9
10
(MAXIMUM SURFACE YIELD)/(BULK YIELD AT 380 KEV)

Figure 60

this order are typical of those observed in the present work. For larger I_R ratios, however, this procedure over estimates the FWHM by as much as 20 per cent. Once ξ has been established the maximum integrated count per incident microcoulomb for the surface region may be corrected for substrate enhancement and used to evaluate the surface number density of the relevant nuclide.

If $R'_M \max(\xi)$ is the maximum integrated count per microcoulomb in an appropriate region of the characteristic photon spectrum for a surface region of effective thickness ξ corrected for substrate enhancement, and $R_s(Eb)$ is the corresponding integrated count from a standard thick target at a mean incident proton energy Eb,

$$\frac{R_s(Eb)}{R'_M \max(\xi)} = \frac{\phi_7(Eb)}{\phi_5 \max(\xi)}$$

where $\phi_5 \max(\xi)$ and $\phi_7(Eb)$ are defined by Equations (20) and (21) respectively and may be partially evaluated for a given Γ, n and ξ. The surface number density C_M is given by the expression

$$C_M = \frac{R'_M \max(\xi)}{R_s(Eb)} \cdot \frac{(dE/dx)_M}{(dE/dx)_s} \cdot \frac{K_s}{K_M} \cdot C_s \quad \ldots.. \qquad (29)$$

where K_s and K_M are constants for a given Γ, n and ξ and all other terms have been defined previously.

The corresponding bulk yield enhancement due to the presence of the surface region has been treated in a similar manner and is presented in Figure 61. It is considerably less significant than surface yield enhancement and may generally be neglected except for large values of

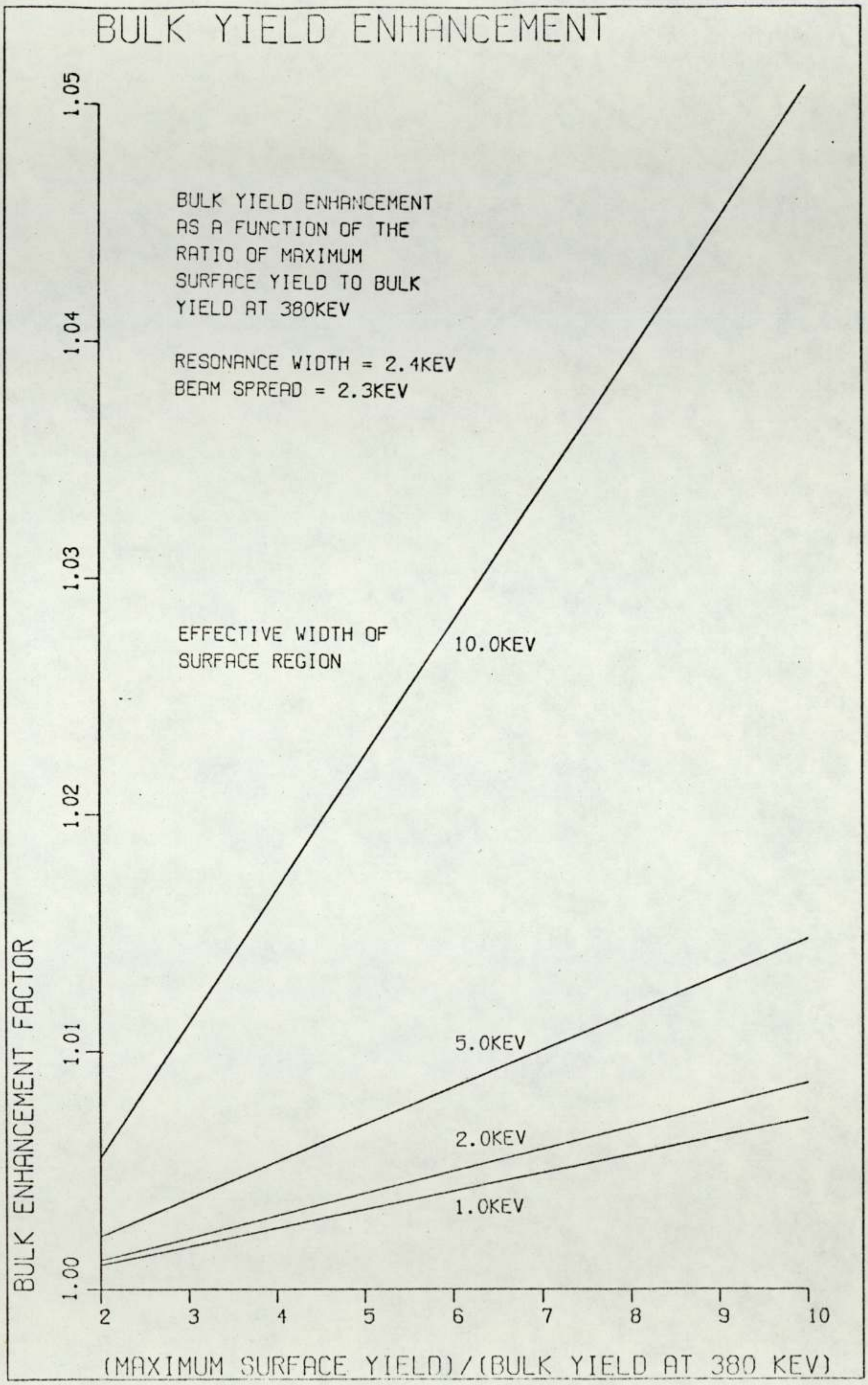
BULK YIELD ENHANCEMENT
BULK YIELD ENHANCEMENT
AS A FUNCTION OF THE
RATIO OF MAXIMUM
SURFACE YIELD TO BULK
YIELD AT 380KEV
RESONANCE WIDTH = 2.4KEV
BEAM SPREAD = 2.3KEV
EFFECTIVE WIDTH OF
SURFACE REGION
10.0KEV
5.0KEV
2.0KEV
1.0KEV
BULK ENHANCEMENT FACTOR
1.00
1.01
1.02
1.03
1.04
1.05
2
3
4
5
6
7
8
9
10
(MAXIMUM SURFACE YIELD)/(BULK YIELD AT 380 KEV)

Figure 61

ξ and small values of I_R. The bulk fluorine concentration may, therefore, be obtained from Equation (28).

The need to consider only relative stopping power in the evaluation of Equation (28) and (29) was found to be particularly advantageous for the case of a chromium base matrix and a calcium fluoride standard. Although absolute stopping power data for these target media is at variance by approximately 10 to 30 per cent in the energy region considered, relative stopping power data is consistent to within 2 per cent. The relative stopping powers used in the evaluation of the data from chromium plate samples are given below.

$$R_{340} = 1.60 \pm 0.03$$

derived from a weighted average of BADER et al(1956), WILLIAMSON et al. (1966) and the computer codes due to STEWARD (1966) and ARMSTRONG and CHADLER (1973).

$$R_{872} = 1.68 \pm 0.03$$

derived from a weighted average of WILLIAMSON et al.(1966) and the computer codes due to STEWARD and ARMSTRONG and CHADLER (1973).

Analytical determinations were performed using molecular hydrogen ion beams because the resonances in the $F^{19}(p,\alpha\gamma)O^{16}$ reaction cross-section considered most suitable were not within the mass-one capabilities of the Dynamitron accelerator. The large effective energy dispersion of molecular hydrogen ion beams renders them unsuitable for analytical work on thin targets although their use to measure bulk concentrations presents no serious difficulty. The only resonances in the $F^{19}(p,\alpha\gamma)O^{16}$ reaction cross-section appropriate for analytical investigation of targets of small effective width that could be observed using the proton beam of the Radiation Centre Dynamitron occur at $E_o = 1090$ keV (Γ=0.7 keV, σ_r= 13m b) and $E_o = 1140$ keV (Γ= 2.5 keV, σ_r = 15 m b). The greatly reduced cross-sections for these resonances were found to require prohibitively long counting periods, however, under conditions of relatively high non-sample fluorine yield due to contamination of the beam transport system.

Limited proton reference data for microcracked chromium plate samples was obtained in the viscinity of the 872 keV resonance after conversion of the Dynamitron accelerator to solid state rectifiers and established the width of the surface region as (70 ± 40). 10^{-4} μm, equivalent to 0.7 ± 0.4 keV at 872 keV and 1.1 ± 0.6 keV at 340 keV. For incident H_2^+ ion beams the average value for the (symmetrical) FWHM of the surface peak in the vicinity of the 872 keV $F^{19}(p,\alpha\gamma)O^{16}$ resonance was 6.6 ± 0.3 keV. The corresponding value in the vicinity of the 340 keV resonance using an incident H_3^+ ion beam was 10.8 ± 0.6 keV. By comparison with the data obtained for standard thin targets using incident H_2^+ and H_3^+ molecular hydrogen ion beams, discussed in Chapter IV, the data obtained for microcracked chromium plate samples under similar conditions is considered to be consistent with a value of (70 ± 40).10^{-4}μm for the width of the surface region.

The corrected surface yield for all samples was found to be constant to within 5 per cent in the vicinity of a given resonance, independent of plating conditions or lateral position on the sample. This is taken to indicate that the effective width of the surface region for all samples studied (approximately forty) is constant to within 5 per cent. The large uncertainty in the value for the effective width of the surface region however introduces a large uncertainty in the evaluation of the concentration. Under the conditions of measurement the maximum thin target yield, and hence the value of the constant K_M in Equation (29), is very sensitive with respect to ξ. In contrast, the constant K_s in the same equation is approximately independent of beam energy dispersion when evaluated at an energy well above the resonance energy. Thus although the relative yield for the surface region is known to within 5 per cent and the stopping power ratio to within 2 per cent the value of the normalizing contant K_s cannot be determined to better than 30 per cent. The absolute surface fluorine concentration has been evaluated on the assumption that the width of the surface region is $(70 \pm 40).10^{-4}$ µm and that all contributions to observed width other than ξ and Γ may be attributed to effective beam energy dispersion. The results are summarized below.

INCIDENT BEAM	FLUORINE NUMBER DENSITY (10^{27} atoms.m^{-3})
H_1^+	3.1 ± 1.1
H_2^+	3.0 ± 0.9
H_3^+	2.8 ± 1.0

Conditions are considerably more favourable for the evaluation of the bulk concentration from Equation (28) as no normalizing constants are required. The bulk fluorine concentration is presented in Table 11 and Figure 62 as a function of the inverse current density. A direct proportionality was observed independent of lateral position on the sample. Microcracking is normally considered to occur only for inverse current densities in the range $4.4.10^{-4}$ m^2.A^{-1}

TABLE 11

Averaged Bulk Fluorine Concentration
in Microcracked Chromium Plate

Inverse Current Density $(m^2.A^{-1}).10^{-4}$	Bulk Fluorine Concentration ppm
1.63	207 ± 41
2.4	289 ± 12
3.26	370 ± 13
3.9	489 ± 17
4.37	570 ± 35
4.89	599 ± 12
5.56	685 ± 11
6.52	828 ± 27
8.15	931 ± 14

* Two Data Points Rejected

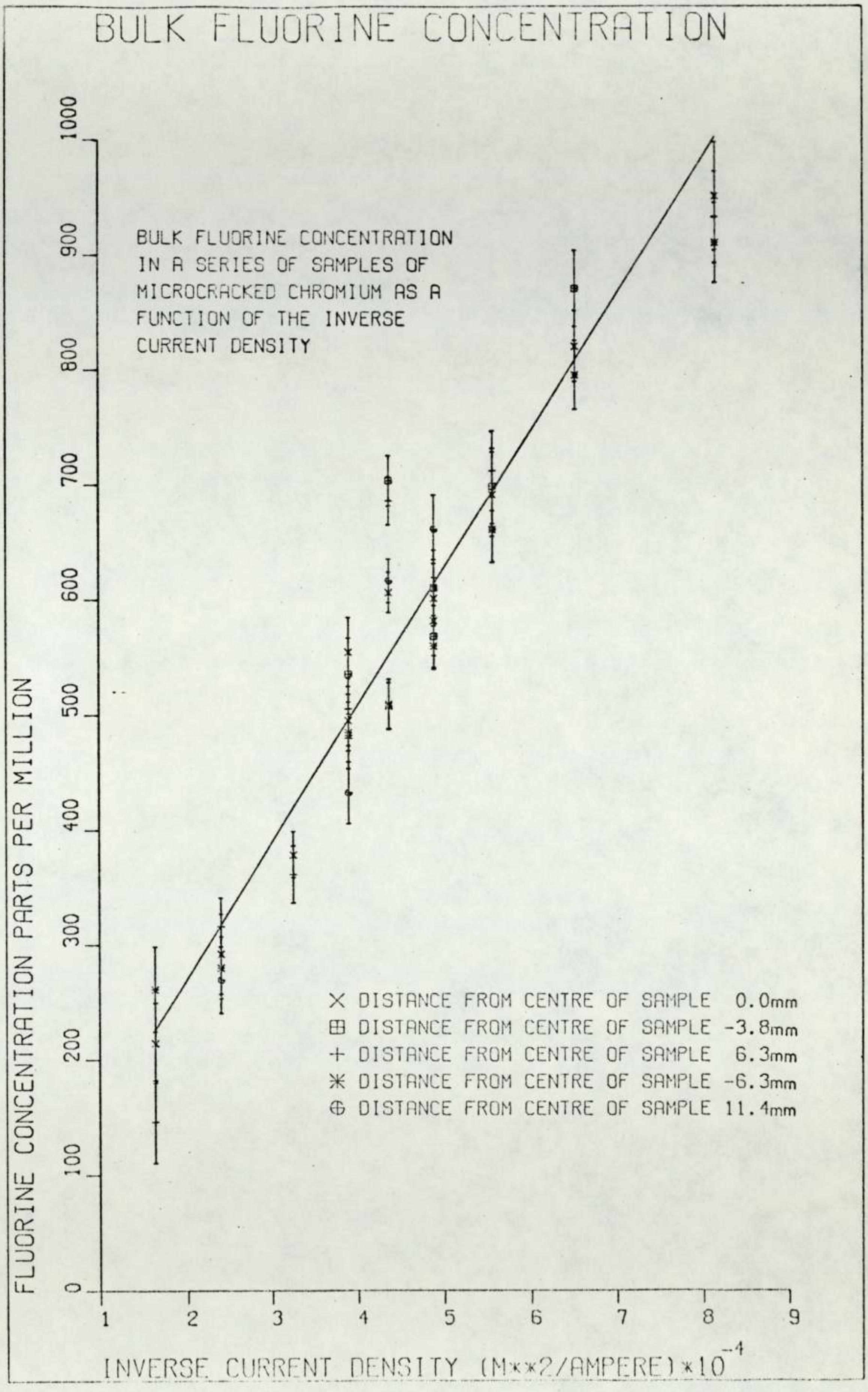
BULK FLUORINE CONCENTRATION
BULK FLUORINE CONCENTRATION IN A SERIES OF SAMPLES OF MICROCRACKED CHROMIUM AS A FUNCTION OF THE INVERSE CURRENT DENSITY
FLUORINE CONCENTRATION PARTS PER MILLION
0
100
200
300
400
500
600
700
800
900
1000
1
2
3
4
5
6
7
8
9
INVERSE CURRENT DENSITY (M**2/AMPERE)*10^{-4}
× DISTANCE FROM CENTRE OF SAMPLE 0.0mm
⊞ DISTANCE FROM CENTRE OF SAMPLE -3.8mm
+ DISTANCE FROM CENTRE OF SAMPLE 6.3mm
✳ DISTANCE FROM CENTRE OF SAMPLE -6.3mm
⊕ DISTANCE FROM CENTRE OF SAMPLE 11.4mm

Figure 62

to $5.6.10^{-4}$ $m^2.A^{-1}$. The data of Figure 62 covers essentially the entire range of inverse current densities for which it is possible to electrodeposit chromium onto a copper backing. We conclude, therefore, that the bulk fluorine concentration of microcracked chromium plate is independent of the presence or quality of microcracking and is simply inversely proportional to the rate of electrodeposition of chromium.

DATA FROM THE ASTON VAN DE GRAAFF

Microcracked chromium plate samples were investigated in the vicinity of the 340 keV $F^{19}(p,\alpha\gamma)O^{16}$ resonance using the proton beam of the 0.5 MV Aston van de Graaff. Insulation breakdown restricted the maximum incident energy to approximately 420 keV.

Figure 63 shows a yield curve obtained using the accelerator control system described by CRUMPTON (1967) and the target assembly described by VILLAITHONG(1971). A similar yield curve obtained using the control system and target assembly described in Chapter II is shown in Figure 64. Despite a notable improvement the energy resolution of the modified system was not sufficient to permit accurate analysis of the surface region and the observed maximum yield was found to vary by as much as 60 per cent for samples prepared under similar conditions.

A typical thick target yield curve from a calcium fluoride standard is shown in Figure 65 and exhibits a high plateau slope of approximately 10 per cent. Spectral displacement due to photomultiplier gain shift was eliminated as a significant cause of the high plateau slope by fitting the prominent first-escape and full-energy peaks of the

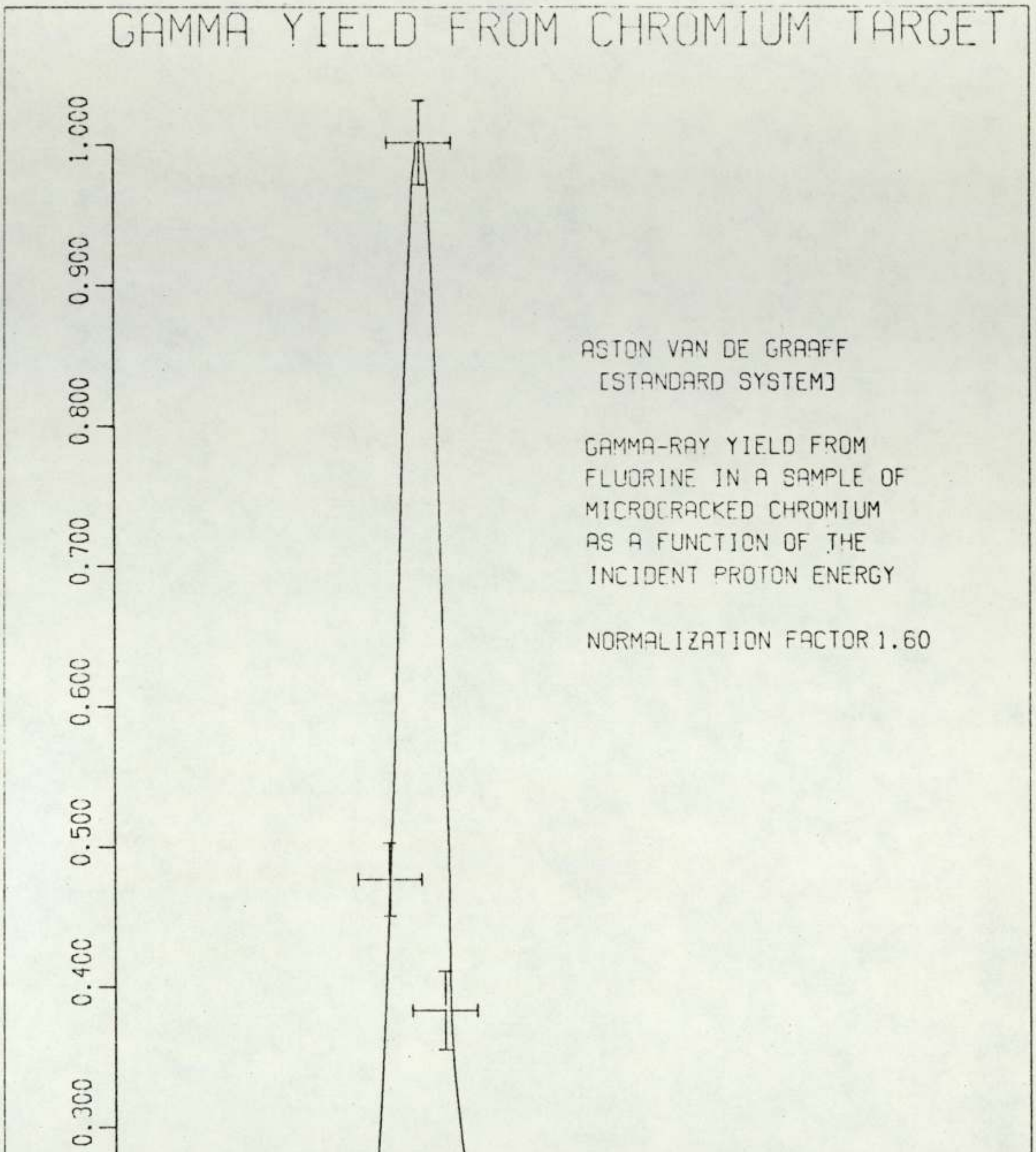
GAMMA YIELD FROM CHROMIUM TARGET
ASTON VAN DE GRAAFF
[STANDARD SYSTEM]
GAMMA-RAY YIELD FROM
FLUORINE IN A SAMPLE OF
MICROCRACKED CHROMIUM
AS A FUNCTION OF THE
INCIDENT PROTON ENERGY
NORMALIZATION FACTOR 1.60
COUNTS/MICROCOULOMB
0.000
0.100
0.200
0.300
0.400
0.500
0.600
0.700
0.800
0.900
1.000
310
320
330
340
350
360
370
380
390
400
PROTON ENERGY (KEV)

Figure 63

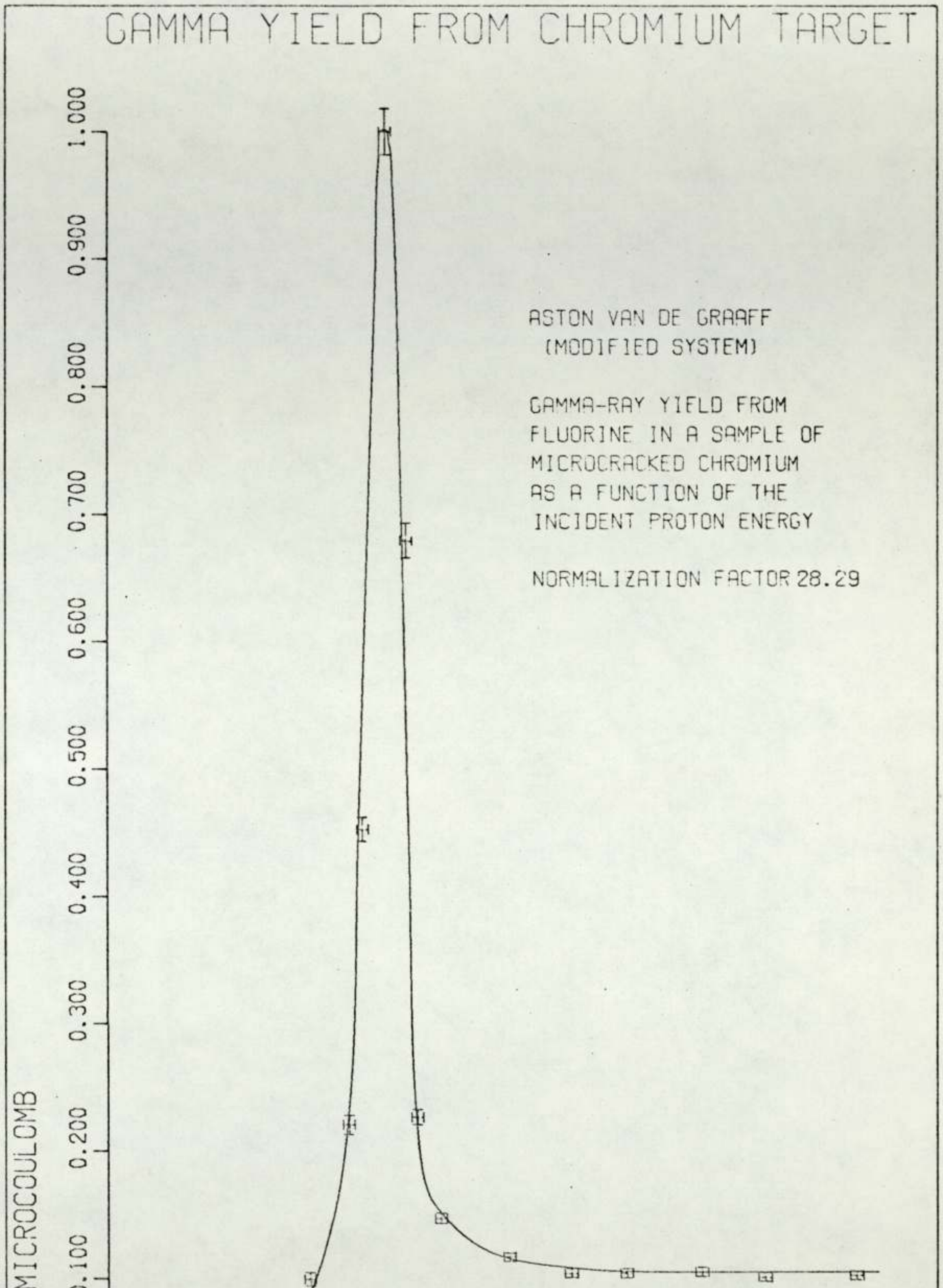
GAMMA YIELD FROM CHROMIUM TARGET
ASTON VAN DE GRAAFF
(MODIFIED SYSTEM)
GAMMA-RAY YIELD FROM
FLUORINE IN A SAMPLE OF
MICROCRACKED CHROMIUM
AS A FUNCTION OF THE
INCIDENT PROTON ENERGY
NORMALIZATION FACTOR 28.29
COUNTS/MICROCOULOMB
-0.000
0.100
0.200
0.300
0.400
0.500
0.600
0.700
0.800
0.900
1.000
310
320
330
340
350
360
370
380
390
400
PROTON ENERGY (KEV)

Figure 64

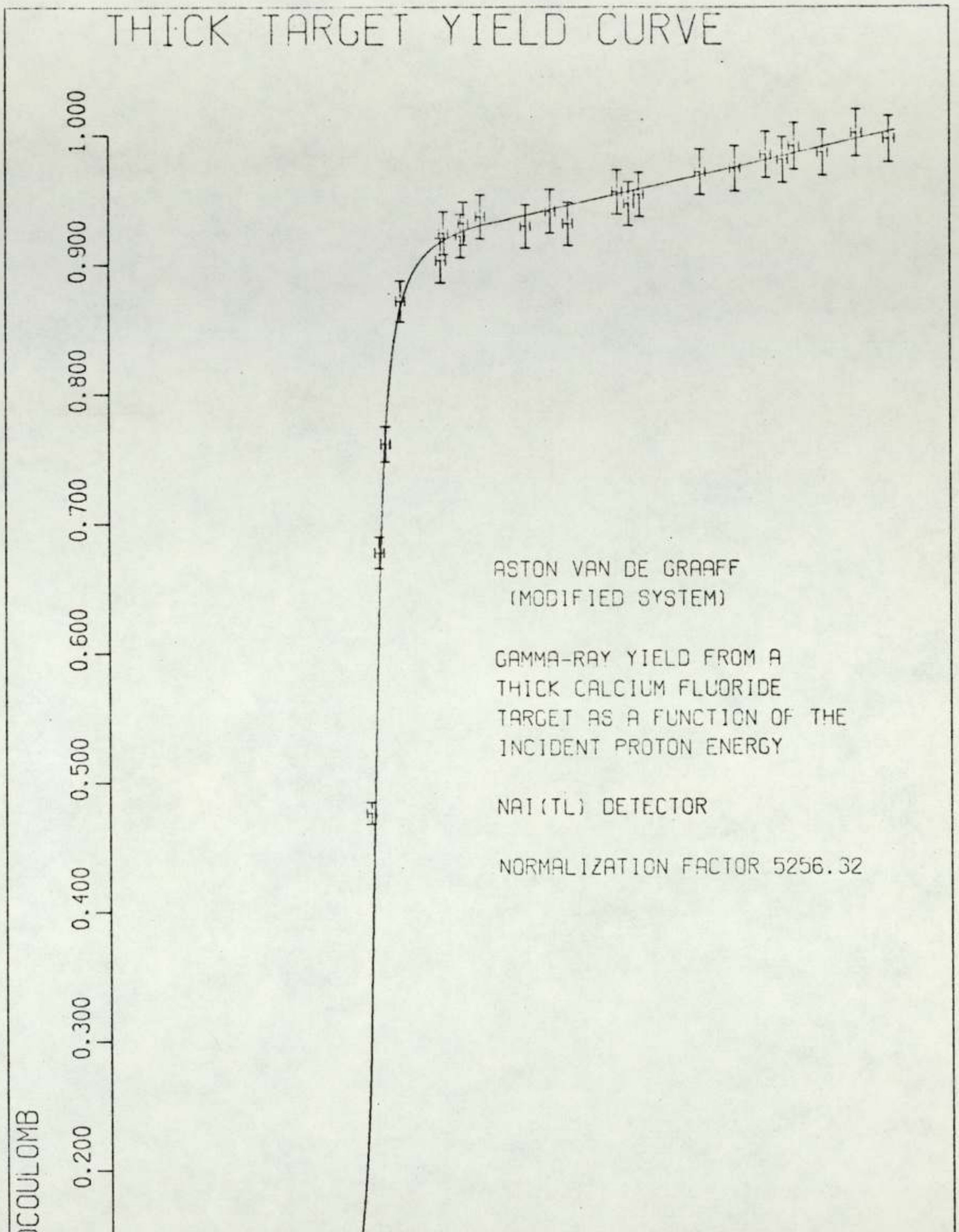
THICK TARGET YIELD CURVE
COUNTS/MICROCOULOMB
0.000
0.100
0.200
0.300
0.400
0.500
0.600
0.700
0.800
0.900
1.000
300
320
340
360
380
400
420
PROTON ENERGY (KEV)
ASTON VAN DE GRAAFF
(MODIFIED SYSTEM)
GAMMA-RAY YIELD FROM A
THICK CALCIUM FLUORIDE
TARGET AS A FUNCTION OF THE
INCIDENT PROTON ENERGY
NAI(TL) DETECTOR
NORMALIZATION FACTOR 5256.32

Figure 65

characteristic photon pulse-height spectrum. Fitting was accomplished using the computer programme "DOGS" [GRIFFITHS (1973)] which employs the procedures developed by MARISCOTTI (1967). All yield curves taken with the NaI(Tl) detector were found to exhibit the same high plateau shape independent of the orientation of the principal axis of the detector with respect to the mass-analyser. A high plateau slope was not, however, a feature of yield curves taken using a Ge(Li) detector. A typical example is shown in Figure 66 and conforms closely to the expected form. The phenomenon was not investigated further as the experimental programme was transferred to the Radiation Centre Dynamitron.

Data for both thin and thick standard targets indicated that beam energy dispersion at the target was a function of accelerator conditions but was typically in the region of 4 to 5 keV. The average value for the FWHM of the surface peak from microcracked chromium plate samples of 5.6 ± 0.3 keV is therefore considered to be consistent with data obtained on the Radiation Centre Dynamitron. The bulk fluorine concentration of microcracked chromium samples derived from data obtained on the Aston Van de Graaff is in agreement with that obtained on the Radiation Centre Dynamitron to within 4 per cent.

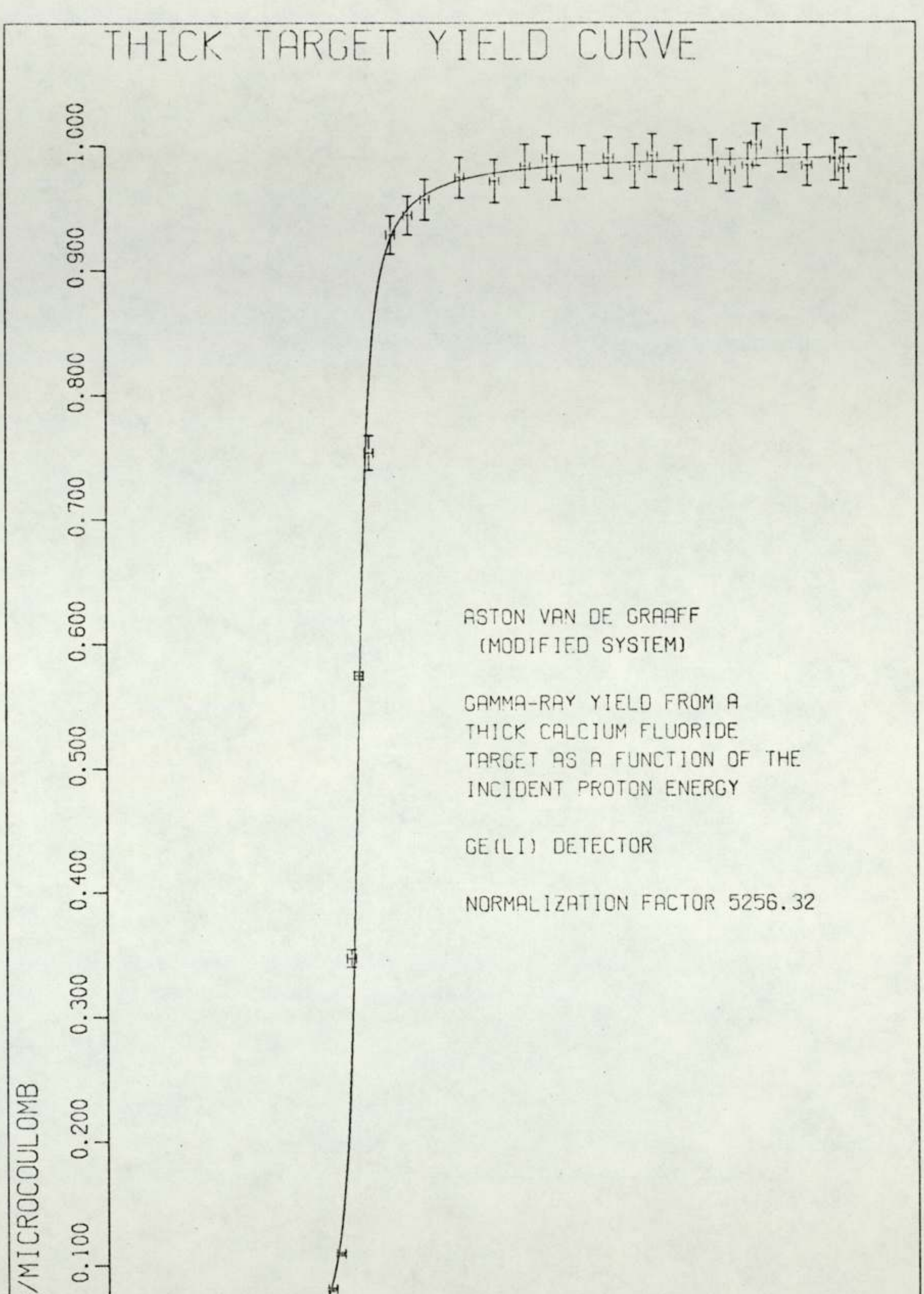
THICK TARGET YIELD CURVE
COUNTS/MICROCOULOMB
0.000
0.100
0.200
0.300
0.400
0.500
0.600
0.700
0.800
0.900
1.000
300
320
340
360
380
400
420
PROTON ENERGY (KEV)
ASTON VAN DE GRAAFF
(MODIFIED SYSTEM)
GAMMA-RAY YIELD FROM A
THICK CALCIUM FLUORIDE
TARGET AS A FUNCTION OF THE
INCIDENT PROTON ENERGY
GE(LI) DETECTOR
NORMALIZATION FACTOR 5256.32

Figure 66

Chapter VII

The Deconvolution of Analytical Yield Data

The Deconvolution of Analytical Yield Curves

The objective of prompt nuclear analysis is the determination of an unknown but desired concentration profile from an experimentally observed yield curve for a known reaction cross-section. The interaction of these three distributions is a superposition problem [SPENCER (1939), (1949)] involving the yield profile, h(s), as the convolution of the concentration profile, g(s), and the reaction cross-section, f(s). In terms of the auxiliary variable u, the convolution of two integratable functions is defined by

$$h(s) = f * g = g * f = \int f(s-u)\, g(u)\, du$$

$$= \int f(u)\, g(s-u)\, du \qquad \ldots\ldots\ldots\ldots(30)$$

where it is assumed that the base domain of integration is the whole of s- space.* Assuming a knowledge of the other two functions the determination of the concentration profile is a mathematical problem involving the solution of the integral equation relating them.

In resonance reaction studies the conditions of measurement impose the constraint that the observed yield curve is discrete rather than continuous. For any point, Y(Eb), on the observed yield curve the integrated count over an appropriate region of the characteristic photon

---

* If s is a one dimensional variable, Equation (30) is termed folding and h(s) is said to be the fold of f(s) with g(s).

pulse-height spectrum from a reaction on a given nuclide induced by a charged particle beam of mean incident energy Eb, may be rigorously defined by the expression,

$$Y(Eb) = a_f\, J\, T\, \Omega \int_{x=o}^{t} \int_{E=o}^{E_1} \int_{E_1=o}^{\infty} g(Eb,E_1)\, f(E_1,E,x)\, \sigma\,(E,\theta\,)\, C(x)\, dE dE_1 dx \quad ..(31)$$

where

$C(x)$ = the concentration profile of the nuclide

$g(Eb,E_1)dE_1$ = the probability of a particle in the incident beam of mean energy Eb having an energy in the interval E_1 to $E_1 + dE_1$

$f(E_1,E,x)dE$ = the probability of a particle incident at an energy E_1 having an energy in the interval E to $E + dE$ at a depth x in the target

$\sigma(E,\theta\,)$ = the reaction cross-section at an energy E with the emission of photon radiation in the direction θ

t = the total pathlength of the incident beam

J = the number of incident particles

T = the detection efficiency

Ω = the geometrical efficiency

a_f = the attenuation factor for the incident particle determined by the probability of scattering, or reaction, before the pathlength t is reached

In order to consider the solution of this equation the effects of incident beam energy dispersion and charged particle straggling will be ignored, as will the attenuation of the incident beam and the difference between range and pathlength. It is further assumed that the observed yields are normalized to comparison standards for unit incident charge so that J, T, Ω and the differential form of the reaction cross-section need not be known. Under these approximations Equation(31) may be expressed as an integral equation of the Volterra form

$$Y(Ep) = K \int_{0}^{Ep} \sigma(E,Ep) \left(\frac{dx}{dE} \right) C(E)\ dE \quad \ldots\ldots\ldots\ldots\ldots\ldots(32)$$

where Ep is the incident particle energy and K is a normalizing constant. Two methods of approach are possible for the solution of equations of this form, convolution and deconvolution.

In the analysis of prompt nuclear reaction data convolution is the more popular of the two methods and has been used extensively [PALMER (1965), OLLERHEAD et al.(1966), DERRY et al. (1971), CHEMIN et al.(1971), BARNES et al.(1973), PRONKO AND PRONKO (1973), CALVERT et al. (1974), WISE et al.(1974)]. An interesting application of successive convolution has been developed by ERGUN (1967) for the analysis of X-ray data.

The technique of deconvolution has not, however, been extensively applied to the analysis of prompt nuclear reaction studies. The advent of the fast Fourier transform algorithm [COOLEY and TUKEY (1965), COOLEY et al.(1969)] has greatly extended the implementation of Fourier methods on digital computers and has led to a resurgence of interest in the use of harmonic analysis [STOKES (1948), PATERSON (1950), DAVIS and HERD (1969), INOUYE et al. (1969)] for the deconvolution of charged particle pulse-height spectra [ZIEGLER and BAGLIN (1970), ZIEGLER et al.(1972)]. Relatively little information has been published on the application of deconvolution techniques to nuclear analysis based on the detection of prompt photon emission [MÖLLER and STARFELT (1967),PORTE et al. (1973), THOMAS and GREA (1975)].

The resolution of Equation (32) for different incident particle energies E_1, E_2 ....E_n is possible only for discrete summation with, for example, at an energy E_1

$$Y(E_1) = K \left[\int_{\Delta E_1} \sigma(E) \left(\frac{dx}{dE}\right) C(E)\, dE + \int_{\Delta E_2} \sigma(E) \left(\frac{dx}{dE}\right) C(E)\, dE + \cdots\cdots \cdots\cdots + \int_{\Delta E_n} \sigma(E) \left(\frac{dx}{dE}\right) C(E)\, dE \right]$$

such that

$$\Delta E_1 = \sum_{i=1}^{n} \Delta E_i$$

For the elaboration of such a system it is assumed that all elements ΔE are equal and that $C(E)$ and (dx/dE) are close enough to constant on any element, therefore

$$\begin{aligned}
Y(E_1) &= K\left[C_1 a_{11} + C_2 a_{12} + \ldots\ldots + C_n a_{1n} \right] \\
Y(E_2) &= K\left[C_1 a_{21} + C_2 a_{22} + \ldots\ldots + C_n a_{2n} \right] \\
&\vdots \qquad\qquad\qquad \vdots \\
Y(E_n) &= K\left[C_1 a_{n1} + C_2 a_{n2} + \ldots\ldots + C_n a_{nn} \right]
\end{aligned}$$

with

$$a_{ij} = \left(\frac{dx}{dE}\right)_j \int_{\Delta E_j} \sigma(E)\, dE$$

or in matrix notation

$$Y = KAC \qquad \ldots\ldots\ldots \quad (33)$$

where A represents a square matrix of order n and Y and C vectors of order n. Expression (33) is a set of n linear equations in n unknowns (the concentrations, $C_j, j = 1,n$) and may be solved by the methods of linear algebra.

The major component of the Breit-Wigner function is strongly localized in the vicinity of the resonance energy. An adequate description of the Volterra integral equation containing this function is therefore possible in discretized form only for small incremental elements ΔE. If the limits of integration are represented by the full range of the incident particle the use of small energy increments requires the solution of a high order system of equations ($n \sim 200$). A system of this order must be considered prohibitively expensive in terms of both data acquisition and computer time required for its solution. For the reaction $F^{19}(p,\alpha\gamma)O^{16}$ at $E_o = 340$ keV (used as a basis for an investigation of the technique of deconvolution) 95.3 per cent of the total integrated cross-section is contained within the energy interval 340 ± 16 keV. A maximum of error of less than 5 per cent is therefore entailed by neglecting the contribution to observed yield for proton energies outside this energy interval. Under this approximation the system order may be reduced to $n \sim 20$.

It has been established (Chapter III) that the convolution integral of a Breit-Wigner is well conditioned with respect to the form of the convoluting function. It follows, therefore, that such integrals are ill-conditioned with respect to the reverse process of deconvolution. It is characteristic of ill-conditioned equations that small percentage changes in the coefficients may lead to large percentage errors in the solution. A direct consequence of this property is that Equations (33) produce wildly oscillating solutions for arbitrary incident particle energies. The subject of ill-conditioning must therefore be considered in some detail.

In the error analysis of matrix computations the use of matrix and vector norms (either implicitly or explicitly) is unavoidable. For the general n x n system of equations denoted by

$$Ax = b$$

the L(2) or Euclidean norms of the vectors x and b are defined by

$$\| x \| = \left[\sum_i | x_i |^2 \right]^{\frac{1}{2}}$$

$$\| b \| = \left[\sum_i | b_i |^2 \right]^{\frac{1}{2}}$$

and are consistent with the Shur or Frobinius matrix norm defined by

$$\| A \|_F = \left[\sum_{ij} | a_{ij} |^2 \right]^{\frac{1}{2}}$$

If the exact solution of $Ax = b$ is denoted by x_e then for perturbations δb in the right hand side

$$A(x_e + \delta x) = b + \delta b \quad , \qquad \delta x = A^{-1} \delta b$$

For any consistent matrix and vector norms

$$\|b\| \leqslant \|A\| \, \|x_e\| \quad , \qquad \|\delta x\| \leqslant \|A^{-1}\| \, \|\delta b\|$$

$$\frac{\|\delta x\|}{\|x_e\|} \leqslant \|A^{-1}\| \, \|A\| \left(\|\delta b\| / \|b\| \right) \quad \dots\dots\dots\dots \qquad (34)$$

giving an upper bound for the relative change in x in terms of the relative change in b. The effect of perturbations in A is more complex as it is possible for A + δA to be singular. If A + δA is non-singular it may be shown [WILKINSON (1966)] that

$$\frac{\|\delta x\|}{\|x_e\|} \leqslant \frac{\|A^{-1}\| \; \|A\|(\|\delta A\|/\|A\|)}{[1 - \|A^{-1}\| \; \|A\| \; (\|\delta A\|/\|A\|)]} \quad \ldots.(35)$$

giving an upper bound for the relative change in x in terms of the relative change in A. The quantity $\|A^{-1}\| \; \|A\|$ is called the condition number of A with respect to the norm involved. For the Shur or Frobinius norm this quantity is known as the spectral condition number of A and is usually denoted by $\kappa(A)$. When κ is large these will always be specific δb and δA for which Equations (34) and (35) are severe overestimates (the so-called"global"uncertainty).

The ill-conditioning of Equations (33) arises from the discretization of the Volterra integral equation and not from the presence of the stocastic in the recorded data. We are, therefore, concerned principally with the degree of ill- conditioning of the coefficient matrix. A convenient measure of matrix ill-conditioning has been given by TURING (1948). The Turing condition numbers are defined by

$$N(A) = \frac{\kappa(A)}{n}$$

and

$$M(A) = n \max_{ij} | a_{ij} | \max_{ij} | a_{ij}^{-1} |$$

with n, the system order and $\max_{ij}|a_{ij}|$ and $\max_{ij}|a_{ij}{}^{-1}|$ the largest terms in the A and A^{-1} matrices respectively. Turing has shown that matrices formed from coefficients chosen from a random normal population are only slightly ill-conditioned and have N-condition numbers of $\sqrt{n}$ and M -condition numbers of $\sqrt{n}\ \ln(n)$. The application of these condition numbers may be illustrated by the trivial set of equations

$$10x + 9y = 19$$
$$9x + 8y = 17$$

which have the exact solution $x = y = 1.0$. The coefficient matrix

$$\begin{pmatrix} 10 & 9 \\ 9 & 8 \end{pmatrix}$$

has an N - condition number of 163.0 and an M-condition number of 200.0 compared with average values of $\sqrt{n} = 1.4$ and $\sqrt{n}\ \ln(n) = 0.98$ for random matrices of the same order. The condition numbers reflect the fact that if the coefficients in the original matrix had been

$$\begin{pmatrix} 10.1 & 9 \\ 9 & 8 \end{pmatrix}$$

the "exact" solution would be $x = 5.0$, $y = -3.5$, so that a 1 per cent change in one coefficient has altered the solutions appreciably. This may be considered a satisfactory example of the application of the definition of ill-conditioning. It should be observed that the condition numbers are applicable only to inversion of a matrix, and not to solution of the equations by elimination. It is difficult to determine the accuracy of the solution of a set of equations without inverting the coefficient matrix.

It is generally true that ill-conditioned matrices are ones which have small determinants, that is, small compared to the magnitudes of the coefficients. An additional test for ill-conditioning is to compute the determinant of the normalized matrix.

$$a_{ij} \rightarrow \alpha_{ij} = \frac{a_{ij}}{\{\Sigma (a_{ij})^2\}^{\frac{1}{2}}} \qquad (i = 1,n; \; j = 1,n)$$

If the determinant is small compared with ±1, the matrix is ill-conditioned. The determinant of the normalized matrix may, however, differ greatly from the condition numbers defined above as a measure of ill-conditioning and is a less reliable indicator.

Initial attempts at the solution of Equations (33) for a system order $n = 21$ yielded concentration factors * oscillating in the range $\pm 1.0 \times 10^8$. These totally useless solutions are not surprising in view of the condition numbers of the coefficient matrix; $M(A) = 11.2 \times 10^9$ (average value 13.95), $N(A) = 18.6 \times 10^7$ (average value 4.58), $\det(\alpha) = 3.16 \times 10^{-45}$. A number of other methods of discretization of the Volterra integral equation were investigated including the generation of empirical yield data outside the range of measurement, polynomial approximation of the integral and the use of the differential form of Equation (32). As no satisfactory reformulation of the problem could be devised which mitigated the basic ill-conditioning of the system it is necessary to consider what steps can be taken to improve

---

*Note. The term "concentration factor" will be used to indicate solutions obtained ignoring the noramlising constant K in Equation (33). For the sake of clarity normalising constants will be omitted from all future equations.

the conditioning of the coefficient matrix.

Essentially two possibilities exist, careful preconditioning of the original equations in order to preserve the diagonal dominance of the coefficient matrix and symmetrical (and severe) truncation of the Breit-Wigner function about its maximum value to elliminate the near singularity of the coefficient matrix due to the almost linear dependence of some of its rows. In the particular application considered the system order was reduced to n = 13 to facilitate preconditioning and the Breit-Wigner function cut at $E_o \pm 2$ keV ($\Gamma = 2.4$ keV). These measures result in a dramatic improvement in the conditioning of the coefficient matrix. After two or three trials a coefficient matrix was evolved with the condition numbers ; $M(A) = 32.5$ (average value 9.25), $N(A) = 1.74$ (average value 3.6), $\det(\alpha) = 0.17$. Although, in general, there is substantial agreement between the two measures of conditioning the M-condition number tends to be larger especially for diagonal or nearly diagonal matrices of the type pertinent to the present problem. The conditioning of the coefficient matrix may therefore be considered to be very good as the best conditioned matrices are the orthogonal ones, which have N-condition numbers of 1.0.

For the above coefficient matrix the solution of Equations (33) presents no problem. The analytical solution may be obtained by premultiplying the yield vector by the inverse coefficient matrix, that is,

$$\mathbf{C} = \mathbf{A}^{-1}\ \mathbf{Y}$$

A typical output from the author's computer programme RANDE 1 ("Ridge or Analytical Deconvolution, Mark 1") is shown in Figures 67 and 68

SPECIMEN OUTPUT FROM PROGRAMME
RANDE1

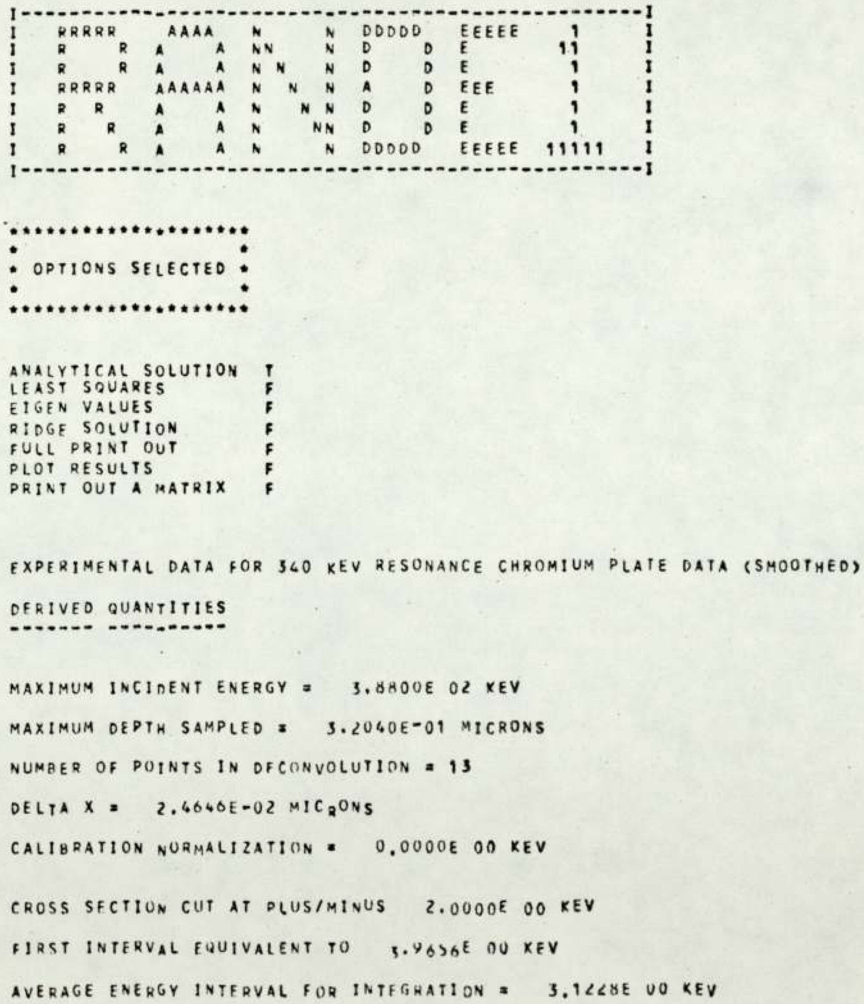

```
I---------------------------------------------------------I
I   RRRRR    AAAA   N     N  DDDDD    EEEEE     1         I
I   R    R  A    A  NN    N  D    D   E        11         I
I   R    R  A    A  N N   N  D    D   E         1         I
I   RRRRR   AAAAAA  N  N  N  A    D   EEE       1         I
I   R  R    A    A  N   N N  D    D   E         1         I
I   R   R   A    A  N    NN  D    D   E         1         I
I   R    R  A    A  N     N  DDDDD    EEEEE   11111       I
I---------------------------------------------------------I


*********************
*                   *
* OPTIONS SELECTED  *
*                   *
*********************


ANALYTICAL SOLUTION  T
LEAST SQUARES        F
EIGEN VALUES         F
RIDGE SOLUTION       F
FULL PRINT OUT       F
PLOT RESULTS         F
PRINT OUT A MATRIX   F


EXPERIMENTAL DATA FOR 340 KEV RESONANCE CHROMIUM PLATE DATA (SMOOTHED)

DERIVED QUANTITIES
------- ----------


MAXIMUM INCIDENT ENERGY =   3.8800E 02 KEV

MAXIMUM DEPTH SAMPLED =   3.2040E-01 MICRONS

NUMBER OF POINTS IN DECONVOLUTION = 13

DELTA X =   2.4646E-02 MICRONS

CALIBRATION NORMALIZATION =   0.0000E 00 KEV

CROSS SECTION CUT AT PLUS/MINUS   2.0000E 00 KEV

FIRST INTERVAL EQUIVALENT TO   3.9656E 00 KEV

AVERAGE ENERGY INTERVAL FOR INTEGRATION =   3.1228E 00 KEV
```

Figure 67

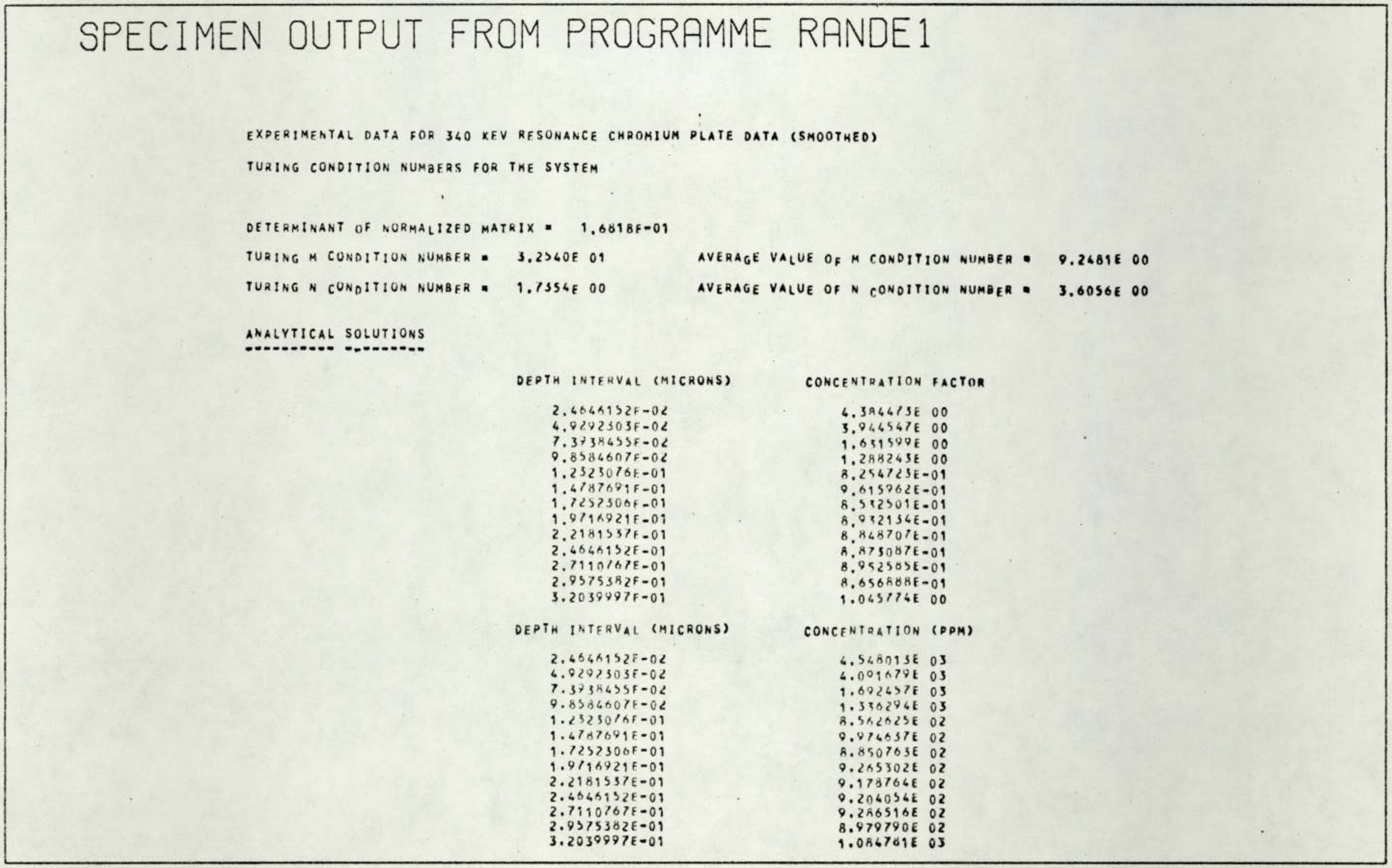

SPECIMEN OUTPUT FROM PROGRAMME RANDE1

```
EXPERIMENTAL DATA FOR 340 KEV RESONANCE CHROMIUM PLATE DATA (SMOOTHED)

TURING CONDITION NUMBERS FOR THE SYSTEM


DETERMINANT OF NORMALIZED MATRIX =   1,6818F-01

TURING M CONDITION NUMBER =   3,2540E 01          AVERAGE VALUE OF M CONDITION NUMBER =   9.2481E 00

TURING N CONDITION NUMBER =   1,7354E 00          AVERAGE VALUE OF N CONDITION NUMBER =   3.6056E 00

ANALYTICAL SOLUTIONS
---------- ---------

                          DEPTH INTERVAL (MICRONS)          CONCENTRATION FACTOR

                             2,4646152F-02                      4,384473E 00
                             4,9292303F-02                      3,944547E 00
                             7,3738455F-02                      1,631599E 00
                             9,8584607F-02                      1,288243E 00
                             1,2323076E-01                      8,254723E-01
                             1,4787691F-01                      9,615962E-01
                             1,7252306F-01                      8,532501E-01
                             1,9716921E-01                      8,932134E-01
                             2,2181537F-01                      8,848707E-01
                             2,4646152F-01                      8,873087E-01
                             2,7110767E-01                      8,952585E-01
                             2,9575382F-01                      8,656888E-01
                             3.2039997F-01                      1.045774E 00

                          DEPTH INTERVAL (MICRONS)          CONCENTRATION (PPM)

                             2,4646152F-02                      4,548013E 03
                             4.9292303F-02                      4.091679E 03
                             7.3738455F-02                      1.692457E 03
                             9.8584607E-02                      1.336294E 03
                             1.2323076F-01                      8.562625E 02
                             1.4787691E-01                      9.974637E 02
                             1.7252306F-01                      8.850763E 02
                             1.9716921E-01                      9.265302E 02
                             2.2181537E-01                      9.178764E 02
                             2.4646152E-01                      9.204054E 02
                             2.7110767E-01                      9.286516E 02
                             2.9575382E-01                      8.979790E 02
                             3.2039997E-01                      1.084761E 03
```

Figure 68

corresponding to an analysis of fluorine in a sample of microcracked chromium plate. A concentration profile for the same data is illustrated in Figure 69, and conforms closely to that of the model discussed in Chapter Vl. The bulk fluorine concentration (∿ 930 ppm) is in very good agreement with that obtained by other methods of solution (plating conditions $8.15 \times 10^{-4}\ m^{2}.A^{-1}$). The surface concentration, however, is low by a factor of approximately seven, a point considered in a later section. The enhanced values of the concentration factors for the first and last elements arise from the measures taken to improve the conditioning of the coefficient matrix. To maintain diagonal dominance for the first and last rows of coefficient matrix it is necessary to ignore approximately one-third of the assumed cross-section which leads to inflated values for C_1 and C_n. The solutions illustrated were derived from smoothed values [SAVITZKY and GOLAY (1964)] for observed yield. The presence of the stocastic does not, however, significantly alter the solutions as indicated by the broken lines in Figure 69 corresponding to solutions obtained using "raw" yield data.

INCIDENT BEAM ENERGY DISPERSION

The effects of incident beam energy dispersions may be considered by replacing the Breit-Wigner cross-section in Equation (32) with an "effective" reaction cross-section similar to that defined by Equation (19). If incident beam energy dispersion is represented by the unit-area slit-function, D (E_v), (defined in Chapter III) the basic formulation of the problem is unaltered but the elements of the coefficient matrix are now given by

$$a_{ij} = \left(\frac{dx}{dE}\right)_j \int_{\Delta E_v} \int_{\Delta E_j} D(E_v)\, \sigma(E)\, dE\, dE_v$$

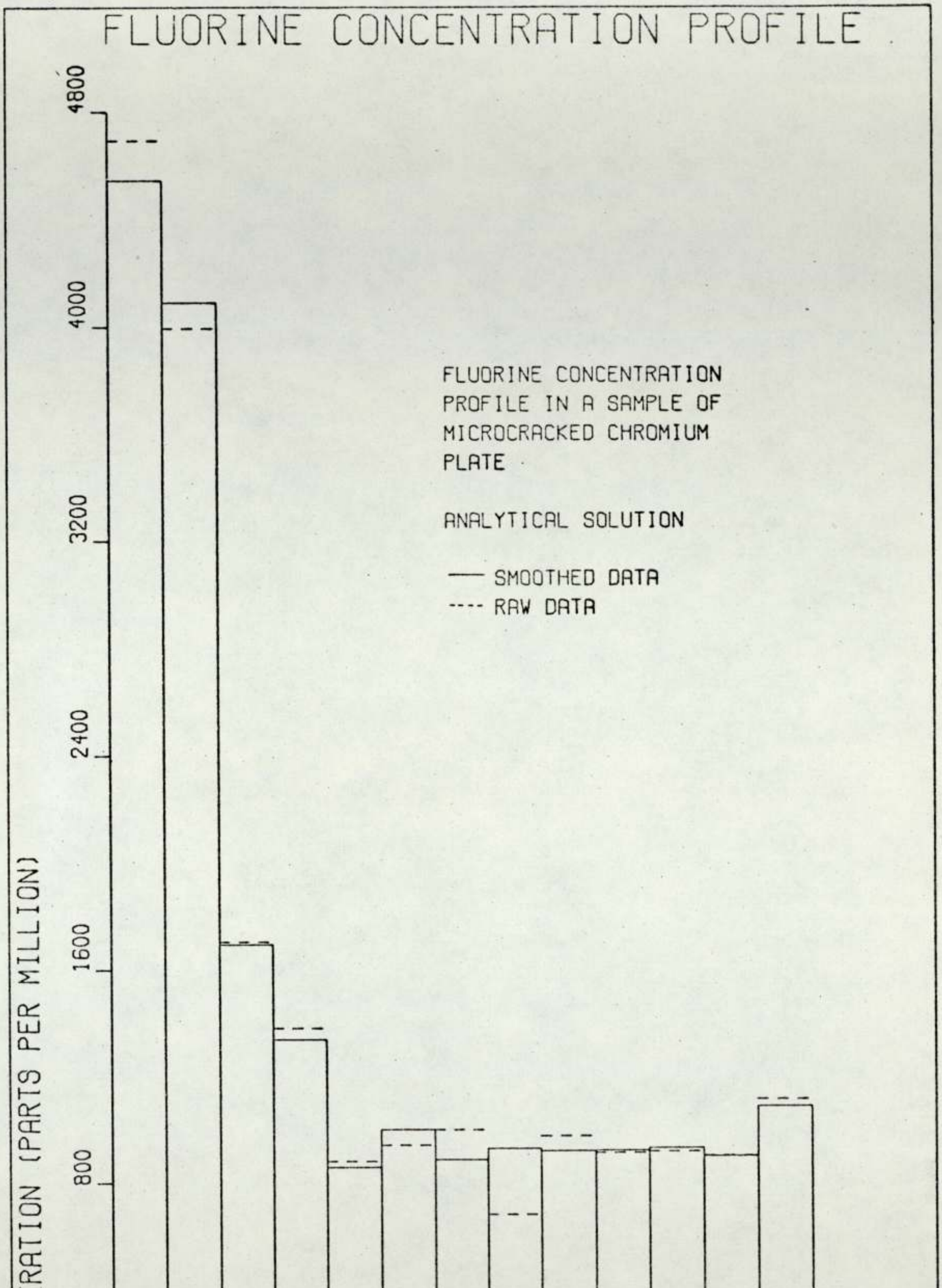
FLUORINE CONCENTRATION PROFILE
4800
4000
3200
2400
1600
800
0
CONCENTRATION (PARTS PER MILLION)
FLUORINE CONCENTRATION PROFILE IN A SAMPLE OF MICROCRACKED CHROMIUM PLATE
ANALYTICAL SOLUTION
SMOOTHED DATA
RAW DATA
0.00
0.05
0.10
0.15
0.20
0.25
0.30
0.35
DEPTH (MICRONS)

Figure 69

The inclusion of incident beam energy dispersion does, however, modify the conditioning of the coefficient matrix as indicated below.

Beam Energy Dispersion (keV)	Condition Numbers N(A)	M(A)	det(α)
2.0	2.058	37.62	0.108
4.0	5.004	89.31	1.9×10^{-2}
8.0	17.5	240.5	-1.16×10^{-3}

For 2 keV beam energy dispersion the conditioning of the coefficient matrix is sufficiently good to permit solution by the methods previously described. For 4 keV beam energy dispersion the analytical solution is rather poor, however, and for 8 keV beam energy dispersion* totally useless. The ill-conditioning could be alleviated by preconditioning the equations for wider energy increments, ΔE, and a reduced system order, n. In order to investigate how much useful information can be extracted under particularly unfavourable conditions we will consider alternative methods of solution of Equations (33).

Computationally a better method of approach is to determine the unknown concentrations C_j $(j = 1,n)$ from the differentiated form of Equations (33) invoking the criterion of least-squares. In a least squares sense the best solution is considered to be that which

*Note. It is necessary to consider large values of beam energy dispersion as the data corresponds to measurements taken using an incident H_3^+ molecular hydrogen ion beam.

minimizes the sum of the squared residuals defined by

$$S = \sum_{i=1}^{n} \left(Y_i - \sum_{j=1}^{n} a_{ij} C_j \right)^2 \qquad \ldots\ldots\ldots\ldots\ldots\ldots\ldots\ldots\ldots(36)$$

The minimum value of S occurs when the n partial derivatives of S with respect to the parameters C_j simultaneously vanish, that is when

$$\frac{\delta S}{\delta C_j} \equiv -2 \sum_{i=1}^{n} (Y_i - \sum_{j=1}^{n} a_{ij} C_j) \cdot (a_{ij}) = 0 \qquad \ldots\ldots\ldots\ldots(37)$$

The constraints imposed by Equations (37) form a system of n independent equations, known as the normal equations, which are linear in the parameters C_j and are defined by

$$\mathbf{Z} = \mathbf{BC} \qquad \ldots\ldots\ldots\ldots\ldots\ldots\ldots\ldots\ldots\ldots(38)$$

where the elements of the column vector **Z** are given by

$$Z_j = \sum_{i=1}^{n} \left(a_{ij} Y_j \right) \qquad (j = 1,n)$$

and the elements of the normal matrix **B** by

$$b_{ij} = \sum_{k=1}^{n} (a_{ki}) \cdot (a_{kj}) \qquad (i = 1, n; j = 1,n)$$

The solution of Equations (38) is a set of parameter values C_j $(j = 1, n)$ that minimizes the sum of the squared residuals, S.

A major difficulty in the application of least squares techniques to the solution of ill-conditioned multivariate problems is that within the accuracy of the computation there is a wide range of coefficient values which yield essentially the same residual error S.

A least squares solution of the Volterra equation with 8 keV beam energy dispersion is shown in Figures 70 to 72 and exhibits marked oscillation and negative concentration factors.

The unstable solutions arise from the application of a first-degree measure to a high- degree quantity, namely volume and its multidimensional generalization. Multivariable problems have a structure entirely different from that of a single variable one. The difficulties engendered by these differences have been referred to by several authors as "the curse of dimensionality". Thus even if it is possible to reduce a multidimensional volume of uncertainty to a fixed fraction, this fraction would have to be extremely small before the ranges of the individual variables are significantly reduced. Determining a true set of optimum conditions in n-dimensional hyperspace is extremely difficult. A close practical approximation to the optimum may, however, be obtained using the technique of ridge analysis.

RIDGE ANALYSIS

Ridge analysis has been discussed in detail by HOERL (1959), (1962), WILDE (1964) and WILDE and BEIGHTLER (1967). Its application to the enhancement of electron probe resolution has been considered by RAPPERPORT (1969). The technique has not been previously applied to the problem under investigation. The basis of ridge analysis is the inclusion of an additional constraint to the least-squares solution, as proposed by LEVENBERG (1944), which determines how stable the solution is and simultaneously shows the best compromise if it is unstable.

SPECIMEN OUTPUT FROM PROGRAMME RANDE2

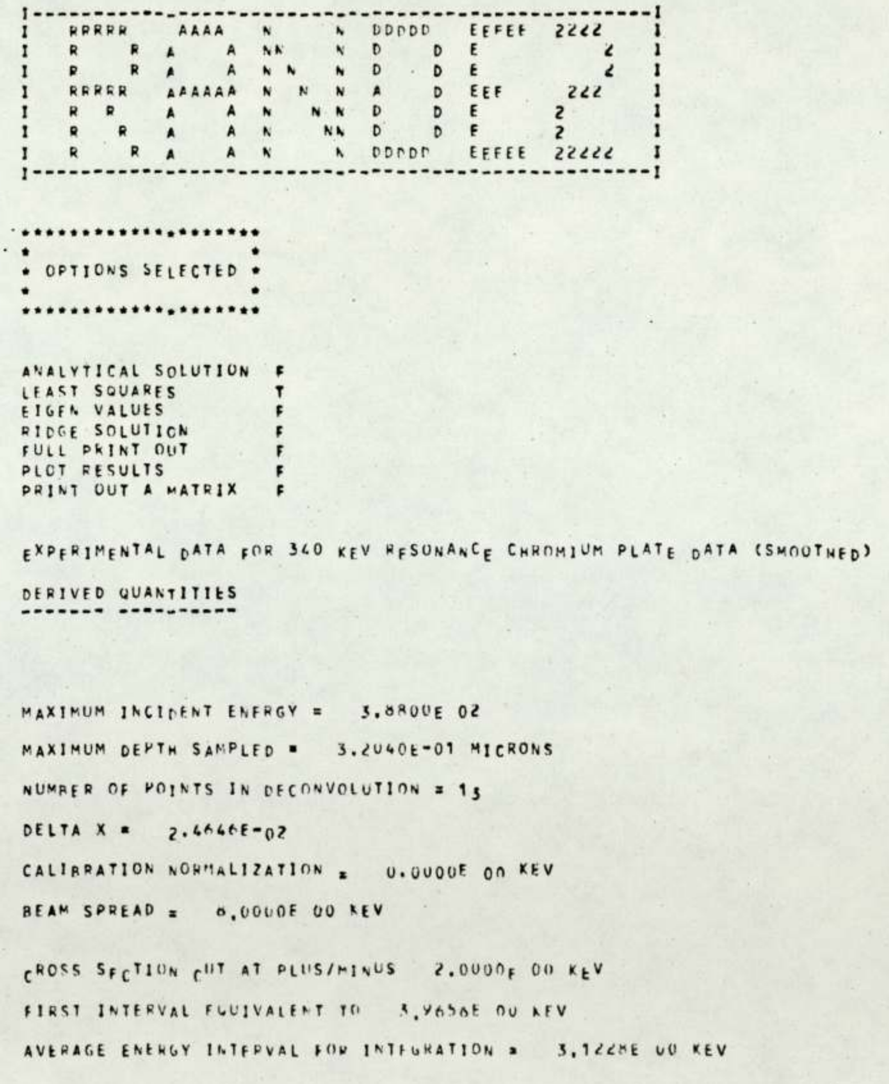

```
I----------------------------------------------------------I
I   RRRRR    AAAA   N     N DDDDD   EEEEE  2222            I
I   R    R  A    A  NN    N D    D  E          2           I
I   R    R  A    A  N N   N D    D  E          2           I
I   RRRRR   AAAAAA  N  N  N D    D  EEE     222            I
I   R  R    A    A  N   N N D    D  E      2               I
I   R   R   A    A  N    NN D    D  E      2               I
I   R    R  A    A  N     N DDDDD   EEEEE  22222           I
I----------------------------------------------------------I

********************
*                  *
* OPTIONS SELECTED *
*                  *
********************


ANALYTICAL SOLUTION  F
LEAST SQUARES        T
EIGEN VALUES         F
RIDGE SOLUTION       F
FULL PRINT OUT       F
PLOT RESULTS         F
PRINT OUT A MATRIX   F

EXPERIMENTAL DATA FOR 340 KEV RESONANCE CHROMIUM PLATE DATA (SMOOTHED)

DERIVED QUANTITIES
------- ----------



MAXIMUM INCIDENT ENERGY =   3.8800E 02

MAXIMUM DEPTH SAMPLED =   3.2040E-01 MICRONS

NUMBER OF POINTS IN DECONVOLUTION = 15

DELTA X =   2.4646E-02

CALIBRATION NORMALIZATION =   0.0000E 00 KEV

BEAM SPREAD =   0.0000E 00 KEV

CROSS SECTION CUT AT PLUS/MINUS   2.0000E 00 KEV

FIRST INTERVAL EQUIVALENT TO   3.9656E 00 KEV

AVERAGE ENERGY INTERVAL FOR INTEGRATION =   3.1228E 00 KEV
```

Figure 70

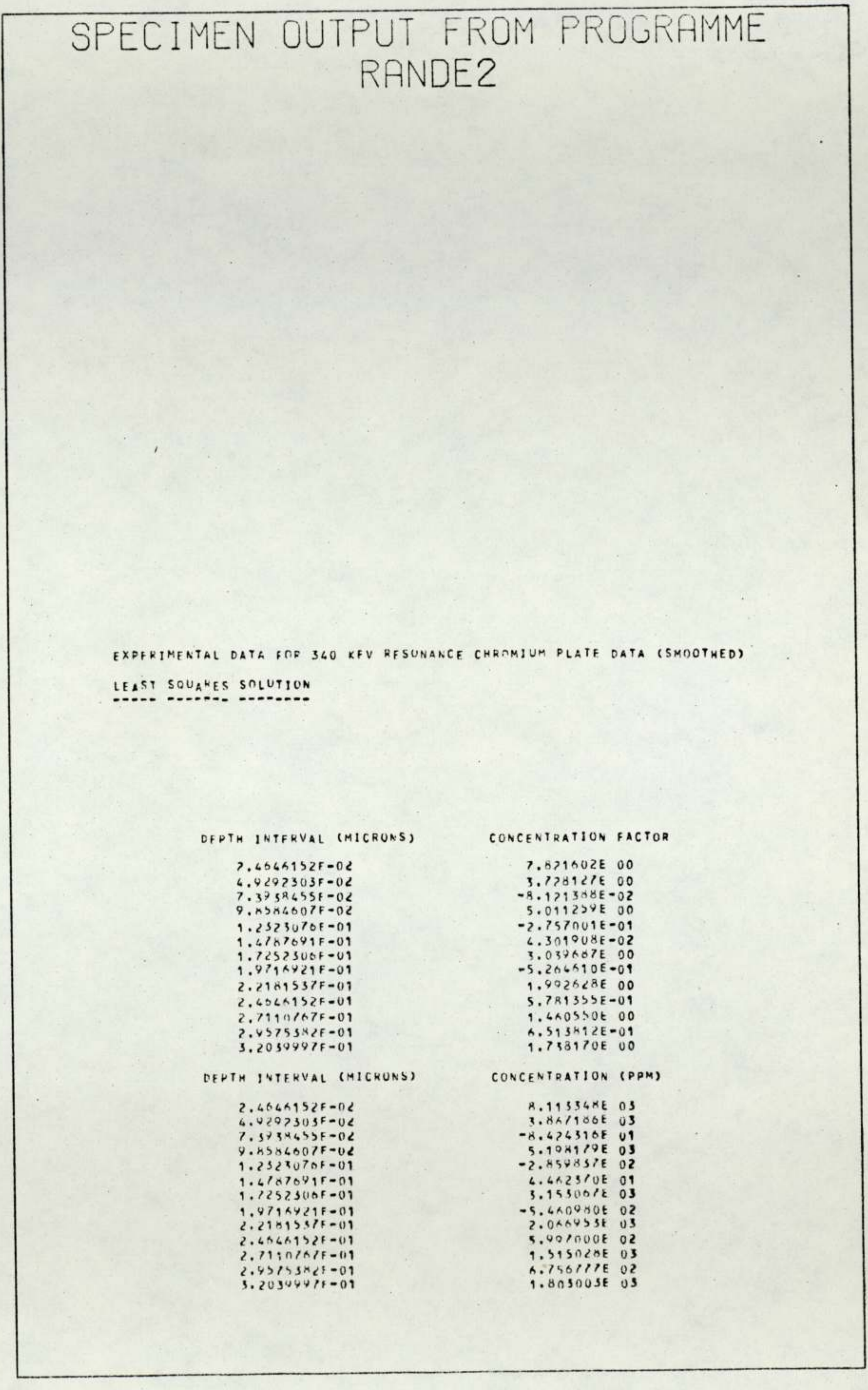

SPECIMEN OUTPUT FROM PROGRAMME
RANDE2

```
EXPERIMENTAL DATA FOR 340 KEV RESONANCE CHROMIUM PLATE DATA (SMOOTHED)

LEAST SQUARES SOLUTION
----- ------- --------



          DEPTH INTERVAL (MICRONS)          CONCENTRATION FACTOR

               2.4646152F-02                     7.821602E 00
               4.9292303F-02                     3.728127E 00
               7.3938455F-02                    -8.121388E-02
               9.8584607F-02                     5.011259E 00
               1.2323076F-01                    -2.757001E-01
               1.4787691F-01                     4.301908E-02
               1.7252306F-01                     3.039687E 00
               1.9716921F-01                    -5.264610E-01
               2.2181537F-01                     1.992628E 00
               2.4646152F-01                     5.781355E-01
               2.7110767F-01                     1.460550E 00
               2.9575382F-01                     6.513812E-01
               3.2039997F-01                     1.738170E 00

          DEPTH INTERVAL (MICRONS)          CONCENTRATION (PPM)

               2.4646152F-02                     8.113348E 03
               4.9292303F-02                     3.867186E 03
               7.3938455F-02                    -8.424316E 01
               9.8584607F-02                     5.198179E 03
               1.2323076F-01                    -2.859837E 02
               1.4787691F-01                     4.462370E 01
               1.7252306F-01                     3.153067E 03
               1.9716921F-01                    -5.460980E 02
               2.2181537F-01                     2.066953E 03
               2.4646152F-01                     5.997000E 02
               2.7110767F-01                     1.515028E 03
               2.9575382F-01                     6.756777E 02
               3.2039997F-01                     1.803003E 03
```

Figure 71

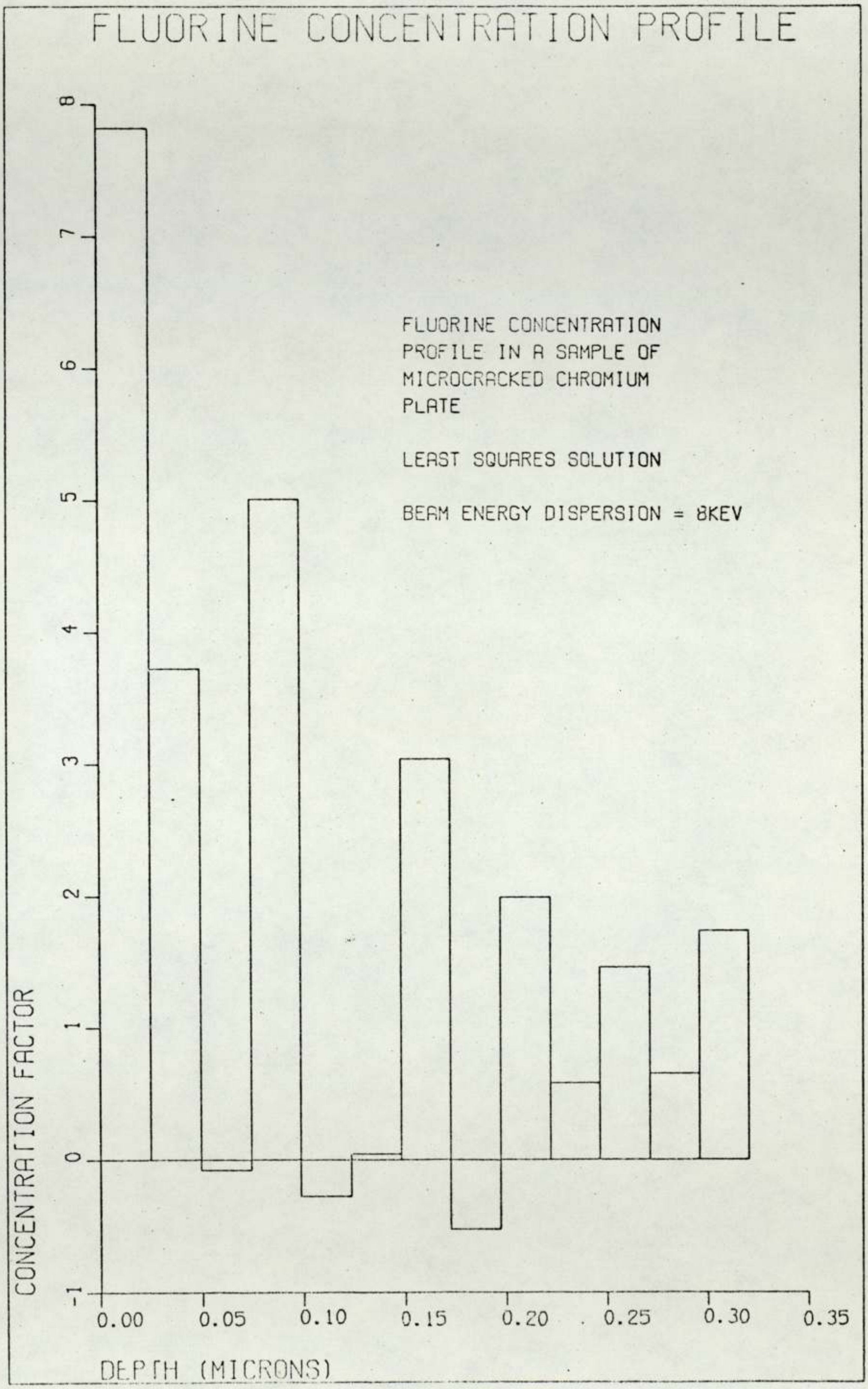
FLUORINE CONCENTRATION PROFILE
FLUORINE CONCENTRATION PROFILE IN A SAMPLE OF MICROCRACKED CHROMIUM PLATE
LEAST SQUARES SOLUTION
BEAM ENERGY DISPERSION = 8KEV
CONCENTRATION FACTOR
8
7
6
5
4
3
2
1
0
-1
0.00
0.05
0.10
0.15
0.20
0.25
0.30
0.35
DEPTH (MICRONS)

Figure 72

In the application of ridge analysis it is necessary to be able to define distances in hyperspace. To avoid dimensional inhomogeneity it is necessary to apply suitable transformations to the independent variables to remove their physical units. In the following discussion it will be assumed that this transformation has been made by dividing by a unit constant of the appropriate dimensions.

For a problem in n variables it is possible to characterize all values of the residual error, S, in n-dimensional hyperspace. For given values of the dependent variable, S, all possible values of the independent variables, C_j, are defined by hypercontours in the given hyperspace. Ridge analysis investigates the maximum and minimum values of S on n-dimensional spheres of various radii centred on the origin. These maximum and minimum values when plotted against their distance from the origin define the so-called ridges of the function. The distance from the origin is known as the radius of interest, R, and is given by the root sum of squares of the coefficients, that is,

$$R = \sum_{j=1}^{n} \left\{ (C_j)^2 \right\}^{\frac{1}{2}} \quad \dots\dots\dots\dots\dots\dots\dots\dots (39)$$

It has been established [HOERL (1959)] that simultaneous minimization of S and R produces the most stable solution to ill-conditioned problems.

Computationally the ridge values are determined from Equations (38) by introducing the dummy parameter λ,

$$Z = (B - \lambda)\ C \quad \dots\dots\dots\dots (40)$$

In this respect it is necessary to introduce the concept of eigenvalue [WILKINSON (1965)]. By definition an eigenvalue is a value of λ which makes the determinant of a matrix equal to zero, that is,

$$|(B - \lambda I)| = 0 \qquad \text{..................(41)}$$

where I is an identity matrix of the same order as B. Equation (41) is known as the characteristic equation of B and is of degree n in λ.

A maximum likelihood solution for ridge analysis has not been theoretically derived. It has been established, however,[HOERL (1959)] that the minimum ridge is defined by a λ value less than the minimum eigenvalue of the normal matrix. The ridge solution corresponds to the point on the curve of residual error against radius where the residual error is increasing rapidly.

In the practical application of ridge analysis a preliminary investigation is made to determine the eigenvalues of the normal matrix using Equation (41). The normal matrix is then augmented by a λ value less than the minimum eigenvalue and the solutions, C_j, determined by premultiplying the vector Z by the inverse augmented normal matrix. Once the solutions have been determined S and R may be calculated from Equations (36) and (39). The process is repeated for different assumed values of λ(less than the minimum eigenvalue) until the optimum solution is located. This may be obtained either visually, from a plot of residual error against radius, or by computing the maximum of the second derivative of the root sum of squares error, $S^{\frac{1}{2}}$, with respect to the radius, R, by successive evaluation for various values of λ, using the expression given by HOERL (1962),

$$\frac{d^2(S^{\frac{1}{2}})}{dR^2} = \frac{P - (\lambda R)^2/S}{S^{\frac{1}{2}}}$$

where

$$P = \frac{R^2}{C^T(B - \lambda I)^{-1}C} + \lambda$$

B = the normal matrix

$(B- \lambda I)^{-1}$ = the inverse of the normal matrix augmented by the λ value selected

C^T = the transpose (a row vector) of the column vector of solution values

and all other terms have been defined previously.

The shape of the ridge determines how sensitive the solution is relative to the available data and therefore determines the number of iterations required to locate the optimum solutions. A considerable saving in computation time can often be achieved by the use of efficient and rapidly convergent search techniques such as the "Fibonacci Search" or "Search by the Golden Ratio" which are discussed in detail by WILDE(1964). Search techniques should, however, be applied with some caution as many problems give rise to "dangerous ridges"[WILDE (1964)] for which most search techniques break-down completely or fail to converge to the correct value. It is generally advisable to investigate secondary ridges for S in order to guarantee the correct optimum.

The ridge solution for the case of 8 keV incident beam energy dispersion is shown in Figures 73 and 74 and although far from perfect it is appreciably better than the corresponding least squares solution (Figure 72). The failure of the ridge solution (in common with all

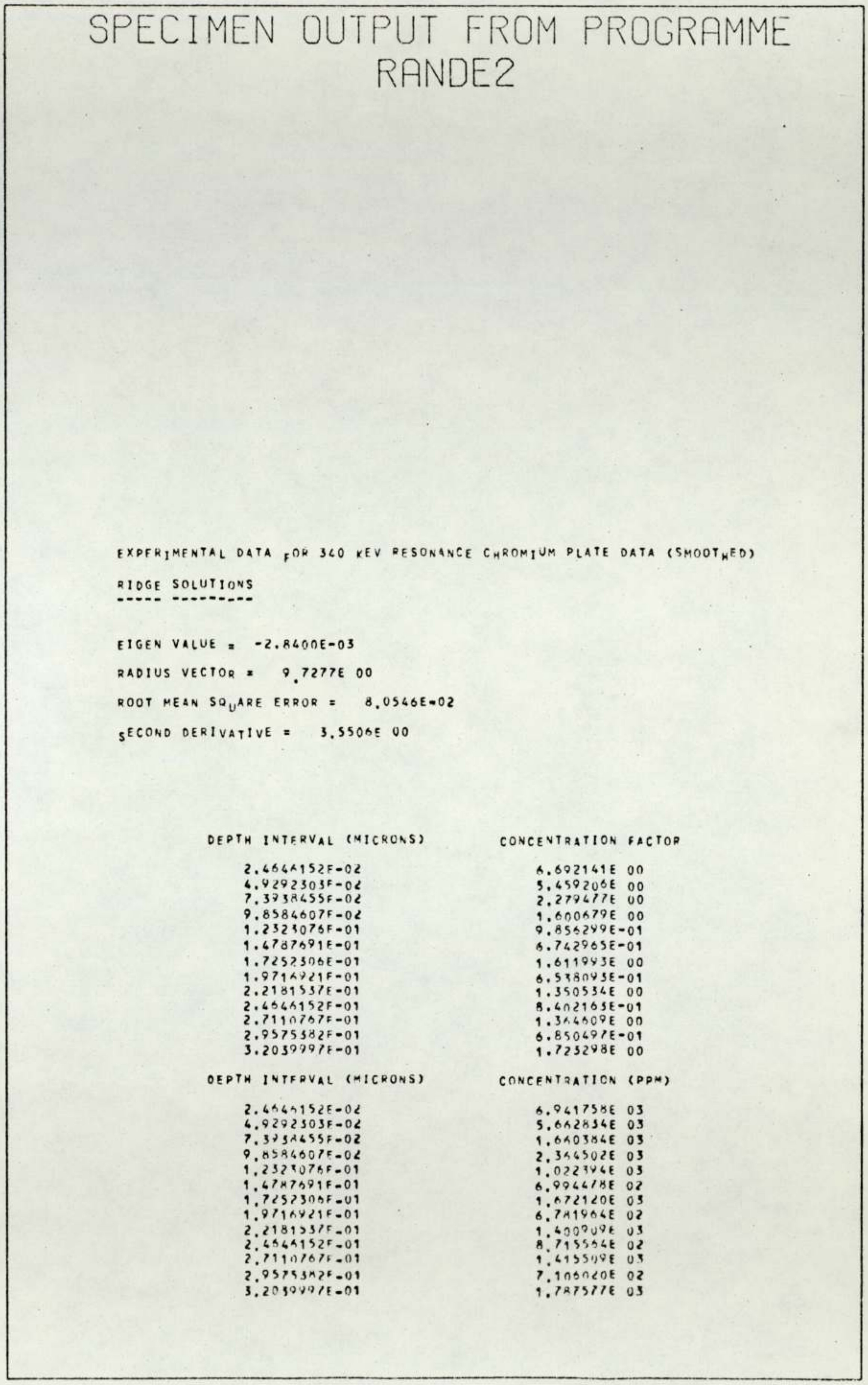

SPECIMEN OUTPUT FROM PROGRAMME
RANDE2

```
EXPERIMENTAL DATA FOR 340 KEV RESONANCE CHROMIUM PLATE DATA (SMOOTHED)

RIDGE SOLUTIONS
----- ---------

EIGEN VALUE =  -2.8400E-03

RADIUS VECTOR =   9.7277E 00

ROOT MEAN SQUARE ERROR =   8.0546E-02

SECOND DERIVATIVE =   3.5506E 00



      DEPTH INTERVAL (MICRONS)              CONCENTRATION FACTOR

           2.4646152F-02                        6.692141E 00
           4.9292303F-02                        5.459206E 00
           7.3938455F-02                        2.279477E 00
           9.8584607F-02                        1.600679E 00
           1.2323076F-01                        9.856299E-01
           1.4787691E-01                        6.742965E-01
           1.7252306E-01                        1.611993E 00
           1.9716921F-01                        6.538093E-01
           2.2181537E-01                        1.350534E 00
           2.4646152F-01                        8.402165E-01
           2.7110767F-01                        1.364609E 00
           2.9575382F-01                        6.850497E-01
           3.2039997E-01                        1.723298E 00

      DEPTH INTERVAL (MICRONS)              CONCENTRATION (PPM)

           2.4646152E-02                        6.941758E 03
           4.9292303F-02                        5.662834E 03
           7.3938455F-02                        1.660384E 03
           9,8584607F-02                        2,344502E 03
           1,2323076F-01                        1,022394E 03
           1,4787691F-01                        6,994478E 02
           1,7252306F-01                        1,672120E 03
           1,9716921F-01                        6,781964E 02
           2,2181537F-01                        1,400909E 03
           2,4646152F-01                        8,715564E 02
           2,7110767F-01                        1,415509E 03
           2,9575382F-01                        7,106020E 02
           3,2039997E-01                        1,787577E 03
```

Figure 73

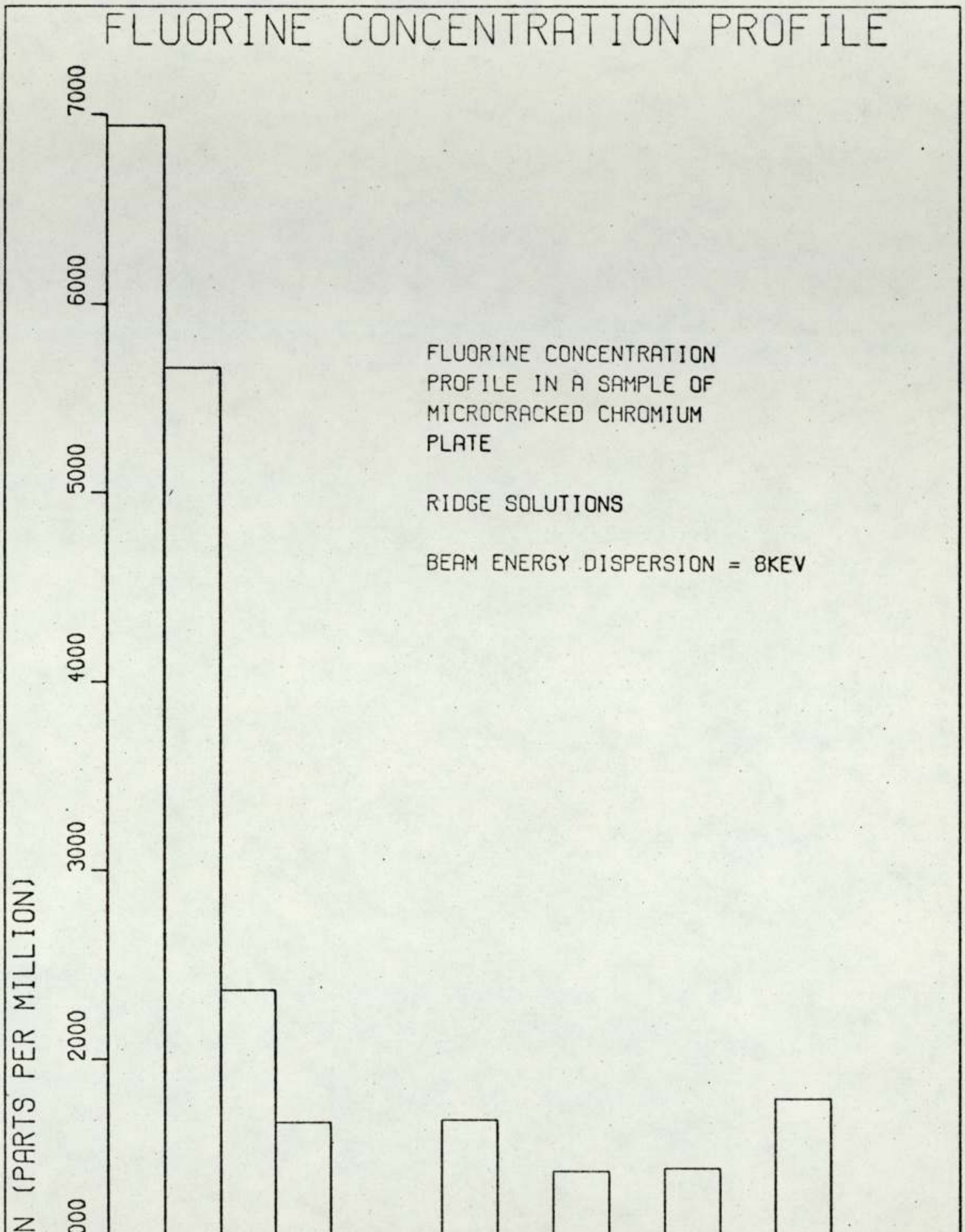
FLUORINE CONCENTRATION PROFILE
FLUORINE CONCENTRATION PROFILE IN A SAMPLE OF MICROCRACKED CHROMIUM PLATE
RIDGE SOLUTIONS
BEAM ENERGY DISPERSION = 8KEV
CONCENTRATION (PARTS PER MILLION)
0
1000
2000
3000
4000
5000
6000
7000
0.00
0.05
0.10
0.15
0.20
0.25
0.30
0.35
DEPTH (MICRONS)

Figure 74

the methods investigated) to reproduce the surface concentration arises from the limited validity of the equations on which the solutions are based. It has been established (Chapter VI) that the effective width of the surface region in samples of microcracked chromium plate is approximately 1 keV whereas the resolution of the solutions discussed is approximately 4 keV. An accurate representation of the surface region is therefore possible only by decreasing the energy increment ΔE either by increasing the system order or reducing the maximum incident particle energy used in the solution.

Although deconvolution is inherently more difficult to apply than the analogous technique of convolution it does offer a number of distinct advantages. In cases where the analytical or least squares solutions are valid, once a satisfactory system of equations has been evolved any number of corresponding yield curves may be analysed by applying the same inverse matrix to each of the yield vectors. Deconvolution does not require a priori knowledge of the functional form of the concentration profile and is therefore very general in application. These advantages are gained, however, at the expense of the greater complexity of the mathematical and computational methods required to obtain satisfactory solutions.

We have established that difficulties encountered in the deconvolution of analytical yield data from prompt nuclear resonance reactions arise from the nature of the Breit-Wigner reaction cross-section and the discretization of the Volterra integral equation. Computational techniques have been described which alleviate the basic ill-conditioning of integral equations of the Volterra form and permit the attainment of stable solutions.

Conclusions

Conclusions

The phenomena associated with molecular hydrogen ion beams would, in general, render them unsuitable for the analysis of regions of small effective width. The marked changes in the shape of observed yield curves taken with molecular hydrogen ion beams due to the presence of beam induced contaminants could, however, be exploited to provide a very sensitive analylitcal technique for the investigation of surface regions.

The comparison of proton stopping power and range data has revealed a significant lack of agreement among established data sets particularly for low energy protons incident on low-Z target media. The two most widely used data sets in analytical applications, the tabulations of JANNI (1966) and WILLIAMSON et al. (1966), yield stopping power and range data well outside the general concensus of opinion for proton energies of less than 1 MeV. There is, therefore, considerable scope for an extended and comprehensive comparison of stopping power and range data.

The investigation of fluorine in samples of microcracked chromium plate has established a fluorine concentration of approximately 3.0×10^{27} atoms.m^{-3} restricted to a surface region of approximately 6 nm. The surface concentration was found to be independent of plating conditions. The lower and homogeneous bulk fluorine concentration of the samples was observed to be inversely proportioned to plating current density but independent of the presence or quality of microcracking.

It has been established that the convolution integral of the Breit-Wigner is well conditioned with respect to the form of the convoluting function. As a consequence of this property the technique of convolution does not permit a unique determination of an unknown concentration profile. A variety of empirical convoluting functions will, in general, result in a satisfactory "fit" within the accuracy of experimental data.

The study of the complementary technique of deconvolution has established the necessary conditions for the solution of the Volterra integral equation. The procedures developed have general application to the large class of problems which yield integral equations of this form. A considerable extension of the present work is possible by the inclusion of "straggling effects" which have not been considered in the solutions described. Alternative methods of discretization could also be investigated.

Appendix I

The Convolution of a Gaussian and a Breit-Wigner

The Convolution of a Gaussian and a Breit-Wigner

If the incident beam energy dispersion is represented by the pure Gaussian

$$G(E) = (1/\theta\pi^{\frac{1}{2}}) \,.\, \exp\left\{-(E/\theta)^2\right\}$$

and the reaction cross-section is of the Breit-Wigner form

$$\sigma(E) = \frac{\Gamma}{2\pi} \;.\; \frac{1}{E^2 + (\Gamma/2)^2}$$

the observed function is given by the convolution

$$I(E) = \int_{-\infty}^{\infty} G(E')\sigma(E-E')\, dE'$$

$$= (\Gamma/2\theta\ \pi)^{3/2} \int_{-\infty}^{\infty} \frac{1}{E'^2 + (\Gamma/2)^2} \;.\; \exp\left\{-\left(\frac{E - E'}{\theta}\right)^2\right\} dE'$$

$$\equiv (\Gamma/2\theta\pi^{3/2}).T$$

let

$$x = (E - E')/\theta$$

$$dx = -E'/\theta$$

therefore

$$T = (1/\theta) \int_{-\infty}^{\infty} \frac{\exp(-x^2)}{(E/\theta - x)^2 + (\Gamma/2\theta)^2} \, dx$$

Making the further substitution $a = E/\theta$, $b = \Gamma/2\theta$

and rearranging

$$b\theta\,T = \int_{-\infty}^{\infty} \frac{b \exp(-x^2)}{(a - x)^2 + b^2} \quad \ldots\ldots\ldots\ldots\ldots\ldots\ldots \quad (1)$$

The integral in Equation (1) is of a standard form| ABROWITZ and STEGUN (1965) |

$$\int_{-\infty}^{\infty} \frac{y \exp(-t^2)}{(x-t)^2 + y^2}\, dt = \pi \operatorname{Re} \omega(x + iy)$$

where $\omega(Z)$ is the complex error function.

Hence using this result and substituting back for a, b and x

$$T = (2\pi/\Gamma) \,.\, \operatorname{Re} \omega\left(\frac{E}{\theta} + i\frac{\Gamma}{2\theta}\right)$$

Therefore

$$I(E) = (1/\theta\pi^{\frac{1}{2}}) \,.\, \operatorname{Re}\omega\left(\frac{E}{\theta} + i\,\frac{\Gamma}{2\theta}\right)$$

where

$$\omega(Z) = \exp(-Z^2) \,.\, \operatorname{erfc}(-iZ)$$

$$\operatorname{erfc} Z = 1 - \operatorname{erf} Z$$

$$\operatorname{erf} Z = (2/\pi^{\frac{1}{2}}) \int_0^Z \exp(-t^2)\, dt$$

Appendix II

Comparison of Stopping Power Data

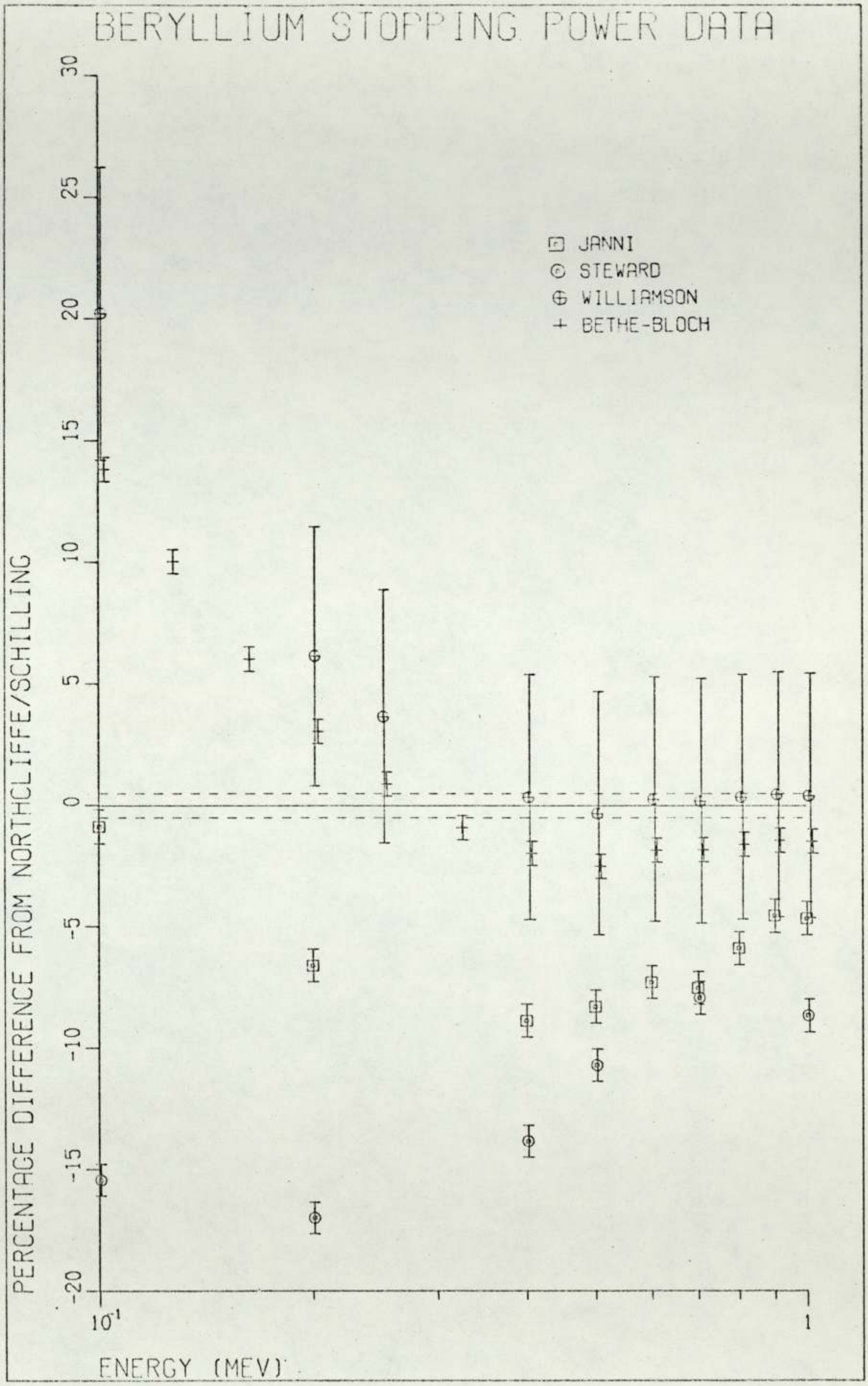
BERYLLIUM STOPPING POWER DATA
JANNI
STEWARD
WILLIAMSON
BETHE-BLOCH
PERCENTAGE DIFFERENCE FROM NORTHCLIFFE/SCHILLING
30
25
20
15
10
5
0
-5
-10
-15
-20
10^{-1}
1
ENERGY (MEV)

Figure 1

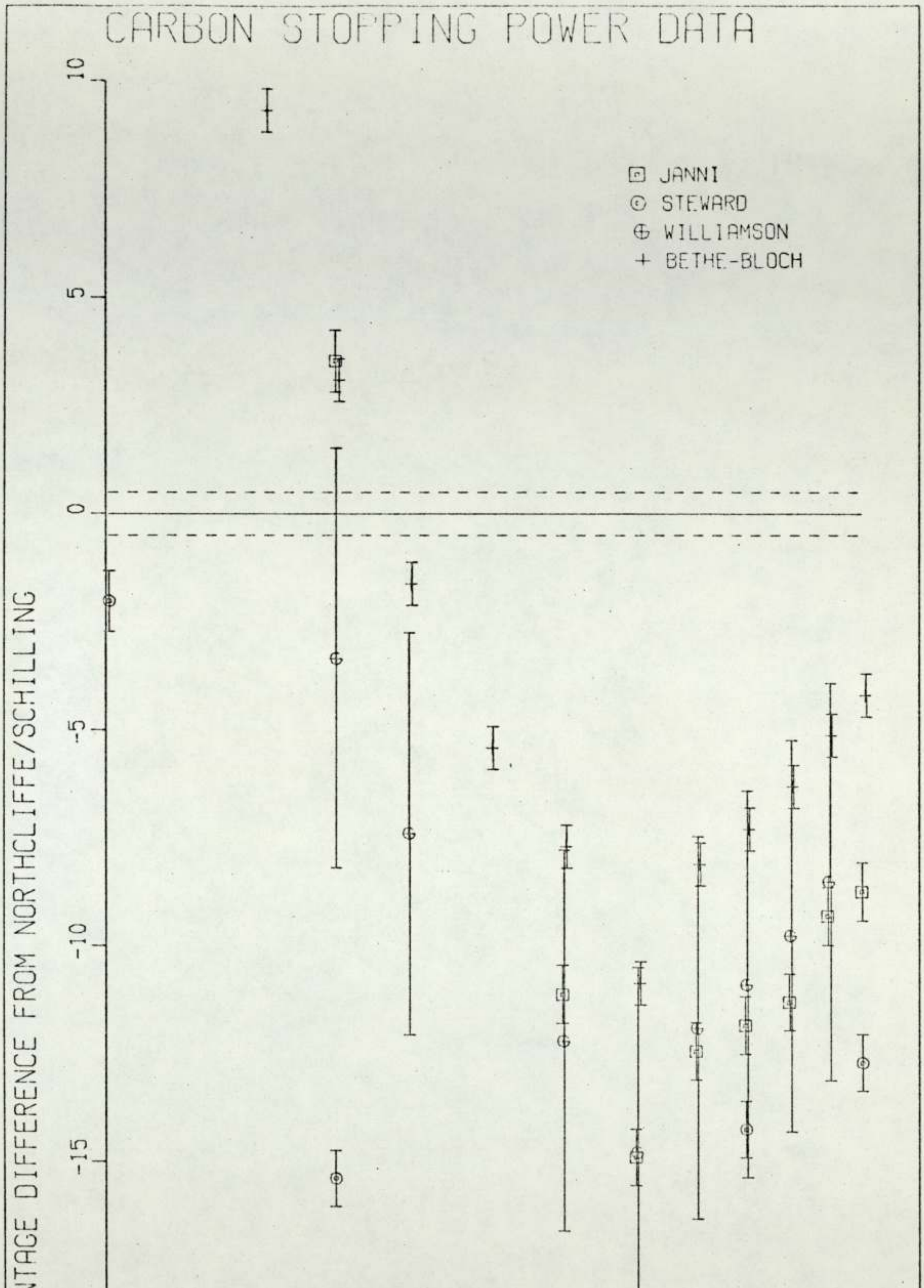
CARBON STOPPING POWER DATA
▣ JANNI
© STEWARD
⊕ WILLIAMSON
+ BETHE-BLOCH
10
5
0
-5
-10
-15
-20
PERCENTAGE DIFFERENCE FROM NORTHCLIFFE/SCHILLING
10^{-1}
1
ENERGY (MEV)

Figure 2

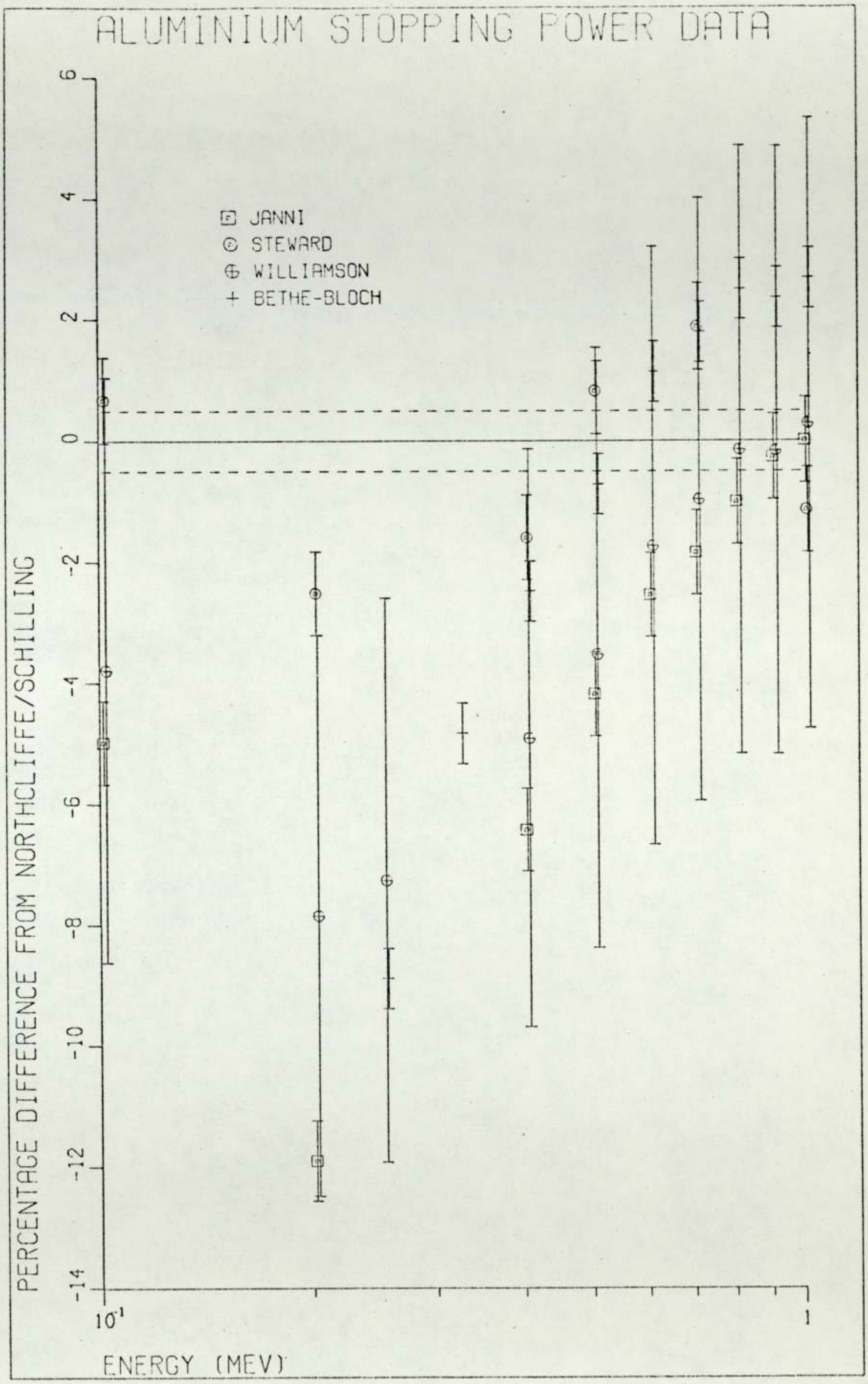
ALUMINIUM STOPPING POWER DATA
JANNI
STEWARD
WILLIAMSON
+ BETHE-BLOCH
PERCENTAGE DIFFERENCE FROM NORTHCLIFFE/SCHILLING
6
4
2
0
-2
-4
-6
-8
-10
-12
-14
10^{-1}
1
ENERGY (MEV)

Figure 3

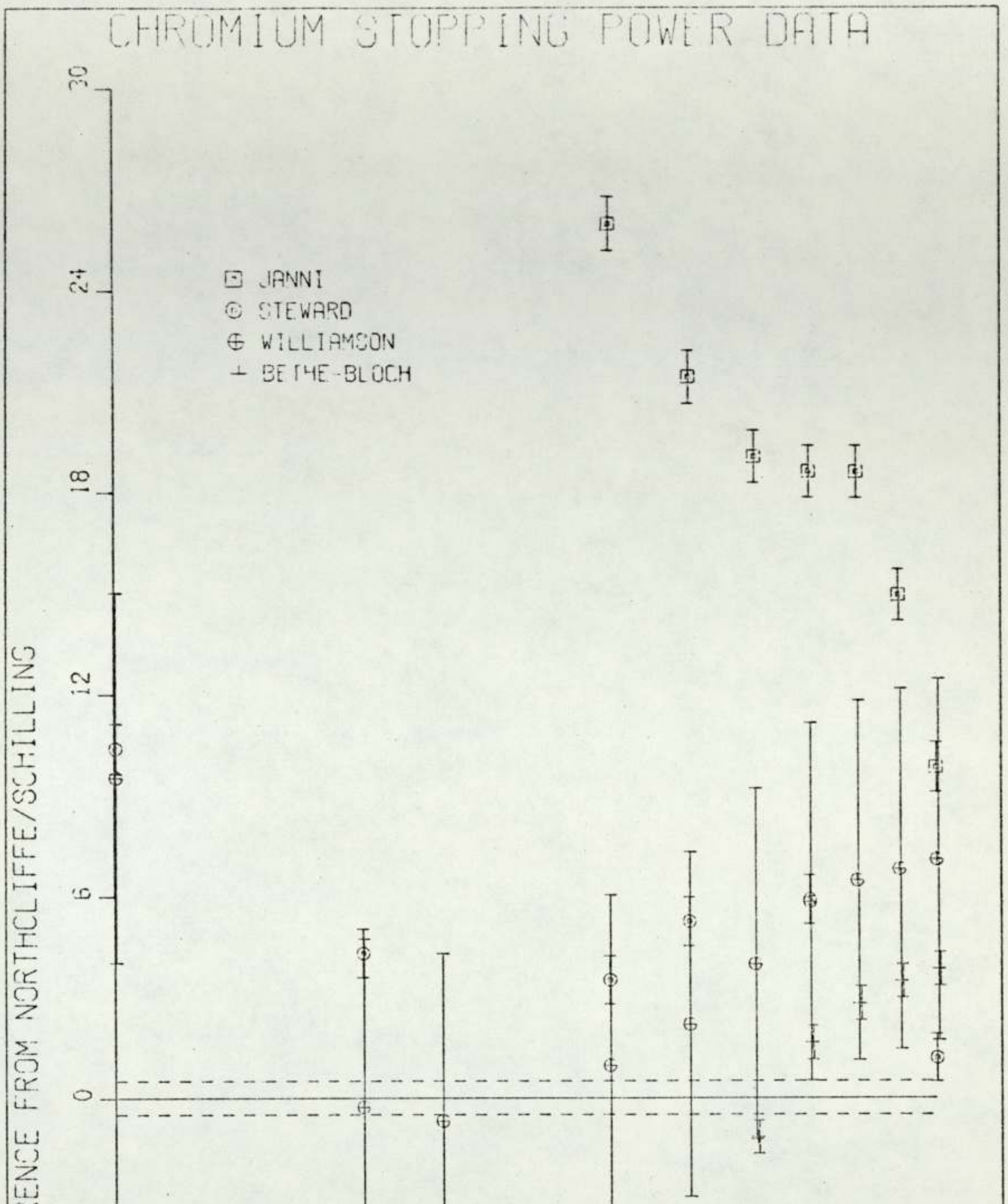
CHROMIUM STOPPING POWER DATA
JANNI
STEWARD
WILLIAMSON
BETHE-BLOCH
PERCENTAGE DIFFERENCE FROM NORTHCLIFFE/SCHILLING
30
24
18
12
6
0
-6
-12
10⁻¹
1
ENERGY (MEV)

Figure 4

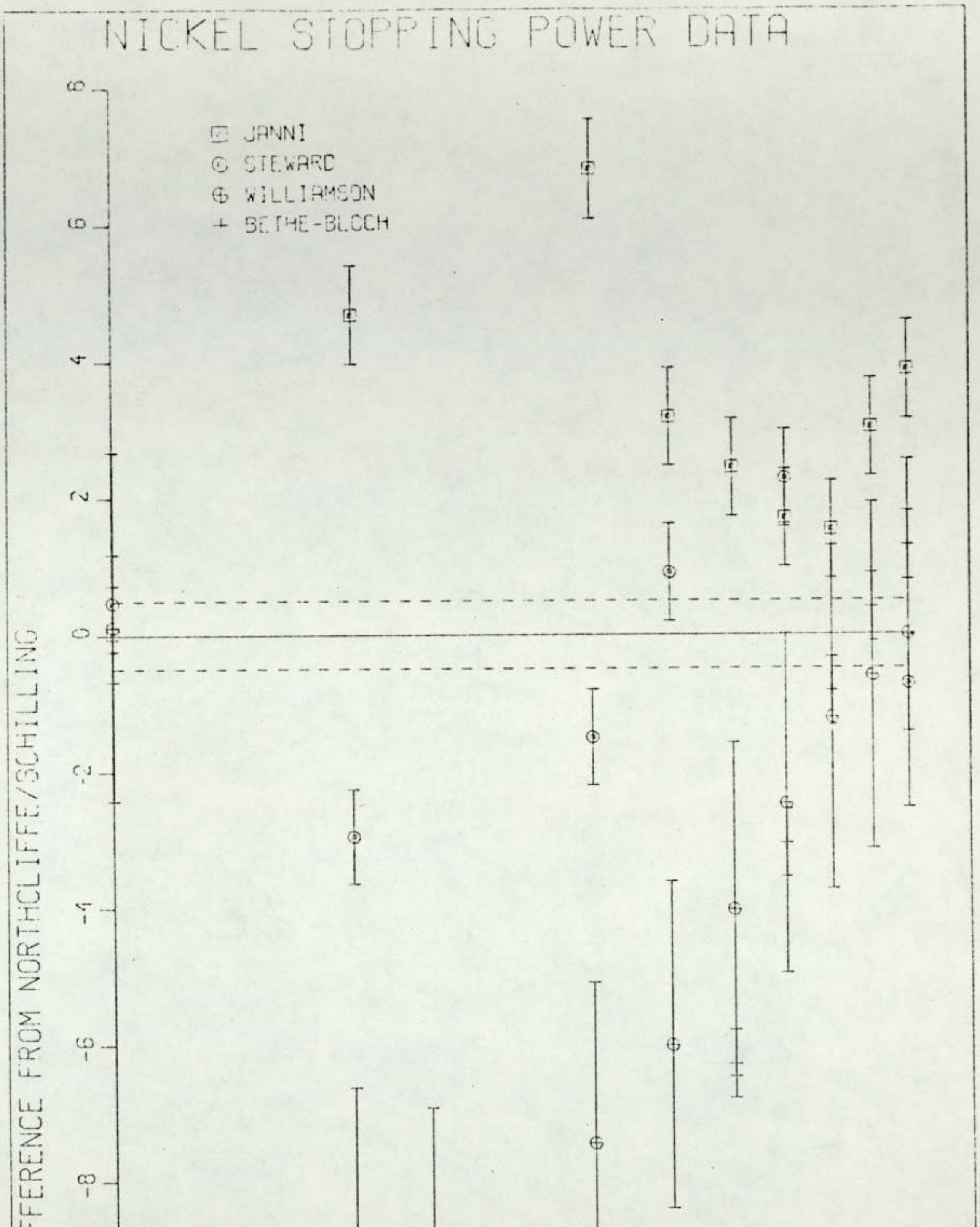
NICKEL STOPPING POWER DATA
JANNI
STEWARD
WILLIAMSON
BETHE-BLOCH
PERCENTAGE DIFFERENCE FROM NORTHCLIFFE/SCHILLING
8
6
4
2
0
-2
-4
-6
-8
-10
-12
10^1
1
ENERGY (MEV)

Figure 5

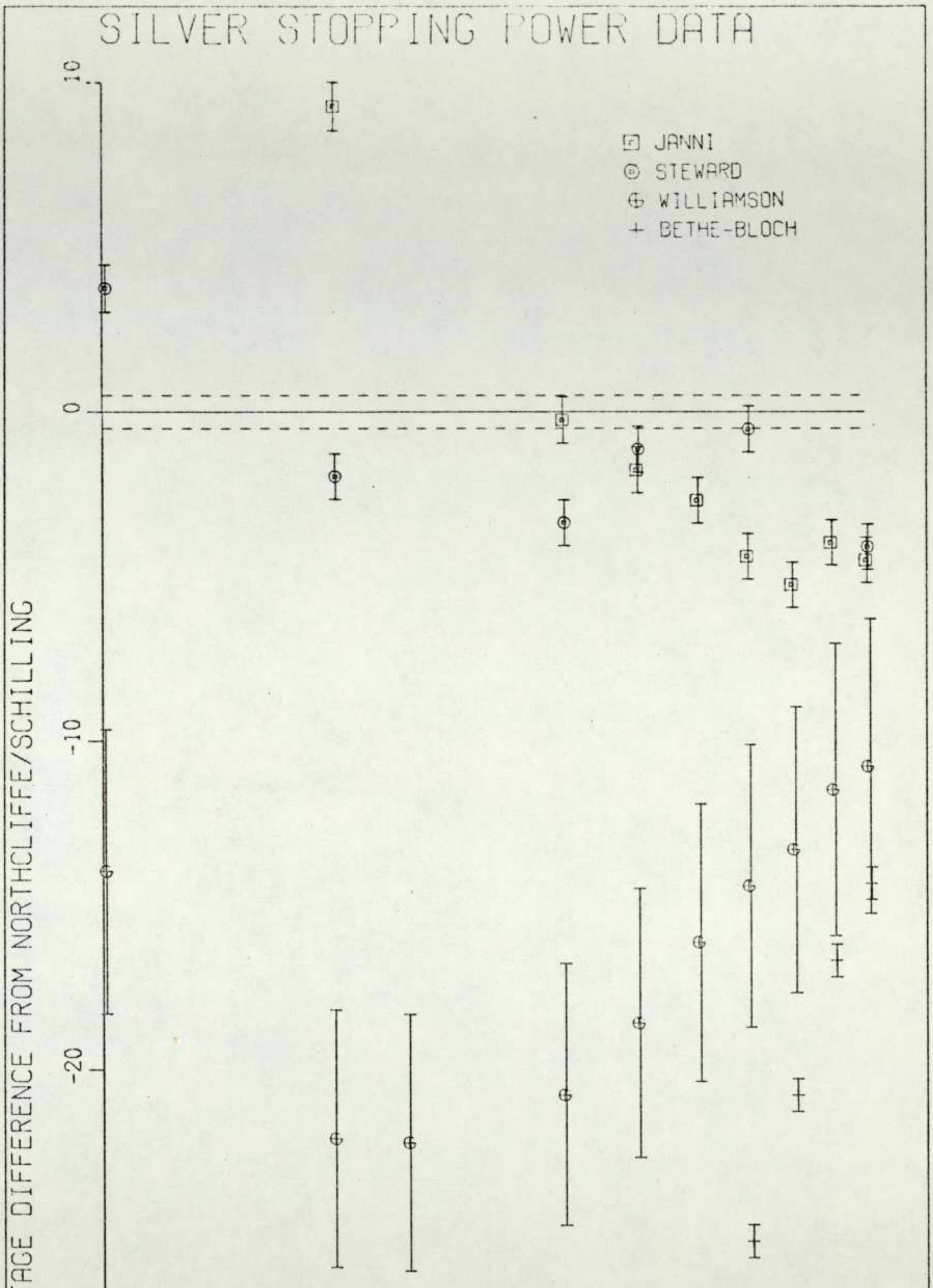
SILVER STOPPING POWER DATA
⊡ JANNI
⊙ STEWARD
⊕ WILLIAMSON
+ BETHE-BLOCH
PERCENTAGE DIFFERENCE FROM NORTHCLIFFE/SCHILLING
10
0
-10
-20
-30
10^{-1}
1
ENERGY (MEV)

Figure 6

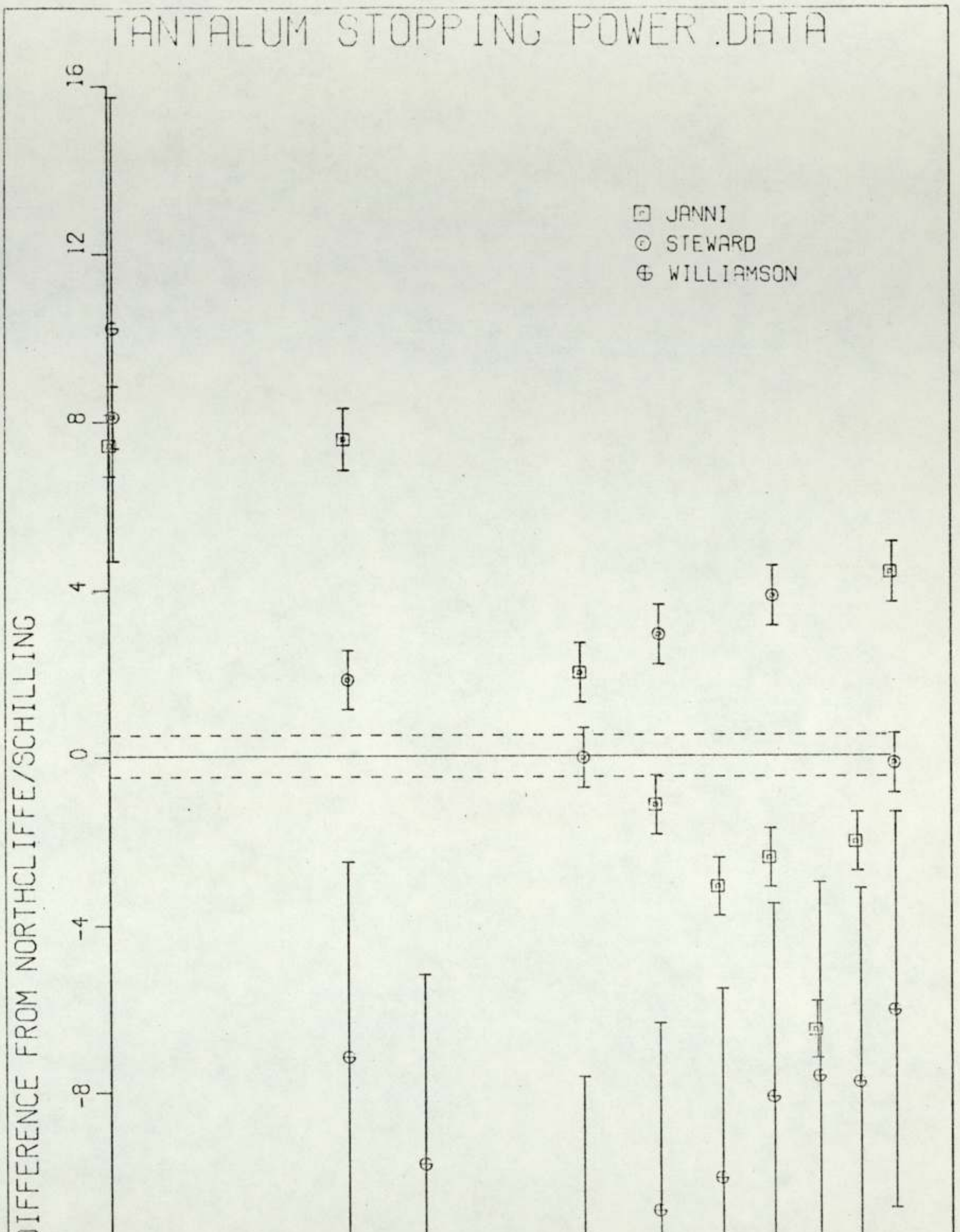
TANTALUM STOPPING POWER.DATA
⊡ JANNI
⊙ STEWARD
⊕ WILLIAMSON
PERCENTAGE DIFFERENCE FROM NORTHCLIFFE/SCHILLING
16
12
8
4
0
-4
-8
-12
-16
10^{-1}
1
ENERGY (MEV)

Figure 7

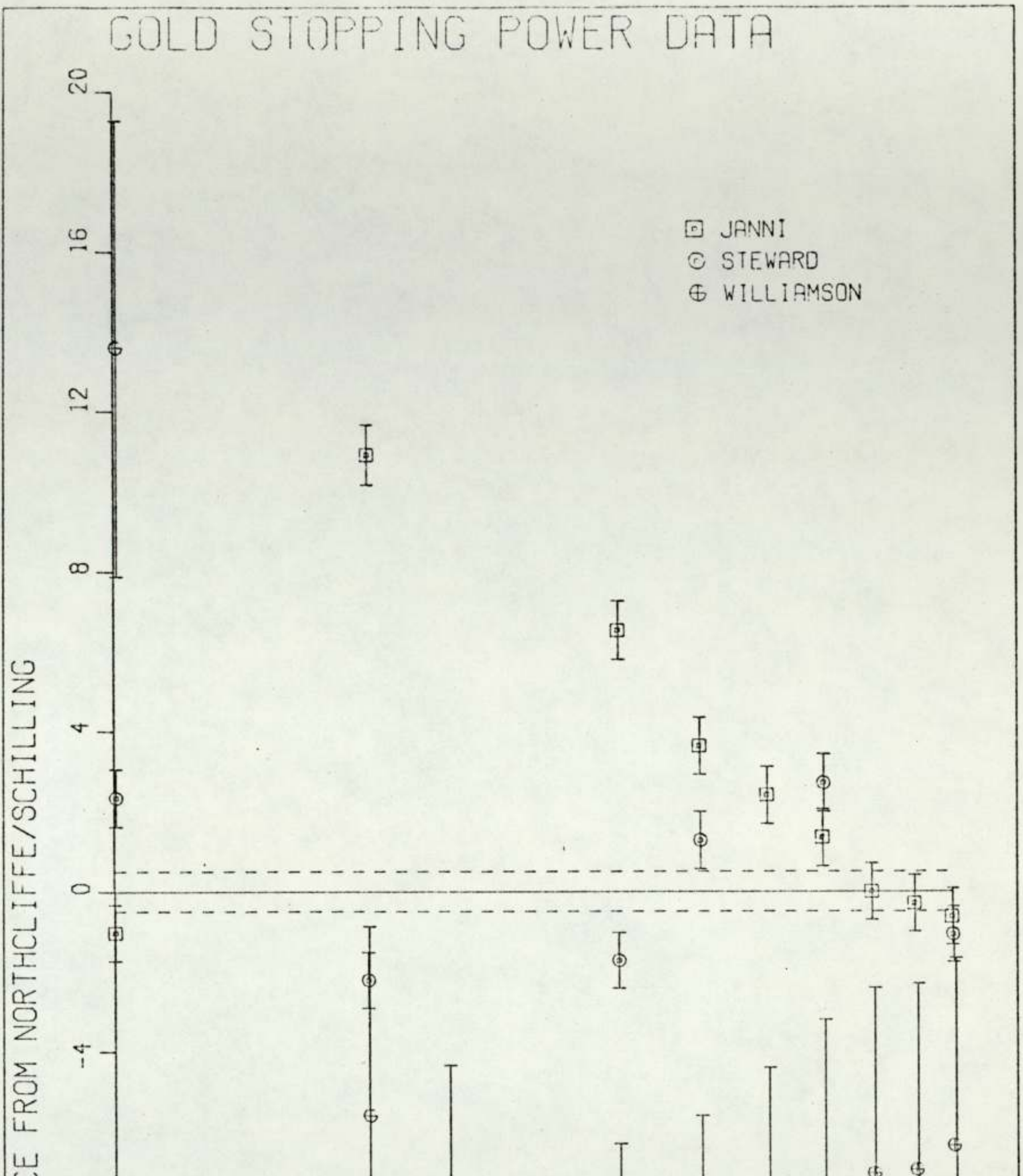
GOLD STOPPING POWER DATA
JANNI
STEWARD
WILLIAMSON
PERCENTAGE DIFFERENCE FROM NORTHCLIFFE/SCHILLING
20
16
12
8
4
0
-4
-8
-12
-16
10^{-1}
1
ENERGY (MEV)

Figure 8

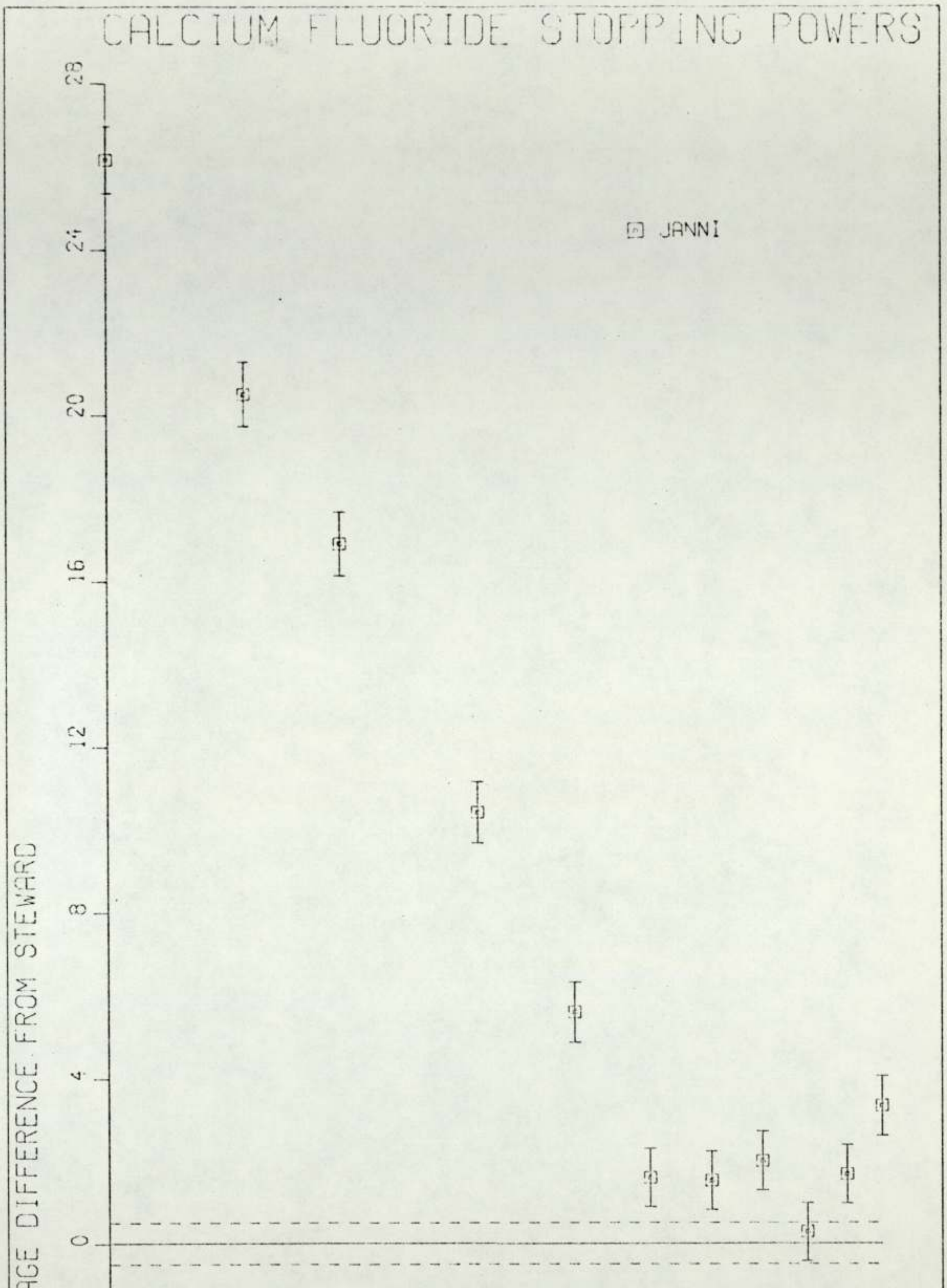
CALCIUM FLUORIDE STOPPING POWERS
JANNI
PERCENTAGE DIFFERENCE FROM STEWARD
28
24
20
16
12
8
4
0
-4
10^1
1
ENERGY (MEV)

Figure 9

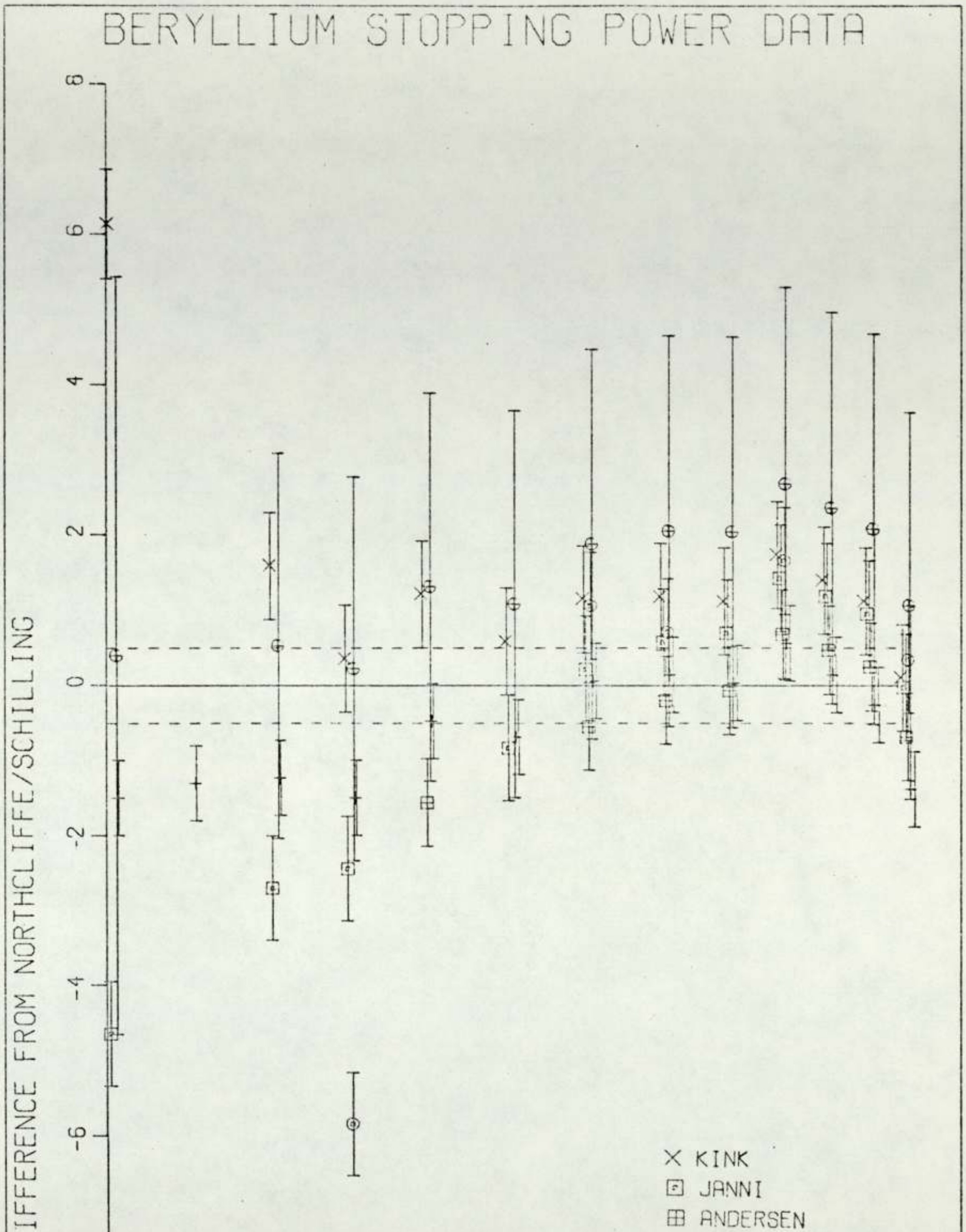
BERYLLIUM STOPPING POWER DATA
PERCENTAGE DIFFERENCE FROM NORTHCLIFFE/SCHILLING
8
6
4
2
0
-2
-4
-6
-8
-10
1
10
ENERGY (MEV)
× KINK
⊡ JANNI
⊞ ANDERSEN
⊙ STEWARD
⊕ WILLIAMSON
+ BETHE-BLOCH

Figure 10

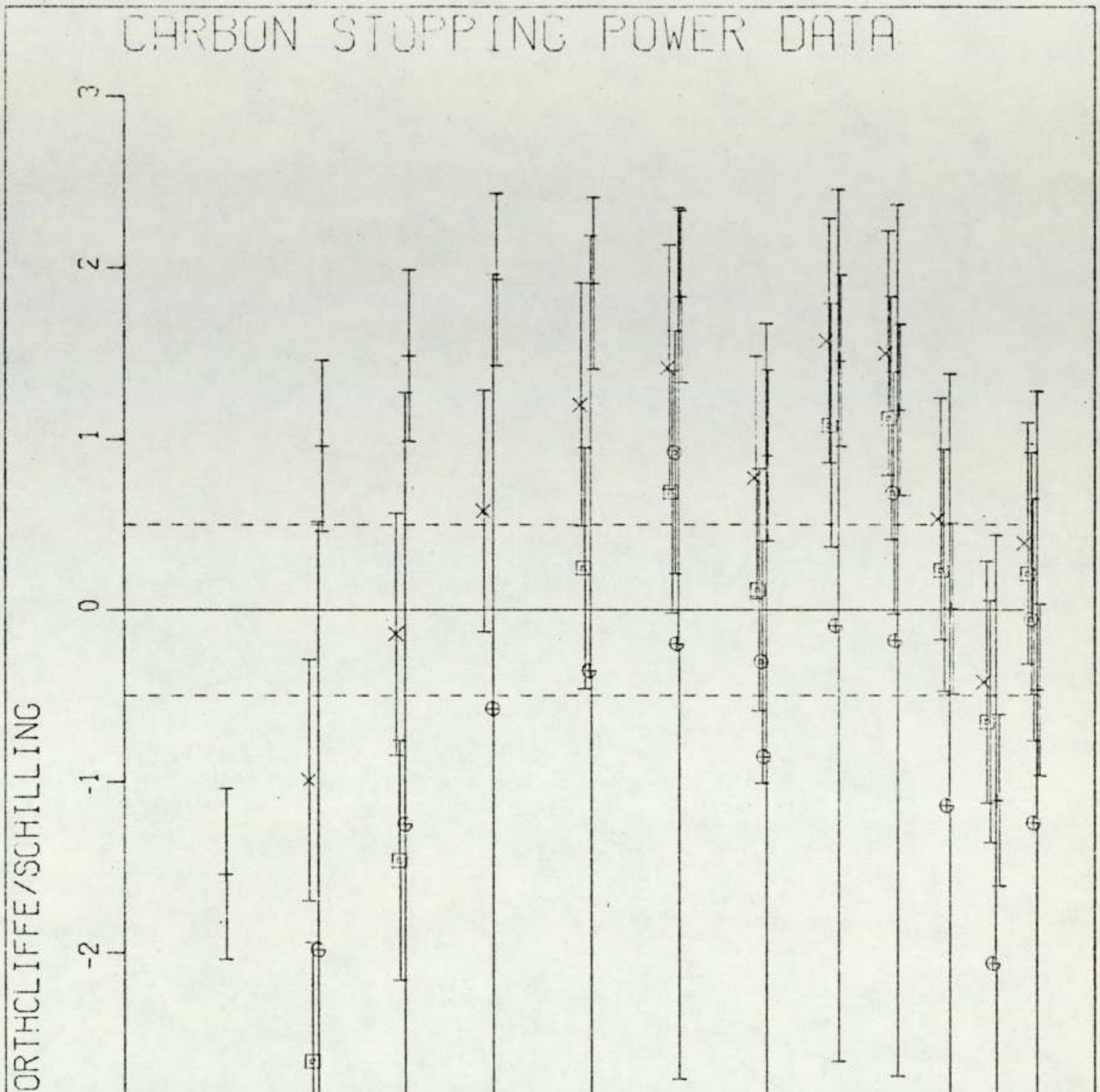
CARBON STOPPING POWER DATA
PERCENTAGE DIFFERENCE FROM NORTHCLIFFE/SCHILLING
3
2
1
0
-1
-2
-3
-4
-5
-6
1
10
ENERGY (MEV)
× KINK
⊡ JANNI
⊙ STEWARD
⊕ WILLIAMSON
+ BETHE-BLOCH

Figure 11

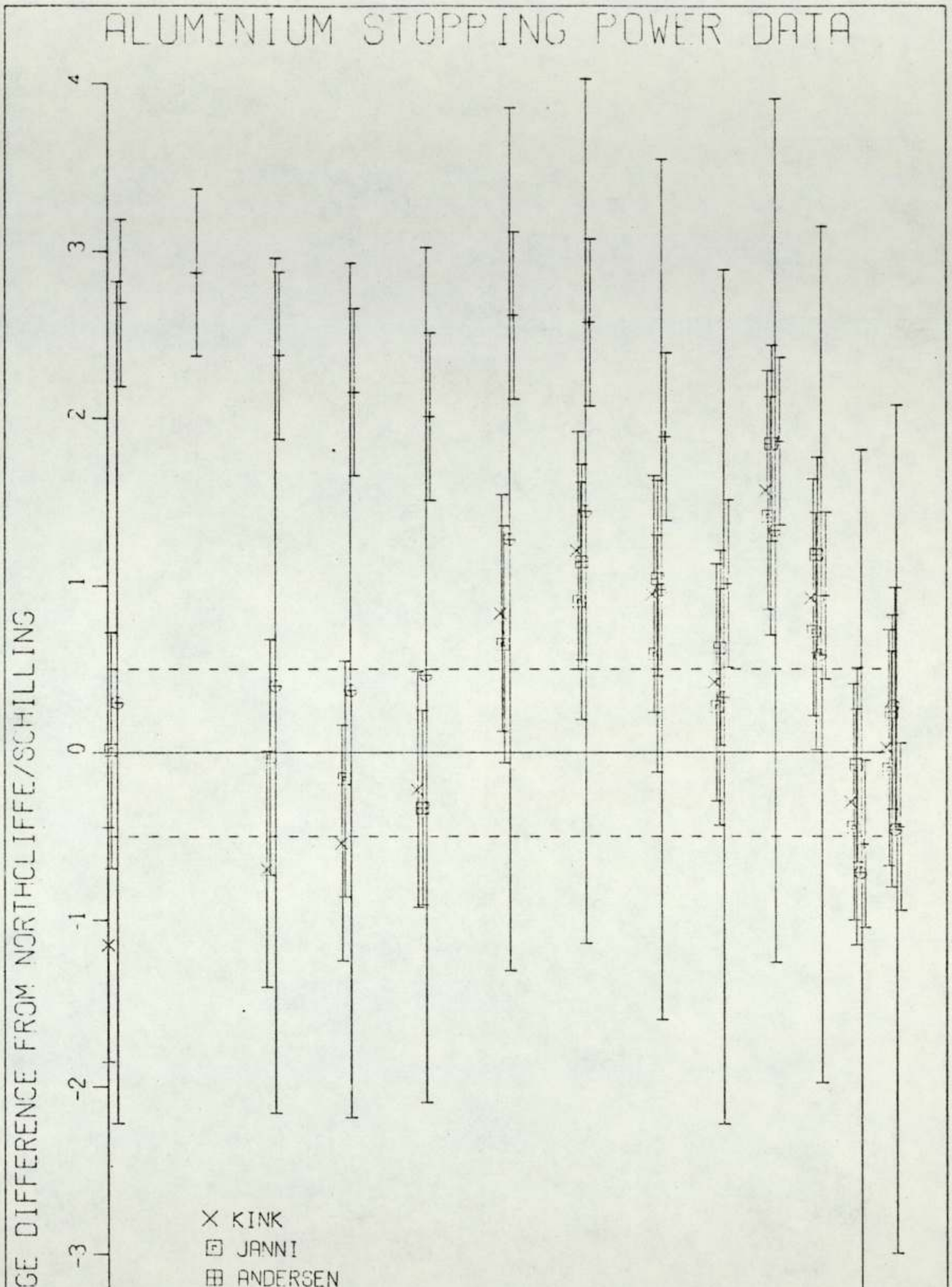
ALUMINIUM STOPPING POWER DATA
PERCENTAGE DIFFERENCE FROM NORTHCLIFFE/SCHILLING
4
3
2
1
0
-1
-2
-3
-4
1
10
ENERGY (MEV)
× KINK
⊡ JANNI
⊞ ANDERSEN
⊙ STEWARD
⊕ WILLIAMSON
+ BETHE-BLOCH

Figure 12

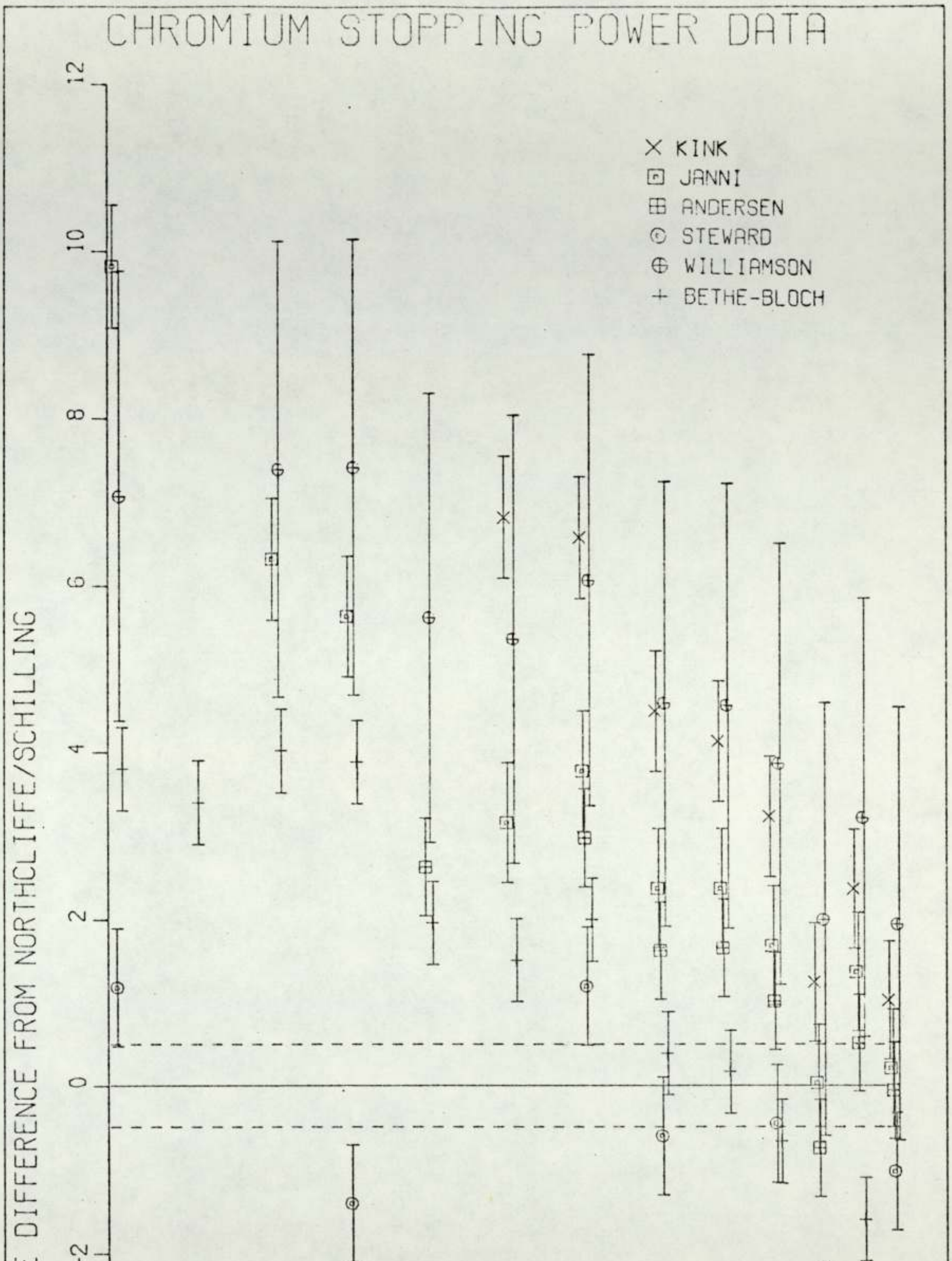
CHROMIUM STOPPING POWER DATA
× KINK
⊡ JANNI
⊞ ANDERSEN
⊙ STEWARD
⊕ WILLIAMSON
+ BETHE-BLOCH
PERCENTAGE DIFFERENCE FROM NORTHCLIFFE/SCHILLING
12
10
8
6
4
2
0
-2
-4
1
10
ENERGY (MEV)

Figure 13

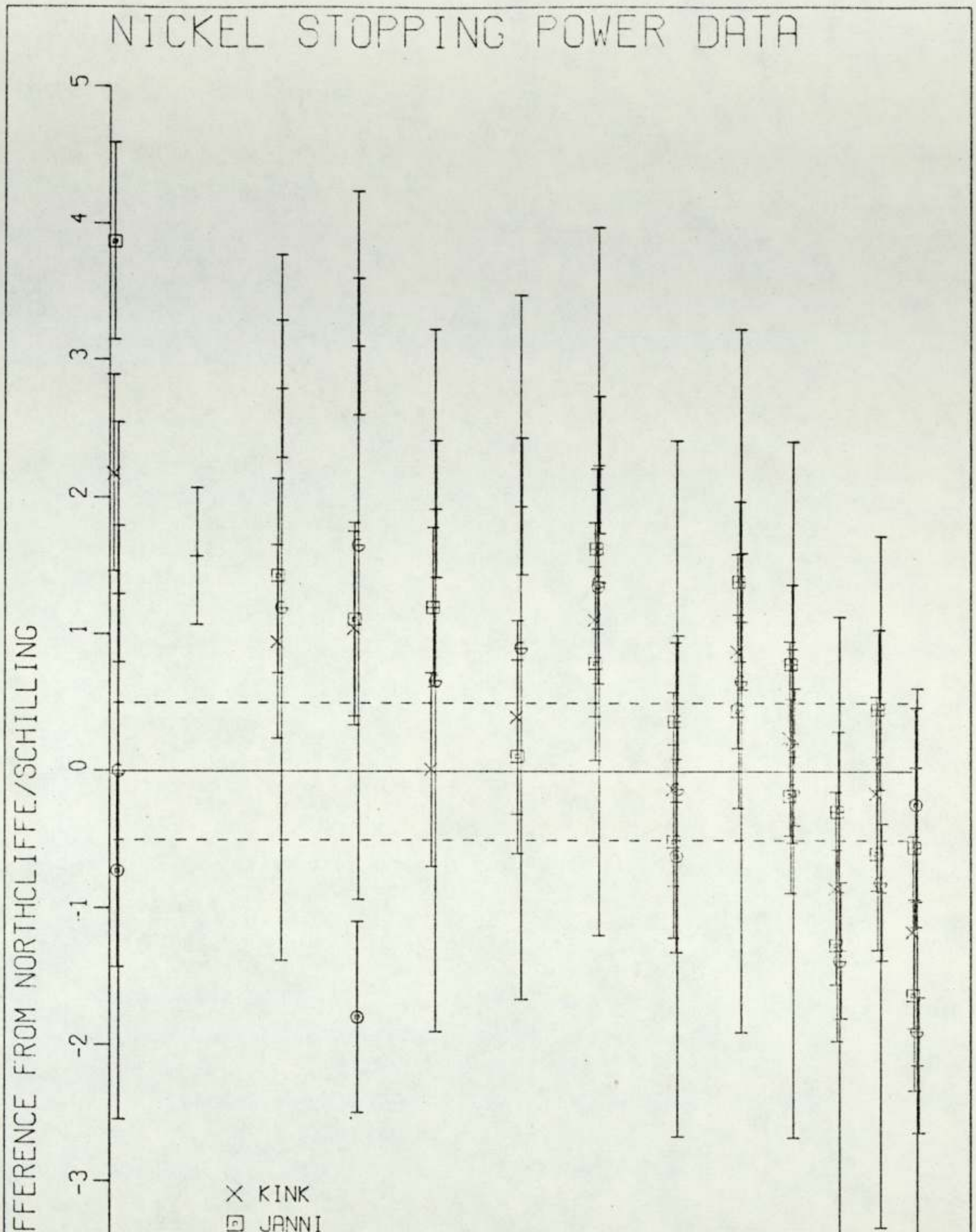
NICKEL STOPPING POWER DATA
PERCENTAGE DIFFERENCE FROM NORTHCLIFFE/SCHILLING
5
4
3
2
1
0
-1
-2
-3
-4
-5
1
10
ENERGY (MEV)
× KINK
⊡ JANNI
⊞ ANDERSEN
⊙ STEWARD
⊕ WILLIAMSON
+ BETHE-BLOCH

Figure 14

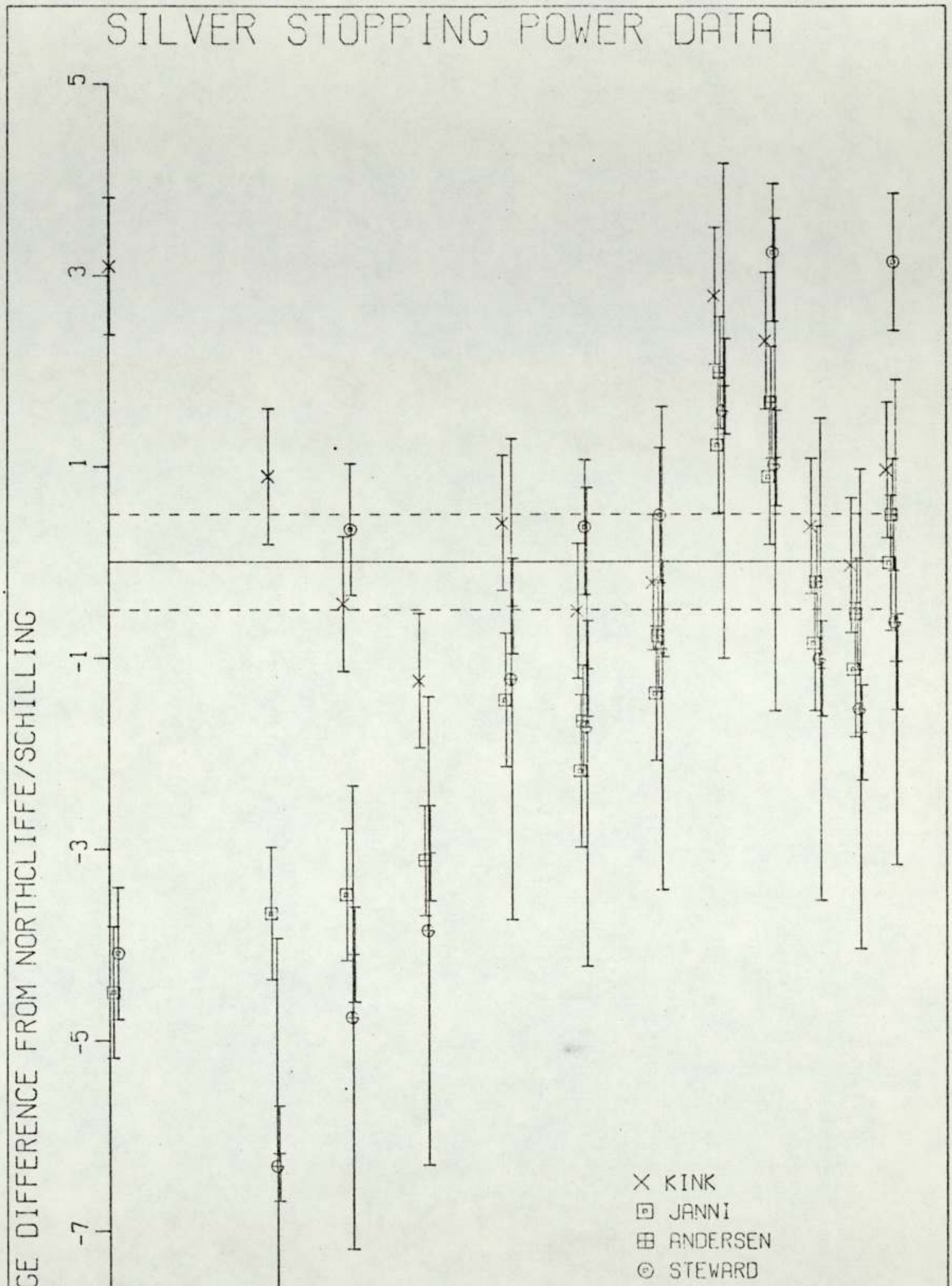

SILVER STOPPING POWER DATA
PERCENTAGE DIFFERENCE FROM NORTHCLIFFE/SCHILLING
5
3
1
-1
-3
-5
-7
-9
1
10
ENERGY (MEV)
× KINK
⊡ JANNI
⊞ ANDERSEN
⊙ STEWARD
⊕ WILLIAMSON
+ BETHE-BLOCH

Figure 15

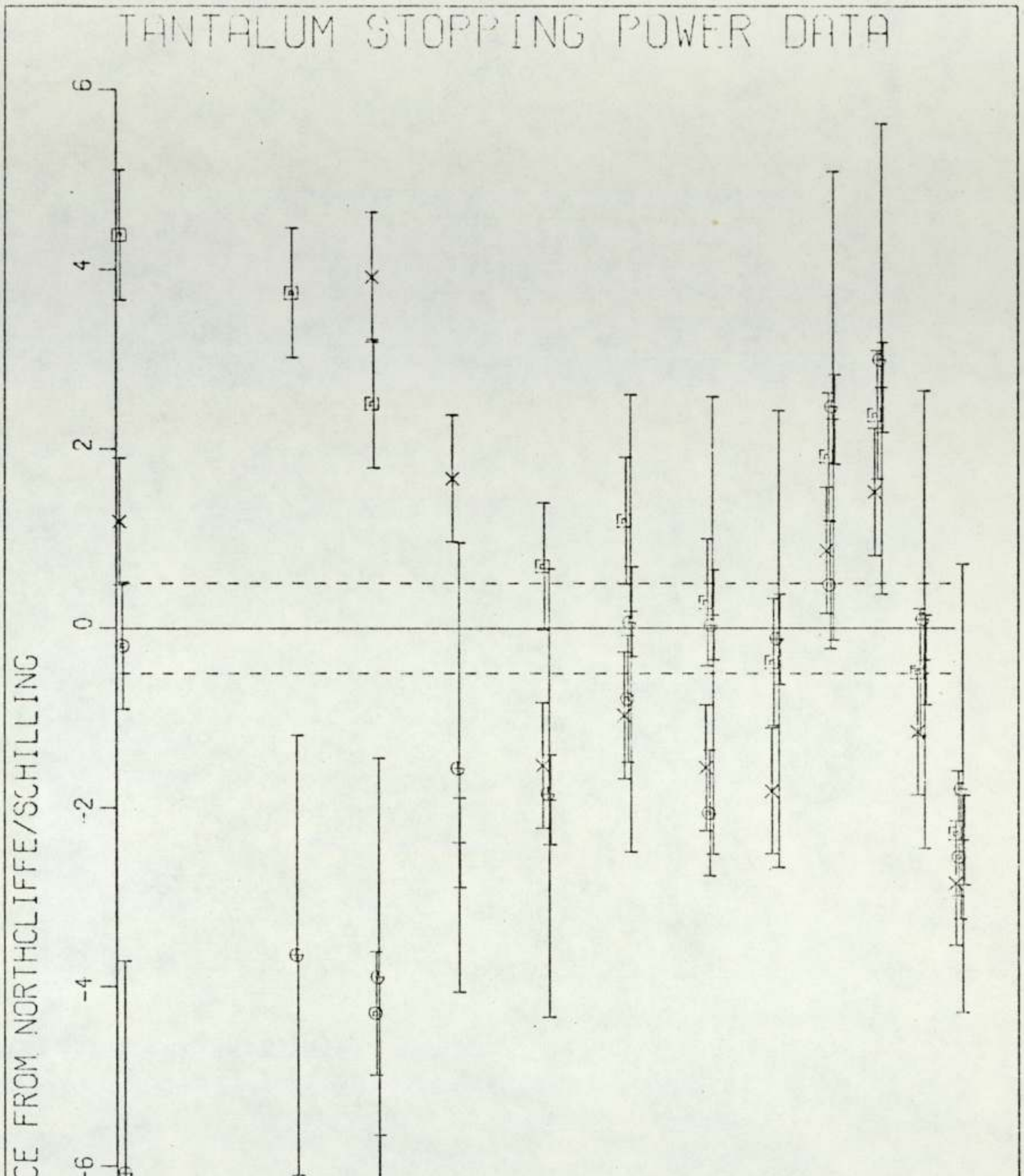
TANTALUM STOPPING POWER DATA
PERCENTAGE DIFFERENCE FROM NORTHCLIFFE/SCHILLING
6
4
2
0
-2
-4
-6
-8
-10
1
10
ENERGY (MEV)
× KINK
⊡ JANNI
⊙ STEWARD
⊕ WILLIAMSON
+ BETHE-BLOCH

Figure 16

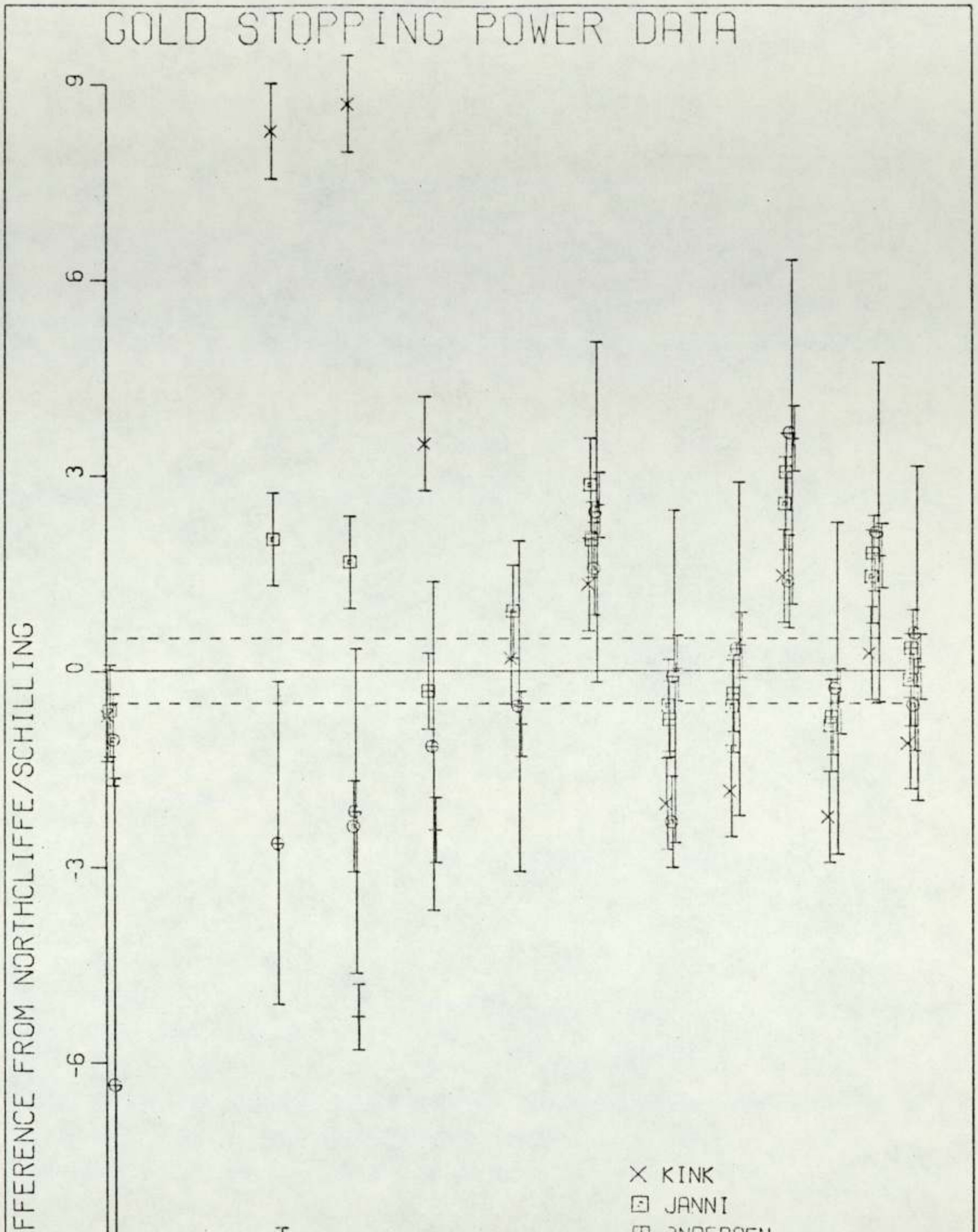
GOLD STOPPING POWER DATA
PERCENTAGE DIFFERENCE FROM NORTHCLIFFE/SCHILLING
9
6
3
0
-3
-6
-9
-12
1
10
ENERGY (MEV)
× KINK
⊡ JANNI
⊞ ANDERSEN
⊙ STEWARD
⊕ WILLIAMSON
+ BETHE-BLOCH

Figure 17

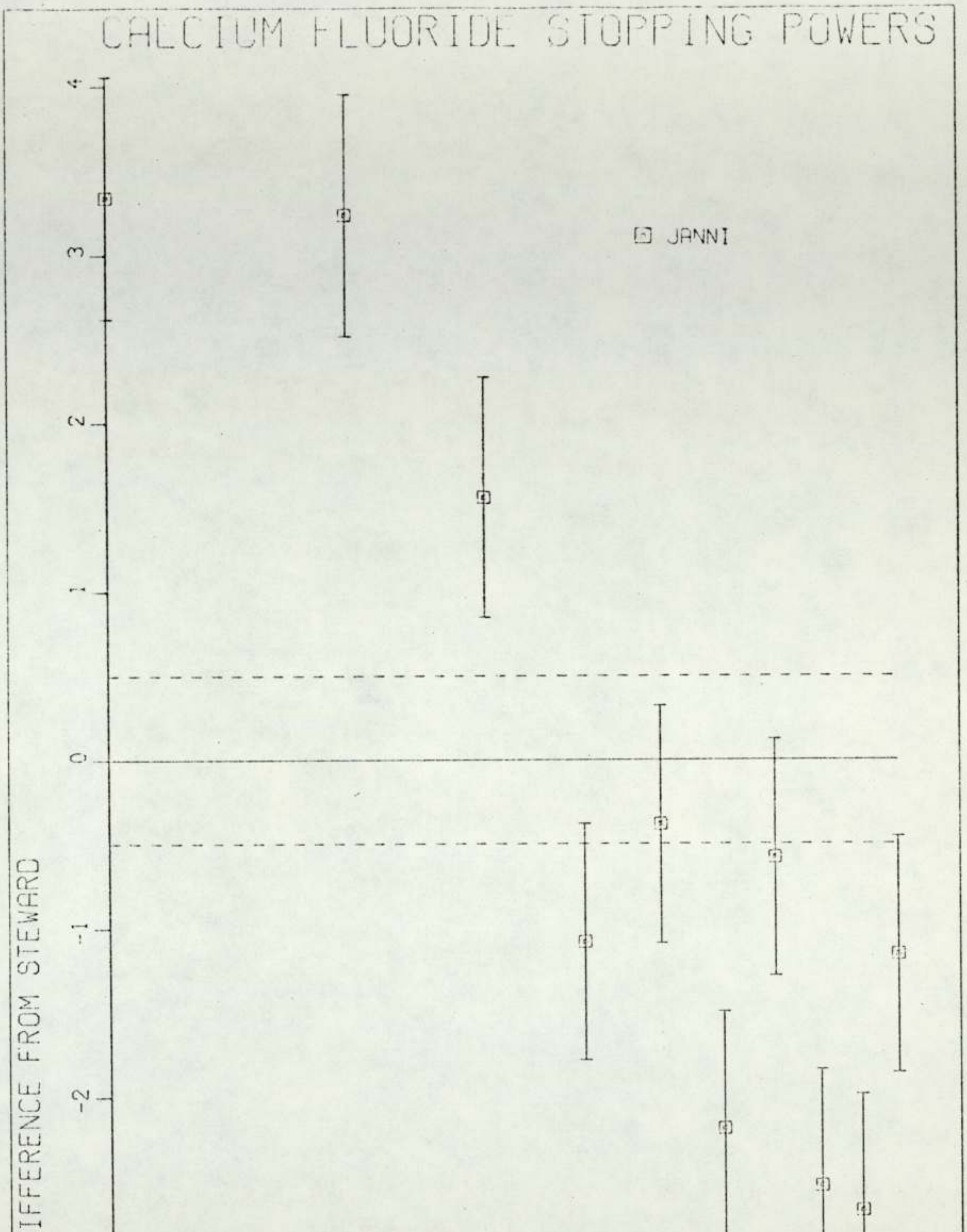
CALCIUM FLUORIDE STOPPING POWERS
PERCENTAGE DIFFERENCE FROM STEWARD
4
3
2
1
0
-1
-2
-3
-4
JANNI
1
10
ENERGY (MEV)

Figure 18

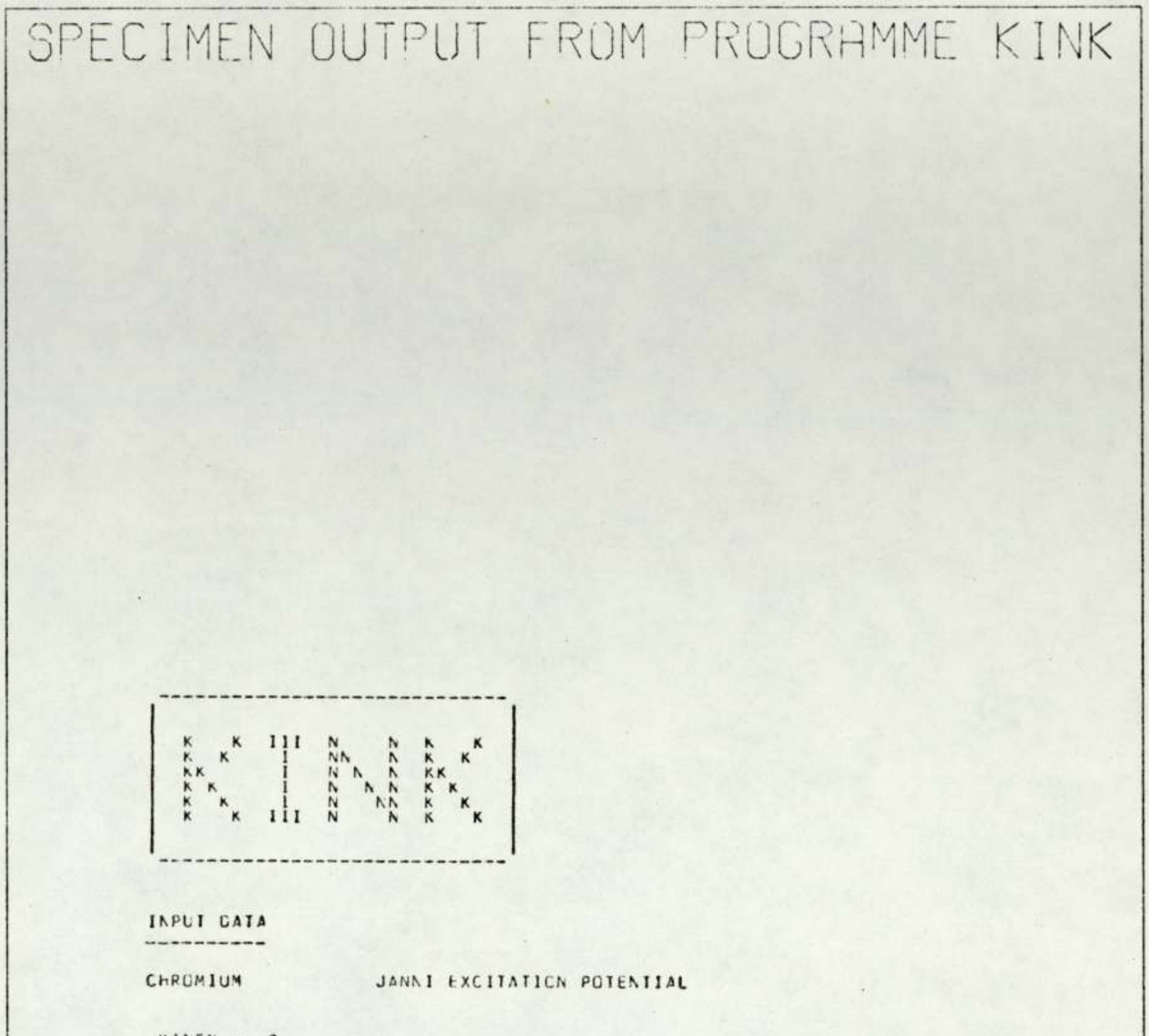

```
SPECIMEN OUTPUT FROM PROGRAMME KINK




 ------------------------------
|                               |
|  K   K  III N    N  K   K     |
|  K  K    I  NN   N  K  K      |
|  KK      I  N N  N  KK        |
|  K K     I  N  N N  K K       |
|  K  K    I  N   NN  K  K      |
|  K   K  III N    N  K   K     |
|                               |
 ------------------------------

INPUT DATA
----------

CHROMIUM              JANNI EXCITATION POTENTIAL

 KINEM =  0
 KRCOIL=  0
 KSPRED=  1
 KSMEAR=  0
 KRSCVR=  0
 KDTDX =  1
 KTHRSH=  0


          INCIDENT PARTICLE                          TARGET PARTICLE
   MASS          CHARGE         ENERGY        MASS         CHARGE         ENERGY
 1.007590     1.000000      1.000000    52.010000    24.000000      0.0


 FINAL ENERGY    ENERGY STEP
   10.0000           0.1000

  TARGET THICKNESS   =      4.000    MILLIGRAMS/SQ.CM.
  TARGET ANGLE       =      0.0      DEG.
  TARGET DENSITY     =      7.200    GRAMS/CC.
  NO. OF ATOMS/MOL.  =      1.000
  EXCITATION POTL.   =    244.400    ELECTRON VOLTS


OPTIONS SPECIFIED
-----------------

-CALCULATION OF STOPPING POWERS,RANGES,ENERGY SPREAD AND EFFECTIVE CHARGES
-WITH CALCULATION OF ENERGY LOSS AND SPREAD IN TARGET


DERIVED QUANTITIES
------------------

  AKI = 0.4787470+03
```

Figure 19

SPECIMEN OUTPUT FROM PROGRAMME KINK

```
CHROMIUM            JANNI EXCITATION POTENTIAL

INCIDENT   MEAN      ENERGY      REDUCED    STOPPING      STOPPING         RANGE          RANGE        STRAGGLING   ENERGY      GAMMA3  EFFECTIVE
ENERGY     ENERGY    LOSS        ENERGY     POWER         POWER          DIFFERENCE     DIFFERENCE    STD. DEVN    SPREAD               CHARGE
MEV.       MEV.      MEV.                   MEV/MM.     MEV-CMSQ/MG.       MM.          MG/CMSQ      PER CENT     MEV.
 1.0000    0.6439    0.7121      5.730    0.1282D+03    0.1780D+00    0.2761D-02    0.1998D+01       2.915      0.0504      0.041    1.0000
 1.1000    0.7825    0.6351      6.962    0.1143D+03    0.1588D+00    0.3896D-02    0.2805D+01       2.636      0.0484      0.051    1.0000
 1.2000    0.9049    0.5823      8.086    0.1048D+03    0.1456D+00    0.5041D-02    0.3629D+01       2.473      0.0460      0.059    1.0000
 1.3000    1.0251    0.5418      9.155    0.9752D+02    0.1354D+00    0.6219D-02    0.4478D+01       2.361      0.0443      0.067    1.0000
 1.4000    1.1456    0.5088     10.191    0.9159D+02    0.1272D+00    0.7440D-02    0.5357D+01       2.277      0.0432      0.075    1.0000
 1.5000    1.2594    0.4811     11.203    0.8660D+02    0.1203D+00    0.8705D-02    0.6268D+01       2.210      0.0424      0.082    1.0000
 1.6000    1.3714    0.4573     12.198    0.8231D+02    0.1143D+00    0.1002D-01    0.7212D+01       2.155      0.0418      0.090    1.0000
 1.7000    1.4818    0.4364     13.190    0.7855D+02    0.1091D+00    0.1138D-01    0.8191D+01       2.109      0.0414      0.097    1.0000
 1.8000    1.5911    0.4179     14.151    0.7522D+02    0.1045D+00    0.1278D-01    0.9204D+01       2.069      0.0406      0.104    1.0000
 1.9000    1.6994    0.4013     15.113    0.7223D+02    0.1003D+00    0.1424D-01    0.1025D+02       2.035      0.0404      0.111    1.0000
 2.0000    1.8068    0.3863     16.068    0.6953D+02    0.9658D-01    0.1574D-01    0.1133D+02       2.004      0.0402      0.118    1.0000
 2.1000    1.9137    0.3727     17.017    0.6709D+02    0.9316D-01    0.1729D-01    0.1245D+02       1.977      0.0400      0.125    1.0000
 2.2000    2.0199    0.3602     17.961    0.6483D+02    0.9004D-01    0.1888D-01    0.1359D+02       1.952      0.0399      0.132    1.0000
 2.3000    2.1257    0.3487     18.900    0.6276D+02    0.8717D-01    0.2052D-01    0.1477D+02       1.930      0.0398      0.139    1.0000
 2.4000    2.2310    0.3380     19.835    0.6085D+02    0.8451D-01    0.2221D-01    0.1599D+02       1.910      0.0397      0.146    1.0000
 2.5000    2.3359    0.3282     20.767    0.5907D+02    0.8204D-01    0.2394D-01    0.1723D+02       1.891      0.0396      0.152    1.0000
 2.6000    2.4405    0.3190     21.696    0.5741D+02    0.7974D-01    0.2571D-01    0.1851D+02       1.874      0.0395      0.159    1.0000
 2.7000    2.5448    0.3104     22.622    0.5586D+02    0.7759D-01    0.2753D-01    0.1983D+02       1.858      0.0395      0.166    1.0000
 2.8000    2.6488    0.3023     23.545    0.5441D+02    0.7558D-01    0.2940D-01    0.2117D+02       1.844      0.0394      0.173    1.0000
 2.9000    2.7526    0.2947     24.466    0.5305D+02    0.7368D-01    0.3131D-01    0.2254D+02       1.830      0.0394      0.179    1.0000
 3.0000    2.8562    0.2876     25.386    0.5177D+02    0.7190D-01    0.3327D-01    0.2395D+02       1.817      0.0393      0.186    1.0000
 3.1000    2.9596    0.2809     26.303    0.5056D+02    0.7022D-01    0.3526D-01    0.2539D+02       1.805      0.0393      0.192    1.0000
 3.2000    3.0627    0.2745     27.218    0.4941D+02    0.6863D-01    0.3731D-01    0.2686D+02       1.794      0.0393      0.199    1.0000
 3.3000    3.1658    0.2685     28.132    0.4832D+02    0.6712D-01    0.3939D-01    0.2836D+02       1.783      0.0392      0.206    1.0000
 3.4000    3.2686    0.2627     29.045    0.4729D+02    0.6568D-01    0.4152D-01    0.2989D+02       1.773      0.0392      0.212    1.0000
 3.5000    3.3714    0.2573     29.956    0.4631D+02    0.6432D-01    0.4369D-01    0.3146D+02       1.763      0.0392      0.219    1.0000
 3.6000    3.4740    0.2521     30.866    0.4538D+02    0.6302D-01    0.4590D-01    0.3305D+02       1.754      0.0392      0.225    1.0000
 3.7000    3.5764    0.2471     31.775    0.4449D+02    0.6179D-01    0.4816D-01    0.3467D+02       1.746      0.0391      0.232    1.0000
 3.8000    3.6788    0.2424     32.682    0.4363D+02    0.6060D-01    0.5046D-01    0.3633D+02       1.737      0.0391      0.239    1.0000
 3.9000    3.7811    0.2379     33.589    0.4282D+02    0.5947D-01    0.5280D-01    0.3801D+02       1.729      0.0391      0.245    1.0000
 4.0000    3.8832    0.2336     34.495    0.4204D+02    0.5839D-01    0.5518D-01    0.3973D+02       1.722      0.0391      0.252    1.0000
 4.1000    3.9853    0.2294     35.400    0.4129D+02    0.5735D-01    0.5760D-01    0.4147D+02       1.715      0.0391      0.258    1.0000
 4.2000    4.0873    0.2254     36.304    0.4058D+02    0.5636D-01    0.6006D-01    0.4325D+02       1.708      0.0390      0.265    1.0000
 4.3000    4.1892    0.2216     37.207    0.3989D+02    0.5540D-01    0.6257D-01    0.4505D+02       1.701      0.0390      0.271    1.0000
 4.4000    4.2910    0.2179     38.109    0.3923D+02    0.5448D-01    0.6511D-01    0.4688D+02       1.695      0.0390      0.278    1.0000
 4.5000    4.3928    0.2144     39.011    0.3859D+02    0.5359D-01    0.6770D-01    0.4874D+02       1.689      0.0390      0.284    1.0000
 4.6000    4.4945    0.2110     39.912    0.3797D+02    0.5274D-01    0.7033D-01    0.5064D+02       1.683      0.0390      0.291    1.0000
 4.7000    4.5962    0.2077     40.813    0.3738D+02    0.5192D-01    0.7300D-01    0.5256D+02       1.677      0.0390      0.297    1.0000
 4.8000    4.6977    0.2045     41.712    0.3681D+02    0.5113D-01    0.7570D-01    0.5451D+02       1.672      0.0390      0.304    1.0000
 4.9000    4.7993    0.2015     42.612    0.3626D+02    0.5036D-01    0.7845D-01    0.5649D+02       1.666      0.0389      0.310    1.0000
 5.0000    4.9006    0.1985     43.510    0.3573D+02    0.4962D-01    0.8124D-01    0.5849D+02       1.661      0.0389      0.316    1.0000
 5.1000    5.0022    0.1956     44.408    0.3521D+02    0.4891D-01    0.8407D-01    0.6053D+02       1.656      0.0389      0.323    1.0000
 5.2000    5.1036    0.1929     45.306    0.3472D+02    0.4822D-01    0.8693D-01    0.6259D+02       1.651      0.0389      0.329    1.0000
 5.3000    5.2049    0.1902     46.203    0.3423D+02    0.4755D-01    0.8984D-01    0.6468D+02       1.647      0.0388      0.336    1.0000
 5.4000    5.3062    0.1876     47.100    0.3377D+02    0.4690D-01    0.9279D-01    0.6681D+02       1.642      0.0388      0.342    1.0000
 5.5000    5.4075    0.1851     47.996    0.3331D+02    0.4627D-01    0.9577D-01    0.6895D+02       1.638      0.0388      0.349    1.0000
 5.6000    5.5087    0.1826     48.892    0.3289D+02    0.4566D-01    0.9879D-01    0.7113D+02       1.633      0.0388      0.355    1.0000
 5.7000    5.6099    0.1803     49.787    0.3245D+02    0.4507D-01    0.1019D+00    0.7334D+02       1.629      0.0387      0.362    1.0000
 5.8000    5.7110    0.1780     50.682    0.3204D+02    0.4450D-01    0.1050D+00    0.7557D+02       1.625      0.0387      0.368    1.0000
 5.9000    5.8121    0.1758     51.577    0.3164D+02    0.4394D-01    0.1081D+00    0.7783D+02       1.621      0.0387      0.374    1.0000
```

Figure 20

SPECIMEN OUTPUT FROM PROGRAMME KINK

```
CHROMIUM          JANNI EXCITATION POTENTIAL

 INCIDENT   MEAN      ENERGY    REDUCED    STOPPING      STOPPING       RANGE        RANGE       STRAGGLING   ENERGY    GAMMA3  EFFECTIVE
 ENERGY     ENERGY    LOSS      ENERGY     POWER         POWER        DIFFERENCE   DIFFERENCE    STD. DEVN    SPREAD             CHARGE
  MEV.      MEV.      MEV.                 MEV/MM.     MEV-CMSQ/MG.     MM.         MG/CMSQ     PER CENT     MEV.
  6.0000    5.9132    0.1736    52.471    0.3125D+02    0.4340D-01    0.1113D+00    0.8012D+02      1.618      0.0387     0.381    1.0000
  6.1000    6.0143    0.1715    53.365    0.3087D+02    0.4287D-01    0.1145D+00    0.8244D+02      1.614      0.0387     0.387    1.0000
  6.2000    6.1153    0.1694    54.258    0.3050D+02    0.4236D-01    0.1178D+00    0.8478D+02      1.610      0.0386     0.394    1.0000
  6.3000    6.2163    0.1674    55.152    0.3014D+02    0.4186D-01    0.1210D+00    0.8715D+02      1.607      0.0386     0.400    1.0000
  6.4000    6.3173    0.1655    56.044    0.2979D+02    0.4137D-01    0.1244D+00    0.8955D+02      1.603      0.0386     0.406    1.0000
  6.5000    6.4182    0.1636    56.937    0.2945D+02    0.4090D-01    0.1277D+00    0.9198D+02      1.600      0.0386     0.413    1.0000
  6.6000    6.5191    0.1618    57.829    0.2912D+02    0.4044D-01    0.1312D+00    0.9443D+02      1.597      0.0386     0.419    1.0000
  6.7000    6.6200    0.1600    58.721    0.2879D+02    0.3999D-01    0.1346D+00    0.9691D+02      1.593      0.0385     0.426    1.0000
  6.8000    6.7209    0.1582    59.613    0.2848D+02    0.3955D-01    0.1381D+00    0.9942D+02      1.590      0.0385     0.432    1.0000
  6.9000    6.8218    0.1565    60.504    0.2817D+02    0.3912D-01    0.1416D+00    0.1020D+03      1.587      0.0385     0.438    1.0000
  7.0000    6.9226    0.1548    61.395    0.2787D+02    0.3871D-01    0.1452D+00    0.1045D+03      1.584      0.0385     0.445    1.0000
  7.1000    7.0234    0.1532    62.286    0.2758D+02    0.3830D-01    0.1488D+00    0.1071D+03      1.581      0.0384     0.451    1.0000
  7.2000    7.1242    0.1516    63.176    0.2729D+02    0.3790D-01    0.1524D+00    0.1097D+03      1.578      0.0384     0.458    1.0000
  7.3000    7.2250    0.1501    64.067    0.2701D+02    0.3752D-01    0.1561D+00    0.1124D+03      1.576      0.0384     0.464    1.0000
  7.4000    7.3257    0.1486    64.957    0.2674D+02    0.3714D-01    0.1598D+00    0.1150D+03      1.573      0.0384     0.470    1.0000
  7.5000    7.4265    0.1471    65.846    0.2647D+02    0.3677D-01    0.1635D+00    0.1177D+03      1.570      0.0384     0.477    1.0000
  7.6000    7.5272    0.1456    66.736    0.2621D+02    0.3641D-01    0.1673D+00    0.1204D+03      1.567      0.0383     0.483    1.0000
  7.7000    7.6279    0.1442    67.625    0.2596D+02    0.3605D-01    0.1711D+00    0.1232D+03      1.565      0.0383     0.490    1.0000
  7.8000    7.7286    0.1428    68.514    0.2571D+02    0.3571D-01    0.1750D+00    0.1260D+03      1.562      0.0383     0.496    1.0000
  7.9000    7.8293    0.1415    69.403    0.2546D+02    0.3537D-01    0.1788D+00    0.1288D+03      1.560      0.0383     0.502    1.0000
  8.0000    7.9299    0.1401    70.292    0.2523D+02    0.3504D-01    0.1828D+00    0.1316D+03      1.557      0.0382     0.509    1.0000
  8.1000    8.0306    0.1388    71.180    0.2499D+02    0.3471D-01    0.1867D+00    0.1344D+03      1.555      0.0382     0.515    1.0000
  8.2000    8.1312    0.1376    72.068    0.2476D+02    0.3439D-01    0.1907D+00    0.1373D+03      1.553      0.0381     0.521    1.0000
  8.3000    8.2318    0.1363    72.956    0.2454D+02    0.3408D-01    0.1948D+00    0.1402D+03      1.550      0.0381     0.528    1.0000
  8.4000    8.3324    0.1351    73.844    0.2432D+02    0.3378D-01    0.1988D+00    0.1432D+03      1.548      0.0380     0.534    1.0000
  8.5000    8.4330    0.1339    74.732    0.2411D+02    0.3348D-01    0.2029D+00    0.1461D+03      1.546      0.0380     0.540    1.0000
  8.6000    8.5336    0.1327    75.619    0.2389D+02    0.3319D-01    0.2071D+00    0.1491D+03      1.544      0.0379     0.547    1.0000
  8.7000    8.6342    0.1316    76.506    0.2369D+02    0.3290D-01    0.2113D+00    0.1521D+03      1.541      0.0379     0.553    1.0000
  8.8000    8.7348    0.1305    77.393    0.2348D+02    0.3262D-01    0.2155D+00    0.1551D+03      1.539      0.0379     0.559    1.0000
  8.9000    8.8353    0.1294    78.280    0.2329D+02    0.3234D-01    0.2197D+00    0.1582D+03      1.537      0.0378     0.566    1.0000
  9.0000    8.9359    0.1283    79.166    0.2309D+02    0.3207D-01    0.2240D+00    0.1613D+03      1.535      0.0378     0.572    1.0000
  9.1000    9.0364    0.1272    80.053    0.2290D+02    0.3181D-01    0.2283D+00    0.1644D+03      1.533      0.0377     0.579    1.0000
  9.2000    9.1369    0.1262    80.939    0.2271D+02    0.3154D-01    0.2327D+00    0.1675D+03      1.531      0.0377     0.585    1.0000
  9.3000    9.2374    0.1252    81.825    0.2253D+02    0.3129D-01    0.2371D+00    0.1707D+03      1.529      0.0376     0.591    1.0000
  9.4000    9.3379    0.1241    82.711    0.2235D+02    0.3104D-01    0.2415D+00    0.1739D+03      1.527      0.0376     0.598    1.0000
  9.5000    9.4384    0.1232    83.597    0.2217D+02    0.3079D-01    0.2460D+00    0.1771D+03      1.525      0.0375     0.604    1.0000
  9.6000    9.5389    0.1222    84.482    0.2199D+02    0.3055D-01    0.2505D+00    0.1803D+03      1.523      0.0375     0.610    1.0000
  9.7000    9.6394    0.1212    85.368    0.2182D+02    0.3031D-01    0.2550D+00    0.1836D+03      1.522      0.0375     0.617    1.0000
  9.8000    9.7398    0.1203    86.253    0.2165D+02    0.3008D-01    0.2596D+00    0.1869D+03      1.520      0.0374     0.623    1.0000
  9.9000    9.8403    0.1194    87.138    0.2149D+02    0.2985D-01    0.2642D+00    0.1902D+03      1.518      0.0374     0.629    1.0000
 10.0000    9.9408    0.1185    88.023    0.2133D+02    0.2962D-01    0.2688D+00    0.1936D+03      1.516      0.0374     0.636    1.0000

RANGE DIFFERENCES ARE FROM       0.22 MEV.
```

Figure 21

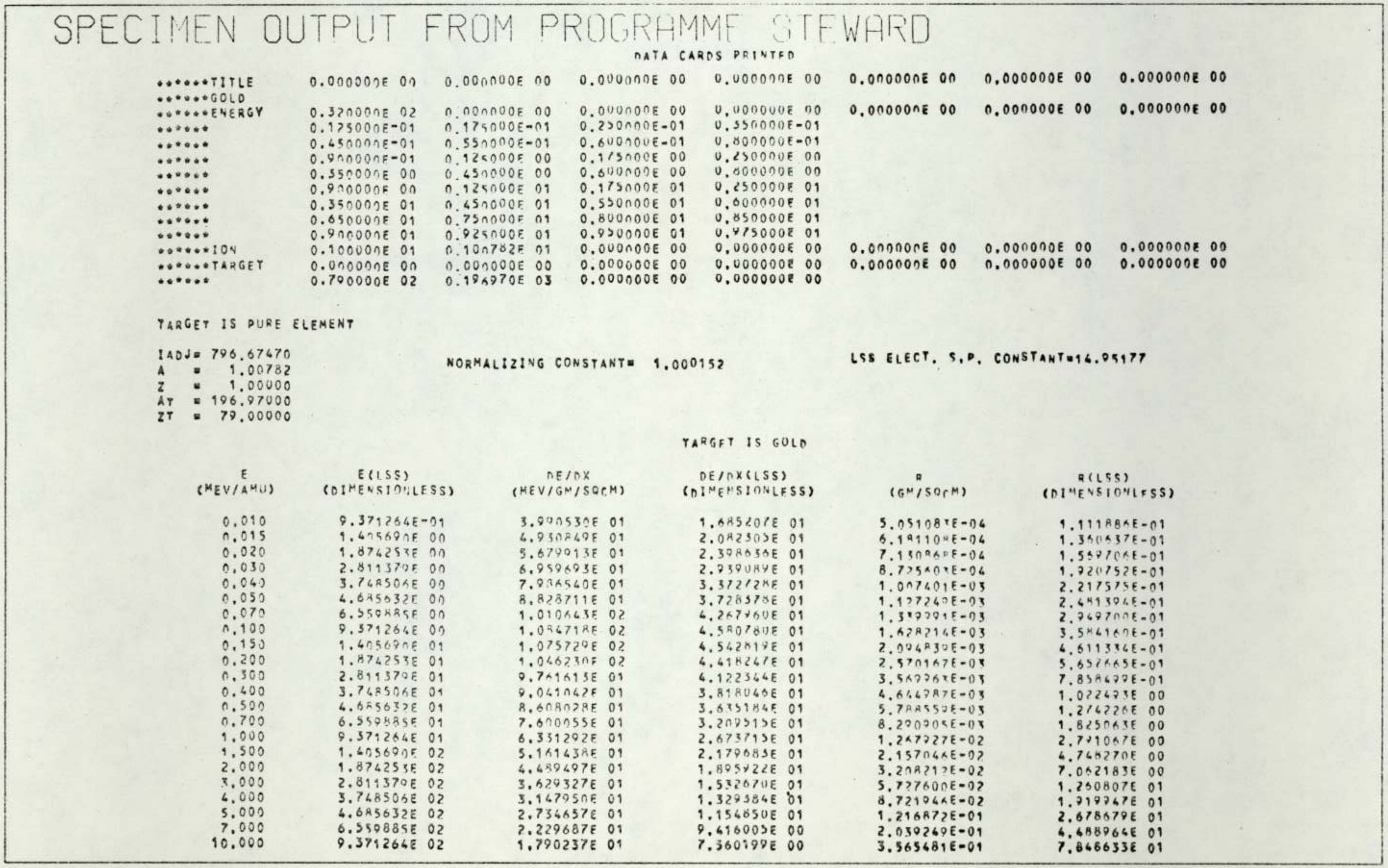

```
SPECIMEN OUTPUT FROM PROGRAMME STEWARD
                                          DATA CARDS PRINTED

******TITLE      0.000000E 00   0.000000E 00   0.000000E 00   0.000000E 00   0.000000E 00   0.000000E 00   0.000000E 00
******GOLD
******ENERGY     0.320000E 02   0.000000E 00   0.000000E 00   0.000000E 00   0.000000E 00   0.000000E 00   0.000000E 00
******           0.125000E-01   0.175000E-01   0.250000E-01   0.350000E-01
******           0.450000E-01   0.550000E-01   0.600000E-01   0.800000E-01
******           0.900000E-01   0.125000E 00   0.175000E 00   0.250000E 00
******           0.350000E 00   0.450000E 00   0.600000E 00   0.800000E 00
******           0.900000E 00   0.125000E 01   0.175000E 01   0.250000E 01
******           0.350000E 01   0.450000E 01   0.550000E 01   0.600000E 01
******           0.650000E 01   0.750000E 01   0.800000E 01   0.850000E 01
******           0.900000E 01   0.925000E 01   0.950000E 01   0.975000E 01
******ION        0.100000E 01   0.100782E 01   0.000000E 00   0.000000E 00   0.000000E 00   0.000000E 00   0.000000E 00
******TARGET     0.000000E 00   0.000000E 00   0.000000E 00   0.000000E 00   0.000000E 00   0.000000E 00   0.000000E 00
******           0.790000E 02   0.196970E 03   0.000000E 00   0.000000E 00

TARGET IS PURE ELEMENT

IADJ= 796.67470
A   =   1.00782           NORMALIZING CONSTANT=  1.000152                           LSS ELECT. S.P. CONSTANT=14.95177
Z   =   1.00000
AT  = 196.97000
ZT  =  79.00000

                                                  TARGET IS GOLD

      E              E(LSS)               DE/DX              DE/DX(LSS)               R                 R(LSS)
  (MEV/AMU)     (DIMENSIONLESS)      (MEV/GM/SQCM)      (DIMENSIONLESS)         (GM/SQCM)         (DIMENSIONLESS)

    0.010        9.371264E-01        3.990530E 01        1.685207E 01        5.051083E-04        1.111886E-01
    0.015        1.405690E 00        4.930849E 01        2.082305E 01        6.191108E-04        1.360637E-01
    0.020        1.874253E 00        5.679913E 01        2.398636E 01        7.130868E-04        1.559706E-01
    0.030        2.811379E 00        6.959693E 01        2.939089E 01        8.725403E-04        1.920752E-01
    0.040        3.748506E 00        7.936540E 01        3.372728E 01        1.007401E-03        2.217575E-01
    0.050        4.685632E 00        8.828711E 01        3.728378E 01        1.127249E-03        2.481394E-01
    0.070        6.559885E 00        1.010643E 02        4.267960E 01        1.389291E-03        2.949700E-01
    0.100        9.371264E 00        1.084718E 02        4.580780E 01        1.628214E-03        3.584160E-01
    0.150        1.405690E 01        1.075729E 02        4.542819E 01        2.094839E-03        4.611334E-01
    0.200        1.874253E 01        1.046230E 02        4.418247E 01        2.570167E-03        5.657665E-01
    0.300        2.811379E 01        9.761613E 01        4.122344E 01        3.562263E-03        7.858499E-01
    0.400        3.748506E 01        9.041042E 01        3.818046E 01        4.644787E-03        1.022493E 00
    0.500        4.685632E 01        8.608028E 01        3.635184E 01        5.788559E-03        1.274226E 00
    0.700        6.559885E 01        7.600055E 01        3.209515E 01        8.290905E-03        1.825063E 00
    1.000        9.371264E 01        6.331292E 01        2.673715E 01        1.247227E-02        2.771067E 00
    1.500        1.405690E 02        5.161438E 01        2.179683E 01        2.157046E-02        4.748270E 00
    2.000        1.874253E 02        4.489497E 01        1.895922E 01        3.208212E-02        7.062183E 00
    3.000        2.811379E 02        3.629327E 01        1.532670E 01        5.727600E-02        1.260807E 01
    4.000        3.748506E 02        3.147950E 01        1.329384E 01        8.721946E-02        1.919947E 01
    5.000        4.685632E 02        2.734657E 01        1.154850E 01        1.216872E-01        2.678679E 01
    7.000        6.559885E 02        2.229687E 01        9.416005E 00        2.039249E-01        4.488964E 01
   10.000        9.371264E 02        1.790237E 01        7.360199E 00        3.565481E-01        7.846633E 01
```

Figure 22

SPECIMEN OUTPUT FROM PROGRAMME STEWARD

```
                                                                          E              DE/DX                R(E)
                                                                      (MEV/AMU)     (MEV/GM/SQCM)        (GM/SQCM)

                                                                       0.0125       4.460680E 01        5.616096E-04
                                                                       0.0175       5.305381E 01        6.655988E-04
                                                                       0.0250       6.319803E 01        7.928236E-04
                                                                       0.0350       7.473116E 01        9.309807E-04
                                                                       0.0450       8.407625E 01        1.067325E-03
                                                                       0.0550       9.148140E 01        1.180434E-03
                                                                       0.0600       9.467569E 01        1.233620E-03
    E             DE/DX            R(E)         SLOPF OF DE/DX         0.0800       1.035334E 02        1.436065E-03
(MEV/AMU)     (MEV/GM/SQCM)      (GM/SQCM)         (SQCM/GM)           0.0900       1.060026E 02        1.532140E-03
                                                                       0.1250       1.080223E 02        1.861527E-03
   0.0100      3.990530E 01      5.051083E-04      0.000000E 00        0.1750       1.060980E 02        2.332503E-03
   0.0150      4.930849E 01      6.181108E-04      1.676266E 03        0.2500       1.011196E 02        3.070065E-03
   0.0200      5.679913E 01      7.130868E-04      1.414279E 03        0.3500       9.401327E 01        4.107475E-03
   0.0300      6.959693E 01      8.725603E-04      1.144359E 03        0.4500       8.824535E 01        5.216773E-03
   0.0400      7.936540E 01      1.007401E-03      9.272533E 02        0.6000       8.104041E 01        7.039732E-03
   0.0500      8.828711E 01      1.127249E-03      7.683872E 02        0.8000       7.177134E 01        9.753694E-03
   0.0700      1.010643E 02      1.339991E-03      4.783589E 02        0.9000       6.754213E 01        1.171448E-02
   0.1000      1.084718E 02      1.628214E-03      1.464355E 02        1.2500       5.746365E 01        1.712487E-02
   0.1500      1.075729E 02      2.094839E-03     -3.818867E 01        1.7500       4.825468E 01        2.682629E-02
   0.2000      1.046230E 02      2.570167E-03     -6.220080E 01        2.5000       4.059412E 01        4.467906E-02
   0.3000      9.761613E 01      3.569963E-03     -7.051136E 01        3.5000       3.398630E 01        7.224773E-02
   0.4000      9.041042E 01      4.644987E-03     -5.723139E 01        4.5000       2.941304E 01        1.044533E-01
   0.5000      8.608028E 01      5.788559E-03     -4.531255E 01        5.5000       2.608415E 01        1.422466E-01
   0.7000      7.600055E 01      8.290905E-03     -4.678990E 01        6.0000       2.482177E 01        1.628060E-01
   1.0000      6.331292E 01      1.267927E-02     -3.493311E 01        6.5000       2.355930E 01        1.833654E-01
   1.5000      5.161438E 01      2.157046E-02     -1.827495E 01        7.5000       2.156446E 01        2.293621E-01
   2.0000      4.489497E 01      3.208212E-02     -1.173462E 01        8.0000       2.083204E 01        2.547993E-01
   3.0000      3.679327E 01      5.727600E-02     -6.655654E 00        8.5000       2.009967E 01        2.802365E-01
   4.0000      3.147950E 01      8.721946E-02     -4.438618E 00        9.0000       1.936721E 01        3.056737E-01
   5.0000      2.734657E 01      1.216872E-01     -3.568979E 00        9.2500       1.900100E 01        3.183923E-01
   7.0000      2.229687E 01      2.039249E-01     -2.084531E 00        9.5000       1.863479E 01        3.311109E-01
  10.0000      1.790237E 01      3.565481E-01      0.000000E 00        9.7500       1.826858E 01        3.438295E-01
```

Figure 23

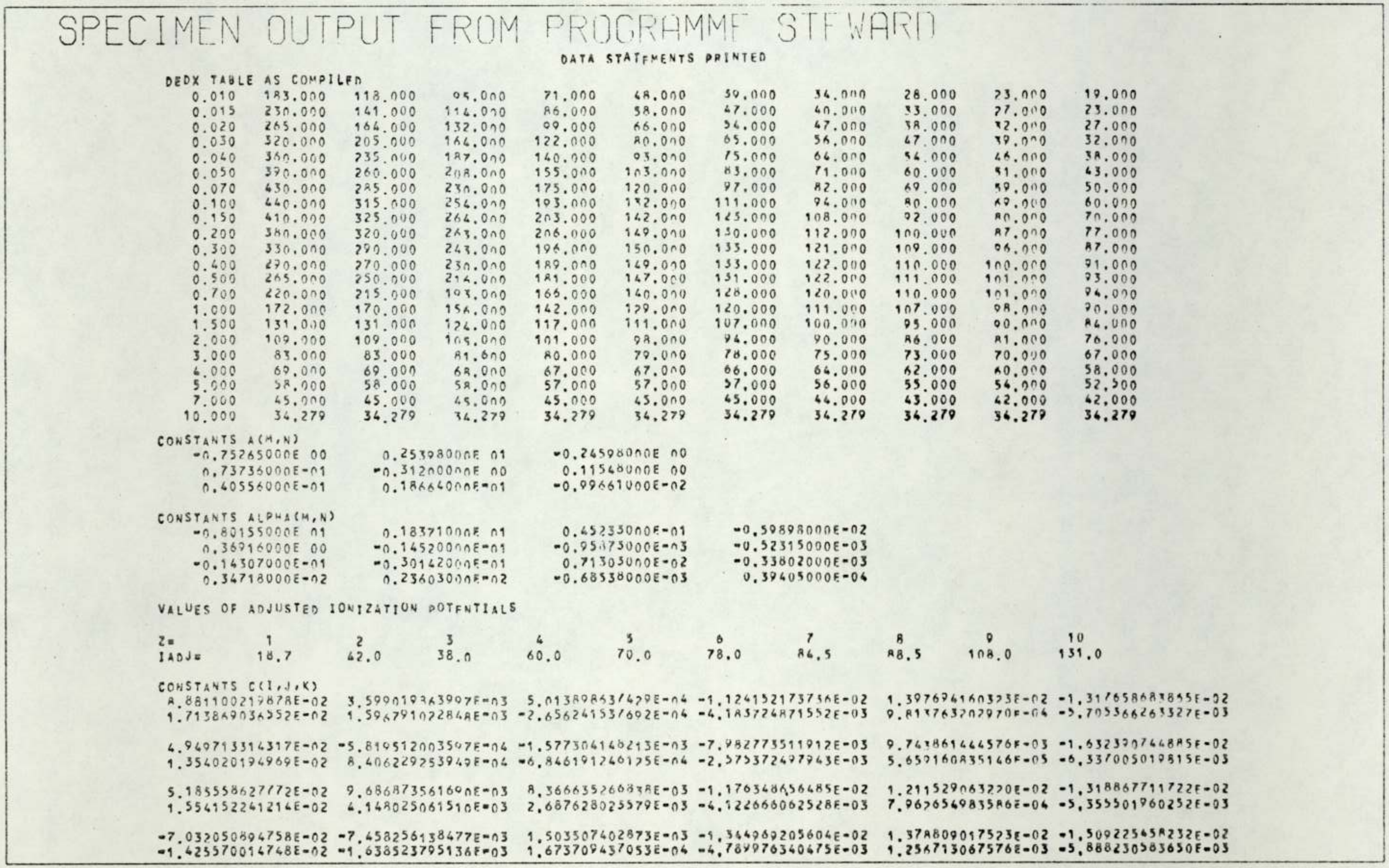

```
SPECIMEN OUTPUT FROM PROGRAMME STEWARD
                                        DATA STATEMENTS PRINTED
 DEDX TABLE AS COMPILED
    0.010   183.000   118.000    95.000    71.000    48.000    39.000    34.000    28.000    23.000    19.000
    0.015   230.000   141.000   114.000    86.000    58.000    47.000    40.000    33.000    27.000    23.000
    0.020   265.000   164.000   132.000    99.000    66.000    54.000    47.000    38.000    32.000    27.000
    0.030   320.000   205.000   164.000   122.000    80.000    65.000    56.000    47.000    39.000    32.000
    0.040   360.000   235.000   187.000   140.000    93.000    75.000    64.000    54.000    46.000    38.000
    0.050   390.000   260.000   208.000   155.000   103.000    83.000    71.000    60.000    51.000    43.000
    0.070   430.000   285.000   230.000   175.000   120.000    97.000    82.000    69.000    59.000    50.000
    0.100   440.000   315.000   254.000   193.000   132.000   111.000    94.000    80.000    69.000    60.000
    0.150   410.000   325.000   264.000   203.000   142.000   125.000   108.000    92.000    80.000    70.000
    0.200   380.000   320.000   263.000   206.000   149.000   130.000   112.000   100.000    87.000    77.000
    0.300   330.000   290.000   243.000   196.000   150.000   133.000   121.000   109.000    96.000    87.000
    0.400   290.000   270.000   230.000   189.000   149.000   133.000   122.000   110.000   100.000    91.000
    0.500   265.000   250.000   214.000   181.000   147.000   131.000   122.000   111.000   101.000    93.000
    0.700   220.000   215.000   193.000   166.000   140.000   128.000   120.000   110.000   101.000    94.000
    1.000   172.000   170.000   156.000   142.000   129.000   120.000   111.000   107.000    98.000    90.000
    1.500   131.000   131.000   124.000   117.000   111.000   107.000   100.000    95.000    90.000    84.000
    2.000   109.000   109.000   105.000   101.000    98.000    94.000    90.000    86.000    81.000    76.000
    3.000    83.000    83.000    81.600    80.000    79.000    78.000    75.000    73.000    70.000    67.000
    4.000    69.000    69.000    68.000    67.000    67.000    66.000    64.000    62.000    60.000    58.000
    5.000    58.000    58.000    58.000    57.000    57.000    57.000    56.000    55.000    54.000    52.500
    7.000    45.000    45.000    45.000    45.000    45.000    45.000    44.000    43.000    42.000    42.000
   10.000    34.279    34.279    34.279    34.279    34.279    34.279    34.279    34.279    34.279    34.279

 CONSTANTS A(M,N)
    -0.75265000E 00      0.25398000E 01     -0.24598000E 00
     0.73736000E-01     -0.31200000E 00      0.11548000E 00
     0.40556000E-01      0.18664000E-01     -0.99661000E-02

 CONSTANTS ALPHA(M,N)
    -0.80155000E 01      0.18371000E 01      0.45233000E-01     -0.59898000E-02
     0.36916000E 00     -0.14520000E-01     -0.95873000E-03     -0.52315000E-03
    -0.14307000E-01     -0.30142000E-01      0.71303000E-02     -0.33802000E-03
     0.34718000E-02      0.23603000E-02     -0.68538000E-03      0.39405000E-04

 VALUES OF ADJUSTED IONIZATION POTENTIALS

 Z=          1         2         3         4         5         6         7         8         9        10
 IADJ=     18.7      42.0      38.0      60.0      70.0      78.0      84.5      88.5     108.0     131.0

 CONSTANTS C(I,J,K)
  8.881100219878E-02  3.599019363997E-03  5.013898637429E-04 -1.124152173736E-02  1.397694160323E-02 -1.317658683855E-02
  1.713849036552E-02  1.596791022848E-03 -2.656241537692E-04 -4.183724871552E-03  9.813763207970E-04 -5.705366263327E-03

  4.949713314317E-02 -5.819512003597E-04 -1.577304148213E-03 -7.982773511912E-03  9.743861444576E-03 -1.632390744885E-02
  1.354020194969E-02  8.406229253949E-04 -6.846191246125E-04 -2.575372497943E-03  5.659160835146E-05 -6.337005019815E-03

  5.185558627772E-02  9.686873561690E-03  8.366635266838E-03 -1.176348656485E-02  1.211529063220E-02 -1.318867711722E-02
  1.554152241214E-02  4.148025061510E-03  2.687628025579E-03 -4.122666062528E-03  7.962654983586E-04 -5.355501960252E-03

 -7.032050894758E-02 -7.458256138477E-03  1.503507402873E-03 -1.344969205604E-02  1.378809017523E-02 -1.509225458232E-02
 -1.425570014748E-02 -1.638523795136E-03  1.673709437053E-04 -4.789976340475E-03  1.256713067576E-03 -5.888230583650E-03
```

Figure 24

Appendix III

Comparison of Range Data

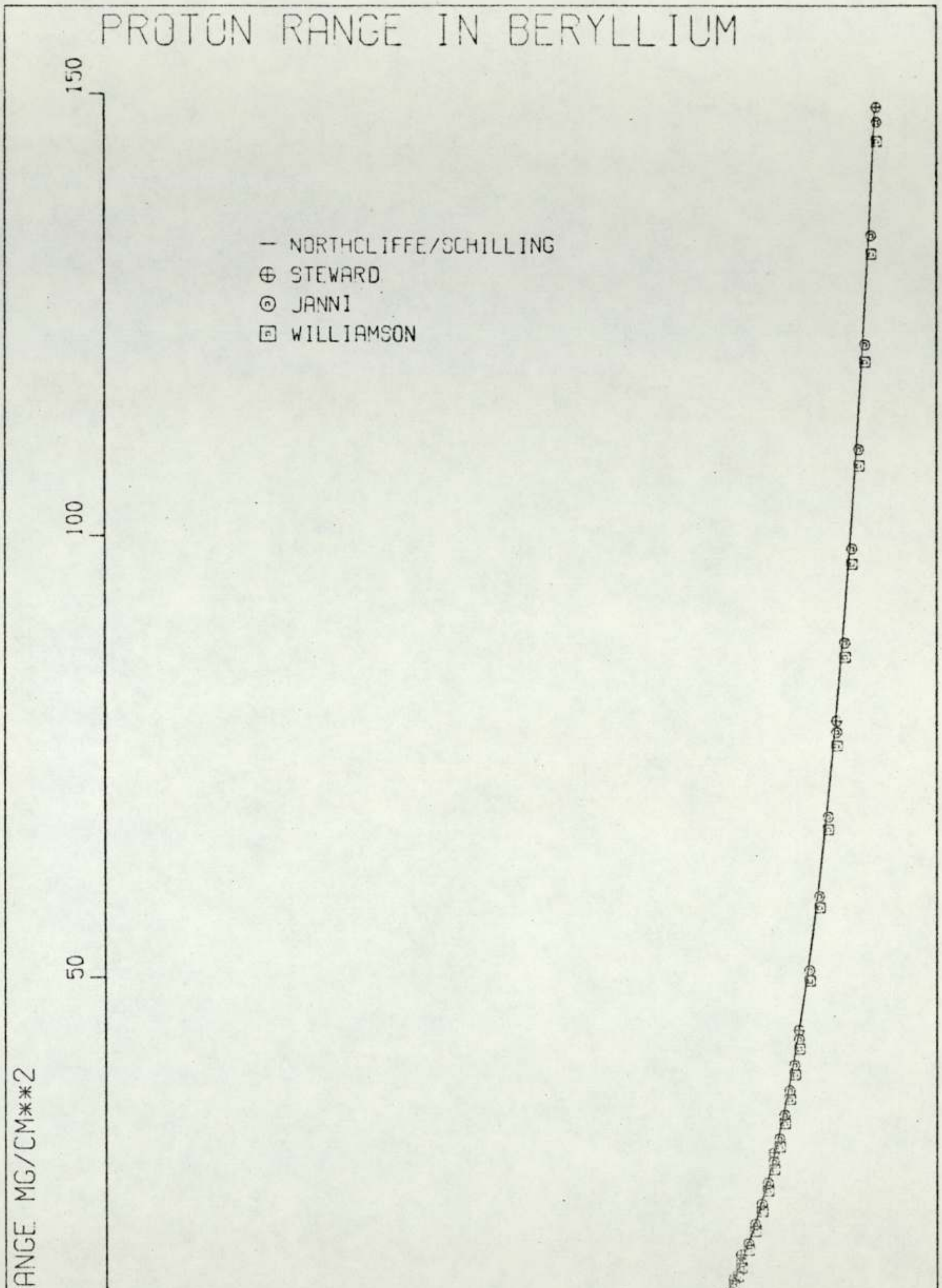
PROTON RANGE IN BERYLLIUM
— NORTHCLIFFE/SCHILLING
⊕ STEWARD
⊙ JANNI
⊡ WILLIAMSON
PROTON RANGE MG/CM**2
0
50
100
150
10^{-2}
10^{-1}
1
10
ENERGY (MEV)

Figure 1

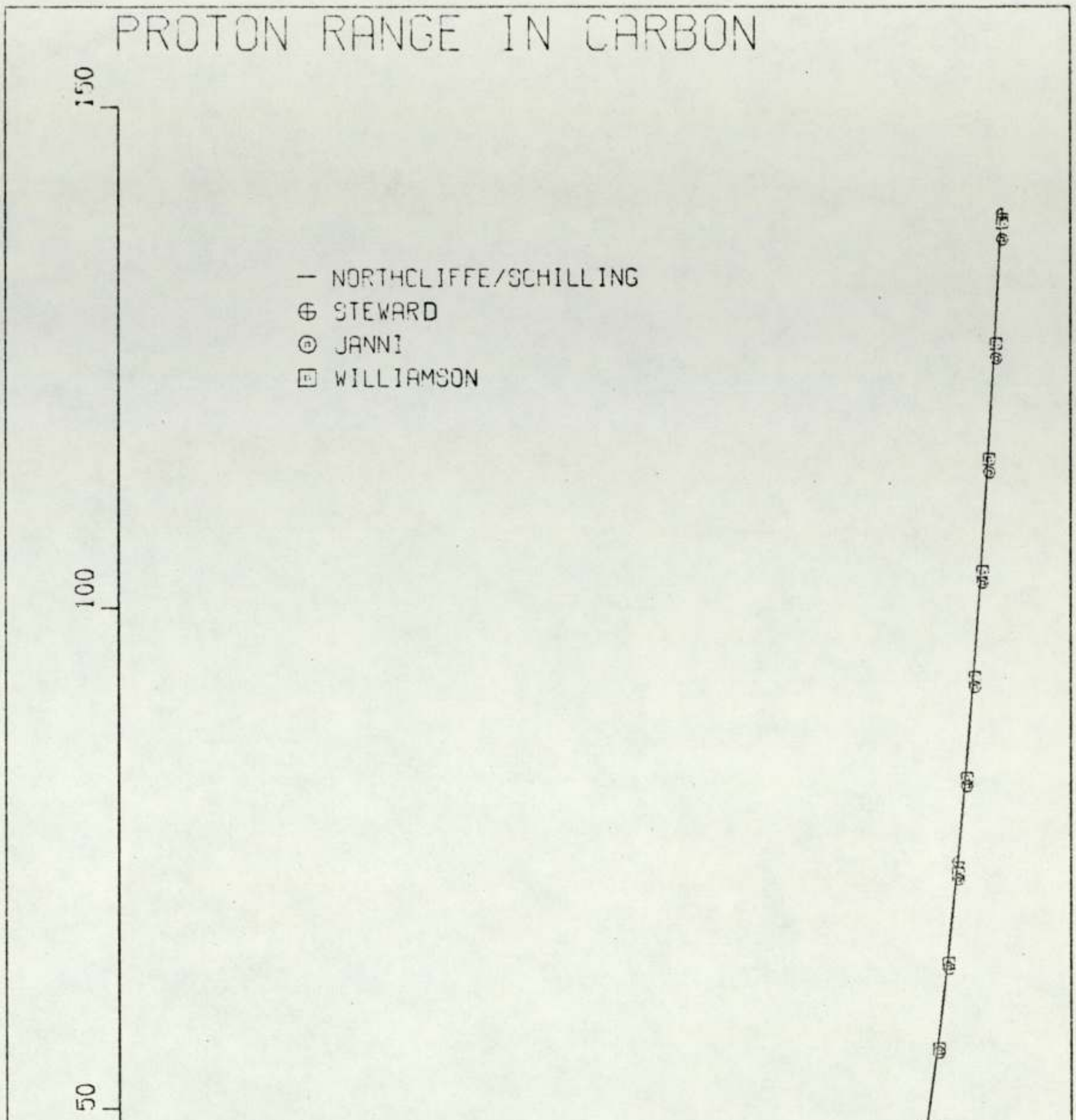
PROTON RANGE IN CARBON
— NORTHCLIFFE/SCHILLING
⊕ STEWARD
⊙ JANNI
⊡ WILLIAMSON
PROTON RANGE MG/CM**2
0
50
100
150
10^{2}
10^{1}
1
10
ENERGY (MEV)

Figure 2

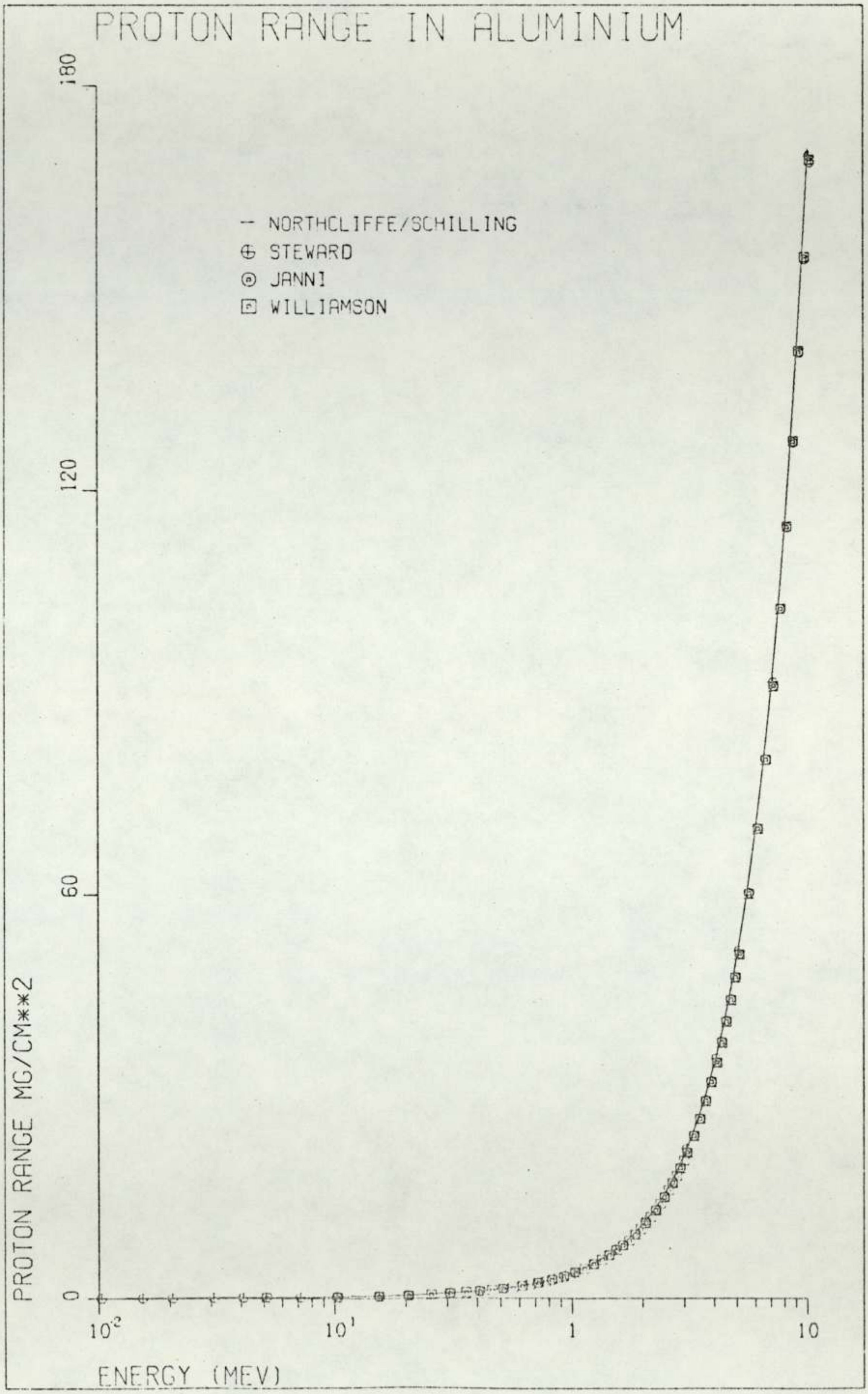
PROTON RANGE IN ALUMINIUM
— NORTHCLIFFE/SCHILLING
⊕ STEWARD
⊙ JANNI
⊡ WILLIAMSON
180
120
60
0
PROTON RANGE MG/CM**2
10^{2}
10^{1}
1
10
ENERGY (MEV)

Figure 3

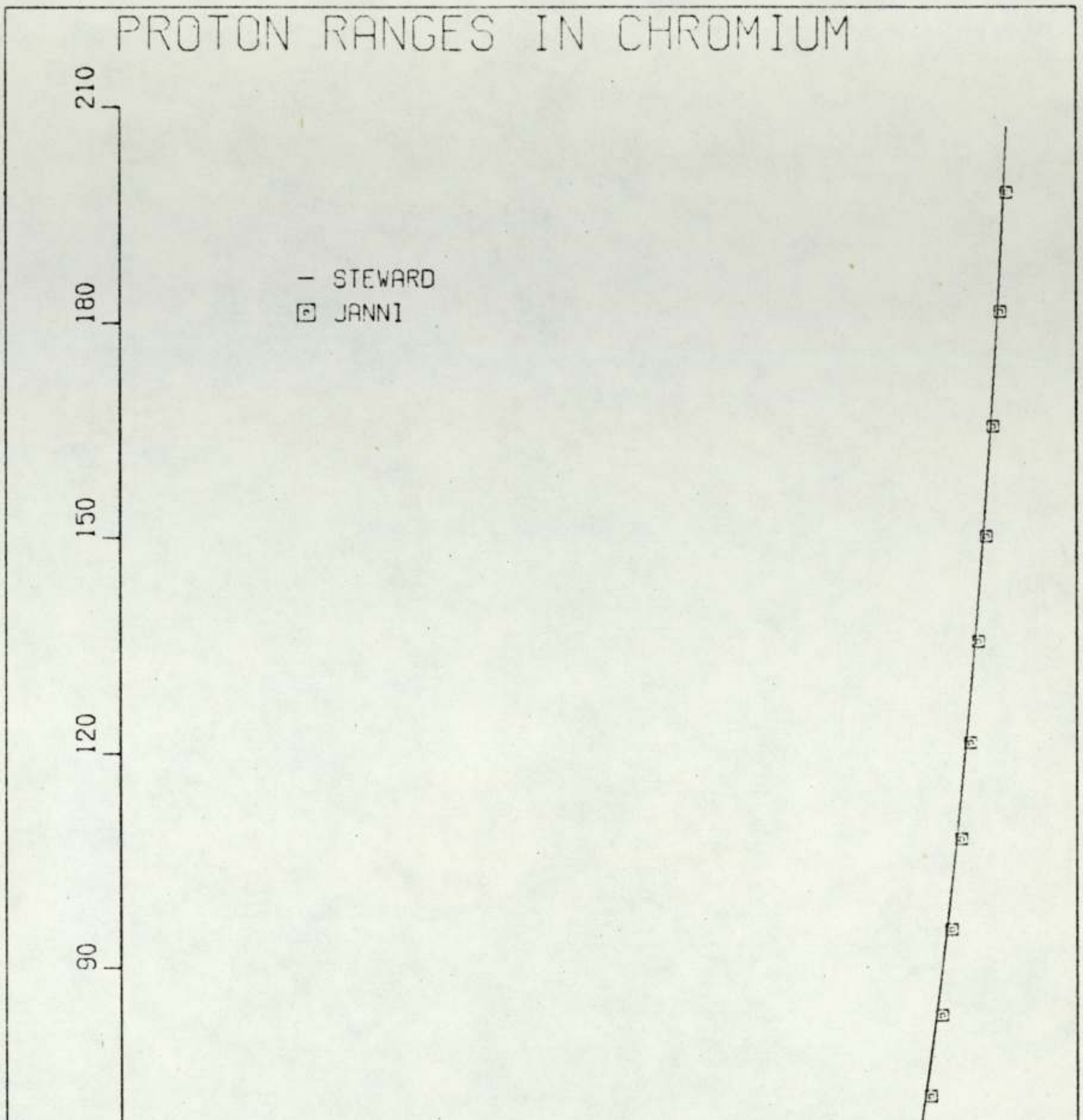
PROTON RANGES IN CHROMIUM
210
180
150
120
90
60
30
0
PROTON RANGE MG/CM**2
– STEWARD
⊡ JANNI
10^{-2}
10^{-1}
1
10
ENERGY (MEV)

Figure 4

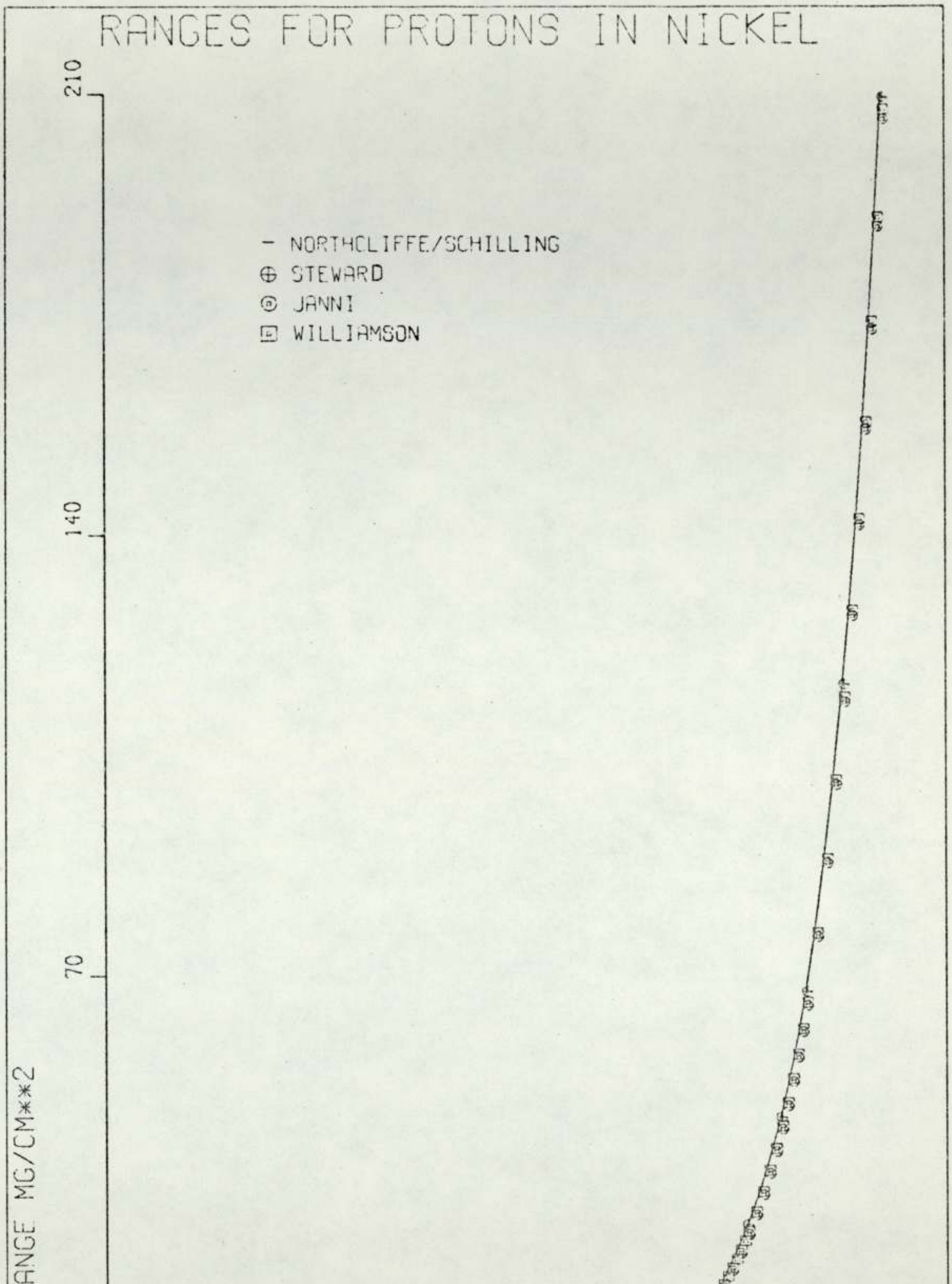
RANGES FOR PROTONS IN NICKEL
— NORTHCLIFFE/SCHILLING
⊕ STEWARD
⊙ JANNI
⊡ WILLIAMSON
PROTON RANGE MG/CM**2
210
140
70
0
10^{-2}
10^{-1}
1
10
ENERGY (MEV)

Figure 5

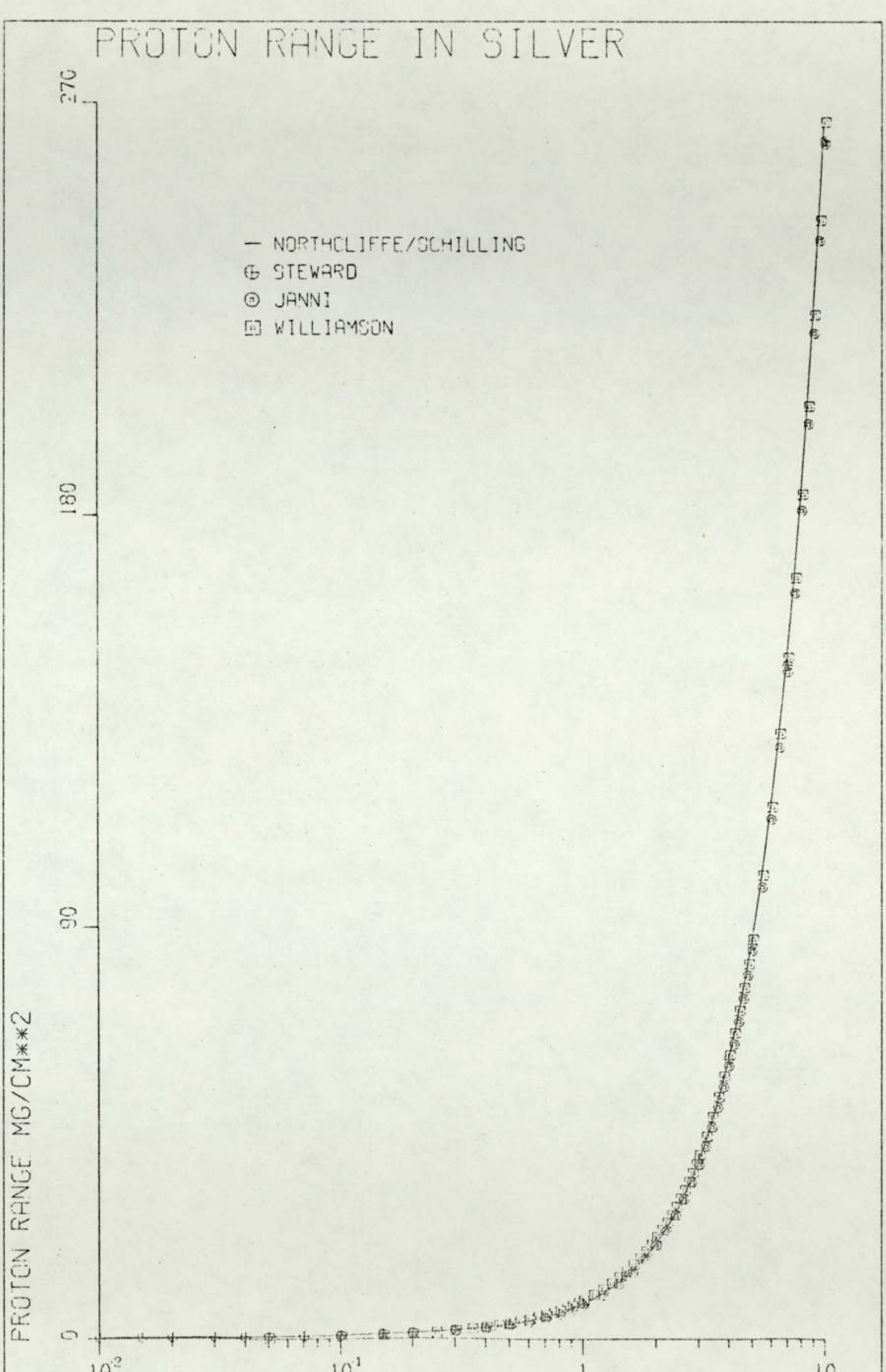
PROTON RANGE IN SILVER
— NORTHCLIFFE/SCHILLING
⊕ STEWARD
⊙ JANNI
⊞ WILLIAMSON
PROTON RANGE MG/CM**2
270
180
90
0
10^{-2}
10^{-1}
1
10
ENERGY (MEV)

Figure 6

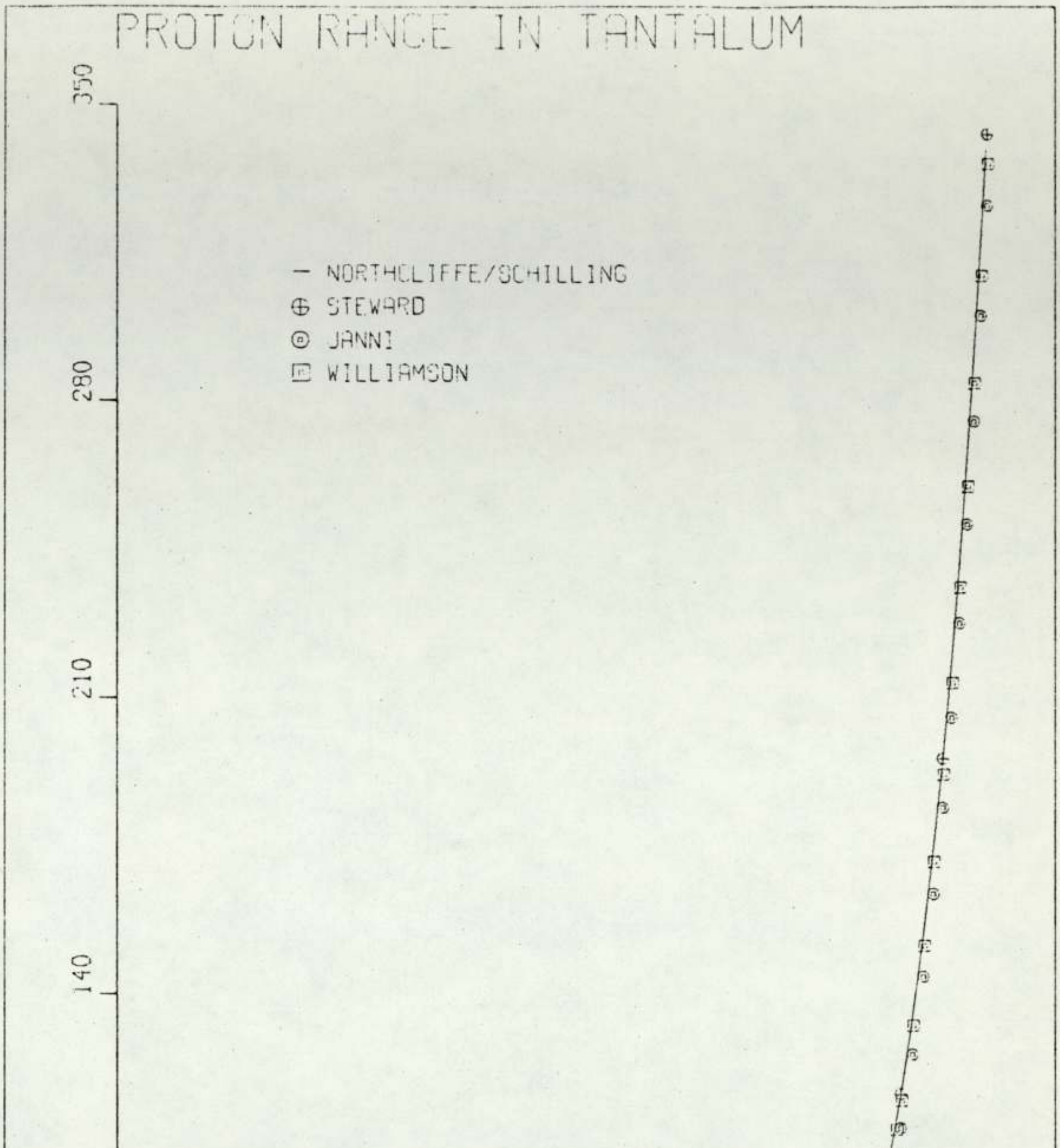

PROTON RANGE IN TANTALUM
— NORTHCLIFFE/SCHILLING
⊕ STEWARD
◎ JANNI
⊡ WILLIAMSON
PROTON RANGE MG/CM**2
0
70
140
210
280
350
10^{2}
10^{1}
1
10
ENERGY (MEV)

Figure 7

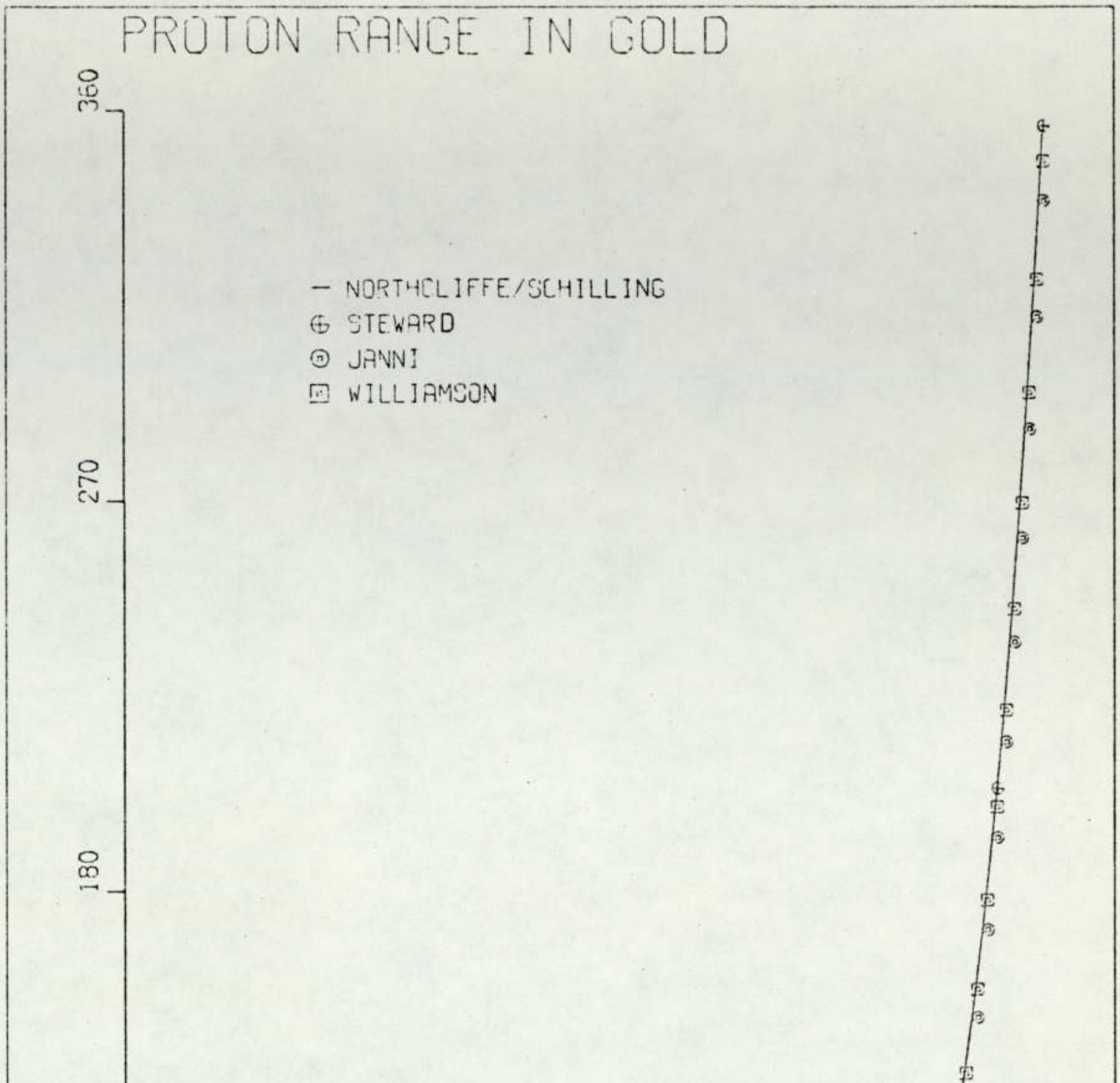
PROTON RANGE IN GOLD
— NORTHCLIFFE/SCHILLING
⊕ STEWARD
⊙ JANNI
⊡ WILLIAMSON
PROTON RANGE MG/CM**2
0
90
180
270
360
10^{-2}
10^{-1}
1
10
ENERGY (MEV)

Figure 8

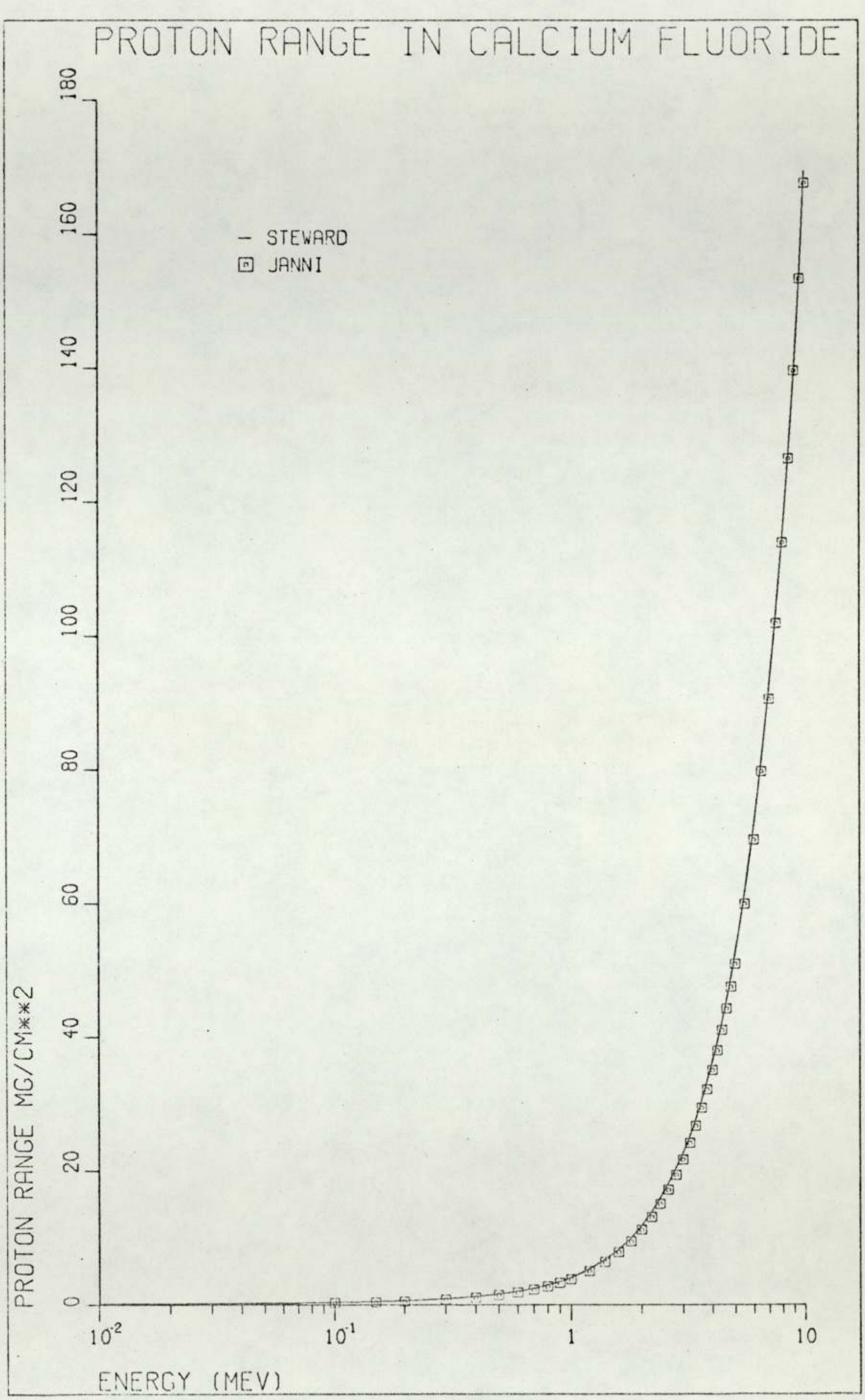
PROTON RANGE IN CALCIUM FLUORIDE
— STEWARD
⊡ JANNI
PROTON RANGE MG/CM**2
0
20
40
60
80
100
120
140
160
180
10^{-2}
10^{-1}
1
10
ENERGY (MEV)

Figure 9

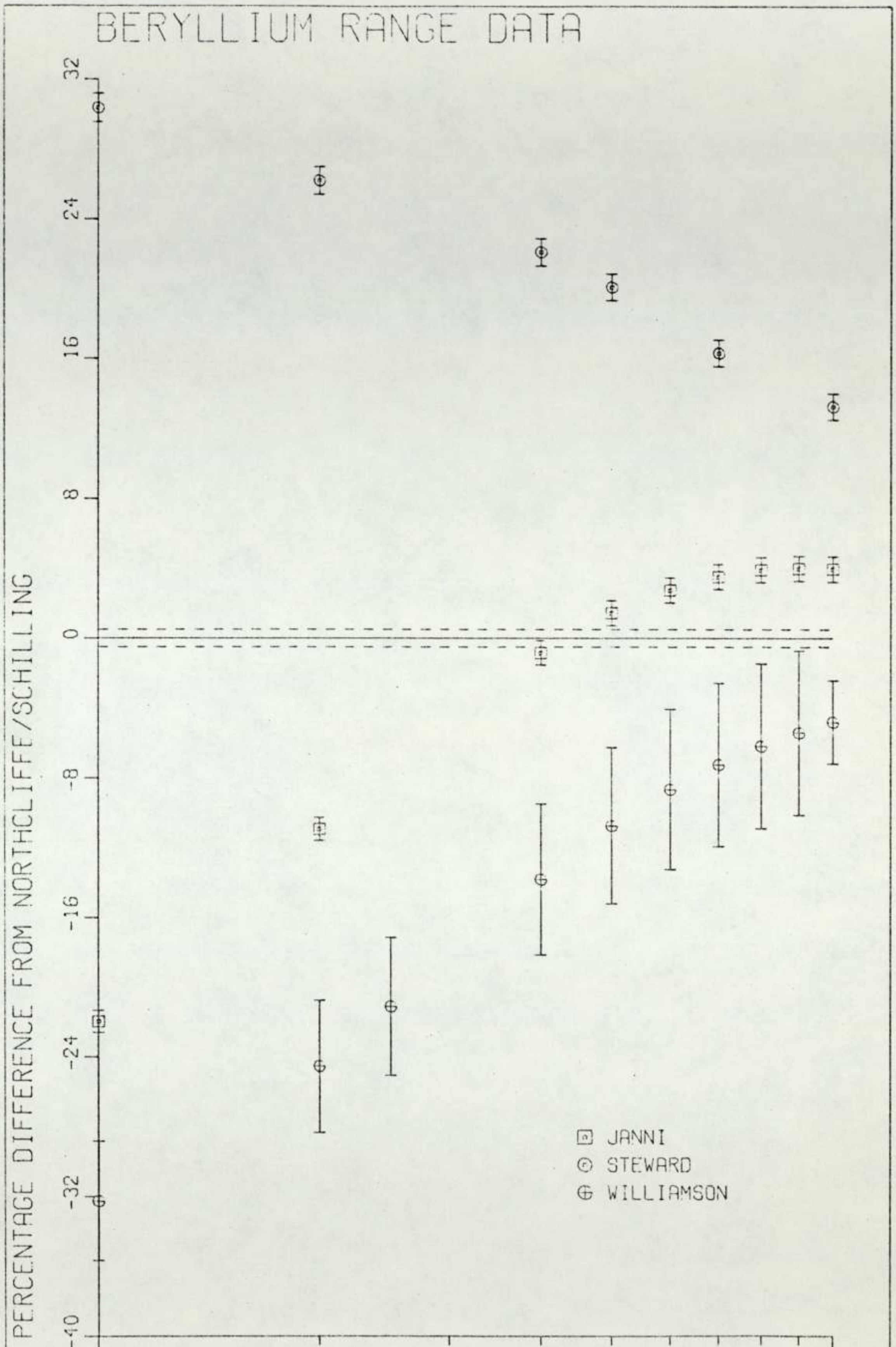
BERYLLIUM RANGE DATA
PERCENTAGE DIFFERENCE FROM NORTHCLIFFE/SCHILLING
32
24
16
8
0
-8
-16
-24
-32
-40
10^{-1}
1
ENERGY (MEV)
JANNI
STEWARD
WILLIAMSON

Figure 10

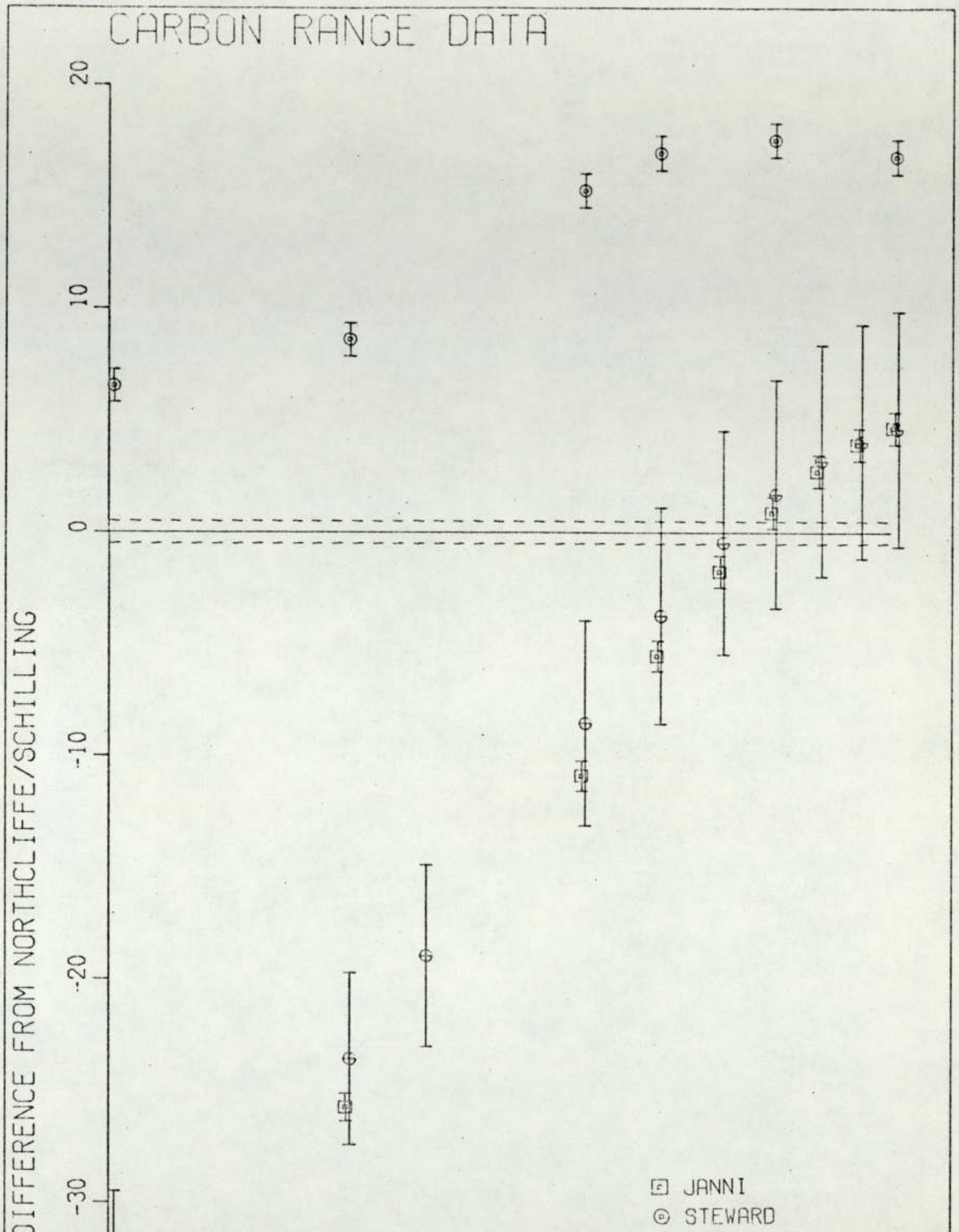
CARBON RANGE DATA
PERCENTAGE DIFFERENCE FROM NORTHCLIFFE/SCHILLING
20
10
0
-10
-20
-30
-40
10^{-1}
1
ENERGY (MEV)
JANNI
STEWARD
WILLIAMSON

Figure 11

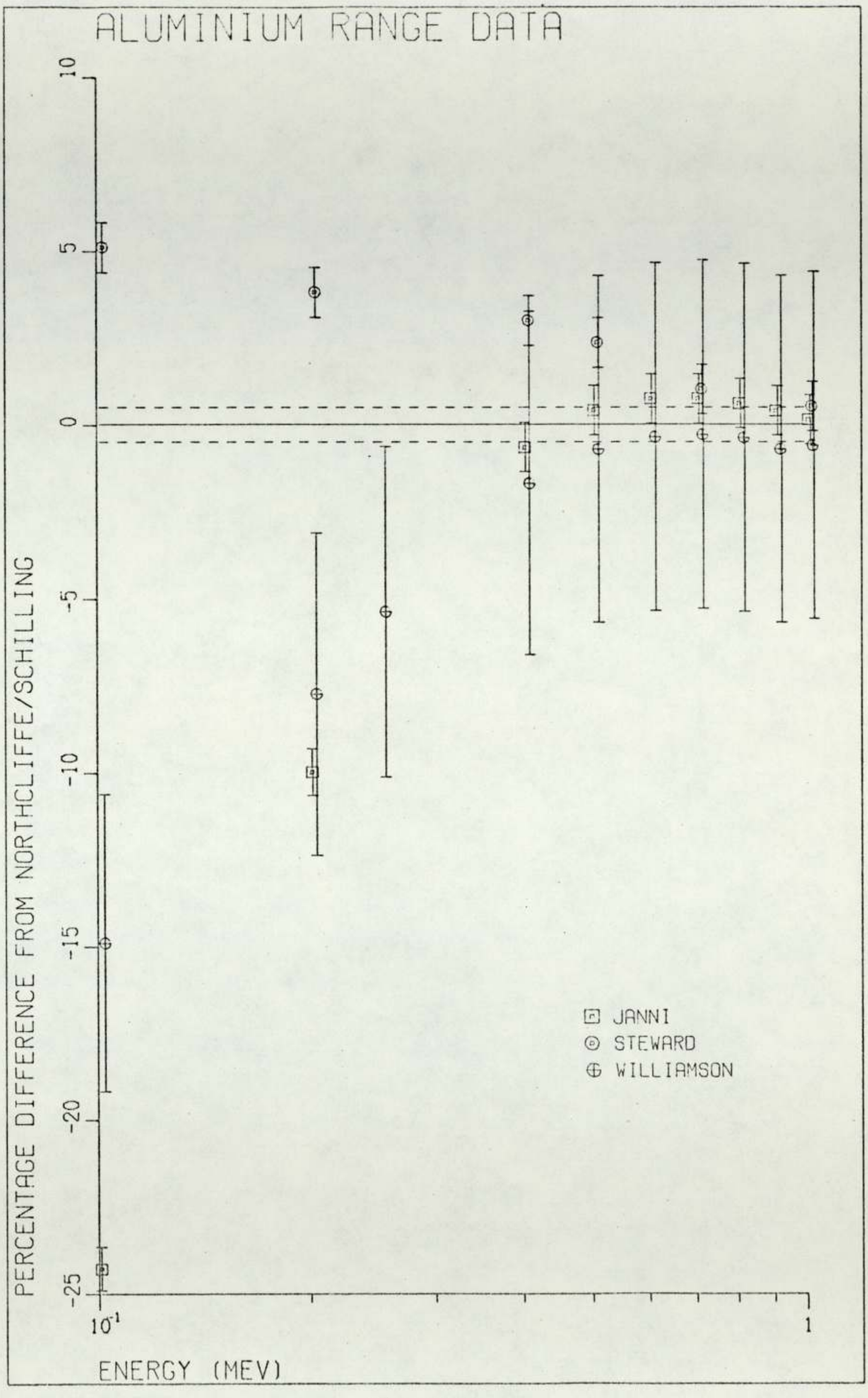
ALUMINIUM RANGE DATA
PERCENTAGE DIFFERENCE FROM NORTHCLIFFE/SCHILLING
10
5
0
-5
-10
-15
-20
-25
10^{-1}
1
ENERGY (MEV)
⊡ JANNI
⊙ STEWARD
⊕ WILLIAMSON

Figure 12

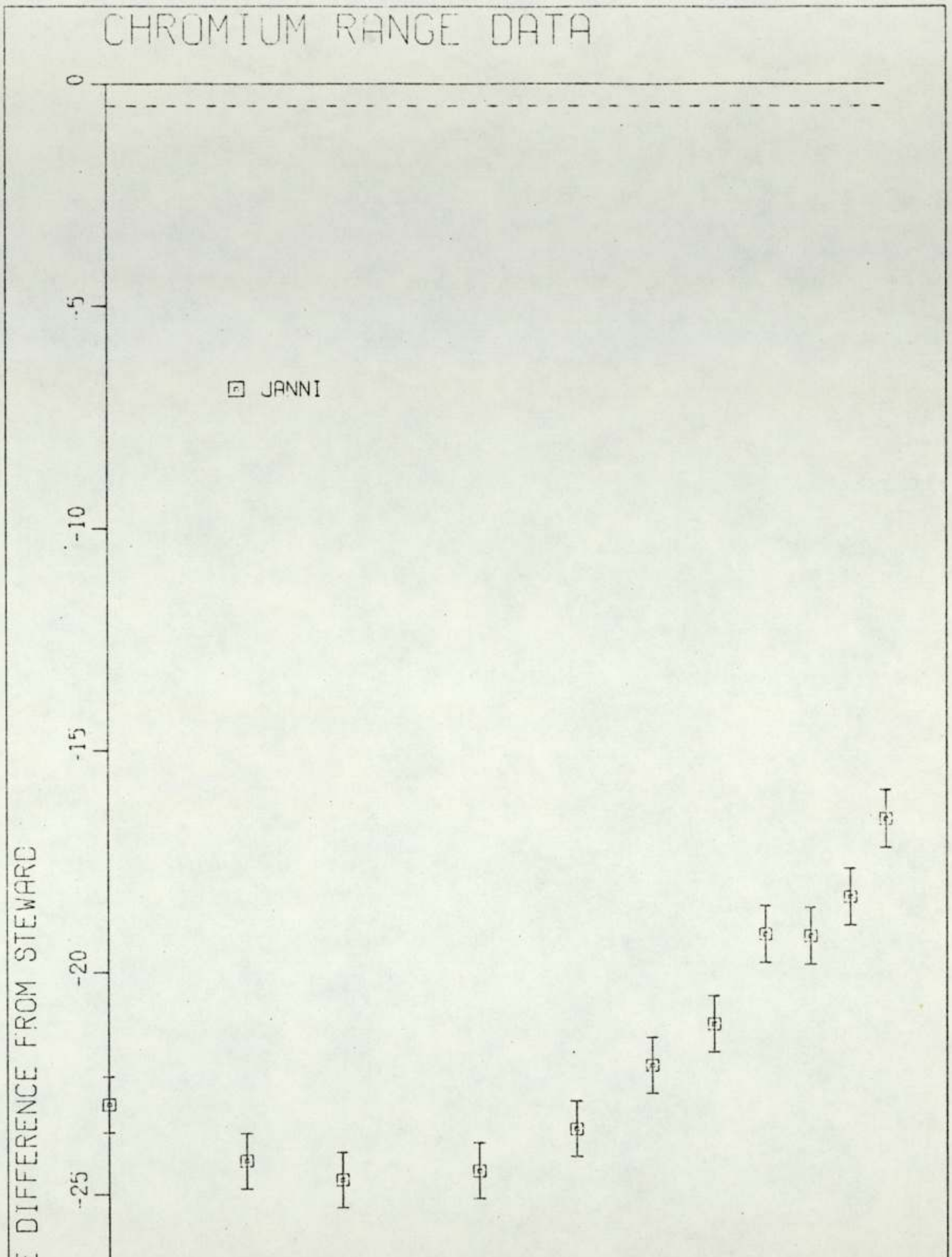
CHROMIUM RANGE DATA
JANNI
0
-5
-10
-15
-20
-25
-30
PERCENTAGE DIFFERENCE FROM STEWARD
10^{-1}
1
ENERGY (MEV)

Figure 13

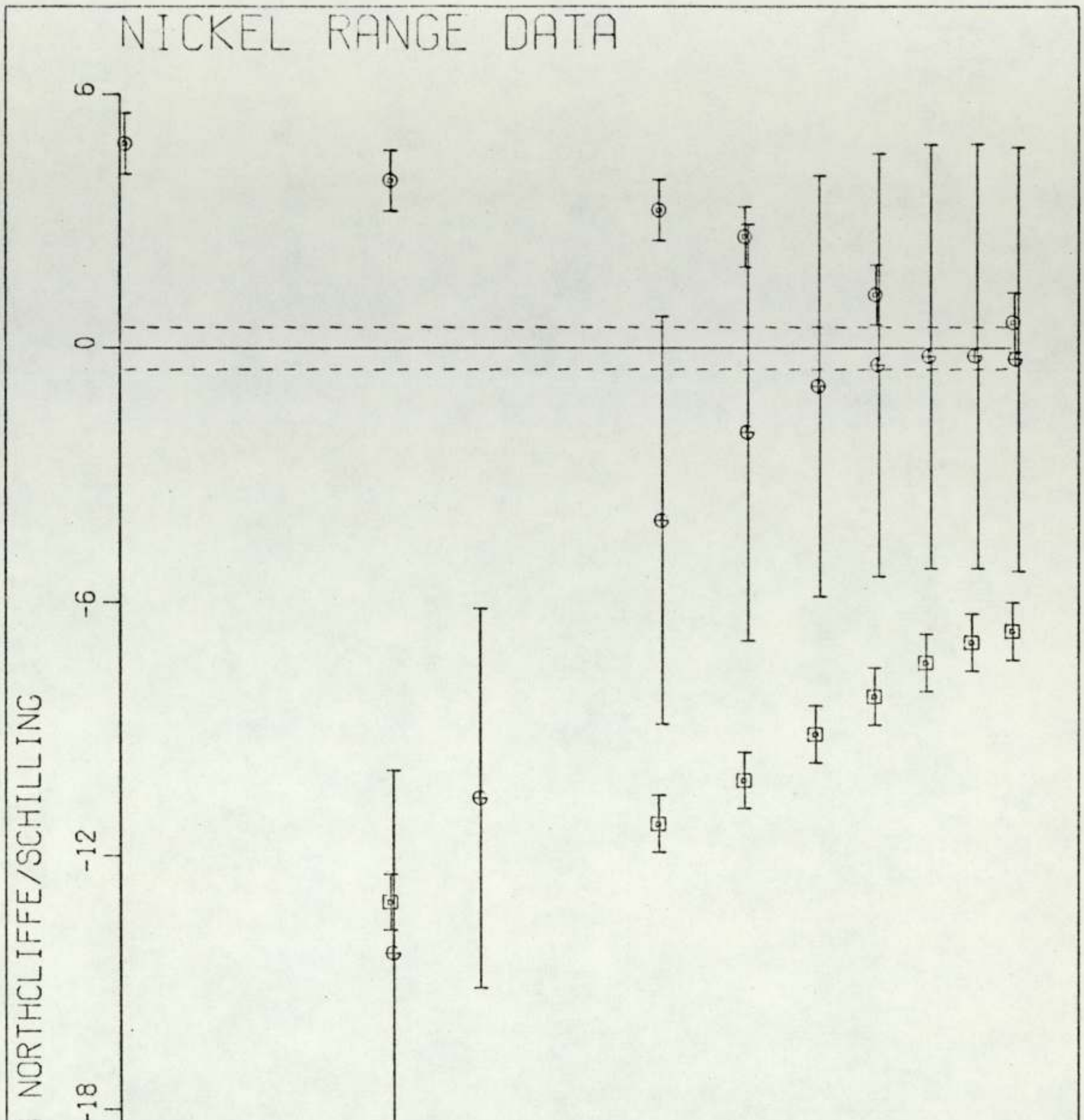
NICKEL RANGE DATA
6
0
-6
-12
-18
-24
-30
PERCENTAGE DIFFERENCE FROM NORTHCLIFFE/SCHILLING
10^{-1}
1
ENERGY (MEV)
⊡ JANNI
⊙ STEWARD
⊕ WILLIAMSON

Figure 14

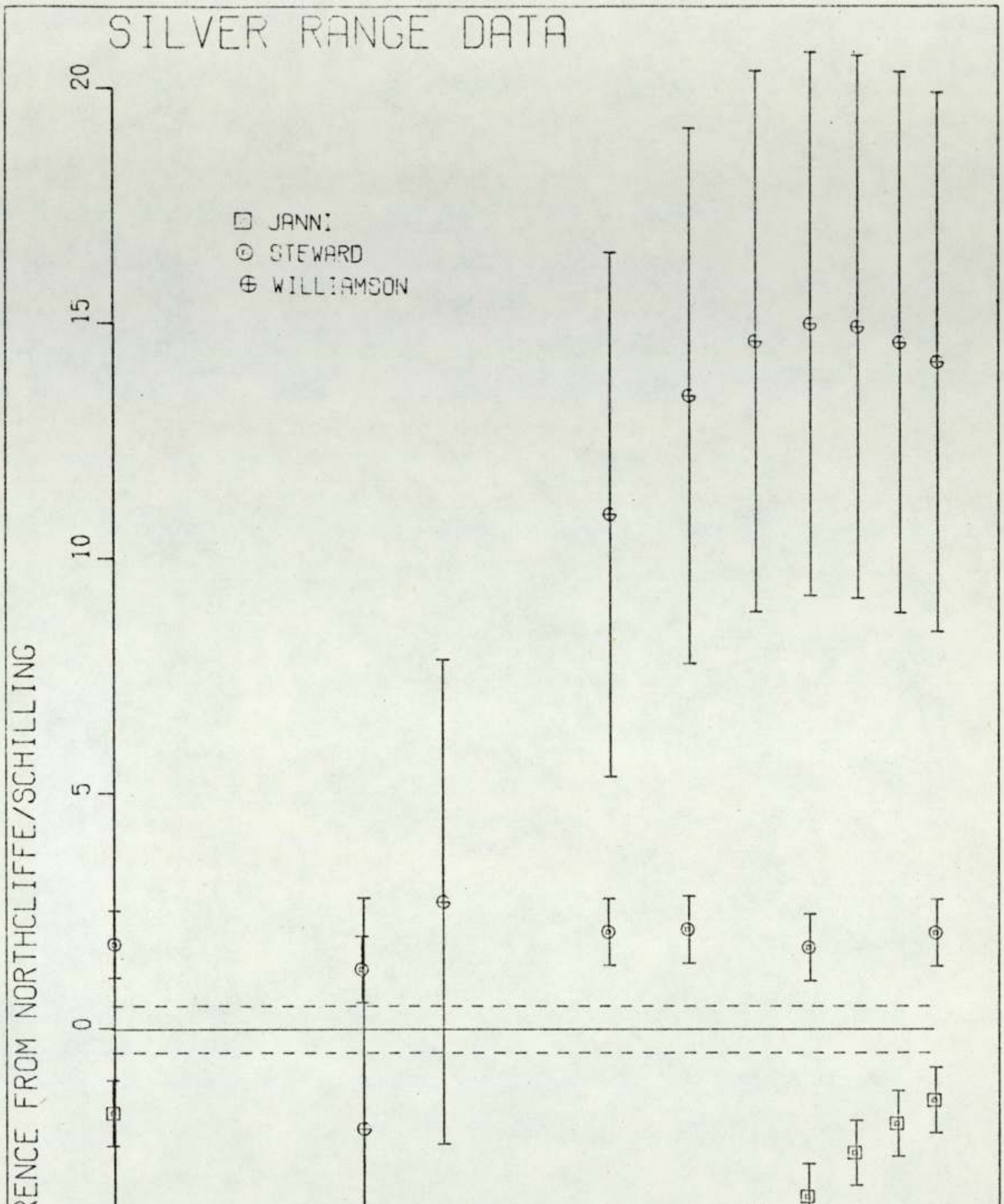
SILVER RANGE DATA
JANNI
STEWARD
WILLIAMSON
PERCENTAGE DIFFERENCE FROM NORTHCLIFFE/SCHILLING
20
15
10
5
0
-5
-10
10^{-1}
1
ENERGY (MEV)

Figure 15

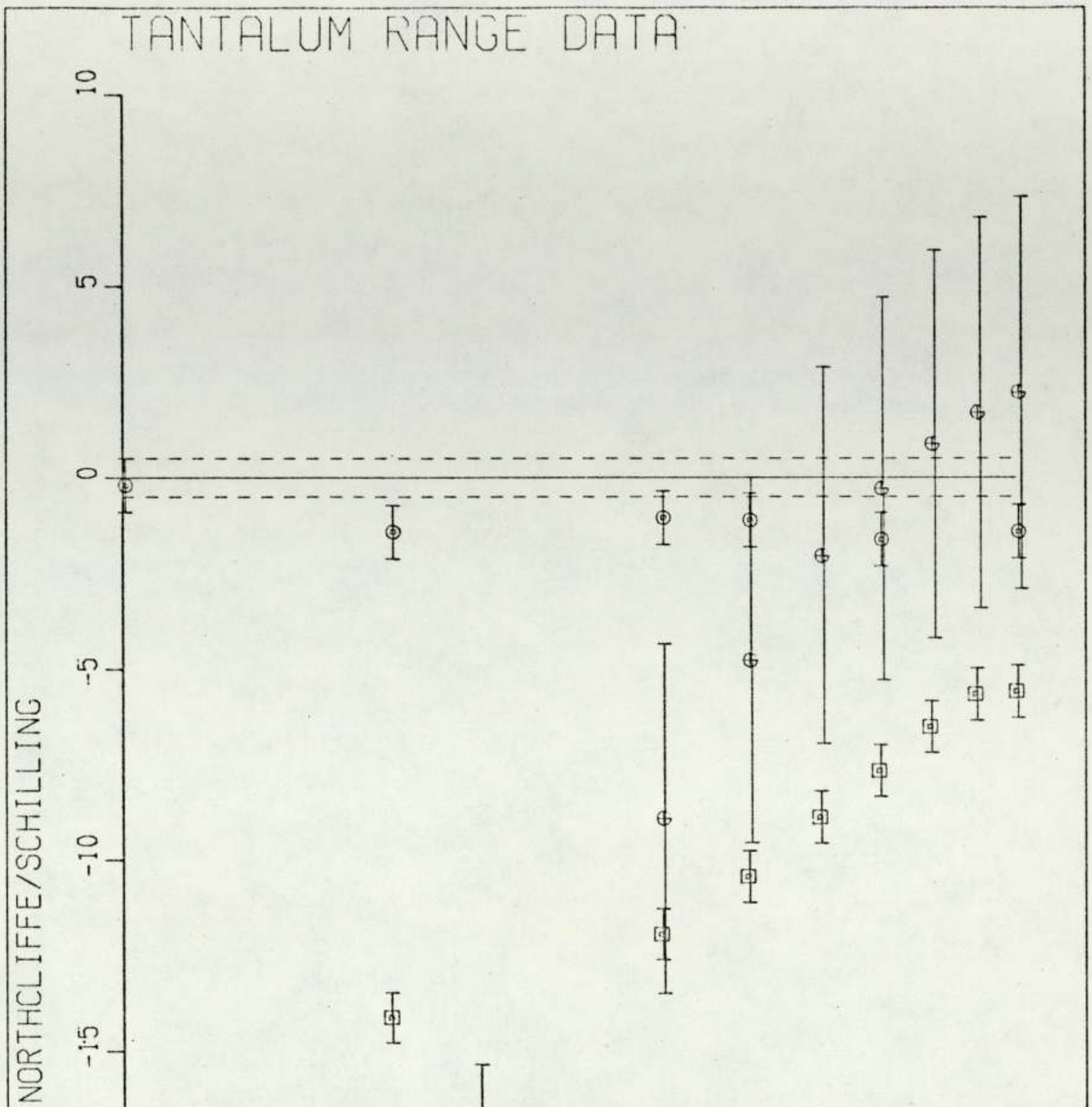
TANTALUM RANGE DATA
PERCENTAGE DIFFERENCE FROM NORTHCLIFFE/SCHILLING
10
5
0
-5
-10
-15
-20
-25
-30
10⁻¹
1
ENERGY (MEV)
⊡ JANNI
⊙ STEWARD
⊕ WILLIAMSON

Figure 16

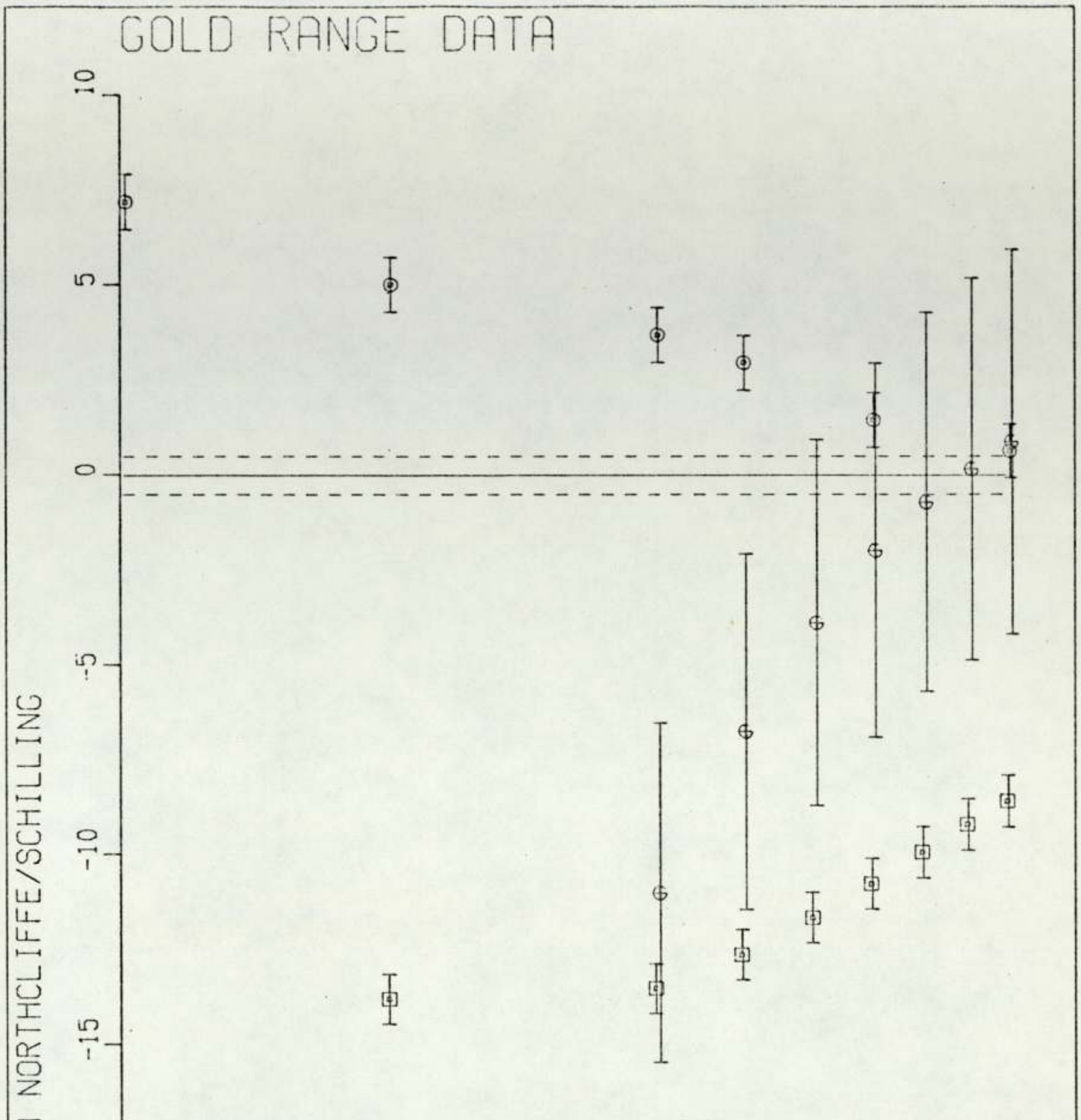

GOLD RANGE DATA
PERCENTAGE DIFFERENCE FROM NORTHCLIFFE/SCHILLING
10
5
0
-5
-10
-15
-20
-25
-30
10⁻¹
1
ENERGY (MEV)
JANNI
STEWARD
WILLIAMSON

Figure 17

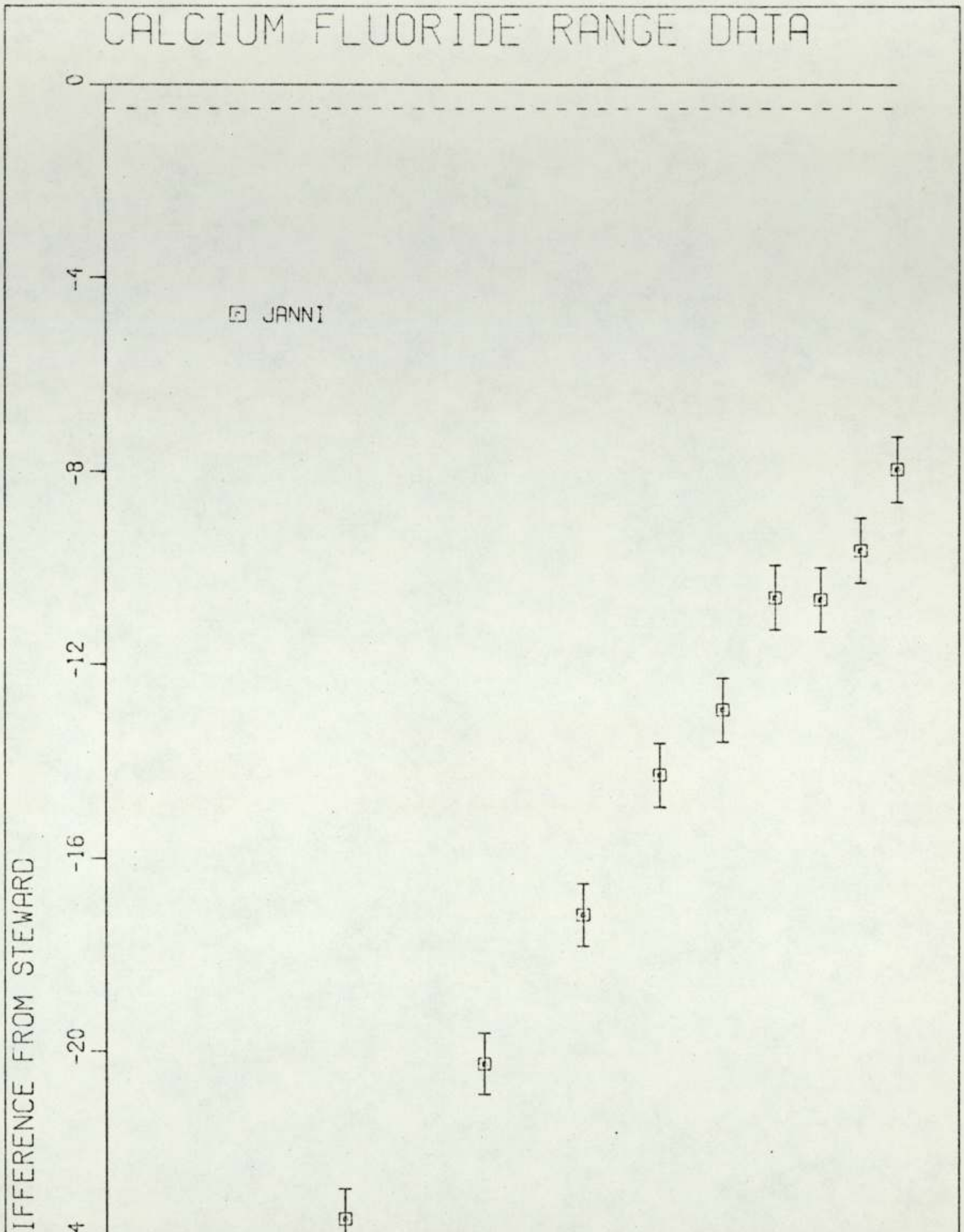
CALCIUM FLUORIDE RANGE DATA
0
-4
-8
-12
-16
-20
-24
-28
PERCENTAGE DIFFERENCE FROM STEWARD
JANNI
10^{-1}
1
ENERGY (MEV)

Figure 18

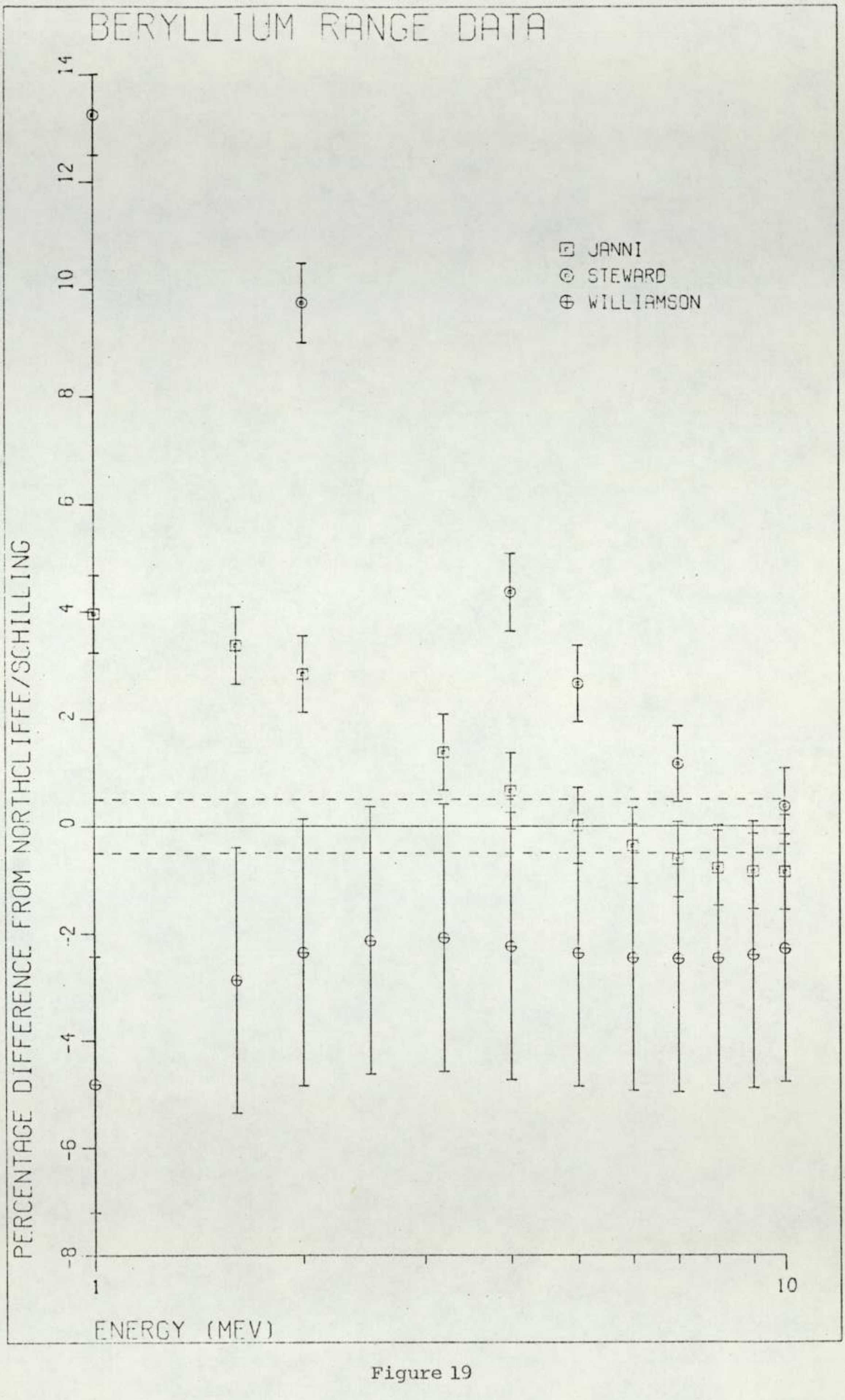
BERYLLIUM RANGE DATA
JANNI
STEWARD
WILLIAMSON
PERCENTAGE DIFFERENCE FROM NORTHCLIFFE/SCHILLING
14
12
10
8
6
4
2
0
-2
-4
-6
-8
1
10
ENERGY (MEV)

Figure 19

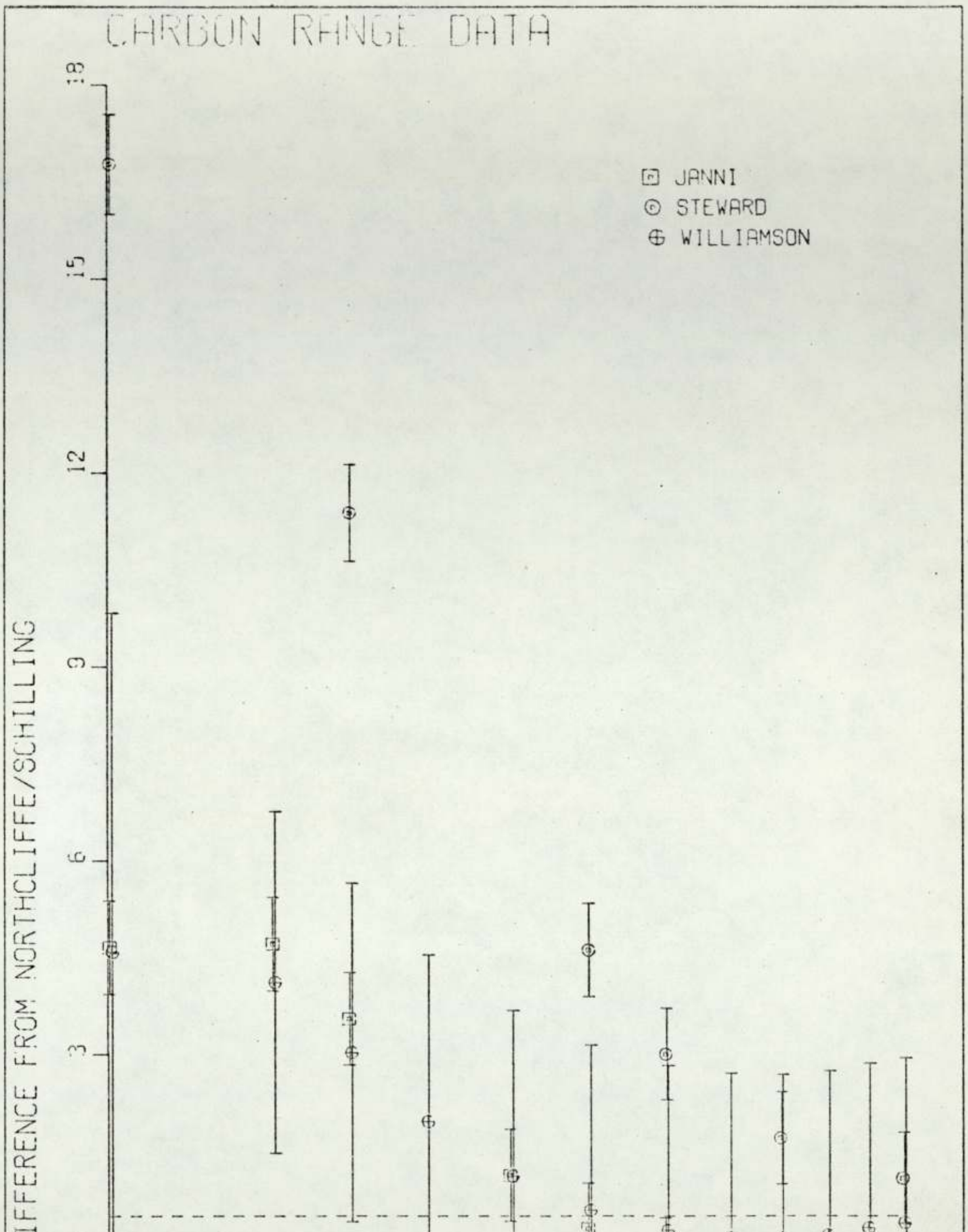
CARBON RANGE DATA
JANNI
STEWARD
WILLIAMSON
PERCENTAGE DIFFERENCE FROM NORTHCLIFFE/SCHILLING
18
15
12
9
6
3
0
-3
1
10
ENERGY (MEV)

Figure 20

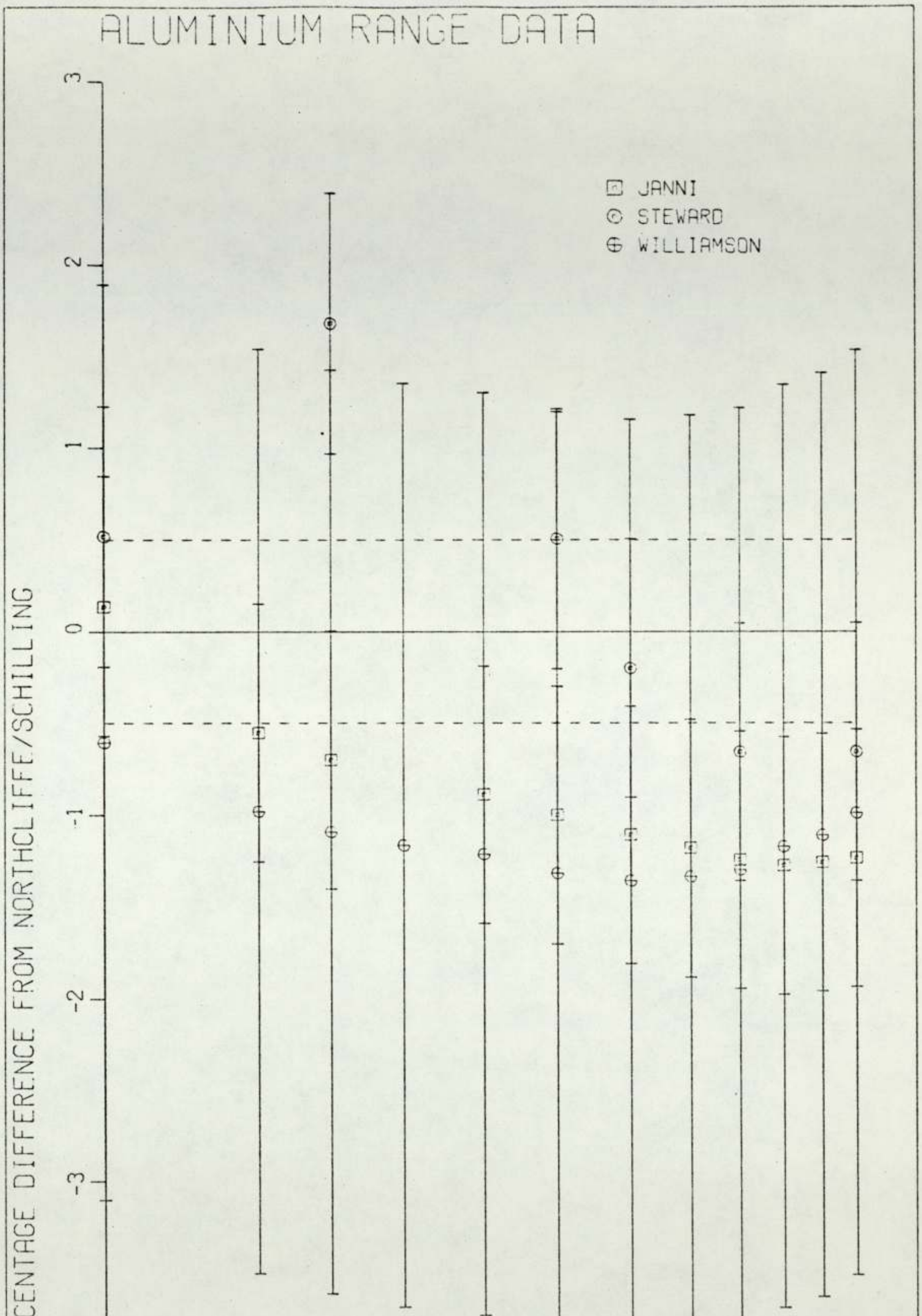
ALUMINIUM RANGE DATA
JANNI
STEWARD
WILLIAMSON
PERCENTAGE DIFFERENCE FROM NORTHCLIFFE/SCHILLING
3
2
1
0
-1
-2
-3
-4
1
10
ENERGY (MEV)

Figure 21

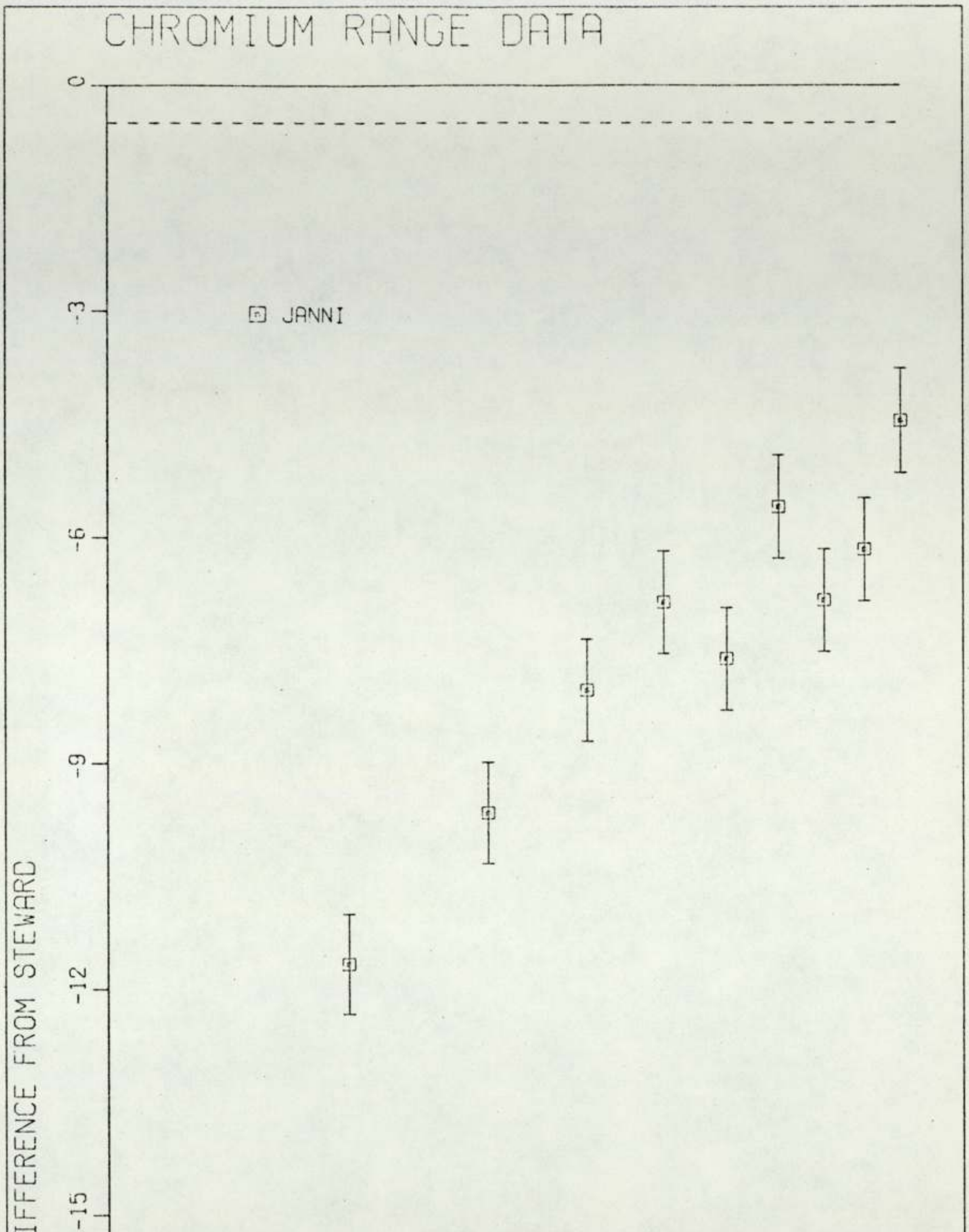
CHROMIUM RANGE DATA
0
-3
-6
-9
-12
-15
-18
⊡ JANNI
PERCENTAGE DIFFERENCE FROM STEWARD
1
10
ENERGY (MEV)

Figure 22

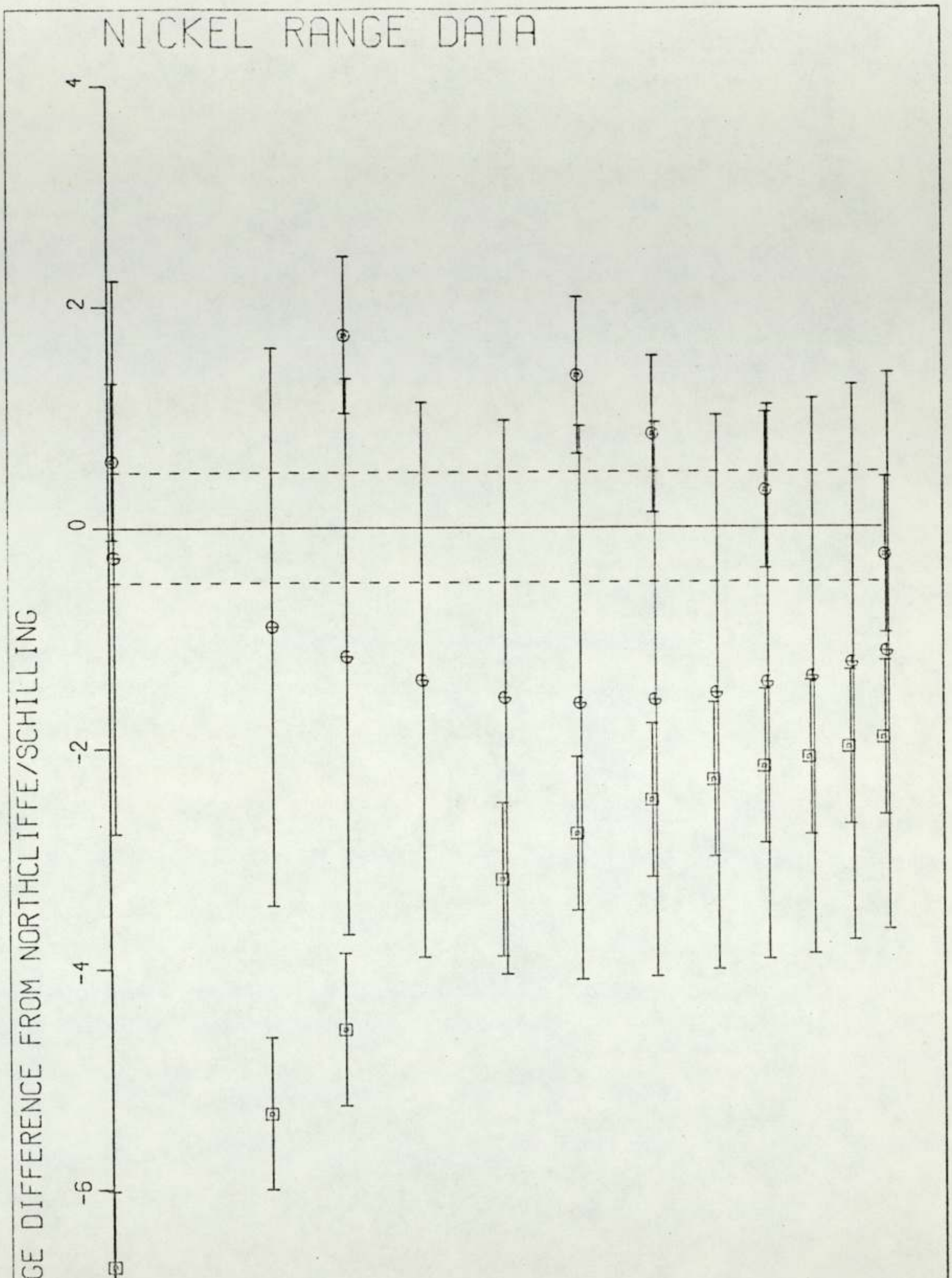
NICKEL RANGE DATA
4
2
0
-2
-4
-6
-8
PERCENTAGE DIFFERENCE FROM NORTHCLIFFE/SCHILLING
1
10
ENERGY (MEV)

Figure 23

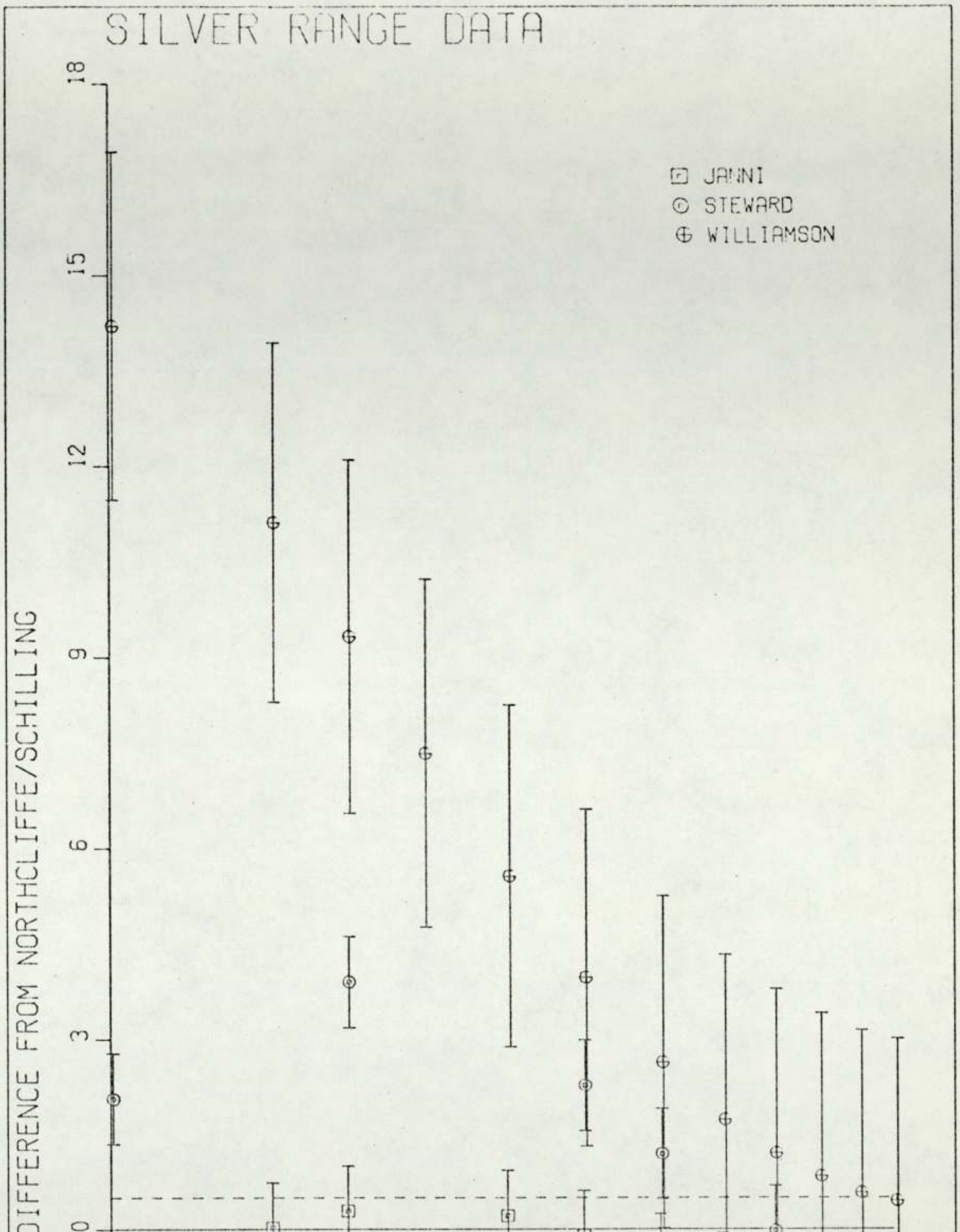
SILVER RANGE DATA
JANNI
STEWARD
WILLIAMSON
PERCENTAGE DIFFERENCE FROM NORTHCLIFFE/SCHILLING
18
15
12
9
6
3
0
-3
1
10
ENERGY (MEV)

Figure 24

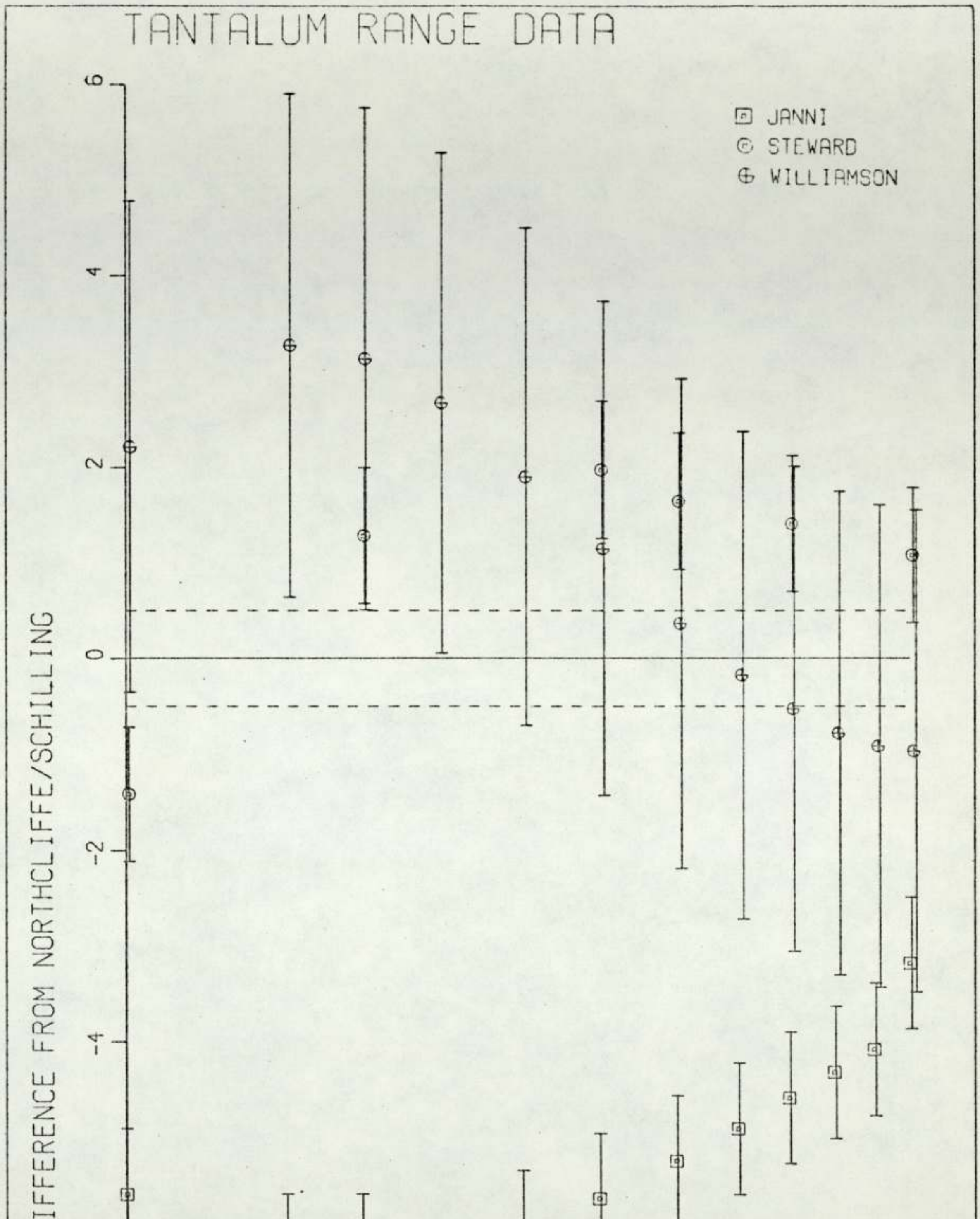
TANTALUM RANGE DATA
JANNI
STEWARD
WILLIAMSON
PERCENTAGE DIFFERENCE FROM NORTHCLIFFE/SCHILLING
6
4
2
0
-2
-4
-6
-8
1
10
ENERGY (MEV)

Figure 25

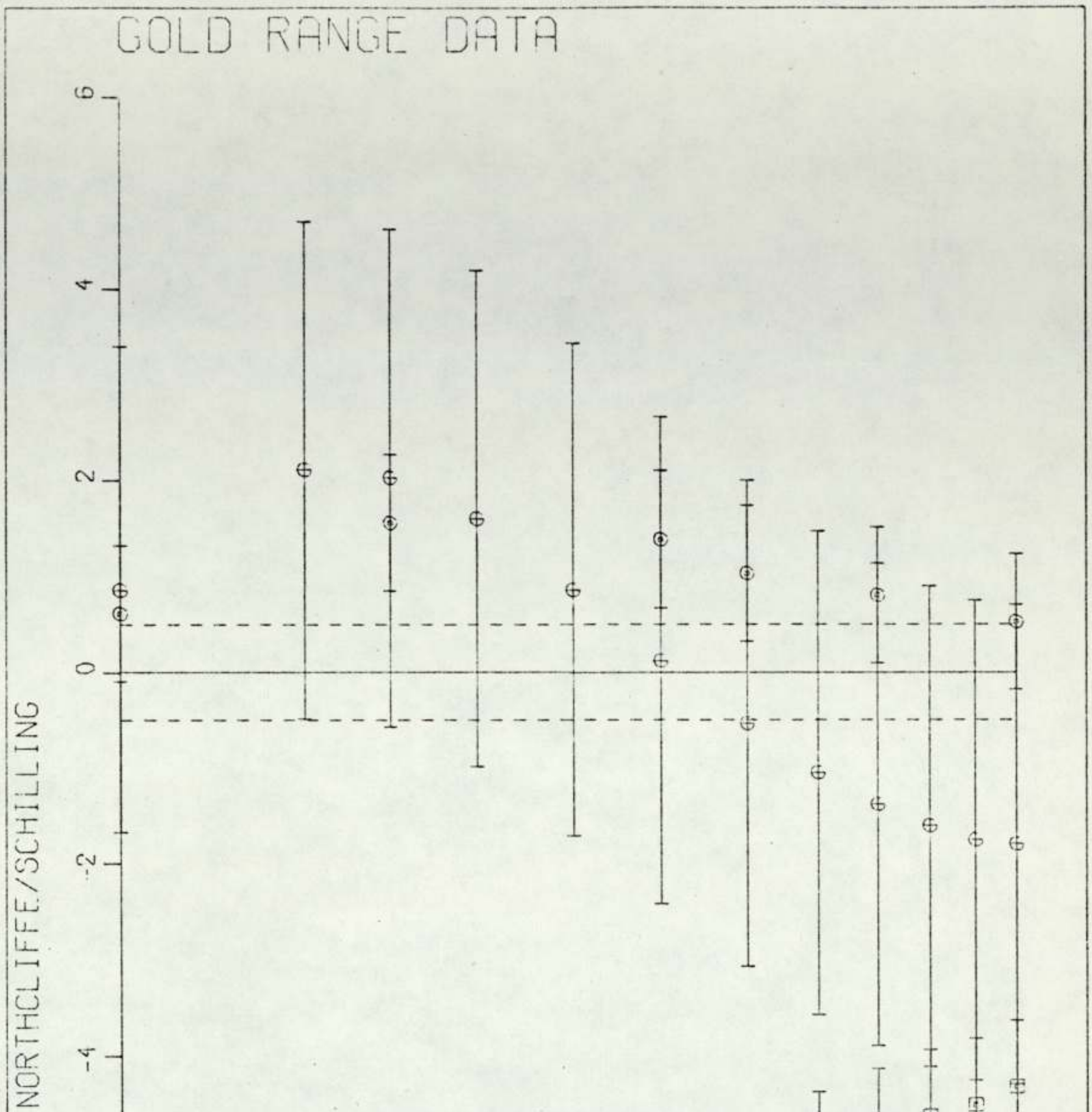
GOLD RANGE DATA
PERCENTAGE DIFFERENCE FROM NORTHCLIFFE/SCHILLING
6
4
2
0
-2
-4
-6
-8
-10
1
10
ENERGY (MEV)
⊡ JANNI
⊙ STEWARD
⊕ WILLIAMSON

Figure 26

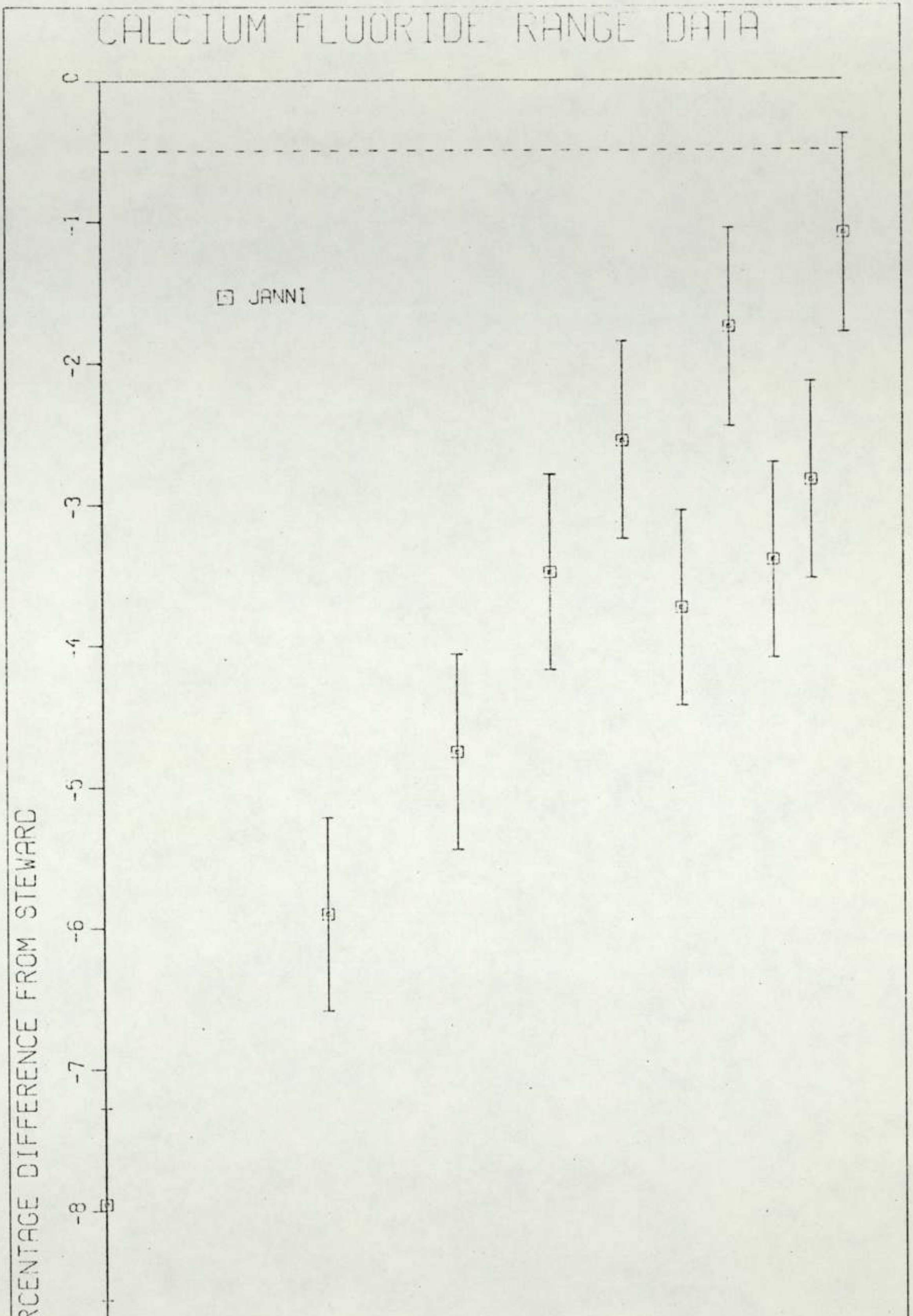
CALCIUM FLUORIDE RANGE DATA
JANNI
PERCENTAGE DIFFERENCE FROM STEWARD
0
-1
-2
-3
-4
-5
-6
-7
-8
-9
1
10
ENERGY (MEV)

Figure 27

Appendix IV

Comparison of Stopping Power Data

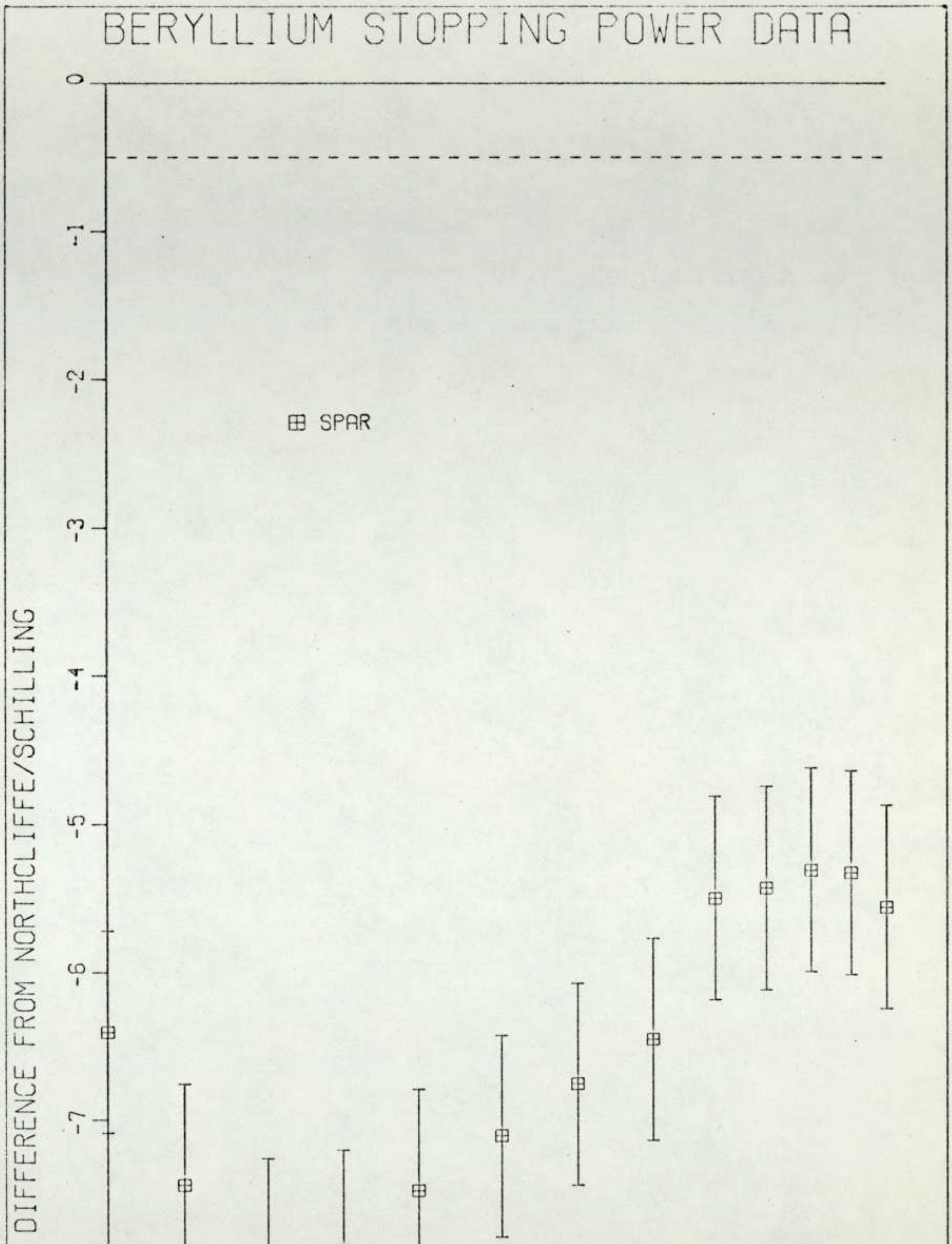
BERYLLIUM STOPPING POWER DATA
⊞ SPAR
PERCENTAGE DIFFERENCE FROM NORTHCLIFFE/SCHILLING
0
-1
-2
-3
-4
-5
-6
-7
-8
-9
10^{-1}
1
ENERGY (MEV)

Figure 1

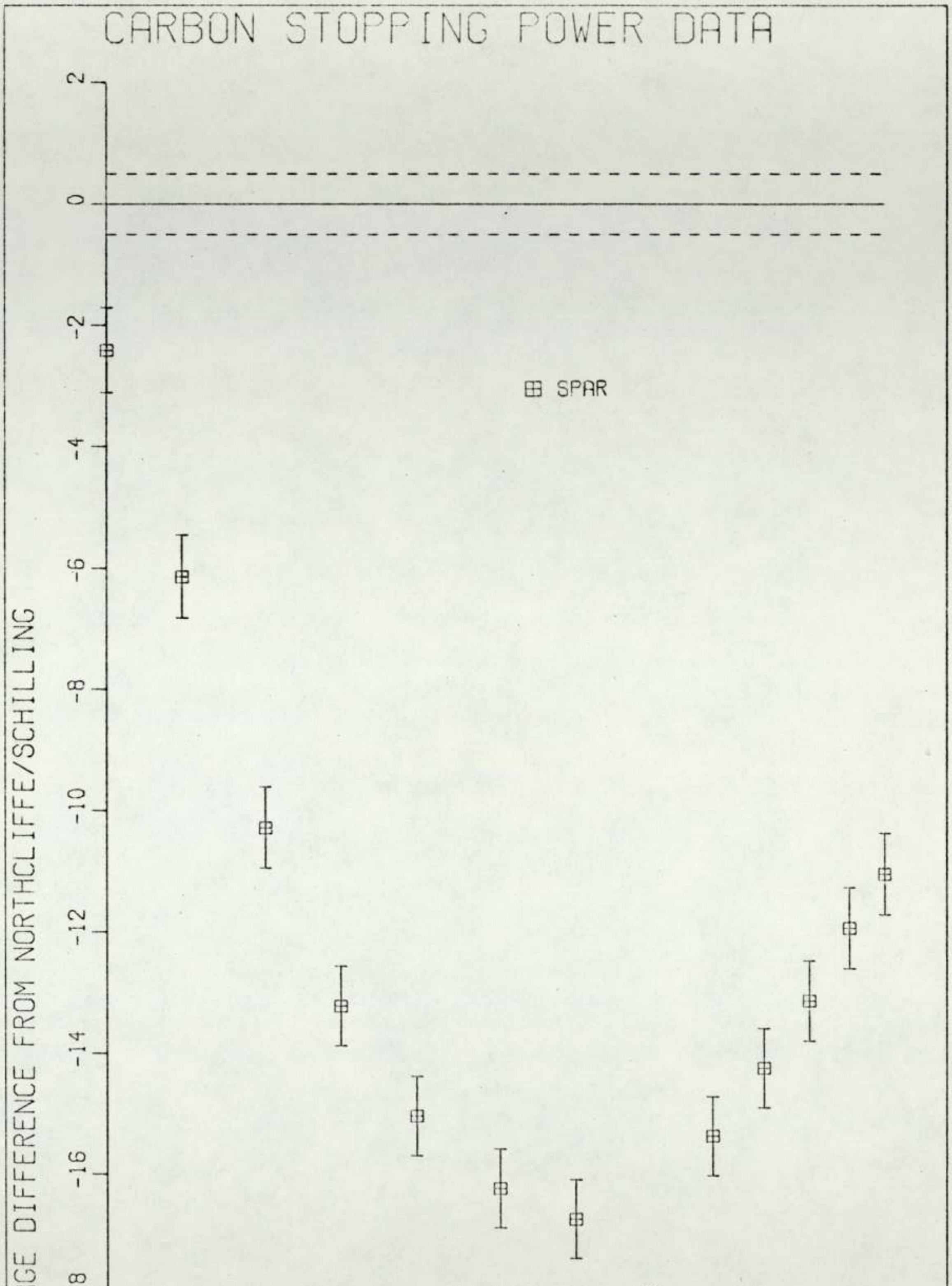
CARBON STOPPING POWER DATA
2
0
-2
-4
-6
-8
-10
-12
-14
-16
-18
-20
PERCENTAGE DIFFERENCE FROM NORTHCLIFFE/SCHILLING
⊞ SPAR
10⁻¹
1
ENERGY (MEV)

Figure 2

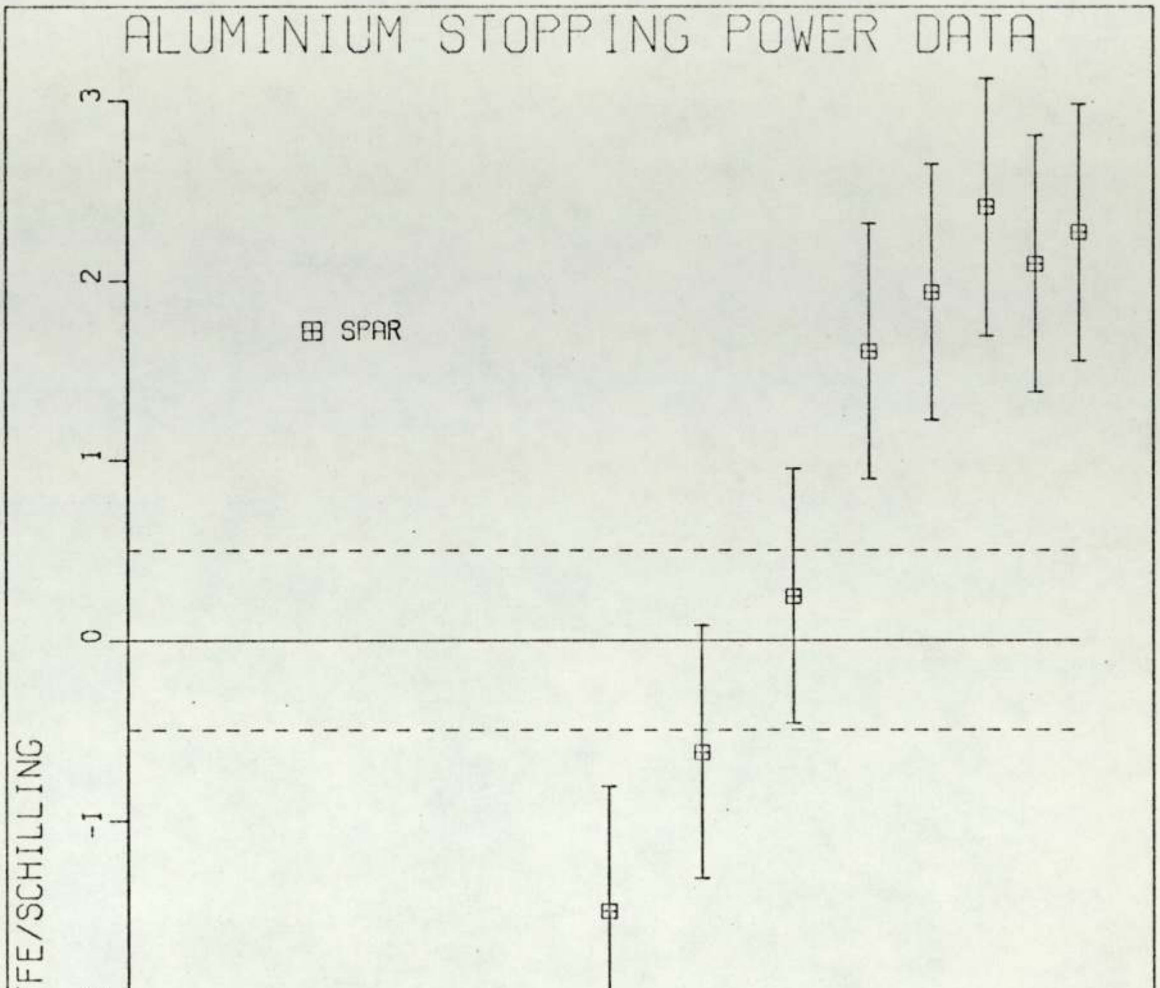
ALUMINIUM STOPPING POWER DATA
⊞ SPAR
PERCENTAGE DIFFERENCE FROM NORTHCLIFFE/SCHILLING
3
2
1
0
-1
-2
-3
-4
-5
-6
10^{-1}
1
ENERGY (MEV)

Figure 3

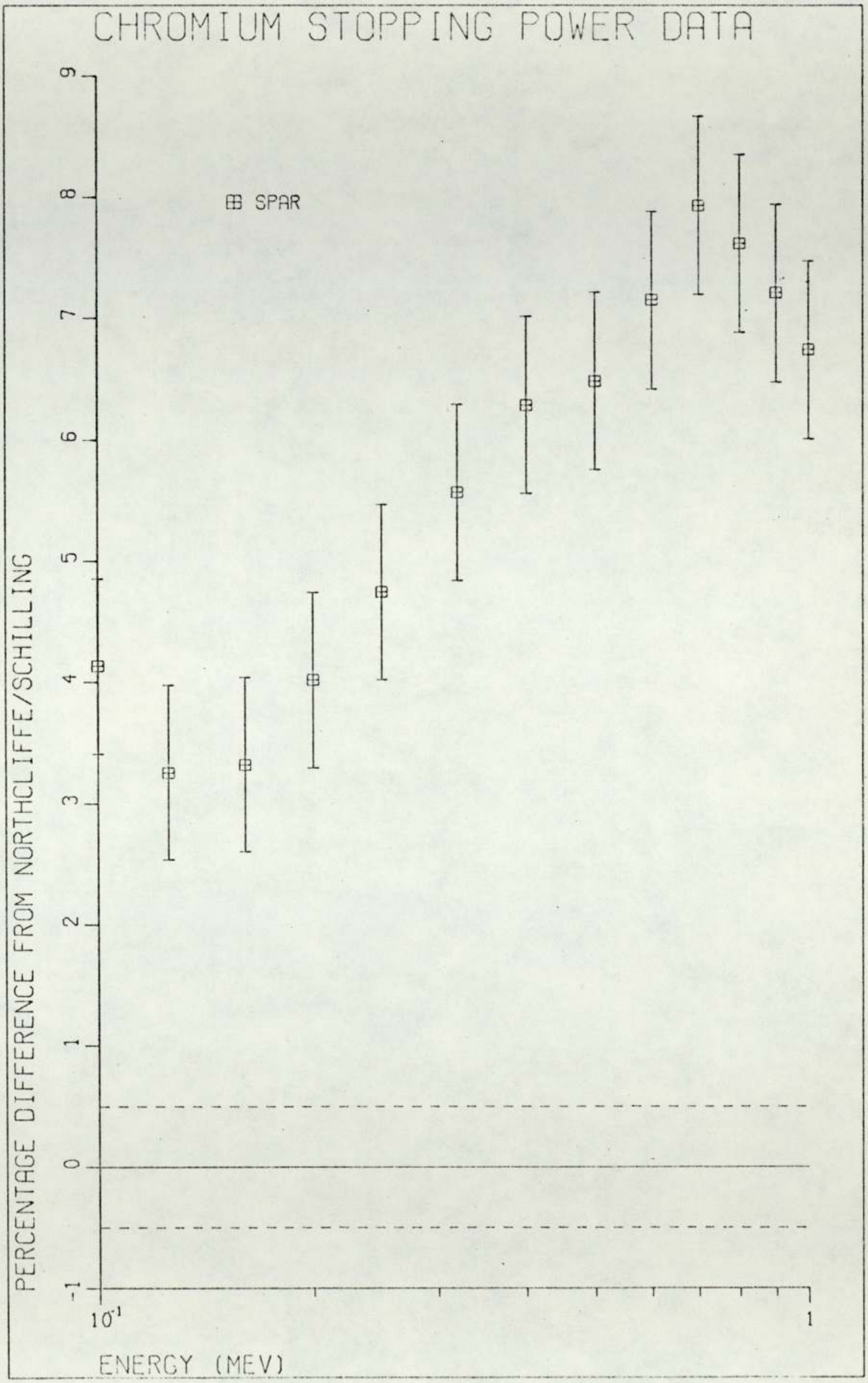
CHROMIUM STOPPING POWER DATA
PERCENTAGE DIFFERENCE FROM NORTHCLIFFE/SCHILLING
⊞ SPAR
9
8
7
6
5
4
3
2
1
0
-1
10^{-1}
1
ENERGY (MEV)

Figure 4

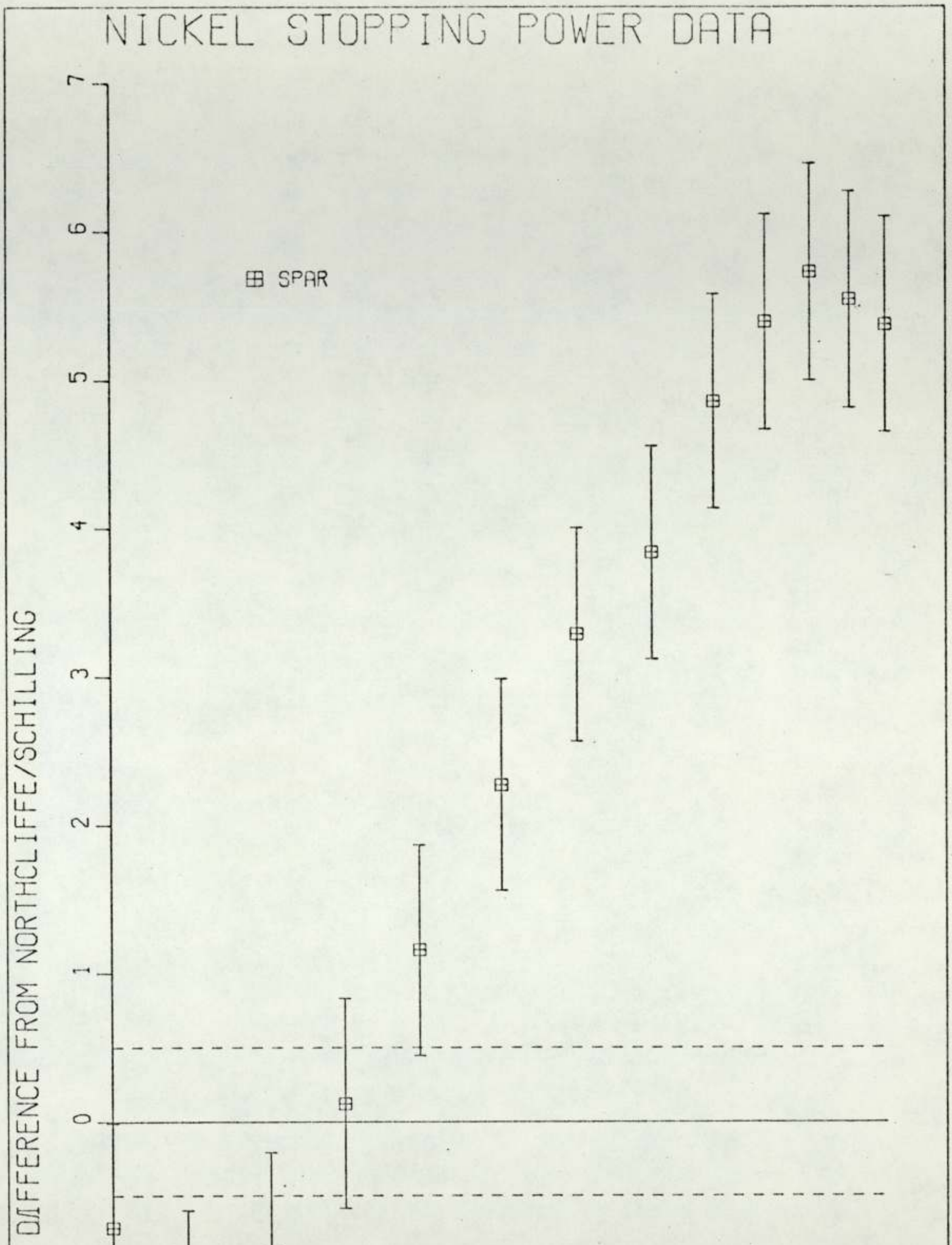
NICKEL STOPPING POWER DATA
PERCENTAGE DIFFERENCE FROM NORTHCLIFFE/SCHILLING
7
6
5
4
3
2
1
0
-1
-2
SPAR
10^{-1}
1
ENERGY (MEV)

Figure 5

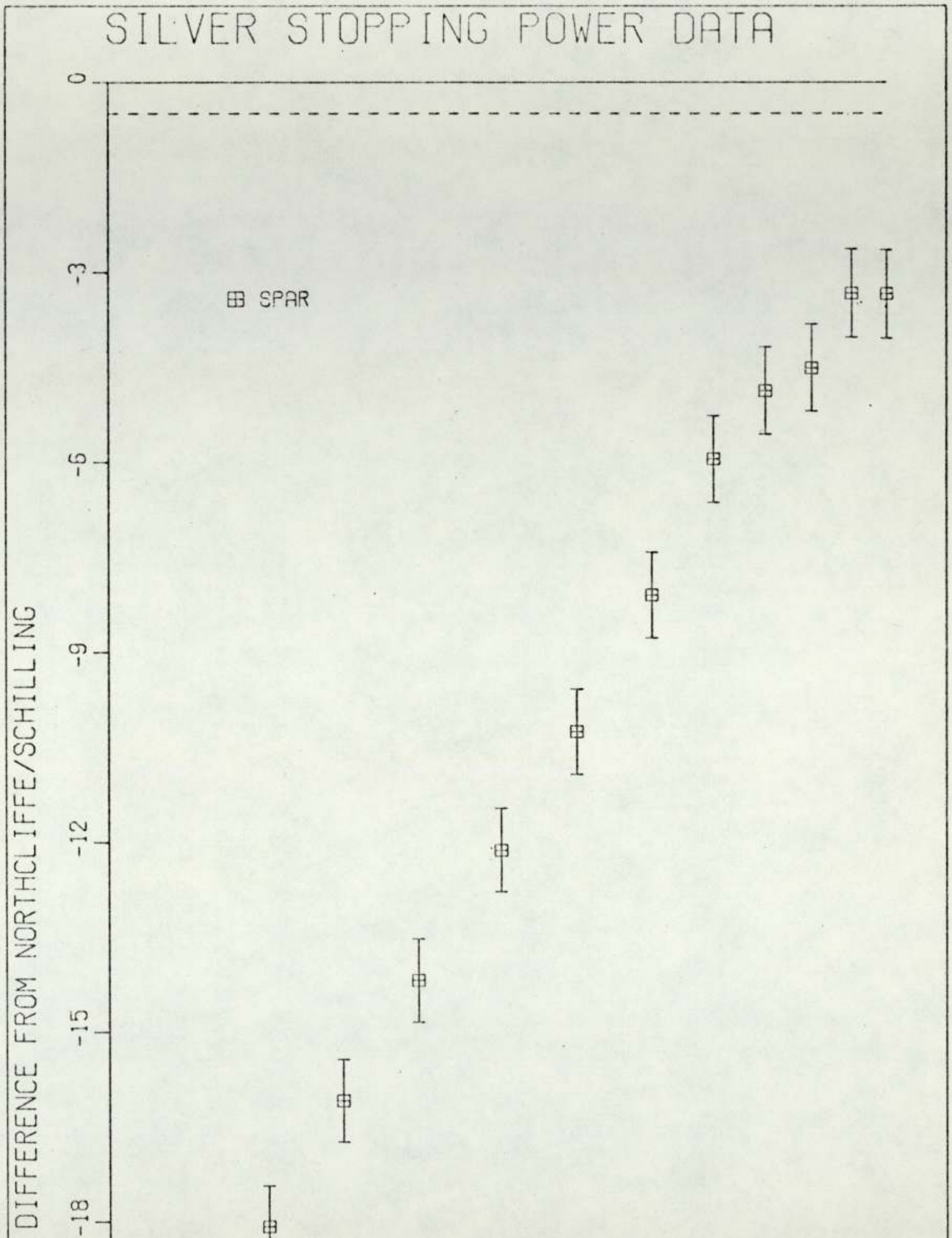
SILVER STOPPING POWER DATA
0
-3
-6
-9
-12
-15
-18
-21
⊞ SPAR
PERCENTAGE DIFFERENCE FROM NORTHCLIFFE/SCHILLING
10⁻¹
1
ENERGY (MEV)

Figure 6

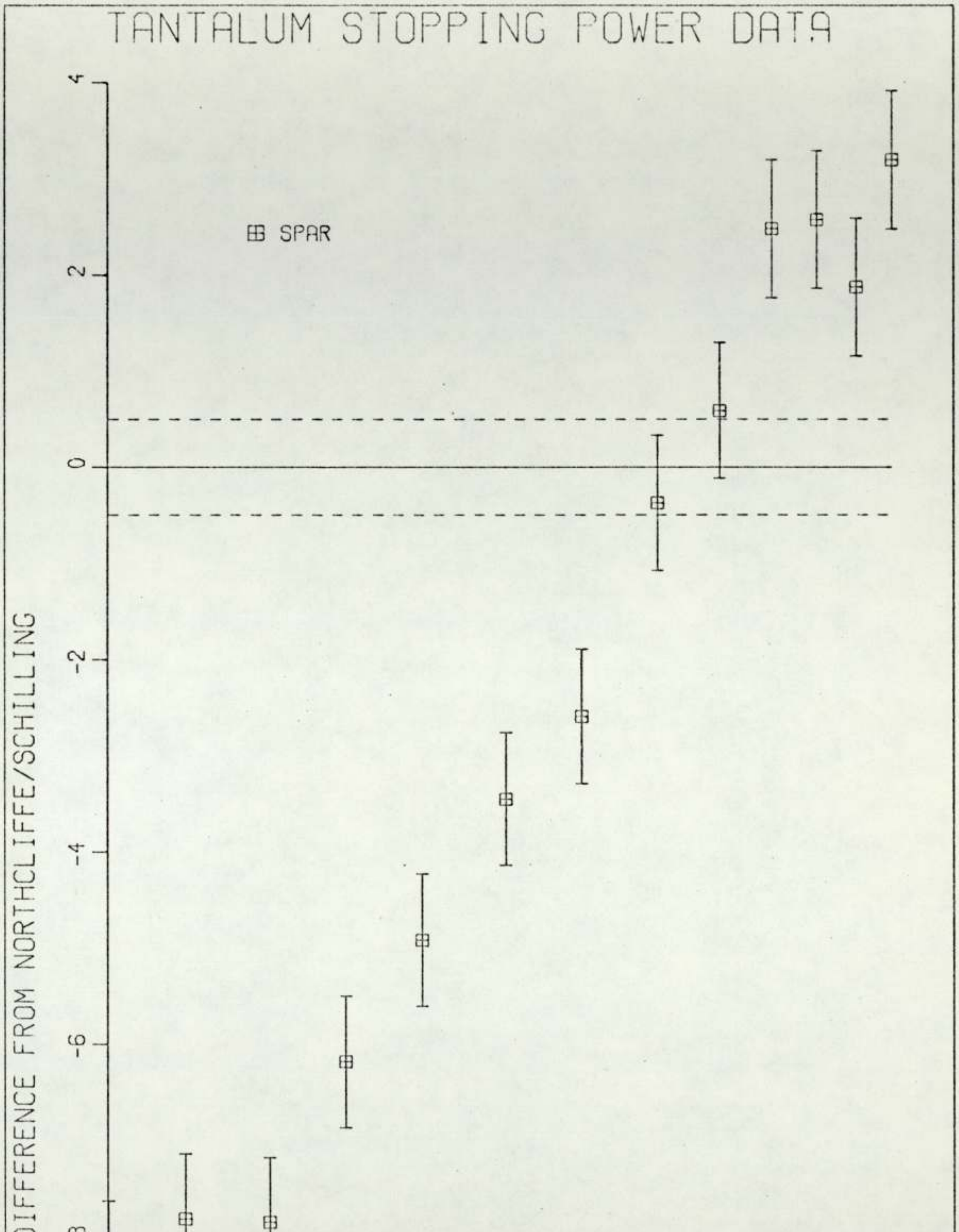
TANTALUM STOPPING POWER DATA
⊞ SPAR
PERCENTAGE DIFFERENCE FROM NORTHCLIFFE/SCHILLING
4
2
0
-2
-4
-6
-8
-10
10^{-1}
1
ENERGY (MEV)

Figure 7

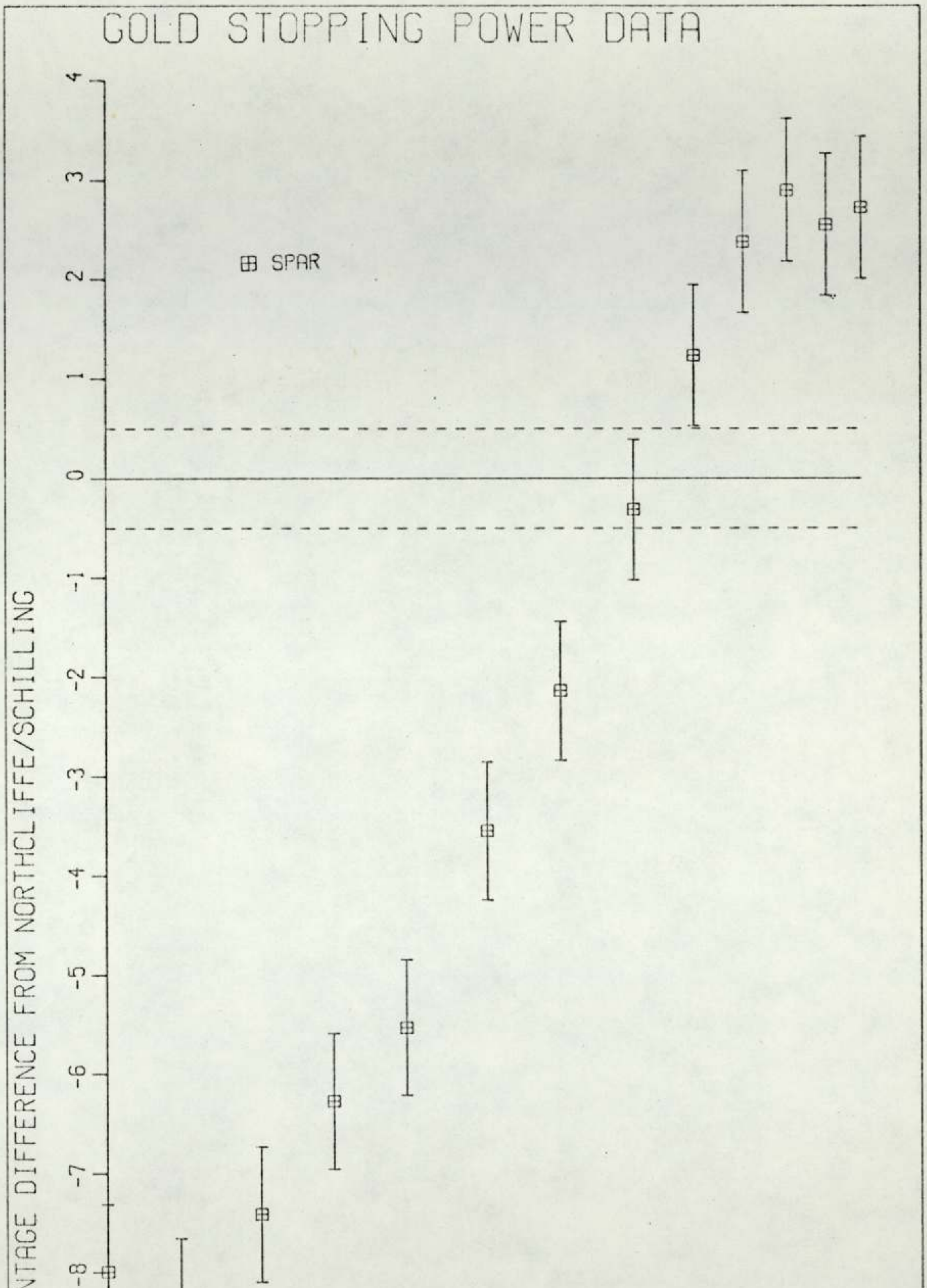
GOLD STOPPING POWER DATA
⊞ SPAR
PERCENTAGE DIFFERENCE FROM NORTHCLIFFE/SCHILLING
4
3
2
1
0
-1
-2
-3
-4
-5
-6
-7
-8
-9
10^{-1}
1
ENERGY (MEV)

Figure 8

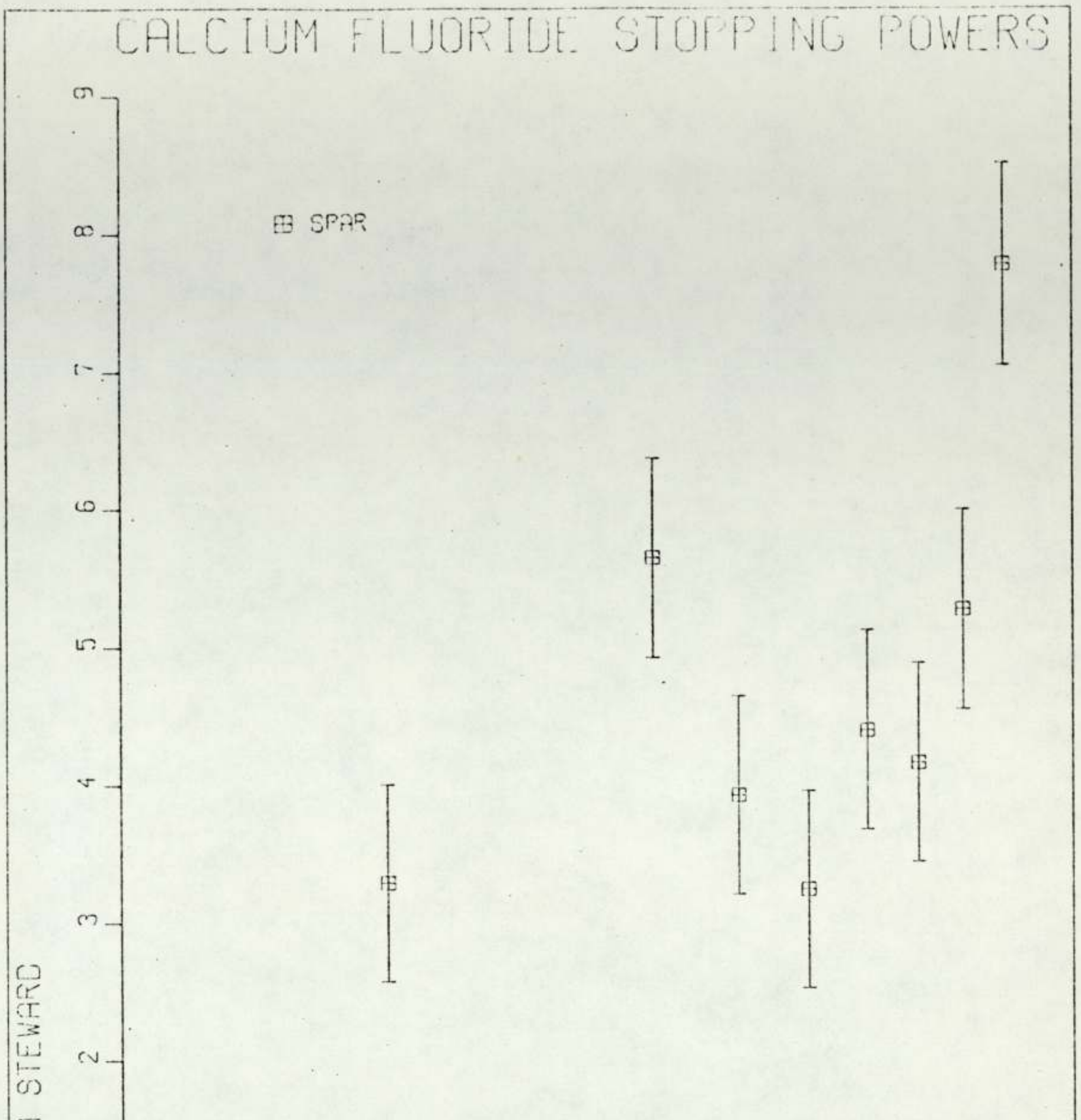
CALCIUM FLUORIDE STOPPING POWERS
⊞ SPAR
PERCENTAGE DIFFERENCE FROM STEWARD
9
8
7
6
5
4
3
2
1
0
-1
-2
10^1
1
ENERGY (MEV)

Figure 9

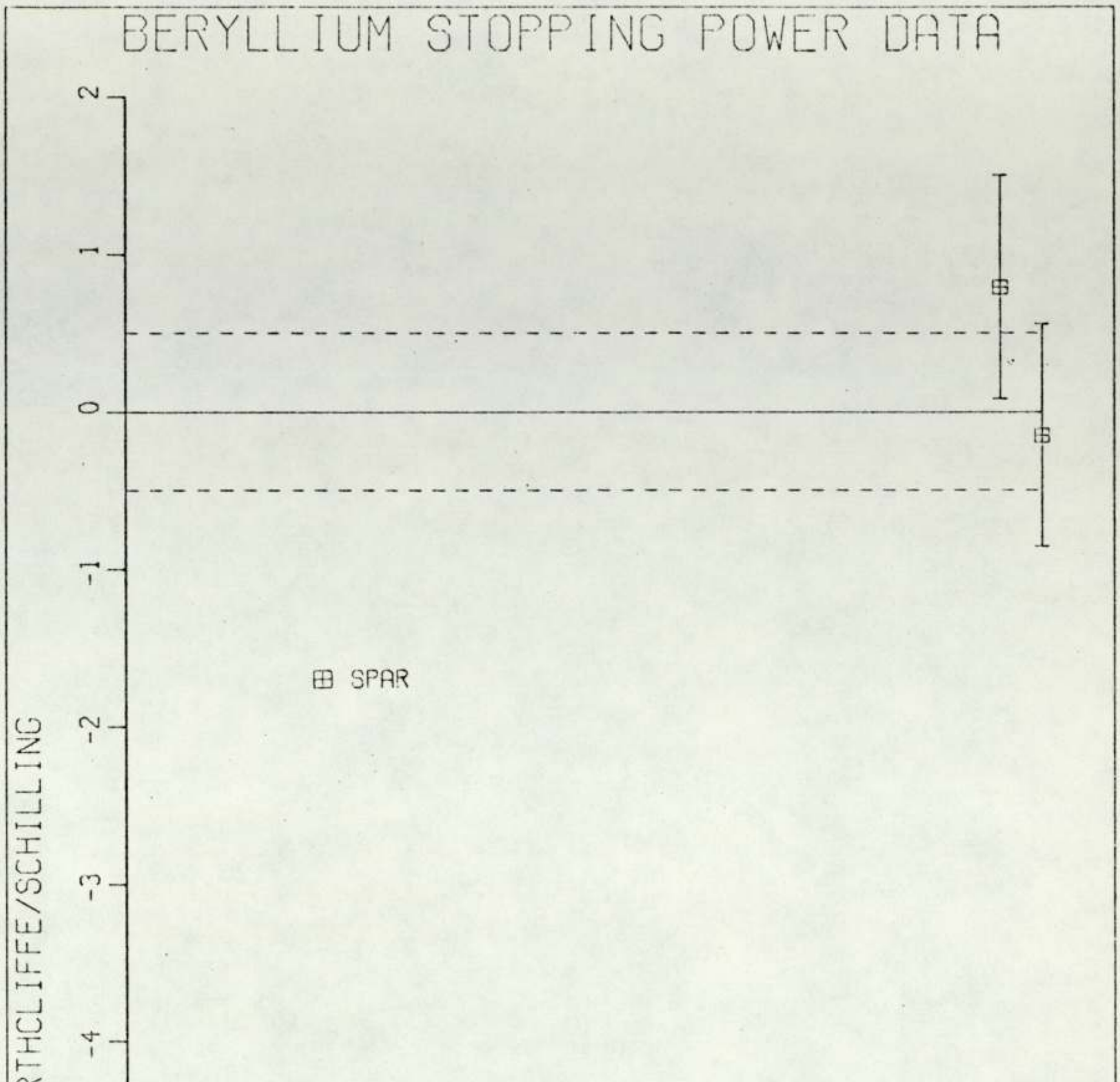
BERYLLIUM STOPPING POWER DATA
PERCENTAGE DIFFERENCE FROM NORTHCLIFFE/SCHILLING
2
1
0
-1
-2
-3
-4
-5
-6
-7
-8
⊞ SPAR
1
10
ENERGY (MEV)

Figure 10

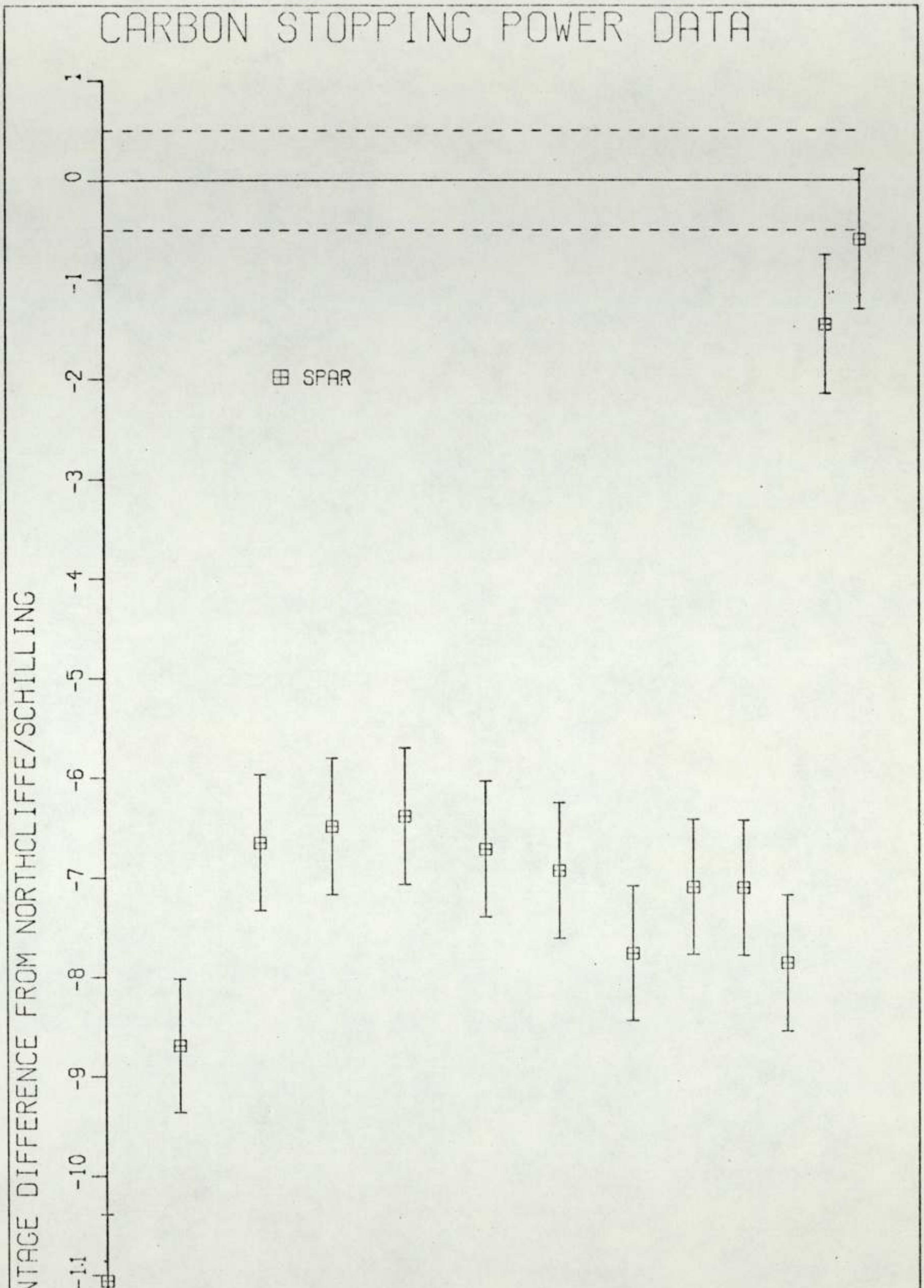
CARBON STOPPING POWER DATA
PERCENTAGE DIFFERENCE FROM NORTHCLIFFE/SCHILLING
ENERGY (MEV)
⊞ SPAR
1
0
-1
-2
-3
-4
-5
-6
-7
-8
-9
-10
-11
-12
1
10

Figure 11

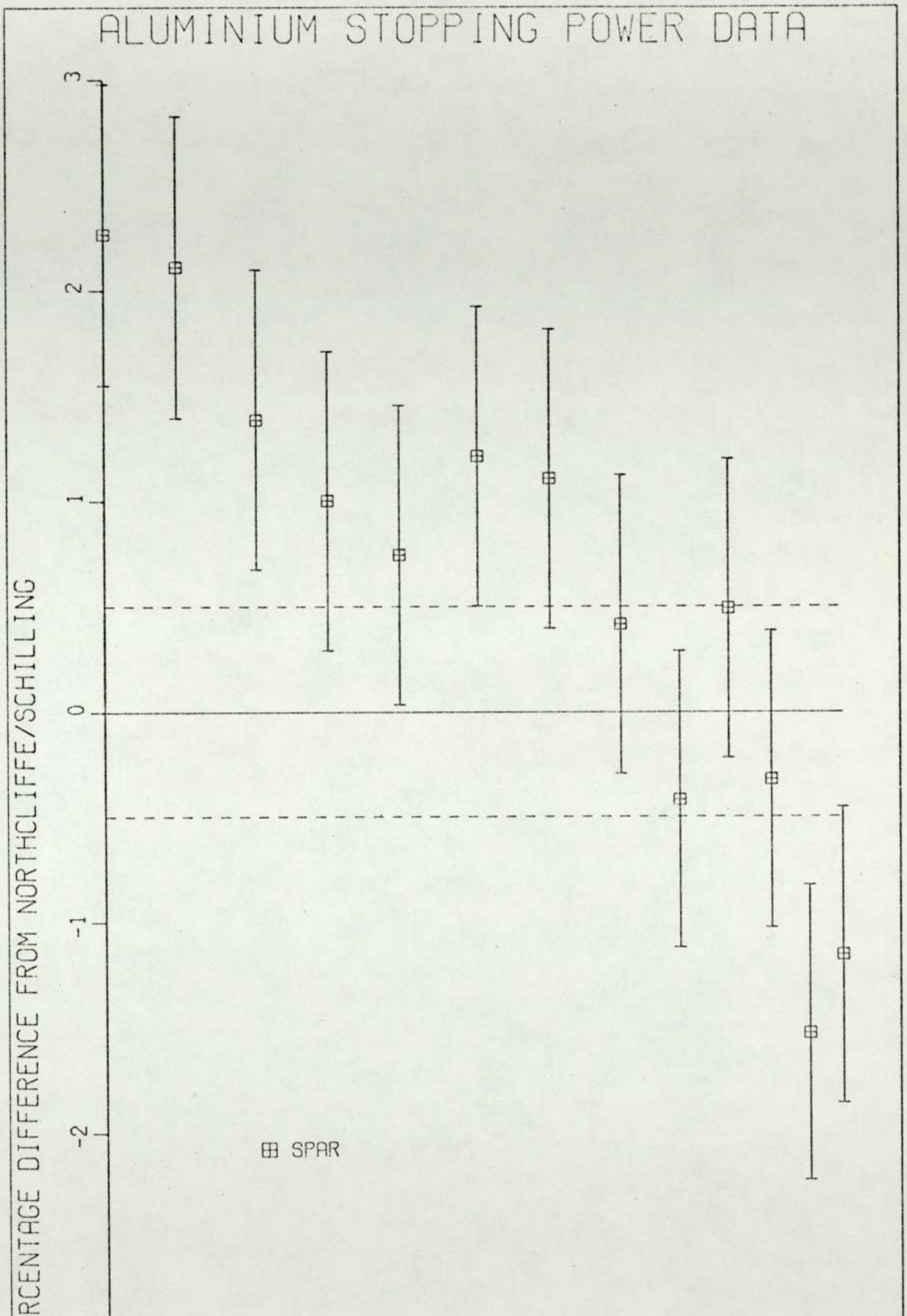
ALUMINIUM STOPPING POWER DATA
PERCENTAGE DIFFERENCE FROM NORTHCLIFFE/SCHILLING
3
2
1
0
-1
-2
-3
⊞ SPAR
1
10
ENERGY (MEV)

Figure 12

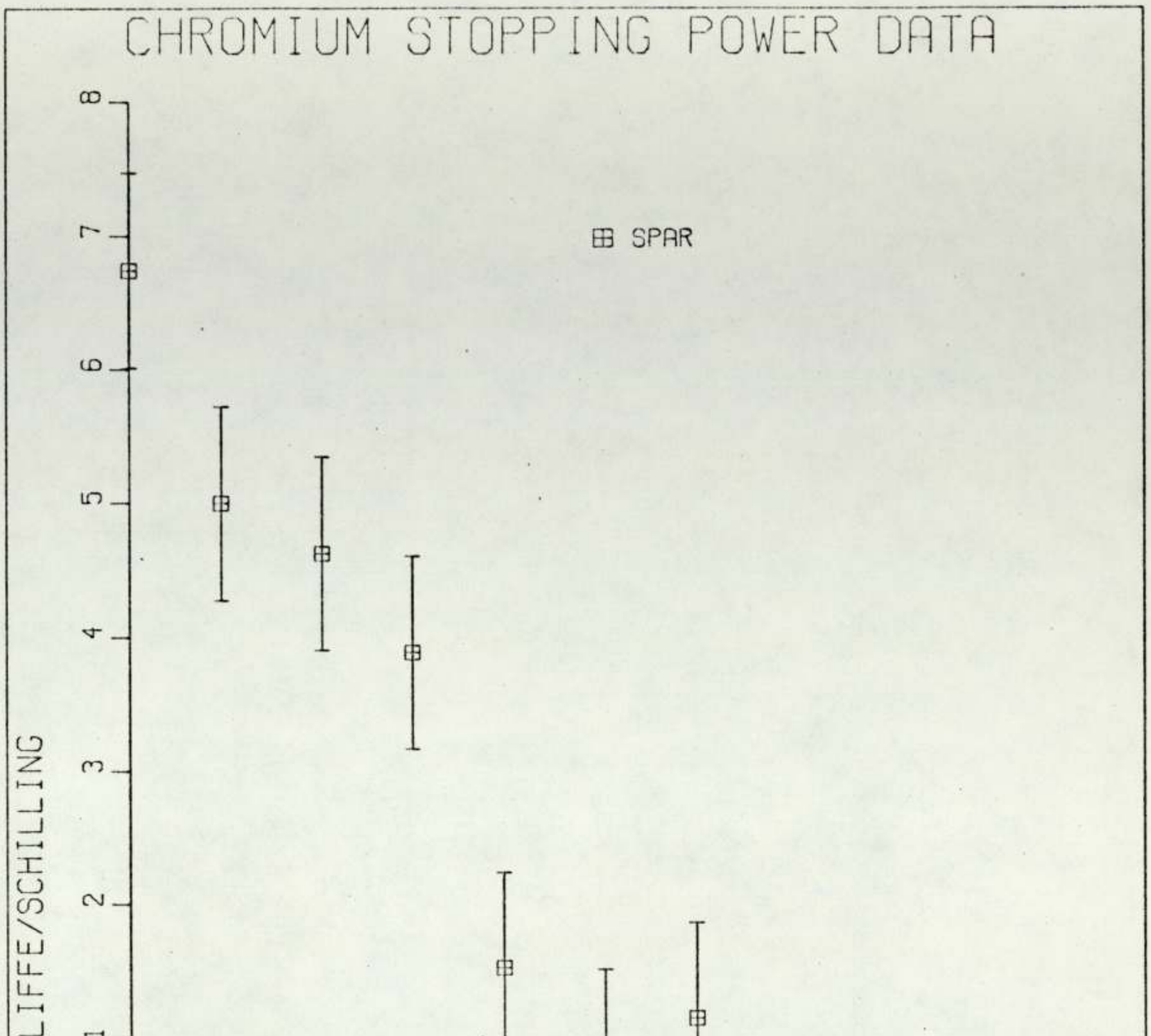
CHROMIUM STOPPING POWER DATA
⊞ SPAR
PERCENTAGE DIFFERENCE FROM NORTHCLIFFE/SCHILLING
8
7
6
5
4
3
2
1
0
-1
-2
-3
-4
1
10
ENERGY (MEV)

Figure 13

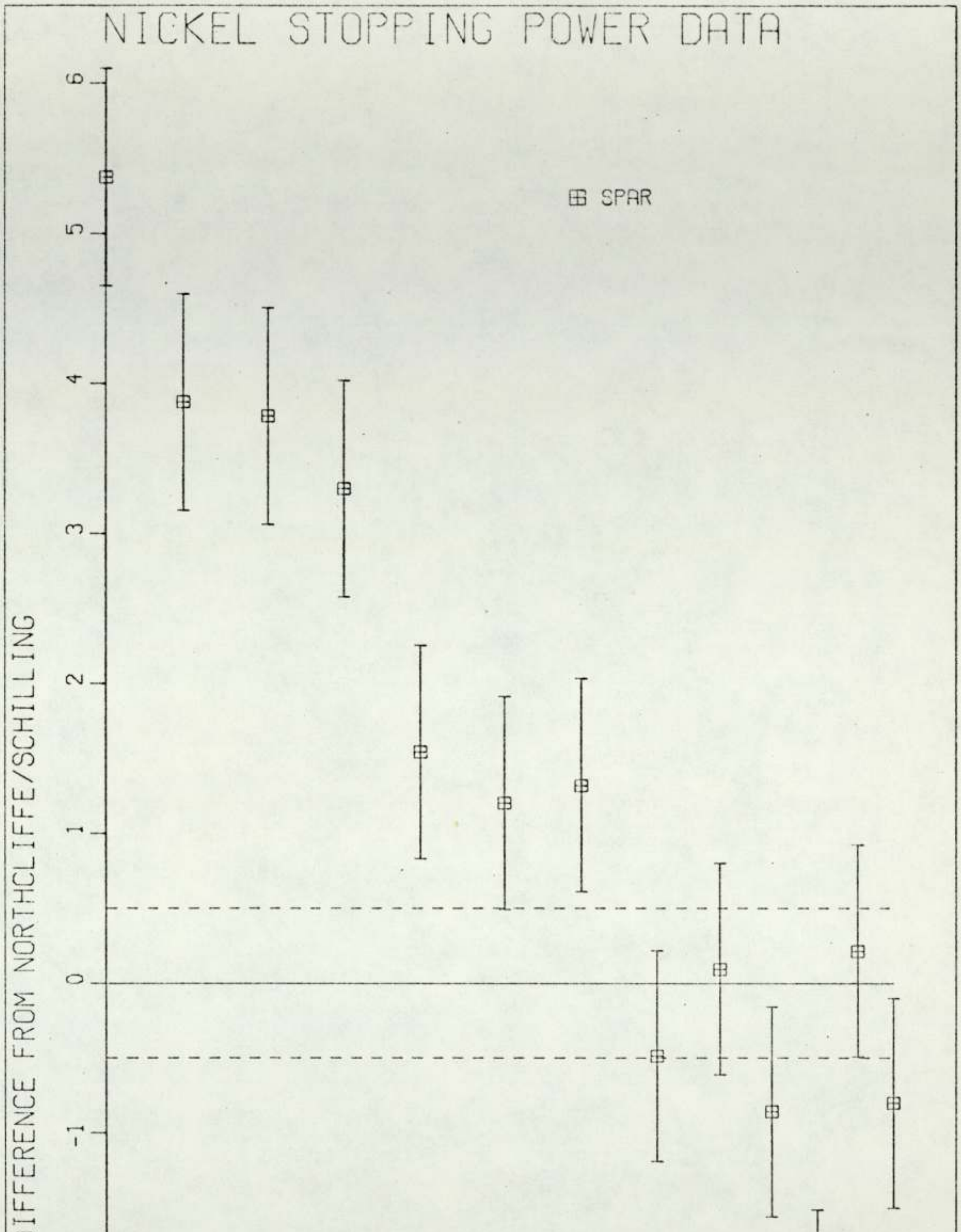
NICKEL STOPPING POWER DATA
⊞ SPAR
PERCENTAGE DIFFERENCE FROM NORTHCLIFFE/SCHILLING
6
5
4
3
2
1
0
-1
-2
-3
1
10
ENERGY (MEV)

Figure 14

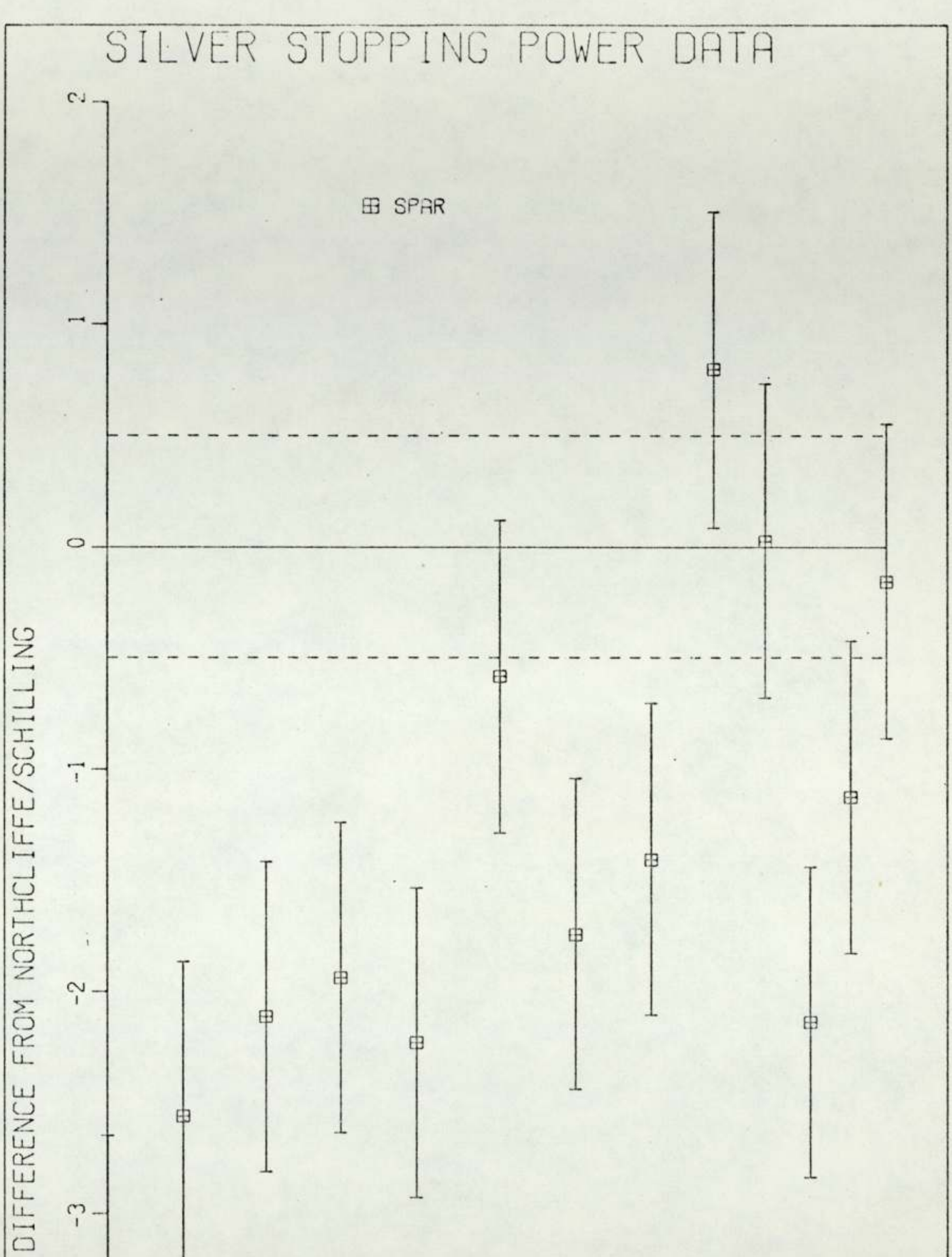
SILVER STOPPING POWER DATA
⊞ SPAR
PERCENTAGE DIFFERENCE FROM NORTHCLIFFE/SCHILLING
2
1
0
-1
-2
-3
-4
1
10
ENERGY (MEV)

Figure 15

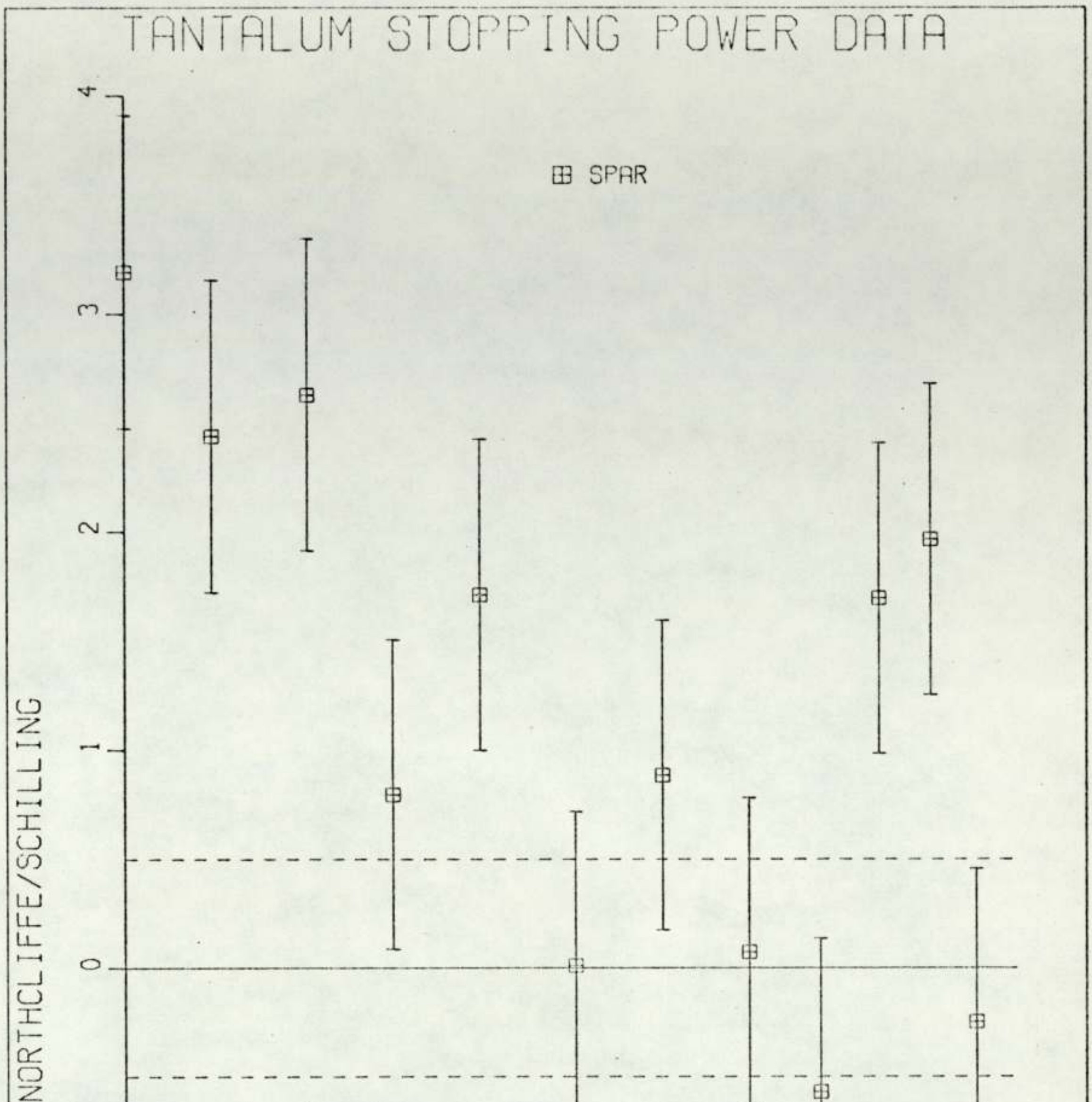
TANTALUM STOPPING POWER DATA
⊞ SPAR
PERCENTAGE DIFFERENCE FROM NORTHCLIFFE/SCHILLING
4
3
2
1
0
-1
-2
-3
1
10
ENERGY (MEV)

Figure 16

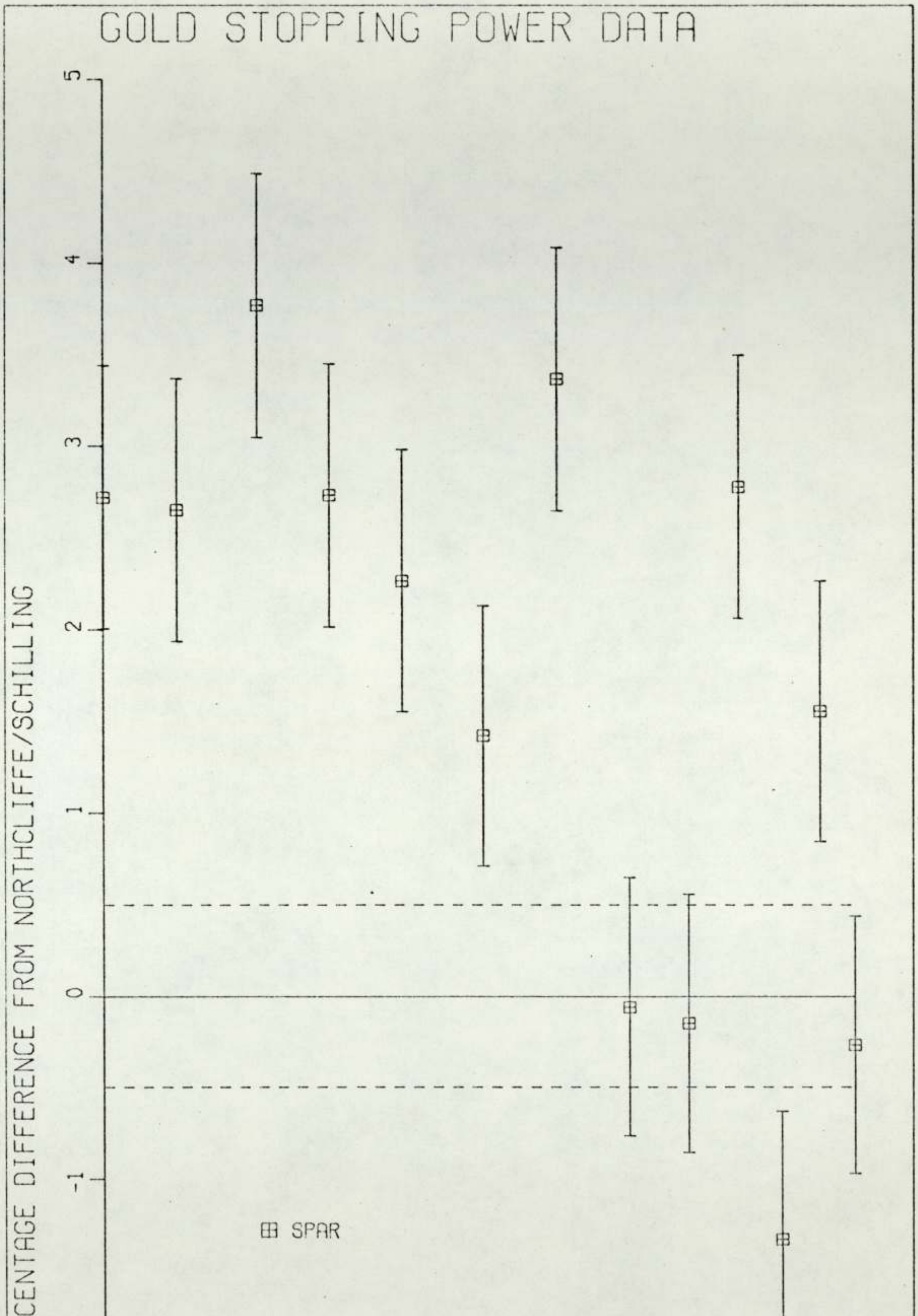
GOLD STOPPING POWER DATA
PERCENTAGE DIFFERENCE FROM NORTHCLIFFE/SCHILLING
5
4
3
2
1
0
-1
-2
1
10
ENERGY (MEV)
⊞ SPAR

Figure 17

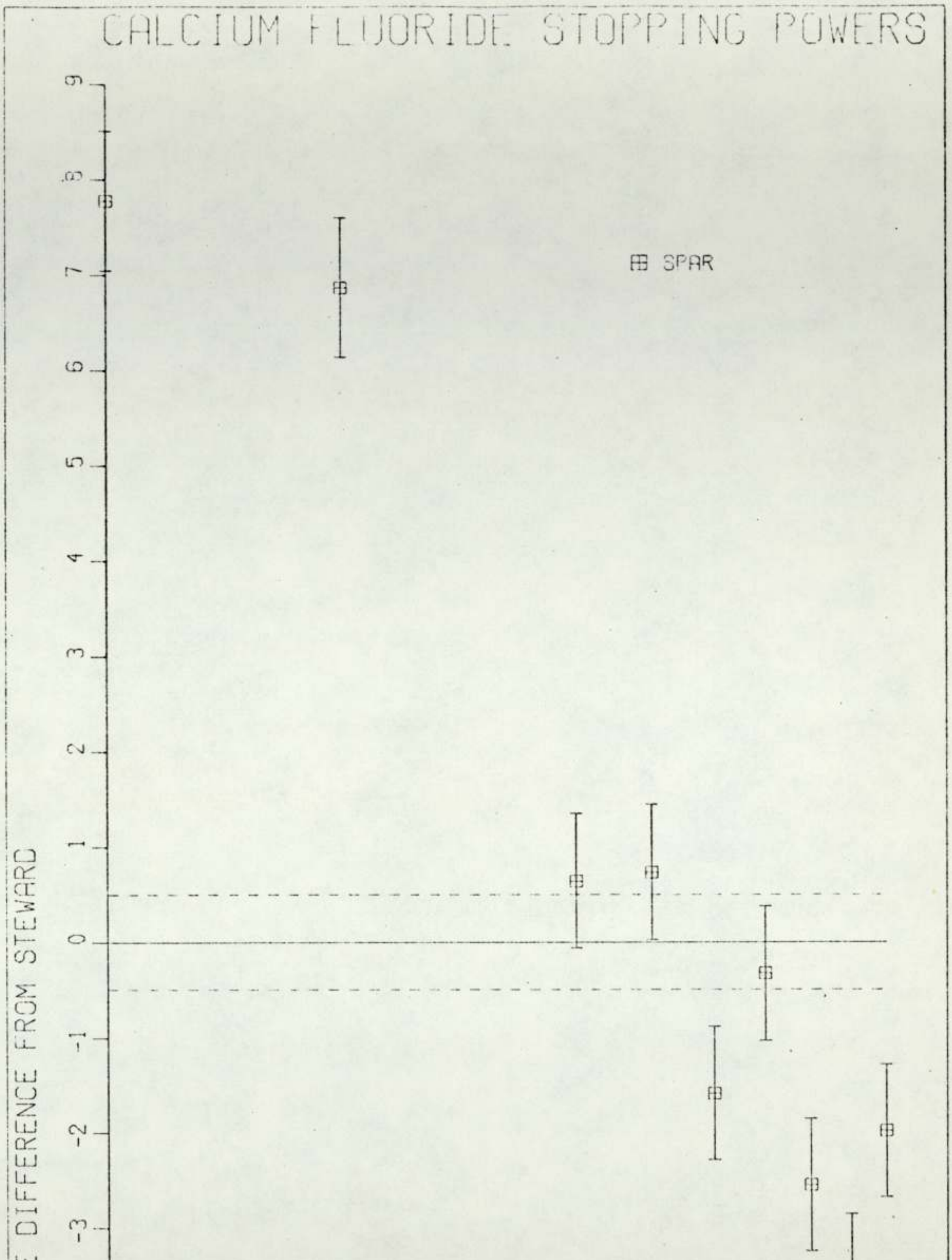
CALCIUM FLUORIDE STOPPING POWERS
PERCENTAGE DIFFERENCE FROM STEWARD
9
8
7
6
5
4
3
2
1
0
-1
-2
-3
-4
-5
1
10
ENERGY (MEV)
⊞ SPAR

Figure 18

SPECIMEN OUTPUT FROM PROGRAMME SPAR

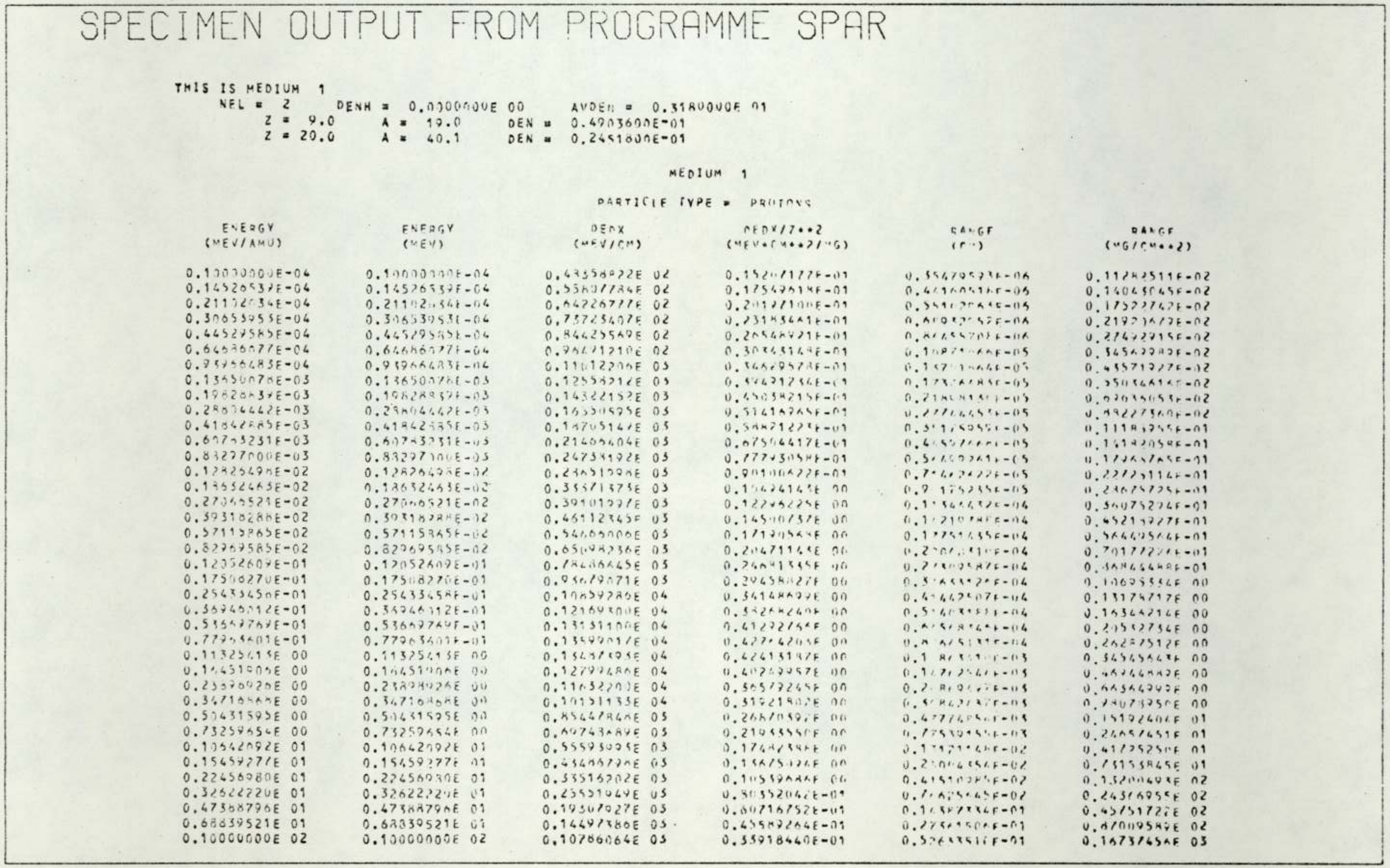

```
THIS IS MEDIUM  1
     NEL =  2      DENH =  0.00000000E 00      AVDEN =  0.31800000E 01
          Z =  9.0      A =  19.0      DEN =  0.49036000E-01
          Z = 20.0      A =  40.1      DEN =  0.24518000E-01

                                        MEDIUM  1

                                   PARTICLE TYPE =  PROTONS

     ENERGY            ENERGY            DEDX              DEDX/Z**2            RANGE             RANGE
   (MEV/AMU)           (MEV)           (MEV/CM)         (MEV*CM**2/MG)          (CM)           (MG/CM**2)

 0.10000000E-04    0.10000000E-04    0.48358822E 02    0.15207177E-01    0.35479573E-06    0.11282511E-02
 0.14526539E-04    0.14526539E-04    0.55807784E 02    0.17549618E-01    0.44166516E-06    0.14045045E-02
 0.21102034E-04    0.21102034E-04    0.64226777E 02    0.20197100E-01    0.55103026E-06    0.17522762E-02
 0.30653953E-04    0.30653953E-04    0.73723407E 02    0.23183461E-01    0.68936057E-06    0.21921672E-02
 0.44529585E-04    0.44529585E-04    0.84425549E 02    0.26548921E-01    0.86455701E-06    0.27492915E-02
 0.64686077E-04    0.64686077E-04    0.96491210E 02    0.30343149E-01    0.10868866E-05    0.34562983E-02
 0.93966483E-04    0.93966483E-04    0.11012206E 03    0.34629578E-01    0.13701864E-05    0.43571927E-02
 0.13650078E-03    0.13650078E-03    0.12558212E 03    0.39491234E-01    0.17306748E-05    0.55035461E-02
 0.19828837E-03    0.19828837E-03    0.14322152E 03    0.45038215E-01    0.21897815E-05    0.69635053E-02
 0.28804442E-03    0.28804442E-03    0.16350595E 03    0.51416765E-01    0.27744453E-05    0.88227360E-02
 0.41842585E-03    0.41842585E-03    0.18705147E 03    0.58821223E-01    0.35175955E-05    0.11185955E-01
 0.60783231E-03    0.60783231E-03    0.21466404E 03    0.67504417E-01    0.44629578E-05    0.14192058E-01
 0.88297000E-03    0.88297000E-03    0.24733192E 03    0.77777305E-01    0.55659261E-05    0.17696765E-01
 0.12826496E-02    0.12826496E-02    0.28651998E 03    0.90100622E-01    0.71462422E-05    0.22725114E-01
 0.18632463E-02    0.18632463E-02    0.33571373E 03    0.10557041E 00    0.90175235E-05    0.28675725E-01
 0.27066521E-02    0.27066521E-02    0.39101997E 03    0.12296225E 00    0.11344432E-04    0.36075224E-01
 0.39318288E-02    0.39318288E-02    0.46112345E 03    0.14500737E 00    0.14218078E-04    0.45213727E-01
 0.57115865E-02    0.57115865E-02    0.54665006E 03    0.17190566E 00    0.17751435E-04    0.56449564E-01
 0.82969585E-02    0.82969585E-02    0.65098236E 03    0.20471143E 00    0.22068310E-04    0.70177274E-01
 0.12052609E-01    0.12052609E-01    0.78486645E 03    0.24681345E 00    0.27315877E-04    0.86864488E-01
 0.17508270E-01    0.17508270E-01    0.93679071E 03    0.29458827E 00    0.33633755E-04    0.10695534E 00
 0.25433458E-01    0.25433458E-01    0.10859280E 04    0.34148697E 00    0.41442507E-04    0.13178717E 00
 0.36946112E-01    0.36946112E-01    0.12169300E 04    0.38268240E 00    0.51459793E-04    0.16364214E 00
 0.53669769E-01    0.53669769E-01    0.13131100E 04    0.41292764E 00    0.64631237E-04    0.20552734E 00
 0.77963601E-01    0.77963601E-01    0.13599017E 04    0.42764205E 00    0.82665133E-04    0.26287512E 00
 0.11325413E 00    0.11325413E 00    0.13487393E 04    0.42413187E 00    0.10863410E-03    0.34545643E 00
 0.16451906E 00    0.16451906E 00    0.12799486E 04    0.40249957E 00    0.14762541E-03    0.46944882E 00
 0.23898026E 00    0.23898026E 00    0.11632203E 04    0.36579245E 00    0.20869497E-03    0.66364993E 00
 0.34716868E 00    0.34716868E 00    0.10151133E 04    0.31921802E 00    0.30840865E-03    0.98073950E 00
 0.50431595E 00    0.50431595E 00    0.85447846E 03    0.26870392E 00    0.47774862E-03    0.15192406E 01
 0.73259654E 00    0.73259654E 00    0.69743689E 03    0.21931978E 00    0.77539155E-03    0.24657451E 01
 0.10642092E 01    0.10642092E 01    0.55593095E 03    0.17482105E 00    0.13121148E-02    0.41725250E 01
 0.15459277E 01    0.15459277E 01    0.43466779E 03    0.13668799E 00    0.23627624E-02    0.75135845E 01
 0.22456980E 01    0.22456980E 01    0.33516202E 03    0.10539686E 00    0.41510984E-02    0.13200493E 02
 0.32622220E 01    0.32622220E 01    0.25551949E 03    0.80352042E-01    0.76657091E-02    0.24376955E 02
 0.47388796E 01    0.47388796E 01    0.19307927E 03    0.60716752E-01    0.14387334E-01    0.45751722E 02
 0.68839521E 01    0.68839521E 01    0.14497386E 03    0.45589264E-01    0.27361506E-01    0.87009589E 02
 0.10000000E 02    0.10000000E 02    0.10786064E 03    0.33918440E-01    0.52633516E-01    0.16737456E 03
```

Figure 19

Appendix V

Comparison of Range Data

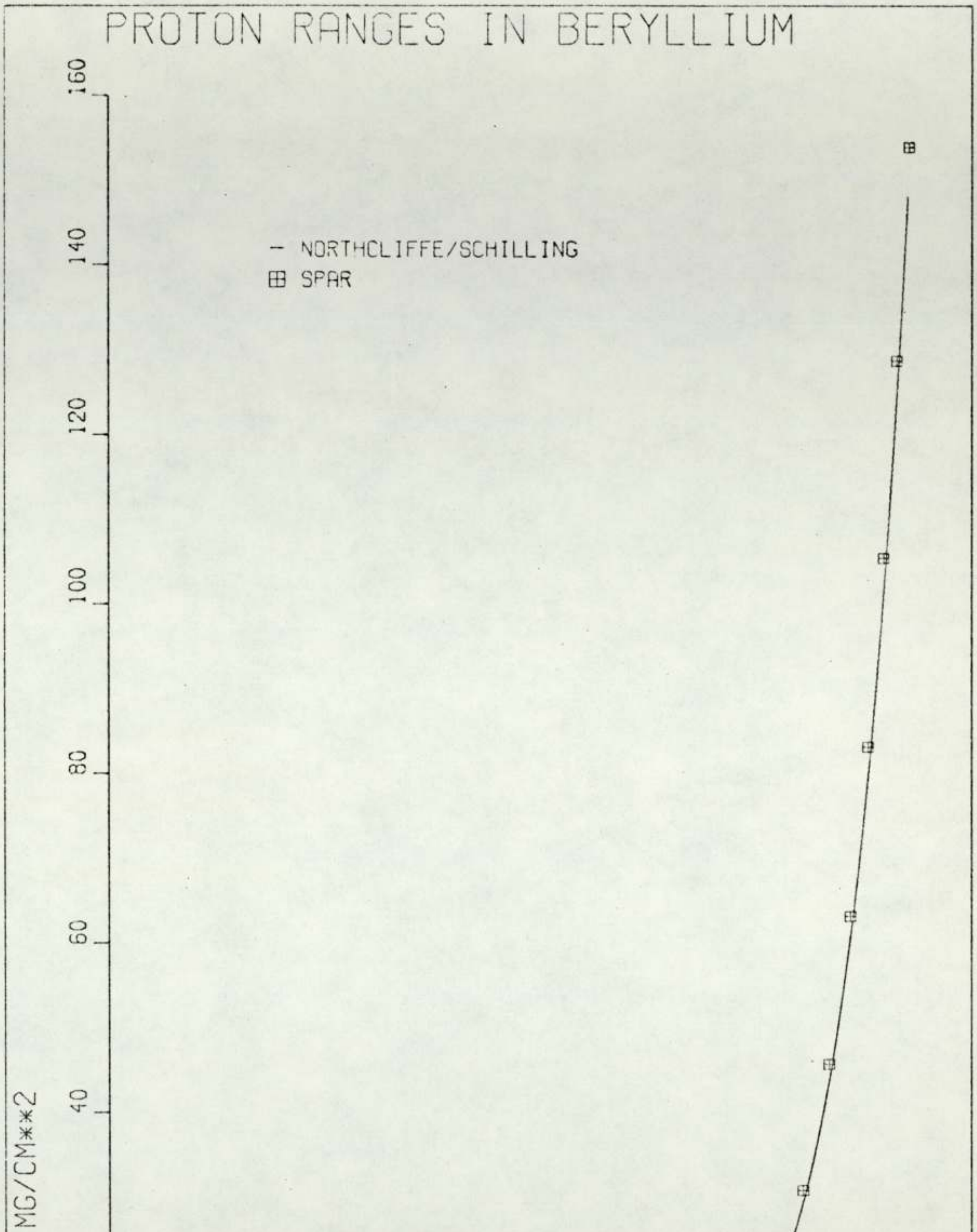
PROTON RANGES IN BERYLLIUM
- NORTHCLIFFE/SCHILLING
⊞ SPAR
PROTON RANGE MG/CM**2
0
20
40
60
80
100
120
140
160
10^2
10^1
1
10
ENERGY (MEV)

Figure 1

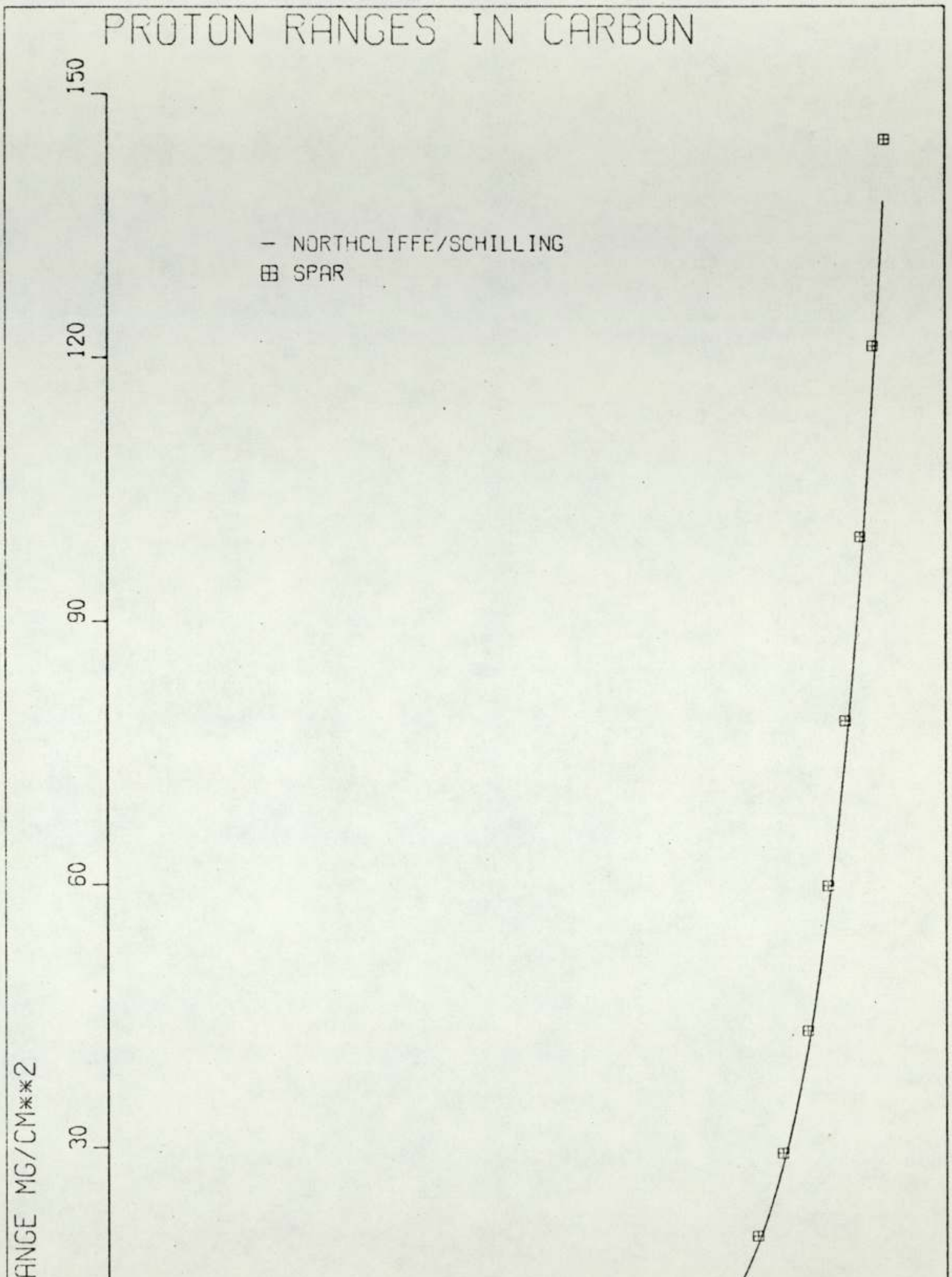
PROTON RANGES IN CARBON
- NORTHCLIFFE/SCHILLING
⊞ SPAR
PROTON RANGE MG/CM**2
0
30
60
90
120
150
10^{-2}
10^{-1}
1
10
ENERGY (MEV)

Figure 2

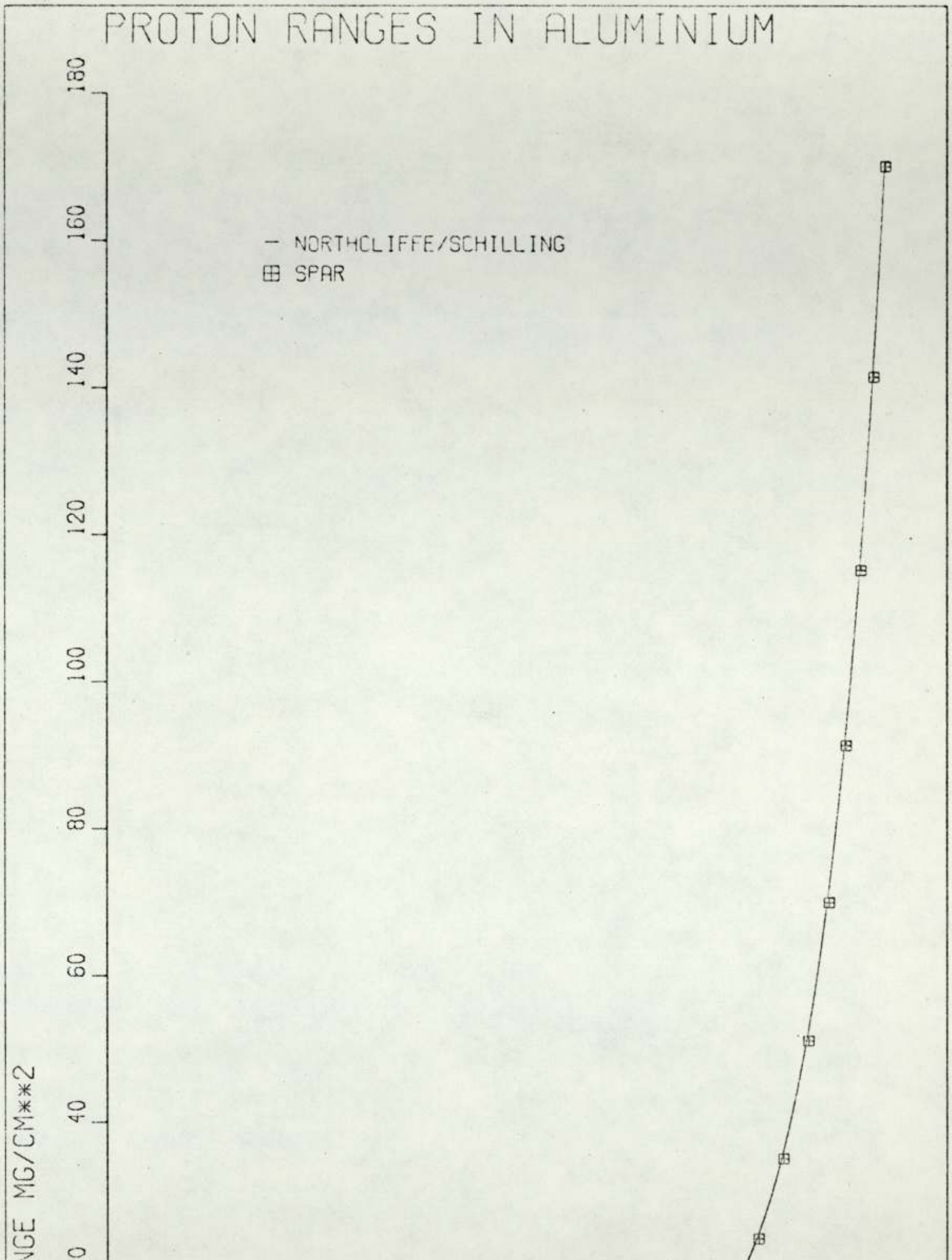
PROTON RANGES IN ALUMINIUM
— NORTHCLIFFE/SCHILLING
⊞ SPAR
PROTON RANGE MG/CM**2
0
20
40
60
80
100
120
140
160
180
10^{-2}
10^{-1}
1
10
ENERGY (MEV)

Figure 3

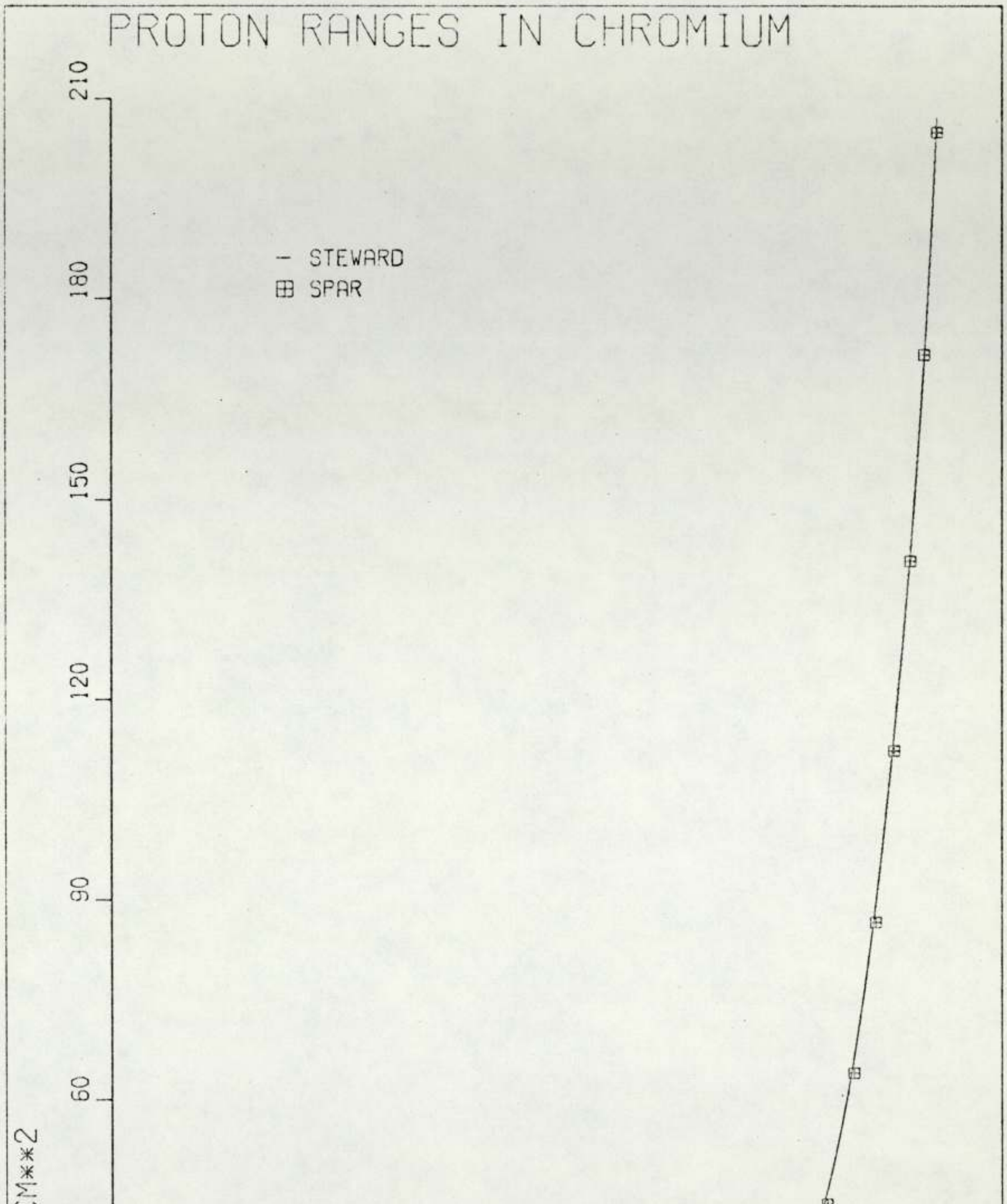
PROTON RANGES IN CHROMIUM
- STEWARD
⊞ SPAR
PROTON RANGE MG/CM**2
0
30
60
90
120
150
180
210
10^{-2}
10^{-1}
1
10
ENERGY (MEV)

Figure 4

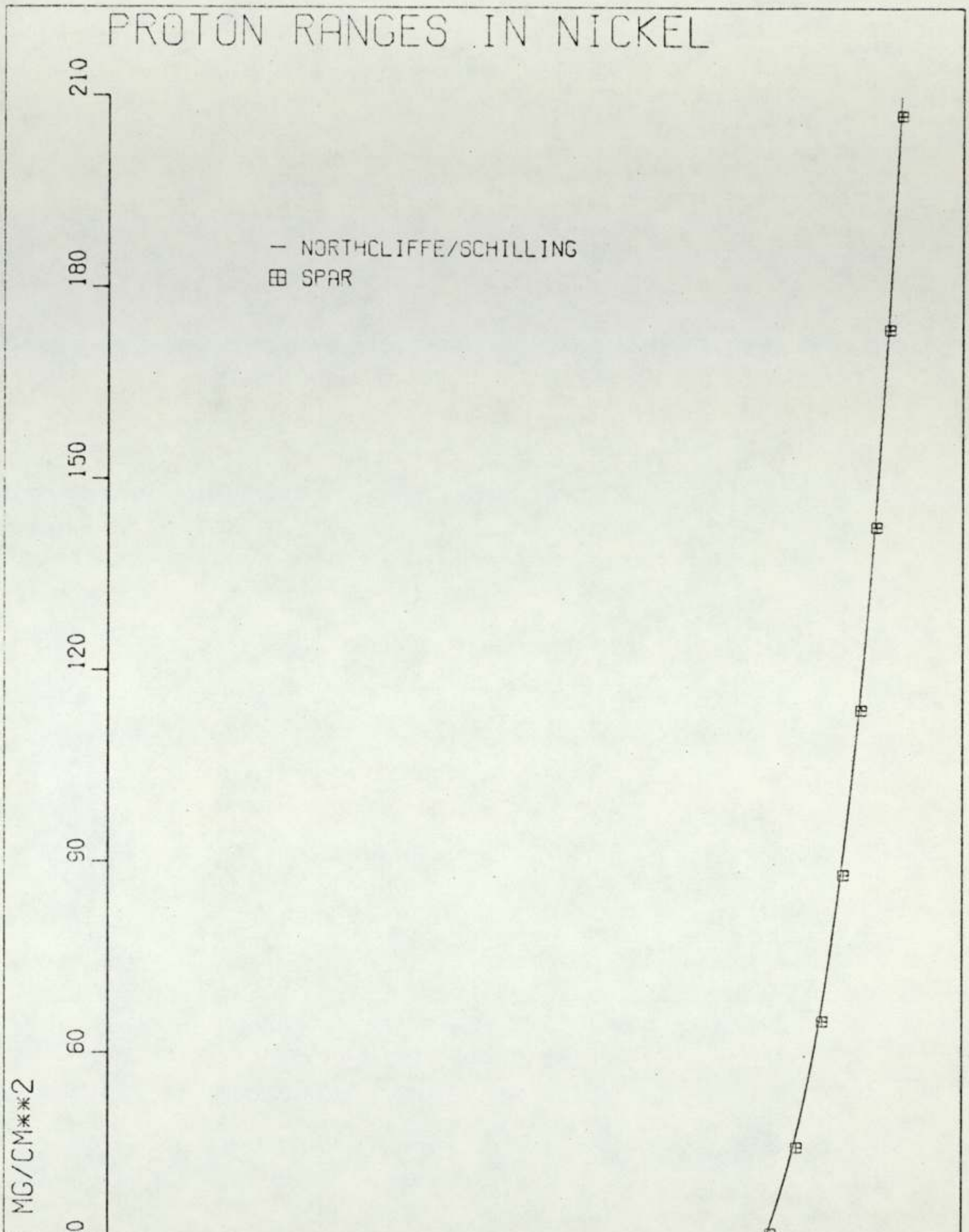
PROTON RANGES IN NICKEL
— NORTHCLIFFE/SCHILLING
⊞ SPAR
PROTON RANGE MG/CM**2
0
30
60
90
120
150
180
210
ENERGY (MEV)
10^2
10^1
1
10

Figure 5

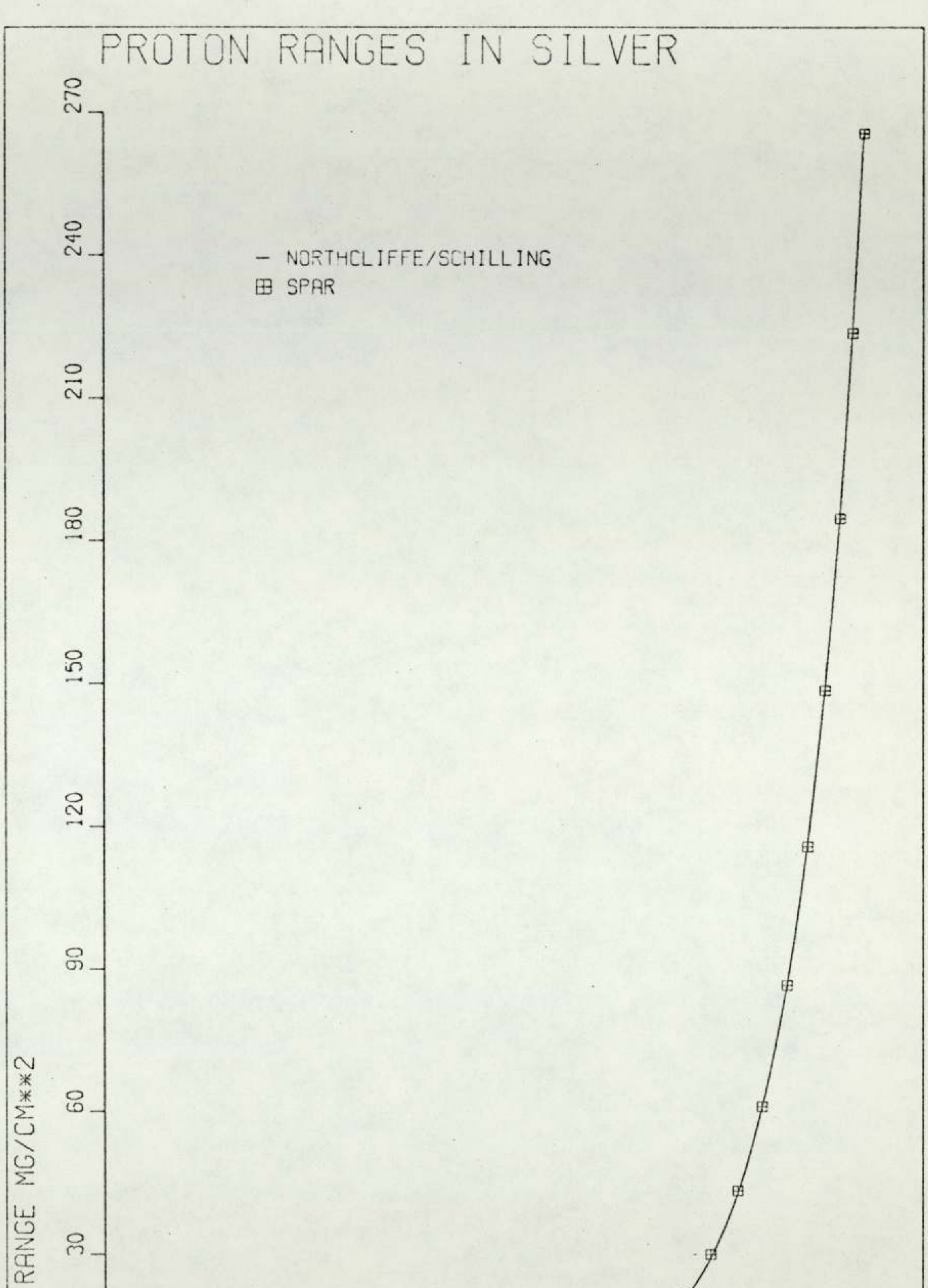
PROTON RANGES IN SILVER
– NORTHCLIFFE/SCHILLING
⊞ SPAR
PROTON RANGE MG/CM**2
0
30
60
90
120
150
180
210
240
270
10^{-2}
10^{-1}
1
10
ENERGY (MEV)

Figure 6

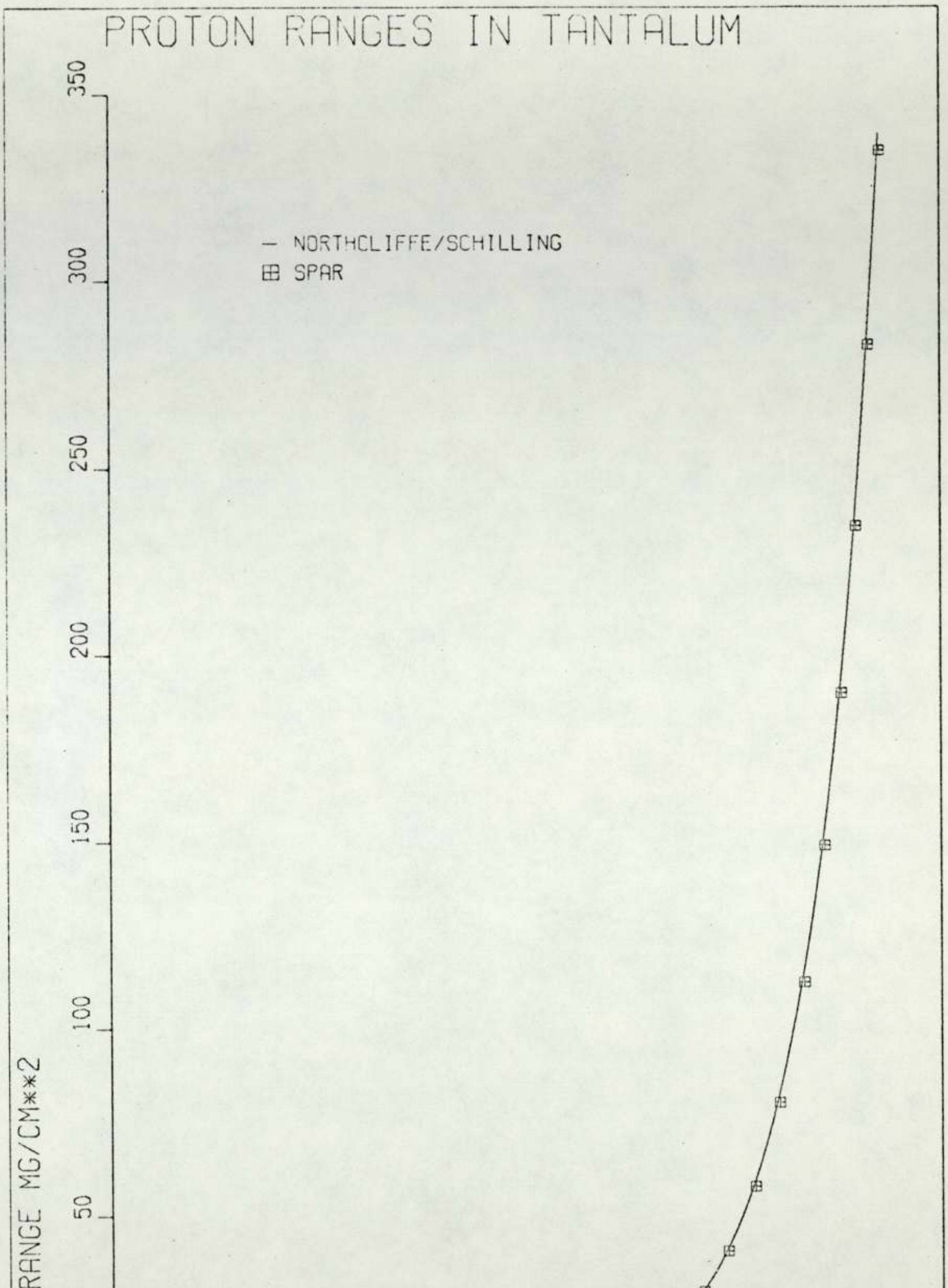
PROTON RANGES IN TANTALUM
— NORTHCLIFFE/SCHILLING
⊞ SPAR
PROTON RANGE MG/CM**2
0
50
100
150
200
250
300
350
10^{-2}
10^{-1}
1
10
ENERGY (MEV)

Figure 7

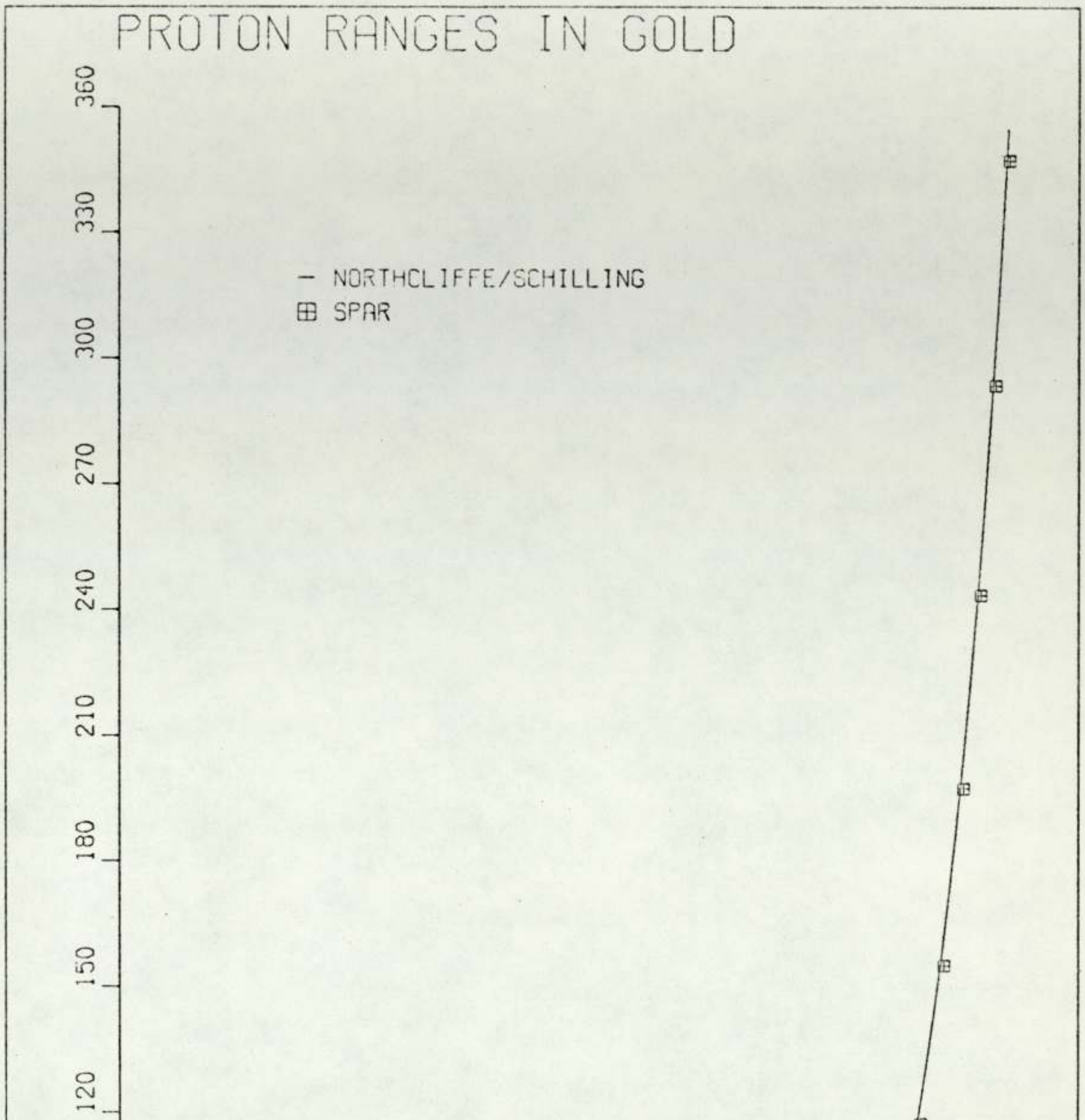
PROTON RANGES IN GOLD
– NORTHCLIFFE/SCHILLING
⊞ SPAR
PROTON RANGE MG/CM**2
0
30
60
90
120
150
180
210
240
270
300
330
360
10^{-2}
10^{-1}
1
10
ENERGY (MEV)

Figure 8

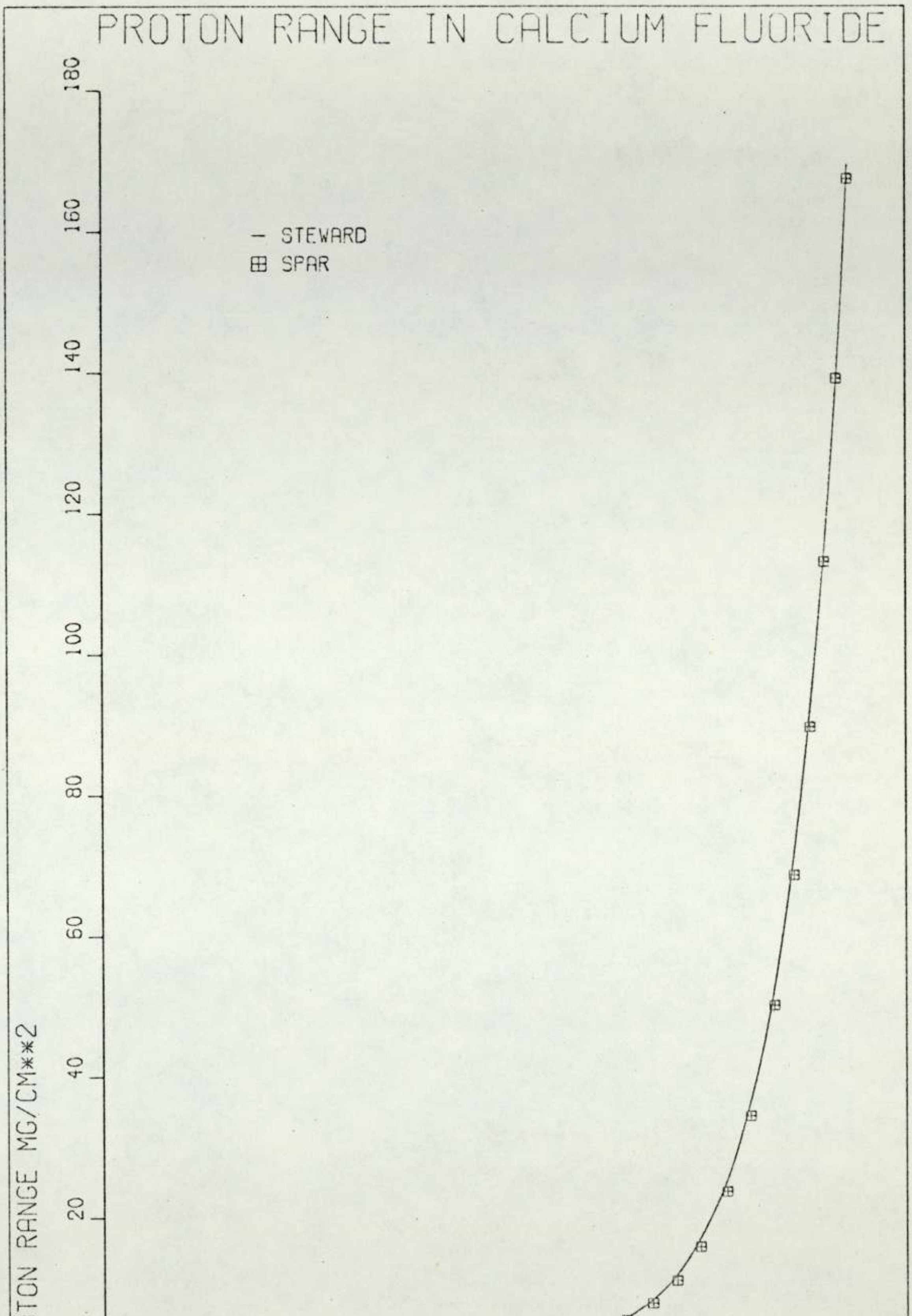
PROTON RANGE IN CALCIUM FLUORIDE
— STEWARD
⊞ SPAR
PROTON RANGE MG/CM**2
0
20
40
60
80
100
120
140
160
180
10^{-2}
10^{-1}
1
10
ENERGY (MEV)

Figure 9

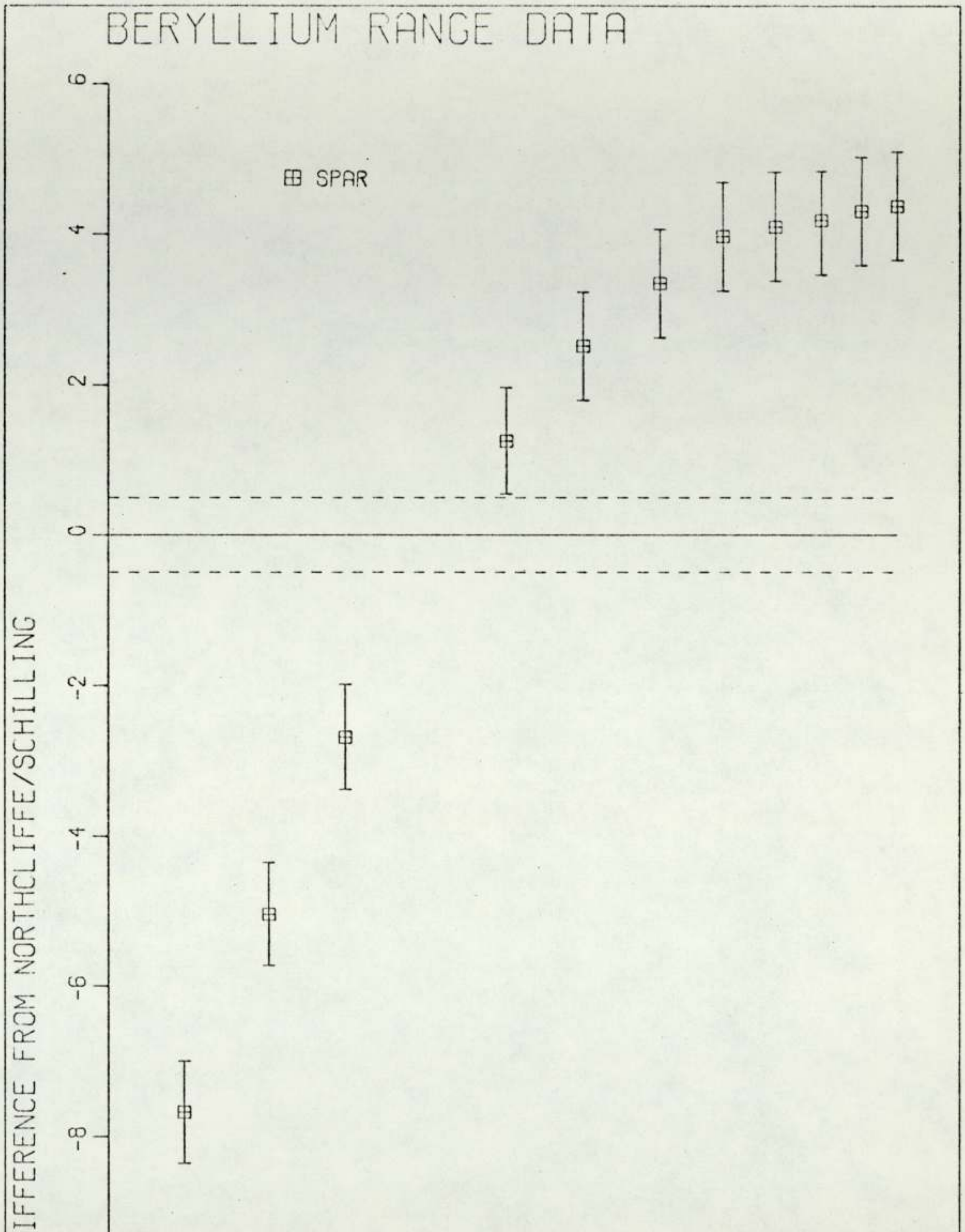
BERYLLIUM RANGE DATA
⊞ SPAR
PERCENTAGE DIFFERENCE FROM NORTHCLIFFE/SCHILLING
6
4
2
0
-2
-4
-6
-8
-10
-12
10^{-1}
1
ENERGY (MEV)

Figure 10

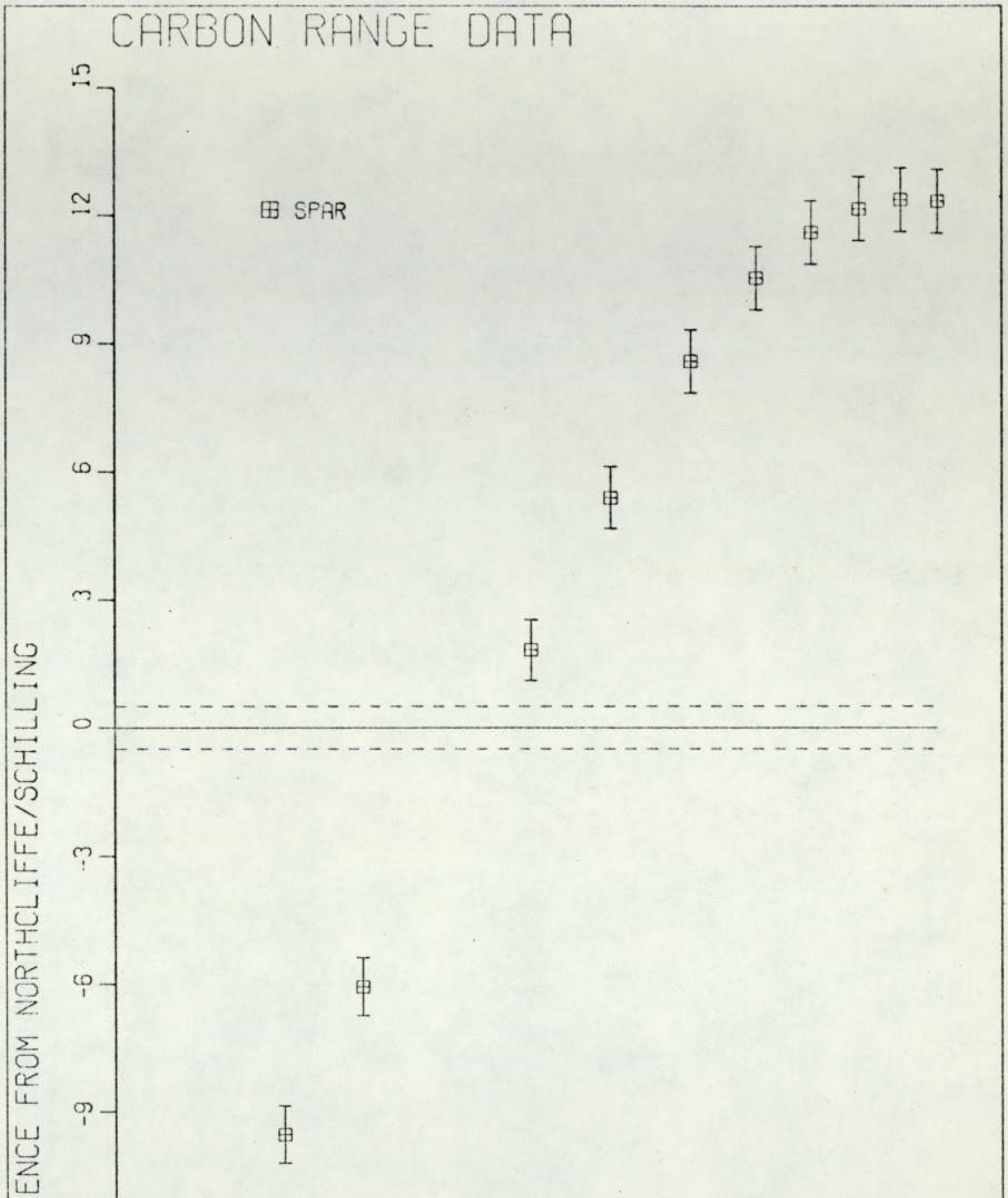
CARBON RANGE DATA
⊞ SPAR
PERCENTAGE DIFFERENCE FROM NORTHCLIFFE/SCHILLING
15
12
9
6
3
0
-3
-6
-9
-12
-15
-18
10^{-1}
1
ENERGY (MEV)

Figure 11

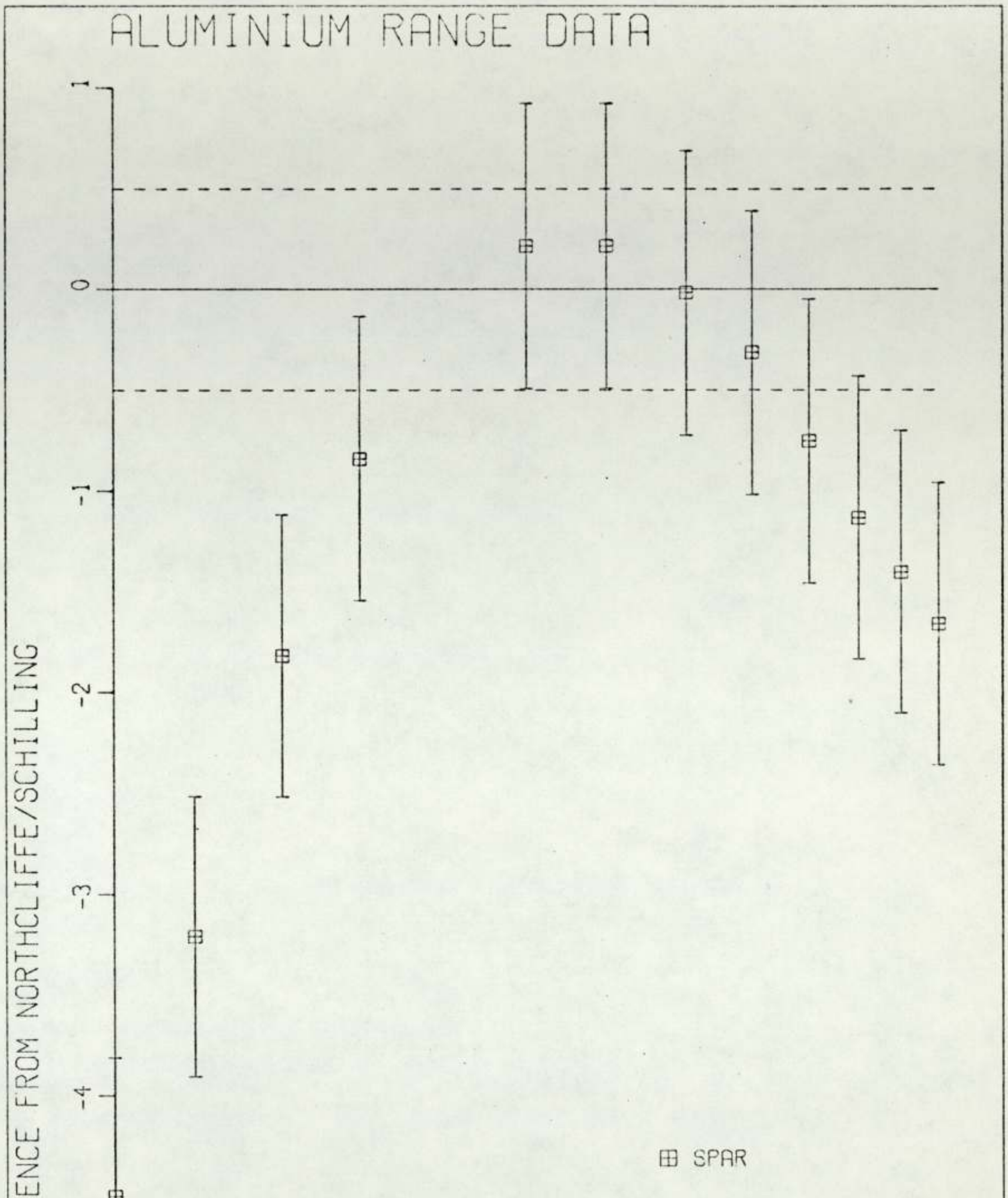
ALUMINIUM RANGE DATA
PERCENTAGE DIFFERENCE FROM NORTHCLIFFE/SCHILLING
1
0
-1
-2
-3
-4
-5
-6
10^{-1}
1
ENERGY (MEV)
⊞ SPAR

Figure 12

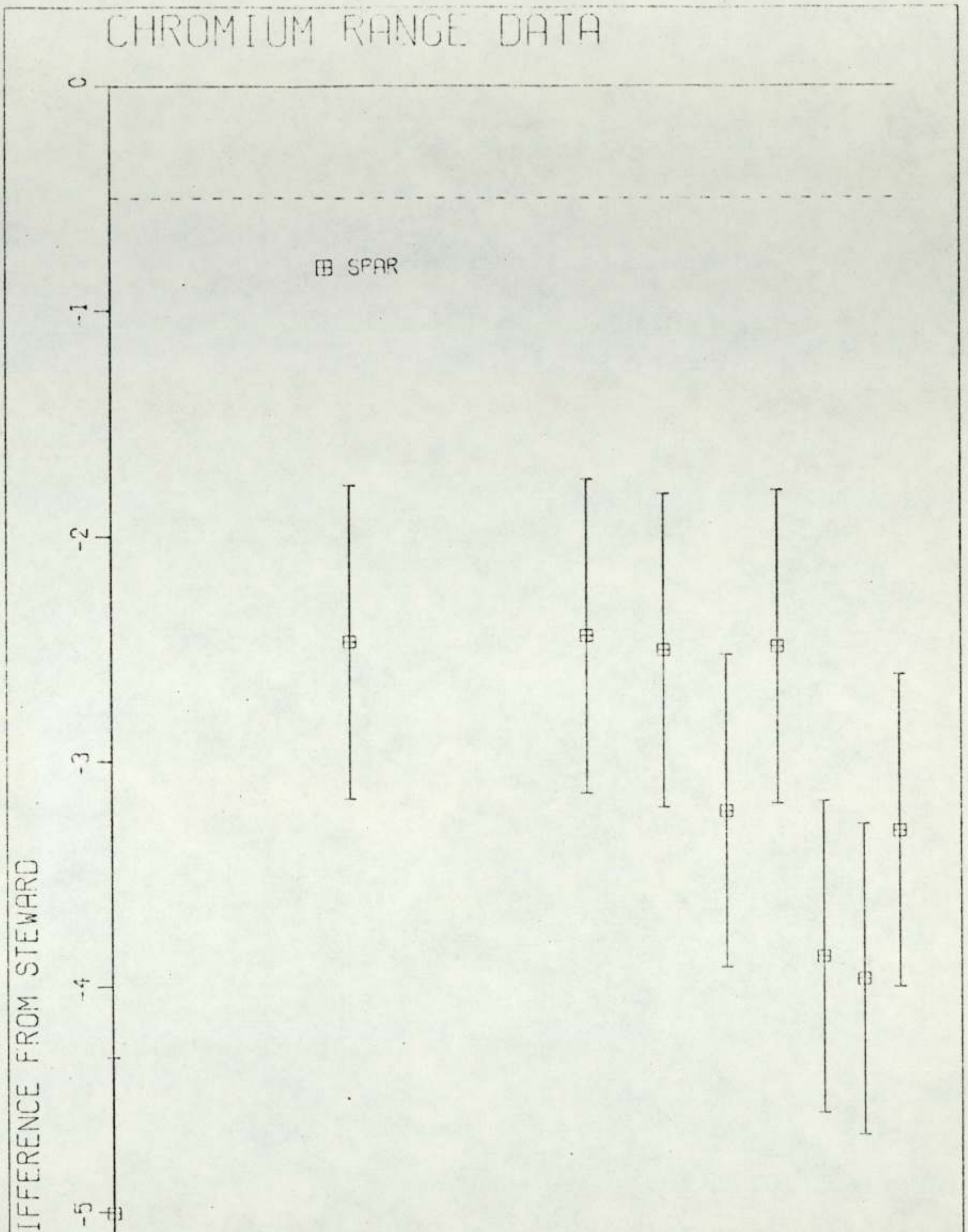
CHROMIUM RANGE DATA
0
-1
-2
-3
-4
-5
-6
⊞ SPAR
PERCENTAGE DIFFERENCE FROM STEWARD
10^1
1
ENERGY (MEV)

Figure 13

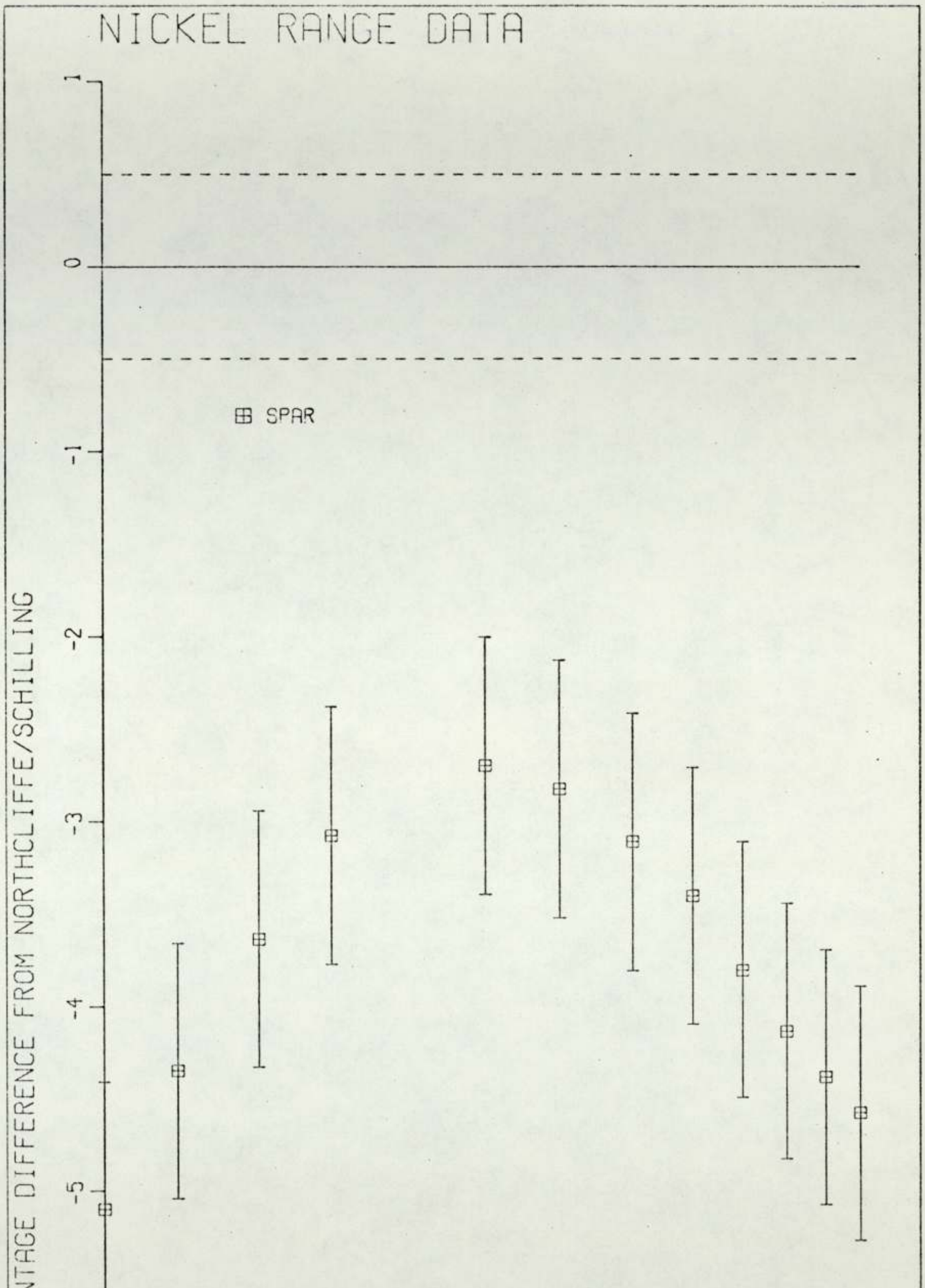
NICKEL RANGE DATA
⊞ SPAR
PERCENTAGE DIFFERENCE FROM NORTHCLIFFE/SCHILLING
1
0
-1
-2
-3
-4
-5
-6
10^1
1
ENERGY (MEV)

Figure 14

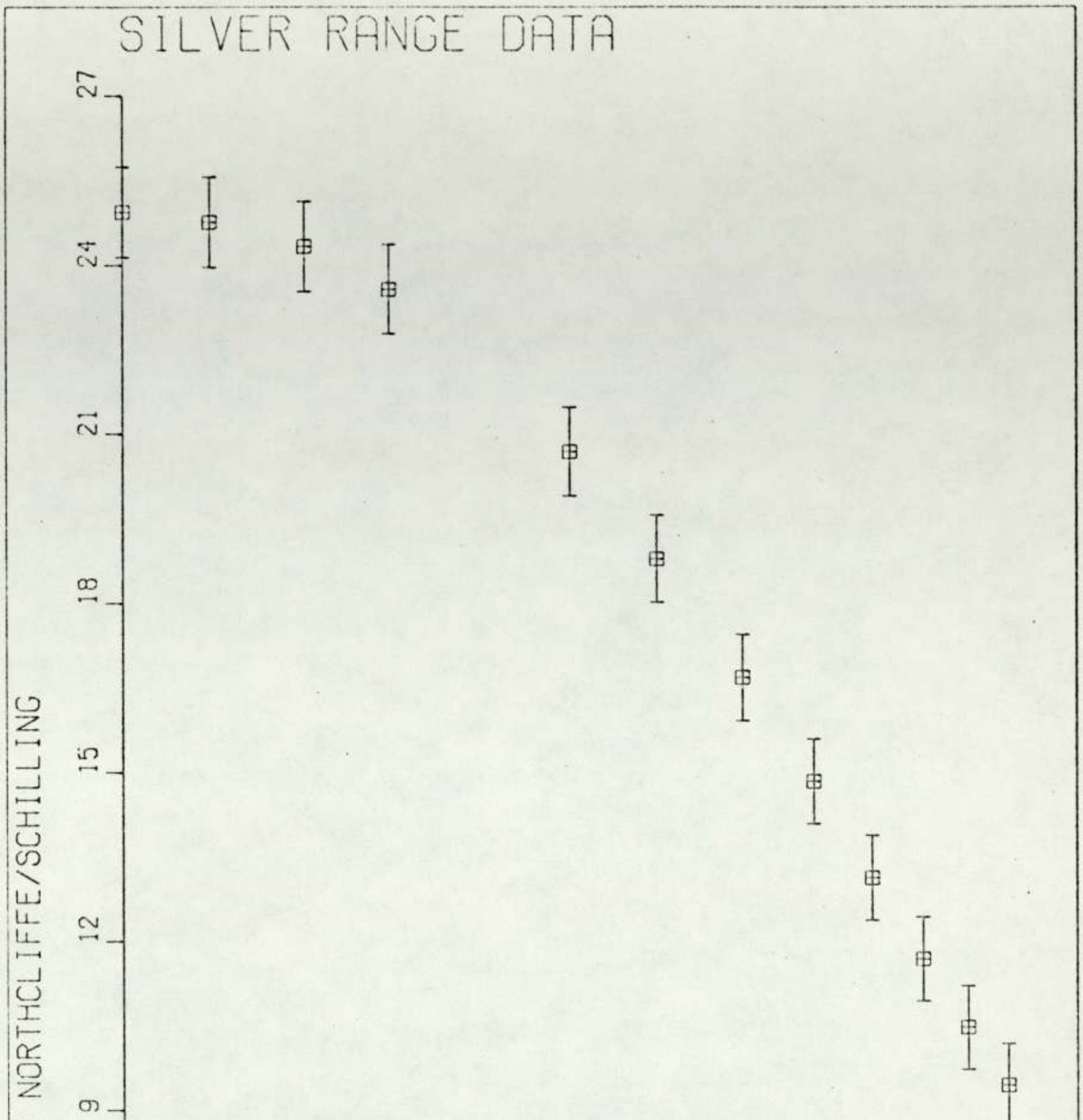
SILVER RANGE DATA
PERCENTAGE DIFFERENCE FROM NORTHCLIFFE/SCHILLING
27
24
21
18
15
12
9
6
3
0
⊞ SPAR
10^1
1
ENERGY (MEV)

Figure 15

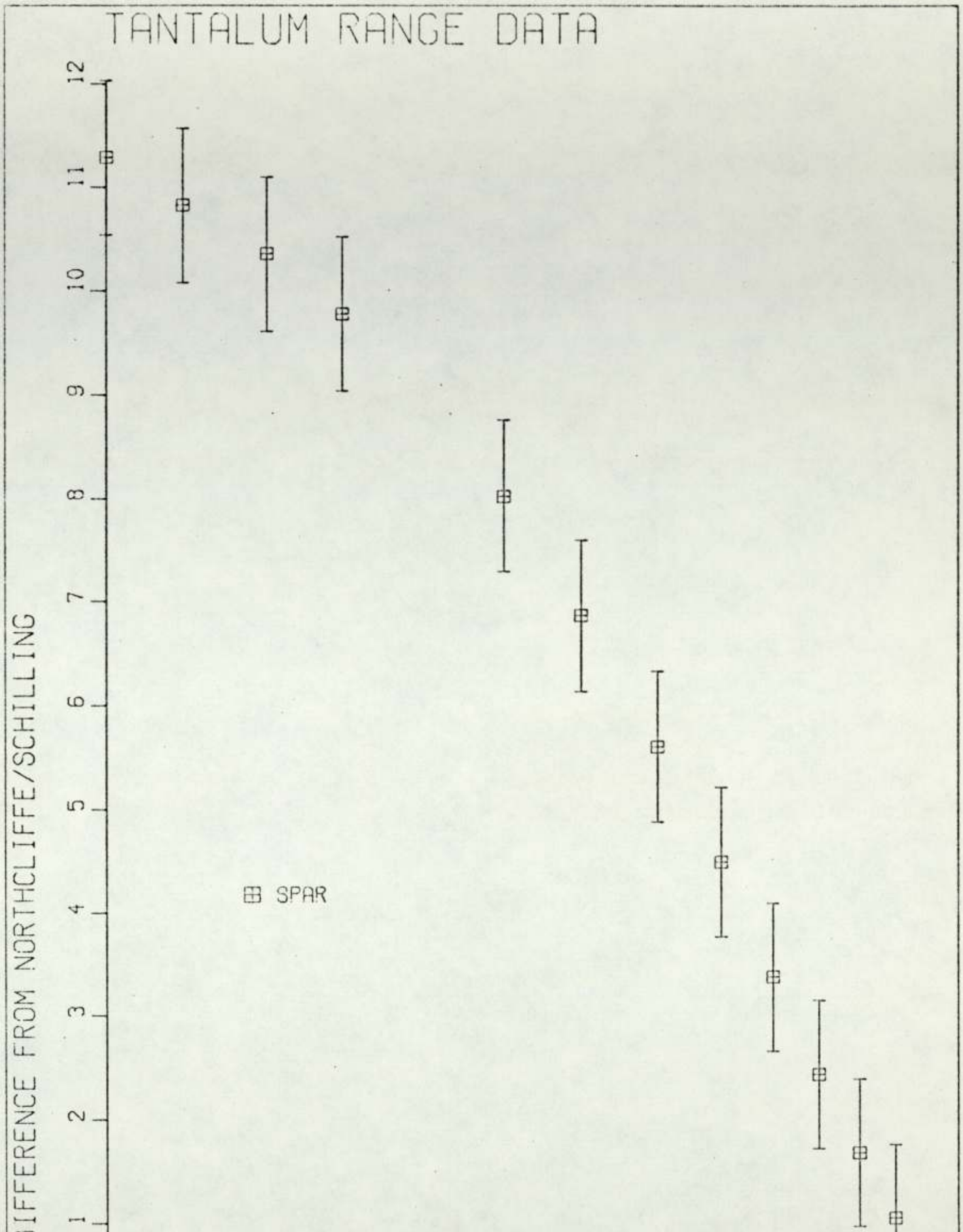
TANTALUM RANGE DATA
PERCENTAGE DIFFERENCE FROM NORTHCLIFFE/SCHILLING
12
11
10
9
8
7
6
5
4
3
2
1
0
-1
⊞ SPAR
10^1
1
ENERGY (MEV)

Figure 16

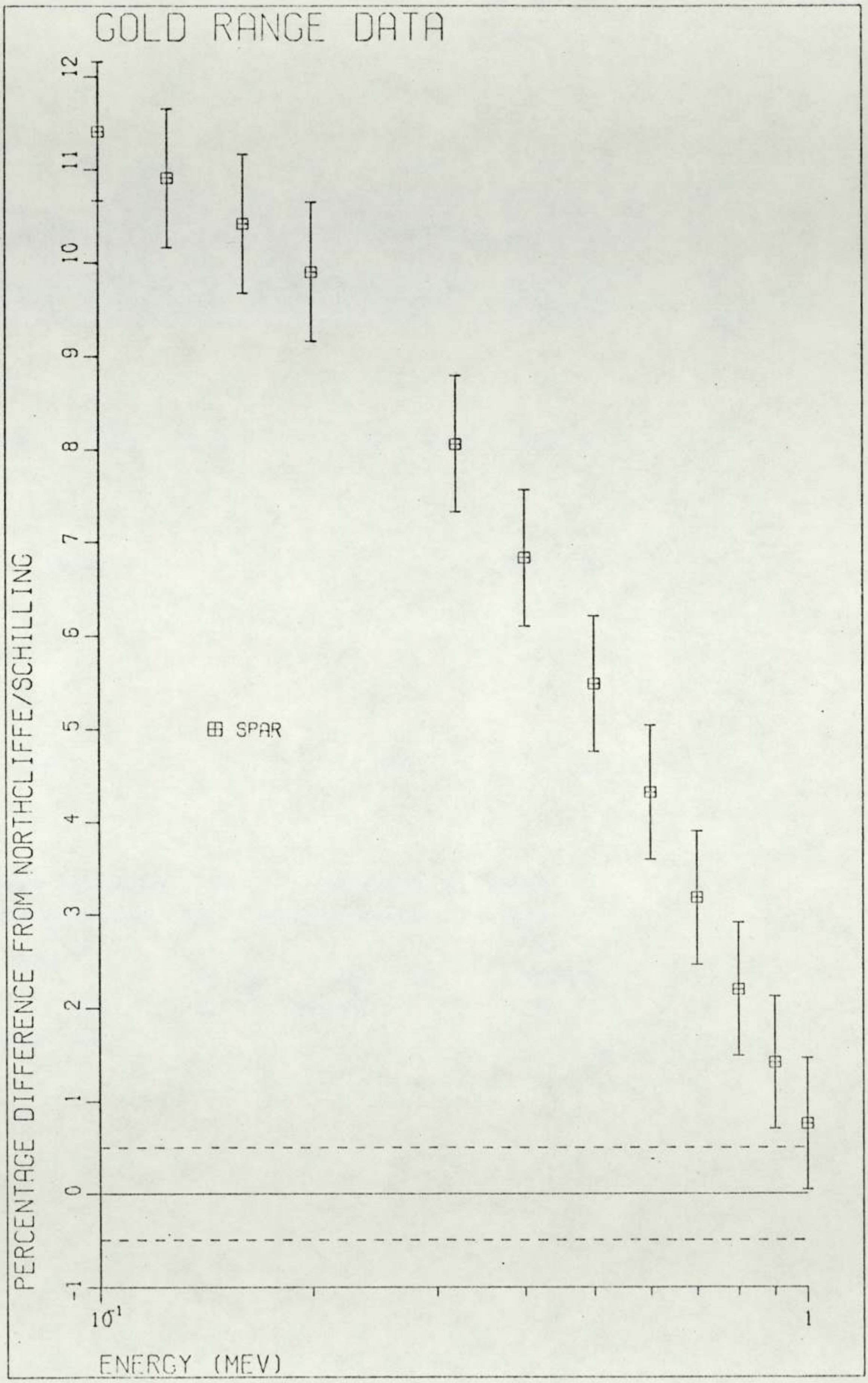
GOLD RANGE DATA
PERCENTAGE DIFFERENCE FROM NORTHCLIFFE/SCHILLING
12
11
10
9
8
7
6
5
4
3
2
1
0
-1
⊞ SPAR
10^1
1
ENERGY (MEV)

Figure 17

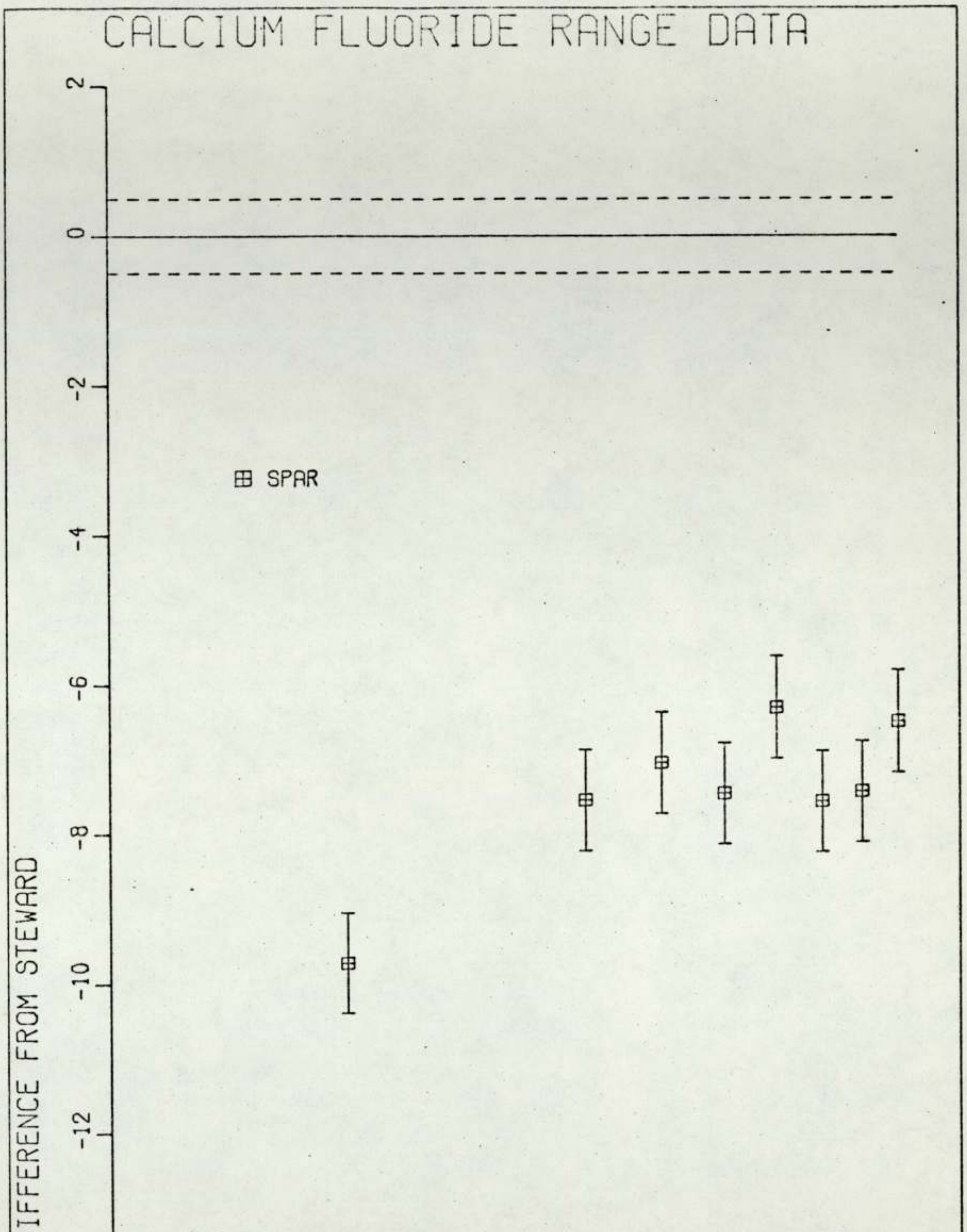
CALCIUM FLUORIDE RANGE DATA
PERCENTAGE DIFFERENCE FROM STEWARD
2
0
-2
-4
-6
-8
-10
-12
-14
-16
⊞ SPAR
10^{-1}
1
ENERGY (MEV)

Figure 18

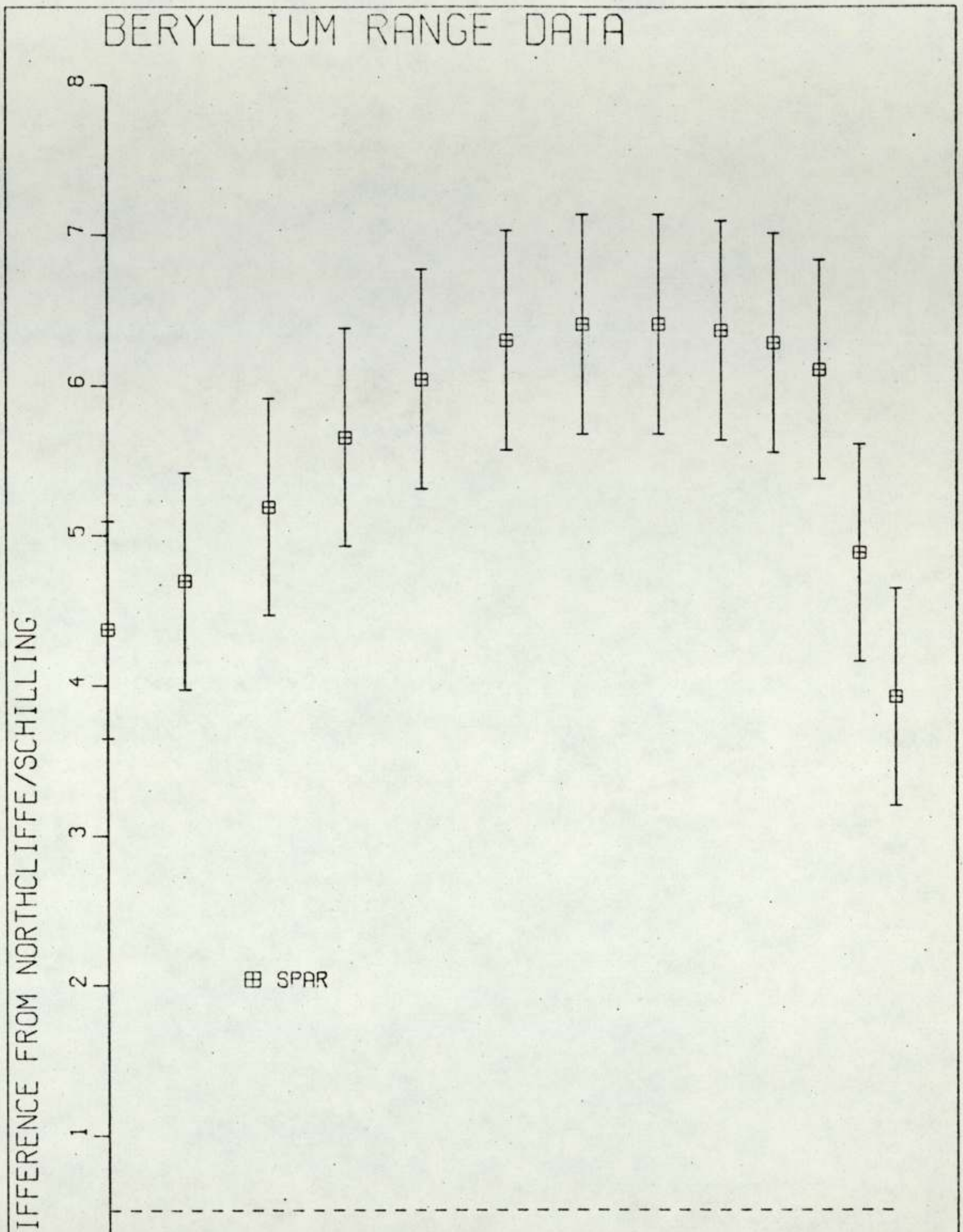
BERYLLIUM RANGE DATA
PERCENTAGE DIFFERENCE FROM NORTHCLIFFE/SCHILLING
8
7
6
5
4
3
2
1
0
-1
1
10
ENERGY (MEV)
⊞ SPAR

Figure 19

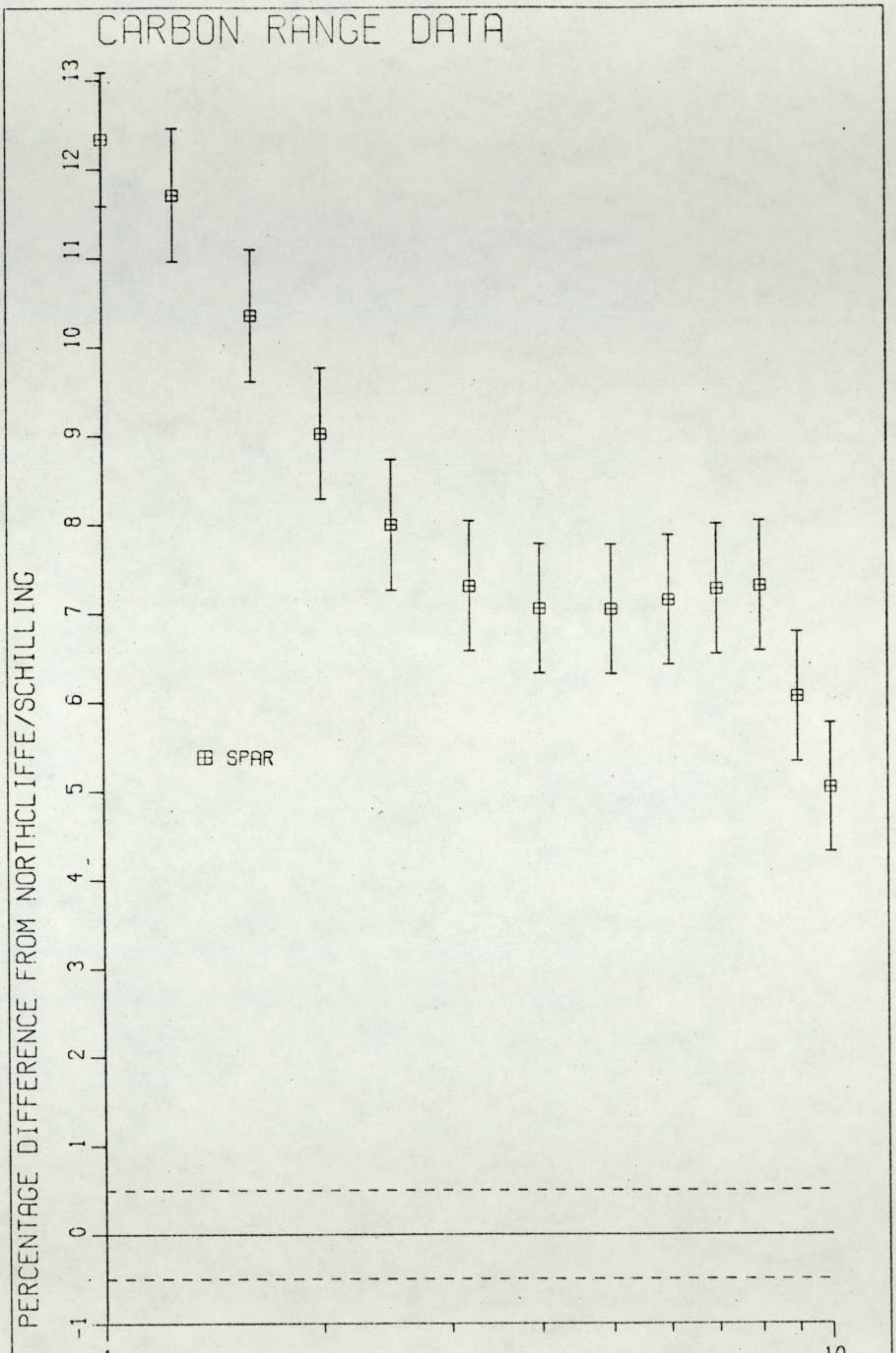
CARBON RANGE DATA
PERCENTAGE DIFFERENCE FROM NORTHCLIFFE/SCHILLING
13
12
11
10
9
8
7
6
5
4
3
2
1
0
-1
⊞ SPAR
1
10
ENERGY (MEV)

Figure 20

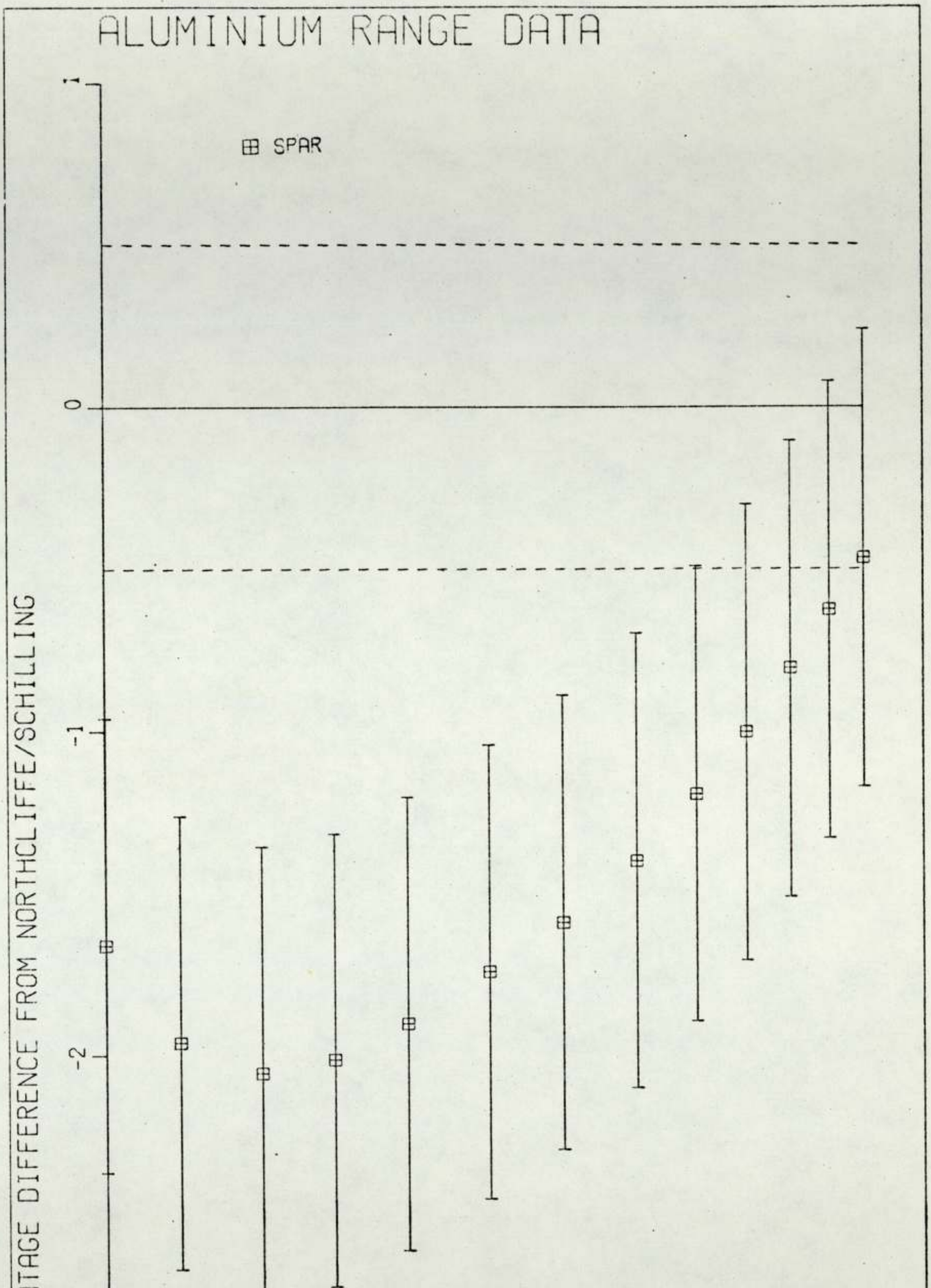
ALUMINIUM RANGE DATA
⊞ SPAR
PERCENTAGE DIFFERENCE FROM NORTHCLIFFE/SCHILLING
1
0
-1
-2
-3
1
10
ENERGY (MEV)

Figure 21

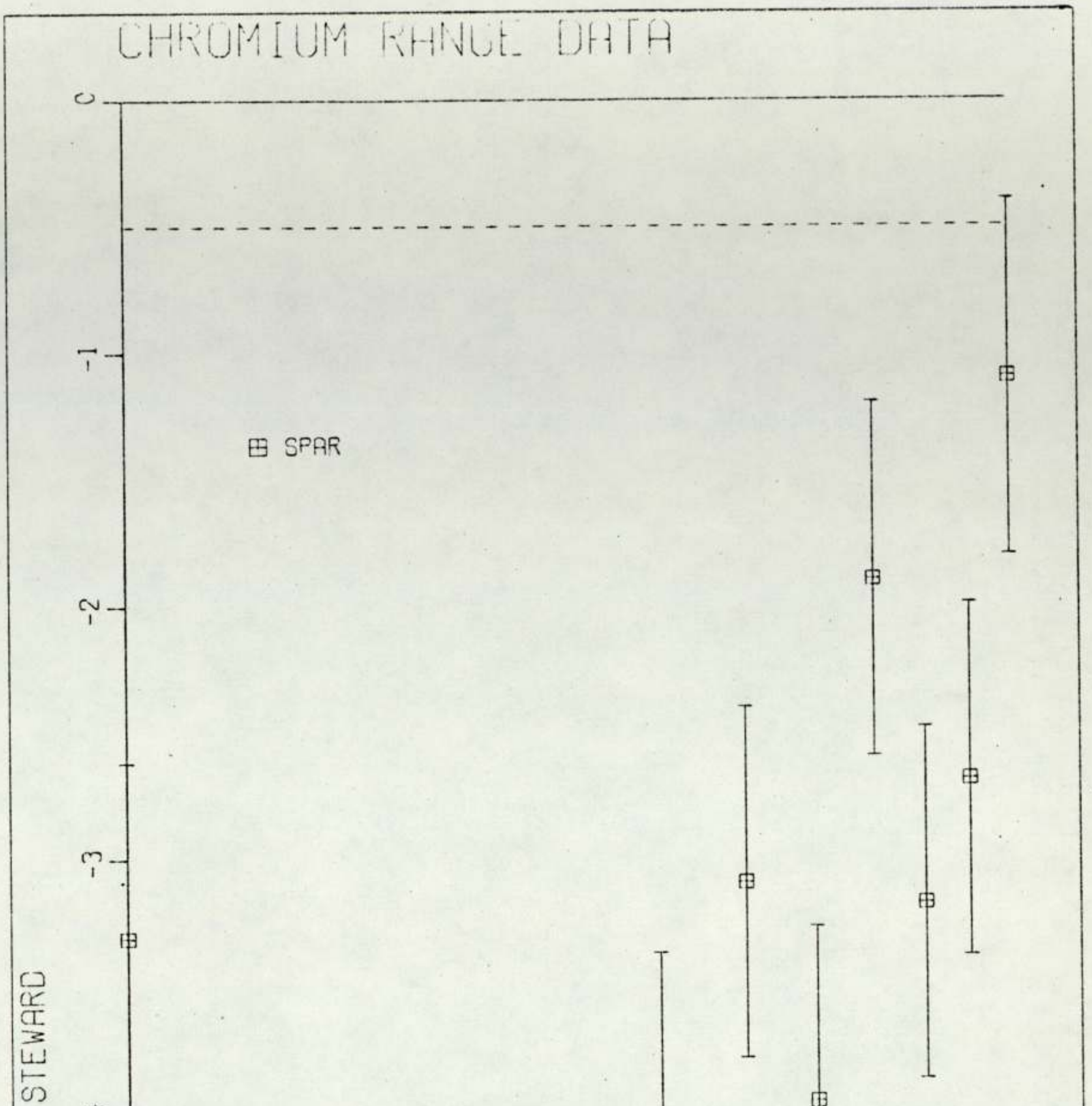
CHROMIUM RANGE DATA
SPAR
PERCENTAGE DIFFERENCE FROM STEWARD
0
-1
-2
-3
-4
-5
-6
1
10
ENERGY (MEV)

Figure 22

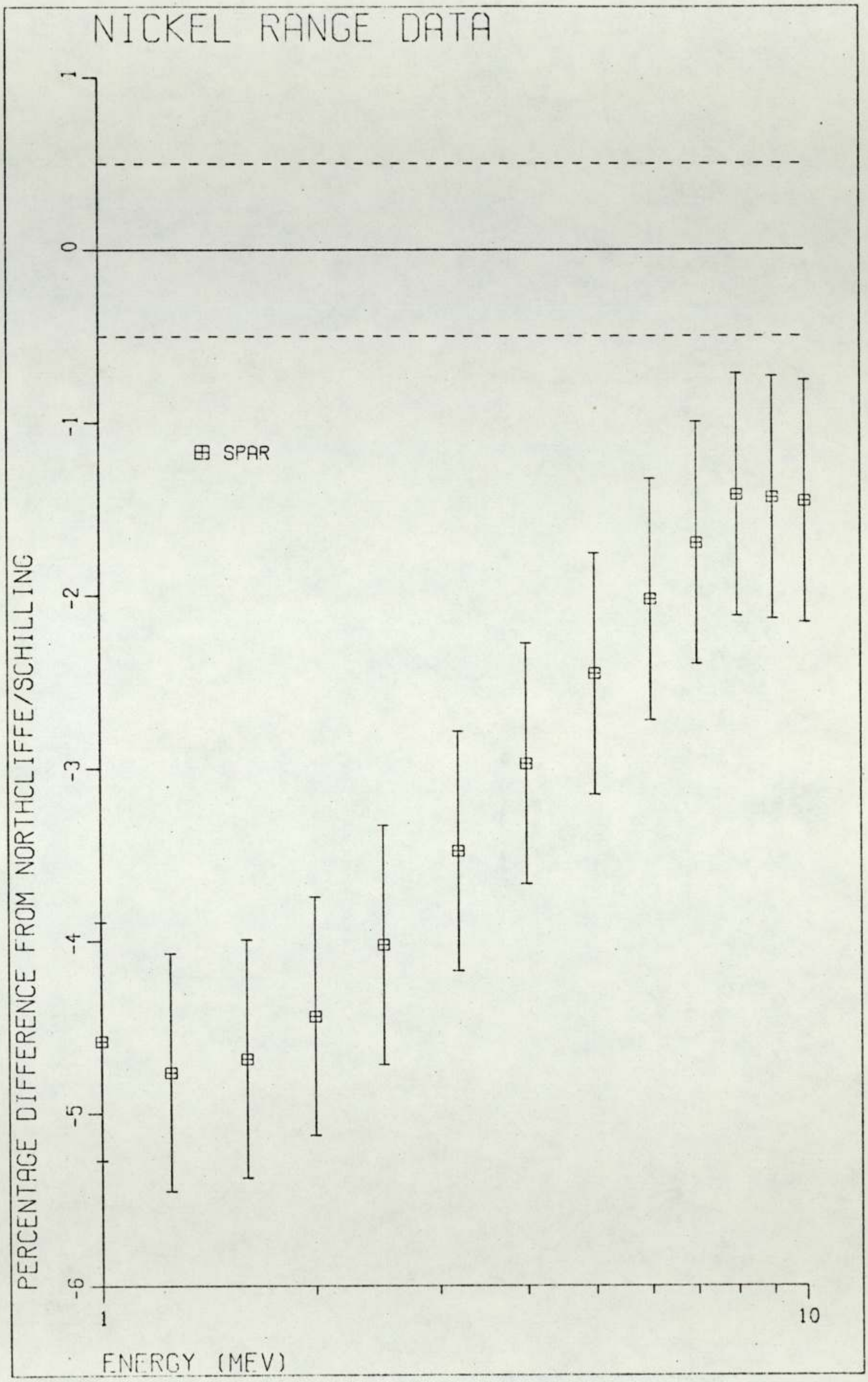
NICKEL RANGE DATA
1
0
-1
-2
-3
-4
-5
-6
⊞ SPAR
PERCENTAGE DIFFERENCE FROM NORTHCLIFFE/SCHILLING
1
10
ENERGY (MEV)

Figure 23

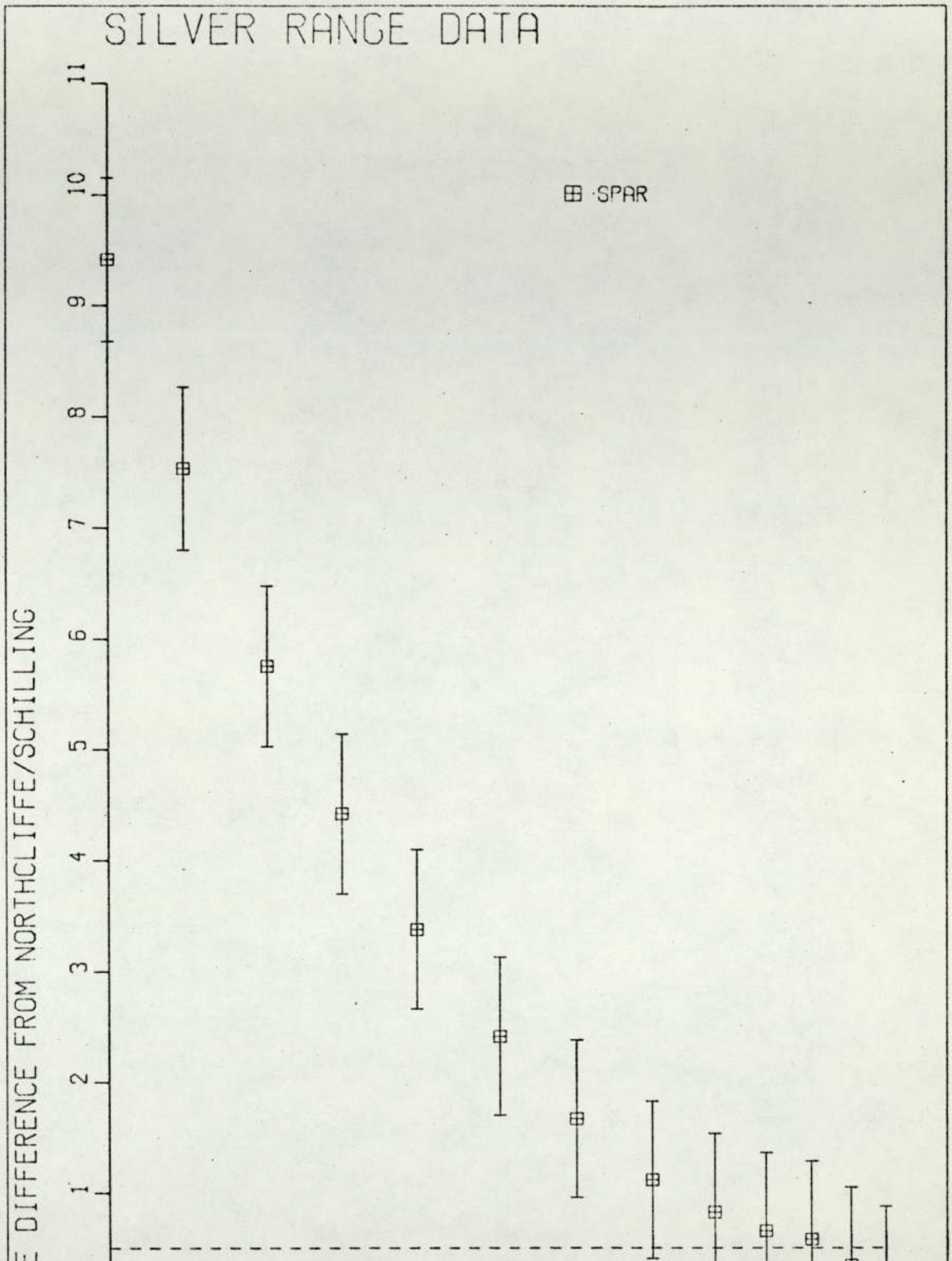
SILVER RANGE DATA
⊞ SPAR
PERCENTAGE DIFFERENCE FROM NORTHCLIFFE/SCHILLING
11
10
9
8
7
6
5
4
3
2
1
0
-1
1
10
ENERGY (MEV)

Figure 24

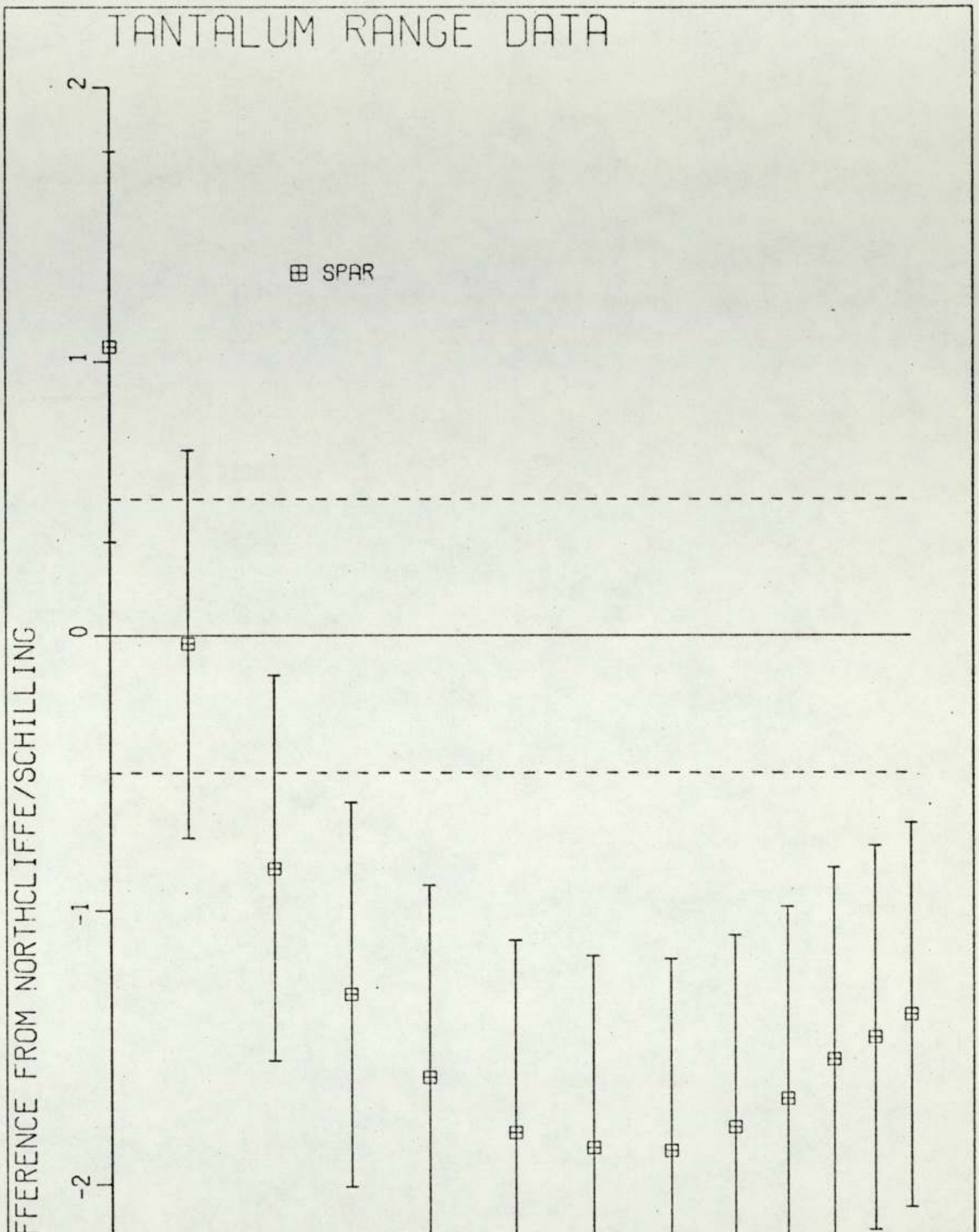
TANTALUM RANGE DATA
⊞ SPAR
PERCENTAGE DIFFERENCE FROM NORTHCLIFFE/SCHILLING
2
1
0
-1
-2
-3
1
10
ENERGY (MEV)

Figure 25

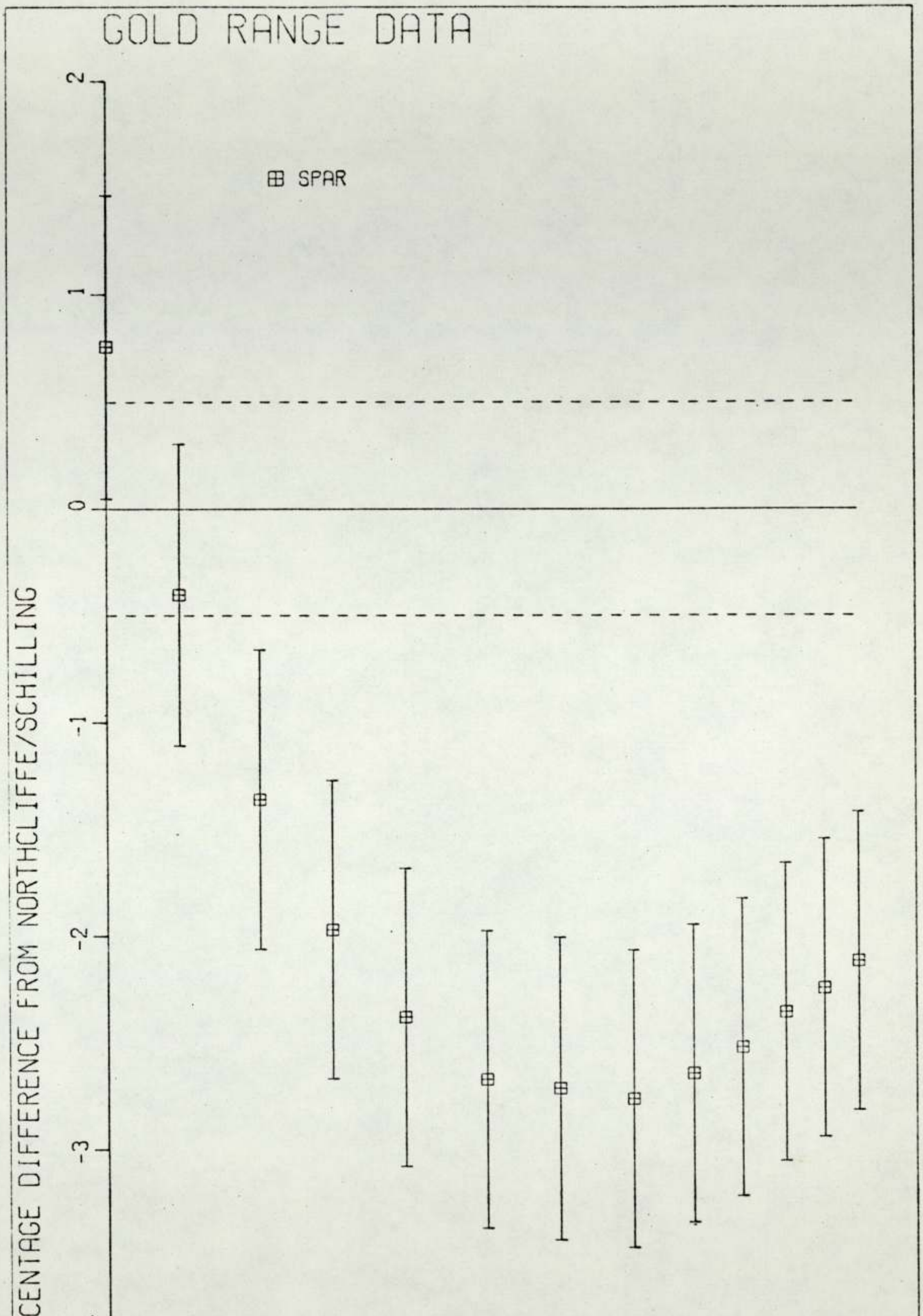
GOLD RANGE DATA
⊞ SPAR
PERCENTAGE DIFFERENCE FROM NORTHCLIFFE/SCHILLING
2
1
0
-1
-2
-3
-4
1
10
ENERGY (MEV)

Figure 26

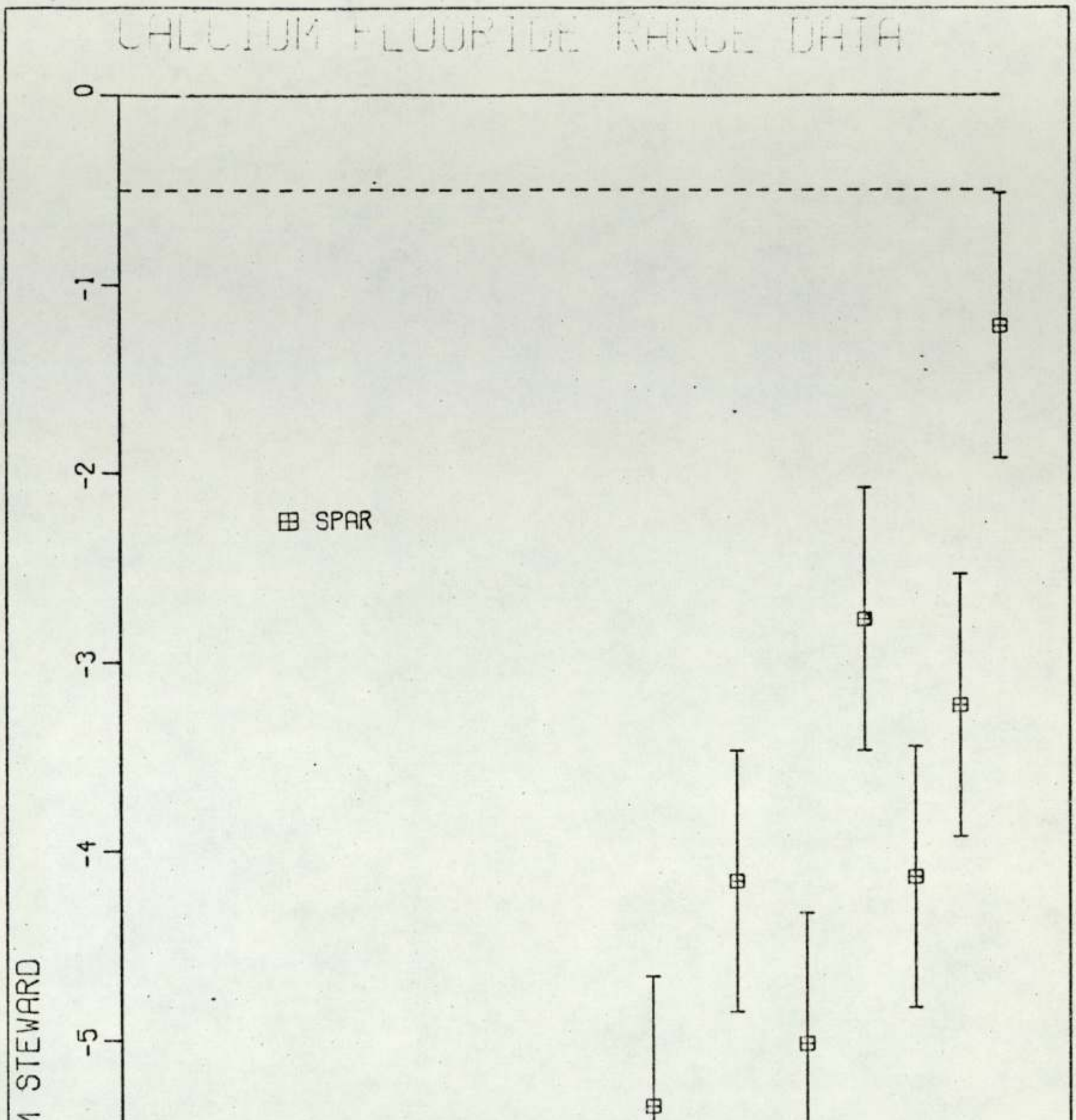
CALCIUM FLUORIDE RANGE DATA
0
-1
-2
-3
-4
-5
-6
-7
-8
PERCENTAGE DIFFERENCE FROM STEWARD
⊞ SPAR
1
10
ENERGY (MEV)

Figure 27

Appendix VI

Charged Particle Straggling

Charged Particle Straggling

Charged particle beams are slowed down in matter by a series of random collisions so that the spatial and temporal distribution of particles can be described only in statistical terms. At any point in an absorber there is a distribution of particle energy values and a corresponding distribution of probable energy loss in the next portion of the beam path, a phenomenon known as "straggling".

There are several theoretical formulations of energy straggling each of which has a limited range of validity. The fundamental physical event which is basic to each of these theories is the single discrete Coulombic collision between an energetic charged particle and an atomic electron. It is convenient to describe the region of validity of each formulation in terms of a parameter, κ, indicative of the ratio of the mean energy loss, ξ, on the pathlength considered, to the largest energy transfer possible in a single collision, ε_{max}. The following definition is taken from SELTZER and BERGER (1964)

$$\kappa = 0.30058 \cdot \frac{mc^2}{\beta^2} \cdot \frac{Z_2}{A_2} \cdot s/_{\varepsilon_{max}} = {}^{\xi}/\varepsilon_{max}$$

where mc^2 is the rest mass of the electron, s the pathlength, βc the velocity of the particle and Z_2 and A_2 the charge and mass of the absorbing medium respectively. The largest energy transfer possible in a single collision between a particle of mass M and a free electron is given by

$$\varepsilon_{max} = \frac{2mc^2\beta^2}{1-\beta^2} \left[1 + \frac{2m}{M} \cdot \frac{1}{(1-\beta^2)^{\frac{1}{2}}} + \left(\frac{m}{M}\right)^2 \right]^{-1}$$

$$\sim \frac{2mc^2 \beta^2}{1 - \beta^2}$$

At the beginning of its penetration when $\kappa \leqslant 0.01$, the energy straggling of a particle beam is described by the LANDAU (1944) distribution. In such cases the distribution of total energy-loss is extremely asymmetric, with a broad peak around the most probable energy-loss and a long tail corresponding to higher energy-losses. The FWHM of the distribution is given by

$$(\mathrm{FWHM})_L = 3.98\ \xi$$

The most probable energy-loss is significantly less than the average energy-loss. The Landau distribution is generally valid for very thin absorbers in which the energy-loss is small compared to the initial kinetic energy.

The transport equation describing the energy-loss of heavy charged particles in thin absorbers has been solved rigorously by VAVILOV (1957) whose distribution is a generalization of the Landau distribution, and is valid in the region $0.01 \leqslant \kappa \leqslant 10$. Evaluation of the Vavilov distribution is made difficult by the fact that it is expressed as an integral over rather complicated functions, so that numerical quadrature is required except in the limiting cases. Numerical evaluation yields a family of curves with the dimensionless parameters κ and β^2 which effect a smooth transition from the Landau distribution and include it as a special case. Vavilov's solution has been tabulated by SELTZER and BERGER (1964), and a computer programme for calculating the distribution has been presented by BADHWAR (1973). The difference between the most probable and average energy- loss has been given in graphical and functional form by SELLERS and HANSER (1972).

When $\kappa \geqslant 10$ the Vavilov solution effects a smooth transition to the BOHR (1915) distribution which holds through the end of the thin absorber region and into the beginning of the thick absorber region. Bohr's distribution , $f_B(\Delta)$, is Gaussian, with

$$f_B(\Delta) = (2\pi\sigma_B^2)^{-\frac{1}{2}} \exp\left[-(\Delta-\bar{\Delta})^2/2\sigma_\beta^{\ 2}\right]$$

and

$$\begin{aligned}\Delta &= T_o - T\\ \bar{\Delta} &= T_o - \bar{T}\end{aligned}$$

where Δ is the energy-loss for a particle at any point in the absorber, T_o is the initial kinetic energy and T the residual kinetic energy. $\bar{\Delta}$ is the average energy-loss. The variance of the distribution is given by

$$\sigma_B^{\ 2} = 0.157\ \rho s\ Z_1^2\ Z_2/A_2$$

where ρs is the absorber thickness and Z_1 the charge of the projectile ion.

At greater depths of penetration, the width and variance of the energy distribution continue to increase. The lower energy particles in the distribution have a higher stopping-power and therefore lose, on average, more energy than the higher energy particles. This effect causes an additional broadening of the energy spectrum. SYMON(1948) improved on Bohr's solution for these cases and gave an approximate solution to the thin absorber case. While Bohr's variance increases directly with absorber thickness Symon adds a term to account for the variation of the stopping-power over the distribution, leading to a variance which increases faster than absorber thickness.

TSCHALÄR (1967) pointed out that Symon neglected a term which contributes strongly to the skewness of the distribution, and thus Symon's distribution erroneously remain practically Gaussian upto very large energy-losses. Tschalär has numerically evaluated the corrected equations and tabulated the distributions and their properties. In general, as the penetration increases, a non-Gaussian low-energy tail begins to reappear. TSCHALÄR (1968) has also shown that when a heavy particle beam has penetrated to such a depth that particles start to be lost by complete stopping the distribution must be propagated numerically.

PAYNE (1969) has given a solution to the problem of predicting energy distributions in thick absorbers by working backwards from the distribution of residual ranges, which remains practically Gaussian throughout the whole depth of penetration. Payne's distributions are similar to those given by Tschalär. Multiple scattering corrections have been included in the Tschalär theory by TSCHALÄR and BICHSEL (1968) and the result tabulated. A graphical presentation has been given by CLARKE (1971).

Many aspects of the theories have been verified experimentally. Work at isolated values of κ [IGO et al. (1953), GOLDING and EISBERG (1957)] and a systematic survey of the Landau transition region ($\kappa > 0.1$) [MACCABEE and RAJU (1965), MACCABEE et al. (1968)] have shown good agreement between the predictions of Vavilov or Symon and experiment. The data of others workers [TSCHALÄR and MACCABEE (1970), PENKROT et al. (1971), NANN and SCHÄFER] and a survey of the Gaussian transition region ($\kappa > 1$) [KOLATA et al. (1968)] have established the validity of the TSCHALÄR theory for large energy loss. Discrepancies have been observed between measured and theoretical straggling distributions for low energy protons [CHILTON et al. (1954), SKOFRONICK et al.(1964), NOSELL (1964)], alpha-particles [FARBI et al. (1967), SYKES and HARRIS (1972)] and heavy ions [ANDEICHIKOV et al. (1974)] although such data is generally outside the region of strict validity of the analytic theories.

REFERENCES

Abramowitz, M. and I.A.Stegun (1965) "Handbook of Mathematical Functions" p302 (Dover, New York)

Adlof, J., J.Sheiffer and C.Urlacher (1966) Anl-Trans-543, Bull.Soc.Chim. Fr. p698

Aguado Bombin, R (1975) Thesis. Univ. Aston in Birmingham

Amsel, G. and D.Samuel (1967) Anal.Chem. 39 p1687

Amsel, G., C.Cherki, G.Feuillade and J.P.Nadai (1969) J.Phys.Chem. Solids 30 p2117

Amsel, G., D.David, G.Beranger, P.Biosot, B.De Gelas and P.Lancombe (1969) J.Nucl.Mater. 29 p144

Amsel, G., J.P.Nadai, E.D'Artemare, D.David, E.Girard and J.Moulin (1971) Nucl.Instrum.Meth. 92 p481

Andersen, S.L., T.Gjötterud, T.Holtebekk and O.Lönsjö (1958)Nucl.Phys. 7 p384

Andersen,H.H. C.C. Hanke, H.Sørensen and P.Vadja (1967) Phys.Rev. 153 p338

Andersen, H.H., C.C.Hanke, H.Sørensen and P.Vadja (1968) Phys.Rev.175 p389

Andersen, H.H., H.Simonsen, H.Sørensen and P.Vadja (1969) Phys.Rev. 186 p372

Andersen. H.H., H.Simonsen and H.Sørensen (1969) Phys.Rev. A125 p171

Antilla, A., and J.Keinonen (1973) Int.J.Appl.Radiat.Isot. 24 p293

Armstrong, T.W. and R.G.Alsmiller (1970) Nucl.Instrum.Meth. 82 p289

Armstrong, T.W., and K.C.Chandler (1973) Nucl.Instrum.Meth. 113 p313

Armstrong, T.W. and K.C.Chandler (1973) Oak Ridge Nat.Lab.Report ORNL - 4869

Armstrong, T.W., and K.C.Chandler (1974) Oak Ridge Nat.Lab.Report ORNL - CCC - 228

Aston, F.W. (1920) Proc.Camb.Phil.Soc. 19 p317

Aston, F.W. (1933)"Mass Spectra and Isotopes" (Arnold)

Avdeichikov, V.V., E.A.Ganza and O.V.Lozhzin(1974) Nucl.Instrum.Meth. 118 p247

Bacher, A.D., E.A. McClatchie, M.S.Zisman, T.A.Weaver and T.A.Tombrello (1972) Nucl.Phys. A181 p453

Bader, M., R.E.Pixley, F.S.Mozer and W.Whaling (1956)

Badhwar, G.D.(1973) Nucl.Instrum.Meth. 109 p119

Barkas, W.H.(1963) Nuclear Research Emulsions 1 p372

Barkas, W.H., and M.J.Berger (1964) Nat.Acad.Sci.Pub. 1133 p103

Barkas, W.H., and S.Von Friesen (1961) Nuovo. Cimento Suppl. 19 p41

Barnes, D.G., J.M.Calvert, K.A.Hay and D.G.Lees (1973) Phil.Mag., 28 p1303

Barnett, C.F., and J.A.Ray (1963) "Physics of Electronic and Atomic Collisions" Proc. 3rd. Int.Conf.(London p743)(North Holland, Amsterdam)

Barouch, E.(1968) Nucl.Instrum.Meth. 61 p113

Bassett, R. (1975) Private Communication

Berger, M.J. (1963)"Methods in Computational Physics" 1 p135 (Academic, New York)

Berger, M.J. and S.M.Seltzer (1964) Nat.Acad.Sci.Pub - 1133 p99

Berkner, K.H., S.N.Kaplan, R.V.Pyle and J.W.Stearns (1966) Phys. Rev. 146 p9

Bethe, H.A.(1930) Ann.der Physik 5 325

Bethe, H.A. (1932) Z.Physik 76 p293

Bichsel, H.(1961)Univ.South Calif. Report - 3 Contract AT(04-3) - 1367

Bichsel, H. (1963) "American Institute of Physics Handbook" Sec.8C (McGraw-Hill, New York)

Bichsel, H. and E.A.Uehling (1960) Phys. Rev. 119 p1670

Bloch, F. (1933) Ann.der Physik 16 p285

Bloch, F.(1933) Z.Physik 81 p363

Bohr,N (1913) Phil.Mag. 25 p10

Bohr, N.(1915) Phil.Mag. 30 p581

Bohr, N.(1948) Mat.Fys.Medd.Dan.Vid.Selsk

Bondelid, R.O., and J.W.Butler (1963) Phys.Rev. 132 p1710

Bondelid, R.O., and C.A.Kennedy (1958) Naval Research Lab.Report NRL - 5083 Washington, D.C.)

Bondelid, R.O., and C.A.Kennedy (1959) Phys.Rev. 115 p1601

Brant, W. (1956) Phys.Rev. 104 p691

Brant, W.(1958) Health Phys. 1 p11

Brant, W. (1958) Phys.Rev. 111 p1042

Brewers, J.M., and F.C.Flack (1968) Nucl.Instrum.Meth. 59 337

Brewers, J.M. and F.C.Flack (1969) Analyst 94 p1

Brown, L (1950) Phys.Rev. 79 p297

Burkig, V.C., and K.R.MacKenzie (1957) Phys.Rev.106 p106

Butler, J.P.(1965) "Radiochemical Methods of Analysis" IAEA, Vienná, 1 , p2391

Cachard, A., J.Pivot, A.Roger, M.Talvat and J.P.Thomas(1971) Rev. Phys.Appl. 6 p279

Calvert, J.M., D.G.Lees, D.J.Derry and D.Barnes (1972) J.Radioanal. Chem. 12 p271

Calvert, J.M., D.J.Derry and D.G.Lees (1974) J.Phys.D: Appl.Phys. 7 p940

Caswell, R.S. and M.J.Berger, (1972) "Theoretical Aspects of Radiation Dosimetry" Conf.Los Alamos Sci.Lab., Oct 2-4 (Los Alamos, New Mexico)

Caudano, R., and J.M.Delfosse (1968) J.Phys. B1 p813

Caywood, J.M., T.A.Tombrello and T.A.Weaver (1971) Phys.Lett. 37A p350

Chambers, E.S.(1965) Phys.Rev. 139 A1068

Chemin,J.F., J.Roturier, B.Saboya and G.Y.Petit (1971) Nucl.Instrum. Meth. 97 p211

Cheng, M.H., M.Chian, E.A.Gislason, B.H.Mahen, C.W. Tsao and A.S. Werner (1970) J.Chem.Phys. 52 p5518

Cherki, C., and J.Siejka (1973) J.Electrochem. Soc. 120 p784

Chilton, A.B., J.N.Cooper, J.C.Harris (1954) Phys.Rev. 93 p413

Choi, D.H., and E.Merzbacher (1969) Phys.Rev. 177 p233

Clarke, M.N.(1974) Private Communication

Churchill, J.L.W. (1951) A.E.I. Report - A166

Cleland, M.R. (1968) 3rd Symp. on "Structure of low-medium Mass Nuclei" p 230 (Lawrence Rad.Lab. Kansas)

Cleland, M.R., and R.Farrell (1965) I.E.E.E. Trans.Nucl.Sci. N.S.12, No.3, p227

Cleland, M.R., P.R.Hanley and C.C.Thomas (1969) I.E.E.E. Trans.Nucl.Sci. NS16 No 3. p113

Coates, L.B. (1973) J.Phys.D: Appl.Phys. 6 p153

Cohen, B.L., and R.A.Moyer (1971) Anal.Chem. 43 p123

Condon, E.U. (1928) Phys.Rev. 32 p858

Cooksen, J.A., A.T.G.Ferguson and F.D.Pilling (1972) J.Radioanal.Chem. 12 p39

Cooley, J.W., P.A.Lewis and P.D.Welch (1969) I.E.E.Trans.on Educt.12 No 1 p27

Cooley, J.W., and J.W.Turkey (1965) Math. of Comp. 19 No90 p297

Coote, G.E., N.E. Whitehead and G.J.McCallum (1972) J.Radioanal. Chem.12 p 491

Cox, B., and C.Roy (1966) Electrochem.Tech. 4 p121

Crumpton, D. (1967) Thesis.Univ.Ast. in Birmingham

Cunha, J.D., and P.M.Corrêa (1975) Nucl.Instrum.Meth. 125 p265

Dahl, P.F., D.G.Costello, and W.L.Walters (1960) Nucl.Phys. 21 p106

Davis, J.B., and H.H.Herd (1969) I.B.M. Journ.Research and Devel.13 p93

Deconnineck, G.J. (1972)J.Radioanal.Chem.12 p157

Dennis, J.K (1965) Trans.of Inst. of Metal Finishing 43 p84

Derry,D.J., D.G.Lees and J.M.Calvert (1971) Proc.Br.Ceram.Soc. 19 p77

Dettman, K., K.G.Harrison and M.W.Lucas (1974) J.Phys.B.At.Mol.Phys. 7 p269

Dunn, G.M., and B.Van Zyl (1967) Phys.Rev. 154 p40

Durup, J., P.Fournier and P.Dông (1969) Int.J.Mass Spec. and Ion Phys. 2 p311

Eastham, D.A. (1975) Nucl.Instrum.Meth. 125 p277

Economou, T.E., A.L.Turkevich, K.P.Sowinski, J.H.Patterson and E.J. Frankgrot (1973) Science 181 p156

Endt, P.M. and C.Van der Leun (1973) Nucl.Phys. A214 p1

Ergun, S.(1967) J.Appl.Crystalography 1 p19

Eyring, H. (1957) Quoted by G.S.Hander and J.R.Arnold (1957) J.Chem. Phys. 27 p144

Fano, U. (1963) Ann.Rev.Nucl.Sci. 13 p1

Fano, U and J.E.Turner (1964) Nat.Acad.Sci.Pub. 1133 p49

Farbi, G., J.Koralyi and V.Svelto (1967) Nucl.Instrum.Meth. 50 p50

Ferai, E. (1940) Phys.Rev. 57 p488

Fiarman, S., and G.Schneider (1972) Environ.Sci.Technol. 6 p79

Fortescue, R.L. and P.D.Hall (1949) Proc.I.E.E. 96 p77

Franck, J.(1925) Trans.Far.Soc. 21 p536

Gass,J.E., H.H.Müller,H.Schmied, L.Jorissen and G.Ziffermayer (1973) Nucl.Instrum.Meth. 106 p109

Gemmell, D.S., J.Remillieux, J.C.Poizat, M.J.Gaillard. R.E.Holland and Z.Vager (1975) Phys.Rev.Lett. 34 p1420

Gibson, D.K., and J.Los (1967) Physika 35 p258

Gibson, D.K., and J.Los (1968) Physika 40 p385

Golding, T.J. and R.M.Eisberg (1957) Phys.Rev. 105 p357

Golicheff, I., M.Loeuillet and C.H.Engelman (1972) J.Radioanal. Chem. 12 p233

Gorodetzky, S., A.Chevallier, A.Pape, J.Cl.Sens, A.M.Dergdolt, M.Bres and R.Armbuster (1967) Nucl.Phys. A91 p133

Green, D., J.Cooper and J.Harris (1955) Phys.Rev. 98 p466

Griffiths, R.(1973) Private Communication

Gyulai J., O.Meyer, J.W.Mayer and J.Rodriguez (1971) J.Appl.Phys. 42 p451

Habanec, J., M. Zarobsky, M., A.Petrina and J.Aousek (1973) J.Radioanal. Chem. 13 p213

Hall, T. (1956) Phys.Rev. 103 p32

Halpern, O. and H.Hall (1948) Phys.Rev. 73 p477

Handley, P. and N.Wells (1973) I.E.E.E. Trans.Nucl.Sci.20 No 3-6 p182

Harrison, K.G. (1971) Thesis Univ.Sussex

Haxby, R.O., W.E.Shoupp, W.E.Stephens and W.H.Wells (1940). Phys. Rev. 58 p1035

Herring, D.F., R.A.Douglas, E.A.Silverstein and R.Chiba (1955)

Hoerl,A.E., (1959) Chem.Eng.Progress 55 p69

Hoerl, A.E.(1962) Chem.Eng.Progress 58 p54

Hunt, S.E. (1952) A.E.I. Report A208

Hunt, S.E., R.A.Pope, W.W.Evans and D.A.Hancock (1958) Brit.J.Appl. Phys. 9 p443

ICRU (1970) Internat.Committ.Rad.Units. and Meas. ICRU Report 16

Igo, G.J., D.D.Clark and R.M.Eisberg (1953) Phys.Rev. 89 p879

Inouye, T., T.Harper and N.C.Rasmussen (1969) Nucl.Instrum.Meth. 67 p125

Janni, J.F. (1966) Air Force Weapons Laboratory Technical Report, AFWL -TR-65-150(unpublished)

Kanner, H. (L951) Phys.Rev. 84 p1211

Kesthelyi, L., I.Berkes, I.Demeter and I.Fodor (1962) Nucl.Phys. 29 p241
Khandelwal, G., and E.Merzbacher (1966) Phys.Rev. 144 p349

Kolata, J.J., T.M.Amos and H.Bichsel (1968) Phys.Rev. 176 p484

Krivan, V.(1972) Z.Anal.Chem. 262 p1

Landau, L., (1944) J.Phys.U.S.S.R. 8 p201

Lea, R.R., D.A.Leich, T.A.Tombrello, J.E.Ericson and I.Freidman (1974) Nature 250 p44

Leich,D.A. and T.A.Tombrello (1973). Nucl.Instrum.Meth. 108 p67

Levenberg, K (1944) Quest.J.Appl.Maths. 2 p164

Lewis, H.W. (1950) Phys.Rev. 78 p526

Lewis, H.W (1961) Phys.Rev. 125 p937

Lindhard, J. and M.Scharff (1961) Phys.Rev. 124 p128

Lindhard, J., M.Scharff and H.E.Schiott (1963) Nat.Fys.Medd.Dan.Vid. Selsk 33 No 14

Lindstrom, W.W., and A.H.Heuer (1974) Nucl.Instrum.Meth. 116 p145

Livingston, M.S. and H.A.Bethe (1937) Rev.Mod.Phys. 9 p261

Lorensen, J. (1974) Nucl.Instrum.Meth. 121 p467

Lucas, M.W.(1975) Private Communication

Lutz,G.T., R.J.Boreni, R.S.Haddock and W.W.Meinke (1968) Nat.Bur. Standards Technical Note - 467

Lyons, P.B., J.W.Toevs and D.G.Sargood (1969) Nucl.Phys. A130 p1

Maccabee, H.D., and M.R.Raju (1965) Nucl.Instrum.Meth. 37 p176

Maccabee, H.D., M.R. Raju and C.A.Tobias (1968) Phys.Rev. 165 p469

Macey, D.J. and W.B.Gilboy (1971) Nucl.Instrum. Meth. 92 p501

Mackintosh, W.D., and J.A.Davies (1969) Anal.Chem. 41 p26A

Mak, B.K., J.R.Bird and T.M.Sabine (1966) Nature 211 p738

MariscottiI., M.A., (1967) Nucl.Instrum.Meth. 50 p309

Mather, R and E.Segrè (1951) Phys.Rev. 84 p191

McClure, G.W.(1963) Phys.Rev. 130 p1852

McClure, G.W.(1965) Phys.Rev. A140 p769

McGowen, J.W.M., and L.Kerwin (1964) Can.J.Phys 42 p972

Meggit, B.T., K.G.Harrison and M.W.Lucas (1973).J.Phys.B; Atom.Mol.Phys 6 pL362

Millar, B., R.Bailey and J.L.W.Churchill (1957) J.Sci.Instrum. 34 p383

Möller, E., and N.Starfelt (1967) Nucl.Instrum.Meth. 50 p225

Möller,E., L.Nilsson and N.Starfelt (1967) Nucl.Instrum.Meth. 50 p270

Monnier, J., H.Hilleret, E.Ligeon and J.B.Quoiran (1972) J.Radioanal. Chem. 12 p353

Moran, T.F., F.C.Petty and A.F.Hedrick (1969) J.Chem.Phys. 51 p2112

Morsell, A.L. (1964) Phys.Rev. 135 pA1436

Mott, N.F.(1931) Proc.Camb. Phil.Soc. 27 p533

Nann,H and W.Shäfer (1972)Nucl.Instrum.Meth. 100 p217

Neild, D.I., D.J.Wise and D.G.Barnes (1972) J.Phys.D. 5 p2292

Neufeld, J., and W.Synder (1957) Phys.Rev. 107 p96

Nicolet, M.A., J.W.Mayer and I.V.Mitchell (1972) Science 177 p841

Northcliffe, L.C., and R.F.Schilling (1970) Nucl.Data Tables A7 p233

O'Connell, B.(1971) Thesis. Univ.Birmingham

Oliver, C., and M.Peisach (172) J.Radioanal, Chem. 11 p105
" " " 12 p313

Ollerhead, R.W., E.Almqvist and J.A.Kuehner (1966) J.Appl.Phys. 37 p2440

Padawer, G.M., (1970) Nucl.Appl.Technol. 9 p856

Padawer, G.M., and E.J.Schneid (1969) Trans.Am.Nucl.Soc. 12 p493

Palmer, D.W. (1965) Nucl.Instrum.Meth. 38 p187

Parkinson, W.C. and J.Bardwick, (1970) Nucl.Instrum.Meth. 78 p245

Paterson, M.S(1950) Proc.Phys.Soc.(Lon) 63A p477

Patterson, J.H., A.L.Turkevitch and E.Franzgrote (1965) J.Geophys.Res. 70 p1311

Payne, M.G.(1969) Phys.Rev.185 p611

Penkrot, J.A., B.L.Cohen, G.R.Rao and R.H.Fulmer Nucl.Instrum.Meth. 96 p505

Pierce, T.B. (1971) Selec.Ann.Rev.Anal.Sci. 1 p133

Pierce, T.B., J.W.McMillan, P.F.Peck and I.G.Jones (1974) Nucl.Instrum. Meth. 118 p115

Poate, J.M., T.M.Buck and B.Schwartz (1973) J.Phys.Chem.Solids 34 p779

Poizat, J.C., and J.Remillieux (1971) Phys.Lett. 34A p53

Poizat, J.C. and J.Remillieux (1972) J.Phys.B 5 pL94

Porte, E., J.Greá, J.P. Sandino, J.P.Thomas and J.Tousset (1973) J. Radioanal. Chem. 16 p493

Pretorius, R. (1972) Radiochem.Radioanal lett. 10 p297

Pretorius, R. and P.Coetzee (1972) J.Radioanal.Chem. 12 p301

Price, P.B., and J.R.Bird (1969) Nucl.Instrum.Meth. 69 p277

Pronko, P.P. and J.G. Pronko (1974) Phys.Rev. B9 p2870

Purser, K.H., P.H.Rose , N.B.Brooks, R.P.Bastide and A.B.Wittkower (1963) Phys.Lett. 6 p176

Guaglia, L., G.Weber and M.Cuypers (1971) Int.J.Appl.Radiat.Isot. 22 p449

Rapperport, E.J.(1969) Advances Electronics and Electron Phys. Supplement 6 p117

Reynolds, H., D.Dunbar, W.Wenzel,and W.Whaling (1953) Phys.Rev. 92 p742

Riviere, A.C., and D.R.Sweetman (1961) ,Proc.Phys.Soc.(Lon) 78 p1215

Rubin, S.(1963) "Thesis on Analytical Chemistry" Vol.4, part 1, p2075

Salmon, L. and D.V.Booker (1972) Report AERE-R7129

Sanders, W.M., B.M.Barnes and D.M.Hale (1972) Conf. 721010-2

Savitzky, A., and M.J.E. Golay (1964) Anal.Chem. 36 p1627

Schwartz, M.E., and L.J.Schaad (1967) J.Chem.Phys. 46 p4112
" " " 47 p5325

Scott, W.T. (1963) Rev.Mod.Phys. 35 p231;

Sellers, R., and F.A.Hanser (1972) Nucl.Instrum.Meth. 104 p233

Seltzer, M., and M.J.Berger (1964) Nat.Acad. Sci.Pub. 1133 p187

Shabason, L., and B.L.Cohen (1973) Anal.Chem. 45 p284

Sippel, R.F.(1959) Phys.Rev.115 p1441

Skofronick, J.G., J.A.Ferry, D.V.Palmer, G.Wendt and R.G.Herb (1964) Phys. Rev. 135A p1429

Spencer, R.C.(1939) Phys.Rev. 55 p239

Spencer, R.C(1949) J.Appl.Phys. 20 p413

Sternheimer, R. (1952) Phys.Rev. 88 p851

Sternheimer, R. (1956) Phys.Rev. 103 p511

Sternheimer, R. (1966) Phys.Rev 145 p247

Steward, P.G.(1968) Thesis. Univ.Calif.Berkeley.

Stokes, A.R.(1948) Proc.Phys.Soc.(Lon) 61 p477

Sweetman, D.R. (1960) Proc.Roy.Soc.(Lon) A256 p416

Sykes, D.A. and S.J.Harris (1972) Nucl.Instrum.Meth. 101 p423

Symon, K.R(1948) Thesis. Univ. Harvard

Thomas, J.R., and J.Grey (1975) Nucl.Instrum.Meth. 126 p303

Thompson, T.J. (1952) Univ.Calif.Rad.Lab. Report UCRL-1910

Thonemann, P.C.(1948) Proc.Phys.Soc., A61 p483

Tombrello, T.A. and J.M.Caywood (1973) Phys.Rev. B8 p3065

Tschalär, C. (1967) Ruth.High Energy Lab.Report RHEL/R146

Tschalär, C. (1967) Nucl.Instrum.Meth. 61 p141

Tschalär, C. (1968) Ruth.High Energy Lab. Report RHEL/R164

Tschalär,C. (1968) Nucl.Instrum. Meth. 64 p237

Tschalär,C., and H.Bichsel (1968). Ruth.High Energy Lab.Report RHEL/R153

Tschalär, C., and H.Bichsel (1968) Nucl.Instrum.Meth. 62 p208

Tschalär, C., and H.D.Maccabee (1970) Phys.Rev. B1 p2863

Turing, A.M. (1948) Quart.J.Mech.Appl.Maths 1 p287

Turkevitch, A.L., E.Frankgrote and J.H.Patterson, (1969) Science 165 p277

Vavilov, P.V. (1957) Soviet Phys. J.E.P.T. 5 p749

Villaithong, E.(1971) Thesis. Univ. Aston in Birmingham

Volger, M., and W.Seibt (1968) Z.Physik 210 p337

Walske, M.C. (1952) Phys.Rev. 88 p1283

Walske, M.C. (1956) Phys.Rev. 101 p94)

Walters, W.L., D.G.Costello, J.G.Skofronick and D.W.Palmer (1961) Phys.Rev. 125 p1012

Walters, W.L., D.G.Costello, J.G.Skofronick and D.W.Palmer (1961) Phys. Rev.Lett 7 p284

Wilde, D.J. (1964)"Optimum Seeking Methods" (Prentice-Hall, New Jersey)

Wilde, D.J., and C.S.Beightler (1967) "Foundations of Optimization" (Prentice-Hall, New Jersey)

Wilkinson, D.H. (1971) Nucl.Instrum.Meth. 95 p259

Wilkinson, J.H. (1967) "Mathematical Methods for Digital Computers" Vol.2. Editors Ralston,A., and H.S.Wilf p65 (John Wiley, New York)

Wilkinson, J.H., (1967) "The Algebraic Eigenvalue Problem" (Clarendon Press, Oxford)

Williams, J.F., and D.N.F.Dunbar (1966) Phys.Rev. 149 p62

Williams, J.F. (1975) Nucl.Instrum.Meth. 126 p205

Williamson, C.F., J.P.Boujot and J.Picard (1966) Rapport CEA-R3042

Wise, P.J., D.G.Barnes and D.J.Neild (1974) J.Phys. D7 p1475

Wolicks, E.A., and A.R.Knudson (1967) Int.J.Appl.Radiat.Isot. 18 p429

Yang, C.N. (1951) Phys.Rev. 84 p599

Ziegler, J.F., and J.E.E.Baglin (1971) J.Appl.Phys. 42 p2031

Ziegler, J.F., and J.E.E. Baglin (1972) J.Appl.Phys. 43 p3809